Transactions of the ASME®

Journal of Fluids Engineering

Published Bimonthly by The American Society of Mechanical Engineers

VOLUME 125 • NUMBER 3 • MAY 2003

TECHNICAL PAPERS

401 On the Anisotropy of Axisymmetric Strained Turbulence in the Dissipation Range
J. Jovanović, I. Otić, and P. Bradshaw

414 Dense Gas Thermodynamic Properties of Single and Multicomponent Fluids for Fluid Dynamics Simulations
Piero Colonna and Paolo Silva

428 The Spatial Stability of Natural Convection Flow on Inclined Plates
Anatoli Tumin

438 Separated Flow in Bends of Arbitrary Turning Angles, Using the Hodograph Method and Kirchhoff's Free Streamline Theory
S. S. Chu

443 Slip Flow in a Curved Tube
C. Y. Wang

447 Sensitivity Evaluation of a Transport-Based Turbulent Cavitation Model
Rajkumar Vaidyanathan, Inanc Senocak, Jiongyang Wu, and Wei Shyy

459 Computations of the Compressible Multiphase Flow Over the Cavitating High-Speed Torpedo
F. M. Owis and Ali H. Nayfeh

469 Experiments and Modeling in Bubbly Flows at Elevated Pressures
Ranganathan Kumar, Thomas A. Trabold, and Charles C. Maneri

479 Measurement of Void Fraction in Magnetic Fluid Using Electromagnetic Induction
S. Shuchi, H. Yamaguchi, and M. Takemura

486 Large Eddy Simulation of Flow in a Stirred Tank
H. S. Yoon, S. Balachandar, M. Y. Ha, and K. Kar

500 Numerical Study of the Flow Around a Bus-Shaped Body
Siniša Krajnović and Lars Davidson

510 Blast Wave Reflection From Wedges
O. Igra, G. Hu, J. Falcovitz, and W. Heilig

520 Modeling of Combustion in Gasoline Direct Injection Engines for the Optimization of Engine Management System Through Reduction of Three-Dimensional Models to ($n \times$ One-Dimensional) Models
P. Emery, F. Maroteaux, and M. Sorine

533 Analysis of a Turbulent Propeller Inflow
Stephen A. Huyer and Stephen R. Snarski

543 Discrete Noise Prediction of Variable Pitch Cross-Flow Fans by Unsteady Navier-Stokes Computations
Yong Cho and Young J. Moon

551 Vortex-Induced Characteristics of Two Fixed-Supported Elastic Cylinders
Z. J. Wang, Y. Zhou, and R. M. C. So

561 Measurements Within Vortex Cores in a Turbulent Jet
Amit Agrawal and Ajay K. Prasad

569 Momentum Thickness Measurements for Thick Axisymmetric Turbulent Boundary Layers
Kimberly M. Cipolla and William L. Keith

(Contents continued on inside back cover)

Transactions of the ASME, Journal of Fluids Engineering (ISSN 0098-2202) is published bimonthly (Jan., Mar., May, July, Sept., Nov.) by The American Society of Mechanical Engineers, Three Park Avenue, New York, NY 10016. Periodicals postage paid at New York, NY and additional mailing offices.
POSTMASTER: Send address changes to Transactions of the ASME, Journal of Fluids Engineering, c/o THE AMERICAN SOCIETY OF MECHANICAL ENGINEERS, 22 Law Drive, Box 2300, Fairfield, NJ 07007-2300.
CHANGES OF ADDRESS must be received at Society headquarters seven weeks before they are to be effective. Please send old label and new address.
STATEMENT from By-Laws. The Society shall not be responsible for statements or opinions advanced in papers or ... printed in its publications (B7.1, Par. 3).

INDEXED by Applied Mechanics Reviews and Engineering Information, Inc. Canadian Goods & Services Tax Registration #126148048.

(**Contents continued**)

Journal of Fluids Engineering **Volume 125, Number 3** **MAY 2003**

576 Analysis for the Effect of Inverter Ripple Current on Fuel Cell Operating Condition
Randall S. Gemmen

TECHNICAL BRIEFS

586 Computational Fluid Dynamics Performance Estimation of Turbo Booster Vacuum Pump
H.-P. Cheng, C.-J. Chen, and P.-W. Cheng

590 Prediction Relations for Pressure Drop Across Finned Sections
Daeho Im and H. S. Ghazi

595 Oxidation Effect on the Monosized Droplets Generation of the Liquid Metal Jet
Wei-Hsiang Lai and Chia-Chin Chen

597 The Shear Layers of a Two-Dimensional Jet Excited by Flexible Wires
Ming-huei Yu, Yi-chun Liao, and Chung-ho Tseng

ANNOUNCEMENTS AND SPECIAL NOTES

600 2003 Fluids Engineering Calendar

602 17th ASME Freeman Scholar Program in Fluids Engineering—Announcement

603 Compact Heat Exchangers and Enhancement Technology for the Process Industries IV—Announcement

604 Information for Authors

The ASME Journal of Fluids Engineering is abstracted and indexed in the following:

Applied Science & Technology Index, AMR Abstracts Database, Chemical Abstracts, Chemical Engineering and Biotechnology Abstracts (Electronic equivalent of Process and Chemical Engineering), Civil Engineering Abstracts, Computer & Information Systems Abstracts, Corrosion Abstracts, Current Contents, Ei EncompassLit, Electronics & Communications Abstracts, Engineered Materials Abstracts, Engineering Index, Environmental Engineering Abstracts, Environmental Science and Pollution Management, Excerpta Medica, Fluidex, Index to Scientific Reviews, INSPEC, International Building Services Abstracts, Mechanical & Transportation Engineering Abstracts, Mechanical Engineering Abstracts, METADEX (The electronic equivalent of Metals Abstracts and Alloys Index), Petroleum Abstracts, Process and Chemical Engineering, Referativnyi Zhurnal, Science Citation Index, SciSearch (The electronic equivalent of Science Citation Index), Shock and Vibration Digest, Solid State and Superconductivity Abstracts, Theoretical Chemical Engineering

On the Anisotropy of Axisymmetric Strained Turbulence in the Dissipation Range

J. Jovanović
Senior Research Scientist

I. Otić
Ph.D. student

P. Bradshaw[a]
Professor of Engineering, Emeritus

Lehrstuhl für Strömungsmechanik,
Universität Erlangen-Nürnberg,
Cauerstrasse 4,
D-91058 Erlangen, Germany

Partition of the stress dissipation has been studied in an axisymmetric strained flow field to assess the possible existence of local isotropy for turbulence at small scales. This is a simple flow to study because the axes of anisotropy of the Reynolds stresses and of the dissipation tensor are aligned. Using invariant theory, the relationship between the stress and dissipation tensors was derived, satisfying restrictions for the limiting states of turbulence and the assumed behavior for large Reynolds number and small anisotropy. The role of the anisotropy in constraining models for the turbulent dissipation rate and the pressure-strain correlations is discussed. Comparisons of the resulting closure with experimental data for several axisymmetric flows are good within the limitations of the data. [DOI: 10.1115/1.1568355]

1 Introduction

Modern developments in the statistical theory of turbulence were initiated by Kolmogorov [1], who introduced the concept of local isotropy for small-scale dissipative fluctuations. This concept is based on the hypothesis that during energy transfer through the spectrum from large eddies to small (a nonlinear process) the turbulence loses orientation, so that the small-scale statistics are isotropic, at sufficiently high Reynolds numbers, irrespective of the orientation at large scales. A consequence is that partition of the stress dissipation[1]

$$\epsilon_{ij}=\nu\overline{\frac{\partial u_i}{\partial x_k}\frac{\partial u_j}{\partial x_k}} \tag{1}$$

must obey the isotropic relation

$$\epsilon_{ij}=\frac{1}{3}\epsilon\delta_{ij}, \tag{2}$$

where ϵ is the trace of ϵ_{ij}.

Note that if the Reynolds number is very high, Kolmogorov's hypothesis implies statistical isotropy at scales significantly larger than the dissipation range. Another obvious but important consequence of local isotropy is that there can be no source ("production") of dissipation rate due to mean-flow deformation. This was the central message that emerged from the work of Kolmogorov [2] which now stands as a cornerstone of two-equation modeling of turbulence.

Launder [3] pointed out a serious deficiency in the frequency equation proposed by Kolmogorov [2] to compute ϵ. Owing to the lack of a source term, it cannot satisfy the equilibrium constraint

$$\epsilon\simeq-\overline{u_iu_j}\frac{\partial\overline{U_i}}{\partial x_j}, \tag{3}$$

for shear flows near walls. However, the assumption of local *homogeneity* permits a more realistic description of the small-scale structure of turbulence, leading to a form of the dissipation rate equation with a source term proportional to the mean flow deformation, which allows the equilibrium constraint to be satisfied (Chou [4], Kolovandin and Vatutin [5], Jovanović, Ye, and Durst [6,7]). It must be remembered that ϵ plays two roles in turbulence modeling; as the viscous dissipation, and as the rate of transfer of turbulent kinetic energy from the large eddies to the smallest. This rate of energy transfer is *determined* by the large eddies, those which carry the Reynolds stresses, and when ϵ is used to parameterize terms in equations for the Reynolds stresses it is playing its second role.

In locally homogeneous turbulence there is likely to be a close relation between the production of dissipation rate by the mean flow deformation and the partition of the dissipation tensor into its components. This has been reported by Chou [4], Kolovandin and Vatutin [5], and Jovanović, Ye, and Durst [6]. The conjecture made by Kolmogorov [2] that the production of dissipation is zero in locally isotropic turbulence is a special case. The outstanding question is, therefore, whether and how the small-scale part of the turbulence reaches the state of vanishing anisotropy (Durbin and Speziale [8], and Lumley [9]).

There have been many experiments to find the regions of applicability of the hypothesis of local isotropy, without definite conclusions (Batchelor [10], Uberoi [11], Monin and Yaglom [12], Antonia, Anselment and Chambers [13], and Saddoughi and Veeravalli [14]). One possibility of making progress is to study turbulent flows with mean flow deformation but for which an exact analytical expression can be derived for partition of the dissipation tensor, leading to conditions for vanishing anisotropy in the dissipation range.

A suitable nontrivial flow to study is axisymmetric strained turbulence, in which, as is fairly easy to show, the directions of anisotropy of the Reynolds stresses and of the dissipation tensor are aligned. Kinematic considerations imply that these anisotropies are identical for two limiting states of turbulence, i.e., for the two-component isotropic state and the one-component state. The same is suggested for small Reynolds number and arbitrary anisotropy of turbulence. This implies restrictions on the possible

---

[a] Permanent address: Thermosciences Division, Mechanical Engineering Department, Stanford University, Stanford, CA 94305-3030.

Contributed by the Fluids Engineering Division for publication in the JOURNAL OF FLUIDS ENGINEERING. Manuscript received by the Fluids Engineering Division February 27, 2002; revised manuscript received December 4, 2002. Associate Editor: G. E. Karniadakis.

[1] The total average turbulent dissipation rate $\overline{\epsilon}$ is

$$\overline{\epsilon}=\nu\overline{\frac{\partial u_i}{\partial x_k}\left(\frac{\partial u_i}{\partial x_k}+\frac{\partial u_k}{\partial x_i}\right)}=\nu\overline{\frac{\partial u_i}{\partial x_k}\frac{\partial u_i}{\partial x_k}}+\nu\frac{\partial^2\overline{u_iu_k}}{\partial x_i\partial x_k}.$$

We will neglect the second term which is almost always very small.

existence of local isotropy. Using the invariant theory of Lumley [15] we shall provide a rational description of the partition process, satisfying the limiting states of turbulence and the assumed behavior for large Reynolds number and small anisotropy. Form this we derive a fully closed model for axisymmetric strained turbulence.

Invariant theory for development of turbulence closures provides exact results only in rather rare circumstances. In more general situations only approximate results can be obtained. The errors resulting from simple analytic approximations of the unknown correlation functions needed in applications of invariant theory can be estimated from the exact expression for the turbulent effective viscosity deduced by Jovanović and Otić [16], to show that they are smaller than about ±30%. Comparison of the theoretical results with direct numerical simulations (DNS) actually show considerably better agreement. In the text to follow the equality sign is used only for the exact relations, and the symbols $\simeq$ and $\approx$ (in that order) imply increasing uncertainty of the results.

2 Partition of the Stress Dissipation in Axisymmetric Turbulence

Let the turbulence be statistically axisymmetric. We may then write

$$\overline{u_i u_j} = A\delta_{ij} + B\kappa_i\kappa_j, \tag{4}$$

$$\epsilon_{ij} = C\delta_{ij} + D\kappa_i\kappa_j, \tag{5}$$

where $\overline{u_i u_j}$ is the stress tensor, A, B, C, and D are scalar functions, and $\boldsymbol{\kappa}$ is the unit vector constructed in such a way that (4) and (5) are invariant under rotation about the axis defined by its scalar arguments. Contracting (4) and (5) we find

$$B = q^2 - 3A, \tag{6}$$

$$D = \epsilon - 3C, \tag{7}$$

where q^2 is the trace of the stress tensor, $q^2 = \overline{u_s u_s}$. Thus we may write

$$\overline{u_i u_j} = A\delta_{ij} + (q^2 - 3A)\kappa_i\kappa_j, \tag{8}$$

$$\epsilon_{ij} = C\delta_{ij} + (\epsilon - 3C)\kappa_i\kappa_j. \tag{9}$$

We can eliminate $\boldsymbol{\kappa}$ from (8) and (9) to obtain

$$\frac{\epsilon_{ij}}{\epsilon} - \frac{1}{3}\delta_{ij} = \frac{q^2}{\epsilon}\frac{\epsilon - 3C}{q^2 - 3A}\left(\frac{\overline{u_i u_j}}{q^2} - \frac{1}{3}\delta_{ij}\right). \tag{10}$$

Following Lumley [15], we introduce the anisotropy tensors

$$a_{ij} = \frac{\overline{u_i u_j}}{q^2} - \frac{1}{3}\delta_{ij}, \tag{11}$$

$$e_{ij} = \frac{\epsilon_{ij}}{\epsilon} - \frac{1}{3}\delta_{ij}, \tag{12}$$

and their scalar invariants

$$a_{ss} = 0, \tag{13}$$

$$e_{ss} = 0, \tag{14}$$

$$\mathrm{II}_{\mathrm{a}} = a_{ij}a_{ji}, \tag{15}$$

$$\mathrm{II}_{\mathrm{e}} = e_{ij}e_{ji}, \tag{16}$$

$$\mathrm{III}_{\mathrm{a}} = a_{ij}a_{jk}a_{ki}, \tag{17}$$

$$\mathrm{III}_{\mathrm{e}} = e_{ij}e_{jk}e_{ki}. \tag{18}$$

Hence, (10) may be written as follows (Jovanović and Otić [16]):

$$e_{ij} = \mathcal{A}a_{ij}, \tag{19}$$

with

$$\mathcal{A} = \frac{q^2}{\epsilon}\frac{\epsilon - 3C}{q^2 - 3A}. \tag{20}$$

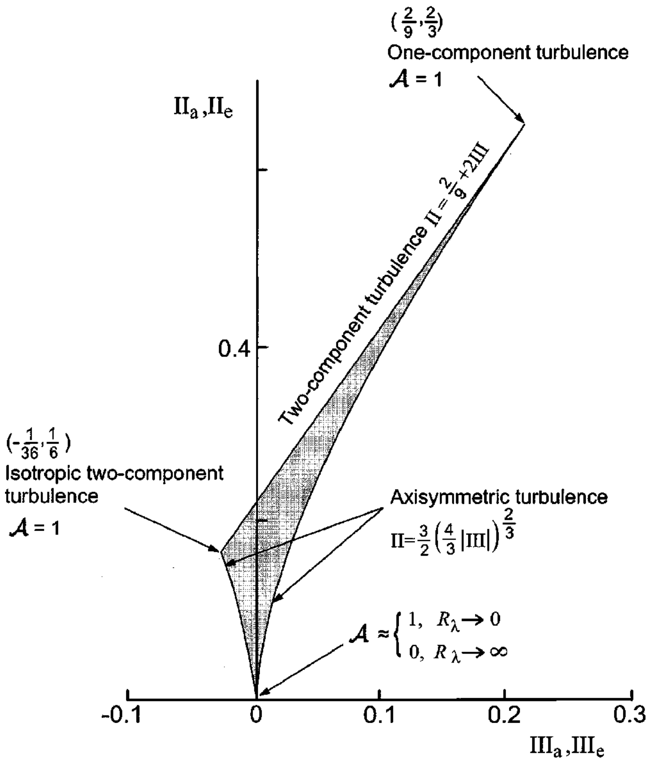

Fig. 1 Anisotropy invariant map and values of the invariant function $\mathcal{A}$ for the limiting states of turbulence, with coordinates of the vertices in parentheses

Multiplying (19) with a_{ij} and e_{ij}, we may express $\mathcal{A}$ in terms of the invariants:

$$\mathcal{A} = \left(\frac{\mathrm{II_e}}{\mathrm{II_a}}\right)^{1/2}. \tag{21}$$

Hence the following relationship holds exactly in axisymmetric turbulence:

$$e_{ij} = \left(\frac{\mathrm{II_e}}{\mathrm{II_a}}\right)^{1/2} a_{ij}. \tag{22}$$

As expected, there is very good agreement between this result and the DNS of Rogallo [17] (see Ye [18]).

3 Construction of the Invariant Function $\mathcal{A}$

We now use invariant theory to determine the scalar function $\mathcal{A}$ for the limiting states of turbulence, for later use in (19).

Lumley [15] showed that in axisymmetric turbulence the invariants II and III are related by

$$\mathrm{II} = \frac{3}{2}\left(\frac{4}{3}\left|\mathrm{III}\right|\right)^{2/3} \tag{23}$$

while in two-component turbulence,

$$\mathrm{II} = \frac{2}{9} + 2\mathrm{III}. \tag{24}$$

Plotted in the III–II plane, these relations (of which (23) yields left-running and right-running branches) define the anisotropy invariant map. As shown by Lumley [15], the curvilinear triangle contains all physically realizable states of turbulence: see Fig. 1, which shows the values of II, III, and $\mathcal{A}$ at the three vertices. The origin corresponds to (three-dimensional) isotropic turbulence in which the anisotropy invariants are of course zero. Note that the above relations between the invariants of a_{ij} and e_{ij} are valid on the bounding lines of the anisotropy map but not elsewhere.

For two-component isotropic turbulence, and also for the one-component state,

$$\mathrm{II_a} = \mathrm{II_e}, \tag{25}$$

and therefore for these cases $\mathcal{A}$ is given by

$$(\mathcal{A})_{2\mathrm{C-iso}} = 1, \tag{26}$$

$$(\mathcal{A})_{1\mathrm{C}} = 1. \tag{27}$$

For very small Reynolds number, the dissipation and energy-containing ranges of the spectrum overlap, with little separation between the corresponding length scales, and therefore we may assume that (Rotta [19])

$$\mathcal{A} \to 1, \quad R_\lambda \to 0 \tag{28}$$

holds for arbitrary anisotropy. Here R_λ is the turbulent Reynolds number:

$$R_\lambda = \frac{q\lambda}{\nu}, \tag{29}$$

based on the Taylor microscale λ. The microscale is strictly defined in terms of the mean-square derivative of the streamwise velocity fluctuation but for practical purposes usually defined so that

$$\epsilon = 5\,\nu \frac{q^2}{\lambda^2}. \tag{30}$$

The two forms of the definition are the same in isotropic turbulence. The Reynolds number of the energy-containing eddies (those which contribute most to q^2 and whose length scale is of the order of q^3/ϵ) is related to R_λ by $q^4/(\epsilon\nu) = R_\lambda^2/5$. Note that $q^4/(\epsilon\nu)$ is just four times the Reynolds number $k^2/(\epsilon\nu)$ used in many turbulence models, where k is the turbulent kinetic energy $k = q^2/2$. It is traditional in basic studies to quote the microscale Reynolds number but it is simply $q^4/(\epsilon\nu)$ in disguise. Also, λ is not the length scale of any representative group of eddies.

Since the limits (26) and (27) are fixed, the only logical way to approach the hypothesis of locally isotropic turbulence in the sense suggested by Kolmogorov [1] is to assume

$$\mathcal{A} \to 0, \quad \mathrm{II_a} \to 0 \quad \text{and} \quad R_\lambda \to \infty. \tag{31}$$

For vanishing anisotropy of turbulence and large Reynolds number, ϵ may be related to the "integral" length scale L_f of the energy-containing range (Kolmogorov [20], and Sreenivasan [21]) by

$$\epsilon \simeq 0.192 \frac{q^3}{L_f}, \quad R_\lambda \gg 1. \tag{32}$$

In this case of isotropic turbulence we see that the integral length scale is directly proportional to $q^3/\epsilon \equiv L$. At very low Reynolds numbers, e.g., in the "final decay period" of classical grid-generated turbulence, the relationship between λ and L_f can be derived analytically to yield (Hinze [22], p. 210)

$$L_f = \frac{1}{2}\left(\frac{\pi}{2}\right)^{1/2} \lambda, \quad R_\lambda \ll 1. \tag{33}$$

Using it the expression for ϵ (30) can be written as

$$\epsilon \simeq 1.959\nu \frac{q^2}{L_f^2}, \quad R_\lambda \ll 1. \tag{34}$$

Following the suggestion of Rotta [19] we combine (32) and (34) to obtain the interpolation formula for ϵ valid for low and large Reynolds numbers:

$$\epsilon \simeq 1.959\nu \frac{q^2}{L_f^2} + 0.192 \frac{q^3}{L_f}. \tag{35}$$

With (30) and (35) we are in a position to correlate the length scale ratio λ/L_f in terms of the Reynolds number

$$\frac{\lambda}{L_f} \simeq -0.049 R_\lambda + \frac{1}{2}(0.009604 R_\lambda^2 + 10.208)^{1/2}, \tag{36}$$

which attains a maximum value of 1.597, say 1.6, when $R_\lambda \to 0$ and vanishes for $R_\lambda \to \infty$. It is suitable to normalize the above relation and introduce the function

$$\mathcal{W} = \frac{1}{1.597}\frac{\lambda}{L_f} = 0.626 \frac{\lambda}{L_f}, \tag{37}$$

which can be used to match limiting properties of the turbulence functions for very low and very large Reynolds numbers.

We can use the above relationships in conjunction with the weighting technique based on (37) to interpolate between the two quasi-asymptotic limits (28) and (31) suggested for $\mathcal{A}$:

$$\mathcal{A} \to (1-\mathcal{W})(\mathcal{A})_{R_\lambda \to \infty} + \mathcal{W}(\mathcal{A})_{R_\lambda \to 0}, \quad \mathrm{II_a} \to 0. \tag{38}$$

This simple proposal appears to be sufficient to ensure (28) and (31) and is consistent with the concept of asymptotic invariance (Tennekes and Lumley [23], p. 6) which broadly states that the overall behavior of turbulent flows, outside any viscous wall region or "sublayer," is almost independent of the fluid viscosity. The concept of asymptotic invariance is well supported by experimental observations (Corrsin [24], Uberoi [25], Comte-Bellot and Corrsin [26], and Hussain and Ramjee [27]) which show that the direct effects of viscosity, away from viscous wall regions, decrease as the Reynolds number increases.

More general and therefore more complicated formulations than (38) are possible but would require additional constraints or input data. It is not clear if something better than (28) and (31) can be formulated rationally. In the absence of any other information we may conclude that while the proposed interpolation (38) is certainly not exact, it should be close enough to the truth for our present purposes. Using it, we find

$$\mathcal{A} \to \mathcal{W}, \quad \mathrm{II_a} \to 0. \tag{39}$$

The two exact limiting values of $\mathcal{A}$, (26) and (27), can be matched to (39) utilizing properties of the parameter J introduced by Lumley [15]:

$$J = 1 - 9\left(\frac{1}{2}\mathrm{II_a} - \mathrm{III_a}\right). \tag{40}$$

$J=0$ indicates two-component turbulence and $J=1$ corresponds to isotropic turbulence (see (24) and (23), respectively). Thus we may write an approximate expression for $\mathcal{A}$ in the case of initially isotropic turbulence submitted to axisymmetric expansion as

$$\mathcal{A} \simeq (1-J)(\mathcal{A})_{1\mathrm{C}} + J(\mathcal{A})_{\mathrm{iso}}, \quad \mathrm{III_a} > 0 \tag{41}$$

and also for turbulence developing in axisymmetric contraction:

$$\mathcal{A} \simeq (1-J)(\mathcal{A})_{2\mathrm{C-iso}} + J(\mathcal{A})_{\mathrm{iso}}, \quad \mathrm{III_a} < 0. \tag{42}$$

Taking into account (23), (26), (27), (39), (41), and (42), we find

$$\mathcal{A} \approx \begin{cases} 1 + \left\{1 - 9\left[\frac{1}{2}\mathrm{II_a} - \frac{3}{4}\left(\frac{2}{3}\mathrm{II_a}\right)^{3/2}\right]\right\}(\mathcal{W}-1), & \mathrm{III_a} > 0 \\ 1 + \left\{1 - 9\left[\frac{1}{2}\mathrm{II_a} + \frac{3}{4}\left(\frac{2}{3}\mathrm{II_a}\right)^{3/2}\right]\right\}(\mathcal{W}-1), & \mathrm{III_a} < 0. \end{cases} \tag{43}$$

The forms deduced for $\mathcal{A}$ imply that the anisotropy of ϵ_{ij} will persist at all Reynolds numbers. This conclusion, reached only from kinematical considerations, is in agreement with the experimental results of Garg and Warhaft [28], theoretical consider-

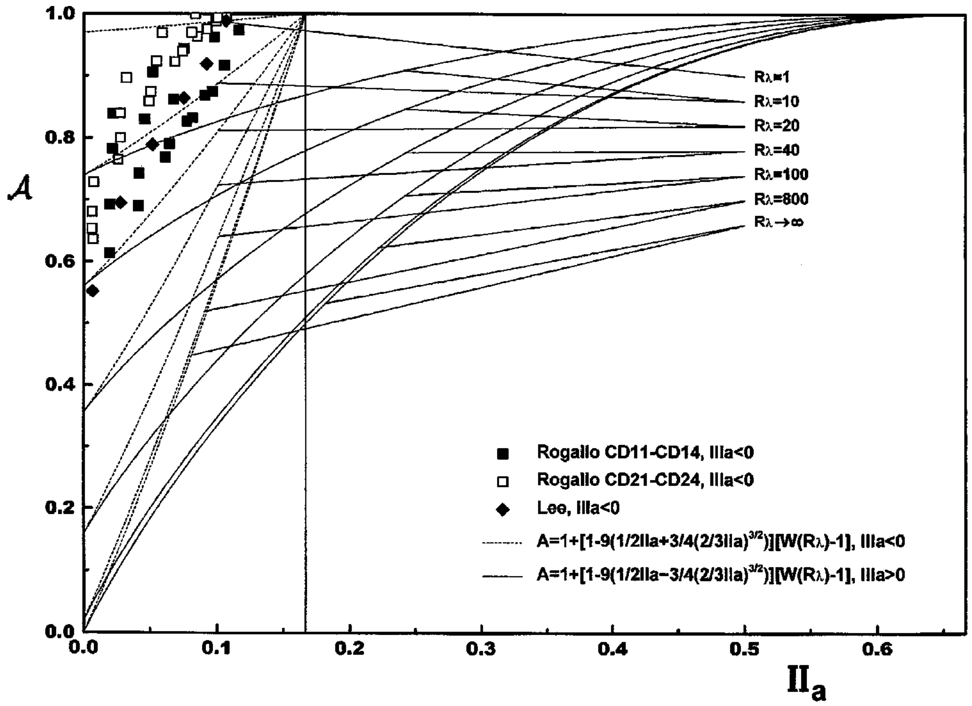

Fig. 2 Distribution of the invariant function $\mathcal{A}$ in axisymmetric strained turbulence. Symbols are the DNS results of Rogallo [17] and Lee [30]. The lines correspond to the suggested forms (43) for $\mathcal{A}$; — — —, $III_a<0$; ——, $III_a<0$.

ations based on the use of evolution equation for ϵ_{ij} by Durbin and Speziale [8] and the numerical simulations of Pumir and Shraiman [29].

Using (43), distributions of $\mathcal{A}$ were calculated for different Reynolds numbers R_λ for turbulence developing in axisymmetric contraction ($III_a<0$) and in axisymmetric expansion ($III_a>0$). The results are plotted against II_a in Fig. 2. It can be seen that $\mathcal{A}$ rises faster with increasing anisotropy in axisymmetric contraction than in axisymmetric expansion. We have indicated on the same diagram the values of $\mathcal{A}$ calculated directly from the DNS results of Rogallo [17] and Lee [30], using (21). These simulations were done at relatively low Reynolds numbers, $R_\lambda \simeq 10-20$.

The database of Rogallo [17] consists of eight different fields and provides information about the evolution of $\mathcal{A}$ in axisymmetric contraction. The DNS database of Lee [30] contains six different fields obtained from simulations of axisymmetric turbulence. He used the spectral code developed by Rogallo [17] with slightly better resolution. Calculated values of $\mathcal{A}$ from these databases agree qualitatively and fairly well quantitatively with expectations based on the application of invariant theory. The simulated and predicted data show a very slow trend in decrease of the anisotropy in ϵ_{ij} with increasing Reynolds number that is in agreement with experimental results of Saddoughi and Veeravalli [14]. According to (43) significant Reynolds number influence on the anisotropy in ϵ_{ij} will persist up to R_λ of the order of 1500.

4 The Dissipation Rate Equation

We shall now demonstrate how the influence of anisotropy of turbulence penetrates into the dynamics of ϵ. For axisymmetric homogeneous turbulence the dissipation rate equation reads

$$\frac{\partial \epsilon}{\partial t} = \underbrace{-2\nu \overline{\frac{\partial u_i}{\partial x_l}\frac{\partial u_k}{\partial x_l}}\frac{\partial \overline{U_i}}{\partial x_k}}_{P_\epsilon^1} \underbrace{-2\nu \overline{\frac{\partial u_s}{\partial x_i}\frac{\partial u_s}{\partial x_k}}\frac{\partial \overline{U_i}}{\partial x_k}}_{P_\epsilon^2} \underbrace{-2\nu \overline{\frac{\partial u_i}{\partial x_l}\frac{\partial u_k}{\partial x_l}\frac{\partial u_i}{\partial x_k}}}_{P_\epsilon^4} \underbrace{-2\nu^2 \overline{\frac{\partial^2 u_i}{\partial x_l \partial x_n}\frac{\partial^2 u_i}{\partial x_l \partial x_n}}}_{\Upsilon}. \tag{44}$$

The time derivative on the left-hand side is strictly the usual "substantial" derivative following the mean motion of the fluid. The first two terms on the right-hand side, P_ϵ^1 and P_ϵ^2, represent the production of ϵ by the mean velocity gradients. These terms involve the following tensors:

$$P_{ik} = 2\nu \overline{\frac{\partial u_i}{\partial x_l}\frac{\partial u_k}{\partial x_l}}, \tag{45}$$

$$R_{ki} = 2\nu \overline{\frac{\partial u_s}{\partial x_i}\frac{\partial u_s}{\partial x_k}}, \tag{46}$$

which have the same trace:

$$P_{ss} = R_{ss} = 2\epsilon. \tag{47}$$

Given the axisymmetry of the whole flow, (45) and (46) must both be axisymmetric, so we can write

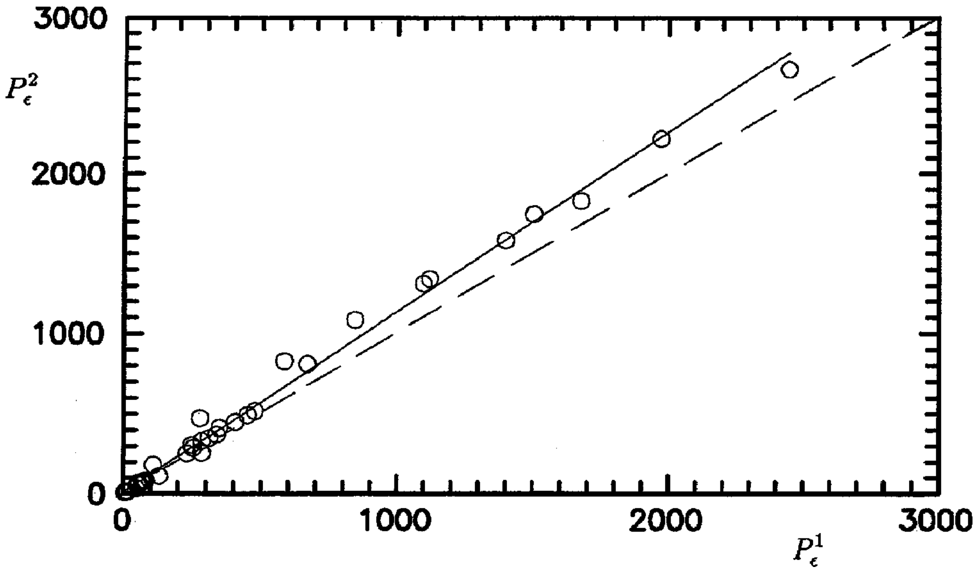

Fig. 3 Cross-plot of P_ϵ^2 as a function of P_ϵ^1 in axisymmetric strained turbulence from the database of Rogallo [17]. The slope of the straight line fitted through the numerical data is 1.12. The dashed line corresponds to the exact analytical solution given by (54).

$$P_{ik}=E\delta_{ik}+F\kappa_i\kappa_k, \tag{48}$$

$$R_{ki}=G\delta_{ki}+H\kappa_k\kappa_i, \tag{49}$$

to show, using the same analytical path as described in Section 2, that these tensors are related as follows:

$$R_{ki}=\left(G-\frac{EH}{F}\right)\delta_{ki}+\frac{H}{F}P_{ik}. \tag{50}$$

Contracting the above equation, and taking into account (47), we get

$$2\epsilon=3\left(G-\frac{EH}{F}\right)+2\frac{H}{F}\epsilon. \tag{51}$$

By comparing left-hand and right-hand sides of (51), we find

$$G=\frac{EH}{F} \quad \text{and} \quad H=F, \tag{52}$$

and therefore

$$P_{ik}=R_{ki}. \tag{53}$$

This result implies that in axisymmetric turbulence the two production terms P_ϵ^1 and P_ϵ^2 of the dissipation rate equation are identical:

$$P_\epsilon^1=P_\epsilon^2. \tag{54}$$

The cross-plot of P_ϵ^1 versus P_ϵ^2 shown in Fig. 3 confirms that the derived relationship (54) holds in axisymmetric turbulence. However, the slope of the straight line fitted through the data of Fig. 3 is 1.12, and we must conclude that the accuracy of these early DNS results is not as high as we would wish.

Using (1) and (45) we write P_ϵ^1 as

$$P_\epsilon^1=-2\epsilon_{ik}\frac{\partial\overline{U_i}}{\partial x_k}. \tag{55}$$

Using (19), we find

$$P_\epsilon^1=-\mathcal{A}\frac{\epsilon\overline{u_iu_k}}{k}\frac{\partial\overline{U_i}}{\partial x_k}\underbrace{-\frac{2}{3}\epsilon(1-\mathcal{A})\frac{\partial\overline{U_i}}{\partial x_k}\delta_{ik}.}_{\substack{=0,\\ \text{for incompressible flow.}}} \tag{56}$$

Thus, for incompressible flow, the source term of the dissipation rate equation is

$$P_\epsilon^1+P_\epsilon^2=-2\mathcal{A}\frac{\epsilon\overline{u_iu_k}}{k}\frac{\partial\overline{U_i}}{\partial x_k}. \tag{57}$$

To formulate a turbulence closure for the difference between the turbulent production of dissipation rate due to vortex stretching, P_ϵ^4, and the viscous destruction, Υ, we can use a result that holds in grid-generated turbulence to get

$$P_\epsilon^4-\Upsilon\simeq-\psi\frac{\epsilon^2}{k}. \tag{58}$$

Using Loitsianski's invariant (Hinze [22], p. 260; Davidson [31]) to estimate ψ in the limit $R_\lambda\to 0$, and Saffman's invariant (Saffman [32] and Kolovandin [33]) in the limit $R_\lambda\to\infty$, we obtain (Jovanović et al. [34])

$$\psi\to\begin{cases}1.4, & R_\lambda\to 0\\ 1.8, & R_\lambda\to\infty\end{cases} \quad \mathrm{II_a}\to 0. \tag{59}$$

DNS results for homogeneous isotropic turbulence (Coleman and Mansour [35] and Mansour and Wray [36]) confirm the accuracy of (59).

Application of the weighting technique based on the length-scale ratio used in the derivation of (39) yields

$$\psi\to 1.8-0.4\mathcal{W}, \quad \mathrm{II_a}\to 0. \tag{60}$$

To complete the closure of the ϵ equation, we must estimate the influence of anisotropy on ψ. This can be done by interpolation if values of ψ are available at the left and right upper vertices of the anisotropy invariant map (Fig. 1), which correspond, respectively, to two-component isotropic turbulence and to the one-component state. Let us denote the values of ψ at these two points by

$$(\psi)_{2\mathrm{C-iso}} = a, \tag{61}$$

$$(\psi)_{1\mathrm{C}} = b. \tag{62}$$

Once more using the tools of invariant theory (Section 3), we obtain

$$\psi \approx \begin{cases} 9b\left[\frac{1}{2}\mathrm{II}_a - \frac{3}{4}\left(\frac{2}{3}\mathrm{II}_a\right)^{3/2}\right] + \left\{1 - 9\left[\frac{1}{2}\mathrm{II}_a - \frac{3}{4}\left(\frac{2}{3}\mathrm{II}_a\right)^{3/2}\right]\right\}(1.8 - 0.4\mathcal{W}), & \mathrm{III}_a > 0 \\ 9a\left[\frac{1}{2}\mathrm{II}_a + \frac{3}{4}\left(\frac{2}{3}\mathrm{II}_a\right)^{3/2}\right] + \left\{1 - 9\left[\frac{1}{2}\mathrm{II}_a + \frac{3}{4}\left(\frac{2}{3}\mathrm{II}_a\right)^{3/2}\right]\right\}(1.8 - 0.4\mathcal{W}), & \mathrm{III}_a < 0. \end{cases} \tag{63}$$

To determine ψ in two-component isotropic turbulence, we used the results for k, ϵ, $\overline{u_i u_j}$ and turbulent microscales $\lambda_{ij} = [\overline{u_i^2}/\overline{(\partial u_i/\partial x_j)^2}]^{1/2}$ obtained by Rogallo [17] for axisymmetric contraction. From the numerical data $\partial\epsilon/\partial t$, P_ϵ^1 and P_ϵ^2 were computed and the decay term $P_\epsilon^4 - \Upsilon$ was deduced from the balance of (44) by difference. Values of ψ computed from eight different fields, using (58), are shown in Fig. 4. These results are somewhat scattered owing to numerical difficulties in evaluating the time derivative of ϵ. Figure 4 indicates that ψ increases continuously with increasing anisotropy and attains a maximum value of about

$$a \approx 2.5, \tag{64}$$

near the isotropic two-component limit (61). This agrees closely with the DNS results of Poinsot [37] for two-dimensional isotropic turbulence, and with computations of the same flow using lattice-Boltzmann automata by Bernsdorf, Brenner, and Durst [38].

Lumley and Newman [39] provided information about the form of ψ in unstrained one-component turbulence. They argued that nonlinear terms in the equation for the two-point correlation vanish in this flow so that ψ can be calculated exactly, to yield

$$b = 1.4, \tag{65}$$

the same result as in the final stage of decay of isotropic turbulence, (59). Examination of the equations for the instantaneous fluctuations shows that b is also 1.4 in one-component turbulence developing in a shear flow.

Lumley and Newman [39] equated "componentality" and "dimensionality" of one-component turbulence, implying that it is also one-*dimensional* turbulence. This assumption is logical but it is not permitted by the dynamic equations for the instantaneous fluctuations for any finite values of the latter. Therefore, if true, the assumption implies that turbulence must vanish completely in the one-component, one-dimensional state, giving:

$$b = 0. \tag{66}$$

DNS results for wall-bounded and free-shear flows support for Lumley and Newman's assumption of the equality of componentality and dimensionality near the 1-C limit. Anisotropy-invariant mapping of turbulence in a channel flow (Fischer, Jovanović, and Durst [40]), indicates that the anisotropy increases towards the right vertex of the anisotropy map when the Reynolds number decreases towards the critical value for relaminarization. DNS results for a sink-flow boundary layer (Spalart [41]) confirm this more directly: the invariants move towards the one-component limit as the acceleration parameter (which is uniquely related to the Reynolds number in this flow) increases towards relaminarization.

Even more convincing evidence suggesting that turbulence vanishes in the one-component state is presented in the work of Seidl [42]. He simulated the flow past a sphere at low Reynolds number. Using an unstructured grid he was able to resolve development of the very thin laminar boundary layer over a sphere, and the near-wake region behind it which undergoes transition, leading to the

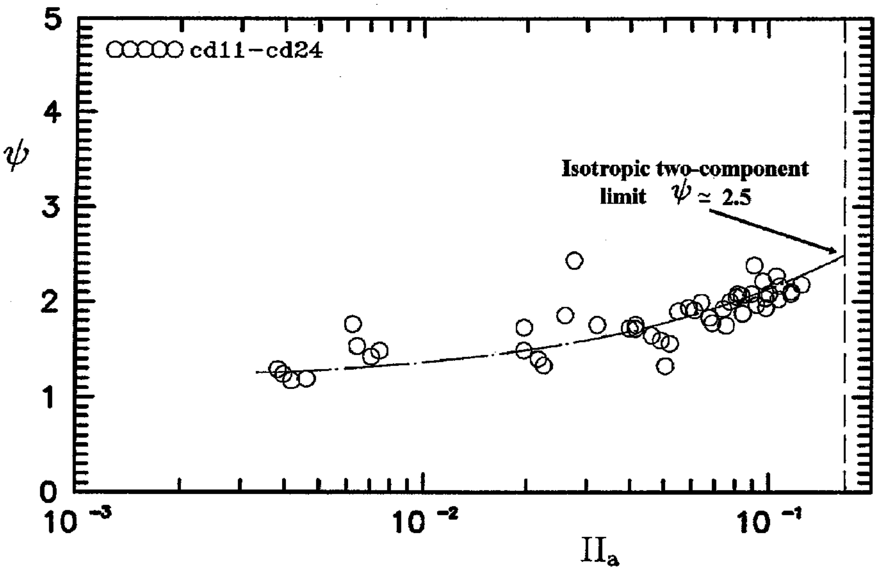

Fig. 4 Variation of ψ with II_a in axisymmetric contraction calculated from the DNS results of Rogallo [17]

rapid development of turbulence. Anisotropy-invariant mapping of turbulence in the near-wake region covers a significant part of the anisotropy invariant map. Contour plots of the turbulent kinetic energy, the dissipation rate and the anisotropy invariants across the wake reveal a significant reduction of turbulence in the shear layer which separates from a sphere. Within this shear layer, which develops oscillations, then rolls up vortex pairs and finally abruptly breaks into turbulence, the flow is very close to the one-component state.

Further evidence suggesting that turbulence vanishes in the one-component state is provided by Jovanović et al. [34], who analyzed DNS results for turbulent channel flow. Using the two-point correlation technique the effect of inhomogeneity near the wall was removed from the data. This allowed them to isolate the influence of anisotropy on the distribution of ψ. Across the logarithmic region the data show that the invariants closely follow the right boundary of the anisotropy map which corresponds to the axisymmetric state. In this region ψ decreases rapidly with increasing anisotropy. If this trend is interpreted in terms of the invariant functions introduced in Section 3 then the data imply that $b \to 0$ in the one-component state. In addition, Jovanović et al. were able to demonstrate that it is essential to reproduce this behavior of ψ in the closure of the dissipation rate equation, in order to achieve equilibrium in the logarithmic region with the proposed form for $\mathcal{A}$ given by (43).

The above discussion suggests that ψ is singular in one-component turbulence, and its properties can be summarized as follows: for relaxation towards isotropic turbulence and also for turbulence developing in pure shear flow, (65) holds. For axisymmetric strained turbulence, (66) is appropriate. The singular behavior of ψ around the one-component limit described above can be incorporated into the turbulence closure using invariant theory (Jovanović et al. [34]).

5 The Intercomponent Energy Transfer

Let us now consider the pressure-strain correlations

$$\Pi_{ij}=\overline{\frac{p}{\rho}\left(\frac{\partial u_i}{\partial x_j}+\frac{\partial u_j}{\partial x_i}\right)}, \tag{67}$$

which are responsible for the intercomponent energy transfer. Using the exact Poisson equation for the pressure fluctuation

$$\frac{1}{\rho}\frac{\partial^2 p}{\partial x_i \partial x_i}=\underbrace{-2\frac{\partial u_k}{\partial x_i}\frac{\partial \overline{U_i}}{\partial x_k}}_{\text{fast}}\underbrace{-\frac{\partial^2}{\partial x_k \partial x_i}(u_k u_i-\overline{u_k u_i})}_{\text{slow}}, \tag{68}$$

we can further split these correlations into the "fast" and "slow" parts (the names are misleading but traditional):

$$\Pi_{ij}=\Pi_{ij}^{\mathrm{f}}+\Pi_{ij}^{\mathrm{s}}, \tag{69}$$

which are associated with the first and second terms on the right-hand side of (68), respectively.

For axisymmetric strained turbulence, the pressure-strain correlations Π_{ij} and the strain rate tensor

$$S_{ij}=\frac{1}{2}\left(\frac{\partial \overline{U_i}}{\partial x_j}+\frac{\partial \overline{U_j}}{\partial x_j}\right), \tag{70}$$

may be written in the form

$$\Pi_{ij}=K\delta_{ij}+L\kappa_i\kappa_j, \tag{71}$$

$$S_{ij}=M\delta_{ij}+N\kappa_i\kappa_j. \tag{72}$$

On combining (4), (71), and (72), the fast and slow parts of Π_{ij} may be expressed as follows (Jovanović and Otić [16]):

$$\Pi_{ij}^{\mathrm{f}}=\mathcal{B}S_{ij}, \tag{73}$$

$$\Pi_{ij}^{\mathrm{s}}=\mathcal{C}a_{ij}, \tag{74}$$

where $\mathcal{B}$ and $\mathcal{C}$ are scalar functions to be determined from various asymptotic considerations.

Chou [4] has shown analytically that the "fast" and "slow" parts of the pressure-strain correlations in homogeneous turbulence can be expressed as separate volume integrals over two-point velocity correlations of second and third order

$$\Pi_{ij}=\underbrace{-\frac{1}{2\pi}\frac{\partial \overline{U_m}}{\partial x_n}\int_V\left(\frac{\partial^2\overline{u_j u_n'}}{\partial \xi_m \partial \xi_i}+\frac{\partial^2\overline{u_i u_n'}}{\partial \xi_m \partial \xi_j}\right)\frac{dV}{|\xi|}}_{\text{fast}}\underbrace{-\frac{1}{4\pi}\int_V\left(\frac{\partial^3\overline{u_j u_m' u_n'}}{\partial \xi_m \partial \xi_n \partial \xi_i}+\frac{\partial^3\overline{u_i u_m' u_n'}}{\partial \xi_m \partial \xi_n \partial \xi_j}\right)\frac{dV}{|\xi|}}_{\text{slow}}. \tag{75}$$

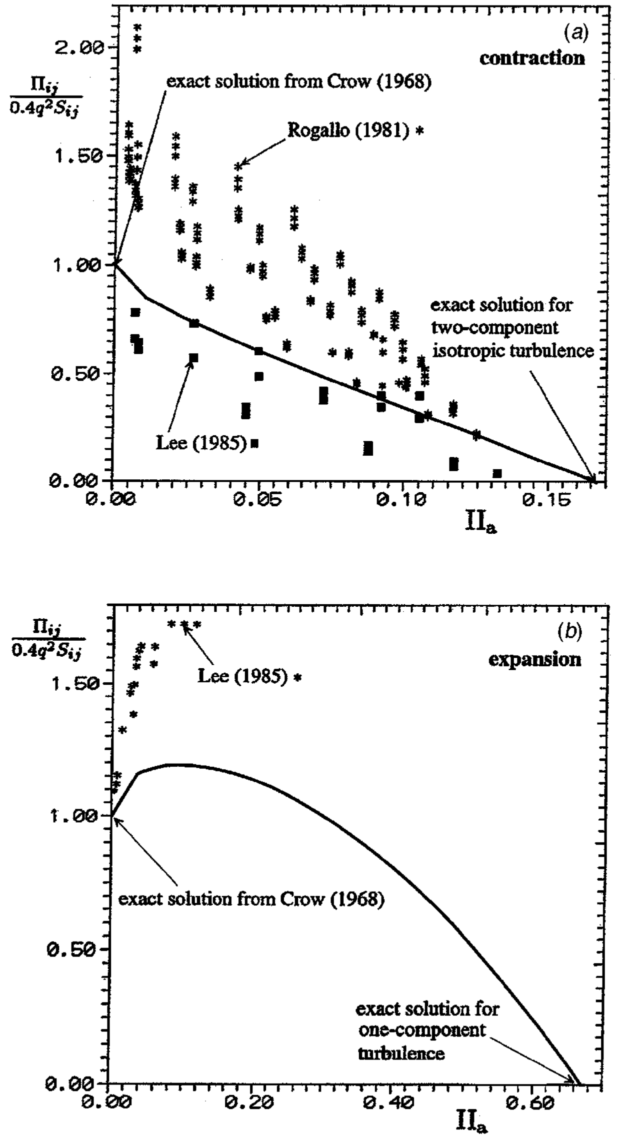

Fig. 5 The pressure-strain correlations in axisymmetric strained turbulence. Symbols are the DNS results of Rogallo [17] and Lee [30]. The lines correspond to the forms (86) and (87) suggested for Π_{ij}^{f}. For large deformations and high Reynolds numbers Π_{ij}^{f} represents the major contribution to the pressure-strain correlations.

Here $\boldsymbol{\xi}$ is the vector which measures the relative distance between two arbitrary points A and B in space:

$$\xi_k = (x_k)_{\mathrm{B}} - (x_k)_{\mathrm{A}}, \tag{76}$$

and the prime indicates the value of the fluctuation at the point B

$$\overline{(u_i)_{\mathrm{A}}(u_j)_{\mathrm{B}}} \equiv \overline{u_i u_j'}, \tag{77}$$

$$\overline{(u_j)_{\mathrm{A}}(u_m u_n)_{\mathrm{B}}} \equiv \overline{u_j u_m' u_n'}. \tag{78}$$

Using kinematic constraints alone, the volume integral for the fast part of Π_{ij} can be evaluated exactly for initially isotropic turbulence exposed to rapid distortion (Crow [43] and Launder, Reece, and Rodi [44]) to yield

$$\Pi_{ij} = \frac{2}{5} q^2 S_{ij}, \quad \mathrm{II_a} \rightarrow 0. \tag{79}$$

From the equation for the anisotropy tensor a_{ij} in homogeneous turbulence (Hallbäck, Groth, and Johansson [45])

$$\frac{\partial a_{ij}}{\partial t} = \frac{1}{q^2}\left[P_{ij} - \left(a_{ij} + \frac{1}{3}\delta_{ij}\right)P_{ss}\right] + \frac{\Pi_{ij}}{q^2} + \frac{2\epsilon}{q^2}(a_{ij} - e_{ij}), \tag{80}$$

where

$$P_{ij} = -\overline{u_i u_k}\frac{\partial \overline{U_j}}{\partial x_k} - \overline{u_j u_k}\frac{\partial \overline{U_i}}{\partial x_k}, \tag{81}$$

we deduce, using (19), (26), and (27), the asymptotic behavior of Π_{ij} as $\partial a_{ij}/\partial t \rightarrow 0$ for the case of initially isotropic turbulence subjected to axisymmetric deformation:

$$(\Pi_{ij})_{\mathrm{2C-iso}} \rightarrow a_{ij}P_{ss} + \frac{1}{3}P_{ss}\delta_{ij} - P_{ij}, \tag{82}$$

$$(\Pi_{ij})_{\mathrm{1C}} \rightarrow a_{ij}P_{ss} + \frac{1}{3}P_{ss}\delta_{ij} - P_{ij}. \tag{83}$$

This behavior suggests that Π_{ij} vanishes in two-component isotropic turbulence and also in the one-component state:

$$(\Pi_{ij})_{\mathrm{2C-iso}} = 0, \tag{84}$$

$$(\Pi_{ij})_{\mathrm{1C}} = 0. \tag{85}$$

Hence we can exactly define the asymptotic behavior of Π_{ij} near all three vertices of the anisotropy invariant map shown in Fig. 1.

The exact analytical results for Π_{ij} in the limiting states of turbulence, (79), (84), and (85), can be used to check the reliability of the DNS results, which we need for modelling when no analytic results are available. In Fig. 5 we show the pressure-strain correlations, normalized by the values for vanishing anisotropy, from the databases of Rogallo [17] and Lee [30].

For axisymmetric contracting turbulence the results shown are to a large extent unrealistic around $\mathrm{II_a} \rightarrow 0$ since these deviate considerably from the exact result derived by Crow [43]. This evidence suggests that something is seriously wrong with the simulation results. The difficulty might be associated with the choice of initial conditions (Lumley [15]).

The DNS results in Fig. 5(*b*), corresponding to turbulence developing in axisymmetric expansion, do seem to be approaching the exact analytical solution (79) as $\mathrm{II_a} \rightarrow 0$. However, the trends in the data with increasing anisotropy open up the possibility of violation of the constraint on Π_{ij} in the one-component limit, derived above. Thus, we cannot provide any firm quantitative conclusion about turbulence closures for the pressure-strain correlations using the data sets shown in Fig. 5. This is a serious deficiency of the 1980-vintage DNS results which are still all that is available for these important ''building-block'' flows.

We now provide a rational construction for Π_{ij}, once more using invariant theory. The analytical behavior of Π_{ij} given by (82) and (83) suggest an approximation for Π_{ij}^f in the following form:

$$\Pi_{ij}^f = a_{ij}P_{ss} + \mathcal{F}\left(\frac{1}{3}P_{ss}\delta_{ij} - P_{ij}\right), \tag{86}$$

where

$$\mathcal{F} \approx \begin{cases} 0.6 + 3.6\left[\frac{1}{2}\mathrm{II_a} - \frac{3}{4}\left(\frac{2}{3}\mathrm{II_a}\right)^{3/2}\right], & \mathrm{III_a} > 0 \\ 0.6 + 3.6\left[\frac{1}{2}\mathrm{II_a} + \frac{3}{4}\left(\frac{2}{3}\mathrm{II_a}\right)^{3/2}\right], & \mathrm{III_a} < 0. \end{cases} \tag{87}$$

Closure for the slow part of Π_{ij} can be formulated using the transport equation for a_{ij} in decaying homogeneous axisymmetric turbulence without mean velocity gradients:

$$2k\frac{\partial a_{ij}}{\partial t} = \Pi_{ij}^s + 2\epsilon a_{ij} - 2\mathcal{A}\epsilon a_{ij}. \tag{88}$$

For $\mathrm{II_a} \rightarrow 0$, the above equation may be written as follows:

$$\Pi_{ij}^s \rightarrow 2(\mathcal{A})_{\mathrm{iso}}\epsilon a_{ij} - \mathcal{D}\epsilon a_{ij}, \tag{89}$$

where $\mathcal{D}$ is a new scalar function. In the final period of decay of grid turbulence, which corresponds to $R_\lambda \rightarrow 0$ and negligible nonlinear terms, intercomponent energy transfer should be negligible—as is confirmed by the experiments (Batchelor [10])—so that we may write

$$\mathcal{D} \rightarrow 2, \quad \mathrm{II_a} \rightarrow 0 \quad \text{and} \quad R_\lambda \rightarrow 0. \tag{90}$$

Data for the decay of slightly anisotropic grid turbulence (Comte-Bellot and Corrsin [26]) yield the behavior of $\mathcal{D}$ at moderate and high Reynolds numbers (Reynolds [46]):

$$\mathcal{D} \rightarrow 2.5, \quad \mathrm{II_a} \rightarrow 0 \quad \text{and} \quad R_\lambda \rightarrow \infty. \tag{91}$$

Matching (90) and (91)

$$\mathcal{D} \rightarrow 2.5 - 0.5\mathcal{W}, \quad \mathrm{II_a} \rightarrow 0, \tag{92}$$

yields

$$\Pi_{ij}^s \rightarrow (2.5\mathcal{W} - 2.5)\epsilon a_{ij}, \quad \mathrm{II_a} \rightarrow 0. \tag{93}$$

Thus, the form suggested for Π_{ij}^s is obtained by interpolating between the data represented by (93) and exact results (84) and (85) for the limiting states of turbulence:

$$\Pi_{ij}^s = \mathcal{C}a_{ij}, \tag{94}$$

where

$$\mathcal{C} \approx \begin{cases} \left\{1 - 9\left[\frac{1}{2}\mathrm{II_a} - \frac{3}{4}\left(\frac{2}{3}\mathrm{II_a}\right)^{3/2}\right]\right\}(2.5\mathcal{W} - 2.5)\epsilon, & \mathrm{III_a} > 0 \\ \left\{1 - 9\left[\frac{1}{2}\mathrm{II_a} + \frac{3}{4}\left(\frac{2}{3}\mathrm{II_a}\right)^{3/2}\right]\right\}(2.5\mathcal{W} - 2.5)\epsilon, & \mathrm{III_a} < 0. \end{cases} \tag{95}$$

6 Comparison of Predictions With the Experimental Data

In this section we use the benchmark set of experimental data for homogeneous flows compiled by Ferziger [47]. We have calculated 13 axisymmetric flows reviewed by Ferziger, using his specified initial values of the Reynolds stress components $\overline{u_i u_j}$ and of the dissipation rate ϵ_0. The data for ϵ_0 provided by Ferziger for homogeneous turbulence with rotation turned out to be quite uncertain. Owing to this reason the values of ϵ_0 for this flow were re-evaluated by curve fitting the experimental data and evaluating the slope at the initial time.

6.1 Reliability of the Experimental Data. Typical turbulence levels measured in grid-generated turbulence are of the order of 0.3–2% (Kovasznay [48]), so the background turbulence level in the test rig must be less than, say, 0.05% so that it can be reliably subtracted. In addition to this, the height (D) of the test section must be much larger than the length scale of the energy-containing eddies, l say, which is of the same order as the mesh size of the grid (M) (Corrsin [24])

$$\frac{D}{l} \sim \frac{D}{M} \gg 1. \tag{96}$$

Measurements of grid-generated turbulence made by Comte-Bellot and Corrsin [26] are the only ones reported in the literature which satisfy these requirements.

A useful class of flows for testing turbulence closures is the passage of grid-generated turbulence through expanding or contracting (and preferably axisymmetric) ducts. All experiments on these flows (Uberoi [11,25], Uberoi and Wallis [49], Hussain and Ramjee [27], and Tan-atichat [50]) were carried out in small medium-quality test rigs with background turbulence levels of 0.2% or more, and with D/l too small to ensure homogeneity. The major purpose of these experiments was to demonstrate the ability of the rapid distortion theory, developed by Batchelor and Proudman [51] and Ribner and Tucker [52], to predict the effect of contraction on turbulence quantities. Even for application to the larger energy-containing eddies alone, this theory, which neglects the viscosity and the nonlinear terms in the equations, requires (Batchelor [10])

$$\frac{l}{L} \sim \frac{l}{D} \gg \frac{q}{U}, \tag{97}$$

where L is the duct length, which is usually not much larger than D. In view of (96), this inequality implies that it is not possible to reach the rapid distortion limit and satisfy constraints for good flow homogeneity. Therefore, the observed deviations of the measurements from rapid distortion theory reported in the literature are not surprising.

A serious problem, arising from inadequate flow quality, occurs in the interpretation of measurements in axisymmetric contractions. When nearly isotropic (grid) turbulence is distorted by contraction, the two lateral components of turbulent intensity increase while the streamwise component decreases, and the grid-induced contribution to the streamwise component may fall below the background turbulence level. The background disturbances originate in part from pressure fluctuations generated by the fan blades and by the turbulent boundary layers on the test section walls. Both of these influences mainly contribute to the longitudinal intensity component of the free stream, and the effect of a contraction is unlikely to be the same as the effect on true turbulence. Thus, the existing experimental data for the streamwise intensity component in contracting ducts are uncertain and should not be used to validate predictions of turbulence models. The radial-component data should be largely free from these objections.

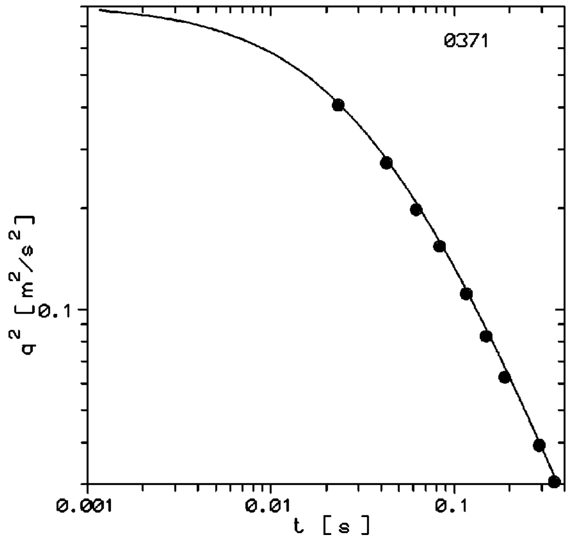

Fig. 6 History of the energy decay of homogeneous isotropic turbulence: ●, Comte-Bellot and Corrsin [26]; ——, predictions

6.2 Dynamic Equations of Axisymmetric Strained Turbulence.

The basic equations for the turbulent stresses $\overline{u_i u_j}$ of axisymmetric strained turbulence are

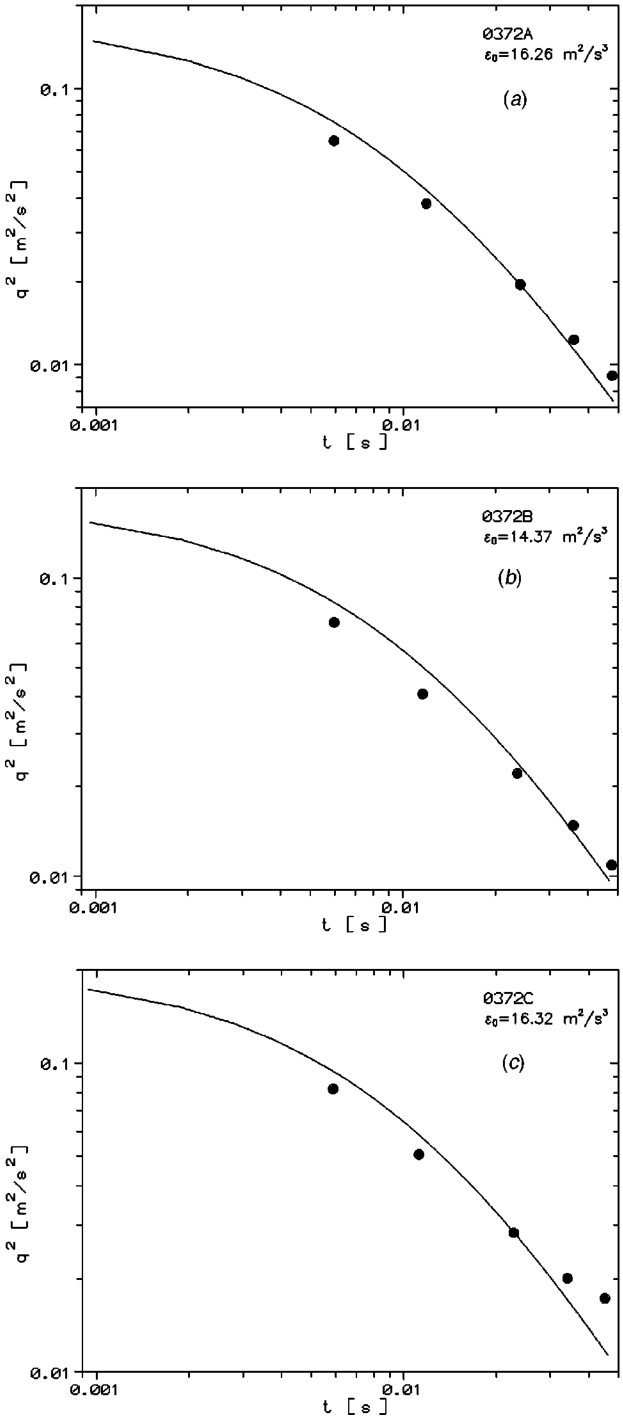

Fig. 7 Histories of the energy decay of nearly homogeneous isotropic turbulence in uniform rotation. (*a*) ●, Wigeland and Nagib [55], Ω=0; ——, predictions; (*b*) ●, Wigeland and Nagib [55], Ω=20 s^{-1}; ——, predictions; (*c*) ●, Wigeland and Nagib [55], Ω=80 s^{-1}; ——, predictions.

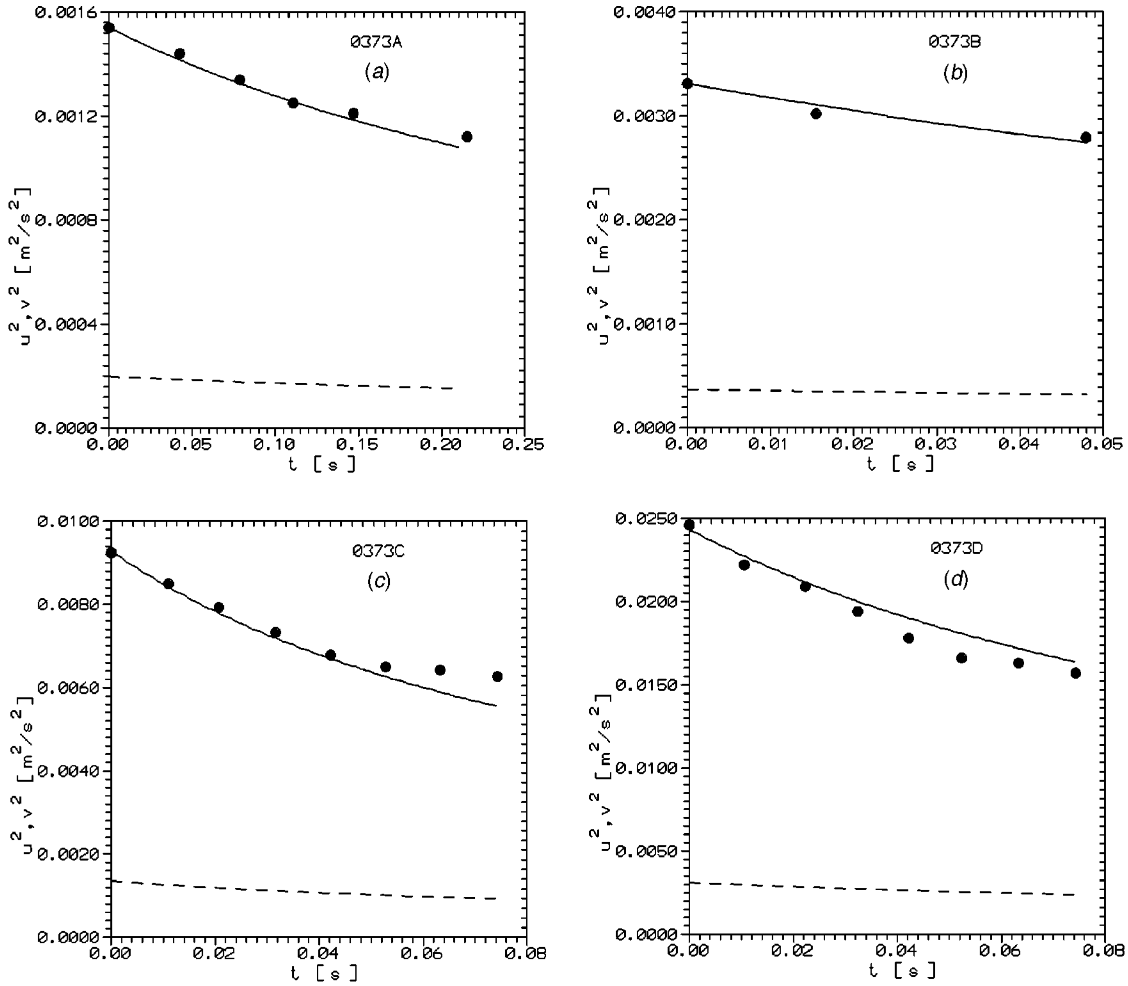

Fig. 8 Histories of the energy components during relaxation from the axisymmetric strain. (*a*) ● $\overline{v^2}$, Uberoi [25], $R_M = UM/\nu = 3710$, contraction=4:1; — — —$\overline{u^2}$, ——$\overline{v^2}$, predictions; (*b*) ● $\overline{v^2}$, Uberoi [25], $R_M = UM/\nu = 3710$, contraction=9:1; — — —$\overline{u^2}$, ——$\overline{v^2}$, predictions; (*c*) ● $\overline{v^2}$, Uberoi [25], $R_M = UM/\nu = 6150$, contraction =4:1; — — —$\overline{u^2}$, ——$\overline{v^2}$, predictions; (*d*) ● $\overline{v^2}$, Uberoi [25], $R_M = UM/\nu = 12300$, contraction=4:1; — — —$\overline{u^2}$, ——$\overline{v^2}$, predictions.

$$\frac{\partial \overline{u_i u_j}}{\partial t} = \underbrace{-\overline{u_i u_k}\frac{\partial \overline{U_j}}{\partial x_k} - \overline{u_j u_k}\frac{\partial \overline{U_i}}{\partial x_k}}_{P_{ij}} + \underbrace{\overline{\frac{p}{\rho}\left(\frac{\partial u_i}{\partial x_j} + \frac{\partial u_j}{\partial x_i}\right)}}_{\Pi_{ij}} \underbrace{- 2\nu \overline{\frac{\partial u_i}{\partial x_k}\frac{\partial u_j}{\partial x_k}}}_{\epsilon_{ij}} . \tag{98}$$

Using (19), (86), and (94), Π_{ij} and ϵ_{ij} can be expressed as

$$\Pi_{ij} = \mathcal{C} a_{ij} + a_{ij} P_{ss} + \mathcal{F}\left(\frac{1}{3} P_{ss} \delta_{ij} - P_{ij}\right), \tag{99}$$

$$\epsilon_{ij} = \mathcal{A} \epsilon a_{ij} + \frac{1}{3} \epsilon \delta_{ij} , \tag{100}$$

so that (98) can be reduced to the form

$$\frac{\partial \overline{u_i u_j}}{\partial t} = P_{ij} + a_{ij} P_{ss} + \mathcal{F}\left(\frac{1}{3} P_{ss} \delta_{ij} - P_{ij}\right) + (\mathcal{C} - 2\mathcal{A}\epsilon) a_{ij} - \frac{2}{3} \epsilon \delta_{ij} . \tag{101}$$

The dissipation equation can be written as

$$\frac{\partial \epsilon}{\partial t} = -2\mathcal{A} \frac{\epsilon \overline{u_i u_k}}{k} \frac{\partial \overline{U_i}}{\partial x_k} - \psi \frac{\epsilon^2}{k} . \tag{102}$$

The scalar functions $\mathcal{A}$, ψ, $\mathcal{F}$, and $\mathcal{C}$ are given by (43), (63), (87), and (95).

6.3 Decay of Homogeneous Isotropic Turbulence. The decay of homogeneous isotropic turbulence is the simplest problem for numerical prediction. The basic experiment is due to Comte-Bellot and Corrsin [26], who carried out the most complete experimental investigations of grid turbulence at moderate and high Reynolds numbers. Figure 6 shows that the numerical predictions match the experiments closely.

6.4 Decay of Initially Isotropic Turbulence in Uniform Rotation. Experiments on the effects of rapid rotation on the decay of grid-generating turbulence include those of Traugott [53], Ibbetson and Tritton [54], Wigeland and Nagib [55], Hopfinger, Browand, and Gagne [56], and more recently Jacquin, Leuchter, Cambon, and Mathieu [57], and Veeravalli [58]. These experiments and the DNS results of Rogallo [17], Bardina, Ferziger, and Rogallo [59], and Speziale, Mansour, and Rogallo [60] show that rapid rotation reduces the dissipation rate and consequently slows the decay of the turbulent kinetic energy. The effects are found to be significant if the turbulent Rossby number is less than unity (approximately):

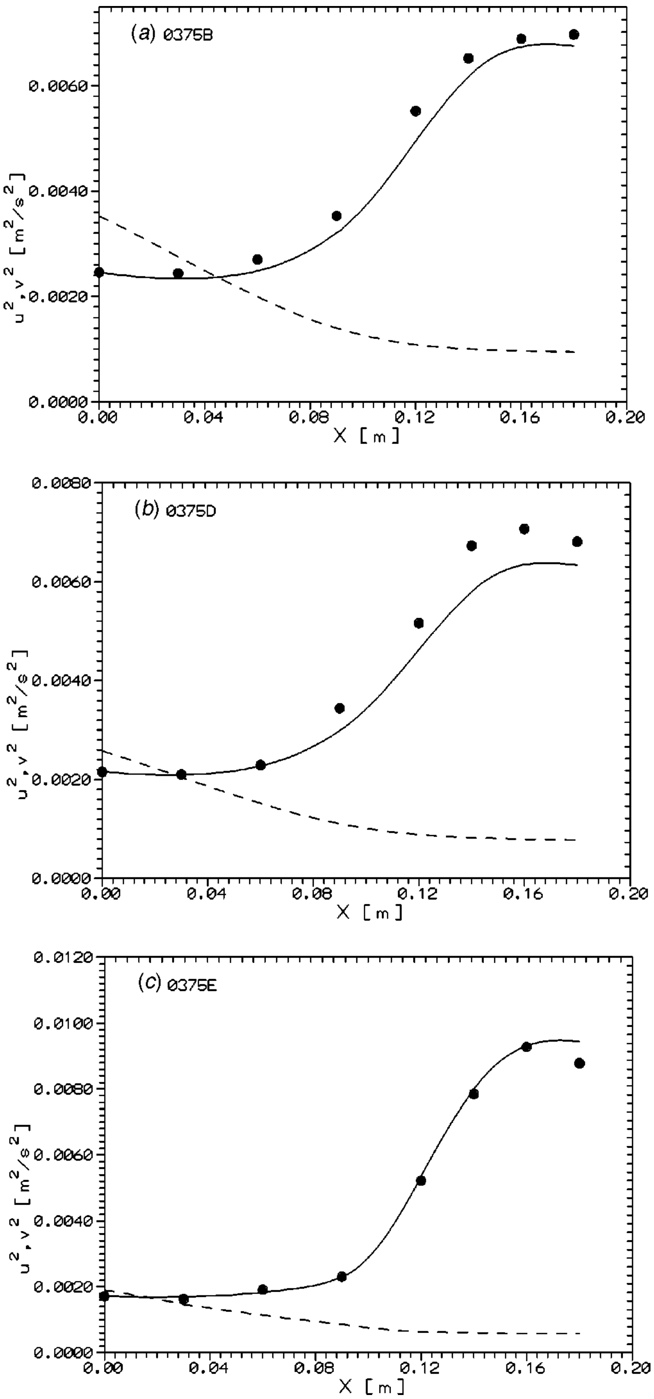

Fig. 9 Variations of the energy components in axisymmetric contraction. (*a*) ● $\overline{v^2}$, Tan-atichat [50], contraction=9:1, — — —$\overline{u^2}$, ——$\overline{v^2}$, predictions. (*b*) ● $\overline{v^2}$, Tan-atichat [50], contraction=9:1, — — —$\overline{u^2}$, ——$\overline{v^2}$, predictions. (*c*) ● $\overline{v^2}$, Tan-atichat [50], contraction=16:1, — — —$\overline{u^2}$, ——$\overline{v^2}$, predictions.

$$R_o = \frac{\epsilon}{\Omega q^2} < 1, \tag{103}$$

where Ω is the rotation rate and ϵ/q^2 represents the vorticity of the energy-containing motion (it is twice Kolmogorov's frequency variable mentioned in Section 1). The mechanism of reduction in dissipation rate is apparently that Coriolis acceleration tends to force elementary vortex lines to lie along the axis, interfering with the vortex-stretching process which transfers energy up the spectrum to the dissipating eddies.

When turbulence is distorted by very rapid deformation, so that the velocity gradients in the mean flow outweigh the gradients in turbulence, e.g.,

$$\frac{\partial \overline{U}}{\partial x} \gg \frac{\partial u}{\partial x}, \tag{104}$$

the governing equations for the turbulent fluctuations can be linearized and nonlinearity due to the inertia terms no longer plays an important role in the dynamics of turbulence. Approaching this limit, the nonlinear spectral transfer process due to the turbulent vortex stretching (P_ϵ^4), which is responsible for production, and any tendency to equi-partition, of ϵ_{ij} (Bradshaw [61]), will be significantly reduced. Thus, the observed trends in the above-mentioned experiments and numerical simulations are not surprising.

Since the instantaneous velocity gradient $\partial u/\partial x$ can be estimated as q/λ (Tennekes and Lumley [23]) we obtain, from (104) and (30),

$$\frac{\mathbf{D}q^2}{\epsilon} \gg \frac{1}{5}R_\lambda, \tag{105}$$

where $\mathbf{D}$ is the magnitude of the deformation tensor $\mathbf{D}^2 = \partial\overline{U_i}/\partial x_k \partial\overline{U_i}/\partial x_k$. Note that the above inequality is stronger than that in (97) by a factor of order $\mathrm{Re}^{1/2}$. For rotational deformation (105) may be written as

$$\frac{1}{\mathrm{R_o}} \gg \frac{1}{5}R_\lambda. \tag{106}$$

This inequality can hardly be satisfied in any flow problem that arises in practice, and therefore the effects reported in the literature can be considered more as the exception than the rule (Batchelor [10]). Figure 7(*a–c*) shows comparisons of the predictions of the above model (which contains no explicit allowance for rotation) and measurements of the decay of initially isotropic turbulence in uniform rotation by Wigeland and Nagib [55]. This figure shows that the discrepancies between the experiments and predictions are small, although the Rossby number $\mathrm{R_o}$ was as small as 0.3. In these experiments $R_\lambda \simeq 20$, suggesting that the inequality (106) is far from being satisfied. From the results shown in Fig. 7, we may conclude that it is not worth the effort to modify the decay term (ψ) of the dissipation rate equation for the effects of rapid rotation on unsheared turbulence.

6.5 Return to Isotropy of Axisymmetric Strained Turbulence. Using (101) and (102), the histories of the energy components measured downstream of an axisymmetric contraction by Uberoi [25] were calculated. The results are compared with the measurements in Fig. 8(*a–d*). The predicted behavior of the lateral velocity component $\overline{v^2}$ for all four cases agrees with the experimental data within the expected accuracy of the latter. We note that the predictions of the flow shown in Fig. 8(*b*), which corresponds to the greatest contraction ratio, also agree with the measurements of the streamwise intensity component $\overline{u^2}$.

6.6 Axisymmetric Contraction of Grid-Generated Turbulence. The development of grid-generated turbulence passing through axisymmetric contractions with area ratios 9:1 and 16:1 was calculated using initial data from the experiments of Tan-atichat [50]. The deformation rate $\mathbf{D}$ was not constant in these experiments, but increased from zero at the entrance, reached a maximum corresponding to the rapid distortion limit (105) half way down the contraction and then decreased to zero at the end of the contraction. Figure 9(*a–f*) shows fair overall agreement between the predicted and measured profiles of $\overline{v^2}$.

7 Conclusions

Analysis of axisymmetric strained turbulence using invariant theory shows that in such turbulence all second-order correlations are aligned with each other. Kinematic constraints arising from the flow axisymmetry have been exploited to obtain analytical closure for the production terms of the dissipation rate equation. All these findings are compared with the available results of direct numerical simulations.

Complete turbulence closure was considered for the dissipation and pressure-strain correlations by assuming that these vary monotonically between the limiting states of turbulence at the vertices of the anisotropy invariant map. This assumption is supported qualitatively by the simulation results. A suitable procedure is suggested for matching the behavior of turbulence around its limiting states and the asymptotic trends for very large and very low Reynolds numbers.

Analytical treatment of axisymmetric turbulence shows that the dynamics of the dissipation correlations are more complicated than those of the pressure-strain correlations, since the behavior of latter can be defined mathematically at the vertices of the anisotropy invariant map. Closures for the partition of the dissipation tensor and for the ‘‘slow’’ part of the pressure-strain correlations indicate that the turbulence functions depend on Reynolds number in the range $R_\lambda < 1500$. The Reynolds number effects are slightly more pronounced for the slow part of the pressure-strain correlations than for the dissipation correlations.

Predictions of axisymmetric flows by the improved turbulence closure, which accounts for the effects of anisotropy of turbulence, agree well with the experimental data.

Acknowledgments

This research received financial support from the Volkswagen-Stiftung within the project ‘‘Development of statistical models of turbulence using the experimental and numerical databases’’ (I/72 857). The authors gratefully acknowledge this support. P. Bradshaw received support (Er 111/1) for his stay at LSTM-Erlangen through the Deutsche Forschungsgemeinschaft (DFG).

References

[1] Kolmogorov, A. N., 1941, ‘‘Local Structure of Turbulence in an Incompressible Fluid at Very High Reynolds Numbers,’’ Dokl. Akad. Nauk SSSR, **30**, pp. 299–303.

[2] Kolmogorov, A. N., 1942, ‘‘Equations of Motion of an Incompressible Turbulent Fluid,’’ Izv. Akad. Nauk SSR Ser. Fiz. Mat. Nauk, **6**, pp. 56–58.

[3] Launder, B. E., 1971, ‘‘Mathematical Models and Turbulence—Lecture 1,’’ Mechanical Engineering Department, Imperial College, London, s. 17.

[4] Chou, P. Y., 1945, ‘‘On the Velocity Correlation and the Solution of the Equation of Turbulent Fluctuation,’’ Q. Appl. Math., **3**, pp. 38–54.

[5] Kolovandin, B. A., and Vatutin, I. A., 1972, ‘‘Statistical Transfer Theory in Non-homogeneous Turbulence,’’ Int. J. Heat Mass Transf., **15**, pp. 2371–2383.

[6] Jovanović, J., Ye, Q.-Y., and Durst, F., 1992, ‘‘Refinement of the Equation for the Determination of Turbulent Micro-scale,’’ Universität Erlangen-Nürnberg, Report Number LSTM 349/T/92.

[7] Jovanović, J., Ye, Q.-Y., and Durst, F., 1995, ‘‘Statistical Interpretation of the Turbulent Dissipation Rate in Wall-Bounded Flows,’’ J. Fluid Mech., **293**, pp. 321–347.

[8] Durbin, P. A., and Speziale, C. G., 1991, ‘‘Local Anisotropy in Strained Turbulence at High Reynolds Numbers,’’ ASME J. Fluids Eng., **113**, pp. 707–709.

[9] Lumley, J. L., 1992, ‘‘Some Comments on Turbulence,’’ Phys. Fluids, **4**, pp. 203–211.

[10] Batchelor, G. K., 1953, *The Theory of Homogeneous Turbulence*, Cambridge University Press, Cambridge, UK, pp. 68–75.

[11] Uberoi, M. S., 1957, ‘‘Equipartition of Energy and Local Isotropy in Turbulent Flows,’’ J. Appl. Phys., **28**, pp. 1165–1170.

[12] Monin, A. S., and Yaglom, A. M., 1975, *Statistical Fluid Mechanics*, Vol. 2, M.I.T. Press, Cambridge, MA, pp. 453–461.

[13] Antonia, R. A., Anselment, F., and Chambers, A. J., 1986, ‘‘Assessment of Local Isotropy Using Measurements in a Turbulent Plane Jet,’’ J. Fluid Mech., **169**, pp. 365–391.

[14] Saddoughi, S. G., and Veeravalli, S. V., 1994, ‘‘Local Isotropy in Turbulent Boundary Layers at High Reynolds Number,’’ J. Fluid Mech., **268**, pp. 333–372.

[15] Lumley, J. L., 1978, ‘‘Computational Modelling of Turbulent Flows,’’ Adv. Appl. Mech., **18**, pp. 123–176.

[16] Jovanović, J., and Otić, I., 2000, ‘‘On the Constitutive Relation for the Reynolds Stresses and the Prandtl-Kolmogorov Hypothesis of Effective Viscosity in Axisymmetric Strained Turbulence,’’ ASME J. Fluids Eng., **122**, pp. 48–50.

[17] Rogallo, R. S., 1981, ‘‘Numerical Experiments in Homogeneous Turbulence,’’ NASA Technical Memo. 81315.

[18] Ye, Q.-Y., 1996, ‘‘Die turbulente Dissipation mechanischer Energie in Scherschichten,’’ Ph.D. thesis, Universität Erlangen-Nürnberg.

[19] Rotta, J. C., 1951, ‘‘Statistische Theorie nichthomogener Turbulenz,’’ Z. Phys., **129**, pp. 547–572.

[20] Kolmogorov, A. N., 1941, ‘‘On Degeneration of Isotropic Turbulence in an Incompressible Viscous Liquid,’’ Dokl. Akad. Nauk SSSR, **6**, pp. 538–540.

[21] Sreenivasan, K. R., 1984, ‘‘On the Scaling of the Turbulence Energy Dissipation Rate,’’ Phys. Fluids, **27**, pp. 1048–1051.

[22] Hinze, J. O., 1975, *Turbulence*, 2nd Ed., McGraw-Hill, New York, p. 260.

[23] Tennekes, H., and Lumley, J. L., 1972, *A First Course in Turbulence*, M.I.T. Press, Cambridge, MA.

[24] Corrsin, S., 1963 ‘‘Turbulence: Experimental Methods,’’ *Handbuch der Physik*, Vol. VIII/2, Springer, Berlin, pp. 524–590.

[25] Uberoi, M. S., 1956, ‘‘Effects of Wind-Tunnel Contraction on Free Stream Turbulence,’’ J. Aero. Sci.,, **23**, pp. 754–764.

[26] Comte-Bellot, G., and Corrsin, S., 1966, ‘‘The Use of a Contraction to Improve the Isotropy of Grid-Generated Turbulence,’’ J. Fluid Mech., **25**, pp. 657–682.

[27] Hussain, A. K. M. F., and Ramjee, V., 1976, ‘‘Effects of the Axisymmetric Contraction Shape on Incompressible Turbulent Flow,’’ ASME J. Fluids Eng., **98**, pp. 58–69.

[28] Garg, S., and Warhaft, Z., 1998, ‘‘On the Small Scale Structure of Simple Shear Flow,’’ Phys. Fluids, **10**, pp. 662–673.

[29] Pumir, A., and Shraiman, B. I., 1995, ‘‘Persistent Small Scale Anisotropy in Homogeneous Shear Flows,’’ Phys. Rev. Lett., **75**, pp. 3114–3117.

[30] Lee, M. J., 1985, ‘‘Numerical Experiments on the Structure of Homogeneous Turbulence,’’ Ph.D. thesis, Stanford University, Stanford, CA.

[31] Davidson, P. A., 2000, ‘‘Was Loitsyansky Correct? A Review of the Arguments,’’ J. Turb.,, **1**, pp. 1–13.

[32] Saffman, P. G., 1967, ‘‘Note on Decay of Homogeneous Turbulence,’’ Phys. Fluids, **10**, pp. 13–49.

[33] Kolovandin, B. A., 1991, ‘‘Modelling the Dynamics of Turbulent Transport Process,’’ Adv. Heat Transfer, **21**, pp. 185–237.

[34] Jovanović, J., Ye, Q.-Y., Jakirlić, S., and Durst, F., 2001, ‘‘Turbulence Closure for the Dissipation Rate Correlations,’’ Universität Ernalngen-Nürnberg, Report Number LSTM 618/T.

[35] Coleman, G. N., and Mansour, N. N., 1991, ‘‘Simulation and Modelling of Homogeneous Compressible Turbulence Under Isotropic Mean Compression,’’ *Proc. Eight. Symp. on Turbulent Shear Flows*, Technische Universität München, Munich, pp. 21.3.1–21.3.6.

[36] Mansour, N. N., and Wray, A. A., 1994, ‘‘Decay of Isotropic Turbulence at Low Reynolds Number,’’ Phys. Fluids, **6**, pp. 808–814.

[37] Poinsot, T. J., 1991, ‘‘Flame Ignition in a Premixed Turbulent Flow,’’ Annual Research Briefs, Center for Turbulence Research, Stanford University, pp. 251–272.

[38] Bernsdorf, J., Brenner, G., and Durst, F., 1998, ‘‘Simulation of a 2D Channel Flow Around a Square Obstacle With Lattice-Boltzmann Automata,’’ Int. J. Mod. Phys. C, **9**, pp. 1129–1141.

[39] Lumley, J. L., and Newman, G., 1977, ‘‘The Return to Isotropy of Homogeneous Turbulence,’’ J. Fluid Mech., **82**, pp. 161–178.

[40] Fischer, M., Jovanović, J., and Durst, F., 2001, ‘‘Reynolds Number Effects in the Near-Wall Region of Turbulent Channel Flows,’’ Phys. Fluids, **13**, pp. 1755–1767.

[41] Spalart, P. R., 1986, ‘‘Numerical Study of Sink-Flow Boundary Layers,’’ J. Fluid Mech., **172**, pp. 307–328.

[42] Seidl, V., 1997, ‘‘Entwicklung und Anwendung eines Parallelen Finite-Volumen-Verfahrens zur Strömungssimulation auf unstrukturierten Gittern mit lokaler Verfeinerung,’’ Institut für Schiffbau, Universität Hamburg, Bericht Nr. 585.

[43] Crow, S. C., 1968, ‘‘Viscoelastic Properties of Fine-Grained Incompressible Turbulence,’’ J. Fluid Mech., **33**, pp. 1–20.

[44] Launder, B. E., Reece, G. J., and Rodi, W., 1975, ‘‘Progress in the Development of a Reynolds Stress Turbulence Closure,’’ J. Fluid Mech., **68**, pp. 537–566.

[45] Hallbäck, M., Groth, J., and Johansson, A. V., 1990, ‘‘An Algebraic Model for Nonisotropic Turbulent Dissipation Rate in Reynolds Stress Closures,’’ Phys. Fluids A, **2**, pp. 1859–1866.

[46] Reynolds, W. C., 1984, ‘‘Physical and Analytical Foundations, Concepts and New Directions in Turbulence Modelling and Simulation,’’ *Turbulence Models and Their Applications*, B. E. Launder, W. C. Reynolds, W. Rodi, J. Mathieu, and D. Jeandel, eds., **2**, CEA-EDF INRIA, Paris, Thermosciences Division, Mechanical Engineering Department, Stanford University, Stanford, CA, pp. 150–294.

[47] Ferziger, J., 1980, ‘‘Homogeneous Turbulent Flows,’’ *Proceedings 1980-81 AFOSR-HTTM Stanford Conference on Complex Turbulent Flows*, S. J. Kline, B. J. Cantwell, and G. M. Lilley, eds., **I**, Stanford University, CEA-EDF INRIA, Eyrolles, Paris, pp. 405–433.

[48] Kovasznay, L. S. G., 1966, ‘‘Turbulence Measurements,’’ *Applied Mechanics Surveys*, ASME, New York, pp. 971–982.

[49] Uberoi, M. S. and Wallis, S., 1966, ‘‘Small Axisymmetric Contraction of Grid Turbulence,’’ J. Fluid Mech., **24**, pp. 539–543.

[50] Tan-atichat, J., 1980, ‘‘Effects of Axisymmetric Contractions on Turbulence of Various Scales,’’ Ph.D. thesis, Illinois Institute of Technology.

[51] Batchelor, G. K., and Proudman, I., 1954, ''The Effect of Rapid Distortion of a Fluid in Turbulent Motion,'' Q. J. Mech. Appl. Math., **7**, pp. 83–103.
[52] Ribner, H. S., and Tucker, M., 1952, ''Spectrum of Turbulence in a Contracting Stream,'' NASA Technical Note 2606.
[53] Traugott, S. C., 1958, ''Influence of Solid-Body Rotation on Screen-Produced Turbulence,'' NACA Technical Note 4135.
[54] Ibbetson, A., and Tritton, D., 1975, ''Experiments on Turbulence in a Rotating Fluid,'' J. Fluid Mech., **68**, pp. 639–672.
[55] Wigeland, R. A., and Nagib, H. M., 1978, ''Grid-Denerated Turbulence With and Without Rotation About the Streamwise Direction,'' Report R78-1, Illinois Institute of Technology.
[56] Hopfinger, E. J., Browand, F. K., and Gagne, Y., 1982, ''Turbulence and Waves in a Rotating Tank,'' J. Fluid Mech., **125**, pp. 505–534.
[57] Jacquin, L., Leuchter, O., Cambon, C., and Mathieu, J., 1990, ''Homogeneous Turbulence in the Presence of Rotation,'' J. Fluid Mech., **220**, pp. 1–52.
[58] Veeravalli, S. V., 1990, ''An Experimental Study of the Effects of Rapid Rotation on Turbulence,'' Annual Research Briefs, Center for Turbulence Research, Stanford University, pp. 203–220.
[59] Bardina, J., Ferziger, J. H., and Rogallo, R. S., 1995, ''Effect of Rotation on Isotropic Turbulence: Computation and Modelling,'' J. Fluid Mech., **154**, pp. 321–336.
[60] Speziale, C. G., Mansour, N. N., and Rogallo, R. S., 1987, ''Decay of Turbulence in a Rapidly Rotating Frame,'' *Studing Turbulence Using Numerical Simulation Databases*, Center for Turbulence Research, Stanford University, Report CTR-S87, pp. 205–212.
[61] Bradshaw, P., 1971, *An Introduction to Turbulence and its Measurement*, Pergamaon, London, pp. 14–17.

Piero Colonna
Faculty of Design, Engineering and Production,
Thermal Power Engineering Section,
Delft University of Technology,
Mekelweg 2,
2628 CD Delft, The Netherlands

Paolo Silva
Dipartimento di Energetica,
Politecnico di Milano,
P.za L. da Vinci, 32,
20133 Milano, Italy

Dense Gas Thermodynamic Properties of Single and Multicomponent Fluids for Fluid Dynamics Simulations

The use of dense gases in many technological fields requires modern fluid dynamic solvers capable of treating the thermodynamic regions where the ideal gas approximation does not apply. Moreover, in some high molecular fluids, nonclassical fluid dynamic effects appearing in those regions could be exploited to obtain more efficient processes. This work presents the procedures for obtaining nonconventional thermodynamic properties needed by up to date computer flow solvers. Complex equations of state for pure fluids and mixtures are treated. Validation of sound speed estimates and calculations of the fundamental derivative of gas dynamics Γ *are shown for several fluids and particularly for Siloxanes, a class of fluids that can be used as working media in high-temperature organic Rankine cycles. Some of these fluids have negative* Γ *regions if thermodynamic properties are calculated with the implemented modified Peng-Robinson thermodynamic model. Results of flow simulations of one-dimensional channel and two-dimensional turbine cascades will be presented in upcoming publications.* [DOI: 10.1115/1.1567306]

1 Introduction

The study of fluid flows involving dense gases, i.e., fluids that cannot be treated as an ideal gas, is of particular interest for several applications. Examples are the hypersonic and transonic wind tunnel design, [1–4], chemicals and fluids transport, [5], heat transfer devices (especially in chemical processes), and supercritical hydrogen to cool hypersonic aircrafts, [6]. One area that can benefit from advances in the mentioned field is turbomachinery design, primarily organic Rankine cycle (ORC) turbines, [7,8], but also compressors and turboexpanders for chemical processes and compressors for refrigeration applications, [9,10]. Other areas which can involve dense gas dynamics are the development of Stirling engines, [11,12], and of thermoacoustic engines, [13].

So-called dense gas effects occur for thermodynamic states at high pressure close to saturation and close to the critical point. The volumetric effect implies that densities are smaller if compared to the ideal gas approximation and the calorimetric effect implies that the heat capacity close to the critical point tends to large values.

For an accurate numerical simulation of dense gas flows these effects must be accounted for and the use of complex thermodynamic models as opposed to the widely adopted ideal gas approximation is mandatory. The introduction of complex thermodynamic models into fluid dynamics numerical schemes is not straightforward, [14–19]; furthermore, modern solvers require the computation of particular thermodynamic functions for time-efficient and accurate implementation. An overview of the mentioned functions, procedures to obtain their algebraic expressions, and their form for several thermodynamic models are outlined in the following. The present study extends the previous work (see, e.g., Refs. [20–22]) regarding the use of complex equations of state (EOS) in fluid dynamic simulations to other accurate EOS and to state-of-the-art EOS for mixtures.

Besides dense gas behavior, nonclassical gasdynamic effects could also occur in the critical or near subcritical dense gas region and are extensively documented in the literature (see, e.g., Ref. [23] for a review and complete references, and also Refs. [24–28] for more recent works). Nonclassical dense gas behavior could be exploited in the design of ORC turbines or other turbomachinery to reduce losses related to shock formation, [7,9,10]. The thermodynamic parameter governing nonclassical behavior is the fundamental derivative of gas dynamics Γ.

Estimates of Γ values for siloxanes, a class of fluids recently proposed and adopted in ORC turbine applications, are also presented. The complete thermodynamic models which are illustrated in the following are implemented in a FORTRAN library, THERMOPROP. The thermodynamic library is part of zFLOW, a computational fluid dynamics (CFD) Euler solver developed in collaboration by the authors and others, [29]. Results for nozzle, shock-tube, and cascade configurations will be presented in upcoming publications.

2 Thermodynamic Properties for Numerical Flow Solvers From Complex Equations of State

A Thermodynamic Models. Using a consistent model for the estimation of thermodynamic properties to be used in a fluid dynamics numerical solver is very important in order to achieve robustness and accuracy. This means that all needed thermodynamic properties must be computed from the minimum set of information, e.g., an EOS in the usual $P=P(v,T)$ form, where P is the pressure, T the temperature, and v the specific volume. The other necessary information is the heat capacity in the ideal gas state as a function of temperature, $C_P^0=C_P^0(T)$, [30].

Multi-parameter equations of state (MEOS) for the estimation of thermodynamic properties of both the liquid and the vapor phase are very accurate even in the closest proximity of the critical point, [31,32], while widely adopted cubic equations of state (CEOS) are inherently inaccurate near the critical point, [33], but need very limited input information and, more importantly, can be extended to multicomponents fluids on a thermodynamically consistent basis, [31,34].

MEOS can be substance-specific, like the modified Keenan-Keyes EOS for water, [30,35], or the Haar-Gallagher EOS for ammonia, [30,36], can fit a specific class of fluids, like the Star-

---

Contributed by the Fluids Engineering Division for publication in the JOURNAL OF FLUIDS ENGINEERING. Manuscript received by the Fluids Engineering Division May 28, 2002; revised manuscript received October 30, 2002. Associate Editor: J. Katz.

ling EOS for light hydrocarbons, [30,37], or can be used for various classes of substances with a comparably lower precision, like the Martin-Hou EOS, [30,38,39]. In order to give an overview of the accuracy of the above-cited models, the overall accuracy of the Starling EOS for light hydrocarbons (23 fluids) can be summarized as follows, [37]: densities are predicted with an average absolute deviation from experimental values of 1.38% for 971 datapoints. Enthalpy departures are predicted with an average absolute deviation from experimental values of 4.05 kJ/kg for 620 datapoints. Vapor pressure are predicted accurately, since the EOS is constrained to measures for 663 points, and are obtained by solving the Gibbs equation, or, which is the same, the equality of fugacities in the vapor and liquid phase. Substance specific EOS are even more precise, like the water and ammonia EOSs.

ThermoProp contains two modules: TPSI, [30], and StanMix, [8]. The mentioned MEOSs are implemented in TPSI and were extended to the calculation of nonconventional thermodynamic functions as shown in the following section. The TPSI database currently includes: ammonia, water, methane, propane, butane, isopentane, pentane, hexane, octane, R11, R12.

StanMix uses the Peng Robinson cubic EOS modified by Stryjeck and Vera in order to achieve high accuracy for saturation pressure estimates of pure fluids, [40]. The correct prediction of saturation properties implies accuracy also in the dense gas region. The model is extended to multicomponent fluids, with the Wong-Sandler (WS) mixing rules [34]. This model can treat even highly nonideal mixtures, [41]. Thermodynamic functions for both pure fluids and mixtures were added to StanMix and are shown in the following section as well. The StanMix database contains data for 53 pure fluids and 66 binary interaction parameters and can easily be expanded as needed.

B Thermodynamic Functions for Modern Flow Solvers. zFlow uses an hybrid between the finite element (FE) and finite volume (FV) methods for the spatial discretization of systems of nonlinear conservation laws such as the Euler equations. The implemented numerical scheme is a high resolution upwind formulation for unstructured grids and general equations of state. The boundary treatment in the case of general gases is also implemented, [29,42,43].

We now briefly outline the nonconventional thermodynamic functions added to the ThermoProp thermodynamic models, starting from the fluid dynamic model implemented in zFlow. This can be regarded as a model procedure for other flow solvers.

The Euler equations in conservative form can be written as

$$\frac{\partial \mathbf{u}}{\partial t}+\sum_{j=1}^{d}\frac{\partial \mathbf{f}_j(\mathbf{u})}{\partial x_j}=0, \tag{2.1}$$

where the conservative variable vector $\mathbf{u}$ and the vector components $\mathbf{f}_j(\mathbf{u})$ of the hyper-flux $\mathbf{F}(\mathbf{u})$ are given by

$$\mathbf{u}=\begin{bmatrix}\rho\\ \rho u^t\\ \rho w_i\end{bmatrix},\quad \mathbf{f}_j(\mathbf{u})=\begin{bmatrix}\rho w_j\\ (\rho u^t+P)w_j\\ \rho w_i w_j+P\delta_{ij}\end{bmatrix}, \tag{2.2}$$

ρ denotes density, u^t the stagnation (or total) energy (i.e., the sum of the internal and kinetic energy), P the pressure, w_j the components of the velocity vector $\mathbf{w}$, and δ_{ij} is the Kroenecker symbol · $A_j(\mathbf{u})$ is the Jacobian matrix of the Euler flux function, i.e.,

$$A_j(\mathbf{u})=\frac{\partial \mathbf{f}_j(\mathbf{u})}{\partial \mathbf{u}}. \tag{2.3}$$

The upwind numerical scheme used in zFlow requires the computation of the following partial derivatives of P:

$$\alpha=\left(\frac{\partial P}{\partial \rho}\right)_u,\quad \beta=\left(\frac{\partial P}{\partial u}\right)_\rho. \tag{2.4}$$

α and β must be evaluated from an EOS in the usual form $P=P(v,T)$, where v is the specific volume and T is the temperature. The sound speed c, defined as

$$c^2=\left(\frac{\partial P}{\partial \rho}\right)_s=-v^2\left(\frac{\partial P}{\partial v}\right)_s, \tag{2.5}$$

is also necessary.

When an implicit time integration scheme is employed, the entropy (s) is one of the prescribed quantities at an inflow boundary. The numerical procedure in this case requires the knowledge of two additional thermodynamic functions, namely

$$\chi=\left(\frac{\partial s}{\partial \rho}\right)_u,\quad \phi=\left(\frac{\partial s}{\partial u}\right)_\rho. \tag{2.6}$$

The Γ function defined as

$$\Gamma=1+\frac{\rho}{c}\left(\frac{\partial c}{\partial \rho}\right)_s=\frac{v^3}{2c^2}\left(\frac{\partial^2 P}{\partial v^2}\right)_s \tag{2.7}$$

is not necessary for the flow field simulation but it is useful to investigate nonclassical gas effects in the dense gas region.

All the mentioned thermodynamic functions can be expressed as algebraic functions of P, v, T starting from an EOS in the usual form $P=P(v,T)$ and an expression of the specific heat in the ideal gas state, $C_P^0(T)$, by using appropriate thermodynamic transformations. The resulting expressions are as follows:

$$c=\sqrt{-v^2\gamma\left(\frac{\partial P}{\partial v}\right)_T} \tag{2.8}$$

$$\beta=\frac{1}{C_v}\left(\frac{\partial P}{\partial T}\right)_v \tag{2.9}$$

$$\alpha=c^2-\beta P v^2 \tag{2.10}$$

$$\chi=-v^2\frac{P}{T} \tag{2.11}$$

$$\phi=\frac{1}{T} \tag{2.12}$$

$$\Gamma=\frac{v^3}{2c^2}\left\{\left(\frac{\partial^2 P}{\partial v^2}\right)_T-3\frac{T}{C_v}\left(\frac{\partial P}{\partial T}\right)_v\left(\frac{\partial^2 P}{\partial v\,\partial T}\right)_{v,T}+\left[\frac{T}{C_v}\left(\frac{\partial P}{\partial T}\right)_v\right]^2\left\{3\left(\frac{\partial^2 P}{\partial T^2}\right)_v+\frac{1}{T}\left(\frac{\partial P}{\partial T}\right)_v\left[1-\frac{T}{C_v}\left(\frac{\partial C_v}{\partial T}\right)_v\right]\right\}\right\}. \tag{2.13}$$

In Eqs. (2.8)–(2.13) the specific heat at constant pressure (C_P), at constant volume (C_v) and their ratio $\gamma=C_P/C_v$ can be calculated as

$$C_v^0(T)=C_p^0(T)-R \tag{2.14}$$

$$C_v=C_v^0(T)+T\int_\infty^v\left(\frac{\partial^2 P}{\partial T^2}\right)_v dv \tag{2.15}$$

$$C_P=C_v-\frac{T(\partial P/\partial T)_v^2}{(\partial P/\partial v)_T} \tag{2.16}$$

$$\gamma=1-\frac{T}{C_v}\frac{(\partial P/\partial T)_v^2}{(\partial P/\partial v)_T}. \tag{2.17}$$

To obtain Eqs. (2.8)–(2.13) from the definitions, thermodynamic relations and rules for partial derivatives transformation are used and details are reported in Appendix A. Expressions specific to the various thermodynamic models implemented in StanMix and TPSI are reported in Appendix B.

Table 1 Comparison between CPU time needed for computing all thermodynamic properties, given 2 input variables, using either analytical expressions for calculating partial derivatives or a numerical discretization procedure, [45]. The *T*, *v* calculation is direct while calculations for other couples of input variables are iterative on *T*, *v*.

Input Variables	Thermodynamic Region	Input Variable 1	Input Variable 2	CPU Time[a] $\frac{f(x+h,y)-f(x,y)}{h}$	CPU Time[a] $\left(\frac{\partial f}{\partial x}\right)_y$
T, v (direct calculation)	dense gas	$T=300°\mathrm{C}$	$v=0.0109\ \mathrm{m}^3/\mathrm{kg}$	1710	137
	perfect gas	$T=300°\mathrm{C}$	$v=0.4116\ \mathrm{m}^3/\mathrm{kg}$	1595	138
T, P	dense gas	$T=300°\mathrm{C}$	$P=22$ bar	1774	107
	perfect gas	$T=300°\mathrm{C}$	$P=1$ bar	1740	106
h, s	dense gas	$h=905.10$ kJ/kg	$s=2.022$ kJ/kg K	22,822	21,307
	perfect gas	$h=977.16$ kJ/kg	$s=2.348$ kJ/kg K	4910	3200

[a] Time in milliseconds for 1000 cycles on an Intel Pentium II Processor, 400 MHz clock frequency, MS Windows NT 4.0 Operating System, Compaq Visual Fortran V6.5a Professional Edition, full optimization mode

The mentioned complex algebraic expressions can be more easily derived using software for symbolic calculations (see, e.g., Ref. [44]) and in some occasions it may prove an indispensable tool. The software, appropriately customized for thermodynamic functions treatment, can easily operate thermodynamic transformations, derivation, and integrations of algebraic expressions.

It is worthwhile noting that all the mentioned thermodynamic functions can be calculated from the EOS, $C_P^0(T)$, the partial derivatives

$$\left(\frac{\partial P}{\partial v}\right)_T, \quad \left(\frac{\partial P}{\partial T}\right)_v, \quad \left(\frac{\partial^2 P}{\partial v^2}\right)_T, \quad \left(\frac{\partial^2 P}{\partial T^2}\right)_v,$$

$$\left(\frac{\partial^2 P}{\partial T \partial v}\right)_{v,T}, \quad \left(\frac{\partial C_v}{\partial T}\right)_v,$$

and the integral

$$\int_\infty^v \left(\frac{\partial^2 P}{\partial T^2}\right)_v dv.$$

The importance of using analytical expression in CFD simulation must be stressed. The use of complex thermodynamic models in numerical flow solvers implies a considerable increase in CPU time if compared to the ideal gas approximation. All partial derivatives could also be computed numerically, using appropriate methods to get the needed accuracy. For example, in TPSI analytical expressions for partial derivatives for the water and ammonia EOSs were impractical to obtain due to the excessive complication of the EOS form, and an adaptive method, [45], was employed. It must be noted though that using analytical expressions greatly reduces the CPU time. Table 1 reports the comparison between the time for calculating all thermodynamic properties using partial derivatives computed with their analytical expression versus numerical discretization using the mentioned robust method. In the reported example, calculating partial derivatives with their analytical expression requires as few as 1/16 less computing time.

3 Sound Speed and the Fundamental Derivative of Gas Dynamics for Several Classes of Fluids

As it is shown in the preceding section, the convective sound speed can be computed from its definition using an EOS in the usual form $P=P(v,T)$. The accuracy of the computed values directly affects the correctness of the computed flow field and, because of its dependence on the derivative of the main thermodynamic variables, relies on the capability of the EOS of correctly describing the combination of volumetric and thermal molecular interaction. This requires a complex EOS, especially if part of the flow field is in thermodynamic states close to the critical region, as it is the case when investigating dense or nonclassical fluid dynamics effects.

Furthermore, the parameter Γ, depending on second partial derivatives, shows a more accentuate dependance on the algebraic form of the EOS and its estimation shows considerable differences as it will be illustrated in Section 3B.

A Sound Speed Estimates. In order to assess the accuracy of the thermodynamic models implemented in THERMOPROP when computing the sound speed, calculations along isotherms and isobars in widely different thermodynamic regions are compared with either experimental measurements or reference data for selected substances. It must be noted that sound speed data for comparison pertaining to fluids whose molecule is sufficiently complex to suppose nonclassical fluid dynamic behavior are not available. Nevertheless, the accuracy of the thermodynamic models implemented in THERMOPROP can be qualitatively extrapolated from the results described in the following.

As a first classical test case, TPSI and STANMIX sound speed computed values for water are compared with reference data made available by the National Institute of Standards and Technologies (NIST), [46]. Figure 1 shows that the accuracy of the modified Keenan and Keyes model implemented in TPSI, [30,35], is very high even in the liquid region and in the proximity of the critical point. Results for the cubic EOS implemented in STANMIX are shown in Fig. 2: As expected, the PRSV EOS is not accurate in the liquid region (calculated points are omitted), and close to the critical point.

Hexane is employed as working fluid in geothermal organic Rankine cycles: sound speed results obtained with the Starling EOS implemented in TPSI for values of pressure and temperature in the vapor phase (Fig. 3) are very accurate if compared to NIST reference data.

In recent years highly accurate speed of sound measurements have become available, thanks also to a recently developed experimental method, [47]. Experimental data for refrigerant R125 found in the literature are compared to STANMIX sound speed calculations in Fig. 4. The available experimental data are in the range 0.5/5 bar and −13/86°C, and therefore the fluid is not far from the ideal gas state. As it can be noted, deviations in this case are very small.

B The Fundamental Derivative Γ for Several Fluids and Mixtures. Classes of fluids that are used in technical applications include organic and inorganic substances. Table 2 reports several classes of fluids and examples of their technical use. All the mentioned fluids can be used in applications that require investigation of dense gas or nonclassical gas effects. Siloxanes were recently proposed and adopted as working fluids for ORC turbines. Together with favorable thermodynamic characteristics with respect to cycle and turbine design, they are thermally stable, atoxic, and scarcely flammable. Moreover, because of their molecular complexity, they may exhibit nonclassical behavior in the dense gas region.

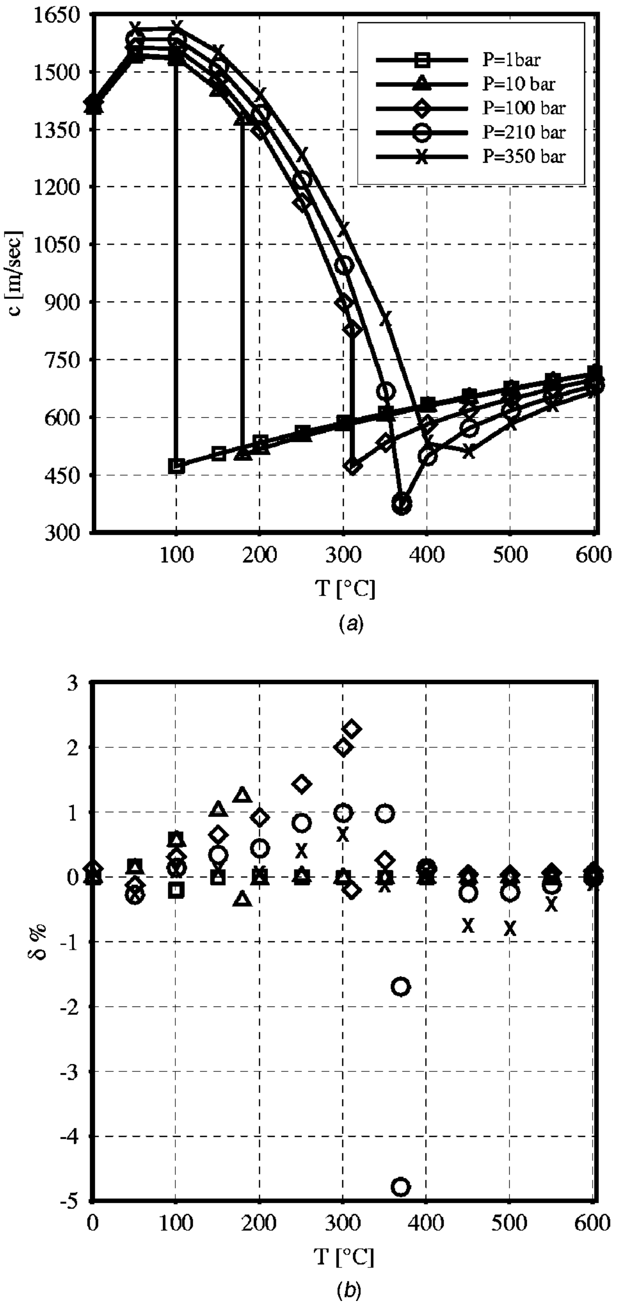

Fig. 1 Water TPSI sound speed estimations comparison with NIST highly accurate data, [62]. δ%: deviation from NIST data; c: TPSI sound speed estimations. Water critical point: $T_c=374.15°C$; $P_c=221$ bar.

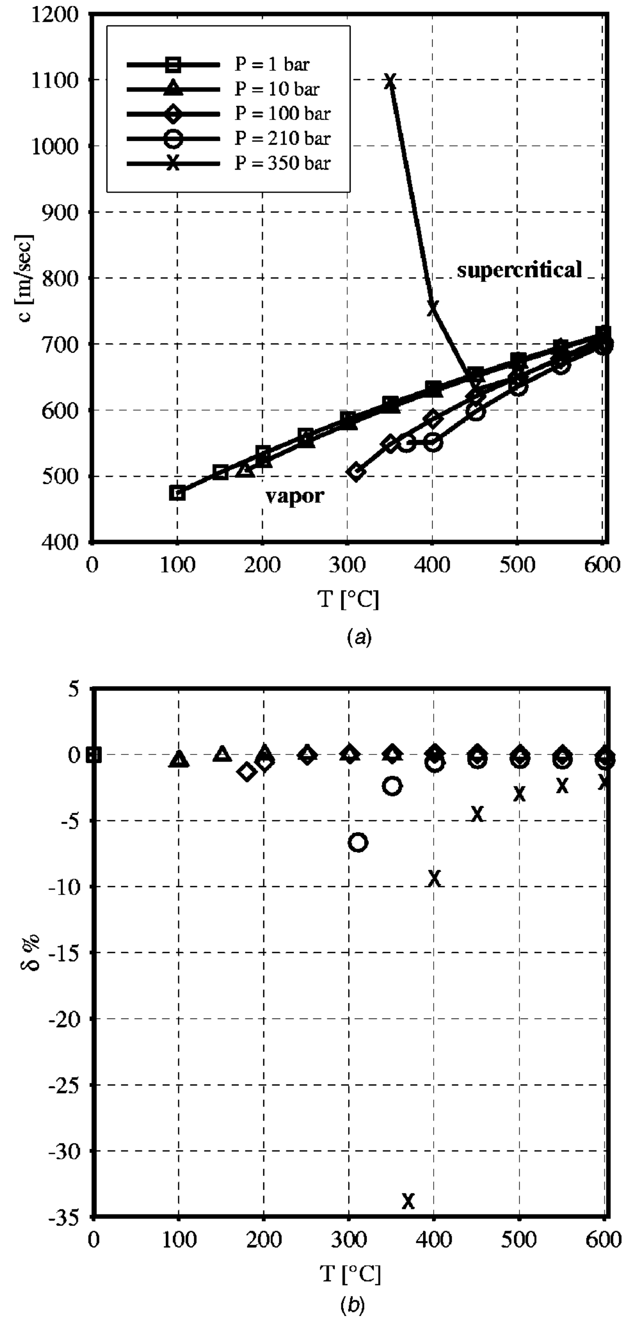

Fig. 2 Water vapor StanMix sound speed estimations comparisons with reference data, [62]. δ%: deviation from NIST data; c: sound speed values calculated by StanMix. Water critical point: $T_c=374.14°C$; $P_c=220.8975$ bar.

1 Comparison With Published Literature. In order to assess differences and further validate Γ calculated with the thermodynamic models implemented in ThermoProp, values along the critical isotherms for several common fluids are compared with curves reported by other investigators, [10,48].

As it can be noted in Figs. 5, 6, and 7 values can differ substantially for relative densities greater than 0.5, and this is expected because differences between thermodynamic models increase in the critical region. Values calculated with substance-specific EOS for water and n-Octane, like the ones implemented in TPSI, are more accurate because those EOS are fitted to experimental data even in the near-critical region while the Martin-Hou EOS, being more general, cannot be as accurate.

Figures 6 and 7 show, moreover, that the cubic EOS of the StanMix model, even if it predicts a quite different curve shape, nevertheless gives values that are intermediate between the Martin-Hou EOS and the substance-specific EOS, except for the region close to the critical point where it is known that CEOS's fail to the predict the correct behavior. This anyhow implies that this simpler EOS can be useful for preliminary investigation of fluids that could exhibit nonclassical behavior, with the advantage of needing less experimental input data for the model.

In Fig. 8, a more comprehensive chart extends the work reported in Ref. [49] with some of the fluids of ThermoProp: It can be seen that in general ThermoProp Γ values are more conservative with respect to predicting nonclassical behavior.

In order to show the thermodynamic region where the turbine expansion of an ORC is located, in Fig. 9 the transformation is

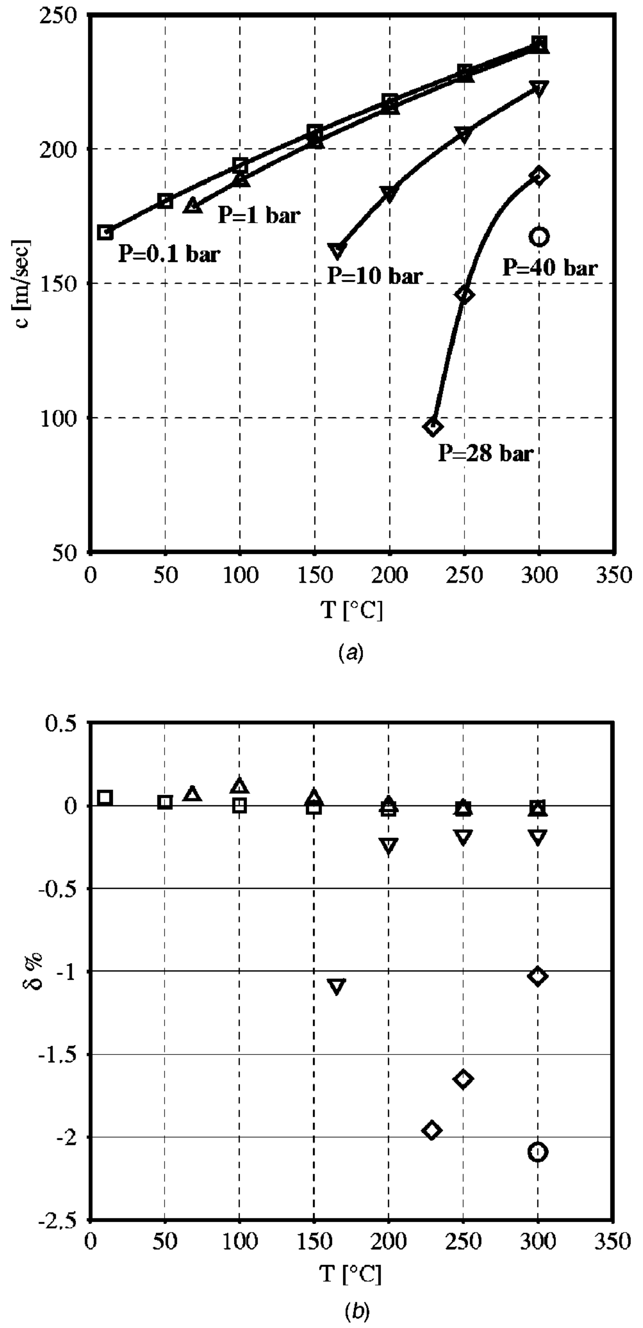

(*a*)

(*b*)

Fig. 3 Hexane TPSI sound speed estimations in the vapor phase versus NIST reference data, [63]. δ%: deviation from NIST data; *c*: TPSI sound speed estimations. Hexane critical point: T_c=232.98°C; P_c=29.27 bar.

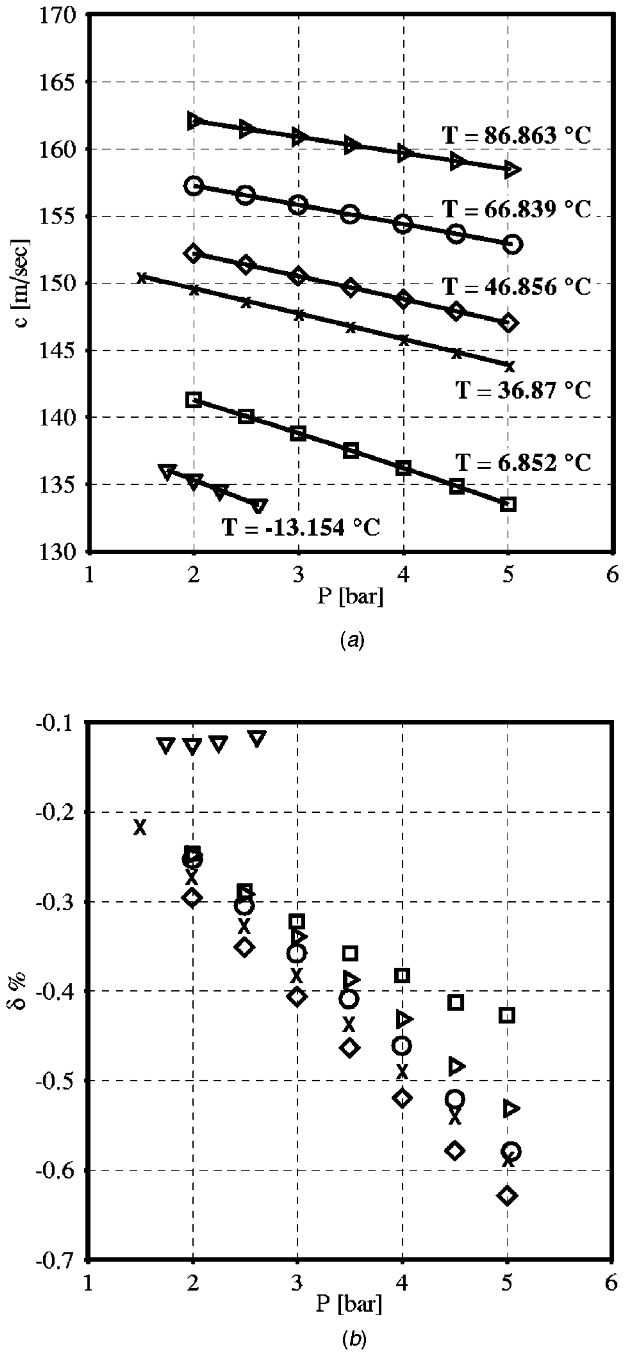

(*a*)

(*b*)

Fig. 4 StanMix sound speed estimations for R125: comparison with experimental data in Ref. [64]. δ%: deviation from experimental data; *c*: sound speed values calculated by StanMix. R125 critical point: T_c=66.25°C; P_c=36.31 bar.

qualitatively represented. In the region where Γ is small even if still positive, nonclassical gasdynamics effects may occur (see, e.g., Ref. [23]).

2 *Siloxanes.* Γ values for siloxanes calculated with StanMix are presented in Fig. 10. In Tables 3 and 4 and in Figs. 10, 11, 12 the common nomenclature for fluids belonging to the siloxane class is the original introduced by Wilcock [50]. Input data for the models are obtained from Dow Corning and thermodynamic properties validation is documented in previous works, [8,51].

In Fig. 10(*a*) are reported Γ curves along the critical isotherms for several linear siloxanes: Note that the values at the critical point are almost the same for all molecules containing the D

Table 2 Classes of fluids for technical applications that can involve their use in the dense gas region

	Fluid	Applications
organic	hydrocarbons	chemical and petrochemical processes, geothermal ORC
	fluorocarbons	chemical processes, refrigeration, geothermal ORC
	siloxanes	high temperature ORC
inorganic	ammonia	refrigeration, Kalina power cycle
	light gases	cryogenic processes, air distillation

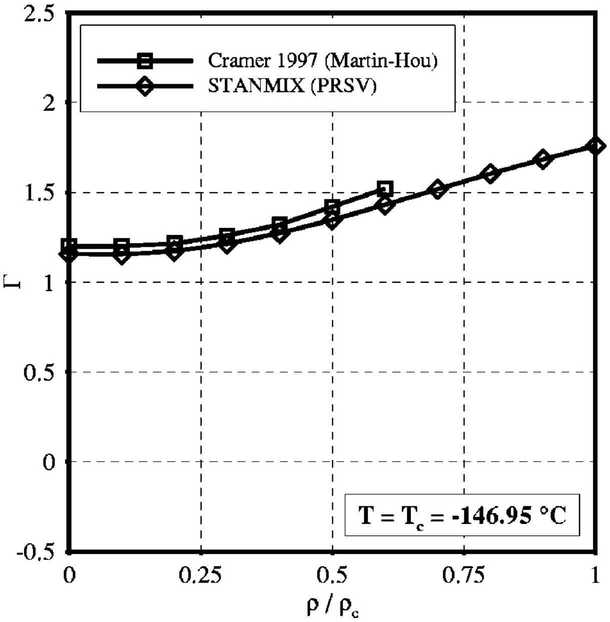

Fig. 5 Comparison between nitrogen Γ along the critical isotherm calculated by StanMix (PRSV EOS) and literature values (Martin-Hou EOS), [10]

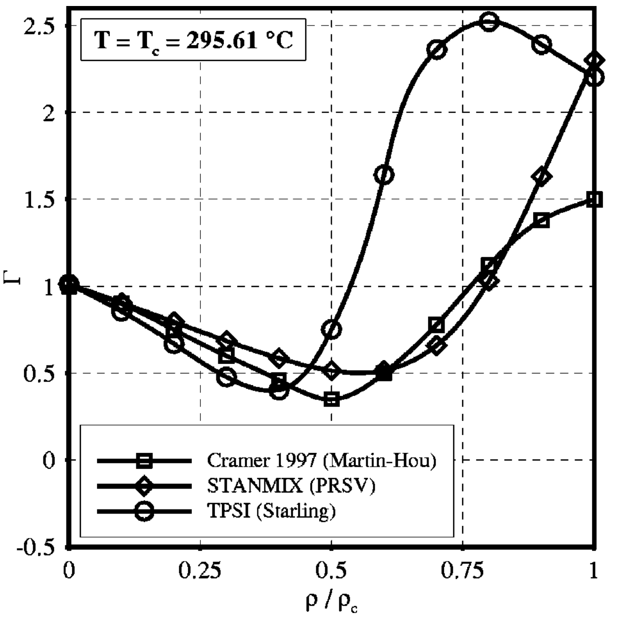

Fig. 7 Comparison between n-Octane Γ along the critical isotherm calculated by StanMix (PRSV EOS), TPSI (Starling), and literature values (Martin-Hou EOS), [10]

groups, $(CH_3)_2SiO$, and it is different for MM which is the simplest molecule and contains only M groups, $(CH_3)_3SiO_{1/2}$. In Fig. 10(*b*) estimates for cyclic siloxanes can be compared to those of linear siloxanes previously outlined: cyclic molecules of comparable molecular weight are slightly less complex, therefore Γ values are higher.

Figure 11 shows Γ values along several isotherms for MD_4M, calculated by StanMix: For subcritical temperature values and for relative specific densities between 1.5 and 2 a negative Γ region is outlined. By observing the shape of Γ curves along isotherms, it can be deduced from Fig. 10 that negative subcritical Γ regions are also found for linear siloxanes lighter than MD_4M, and for cyclic siloxanes. Linear and cyclic siloxanes are therefore very likely Bethe-Zel'dovic-Thompson (BZT) fluids, according to Cramer's definition, [23], of BZT fluids as those having a negative Γ region.

3 Mixtures

(a) Siloxanes. Figure 12 shows a comparison between pure linear siloxanes and equimolar mixtures of the same components. In order to display the calculated Γ values as a function of the

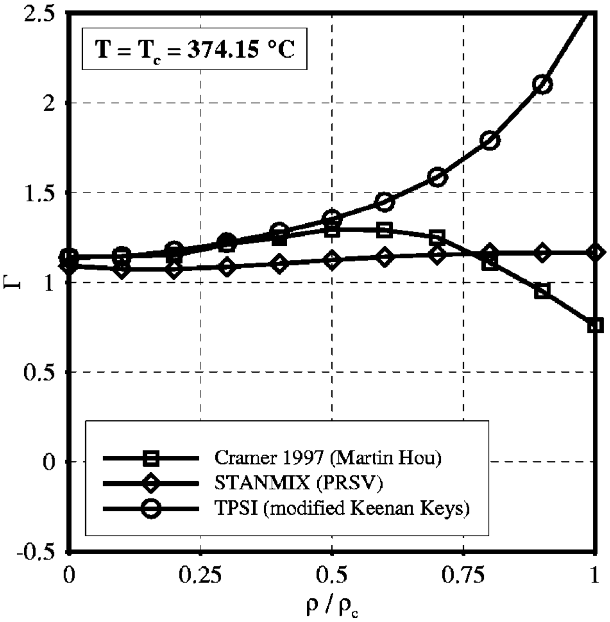

Fig. 6 Comparison between water Γ along the critical isotherm calculated by StanMix (PRSV EOS), TPSI (modified Keenan Keys), and literature values (Martin-Hou EOS), [10]

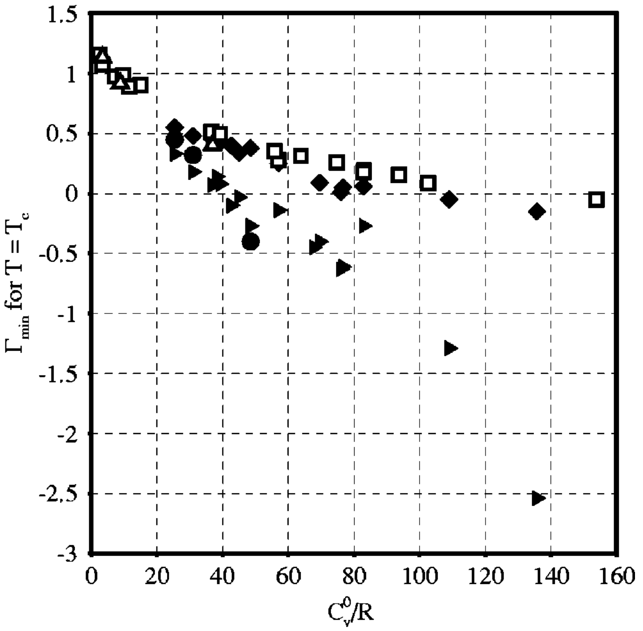

Fig. 8 An overview of minimum Γ along the critical isotherm predicted by StanMix, TPSI and several other equations of state as reported in the literature, [49]. □: StanMix (PRSV EOS), for several fluids; △: TPSI (MEOS), for several fluids; ♦: Martin-Hou, for several fluids; ►: Hirschfelder et al., for several fluids; ●: Benedict-Web-Rubin, for several fluids.

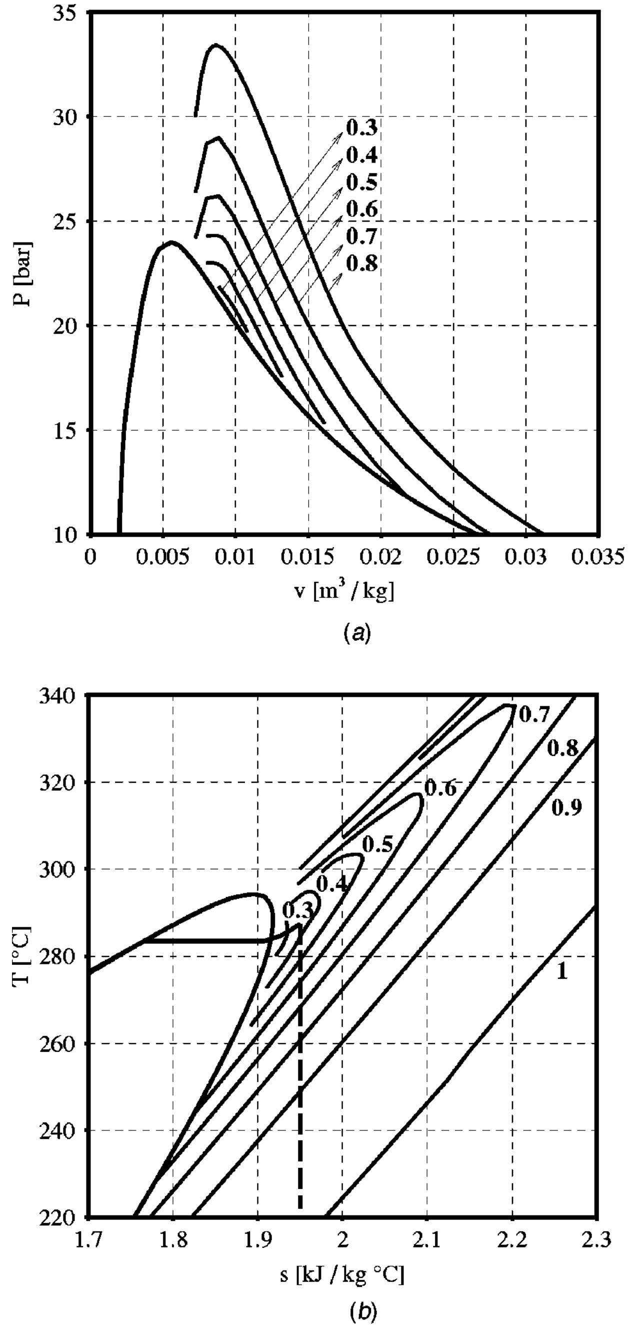

(*a*)

(*b*)

Fig. 9 Iso-Γ curves in the *P*−*v* (*a*) and *T*−*s* (*b*) thermodynamic plane for n-Octane (TPSI). Part of a typical ORC thermodynamic cycle is also represented in (*b*). The turbine expansion transformation for an ORC is qualitatively outlined (dashed line). As it can be noted part of the transformation takes place in the Γ<1 region. All curves are a graphical output from zFLOW.

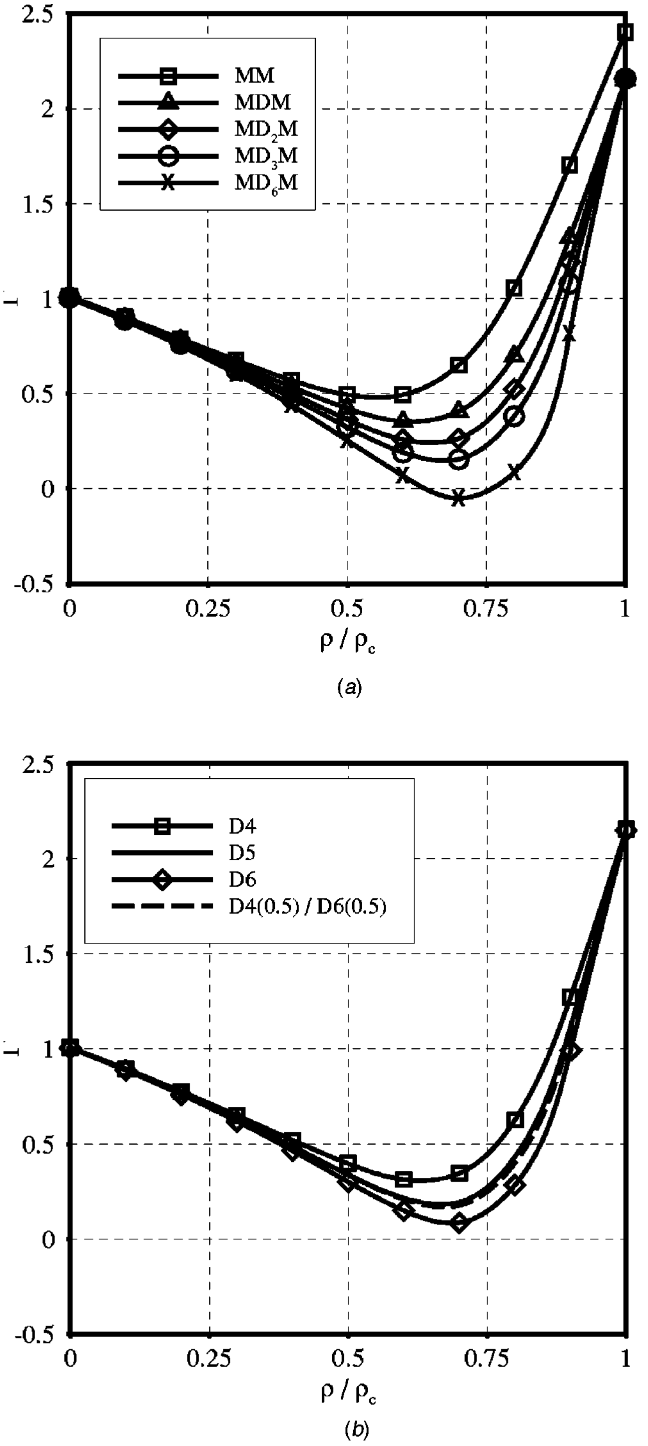

(*a*)

(*b*)

Fig. 10 Γ along the critical isotherm calculated by STANMIX (PRSV EOS) for several linear (*a*) and cyclic (*b*) siloxanes. A comparison between pure fluids and a mixture of the same fluids is also shown (dashed line in (*b*)).

relative density, so that they can be compared with pure fluid calculations and they are consistent with the usual representation of such results, the mixture critical density must also be computed. The direct calculation of the critical point for mixture is not implemented in the STANMIX code yet, therefore at the moment the critical parameters are evaluated graphically from the saturation curves in the $P-v$ plane and extrapolated. This reflects in an uncertainty in the mixture critical volume and therefore in the ρ/ρ_c coordinate. Siloxanes mixtures are almost ideal and very similar to light hydrocarbons with regard to molecular structure, therefore it is believed that their thermodynamic behavior is almost linear with molar composition: in this case, for example, an equimolar mixture of MD_nM and $MD_{n+2}M$ is almost equivalent to $MD_{n+1}M$. This is very well verified for the comparison of $MDM(0.5)/MD_3M(0.5)$ with MD_2M. In the case of the comparison of $MM(0.5)/MD_2M(0.5)$ with MDM, a certain discrepancy can be noted, and it is believed to be due to the slight difference between the MM and the MD_nM molecule structures and to the

Table 3 Basic thermodynamic parameters for lighter linear siloxanes, [61]

Name	Chemical Formula	T_c (°C)	P_c (bar)	MW
MM	$C_6H_{18}OSi_2$	245.60	19.3936	162.379
MDM	$C_8H_{24}O_2Si_3$	291.25	14.3983	236.530
MD_2M	$C_{10}H_{30}O_3Si_4$	326.25	11.7940	310.690
MD_3M	$C_{12}H_{36}O_4Si_5$	355.25	9.96024	384.843
MD_4M	$C_{14}H_{42}O_5Si_6$	380.00	8.77474	459.000

Table 4 Basic thermodynamic parameters for lighter cyclic siloxanes [61]

Name	Chemical Formula	T_c (°C)	P_c (bar)	MW
D_3	$((CH_3)_2SiO)_3$	281.05	16.63	222.464
D_4	$((CH_3)_2SiO)_4$	313.35	13.32	296.618
D_5	$((CH_3)_2SiO)_5$	346.00	11.60	370.773

uncertainty in the critical volume estimation for the mixture. The linear behavior is also very well outlined in Fig. 10(*b*) for cyclic siloxanes: The Γ curve for the equimolar mixture of D_4 and D_6 is almost identical to the curve for D_5.

(b) Other mixtures of technological interest. As a last example of the capability of the mixture model implemented in STANMIX, Fig. 13(*a*) shows Γ curves for air: In this case air is treated as a binary mixture of nitrogen(0.79)/oxygen (0.21) and curves for the pure components are also displayed.

One of the main characteristics of the mixture model coded in STANMIX is that it can treat both quasi-ideal mixtures and highly nonideal mixtures. Figure 13(*b*) shows the calculation of Γ along the critical isotherm for the aqueous 2-propanol mixture.

Mixtures of polar components were recently proposed as working fluids for power cycles (e.g., Kalina cycle [52–57], SMR cycle [58]) and for refrigeration cycles (see, e.g., Ref. [59]).

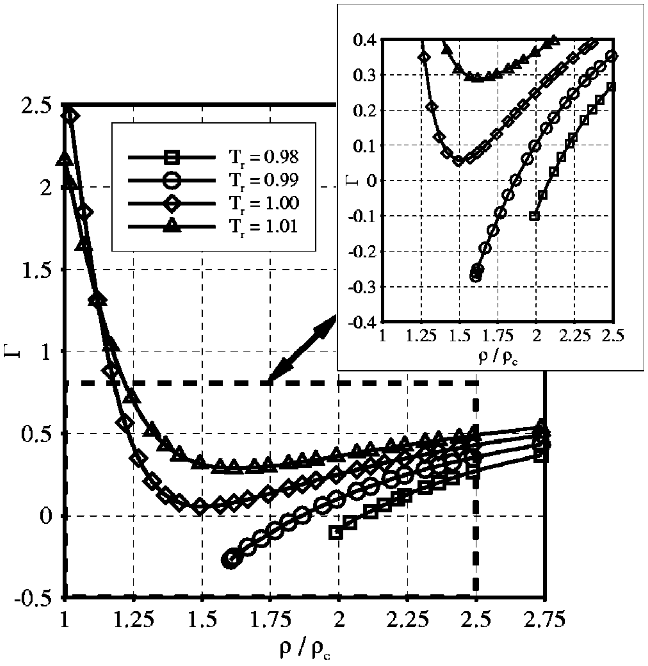

Fig. 11 MD_4M **Γ along several isotherms calculated by STANMIX (PRSV EOS)**

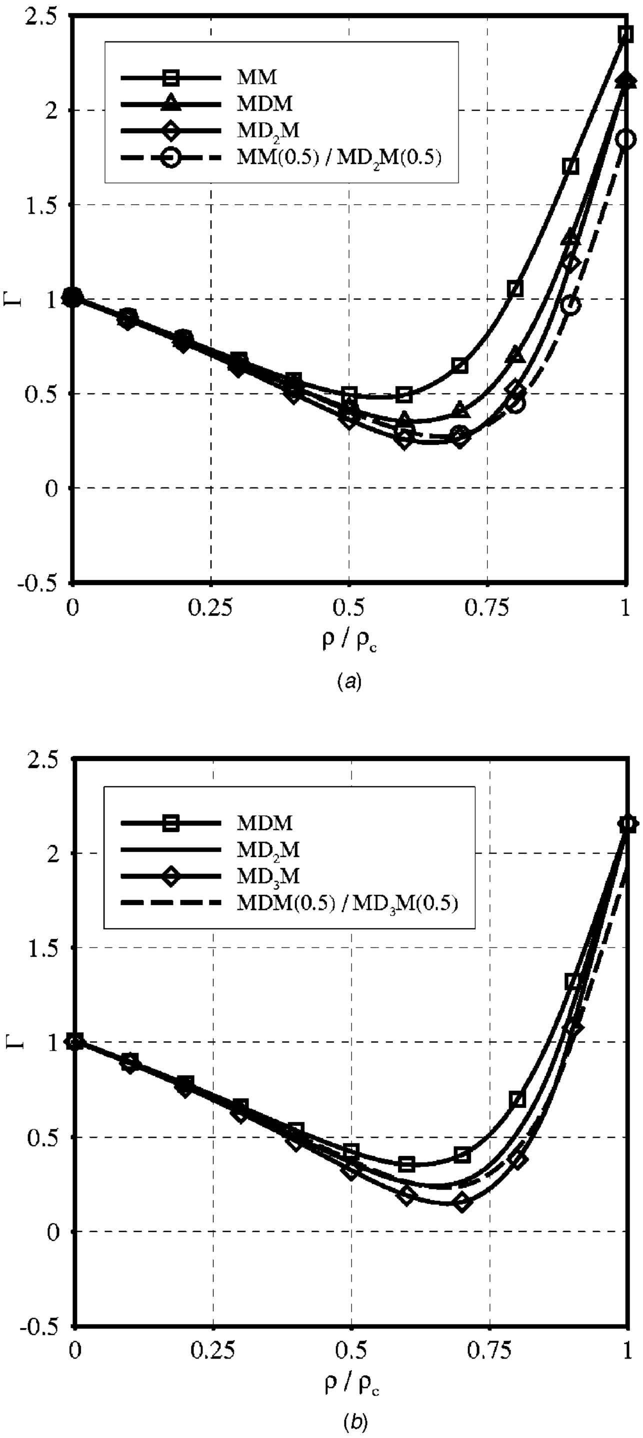

(*a*)

(*b*)

Fig. 12 Γ along the critical isotherm calculated by STANMIX (PRSV EOS) for linear siloxanes. Comparisons between pure fluids and mixtures of the same fluids.

4 Concluding Remarks

Modern numerical schemes for fluid dynamics simulations need complex thermodynamic models if dense or nonclassical gas effects are investigated. Previous work documented the use of Van der Waals or Martin Hou equations of state or other relatively simple models. In this work, the procedures for incorporating more complex EOS and EOS for mixtures in fluid dynamics solvers are presented. In order to speed up calculations, algebraic expressions for nonconventional thermodynamic properties must be

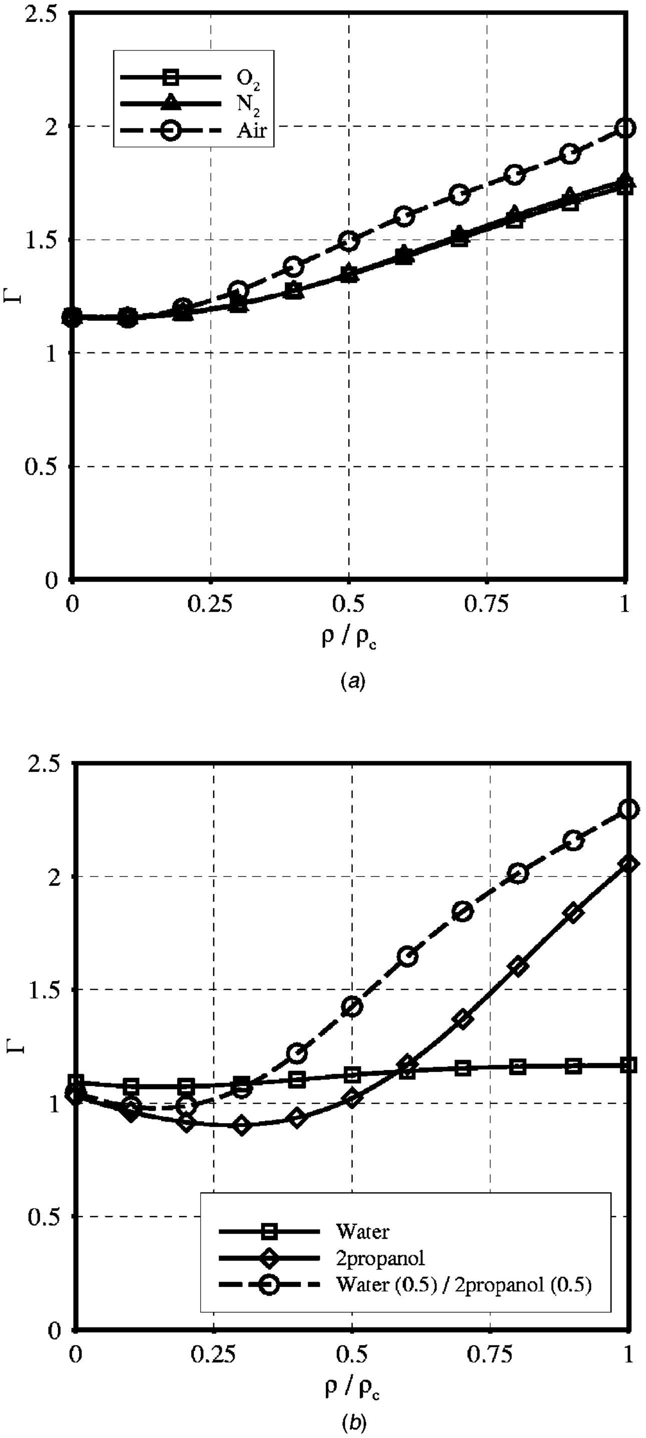

(*a*)

(*b*)

Fig. 13 Γ along the critical isotherm calculated by StanMix (PRSV EOS) for air (*a*) and an equimolar aqueous-2propanol mixture (*b*), a highly nonideal mixture. Air is approximated with a binary mixture of 0.79 nitrogen and 0.21 oxygen (mole fractions).

added to common thermodynamic properties programs. The accuracy of the implemented thermodynamic models can be deduced also from the comparison of sound speed estimates with experimental or reference data. The extension of existing thermodynamic models enable us to treat a wide variety of fluids with the PRSV EOS and a smaller but still considerable set of fluids with more complex EOS. The use of state-of-the art mixing rules extends the cubic equation of state model to ideal and highly nonideal mixtures. The evaluation of the fundamental derivative of gasdynamics Γ for Siloxanes is presented for the first time. Siloxanes form a class of substances of technological interest because they can be used as working fluids in organic Rankine cycles. Some of the linear and cyclic siloxanes and their mixtures exhibit negative Γ regions that could be exploited in the design of more efficient turbines. Results of fluid dynamic simulations of mono and two-dimensional channel configurations will be presented in upcoming publications. An extension of the code to the solution of viscous flows and to multiphase fluids is also planned.

Acknowledgments

The authors are very grateful to their friend and colleague S. Rebay for his advice. We also gratefully recognize Prof. W. C. Reynolds, Mechanical Engineering Department, Stanford University, for his guidance in the initial phase of this project and the permit to extend his software TPSI.

Appendix A

Nonconventional Thermodynamic Functions for Computational Fluid Dynamics From Equations of State

1 Partial Derivatives of Pressure: α and β. The definition of α and β is

$$\alpha=\left(\frac{\partial P}{\partial\rho}\right)_u=-v^2\left(\frac{\partial P}{\partial v}\right)_u, \tag{A1}$$

$$\beta=\left(\frac{\partial P}{\partial u}\right)_\rho=\left(\frac{\partial P}{\partial u}\right)_v. \tag{A2}$$

By using the chain rule expansion, β can be written as

$$\beta=\frac{(\partial P/\partial T)_v}{(\partial u/\partial T)_v}. \tag{A3}$$

Therefore it can be evaluated from a volumetric EOS and the specific heat at constant volume as

$$\beta=\frac{1}{C_v}\left(\frac{\partial P}{\partial T}\right)_v. \tag{A4}$$

The relation between α, c, and β can be obtained as shown in the following. Using the chain rule expansion yields

$$\begin{gathered}\left(\frac{\partial P}{\partial v}\right)_u\left(\frac{\partial v}{\partial u}\right)_P\left(\frac{\partial u}{\partial P}\right)_v=-1,\\ \left(\frac{\partial P}{\partial v}\right)_u=-\left(\frac{\partial u}{\partial v}\right)_P\left(\frac{\partial P}{\partial u}\right)_v=-\left(\frac{\partial u}{\partial v}\right)_P\beta.\end{gathered} \tag{A5}$$

Therefore α can be written as

$$\alpha=v^2\beta\left(\frac{\partial u}{\partial v}\right)_P. \tag{A6}$$

The latter partial derivative can be written as

$$\left(\frac{\partial u}{\partial v}\right)_P=\frac{(\partial u/\partial T)_P}{(\partial v/\partial T)_P}, \tag{A7}$$

and from usual thermodynamic derivation,

$$\left(\frac{\partial u}{\partial T}\right)_P=C_v+\left[T\left(\frac{\partial P}{\partial T}\right)_v-P\right]\left(\frac{\partial v}{\partial T}\right)_P. \tag{A8}$$

By substituting Eq. (*A*7) in Eq. (*A*6) and simplifying, the expression for α becomes

$$\alpha=v^2\beta\left[\frac{C_v}{(\partial v/\partial T)_P}+T\left(\frac{\partial P}{\partial T}\right)_v-P\right]. \tag{A9}$$

Using the chain rule yields

$$\left(\frac{\partial v}{\partial T}\right)_P=-\left(\frac{\partial P}{\partial T}\right)_v\left(\frac{\partial v}{\partial P}\right)_T. \tag{A10}$$

By recalling that the relation between C_P and C_v is

$$C_P=C_v-\frac{T(\partial P/\partial T)_v^2}{(\partial P/\partial v)_T}, \tag{A11}$$

the following expression is obtained:

$$\left(\frac{\partial v}{\partial P}\right)_T=\frac{C_v-C_P}{T(\partial P/\partial T)_v^2}. \tag{A12}$$

Substituting Eq. (A12) in Eq. (A10) yields

$$\left(\frac{\partial v}{\partial T}\right)_P=\frac{C_P-C_v}{T(\partial P/\partial T)_v}. \tag{A13}$$

From Eq. (2.8), the specific volume can be written as

$$v^2=-\frac{c^2}{\gamma(\partial P/\partial v)_T}, \tag{A14}$$

therefore substituting Eq. (A13), Eq. (A4), and Eq. (A14) in Eq. (A9) yields

$$\alpha=-\frac{c^2}{\gamma(\partial P/\partial v)_T}\frac{1}{C_v}\left(\frac{\partial P}{\partial T}\right)_v\left[\frac{C_vT(\partial P/\partial T)_v}{C_P-C_v}+T\left(\frac{\partial P}{\partial T}\right)_v\right]-\beta Pv^2. \tag{A15}$$

By carrying out straightforward simplifications and by recalling that

$$C_P-C_v=-T\left(\frac{\partial P}{\partial T}\right)_v^2\left(\frac{\partial v}{\partial P}\right)_T, \tag{A16}$$

the following expression is finally obtained:

$$\alpha=c^2-\beta Pv^2. \tag{A17}$$

2 Partial Derivatives of Entropy: χ and ϕ. The definition of χ and ϕ is

$$\chi=\left(\frac{\partial s}{\partial \rho}\right)_u=-v^2\left(\frac{\partial s}{\partial v}\right)_u \tag{A18}$$

$$\phi=\left(\frac{\partial s}{\partial u}\right)_\rho=\left(\frac{\partial s}{\partial u}\right)_v. \tag{A19}$$

The differential of entropy can be expressed as

$$ds=\frac{1}{T}du-\frac{P}{T}dv.$$

Therefore,

$$\left(\frac{\partial s}{\partial v}\right)_u=\frac{P}{T},$$

$$\left(\frac{\partial s}{\partial u}\right)_v=\frac{1}{T},$$

$$\chi=-v^2\frac{P}{T}, \tag{A20}$$

$$\phi=\frac{1}{T}. \tag{A21}$$

3 The Fundamental Derivative of Gas Dynamics: Γ. The expression of Γ in terms which allow its calculation from a volumetric EOS is reported, for instance, in Refs. [23], [60]. We hereby report its derivation.

The parameter Γ is defined as

$$\Gamma=1+\frac{\rho}{c}\left(\frac{\partial c}{\partial \rho}\right)_s=\frac{v^3}{2c^2}\left(\frac{\partial^2 P}{\partial v^2}\right)_s. \tag{A22}$$

The composite derivative rule applied to $(\partial^2P/\partial v^2)_s$ can explicitly be written as

$$\left[\frac{\partial}{\partial v}\left(\frac{\partial P}{\partial v}\right)_s\right]_s=\left(\frac{\partial^2 P}{\partial v^2}\right)_s=\left[\frac{\partial}{\partial v}\left(\frac{\partial P}{\partial v}\right)_s\right]_T+\left[\frac{\partial}{\partial T}\left(\frac{\partial P}{\partial v}\right)_s\right]_v\left(\frac{\partial T}{\partial v}\right)_s.$$

Substituting for $(\partial^2P/\partial v^2)_s$ the following expression is obtained:

$$\begin{aligned}\left(\frac{\partial^2 P}{\partial v^2}\right)_s&=\frac{\partial}{\partial v}\left[\left(\frac{\partial P}{\partial T}\right)_v\left(\frac{\partial T}{\partial v}\right)_s+\left(\frac{\partial P}{\partial v}\right)_T\right]_T\\&\quad+\left\{\frac{\partial}{\partial T}\left[\left(\frac{\partial P}{\partial T}\right)_v\left(\frac{\partial T}{\partial v}\right)_s+\left(\frac{\partial P}{\partial v}\right)_T\right]_v\right\}\left(\frac{\partial T}{\partial v}\right)_s\\&=\left(\frac{\partial^2 P}{\partial v\,\partial T}\right)_{v,T}\left(\frac{\partial T}{\partial v}\right)_s+\frac{\partial}{\partial v}\left[\left(\frac{\partial T}{\partial v}\right)_s\right]_T\left(\frac{\partial P}{\partial T}\right)_v+\left(\frac{\partial^2 P}{\partial v^2}\right)_T\\&\quad+\left(\frac{\partial^2 P}{\partial T^2}\right)_v\left(\frac{\partial T}{\partial v}\right)_s^2+\left(\frac{\partial^2 P}{\partial v\,\partial T}\right)_{v,T}\left(\frac{\partial T}{\partial v}\right)_s\\&\quad+\left(\frac{\partial P}{\partial T}\right)_v\frac{\partial}{\partial T}\left[\left(\frac{\partial T}{\partial v}\right)_s\right]_v\left(\frac{\partial T}{\partial v}\right)_s\\&=2\left(\frac{\partial^2 P}{\partial v\,\partial T}\right)_{v,T}\left(\frac{\partial T}{\partial v}\right)_s+\frac{\partial}{\partial v}\left[\left(\frac{\partial T}{\partial v}\right)_s\right]_T\left(\frac{\partial P}{\partial T}\right)_v+\left(\frac{\partial^2 P}{\partial v^2}\right)_T\\&\quad+\left(\frac{\partial^2 P}{\partial T^2}\right)_v\left(\frac{\partial T}{\partial v}\right)_s^2+\left(\frac{\partial P}{\partial T}\right)_v\frac{\partial}{\partial T}\left[\left(\frac{\partial T}{\partial v}\right)_s\right]_v\left(\frac{\partial T}{\partial v}\right)_s.\end{aligned} \tag{A23}$$

From usual thermodynamic derivation,

$$\left(\frac{\partial T}{\partial v}\right)_s=-\frac{T}{C_v}\left(\frac{\partial P}{\partial T}\right)_v. \tag{A24}$$

Equation (A24) can be substituted in Eq. (A23) and the following expression is obtained:

$$\begin{aligned}\left(\frac{\partial^2 P}{\partial v^2}\right)_s&=-2\frac{T}{C_v}\left(\frac{\partial^2 P}{\partial v\,\partial T}\right)_{v,T}\left(\frac{\partial P}{\partial T}\right)_v+\frac{\partial}{\partial v}\left[-\frac{T}{C_v}\left(\frac{\partial P}{\partial T}\right)_v\right]_T\left(\frac{\partial P}{\partial T}\right)_v\\&\quad+\left(\frac{\partial^2 P}{\partial v^2}\right)_T+\left(\frac{\partial^2 P}{\partial T^2}\right)_v\left[-\frac{T}{C_v}\left(\frac{\partial P}{\partial T}\right)_v\right]^2\\&\quad+\left(-\frac{T}{C_v}\right)\left(\frac{\partial P}{\partial T}\right)_v^2\frac{\partial}{\partial T}\left[-\frac{T}{C_v}\left(\frac{\partial P}{\partial T}\right)_v\right]_v.\end{aligned}$$

By developing the partial derivatives and appropriately collecting terms, $(\partial^2P/\partial v^2)_s$ can be written as

$$\begin{aligned}\left(\frac{\partial^2 P}{\partial v^2}\right)_s&=\left(\frac{\partial^2 P}{\partial v^2}\right)_T-3\frac{T}{C_v}\left(\frac{\partial P}{\partial T}\right)_v\left(\frac{\partial^2 P}{\partial v\,\partial T}\right)_{v,T}+3\frac{T}{C_v^2}\left(\frac{\partial P}{\partial T}\right)_v^2\left(\frac{\partial C_v}{\partial v}\right)_T\\&\quad+\frac{T}{C_v^2}\left(\frac{\partial P}{\partial T}\right)_v^3\left[1-\frac{T}{C_v}\left(\frac{\partial C_v}{\partial T}\right)_v\right].\end{aligned}$$

Furthermore, the partial derivative of the specific heat with respect to the specific volume at constant temperature can be expressed as

$$\left(\frac{\partial C_v}{\partial v}\right)_T=\frac{\partial}{\partial v}\left[\left(\frac{\partial u}{\partial T}\right)_v\right]_T=\frac{\partial}{\partial T}\left[\left(\frac{\partial u}{\partial v}\right)_T\right]_v$$

$$=\frac{\partial}{\partial T}\left[T\left(\frac{\partial P}{\partial T}\right)_v-P\right]_v=T\left(\frac{\partial^2 P}{\partial T^2}\right)_v .$$

Therefore the final expression for $(\partial^2 P/\partial v^2)_s$ is

$$\left(\frac{\partial^2 P}{\partial v^2}\right)_s=\left(\frac{\partial^2 P}{\partial v^2}\right)_T-3\frac{T}{C_v}\left(\frac{\partial P}{\partial T}\right)_v\left(\frac{\partial^2 P}{\partial v\,\partial T}\right)_{v,T}+3\frac{T^2}{C_v^2}\left(\frac{\partial P}{\partial T}\right)_v^2\left(\frac{\partial^2 P}{\partial T^2}\right)_v$$

$$+\frac{T}{C_v^2}\left(\frac{\partial P}{\partial T}\right)_v^3\left[1-\frac{T}{C_v}\left(\frac{\partial C_v}{\partial T}\right)_v\right]$$

$$=\left(\frac{\partial^2 P}{\partial v^2}\right)_T-3\frac{T}{C_v}\left(\frac{\partial P}{\partial T}\right)_v\left(\frac{\partial^2 P}{\partial v\,\partial T}\right)_{v,T}+\left[\frac{T}{C_v}\left(\frac{\partial P}{\partial T}\right)_v\right]^2$$

$$\times\left\{3\left(\frac{\partial^2 P}{\partial T^2}\right)_v+\frac{1}{T}\left(\frac{\partial P}{\partial T}\right)_v\left[1-\frac{T}{C_v}\left(\frac{\partial C_v}{\partial T}\right)_v\right]\right\}. \qquad (A25)$$

This expression compares with the one reported in Ref. [60].

By recalling that

$$C_v=C_v^0(T)+T\int_\infty^v\left(\frac{\partial^2 P}{\partial T^2}\right)_v dv \qquad (A26)$$

and

$$\left(\frac{\partial C_v}{\partial T}\right)_v=\frac{dC_v^0}{dT}+\frac{\partial}{\partial T}\left[T\int_\infty^v\left(\frac{\partial^2 P}{\partial T^2}\right)_v dv\right]_v, \qquad (A27)$$

the fundamental derivative of gasdynamics can be obtained analytically from an equation of state in the classical form $P=P(v,T)$ and by $C_v^0(T)$ or $C_p^0(T)$ as follows:

$$\Gamma=\frac{v^3}{2c^2}\left\{\left(\frac{\partial^2 P}{\partial v^2}\right)_T-3\frac{T}{C_v}\left(\frac{\partial P}{\partial T}\right)_v\left(\frac{\partial^2 P}{\partial v\,\partial T}\right)_{v,T}\right.$$

$$\left.+\left[\frac{T}{C_v}\left(\frac{\partial P}{\partial T}\right)_v\right]^2\left\{3\left(\frac{\partial^2 P}{\partial T^2}\right)_v+\frac{1}{T}\left(\frac{\partial P}{\partial T}\right)_v\left[1-\frac{T}{C_v}\left(\frac{\partial C_v}{\partial T}\right)_v\right]\right\}\right\}. \qquad (A28)$$

Appendix B

Nonconventional Thermodynamic Functions for Computational Fluid Dynamics for Several Equations of State

1. PRSV Equations of State. The Peng-Robinson equation of state is

$$P=\frac{RT}{(v-b)}-\frac{a(T)}{v(v+b)+b(v-b)}. \qquad (B1)$$

The parameter a introduced in the Styjeck-Vera modification of the PR EOS is given by

$$a(T)=a_c\times\alpha(T),$$

where

$$a_c=0.457235\frac{R^2T_c}{P_c},$$

$$\alpha(T)=[1+k(1-T_r^{0.5})]^2,$$

$$k=k_0+k_1(1+T_r^{0.5})(0.7-T_r)\quad\text{for}\quad T_r<1;\quad k_1=0\quad\text{for}\quad T_r\geqslant 1,$$

$$k_0=0.378893+1.4897153\omega-0.17131848\omega^2+0.0196554\omega^3.$$

T_c is the critical temperature and $T_r=T/T_c$. k_1 is obtained from saturation-pressure fitting of experimental data or from fitting values to an accurate $P^{\text{sat}}=P(T^{\text{sat}})$ equation.

For a pure fluid the parameter b is not a function of temperature, while for a mixture, the mixing rules introduce a weak dependence on T. For this reason the pressure derivatives for a pure fluid differ from the mixtures ones.

The derivatives of P with respect to v at constant T is the same for pure fluids and multicomponent fluids:

$$\left(\frac{\partial P}{\partial v}\right)_T=\frac{-RT}{(b-v)^2}+\frac{2a(b+v)}{(v^2+2bv-b^2)}, \qquad (B2)$$

$$\left(\frac{\partial^2 P}{\partial v^2}\right)_T=2\left(\frac{RT}{(v-b)^3}-\frac{a(3v^2+6vb+5b^2)}{(v^2+2vb-b^2)^3}\right). \qquad (B3)$$

The derivatives of P with respect to T at constant v are different depending on the single-component or multicomponent case. For a pure fluid,

$$\left(\frac{\partial P}{\partial T}\right)_v=\frac{R}{(b-v)}+\frac{a'(T)}{(b^2-2bv-v^2)}, \qquad (B4)$$

$$\left(\frac{\partial^2 P}{\partial T^2}\right)_v=-\frac{a''(T)}{b(v-b)+v(v+b)}, \qquad (B5)$$

$$\left(\frac{\partial^2 P}{\partial v\,\partial T}\right)_{T,v}=-\frac{RT}{(v-b)^2}+2a'(T)\frac{2(v+b)}{(v^2+2vb-b^2)^2}. \qquad (B6)$$

The derivatives of $a(T)$ are omitted for brevity. The integral for the real gas correction is given by

$$\int_\infty^v\left(\frac{\partial^2 P}{\partial T^2}\right)_v dv=a''(T)\frac{\operatorname{Log}\left[\dfrac{z+(1+\sqrt{2})B}{Z+(1-\sqrt{2})B}\right]}{2\sqrt{2}b} \qquad (B7)$$

with

$$Z=\frac{Pv}{RT};\quad B=\frac{bRT}{P}. \qquad (B8)$$

For the expression of $(\partial C_v/\partial T)_v$, it is useful to define

$$Y=\frac{Z+(1+\sqrt{2})B}{Z+(1-\sqrt{2})B}. \qquad (B9)$$

The partial derivative of the specific heat with respect to T at constant v is given by

$$\left(\frac{\partial C_v}{\partial T}\right)_v=\frac{dC_v^0}{dT}+\frac{1}{2\sqrt{2}b}\operatorname{Log}(Y)(Ta'''(T)+a''(T))$$

$$+\frac{T}{2\sqrt{2}bY}a''(T)\frac{\partial Y}{\partial T} \qquad (B10)$$

with

$$\frac{\partial Y}{\partial T}=\frac{\partial Z/\partial T+(1+\sqrt{2})\partial B/\partial T}{Z-(\sqrt{2-1})B}$$

$$-\frac{[Z+(1+\sqrt{2})B][\partial Z/\partial T+(1-\sqrt{2})\partial B/\partial T]}{[Z-(\sqrt{2-1})B]^2}.$$

2 PRSV EOS and WS Mixing Rules. The WS mixing rules for the a and b parameters are given by

$$b_{\text{mixture}}=\frac{Q}{1-D}, \qquad (B12)$$

$$a_{\text{mixture}}=RT\frac{QD}{1-D}, \qquad (B13)$$

where

$$Q=\sum_i \sum_j x_i x_j \left(b-\frac{a}{RT}\right)_{i,j}, \tag{B14}$$

$$D=\sum_i x_i \frac{a_i}{b_i RT}+\frac{G^E_{P\to 0}}{RT}. \tag{B15}$$

In the above expression, a_i and b_i are the CEOS coefficients for the pure components and x_i are the mole fractions of the components. The excess Gibbs energy at low pressure, $G^E_{P\to 0}$, must be determined from a low pressure liquid activity coefficient model. The binary interaction parameter, k_{ij} contained in the combining rule

$$b_{ij}-\frac{a_{ij}}{RT}=\left[\left(b_i-\frac{a_i}{RT}\right)+\left(b_j-\frac{a_j}{RT}\right)\right]\frac{(1-k_{ij})}{2}, \tag{B16}$$

must be computed from the same liquid model.

The derivatives of P with respect to T at constant v for a multicomponent fluid are given by

$$\left(\frac{\partial P}{\partial T}\right)_v=\frac{RTb'(T)}{(b-v)^2}+\frac{R}{(b-v)}+\frac{a'(T)}{(b^2-2bv-v^2)}-\frac{2a(b-v)b'(T)}{(v^2+2bv-b^2)^2}, \tag{B17}$$

$$\begin{aligned}\left(\frac{\partial^2 P}{\partial T^2}\right)_v=&\frac{2Rb'(T)}{(v-b)^2}+\frac{2RT(b'(T))^2}{(v-b)^3}\\&+\frac{2a'(T)[vb'(T)+(v-b)b'(T)-bb'(T)]}{[(v-b)b+v(v+b)]^2}\\&-\frac{a''(T)}{(v-b)b+v(v+b)}+\frac{RTb''(T)}{(v-b)^2}\\&+\frac{a[-2(b'(T))^2+vb''(T)+(v-b)b''(T)-bb''(T)]}{[b(v-b)+v(v+b)]^2},\end{aligned} \tag{B18}$$

$$\left(\frac{\partial^2 P}{\partial v\,\partial T}\right)_{T,v}=-\frac{RT}{(v-b)^2}+\frac{2(v+b)a'(T)}{(v^2+2vb-b^2)^2}-\frac{2[a(v-b)^3(3v^2-2vb-3b^2)+RT(v^2+2vb-b^2)^3]b'(T)}{(v^3+v^2b-3vb^2+b^3)^3}. \tag{B19}$$

The temperature derivatives of the a and b parameters for the PRSV EOS and the WS mixing rules can be expressed as follows:

$$W_1=Q\cdot D+D\cdot T\cdot Q'(T)+D'(T)\cdot Q\cdot T, \tag{B20}$$

$$W_2=T\cdot Q\cdot D\cdot D'(T), \tag{B21}$$

$$W_3=1-D, \tag{B22}$$

$$b'(T)=\frac{W_1}{W_3}+\frac{W_2}{W_3^2}, \tag{B23}$$

$$a'(T)=R\left(\frac{W_1}{W_3}+\frac{W_2}{W_3^2}\right)=Rb'(T). \tag{B24}$$

The second temperature derivatives of a and b are omitted for brevity. They can be obtained in a similar way.

The derivatives of Q and D are given by

$$D'(T)=\sum_i x_i\frac{(-a_i+Ta_i'(T))}{b_iRT^2}-\frac{g^E_{\mathrm{low}P}(x_i)}{\sigma RT^2}, \tag{B25}$$

$$Q'(T)=\sum_i\sum_j\frac{1}{2RT}\left(\frac{a_i+a_j}{T}-a_i'(T)-a_j'(T)\right)x_ix_j(1-k_{i,j}), \tag{B26}$$

$$D''(T)=\sum_i x_i\left[\frac{1}{b_iRT}a_i''(T)-\frac{2}{b_iRT^3}(Ta_i'(T)-a_i)\right]+\frac{g^E_{\mathrm{low}P}(x_i)}{\sigma RT^3}, \tag{B27}$$

$$Q''(T)=\sum_i\sum_j\frac{1}{RT}\left[(a_i'(T)-a_j'(T))\frac{1}{T}-(a_i''(T)-a_j''(T))\frac{1}{2}-\frac{a_i+a_j}{T^2}\right]x_ix_j(1-k_{i,j}). \tag{B28}$$

By imposing that b does not depend on the temperature, the expression valid for pure fluids is obtained.

The integral for the real gas correction is given by

$$\begin{aligned}\int_\infty^v\left(\frac{\partial^2 P}{\partial T^2}\right)_v dv=&-\frac{RT(b'(T))^2}{(b-v)^2}+\frac{R[2b'(T)+Tb''(T)]}{(b-v)}-\frac{2a(b'(T))^2(b-3v)}{(v^2+2bv-b^2)^2}\\&+\frac{2bva'(T)b'(T)+(bvb''(T)-2b(b'(T))^2-2v(b'(T))^2)}{b^2(v^2+2bv-b^2)^2}+\frac{b^2a''(T)+2a(b'(T))^2-b[ab''(T)+2a'(T)b'(T)]}{2\sqrt{2}2b^3}\\&\times\mathrm{Log}\left[\frac{Z+(1+\sqrt{2})B}{Z+(1-\sqrt{2})B}\right].\end{aligned} \tag{B29}$$

For the computation of the fundamental derivative of gas dynamics, the partial derivative $(\partial C_v/\partial T)_v$ must also be computed. This derivative involves, furthermore, the computation of $a'''(T)$, $b'''(T)$. In this case the use of a software for automated symbolical computation is mandatory and the resulting expressions are omitted for brevity.

3 Starling EOS. The Starling EOS is in the form

$$P=\rho RT+\left(B_0RT-A_0-\frac{C_0}{T^2}+\frac{D_0}{T^3}+\frac{E_0}{T^4}\right)\rho^2+\left(bRT-a-\frac{b}{T}\right)\rho^3+\alpha\left(a+\frac{d}{T}\right)\rho^6+c\,\frac{\rho^3}{T^2}(1+\theta\rho^2)e^{-\theta\rho^2}. \tag{B30}$$

All thermodynamic functions can be expressed starting from the following expressions:

$$\left(\frac{\partial P}{\partial v}\right)_T=-\frac{RT}{v^2}-2\,\frac{B_0RT-A_0-\frac{C_0}{T^2}+\frac{D_0}{T^3}-\frac{E_0}{T^4}}{v^3}-3\,\frac{bRT-a-\frac{d}{T}}{v^4}-6\,\frac{\alpha\left(a+\frac{d}{T}\right)}{v^7}-3\,\frac{c\left(1+\frac{\theta}{v^2}\right)e^{-\theta/v^2}}{v^4T^2}-2\,\frac{c\,\theta e^{-\theta/v^2}}{v^6T^2}+2\,\frac{c\left(1+\frac{\theta}{v^2}\right)\theta e^{-\theta/v^2}}{v^6T^2}, \tag{B31}$$

$$\left(\frac{\partial P}{\partial T}\right)_v=\frac{T}{v}+\frac{B_0R+2\,\frac{C_0}{T^3}-3\,\frac{D_0}{T^4}+4\,\frac{E_0}{T^5}}{v^2}+\frac{bR-\frac{d}{T^2}}{v^3}-\frac{\alpha d}{T^2v^6}-2\,\frac{c\left(1+\frac{\theta}{v^2}\right)e^{-\theta/v^2}}{v^3T^3}, \tag{B32}$$

$$\left(\frac{\partial^2 P}{\partial T^2}\right)_v=\frac{-6\,\frac{C_0}{T^4}+12\,\frac{D_0}{T^5}-20\,\frac{E_0}{T^6}}{v^2}-\frac{2d}{T^3v^3}+\frac{2\alpha d}{T^3v^6}+6\,\frac{c\left(1+\frac{\theta}{v^2}\right)e^{-\theta/v^2}}{v^3T^4}, \tag{B33}$$

$$\left(\frac{\partial^2 P}{\partial v^2}\right)_T=2\,\frac{RT}{v^3}+6\,\frac{B_0RT-A_0-\frac{C_0}{T^2}+\frac{D_0}{T^3}-\frac{E_0}{T^4}}{v^4}+12\,\frac{bRT-a-\frac{d}{T}}{v^5}+42\,\frac{\alpha\left(a+\frac{d}{T}\right)}{v^8}+12\,\frac{c\left(1+\frac{\theta}{v^2}\right)e^{-\theta/v^2}}{v^5T^2}+18(1-\theta)\,\frac{c\,\theta e^{-\theta/v^2}}{v^7T^2}-\left(1+\frac{\theta}{v^2}\right)\frac{4ce^{-\theta/v^2}}{v^9T^2}\,\theta, \tag{B34}$$

$$\left(\frac{\partial^2 P}{\partial v\,\partial T}\right)_{T,v}=-\frac{R}{v^2}-\frac{2}{v^3}\left(B_0R+\frac{2C_0}{T^3}-\frac{3D_0}{T^4}+\frac{4E_0}{T^5}\right)-\frac{3}{v^4}\,\frac{\alpha d}{T^2v^7}+\frac{6}{v^4T^3}\left(1+\frac{\theta}{v^2}\right)e^{-\theta/v^2}-\frac{4}{v^6T^3}\,c\,\theta e^{-\theta/v^2}\frac{\theta}{v^2}, \tag{B35}$$

$$\int_\infty^v\left(\frac{\partial^2 P}{\partial T^2}\right)_v dv=-\frac{6c}{\theta T^4}+\frac{e^{-\theta/v^2}}{5\,\theta T^6v^5}(30v^4C_0T^2\theta e^{\theta/v^2}-60v^4D_0T\theta e^{\theta/v^2}+100v^4E_0\theta e^{\theta/v^2}+5dT^3v^3\theta e^{\theta/v^2}-2\,\alpha dT^3\theta e^{\theta/v^2}+30cT^2v^5+15cT^2v^3\theta). \tag{B36}$$

The expression for $(\partial C_v/\partial T)_v$ is omitted because it is too lengthy.

4 Martin-Hou EOS. The Martin-Hou EOS is in the form

$$P=\frac{RT}{v-b}+\sum_{i=2}^{5}\frac{1}{(v-b)^i}(A_i+B_iT+C_ie^{-kT/T_C})+\frac{A_6+B_6T+C_6e^{-kT/T_C}}{e^{\alpha v}(1+ce^{\alpha v})}. \tag{B37}$$

All thermodynamic functions can be expressed starting from the following expressions:

$$\left(\frac{\partial P}{\partial v}\right)_T=-\frac{Rt}{(v-b)^2}-\sum_{i=2}^{5}\frac{i}{(v-b)^{i+1}}(A_i+B_iT+C_ie^{-kT/T_C})-\frac{\alpha(A_6+B_6T+C_6e^{-kT/T_C})}{e^{\alpha v}}, \tag{B38}$$

$$\left(\frac{\partial P}{\partial T}\right)_v=\frac{RT}{v-b}+\sum_{i=2}^{5}\frac{1}{(v-\mathbf{n})^i}\left(B_i-\frac{C_ike^{-kT/T_C}}{T_C}\right)+\frac{1}{e^{\alpha v}}\left(B_6-\frac{C_6ke^{-kT/T_C}}{T_C}\right), \tag{B39}$$

$$\left(\frac{\partial^2 P}{\partial T^2}\right)_v=\sum_{i=2}^{5}\frac{1}{(v-b)^i}\left(\frac{C_ik^2e^{-kT/T_C}}{T_C^2}\right)+\frac{C_6k^2e^{-kT/T_C}}{T_C^2e^{\alpha v}}, \tag{B40}$$

$$\left(\frac{\partial^2 P}{\partial v^2}\right)_T=2\,\frac{RT}{(v-b)^3}+\sum_{i=2}^{5}\frac{i^2+i}{(v-b)^{i+2}}(A_i+B_iT+C_ie^{-kT/T_C})+\alpha^2\frac{A_6+B_6T+C_6e^{-kT/T_C}}{e^{\alpha v}}, \tag{B41}$$

$$\left(\frac{\partial^2 P}{\partial v\,\partial T}\right)_{T,v}=-\frac{RT}{(v-b)^2}-\sum_{i=2}^{5}\frac{i}{(v-b)^{i+1}}\left(B_i-\frac{C_ike^{-kT/T_C}}{T_C}\right)-\frac{\alpha}{e^{\alpha v}}\left(B_6-\frac{C_6ke^{-kT/T_C}}{T_C}\right), \tag{B42}$$

$$\left(\frac{\partial^2 P}{\partial T^2}\right)_v=\sum_{i=2}^{5}\frac{1}{(v-b)^i}\left(\frac{C_ik^2e^{-kT/T_C}}{T_C^2}\right)+\frac{C_6k^2e^{-kT/T_C}}{T_C^2e^{\alpha v}}, \tag{B43}$$

$$\int_\infty^v\left(\frac{\partial^2 P}{\partial T^2}\right)_v dv=-\frac{1}{12}k^2[(12C_2v^3-36C_2v^2b+36C_2vb^2-12C_3b^3+6C_3v^2-12C_3vb+6C_3b^2+4C_4v-4C_4b+3C_5)e^{\alpha v}\alpha+12C_6v^4-48C_6v^3b+72C_6v^2b^2-48C_6vb^3+12C_6b^4]\,\frac{e^{(-kT+v\alpha T_C/T_C)}}{[(b-v)^4T_C^2\alpha]}. \tag{B44}$$

Note that the above expression is valid if $\alpha>0$ or $\alpha=0$ and $C_6=0$. This is verified for all fluids in the TPSI database. The expression for $(\partial C_v/\partial T)_v$ is omitted for brevity.

References

[1] Wagner, B., and Schmidt, W., 1978, ''Theoretical Investigation of Real Gas Effects in Cryogenic Wind Tunnels,'' AIAA J., **16**, pp. 580–586.

[2] Anderson, W. K., May 1991, ''Numerical Study of the Aerodynamic Effects of Using Sulfur Hexafluoride as a Test Gas in Wind Tunnels,'' NASA Technical Paper 3086, NASA Langley Research Center, Hampton, VA.

[3] Anders, J. B., Anderson, W. K., and Murthy, A. V., 1999, ''Transonic Similarity Theory Applied to a Supercritical Airfoil in Heavy Gases,'' J. Aircr., **36**, Nov–Dec, pp. 957–964.

[4] Korte, J. J., 2000, ''Inviscid Design of Hypersonic Wind Tunnel Nozzles for Real Gas,'' E. Camhi, ed., *Proceedings of the 38th Aerospace Sciences Meeting and Exhibit*, Reno, NV, Jan. 10–13, AIAA, Reston, VA, pp. 1–8.

[5] Bober, W., and Chow, W. L., 1990, ''Nonideal Isentropic Gas Flow Through Converging-Diverging Nozzles,'' ASME J. Fluids Eng., **112**, pp. 455–460.

[6] Dziedzidzic, W. M., Jones, S. C., Gould, D. C., and Petley, D. H., 1993, ''Analytical Comparison of Convective Heat Transfer Correlation in Supercritical Hydrogen,'' J. Thermophys. Heat Transfer, **7**, pp. 68–73.

[7] Brown, B. P., and Argrow, B. M., 2000, ''Application of Bethe-Zel'dovic-Thompson Fluids in Organic Rankine Cycle Engines,'' J. Propul. Power., **16** Nov–Dec, pp. 1118–1123.

[8] Angelino, G., and Colonna, P., 1998, ''Multicomponent Working Fluids for Organic Rankine Cycles (ORCs),'' Energy, **23**, pp. 449–463.

[9] Schnerr, G. H., and Leidner, P., 1993, ''Numerical Investigation of Axial Cascades for Dense Gases.'' E. L. Chin, ed., *PICAST'1—Pacific International Conference on Aerospace Science Technology*, Vol. 2, National Cheng Kung University, Publ., Taiwan, pp. 818–825.

[10] Monaco, J. F., Cramer, M. S., and Watson, L. T., 1997, ''Supersonic Flows of Dense Gases in Cascade Configurations,'' J. Fluid Mech., **330**, pp. 31–59.

[11] Angelino, G., and Invernizzi, C., 1996, ''Potential Performance of Real Gas Stirling Cycles Heat Pumps,'' Int. J. Refrig., **19**, p. 390.

[12] Angelino, G., and Invernizzi, C., 2000, ''Real Gas Effects in Stirling Engines,'' *35th Intersociety Energy Conversion Engineering (IECEC)*, Las Vegas, NV July, AIAA, Reston, VA, pp. 69–75.

[13] Fitzgerald, R., 1999, ''Traveling Waves Thermoacustic Heat Engines Attain High Efficiency,'' Phys. Today, **52**, pp. 18–20.

[14] Glaister, P., 1988, ''An Approximate Linearized Riemann Solver for the Euler Equations for Real Gases,'' J. Comput. Phys., **74**, pp. 382–408.

[15] Grossmann, B., and Walters, R. W., 1989, ''Analysis of the Flux-Split Algorithms for Euler's Equations With Real Gases,'' AIAA J., **27**, pp. 524–531.

[16] Vinokur, M., and Montagne', J. L., 1990, ''Generalized Flux-Vector Splitting and Roe Average for an Equilibrium Real Gas,'' J. Comput. Phys., **89**, pp. 276–300.

[17] Liou, M.-S., van Leer, B., and Shuen, J.-S., 1990, ''Splitting of Inviscid Fluxes for Real Gases,'' J. Comput. Phys., **87**, pp. 1–24.

[18] Mottura, L., Vigevano, L., and Zaccanti, M., 1997, ''An Evaluation of Roe's Scheme Generalizations for Equilibrium Real Gas Flows,'' J. Comput. Phys., **138**, pp. 354–339.

[19] Guardone, A., Selmin, V., and Vigevano, L., 1999, ''An Investigation of Roe's Linearization and Average for Ideal and Real Gases,'' Scientific Report DIA-SR 99-01, Politecnico di Milano, Dipartimento di Ingegneria Aerospaziale, Jan.

[20] Drikakis, D., and Tsangaris, S., 1993, ''Real Gas Effects for Compressible Nozzle Flows,'' ASME J. Fluids Eng., **115**, pp. 115–120.

[21] Cravero, C., and Satta, A., 2000, ''A CFD Model for Real Gas Flows,'' ASME Turbo Expo, Munich, May, ASME, New York, pp. 1–10.

[22] Aungier, R. H., 1995, ''A Fast, Accurate Real Gas Equation of State for Fluid Dynamic Analysis Applications,'' ASME J. Fluids Eng., **117**, pp. 277–281.

[23] Cramer, M. S., 1991, *Nonclassical Dynamics of Classical Gases* (Nonlinear Waves in Real Fluids) International Center for Mechanical Sciences, Courses and Lectures, Springer-Verlag, Berlin.

[24] Aldo, A. C., and Argrow, B. M., 1994, ''Dense Gas Flows in Minimum Lenght Nozzles,'' ASME J. Fluids Eng., **117**, pp. 270–276.

[25] Argrow, B. M., 1996, ''Computational Analysis of Dense Gas Shock Tube Flow,'' Shock Waves, **6**, pp. 241–248.

[26] Brown, B. P., and Argrow, B. M., 1998, ''Nonclassical Dense Gas Flows for Simple Geometries,'' AIAA J., **36**, (Oct) pp. 1842–1847.

[27] Brown, B. P., and Argrow, B. M., 1997, ''Two-Dimensional Shock Tube Flow for Dense Gases,'' J. Fluid Mech., **349**, pp. 95–115.

[28] Cramer, M. S., and Park, S., 1999, ''On the Suppression of Shock-Induced Separation in Bethe-Zel'dovich-Thompson Fluids,'' J. Fluid Mech., **393**, pp. 1–21.

[29] Colonna, P., Rebay, S., and Silva, P., 2002, ''Computer Simulations of Dense Gas Flows Using Complex Equations of State for Pure Fluids and Mixtures and State of the Art Numerical Schemes,'' Tech Report Università di Brescia, Brescia, Italy.

[30] Reynolds, W. C., 1979, ''Thermodynamic Properties in S.I.,'' Department of Mechanical Engineering, Stanford University, Stanford, CA.

[31] Sandler, S. I., et al., 1994, *Models for Thermodynamic and Phase Equilibria Calculations*, Marcel Dekker, New York.

[32] Span, R., Wagner, W., Lemmon, E. W., and Jacobsen, R. T., 2001, ''Multiparameter Equations of State—Recent Trends and Future Challanges,'' Fluid Phase Equilib., **183–184**, pp. 1–20.

[33] Smith, D. H., and Fere, M., 1995, ''Improved Phase Boundary for One-Component Vapor-Liquid Equilibrium Incorporating Critical Behavior and Cubic Equations of State,'' Fluid Phase Equilib., **113**, pp. 103–115.

[34] Wong, D. S. H., and Sandler, S. I., 1993, ''A Theoretically Correct Mixing Rule for Cubic Equations of State,'' AIChE J., **38**, pp. 671–680.

[35] Keenan, J. H. et al., 1969, *Steam Tables*, John Wiley and Sons, New York.

[36] Haar, L., and Gallagher, J. S., 1978, ''Thermodynamics Properties of Ammonia,'' J. Phys. Chem. Ref. Data, **7**, pp. 635–791.

[37] Starling, K. E., 1973, *Equation of State and Computer Prediction—Fluid Thermodynamic Properties for Light Petroleum Substances* Gulf Publishing, Houston.

[38] Martin, J. J., and Hou, Y. C., 1955, ''Development of an Equation of State for Gases,'' AIChE J., **1** (June), pp. 142–151.

[39] McLinden, M. O., Lemmon, E. W., and Jacobsen, R. T., 1998, ''Thermodynamic Properties for the Alternative Refrigerants,'' Int. J. Refrig. , **21** (June), pp. 322–338.

[40] Stryjeck, R., and Vera, J. H., 1986, ''PRSV: An Improved Peng-Robinson Equation of State for Pure Compounds and Mixtures,'' Can. J. Chem. Eng., **64**, pp. 323–333.

[41] Prausnitz, J. M., 1995, ''Some New Frontiers in Chemical Engineering Thermodynamics,'' Fluid Phase Equilib., **104**, pp. 1–20.

[42] Bassi, F., Rebay, S., and Savini, M., 1991, ''Transonic and Supersonic Inviscid Computations in Cascades Using Adaptive Unstructured Meshes,'' International Gas Turbine & Aeroengine Congress & Exhibition, Orlando, FL., June 3–6, ASME, New York.

[43] Rebay, S., 1992, ''Soluzione Numerica Adattiva su Reticoli non Strutturati delle Equazioni di Eulero,'' Ph.D. thesis, Politecnico di Milano, Milano.

[44] Taylor, R., 1997, ''Automatic Derivation of Thermodynamic Property Functions Using Computer Algebra,'' Fluid Phase Equilib., **129**, pp. 37–47.

[45] Press, W. H., Teukolsky, S. A., Vetterling, W. T., and Flannery, B. P., 1993, *Numerical Recipes in Fortran 77: The Art of Scientific Computing* (Vol. 2, Numerical Analysis Series), 2nd Ed., Cambridge University Press, Cambridge, UK.

[46] Lemmon, E. W., McLinden, M. O., and Friend, D. G., 2001, Thermophysical Properties of Fluid Systems (NIST Chemistry WebBook, NIST Standard Reference Database Number 69), National Institute of Standards and Technology, Gaithersburg MD.

[47] Moldover, M., Mehl, J. B., and Greenspan, M., 1986, ''Gas-Filled Spherical Resonators: Theory and Experiment,'' J. Acoust. Soc. Am., **79**, pp. 253–272.

[48] Cramer, M. S., November 1989, ''Negative Nonlinearity in Selected Fluorocarbons,'' Phys. Fluids A, **11**, pp. 1894–1897.

[49] Thompson, P. A., and Lambrakis, K. C., 1973, ''Negative Shock Waves,'' J. Fluid Mech., **60**, pp. 187–208.

[50] Wilcock, D. F., 1946, ''Vapor Pressure-Viscosity relations in Methylpolysiloxanes,'' J. Chem. Am. Soc., **68** (Apr) pp. 691–696.

[51] Colonna, P., 1996, ''*Fluidi di Lavoro Multi Componenti Per Cicli Termodinamici di Potenza*,'' Ph.D. thesis, Politecnico di Milano, Milano.

[52] Kalina, A. L., 1984, ''Combined Cycle Systems With Novel Bottoming Cycle,'' ASME J. Eng. Gas Turbines Power, **106**, pp. 737–742.

[53] Ibrahim, M. B., and Kovach, R. M., 1993, ''A Kalina Cycle Application for Power Generation,'' Energy, **18**, pp. 961–969.

[54] Marston, C. H., and Hyre, M., 1995, ''Gas Turbine Bottoming Cycles: Triple-Pressure Steam Versus Kalina,'' ASME J. Eng. Gas Turbines Power, **117**, pp. 10–15.

[55] Marston, C. H., 1990, ''Parametric Analysis of the Kalina Cycle,'' ASME J. Eng. Gas Turbines Power, **112**, pp. 107–116.

[56] Rogdakis, E. D., 1996, ''Thermodynamic Analysis, Parametric Study and Optimum Operation of the Kalina Cycle,'' Int. J. Energy Res., **20**, pp. 359–370.

[57] Heppenstall, T., 1998, ''Advanced Gas Turbine Cycles for Power Generation: A Critical Review,'' Appl. Therm. Eng., **18**, pp. 837–846.

[58] Verschoor, M. J. E., and Brouwer, E. P., 1995, ''Description of the SMR Cycle Which Combines Fluid Elements of Steam and Organic Rankine Cycles,'' Energy, **20**, p. 295.

[59] Orbey, H., and Sandler, S. I., 1995, ''Equation of State Modeling of Refrigerant Mixtures,'' Ind. Eng. Chem. Res., **34**, pp. 2520–2525.

[60] Lambrakis, K. C., and Thompson, P. A., 1972, ''Existence of Real Fluids With Negative Fundamental Derivative,'' Phys. Fluids, **15**, pp. 933–935.

[61] Flaningam, O. L., 1986, ''Vapor Pressures of Poly(Dimethylsiloxane) Oligomers,'' J. Chem. Eng. Data, **31**, pp. 266–272.

[62] Wagner, W., and Pruss, A., 2001, ''New International Formulation for the Thermodynamic Properties of Ordinary Water Substance for General and Scientific Use,'' J. Phys. Chem. Ref. Data, **30**, to be published.

[63] Span, R., 2000, *Multiparameter Equations of State—An Accurate Source of Thermodynamic Property Data*, Springer-Verlag, Berlin.

[64] Grigiante, M., Scalabrin, G., Benedetto, G., Gavioso, R. M., and Spagnolo, R., 2000, ''Vapor Phase Acoustic Measurements for R125 and Development of a Helmholtz Free Energy Equation,'' Fluid Phase Equilib., **174**, pp. 69–79.

The Spatial Stability of Natural Convection Flow on Inclined Plates

Anatoli Tumin
Department of Aerospace
and Mechanical Engineering,
The University of Arizona,
Tucson, AZ 85721
e-mail: tumin@engr.Arizona.edu

The spatial stability of a natural convection flow on upward-facing, heated, inclined plates is revisited. The eigenvalue problem is solved numerically employing two methods: the collocation method with Chebyshev polynomials and the fourth-order Runge-Kutta method. Two modes, traveling waves and stationary longitudinal vortices, are considered. Previous theoretical models indicated that nonparallel effects of the mean flow are significant for the vortex instability mode, but most of them ignored the fact that the eigenfunctions are dependent on the streamwise coordinate as well. In the present work, the method of multiple scales is applied to take the nonparallel flow effects into consideration. The results demonstrate the stabilizing character of the nonparallel flow effects. The vortex instability mode is also considered within the scope of partial differential equations. The results demonstrate dependence of the neutral point on the initial conditions but, farther downstream, the results collapse onto one curve. The marching method is compared with the quasi-parallel normal mode analysis and with theoretical results including correction to nonparallel flow effects. The marching method provides better agreement of theoretical and experimental growth rates. [DOI: 10.1115/1.1566047]

1 Introduction

Natural convection flow is a leading mechanism of mass and heat transfer in many geophysical and technological phenomena. An understanding of the laminar-turbulent transition in such flows will improve predictions of the heat transfer rate and the development of effective methods for flow control. One can find a comprehensive discussion of the buoyancy-induced flows in Ref. [1].

Instability and transition to turbulence of natural convection on inclined plates is of great interest because it is associated with thermal stratification in cryogenic tanks, heat exchangers, etc. Sparrow and Husar [2] observed the generation of an array of longitudinal vortices in the natural convection flow of water on an inclined plate. At some distance downstream, they discovered vortex pairing. The breakdown of the new vortex array led to a turbulent flow. Lloyd and Sparrow [3] investigated, experimentally, the instability of the flow on inclined plates in more detail. They found that there are two modes of the flow instability, depending on the inclination angle of the plate. At angles less than 14° (relative to the vertical), the instability is wave-like (Tollmien-Schlichting type). At angles above 17°, the instability manifests itself as a system of longitudinal vortices. These instability modes coexist at angles between 14° and 17°. Shaukatullah and Gebhart [4] carried out measurements of temperature and of the longitudinal and transverse velocity components in the presence of a vortex array in the flow on a heated, inclined plate. Zuercher et al. [5] visualized the flow field and measured velocity components in the vortices. They re-examined the formation, growth, and pairing of the vortices experimentally. The application of advanced methods of flow control for this type of flow was realized in experiments by Trautman [6].

The linear stability of the flow has been studied theoretically as well (see review by Gebhart et al. [1]). Haaland and Sparrow [7] calculated the neutral stability curves for the vortex mode. They included the nonparallel effect (via streamwise dependence of the basic flow and temperature field) in the leading operator, and they showed that the effect is essential for the stability analysis. Iyer and Kelly [8] analyzed the wave-like and vortex modes within the scope of the spatial linear stability theory. Chen et al. [9] constructed the full eigenspectrum within the temporal linear stability theory and analyzed finite-amplitude longitudinal rolls in an inclined free-convection boundary layer. The latter rolls become unstable with respect to disturbances of a spanwise wave length, which was twice that of the primary rolls. This subharmonic instability explains qualitatively the vortex pairing observed in the experiments.

Despite the number of theoretical results, there are still many questions regarding the theoretical models. Particularly, the experiments deal with spatially developing disturbances, while most of the theoretical work deals with temporal analysis. To our knowledge, the spatial theory of normal modes was considered only by Iyer and Kelly [8], but they still used the parallel flow assumption. The full spatial eigenspectrum (similarly to the temporal theory, [9]) has never been constructed. Other theoretical models take into account the nonparallel effects in the leading operator inconsistently. They ignore the fact that the eigenfunctions (shapes of the disturbance profiles) depend on the streamwise coordinate as well. Lee et al. [10] recognized the importance of the streamwise dependence of the disturbances. They proposed a local nonparallel model where the nonparallel effects are included via consideration of the next term of the Taylor series. Although the model provides a local improvement of the growth rates, the latter cannot be used over a large scale for evaluation of the disturbance amplification. The nonparallel effects were discussed by Wakitani [11] in conjunction with buoyant plumes. He applied the method of multiple scales that had been used for the linear stability analysis of the Blasius boundary layer, [12–15], to a buoyant plume generated above a heated body. This type of analysis has not been carried out yet on the natural convection flow on inclined plates.

The vortex instability mode resembles Görtler vortices, [16]. It is well known that application of the normal mode analysis to Görtler vortices is questionable (at least at some distance from the leading edge), [17], and the neutral point is dependent on the initial disturbance profile. Day et al. [18] carried out a comparison of local and marching analyses of the Görtler instability. They found that, in spite of the initial conditions effect, the solutions of the marching analysis corresponding to the different initial condi-

---

Contributed by the Fluids Engineering Division for publication in the JOURNAL OF FLUIDS ENGINEERING. Manuscript received by the Fluids Engineering Division Nov. 2, 2001; revised manuscript received Nov. 26, 2002. Associate Editors: T. Gatski.

tions further downstream collapse onto one common curve. Luchini and Bottaro [19] analyzed how the universal disturbance shape is approached in the forward marching solution. The marching analysis for a horizontal heated plate was carried out by Hall and Morris [20] in a forced convection boundary layer. Their findings were similar to the case of Görtler instability, [17]. The latter indicates that there is a strong similarity of the phenomena in flows with a vortex instability mode. Jeschke and Beer [21] formulated a consistent system of governing equations for linear and nonlinear vortex instability modes for the case of the natural convection flow along a constant heat-flux inclined flat plate. In their analysis, a normal-mode solution was applied as an initial condition for the marching procedure and the main results were obtained for the nonlinear regime.

The objective of the present work is to analyze the full spatial spectrum of the stability problem in the quasi-parallel approximation and to apply the method of multiple scales to the flow in order to include the nonparallel effects consistently. For the vortex instability mode, the objective is to compare the marching solution and the normal mode analysis for the natural convection flow over an upward-facing, heated, inclined plate of constant surface temperature.

2 The Governing Equations

We consider an upward-facing heated inclined plate of constant surface temperature. A schematic of the flow and the coordinate system are shown in Fig. 1. The coordinate z is normal to the plane shown. The governing equations may be written in the Boussinesq approximation, [1], for the velocity vector $\mathbf{V}$ and the temperature T

$$\nabla \mathbf{V}=0 \tag{1}$$

$$\frac{\partial \mathbf{V}}{\partial t}+(\mathbf{V}\nabla)\mathbf{V}=-\frac{1}{\rho}\nabla p-\mathbf{g}\beta(T-T_\infty)+\nu\nabla^2\mathbf{V} \tag{2}$$

$$\frac{\partial T}{\partial t}+(\mathbf{V}\nabla)T=a\nabla^2 T \tag{3}$$

where $\mathbf{g}$ is the gravity vector; a and ν are the thermal diffusivity and kinematic viscosity, respectively; and β stands for the volumetric thermal expansion coefficient.

2.1 Mean-Flow Equations. The mean flow is considered in a boundary layer approximation when the streamwise pressure gradient is neglected, [7]. The boundary layer equations admit the self-similar solution with the velocity and length scales, $u_{0x}(x)$ and $\delta_x(x)$ correspondingly, as follows:

$$u_{0x}=4\nu\kappa^2 x^{1/2}, \quad \delta_x=\frac{x^{1/4}}{\kappa}, \quad \kappa=\left[\frac{\beta g\cos\theta\Delta T}{4\nu^2}\right]^{1/4} \tag{4}$$

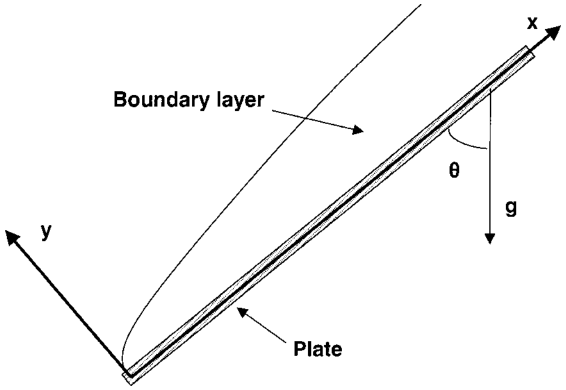

Fig. 1 Schematic of the flow and the coordinate system

where $\Delta T=T_w-T_\infty$, T_w is the wall temperature, and T_∞ stands for temperature of the ambient fluid. The subscript "x" in the definition of the velocity and the length scales emphasizes that they depend on the coordinate x. The boundary layer equations have the following self-similar solutions for temperature, T, and x and y-velocity components, U and V, respectively,

$$T=T_\infty+\Delta T\Phi(\eta) \tag{5}$$

$$U=u_{0x}F'(\eta) \tag{6}$$

$$V=\frac{u_{0x}}{R_x}(\eta F'(\eta)-3F(\eta)) \tag{7}$$

where prime stands for the derivative with respect to the similarity variable, $\eta=y/\delta_x$, and $R_x=u_{0x}\delta_x/\nu=4\kappa x^{3/4}$ is the local Reynolds number. The governing equations for the mean flow are reduced to the following system of ordinary differential equations:

$$F'''+\Phi+3FF''-2(F')^2=0 \tag{8}$$

$$\Phi''+3\mathrm{Pr}F\Phi'=0 \tag{9}$$

where Pr is the Prandtl number. Equations (8) and (9) are solved subject to the following boundary conditions:

$$F(0)=F'(0)=F'(\infty)=\Phi(\infty)=0, \quad \Phi(0)=1. \tag{10}$$

This is the conventional system of governing equations for the natural convection mean flow, but one should keep in mind that the streamwise pressure gradient in the mean-flow equations may be neglected only if $\tan\theta/R_x \ll 1$, as was discussed by Halland and Sparrow [7]. Solution of the mean-flow equations is described elsewhere (see, for example, [1]).

2.2 Governing Equations for the Perturbations

Method of Multiple Scales. We consider the basic flow as a two-dimensional one, while the disturbances might be three-dimensional. The linearized equations, (1)–(3), are written in dimensionless form with the help of the velocity scale u_{0L}, length scale δ_L, and time measuring in units of δ_L/u_{0L}

$$u_{0L}=4\nu\kappa^2 L^{1/2}, \quad \delta_L=\frac{L^{1/4}}{\kappa}, \quad R_L=\frac{u_{0L}\delta_L}{\nu}=4\kappa L^{3/4}$$
$$\hat{x}=\frac{x}{\delta_L}, \quad \hat{y}=\frac{y}{\delta_L}, \quad \hat{z}=\frac{z}{\delta_L}, \quad \hat{t}=\frac{tu_{0L}}{\delta_L} \tag{11}$$

where L is a representative scale in the streamwise direction. The mean-flow profiles $\bar{U}$, V_*, and $\bar{T}$ are defined as $\bar{U}=U/u_{0L}$, $V_*=R_L V/u_{0L}$, and $\bar{T}=(T-T_\infty)/\Delta T$, respectively. The convenience of the fixed scales u_{0L} and δ_L is associated with the independence of the governing equations of the self-similar character of the mean flow, and they can be applied for a general case. In the specific case of a self-similar flow, the functions $U(x,y)$ and $V(x,y)$ could be derived from the solutions in the form of (5)–(7). The governing equations could be written as follows:

$$\frac{\partial u}{\partial \hat{x}}+\frac{\partial v}{\partial \hat{y}}+\frac{\partial w}{\partial \hat{z}}=0 \tag{12}$$

$$R_L\frac{\partial u}{\partial \hat{t}}+R_L u\frac{\partial \bar{U}}{\partial \hat{x}}+R_L\bar{U}\frac{\partial u}{\partial \hat{x}}+R_L v\frac{\partial \bar{U}}{\partial \hat{y}}+V_*\frac{\partial u}{\partial \hat{y}}$$
$$=-R_L\frac{\partial p}{\partial \hat{x}}+\tau+\frac{\partial^2 u}{\partial \hat{x}^2}+\frac{\partial^2 u}{\partial \hat{y}^2}+\frac{\partial^2 u}{\partial \hat{z}^2} \tag{13}$$

$$R_L\frac{\partial v}{\partial \hat{t}}+R_L\bar{U}\frac{\partial v}{\partial \hat{x}}+v\frac{\partial V_*}{\partial \hat{y}}+V_*\frac{\partial v}{\partial \hat{y}}$$
$$=-R_L\frac{\partial p}{\partial \hat{y}}+\tau\tan\theta+\frac{\partial^2 v}{\partial \hat{x}^2}+\frac{\partial^2 v}{\partial \hat{y}^2}+\frac{\partial^2 v}{\partial \hat{z}^2} \tag{14}$$

$$R_L\frac{\partial w}{\partial\hat t}+R_L\overline{U}\frac{\partial w}{\partial\hat x}+V_*\frac{\partial w}{\partial\hat y}=-R_L\frac{\partial p}{\partial\hat z}+\frac{\partial^2 w}{\partial\hat x^2}+\frac{\partial^2 w}{\partial\hat y^2}+\frac{\partial^2 w}{\partial\hat z^2} \tag{15}$$

$$R_L\frac{\partial\tau}{\partial\hat t}+R_L u\frac{\partial\overline{T}}{\partial\hat x}+R_L\overline{U}\frac{\partial\tau}{\partial\hat x}+R_L v\frac{\partial\overline{T}}{\partial\hat y}+V_*\frac{\partial\tau}{\partial\hat y}=\frac{1}{\Pr}\left(\frac{\partial^2\tau}{\partial\hat x^2}+\frac{\partial^2\tau}{\partial\hat y^2}+\frac{\partial^2\tau}{\partial\hat z^2}\right) \tag{16}$$

where u, v, and w are dimensionless x, y, and z-velocity disturbances and p and τ are the dimensionless pressure and temperature disturbances scaled with ρu_{0L}^2 and ΔT, respectively.

Equations (13)–(16) contain terms associated with the divergence of the mean flow, $\partial\overline{U}/\partial\hat x$, $\partial\overline{T}/\partial\hat x\sim O(R_x^{-1})$. We neglect in Eq. (14) the term with $\partial V_*/\partial\hat x$ because it is small in comparison to the others.

In order to apply the method of multiple scales for further analysis, we introduce the "slow" variable $X=\varepsilon\hat x$ with $\varepsilon=R_L^{-1}$. In the normal mode analysis, we are looking for a solution of the linearized equations in the following form:

$$(u,v,w,p,\tau)=(\hat u,\hat v,\hat w,\hat p,\hat\tau)e^{i(\int\alpha d\hat x+\gamma\hat z-\omega\hat t)} \tag{17}$$

where the amplitude functions depend on the coordinate $\hat y$ and the slow variable X. After substituting (17) into (12)–(16), one can arrive at the system of equations

$$i\alpha\hat u+i\gamma\hat w+\frac{\partial\hat v}{\partial\hat y}=-\varepsilon\frac{\partial\hat u}{\partial X} \tag{18}$$

$$iR_L(\alpha\overline{U}-\omega)\hat u+\hat u\frac{\partial\overline{U}}{\partial X}+R_L\hat v\frac{\partial\overline{U}}{\partial\hat y}+V_*\frac{\partial\hat u}{\partial\hat y}+i\alpha R_L\hat p-\hat\tau-\frac{\partial^2\hat u}{\partial\hat y^2}+(\alpha^2+\gamma^2)\hat u=-\frac{\partial\hat p}{\partial X}-\overline{U}\frac{\partial\hat u}{\partial X}+O(\varepsilon) \tag{19}$$

$$iR_L(\alpha\overline{U}-\omega)\hat v+v\frac{\partial V_*}{\partial\hat y}+V_*\frac{\partial\hat v}{\partial\hat y}+R_L\frac{\partial\hat p}{\partial\hat y}-\hat\tau\tan\theta-\frac{\partial^2\hat v}{\partial\hat y^2}+(\alpha^2+\gamma^2)\hat v=-U_L\frac{\partial\hat v}{\partial X}+O(\varepsilon) \tag{20}$$

$$iR_L(\alpha\overline{U}-\omega)\hat w+V_*\frac{\partial\hat w}{\partial\hat y}+iR_L\gamma\hat p-\frac{\partial^2\hat w}{\partial\hat y^2}+(\alpha^2+\gamma^2)\hat w=-\overline{U}\frac{\partial\hat w}{\partial X}+O(\varepsilon) \tag{21}$$

$$iR_L(\alpha\overline{U}-\omega)\hat\tau+\hat u\frac{\partial\overline{T}}{\partial X}+R_L\hat v\frac{\partial\overline{T}}{\partial\hat y}+V_*\frac{\partial\hat\tau}{\partial\hat y}-\frac{1}{\Pr}\frac{\partial^2\hat\tau}{\partial\hat y^2}+\frac{1}{\Pr}(\alpha^2+\gamma^2)\hat\tau=-\overline{U}\frac{\partial\hat\tau}{\partial X}+O(\varepsilon). \tag{22}$$

Equations (12)–(16) are solved subject to the following boundary conditions:

$$\hat y=0:\quad \hat u=\hat v=\hat w=\hat\tau=0,\quad \hat y\to\infty:\quad \hat u,\hat v,\hat w,\hat p,\hat\tau\to 0. \tag{23}$$

Equations (18)–(22) contain terms associated with the nonparallel effects of the mean flow via the mean-flow profiles V_*, $\partial\overline{U}/\partial X$, and $\partial\overline{T}/\partial X$, and the terms originating from dependence of the amplitude functions $\hat u$, $\hat v$, $\hat w$, $\hat p$, and $\hat\tau$ on the slow variable X. If we neglect the latter terms on the right-hand side of Eqs. (18)–(22), we arrive at the conventional local nonparallel analysis. If we additionally neglect all terms resulting from the nonparallel effects of the mean flow, we arrive at the quasi-parallel approximation. In both cases, the amplitude functions depend on the slow variable X as a parameter.

For the method of multiple scales, it will be convenient to introduce the vector function

$$\hat{\mathbf{A}}(y,X)=(\hat u,\partial\hat u/\partial\hat y,\hat v,\hat p,\hat\tau,\partial\hat\tau/\partial\hat y,\hat w,\partial\hat w/\partial\hat y)^t \tag{24}$$

where the superscript "t" stands for transposed. One can obtain the system of differential equations in matrix form as

$$E\frac{\partial\hat{\mathbf{A}}}{\partial\hat y}=H_0\hat{\mathbf{A}}+\varepsilon H_1\hat{\mathbf{A}}+\varepsilon H_2\frac{\partial\hat{\mathbf{A}}}{\partial X} \tag{25}$$

where E, H_0, H_1, and H_2 are 8×8 matrices (see nonzero elements of the matrices in the Appendix). The matrices H_0 and H_2 depend on the mean-flow velocity, $\overline{U}$, and temperature, $\overline{T}$, profiles, but they do not depend on V_* and the derivatives of the profiles with respect to X. The matrix H_1 originates from the divergence of the basic flow. It contains the normal velocity component of the basic flow and the streamwise derivatives of functions $\overline{U}(X,y)$ and $\overline{T}(X,y)$. The last two terms in Eq. (25) will be treated as a perturbation, while the leading operator will correspond to the conventional quasi-parallel approximation.

We are looking for the solution of Eq. (25) in the following form:

$$\hat{\mathbf{A}}=a(X)\hat{\mathbf{A}}^{(0)}(\hat y,X)+\varepsilon\hat{\mathbf{A}}^{(1)}(\hat y,X)+\ \ldots \tag{26}$$

where $a(X)$ is the unknown slow amplitude function. In the leading order of magnitude, we derive the equations in the conventional quasi-parallel approach

$$E\frac{\partial\hat A^{(0)}}{\partial\hat y}=H_0\hat A^{(0)}. \tag{27}$$

Equation (27), together with the boundary conditions on the wall and outside the boundary layer, represents an eigenvalue problem. In the spatial analysis, which is the primary interest in this work, the frequency of the disturbance, ω, and the spanwise wave number, γ, are prescribed, and the complex value α must be determined. If the imaginary part, α_i, is negative, the disturbance grows in the downstream direction, and vice versa.

In the next order of ε, we obtain the inhomogeneous system of equations

$$E\frac{\partial\hat{\mathbf{A}}^{(1)}}{\partial\hat y}-H_0\hat{\mathbf{A}}^{(1)}=aH_1\hat{\mathbf{A}}^{(0)}+aH_2\frac{\partial\hat{\mathbf{A}}^{(0)}}{\partial X}+H_2\hat{\mathbf{A}}^{(0)}\frac{da}{dX}. \tag{28}$$

The solvability condition for Eq. (28) is orthogonality of the right-hand side to solution of the adjoint problem. The latter leads to the ordinary differential equation for the unknown function $a(X)$

$$\frac{da}{dX}=-a\frac{\underbrace{\langle H_1\hat{\mathbf{A}}^{(0)},\mathbf{B}\rangle}_{(1)}+\underbrace{\left\langle H_2\frac{\partial\hat{\mathbf{A}}^{(0)}}{\partial X},\mathbf{B}\right\rangle}_{(2)}}{\langle H_2\hat{\mathbf{A}}^{(0)},\mathbf{B}\rangle} \tag{29}$$

where the inner product $\langle,\rangle$ is defined as

$$\langle\mathbf{f},\mathbf{g}\rangle\equiv\int_0^\infty(\mathbf{f},\mathbf{g})d\hat y \tag{30}$$

and the vector function $\mathbf{B}$ is the solution of the adjoint problem

$$-E\frac{\partial\mathbf{B}}{\partial\hat y}=H_0^*\mathbf{B} \tag{31}$$

$$\hat y=0:\quad B_2=B_4=B_6=B_8=0$$

$$\hat y\to\infty:\quad B_j\to 0,\quad (j=1,\ldots,8).$$

The asterisk in (31) stands for the Hermitian adjoint matrix (we take into account that E is a real diagonal matrix). The numbering of terms in the numerator on the right-hand side of Eq. (29) will be explained in the discussion of the results.

Marching Analysis of the Vortex Mode. As was discussed in the Introduction, there are two modes of the flow instability: a traveling or Tollmien-Schlichting-like mode, and a stationary vortex instability mode. The latter resembles Görtler vortices. It means that the normal mode analysis is questionable at small Reynolds numbers and at small spanwise wave numbers, γ. Also, one should expect that the neutral point is dependent on the initial disturbance profile, [16]. For purposes of deriving the governing partial differential equations specifically for the vortex instability mode, we rescale the disturbance profiles as follows:

$$\overline{u}=u, \quad \overline{v}=v\,\frac{L}{\delta_L}, \quad \overline{w}=w\,\frac{L}{\delta_L}, \quad \overline{p}=p\left(\frac{L}{\delta_L}\right)^2, \quad \overline{\tau}=\tau. \tag{32}$$

As for the Görtler instability, the rescaling reflects that the normal and the spanwise velocity components in the vortex instability mode are of order R_L^{-1} in comparison with the streamwise velocity component, and the pressure disturbance is of order R_L^{-2} in the scale of ρu_{0L}^2. The streamwise coordinate is scaled with L, while the normal and the spanwise coordinates are scaled with δ_L

$$\xi=\frac{x}{L}, \quad \hat{y}=\frac{y}{\delta_L}, \quad \hat{z}=\frac{z}{\delta_L}. \tag{33}$$

Solution of the linearized equations for the disturbances is considered, depending on the $\hat{z}$-coordinate as $\exp(i\gamma\hat{z})$, and it is convenient to substitute $-i\overline{w}\rightarrow\widetilde{w}$ because the latter leads to a system of partial differential equations with real functions only.

We introduce the vector function $\mathbf{f}=(\overline{u},\overline{v},\widetilde{w},\overline{p},\overline{\tau})^t$, and write the governing equations in matrix form as

$$\frac{\partial}{\partial\xi}(A\mathbf{f})=B_0\mathbf{f}+B_1\frac{\partial\mathbf{f}}{\partial\hat{y}}+B_2\frac{\partial^2\mathbf{f}}{\partial\hat{y}^2}. \tag{34}$$

A, B_0, B_1, and B_2 in Eq. (34) are 5×5 matrices (their nonzero elements are given in the Appendix). The solution of Eq. (34) is subject to the following initial and boundary conditions:

$$\begin{aligned} \hat{y}=0: &\quad \overline{u}=\overline{v}=\widetilde{w}=\overline{\tau}=0 \\ \hat{y}\rightarrow\infty: &\quad \overline{u},\overline{v},\widetilde{w},\overline{p},\overline{\tau}\rightarrow 0 \\ \xi=\xi_0: &\quad \mathbf{f}=\mathbf{f}_0(\hat{y}). \end{aligned} \tag{35}$$

Scaling of the dependent and independent variables, (32) and (33), leads to governing equations similar to (12)–(16), where the terms $\partial p/\partial\hat{x}$ and $\partial^2/\partial\hat{x}^2$ do not appear in the leading order.

3 Numerical Methods

3.1 The Spatial Stability Equations. The stability analysis has been carried out employing two numerical methods. The first method is the collocation method with Chebyshev polynomials, described elsewhere (see, for example, [22]). The number of Chebyshev polynomials was chosen to be $N=70$. The boundary condition at $\hat{y}\rightarrow\infty$ was replaced by the following:

$$\hat{y}=\hat{y}_{\max}: \quad \hat{u}=\hat{v}=\hat{w}=\hat{\tau}=0 \tag{36}$$

where $\hat{y}_{\max}=100$. The Chebyshev interval was transformed to the domain $0\leqslant\hat{y}\leqslant\hat{y}_{\max}$. The number of polynomials and the distance was chosen after comparison of the results with different values of $\hat{y}_{\max}$ and N (see the following results). To employ the method, one also needs to define boundary conditions for the pressure disturbance. These are obtained from Eq. (20) evaluated at the boundaries $\hat{y}=0$ and $\hat{y}=\hat{y}_{\max}$. The method reduces the eigenvalue problem to a generalized matrix eigenvalue problem of the form $C\mathbf{X}=\alpha G\mathbf{X}$, where C and G are the square matrices and $\mathbf{X}$ is an eigenvector. The problem was solved using a standard routine from the IMSL Fortran Library, and the full spectrum could be obtained.

Another numerical code employed the fourth-order Runge-Kutta method for solving the ordinary differential equations with a Newton iteration procedure to find an eigenvalue. Four fundamental solutions of Eq. (27) that are decaying at $\hat{y}\rightarrow\infty$ are evaluated in the numerical procedure by employing the Gram-Schmidt orthonormalization. The general solution is obtained as a sum of the fundamental ones. The unknown coefficients are found from the boundary conditions on the wall. To satisfy all boundary conditions (23), a Newton iterative procedure was used to find the unknown eigenvalue α. The method is sensitive to the initial approach to the eigenvalue, and the latter was obtained from the full eigenvalue map. Both codes were developed for nonstationary three-dimensional disturbances. To analyze two-dimensional disturbances, the spanwise wave number, γ, was defined as 10^{-5}. For the purpose of analysis of the stationary disturbances, the frequency, ω, was also chosen equal to 10^{-5}. Comparison of the eigenvalues obtained with smaller values γ and ω showed that they may be considered as limits at $\gamma\rightarrow 0$ and $\omega\rightarrow 0$, respectively.

3.2 The Marching Method. In the present work we adopt the numerical procedure from [23] that was used for the analysis of optimal disturbances in a Blasius boundary layer. Equation (34) is approximated in the streamwise direction with a fully implicit finite difference scheme of the second order (except the first step)

$$\begin{aligned} &\frac{3}{2}(A\mathbf{f})^{n+1}-2(A\mathbf{f})^n+\frac{1}{2}(A\mathbf{f})^{n-1} \\ &\quad=\Delta\xi\left[(B_0\mathbf{f})^{n+1}+\left(B_1\frac{\partial\mathbf{f}}{\partial\hat{y}}\right)^{n+1}+\left(B_2\frac{\partial^2\mathbf{f}}{\partial\hat{y}^2}\right)^{n+1}\right] \\ &\quad n=1,\ldots,M-1 \end{aligned} \tag{37a}$$

$$(A\mathbf{f})^1-(A\mathbf{f})^0=\Delta\xi\left[(B_0\mathbf{f})^1+\left(B_1\frac{\partial\mathbf{f}}{\partial\hat{y}}\right)^1+\left(B_2\frac{\partial^2\mathbf{f}}{\partial\hat{y}^2}\right)^1\right] \tag{37b}$$

where $\Delta\xi=1/M$ is the step along the streamwise coordinate. At each streamwise coordinate ξ, we solve the one-dimensional boundary value problem along the coordinate $\hat{y}$ using the spectral collocation method with Chebyshev polynomials. The Chebyshev interval was transformed to the domain $0\leqslant\hat{y}\leqslant\hat{y}_{\max}$. The resulting linear algebraic system for the coefficients was solved using routine DLSARG from the IMSL Fortran Library. After comparison of results with different $\hat{y}_{\max}$ and different numbers of Chebyshev polynomials, N, values $\hat{y}_{\max}=100$ and $N=100$ were chosen for the present analysis.

4 Results

4.1 Spectra. We begin with consideration of a traveling wave. Figure 2 shows the eigenvalue map within the scope of the spatial theory when all nonparallel terms are excluded. Figure 2(a) illustrates the effect of the number of the Chebyshev polynomials at $\hat{y}_{\max}=100$, while Fig. 2(*b*) shows the effect of the outer boundary, $\hat{y}_{\max}$ at $N=70$. The latter reflects effect of the wall normal resolution. The results justify our choice, $N=70$ and $\hat{y}_{\max}=100$. One can see a number of modes along the imaginary axis α_i. This is a discretization of the continuous spectrum, and the result depends on $y_{\max}$ (Fig. 2(*b*)). Although there are an infinite number of modes with $\alpha_i<0$, they do not represent instability modes. From the analysis of the signaling problem (see discussion in [24] and [25]), one can show that these are the upstream modes. Pure traveling (discrete) modes are shown in Fig. 2 as well. Only one of them is unstable ($\alpha=0.7302-i0.03326$). The latter eigenvalue was also obtained with the second (Runge-Kutta method) code, and the results agree within 0.1%. Corresponding streamwise velocity and temperature profiles are shown in Fig. 3. One can recognize that the streamwise velocity profile is typical for Tollmien-Schlichting-like waves.

In what follows, all results for the vortex instability mode were obtained at $\theta=60°$. One can find from Eqs. (18)–(22) that neglecting viscous terms $\partial^2/\partial x^2$ and rescaling the amplitude functions (32) lead to the governing equations with α, R_L, and θ entering in the combinations αR_L and $R_L\tan\theta$ only. The latter means that the proper presentation of the eigenvalue map will be for $\alpha/\tan\theta$ at a prescribed value of $R_L\tan\theta$. Within the conventional approxima-

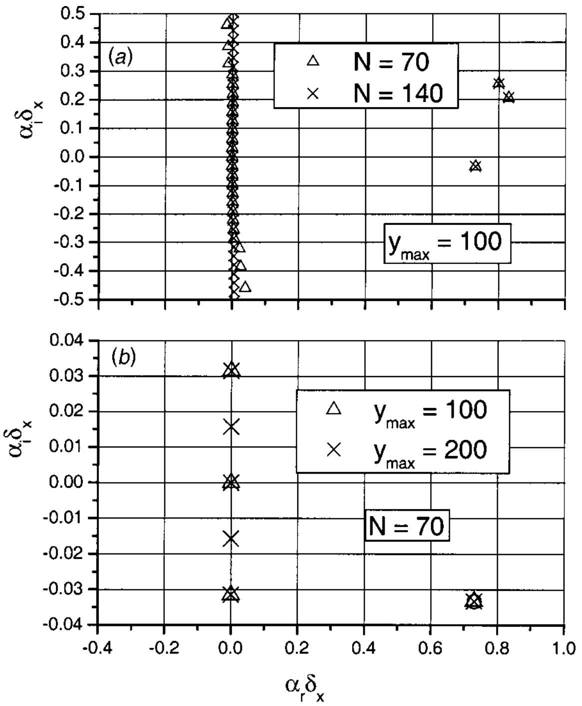

Fig. 2 Eigenvalue map $(R_x=100,\ \theta=5°,\ \omega=0.1,\ \gamma\delta_x=0)$: ×, △ – collocation method; ○ – Runge-Kutta method. Pr=5.5.

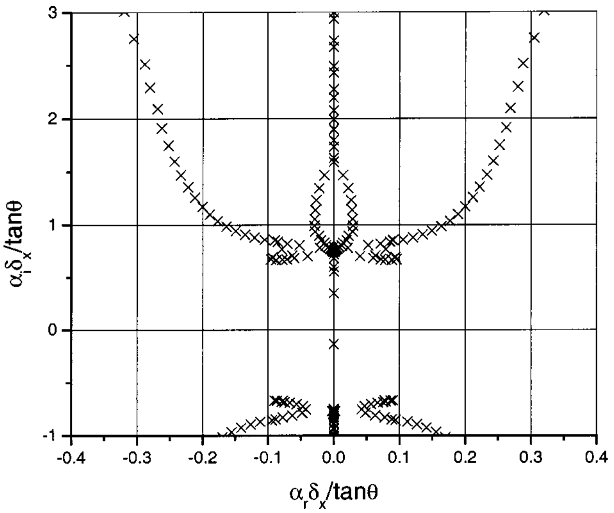

Fig. 4 Eigenvalue map $(R_x \tan\theta=24.26,\ \omega=0,\ \gamma\delta_x=1.292)$ showing the quasi-parallel approximation (×). Pr=5.5.

tion for the vortex instability mode, the result will be independent of the specific angle θ. An example of the eigenvalue map for a steady vortex mode is shown in Fig. 4. In this example, we exclude the terms associated with the nonparallel effects and keep the terms $\partial p/\partial x$ and $\partial^2/\partial x^2$, which are usually not included in an analysis of the vortex mode. The parameters are chosen the same as in the temporal theory of [9]. They correspond to the neutral vortex mode. One can see some discrete modes and discretization of the continuous spectrum. The terms $\partial p/\partial x$ and $\partial^2/\partial x^2$ do not affect the discrete modes, but they affect the upstream branches of the continuous spectrum. The spectra when the latter terms are excluded are shown in Fig. 5 (in quasi-parallel and local nonparallel approximations). Including the terms originating from the mean-flow profiles V_*, $\partial U/\partial\hat{x}$, and $\partial T/\partial\hat{x}$ (local nonparallel approximation) leads to a stabilizing effect, as was established in earlier publications. Figure 6 shows the velocity components of the neutral mode (to be more precise, our calculation demonstrates almost neutral modes, as there is a small imaginary part $\alpha_i/\tan\theta\approx 0.0058$). One can recognize that the eigenfunctions represent streamwise vortices with transversal spacing $\lambda_z=2\pi/\gamma$.

An asymptotic analysis of the Görtler instability, [26], indicates that there is the possibility of a few unstable modes. The highest modes represent two and more layers of counterrotating streamwise vortices. Due to the similarity of Görtler instability and the vortex instability in the natural convection boundary layer, one can expect the appearance of the highest instability modes with an increase of the Reynolds number. Figure 7 shows the eigenvalue map for the vortex modes in the quasi-parallel approximation at two Reynolds numbers. One can see the appearance of the second unstable mode. The shape of the first unstable mode is similar to the shape shown in Fig. 6. The velocity components of the second mode are shown in Fig. 8. These velocity profiles represent two-layer counterrotating streamwise vortices. Because the second unstable mode appears at significantly higher Reynolds number, it does not have a practical interest.

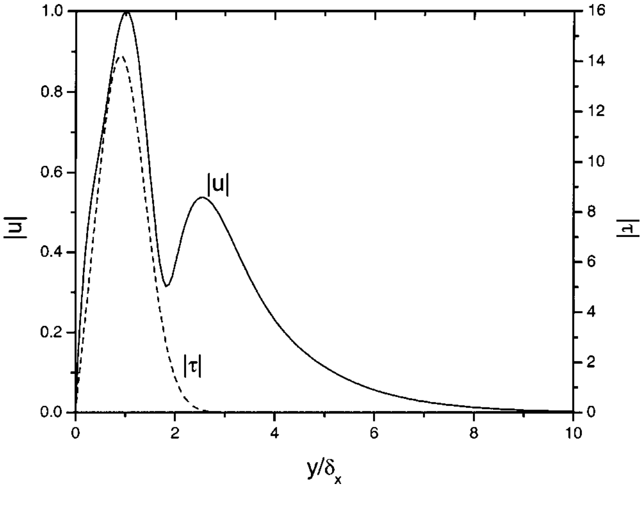

Fig. 3 Profiles of streamwise velocity and temperature disturbances (parameters are the same as in Fig. 2

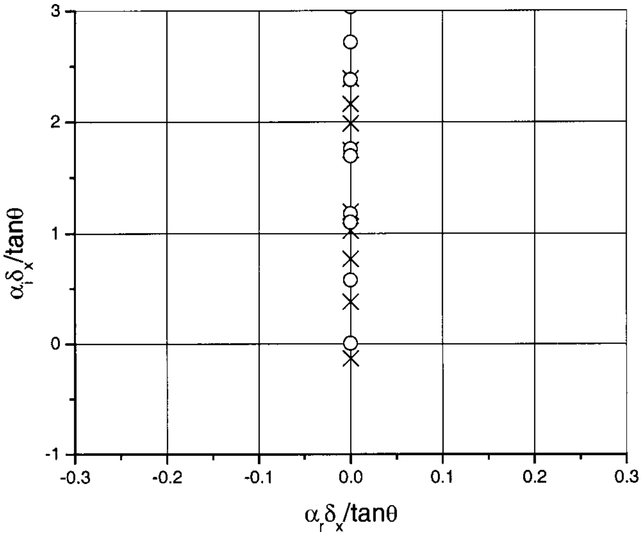

Fig. 5 Eigenvalue map $(R_x \tan\theta=24.26,\ \omega=0,\ \gamma\delta_x=1.292)$: × – quasi-parallel approximation; ○ – local nonparallel model

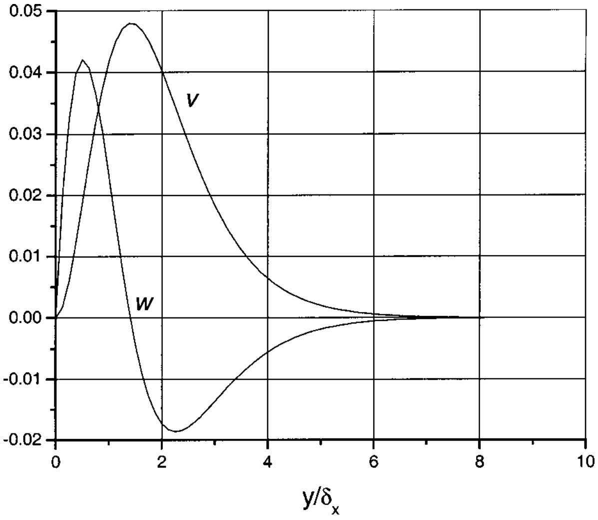

Fig. 6 Velocity disturbance profiles, *v* and *w*, of the neutral vortex mode ($R_x \tan\theta$=24.26, ω=0, $\gamma\delta_x$=1.292). Pr=5.5.

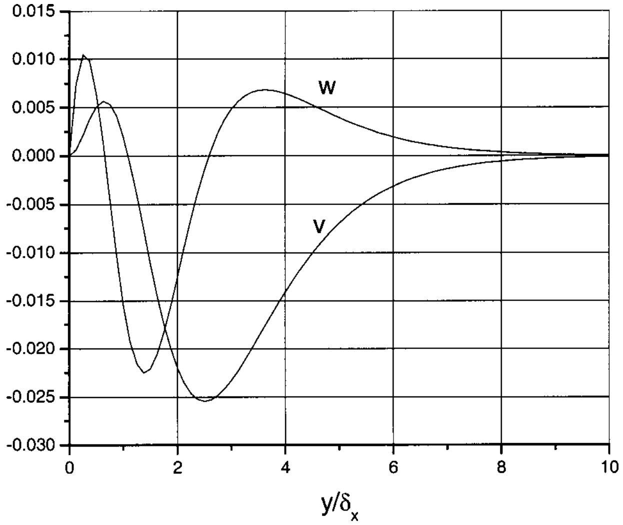

Fig. 8 Velocity disturbance profiles, *v* and *w*, of the second unstable vortex mode ($R_x \tan\theta$=242.6, ω=0, $\gamma\delta_x$=1.292). Pr =5.5.

4.2 The Perturbation Method. We begin with consideration of the nonparallel flow effects on the traveling waves. Because the instability occurs in the form of two-dimensional waves traveling in the streamwise direction, we consider the case of γ=0. Figure 9 shows neutral curves for the traveling waves at Pr=5.5 and two angles, θ, with and without the nonparallel flow effects (following Section 2.2). Amplification or attenuation of the disturbances should be defined in terms of a physical parameter (e.g., energy of the disturbance) because the eigenfunctions depend on the streaming coordinate and the local measurements of the amplitude in an experiment might depend on the coordinate y. All our results illustrating the nonparallel effects are obtained for the maximum streamwise velocity disturbance amplitude. One can see that the nonparallel flow effects have a stabilizing character. The effects become less significant with an increase of the wave number α. The latter is consistent with previous studies of nonparallel flow effects in other types of flows. Figure 10 shows the growth rates at two angles, θ, and three frequencies, ω_0. In all cases, the calculations were started at R_x=15, and the dimensional frequency was kept constant along the streamwise coordinate. The results demonstrate that the nonparallel flow effect is more significant for the low-frequency disturbances and lower Reynolds numbers as it should be because the wavelength becomes comparable with the streamwise scale of the mean flow. In the course of the present work, results by Iyer and Kelly [8] for the quasi-parallel approximation were repeated for the traveling waves at Pr=6.7. The discrepancy in the critical Reynolds numbers was less than 0.5%.

As was discussed earlier, previous works have determined that the nonparallel effects are essential in a stability analysis of the vortex mode. These theoretical models (we call them local nonparallel models) included into the leading operator terms V, $\partial U/\partial x$, and $\partial T/\partial x$ that originated from the mean-flow divergence and skipped terms associated with the dependence of the amplitude functions on the streamwise coordinate. Lee et al. [10] included the derivatives of the amplitude function as the next term of the Taylor series. Figure 11 shows the growth rate, $-\alpha_i$, for the steady vortex mode in the local nonparallel and quasi-parallel models. The results confirm the statement that the nonparallel effects affect the neutral point and the growth rate significantly.

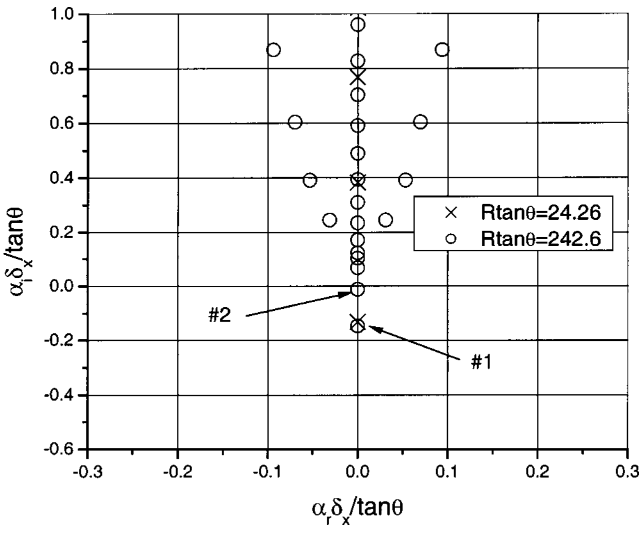

Fig. 7 Eigenvalue maps (ω=0, $\gamma\delta_x$=1.292). Quasi-parallel approximation. Pr=5.5.

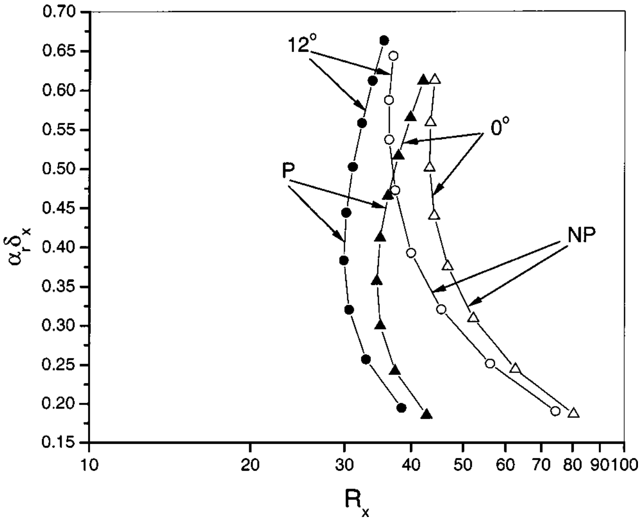

Fig. 9 Neutral curves for the traveling mode, γ=0. Solid symbols (P)–quasi-parallel approximation; open symbols (NP)–nonparallel flow theory. Pr=5.5.

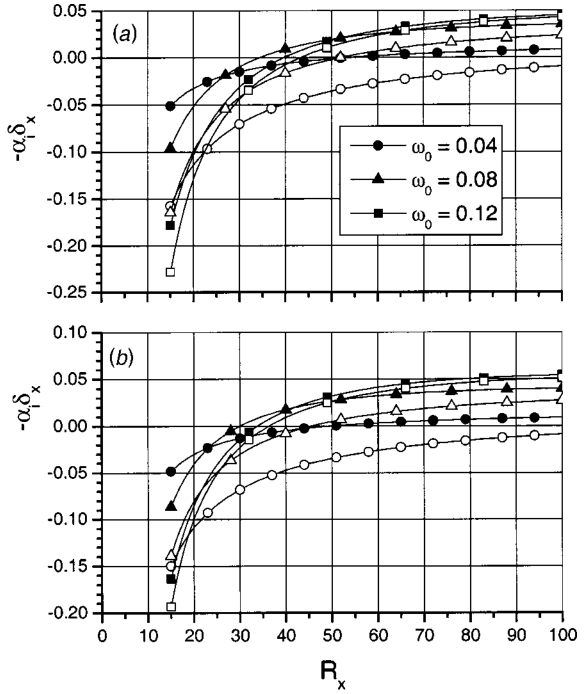

Fig. 10 Growth rates for the traveling modes: (*a*) θ=0°; (*b*) θ=12°. Solid symbols–quasi-parallel approximation; open symbols–nonparallel flow theory. Pr=5.5.

Inclusion of the relatively small terms in the leading operator might be questionable. To clarify it, we considered the perturbation method when the leading operator originates from the quasi-parallel approximation and all terms like V, $\partial U/\partial x$, and $\partial T/\partial x$ are included in the perturbation. As a result, they appear as term 1 in Eq. (29). The result is presented in Fig. 11. One can see that for the chosen parameters, the perturbation method based on the quasi-parallel approximation leads to the same result as the local nonparallel theory when the terms are included into the leading operator. The latter result, as will be shown further, depends on the Reynolds number, R_x, and the spanwise wave number, γ.

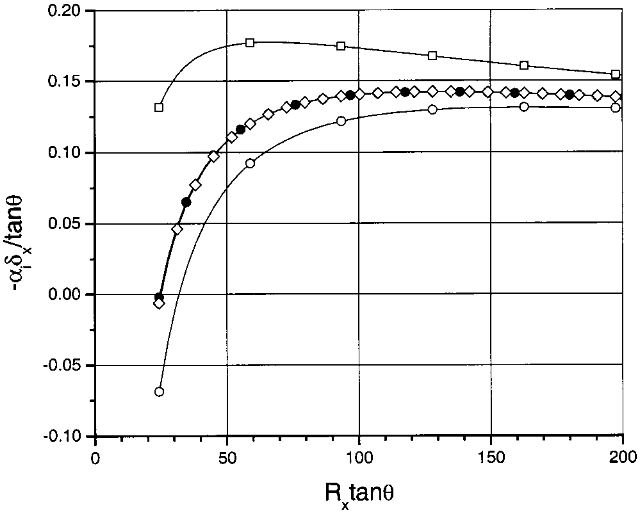

Fig. 11 Comparison of growth rates for different models of the steady vortex mode ($R_x\tan\theta$=24.26, ω=0, $\gamma\delta_x$=1.292): □ – quasi-parallel; ◇ – local nonparallel; ● – perturbation method (term No. 1 in Eq. (29) only); ○ – conventional nonparallel theory (both terms in Eq. (29)). Pr=5.5.

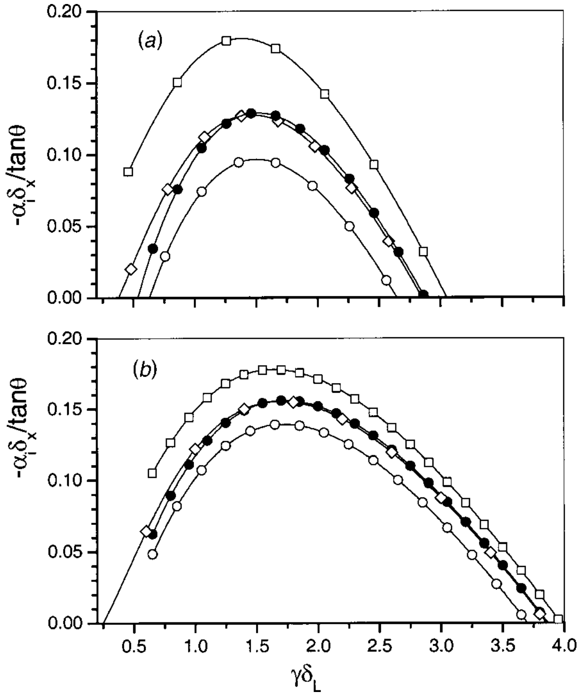

Fig. 12 Effect of spanwise wave number and Reynolds number on the growth rate of the vortex instability mode: (*a*) $R_x\tan\theta$=60; (*b*) $R_x\tan\theta$=120. □ – quasi-parallel; ◇ – local nonparallel; ● – perturbation method (term No. 1 in Eq. (22) only); ○ – conventional nonparallel theory (both terms in Eq. (22)). Pr=6.7.

The conventional consideration of nonparallel effect also includes the derivatives, $\partial/\partial X$, of the amplitude functions in the perturbation of the leading operator (term 2 in Eq. (29)). One can see from Fig. 11 that term 2 in Eq. (29) has significant stabilization in comparison with the input from term 1 only. This result indicates that nonparallel effects must be included consistently when the normal mode consideration is used for the stability analysis.

One can expect that the perturbation method provides more accurate results for higher Reynolds numbers. To illustrate the effect of the Reynolds number and the spanwise wave number, the growth rates are shown in Fig. 12 for two values of $R_x\tan\theta$. Because Chen et al. [9] reported a discrepancy with Haaland and Sparrow [7] for the lower branch of the neutral curve at Pr=6.7, we present the growth rates for this Prandtl number. One can see the stabilizing effect of the nonparallel flow effects on the vortex instability mode. The perturbation method (term 1 in Eq. (29) only) agrees better with the direct local nonparallel analysis at higher Reynolds numbers and higher spanwise wave numbers, γ. From these two examples, one can recognize that the neutral points at small γ corresponding to the local nonparallel flow model (diamonds in Fig. 12) agree with the data presented by Haaland and Sparrow [7].

4.3 The Marching Method. To illustrate dependence on the initial data, we use two runs (similar to the analysis of the Görtler instability in [19]). In the first run, the initial disturbance profiles at $\xi_0=0.02$ were equal to zero everywhere, and only the velocity disturbance $\overline{u}$ at the second grid point ($\hat{y}=5\times10^{-4}$) was equal to 1. In the second run, the initial disturbance profiles were equal to zero everywhere, but the streamwise velocity disturbance was chosen as $\overline{u}=\overline{U}(\xi=1,\hat{y})$. Because the inflow data do not satisfy governing Eqs. (34), there is a transient interval depending on the marching step. For purposes of illustration and to avoid the transient effect, we saved the velocities and pressure and tempera-

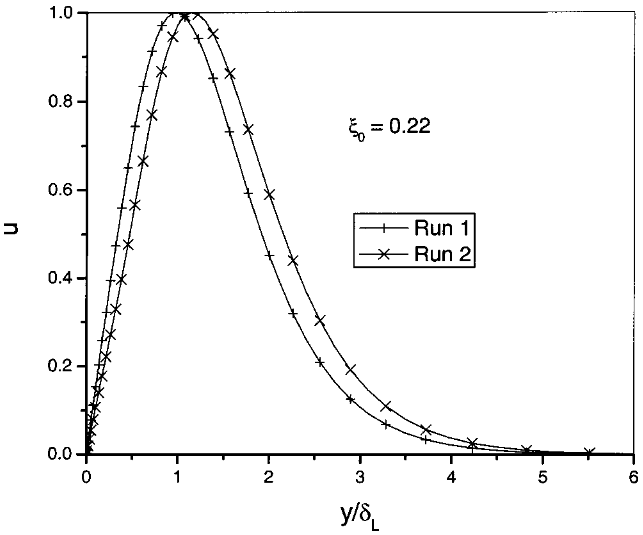

Fig. 13 Comparison of the disturbance velocity profiles at $\xi_0 = 0.22$ used in two runs ($R_L \tan\theta = 145$, $\gamma\delta_L = 1.5$): + – 1st run; × – 2nd run. Pr=5.5.

ture profiles obtained from the previous runs somewhere downstream ($\xi = 0.22$, see Fig. 13) and repeated the runs from this point with different marching steps ($\Delta\xi = 0.02$ and 0.004) using the saved profiles as initial data to check independence of the results of the marching step. Figure 14 shows $\bar{u}_{\max}$ from these two runs, with results normalized to the value $\bar{u}_{\max} = 1$ at $\xi = 1$. One can see that the behavior and growth rates in the vicinity of the neutral point for the first run depends on the initial data but, at some distance downstream, the results collapse onto one curve, similar to the results in Refs. [16–18] in the case of Görtler instability. The disturbance profiles also collapsed onto one another. Figure 15 demonstrates a comparison of growth rates for $u_{\max}$ obtained from three models: quasi-parallel approximation, theory with nonparallel effects, and marching method. In the latter case, the growth rates are evaluated from the first run shown in Fig. 14. One can see that, similar to the case of Görtler instability, the local analysis (quasi-parallel and nonparallel approximations) overestimates the growth rates. The dependence of the growth rate on the parameter γ at $\xi = 1$ is presented in Fig. 16.

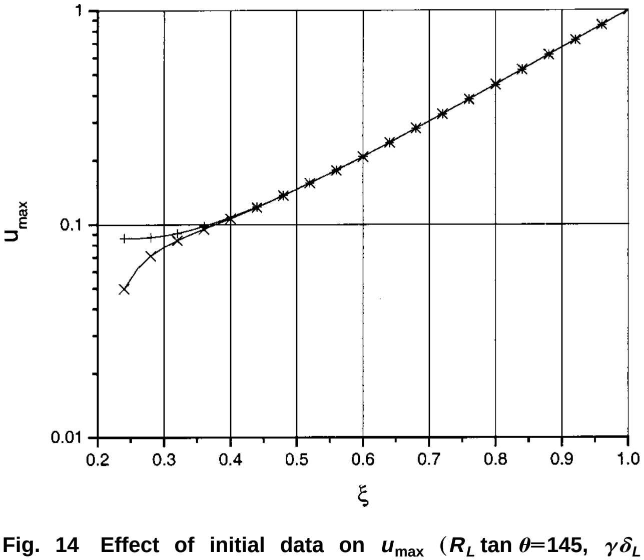

Fig. 14 Effect of initial data on $u_{\max}$ ($R_L \tan\theta = 145$, $\gamma\delta_L = 1.5$): + – 1st run; × – 2nd run. Pr=5.5.

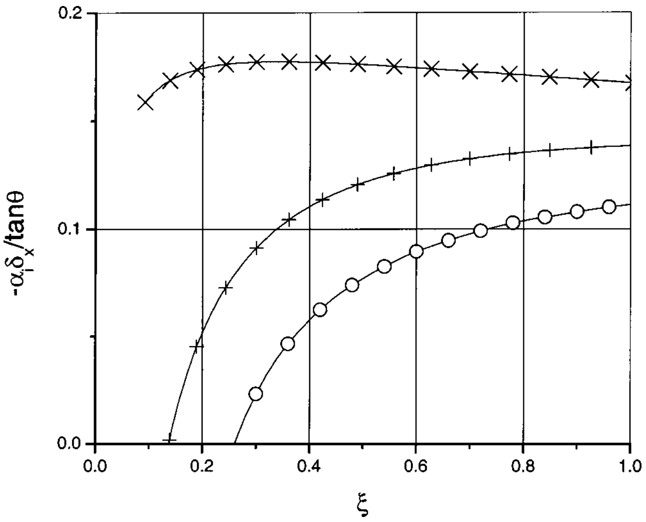

Fig. 15 Comparison of growth rates ($R_L \tan\theta = 145$, $\gamma\delta_L = 1.5$): × – quasi-parallel approximation; + – nonparallel normal mode consideration; ○ – marching method (run 1). Pr=5.5.

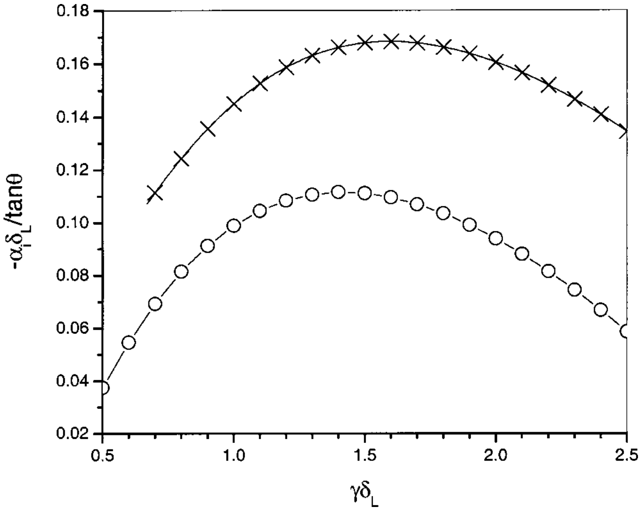

Fig. 16 Comparison of growth rates at $\xi = 1$. $R_L \tan\theta = 145$, Pr =5.5: × – quasi-parallel approximation; ○ – marching method (run 1).

5 Discussion

As follows from the results, the nonparallel flow effects stabilize the traveling and the vortex modes. In most studies of the vortex instability mode, theoretical models ignored the fact that the eigenfunctions depend on the streamwise coordinate. Lee et al. [10] included the dependence on the streamwise coordinate as the first term of the Taylor series. Usually the nonparallel flow effects are discussed in terms of correction of the growth rate, while there is a more significant point that must be addressed for the purpose of consistent comparisons with experimental data. As was mentioned above, the eigenfunction (solution of Eq. (27)) depends on the streamwise coordinate as a parameter. The latter leads to uncertainty of the eigenfunction normalization. How can we compare measurements of a physical parameter (i.e., velocity or temperature disturbance amplitudes) with the theoretical solution, $\hat{\mathbf{A}}^{(0)}(\hat{y},X)\exp[i(\int \alpha d\hat{x} + \gamma\hat{z} - \omega\hat{t})]$, when the uncertainty of normalization for $\hat{\mathbf{A}}^{(0)}(\hat{y},X)$ is not resolved? The same question is applicable to the model of [10]. How do we calculate the partial derivative of the eigenfunction $\partial\hat{\mathbf{A}}^{(0)}(\hat{y},X)/\partial X$? The main advantage of the method of multiple scales used for the stability of the nonparallel flow is that the uncertainty of normalization is resolved. One can easily show, with the help of Eq. (29), that the product $a(X)\hat{\mathbf{A}}^{(0)}(\hat{y},X)$ is invariant with respect to the eigenfunction normalization.

Similar to the Görtler instability in a boundary layer over a curved wall, the presented results illustrate that there is dependence of the vortex instability mode on initial conditions. The physical reason for this dependence is the nonmodal growth mechanism. This mechanism has been of great interest during the last 20 years. One can find a vast bibliography on this topic in [27,28]. In simple words, there is a possibility of combining the *decaying modes* of the spectra (see Fig. 4 or 5) in such way that the solution will possess a strong *transient growth* (nonmodal growth). As follows from the theoretical results, the optimal disturbances are associated with a system of counterrotating streamwise vortices. Although the transient growth phenomenon has not been considered in natural convection boundary layers, we can refer to results related to the problem of Görtler vortices, [29,30]. In other words, one should expect in an experiment that real behavior of the vortex instability mode might be hidden behind the transiently growing streamwise vortices associated with an initial perturbation.

Although interpretation of experimental data on the vortex instability might be complicated because of the coexistence of modal and nonmodal growth, it is tempting to compare theoretical growth rates with the experimental data obtained by Zuercher et al. [5]. The authors determined the spatial growth rates of circulation in the streamwise vortices observed in a boundary layer flow along a heated, inclined plate. They established that the amplitude could be fitted with the help of a universal curve $\Gamma = \tilde{A}\exp(\tilde{B}R_x\tan\theta)$ with $\tilde{B}=0.031$. Comparison with growth rates obtained within the scope of the quasi-parallel approximation in [8] showed that theoretical results significantly overestimate the experimental data. We would like to compare the results of the marching method with the experimental data.

One can easily establish the following relationship between the constant $\tilde{B}$ and our definition of growth rate

$$\frac{d\ln\Gamma}{dx}\,\delta_x=\tilde{B}\,\frac{3R_x\tan\theta}{4}\,\frac{\delta_x}{x}=3\tilde{B}\tan\theta$$
$$\frac{d\ln\Gamma}{dx}\,\frac{\delta_x}{\tan\theta}=3\tilde{B}=0.093. \tag{38}$$

We would like to point out that the experimental observation is consistent with the conclusion that the growth rate should be scaled with tan θ. To compare the absolute values of experimental and theoretical growth rates, we need to choose an appropriate spanwise wave number γ. As follows from Fig. 15 of [5], the authors included in their correlation data the spanwise wavelengths from 7 mm to 11.5 mm at $\theta=30°$ and $\Delta T=10°\mathrm{C}$. The results indicate a shallow peak in the growth rate at the wavelength, λ_z, equal to 10 mm. It was also established in [5] that the streamwise vortices could be clearly observed at $R_x\tan\theta=145$. Therefore, theoretical data from Fig. 16 obtained with the help of the marching method can be used for the comparison. The following equation serves for estimation of the wave number

$$\gamma\delta_L=\frac{2\pi}{\lambda_z}\,\delta_L=\frac{2\pi}{\lambda_z}\,\frac{L^{1/4}}{\kappa}=\frac{2\pi}{\lambda_z\kappa}\left(\frac{R_L}{4\kappa}\right)^{1/3}=\frac{2\pi}{\lambda_z\kappa}\left(\frac{R_L}{4\kappa}\right)^{1/3}. \tag{39}$$

We use Eq. (39) with $R_L\tan\theta=145$, $\lambda_z=10$ mm, and $\theta=30°$. Parameter κ can be obtained from the definition in Eq. (4) with $\Delta T=10°\mathrm{C}$ and $g\beta/\nu^2=5.808\times10^3\ \mathrm{K}^{-1}\ \mathrm{cm}^{-3}$, [9]. Finally, we arrive at the dimensionless wave number $\gamma\delta_L=1.07$. This wave number corresponds to the dimensionless growth rate in Fig. 16 equal to 0.10. The agreement within 10% of the growth rate with the experimental value, 0.093, is promising.

As was discussed above, interpretation of experimental data on the vortex instability might be complicated because of the coexistence of modal and nonmodal growth. Therefore, the design of this kind of experiment and analysis of the experimental data should be accompanied by a comprehensive theoretical analysis. To deal with well-controlled disturbances (even if the basic flow field is well controlled), it is not enough to place some kind of roughness strips to force the streamwise vortices. The strips might generate vortices so that only a small portion will correspond to the instability mode. To resolve this obstacle to the analysis, the receptivity problem must be solved in conjunction with a decomposition of the disturbance field into the discrete and continuous spectra to interpret the experimental data. As an appropriate tool for the receptivity analysis, one can use the adjoint based method, [31,32], within the scope of the full linearized governing equations, (1)–(3), or one can use the parabolized equations for simultaneous receptivity analysis and for the disturbance analysis downstream from the roughness elements, [19]. Effects of the nonlinear regime can be considered within the scope of the model of [21].

Acknowledgments

The author thanks Prof. C. F. Chen for useful and encouraging discussion of the results. The assistance of Mrs. Connie Spencer in the preparation of the manuscript is gratefully acknowledged. The author benefited from the valuable comments and suggestions of five anonymous reviewers.

Appendix

We denote $\Omega=iR_L(\alpha\overline{U}-\omega)+\alpha^2+\gamma^2$ and $D=d/d\hat{y}$, and rewrite the nonzero elements of the matrices E, H_0, H_1, and H_2 in Eq. (25) as follows:

$$E=\mathrm{diag}(1,R_L^{-1},1,1,1,R_L^{-1},1,R_L^{-1})$$

$$H_0^{12}=1,\quad H_0^{21}=\Omega/R_L,\quad H_0^{23}=D\overline{U},\quad H_0^{24}=i\alpha,\quad H_0^{25}=-1/R_L$$

$$H_0^{31}=-i\alpha,\quad H_0^{37}=-i\gamma,\quad H_0^{42}=-\frac{i\alpha}{R_L},\quad H_0^{43}=-\frac{\Omega}{R_L},$$

$$H_0^{45}=\frac{\tan\theta}{R_L}$$

$$H_0^{48}=-\frac{i\gamma}{R_L},\quad H_0^{56}=1,\quad H_0^{63}=\mathrm{Pr}D\overline{T},$$

$$H_0^{65}=[i\mathrm{Pr}R_L(\alpha\overline{U}-\omega)+\alpha^2+\gamma^2]/R_L$$

$$H_0^{78}=1,\quad H_0^{84}=i\gamma,\quad H_0^{87}=\Omega/R_L$$

$$H_1^{21}=-DV_*,\quad H_1^{22}=V_*,\quad H_1^{41}=i\alpha V_*,$$

$$H_1^{43}=-DV_*,\quad H_1^{47}=i\gamma V_*$$

$$H_1^{61}=\mathrm{Pr}\frac{\partial\overline{T}}{\partial X},\quad H_1^{66}=\mathrm{Pr}V_*,\quad H_1^{88}=V_*$$

$$H_2^{21}=\overline{U},\quad H_2^{24}=1,\quad H_2^{31}=-1,\quad H_2^{42}=-1/R_L,\quad H_2^{43}=-\overline{U}$$

$$H_2^{65}=\mathrm{Pr}\overline{U},\quad H_2^{87}=\overline{U}.$$

The matrices A, B_0, B_1, and B_2 in Eq. (34) have the following nonzero elements:

$$A^{11}=1,\quad A^{21}=\overline{U},\quad A^{31}=V_*/4,\quad A^{32}=\overline{U},\quad A^{43}=\overline{U},$$

$$A^{51}=\overline{T},\quad A^{55}=\overline{U}$$

$$B_0^{21}=-0.25\gamma^2,\quad B_0^{22}=-D\overline{U},\quad B_0^{25}=0.25$$

$$B_0^{32}=-0.25\gamma^2-0.5DV_*,\quad B_0^{33}=0.25\gamma V_*,\quad B_0^{35}=R_L\tan\theta/16$$

$$B_0^{43} = -0.25\gamma^2 - 0.25DV_*, \quad B_0^{44} = -\gamma$$

$$B_0^{52} = -D\overline{T}, \quad B_0^{53} = \gamma\overline{T}, \quad B_0^{55} = -0.25\gamma^2/\mathrm{Pr} - 0.25DV_*$$

$$B_1^{12} = -1, \quad B_1^{21} = -0.25V_*, \quad B_1^{32} = -0.5V_*, \quad B_1^{34} = -1$$

$$B_1^{43} = -0.25V_*, \quad B_1^{52} = -\overline{T}, \quad B_1^{55} = -0.25V_*$$

$$B_2^{21} = B_2^{32} = B_2^{43} = B_2^{55} = 0.25.$$

References

[1] Gebhart, B., Jaluria, Y., Mahajan, R. L., and Sammakia, B., 1988, *Buoyancy-Induced Flows and Transport*, Hemisphere, Washington, DC.

[2] Sparrow, E. M., and Husar, R. B., 1969, ''Longitudinal Vortices in Natural Convection Flow on Inclined Plates,'' J. Fluid Mech., **37**, pp. 251–255.

[3] Lloyd, J. R., and Sparrow, E. M., 1970, ''On the Instability of Natural Convection Flow on Inclined Plates,'' J. Fluid Mech., **42**, pp. 465–470.

[4] Shaukatullah, H., and Gebhart, B., 1978, ''An Experimental Investigation of Natural Convection Flow on an Inclined Surface,'' Int. J. Heat Mass Transf., **21**, pp. 1481–1490.

[5] Zuercher, E. J., Jacobs, J. W., and Chen, C. F., 1998, ''Experimental Study of the Stability of Boundary-Layer Flow Along a Heated, Inclined Plate,'' J. Fluid Mech., **367**, pp. 1–25.

[6] Trautman, M. A., 1999, ''The Manipulation of Instability in a Natural Convection Boundary Layer Along a Heated, Inclined Plate,'' Ph.D. thesis, Georgia Institute of Technology, Atlanta, GA.

[7] Haaland, S. E., and Sparrow, E. M., 1973, ''Vortex Instability of Natural Convection Flow on Inclined Surfaces,'' Int. J. Heat Mass Transf., **16**, pp. 2355–2367.

[8] Iyer, P. A., and Kelly, R. E., 1974, ''The Stability of the Laminar Free Convection Flow Induced by a Heated, Inclined Plate,'' Int. J. Heat Mass Transf., **17**, pp. 517–525.

[9] Chen, C. C., Labhabi, A., Chang, H.-C, and Kelly, R. E., 1991, ''Spanwise Pairing of Finite-Amplitude Longitudinal Vortex Rolls in Inclined Free-Convection Boundary Layers,'' J. Fluid Mech., **231**, pp. 73–111.

[10] Lee, H. R., Chen, T. S., and Armaly, B. F., 1992, ''Non-Parallel Thermal Instability of Natural Convection Flow on Non-Isothermal Inclined Flat Plates,'' Int. J. Heat Mass Transf., **35**, pp. 207–220.

[11] Wakitani, S., 1985, ''Non-Parallel-Flow Stability of a Two-Dimensional Buoyant Plume,'' J. Fluid Mech., **159**, pp. 241–258.

[12] Bouthier, M., 1971, ''Stabilité Linéaire des Écoulements Presque Paralléles par la Method des Échelles Multiples,'' C. R. Acad. Sci., Ser., A, **273**, pp. 1101–1104.

[13] Bouthier, M., 1973, ''Stabilité Linéaire des Écoulements Presque Paralléles. Part 1,'' J. Mec., **12**, pp. 75–95.

[14] Gaster, M., 1974, ''On the Effects of Boundary Layer Growth on Flow Stability,'' J. Fluid Mech., **66**, pp. 465–480.

[15] Saric, W. S., and Nayfeh, A. H., 1975, ''Non-Parallel Stability of Boundary-Layer Flows,'' Phys. Fluids, **18**, pp. 945–950.

[16] Saric, W. S., 1994, ''Görtler Vortices,'' Annu. Rev. Fluid Mech., **26**, pp. 379–409.

[17] Hall, P., 1983, ''The Linear Development of Görtler Vortices in Growing Boundary Layers,'' J. Fluid Mech., **130**, pp. 41–58.

[18] Day, H. P., Herbert, T., and Saric, W. S., 1990, ''Comparing Local and Marching Analyses of Görtler Instability,'' AIAA J., **28**, pp. 1010–1015.

[19] Luchini, P., and Bottaro, A., 1998, ''Görtler Vortices: A Backward-in-Time Approach to the Receptivity Problem,'' J. Fluid Mech., **363**, pp. 1–23.

[20] Hall, P., and Morris, H., 1992, ''On the Instability of Boundary Layers on Heated Plates,'' J. Fluid Mech., **245**, pp. 367–400.

[21] Jeschke, P., and Beer, H., 2001, ''Longitudinal Vortices in a Laminar Natural Convection Boundary Layer Flow on an Inclined Flat Plate and Their Influence on Heat Transfer,'' J. Fluid Mech., **432**, pp. 313–339.

[22] Malik, M. R., 1990, ''Numerical Methods for Hypersonic Boundary Layer Stability,'' J. Comput. Phys., **86**, pp. 376–413.

[23] Andersson, P., Berggren, M., and Henningson, D. S., 1999, ''Optimal Disturbances and Bypass Transition in Boundary Layers,'' Phys. Fluids, **11**, pp. 134–147.

[24] Ashpis, D., and Reshotko, E., 1990, ''The Vibrating Ribbon Problem Revisited,'' J. Fluid Mech., **213**, pp. 513–547.

[25] Tumin, A., and Reshotko, E., 2001, ''Spatial Theory of Optimal Disturbances in Boundary Layers,'' Phys. Fluids, **13**, pp. 2097–2104.

[26] Hall, P., 1982, ''Taylor-Görtler Vortices in Fully Developed or Boundary Layer Flows—Linear Theory,'' J. Fluid Mech., **124**, pp. 475–494.

[27] Reshotko, E., 2001, ''Transient Growth: A Factor in Bypass Transition,'' Phys. Fluids, **13**, pp. 1067–1075.

[28] Schmid, P. J., and Henningson, D. S., 2001, *Stability and Transition in Shear Flows* (Applied Mathematical Sciences, **142**), Springer-Verlag, New York.

[29] Cossu, C., Chomaz, J.-M., and Costa, M., 2000, ''Maximum Growth of Görtler Vortices,'' *Laminar-Turbulent Transition*, H. Fasal and W. S. Saric, eds., IUTAM Symposium, Sedona, AZ, Springer-Verlag, New York, pp. 511–516.

[30] Ardonceau, P., and Chevalerie, D. A., 2000, ''Non Normality of the Görtler Operator and Spatial Amplification,'' *Laminar-Turbulent Transition*, H. Fasel and W. S. Saric, eds., IUTAM Symposium, Sedona, AZ, Springer-Verlag, New York, pp. 517–522.

[31] Tumin, A. M., and Fedorov, A. V., 1983, ''Excitation of Instability Waves in a Boundary Layer on a Vibrating Surface,'' J. Appl. Mech. Tech. Phys., **24**, pp. 348–354 (translated from Russian).

[32] Tumin, A., 1996, ''Receptivity of Pipe Poiseuille Flow,'' J. Fluid Mech., **315**, pp. 119–137.

Separated Flow in Bends of Arbitrary Turning Angles, Using the Hodograph Method and Kirchhoff's Free Streamline Theory

S. S. Chu[1]
Department of Information Management,
Fooyin University,
Ta-Liao,
Kaohsiung Hsien,
Taiwan, R.O.C.

The problem of separated flow in bends of arbitrary turning angles has been examined. The method of analysis is based on the inviscid flow theory coupled with Kirchhoff's separation model. The physical flow problem is first transformed to the hodograph domain, and then into a rectangular computational region using properly selected flow parameters. The solution is first established in the hodograph plane. The final flow pattern including the inner and outer walls of the bend, the separation streamline, and other flow properties in the physical plane are subsequently obtained through direct integration. The results of the present analysis are compared with those of Lichtarowicz and Markland as well as Mankbadi and Zaki. [DOI: 10.1115/1.1567311]

Introduction

Problems of separated flow in components of a fluid power system have been very important in determining the energy losses in practical applications, such as the flow in pipes, valves, and fittings including tees, elbows, and bends. When a real fluid passes around a bend, the flow separation usually starts at the inner corner, and a separated flow region may also exist in the outer corner. After separating from the inner corner, the fluid may reattach to the inner wall of the bend. Both the size of the separation region in the outer corner and the reattachment length on the inner wall depend on the Reynolds number of the flow and the geometry of the bend. Solutions of the Navier-Stokes equations are required in order to resolve these phenomena of viscosity. However, such solution procedures are quite tedious. The potential flow theory cannot predict the effects of viscosity directly. Nevertheless, a good theoretical prediction of such viscous dissipation can be derived from an inviscid flow estimate of the size of the separation bubble and the velocity gradient across it. Several previous studies, [1–6], have also shown that the analysis of potential flow with separation often yields results which agree well with the experimental values.

Other than solving the Navier-Stokes equations which requires more computational cost, the separated flow in a two-dimensional bend has been attacked successfully using theoretical treatments based on the free streamline theory for a realistic representation of the potential flow, and the problem was treated by considering the separation occurring only at the inner corner. Lichtarowicz and Markland [2] used the conformal transformation to solve potential flow with separation in a right-angled elbow. However, the confined 90 deg turning angle is sometimes not of much interest for practical situations. Mankbadi and Zaki [1] solved the potential flow with separation in bends of various angles through successive mapping of the hodograph plane. But the solutions of symmetric bend are not in good agreement with those of Lichtarowicz and Markland [2] when the velocity distribution along the separating streamline for the two works are the same; besides, the shape of the resulting separation streamline is also not accurate enough.

Application of the method of hodograph transformation has not been extensively explored for engineering purpose. However, in recent years, a number of studies using the hodograph method have been reported, [7–17], which indicate that the hodograph transformation coupled with numerical computation is particularly efficient for both two-dimensional and axisymmetric flow problems, especially when straight boundaries are involved, such as the flow through certain components of a propulsive system, control valve, and orifice. The simplicity in its specification of the boundary condition of the free boundary problem in the hodograph plane and the ease of finding solution through iterations make this approach very effective and economical in dealing with many problems of this nature. The physical flow problem is first transformed to the hodograph domain, and then into a rectangular computational region using properly selected flow parameters. Kirchhoff's concept of a free streamline is applied to treat the separated flow. The stream function ψ is first established in the hodograph plane. The final flow pattern including the inner and outer walls of the bend, the separation streamline, and other flow properties in the physical plane are subsequently obtained through direct integration. The final results are compared with those of Lichtarowicz and Markland [2] as well as Mankbadi and Zaki [1].

Since the physical geometry of the body involved with the flow is not known before the solution has been established, this solution procedure has been recognized as an indirect method, and its application to finding flow solutions has been rather restrictive. Since the advent of high-speed computers, this deficiency arising from the indirect nature of this method has been considerably suppressed, if not completely eliminated. It is the intention of the present work to show that the proposed method of using the hodograph transformation coupled with numerical iteration is a simple, fast, and accurate solution procedure for treating the present problem of separated flow in bends of arbitrary turning angles.

Analytical Considerations

The method of hodograph transformation is employed to formulate the problem of separated flow in bends of arbitrary turning

---

[1] Former Professor of Aeronautical Engineering, Airforce Academy, Kangshan, Taiwan, R.O.C.

Contributed by the Fluids Engineering Division for publication in the JOURNAL OF FLUIDS ENGINEERING. Manuscript received by the Fluids Engineering Division January 17, 2000, revised manuscript received December 4, 2002. Associate Editor: U. Ghia.

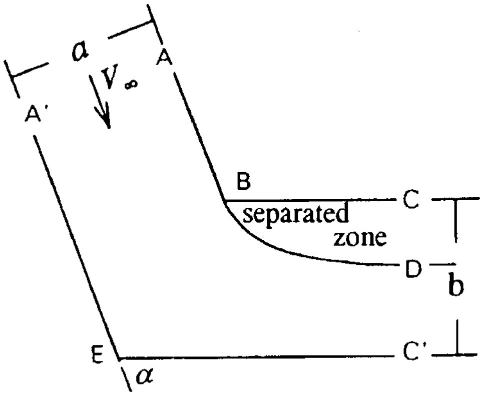

Fig. 1 Schematic of flow inside a bend

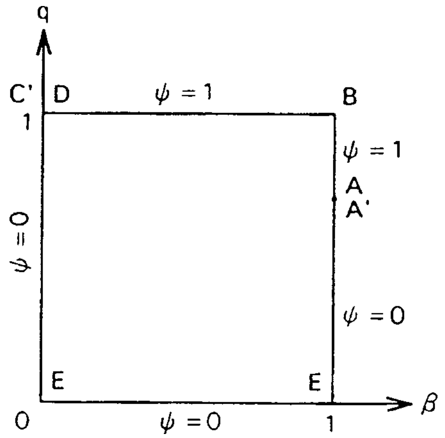

Fig. 2 The hodograph diagram

angles. Kirchhoff's concept of a free streamline is applied to treat the separated flow, [1,18]. The separated free streamline is assumed to start from the inner corner of the bend, gradually turn through the bend angle toward the direction of the after portion of the bend, and asymptotically extend to infinity. That is, the separated free streamline divides the flow field inside the bend into two parts, the main portion of the flow allowing a velocity potential to be defined, and a separated zone bounded by the curved free streamline as shown in Fig. 1, where BD is the separated free streamline. The velocity along the curved free streamline is constant and greater than the upstream uniform velocity, and has been taken as unity in the analysis.

Roshko's free streamline model was applied by Lichtarowicz and Markland [2] to solve the flow around a right-angled elbow. The separation streamline may be regarded as consisting of two parts; the first is a curved part which turns through a right angle, and the second part of the streamline is straight and parallel to the wall. Following Roshko [6,19], the position of the conjuncture point of the two parts of the separation streamline and the variation of velocity along the streamline are functions of the ratio of the velocity at the separation point to the velocity downstream. A constant velocity distribution along the whole line is one of the choices in the Roshko's free streamline model, which then becomes the same as Kirchhoff's model for this choice. Several other variations of the Kirchhoff's free streamline model have also been used successfully in some other flow cases [5,20,21]. However, Kirchhoff's model has been particularly successful in treating internal flows with separation.

By taking the speed V and the streamline angle θ of the flow as the independent variables while treating all other quantities, including the physical coordinates x, y, as the dependent variables, the physical flow problem can be transformed to the hodograph domain. For convenience in computations, it has been found to be more efficient to perform a transformation again using properly selected flow parameters to obtain a rectangular computational region. The solution is thus established first in this rectangular hodograph plane. The hodograph equation governing the steady incompressible potential flow can be written as, [22],

$$V^2\psi_{VV}+V\psi_V+\psi_{\theta\theta}=0 \tag{1}$$

where the subscripts indicate differentiations with $V=\sqrt{u^2+v^2}$ and $\theta=\tan^{-1}(v/u)$. The physical coordinates (x, y) are related to (V,θ) through

$$dx=-(\psi_\theta\cos\theta/V^2+\psi_V\sin\theta/V)dV+(\psi_V\cos\theta -\psi_\theta\sin\theta/V)d\theta \tag{2a}$$

$$dy=(-\psi_\theta\sin\theta/V^2+\psi_V\cos\theta/V)dV+(\psi_V\sin\theta +\psi_\theta\cos\theta/V)d\theta. \tag{2b}$$

Upon introducing the dimensionless variables: $\beta=\theta/\alpha$, $q=V/V_s$, $\psi'=\psi/(V_s b)$ where α is the turning angle of the bend, V_s is the velocity at the separation point, and b is the width of downstream contracted flow, Eq. (1) becomes

$$q^2\psi_{qq}+q\psi_q+\frac{1}{\alpha^2}\psi_{\beta\beta}=0, \tag{3}$$

where the prime on ψ' has been intentionally eliminated for simplicity. The corresponding hodograph now becomes a rectangle as shown in Fig. 2. The values of ψ, β, and q now all vary from zero to unity. The flow field in the $\beta-q$ plane may then be interpreted as a point source at A of total strength aV_∞ and a point sink of equal but opposite strength at D. All the flow from the source is consumed by the sink. The coordinates of the rectangular hodograph are already normalized by the respective reference quantities, and the boundary conditions are completely specified. The solution in the physical plane can then be obtained by integrating the following equations of the transformation:

$$dx=-(\psi_\beta\cos\alpha\beta/\alpha q^2+\psi_q\sin\alpha\beta/q)dq+(\alpha\psi_q\cos\alpha\beta -\psi_\beta\sin\alpha\beta/q)d\beta \tag{4a}$$

$$dy=(-\psi_\beta\sin\alpha\beta/\alpha q^2+\psi_q\cos\alpha\beta/q)dq+(\alpha\psi_q\sin\alpha\beta +\psi_\beta\cos\alpha\beta/q)d\beta. \tag{4b}$$

Once all ψ values are established, solutions in the hodograph domain can be transformed back to the physical plane to obtain the resulting physical flow field. The final flow pattern including the length and location of the inner and outer walls of the bend, the coordinates of the separation streamline, and other flow properties in the physical plane are subsequently obtained through direct integration. The separation streamline is obtained by integrating along the top boundary of the hodograph, while the physical geometry of the four sides of the bend is established through integration along the left and right boundaries. The velocity field of the flow follows immediately from the evaluation of the corresponding physical coordinates. Unlike Lichtarowicz and Markland's [2] work in which the Roshko's free streamline model was applied, no conjuncture point for the separation streamline was invoked in the present work. With the proposed method, only the upstream uniform velocity and the turning angle need to be specified for the calculations of the whole flow field.

Numerical Computation

For solving the hodograph equation, the rectangular hodograph region is divided into a finite difference mesh of uniform size in both β and q directions. A finite difference scheme with second-order central differencing has been constructed to solve the hodograph equation. Upon arranging it in the form of a tridiagonal matrix, the finite difference expression of the hodograph equation may be written as

$$(2q^2\alpha^2\Delta\beta_{ij}^2+q\alpha^2\Delta q_{ij}\Delta\beta_{ij}^2)\psi_{i,j+1}+(-4q^2\alpha^2\Delta\beta_{ij}^2-4\Delta q_{ij}^2)\psi_{i,j}$$
$$+(2q^2\alpha^2\Delta\beta_{ij}^2-q\alpha^2\Delta q_{ij}\Delta\beta_{ij}^2)\psi_{i,j-1}$$
$$=-2\Delta q_{ij}^2(\psi_{i+1,j}+\psi_{i-1,j}). \qquad (5)$$

With the boundary values completely specified in the hodograph domain, solutions of the hodograph equation can be established through iterations for selected values of α and V_∞.

It should be noted that discontinuities of ψ along the boundaries of the hodograph domain are inherent to the method of the hodograph transformation. With the given boundary values, ψ is established within the domain through the successive over-relaxation method. A converged solution is achieved when the variation of ψ at each grid point is within an arbitrarily small margin (e.g., 10^{-5}). Convergence histories of the present work may be depicted by two ways; one is by plotting the maximum variation of ψ in the computational region as a function of iteration cycles, the other representation is the residual versus iteration cycles.

After all $\psi(\beta,q)$ values satisfy the convergence criterion, the derivatives ψ_β and ψ_q can be evaluated for all points, and the x and y values can then be obtained by integrating Eqs. (4*a*) and (4*b*) numerically. Results of the final flow pattern including the inner and outer walls of the bend, the separation streamline, and other flow properties in the physical plane are subsequently obtained. The contraction coefficient defined as $C_C=DC'/AA'$ can be evaluated after the coordinates of B and D are obtained. The pressure distribution along the lower side of the bend can also be established after the velocity distribution is evaluated through the Bernoulli's principle. Although the solution procedure is an indirect approach, it has been found to be more efficient to specify only the bend angle rather than the complete bend geometry.

Results and Discussion

Calculations have been carried out for some cases of flow in bends with different turning angles. A right-angled elbow was first considered. Due to the indirect nature of the hodograph method, a variety of the resulting bend geometries in the physical plane may be yielded by different specified inlet velocities. A simple interpolation procedure will find the value $V_\infty=0.54$ that will produce a symmetrical bend, i.e., a bend with the upstream width equal to the downstream width. The computed solution in the hodograph plane is displayed in Fig. 3. All streamlines emanating from the "sourcelike" point A go to the "sinklike" point C′ as depicted in

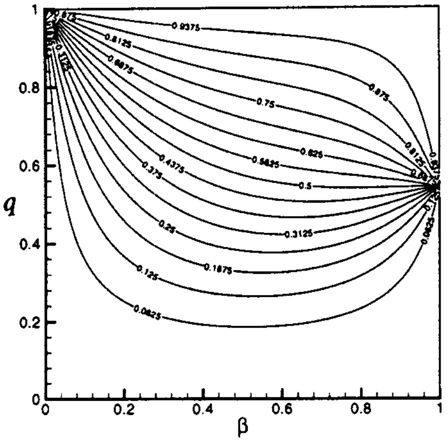

Fig. 3 A typical solution in the hodograph plane

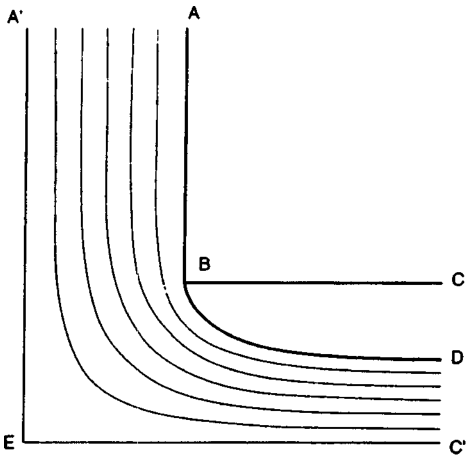

Fig. 4 Solution for a right-angled bend in physical plane

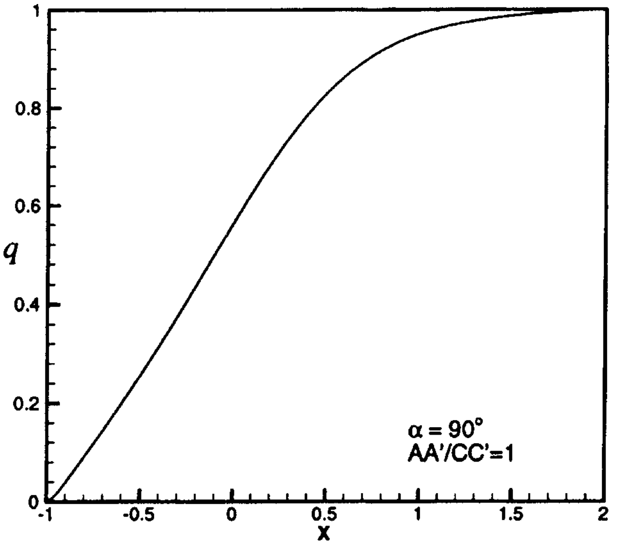

Fig. 5 Velocity distribution along the lower side of a right-angled bend

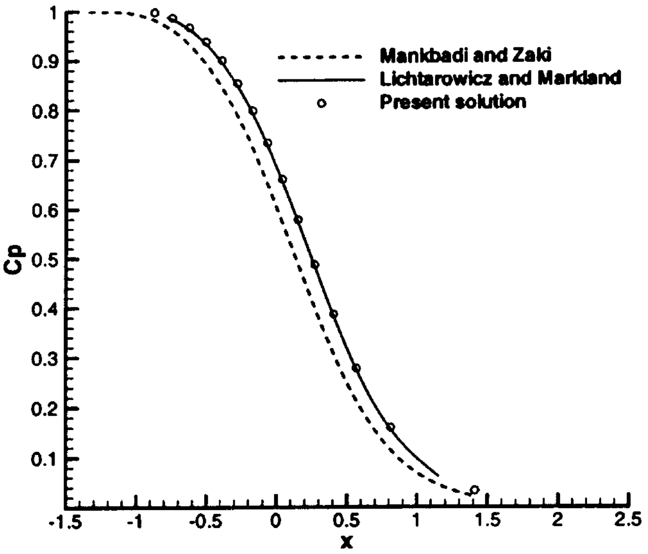

Fig. 6 Pressure coefficient along the lower side of a right-angled bend

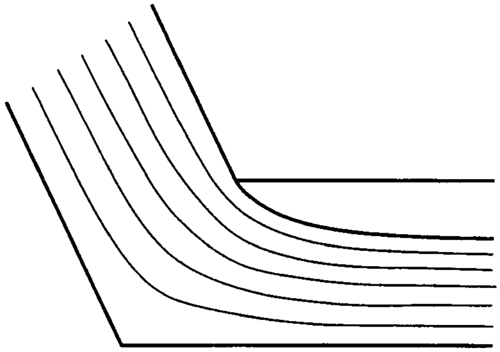

Fig. 7 Solution for a bend of 60 deg in physical plane

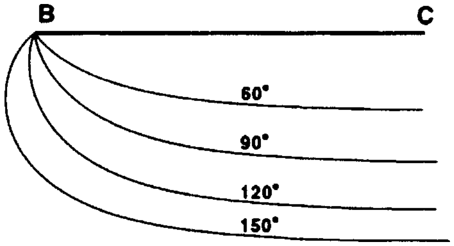

Fig. 8 Free streamlines for different bend angles

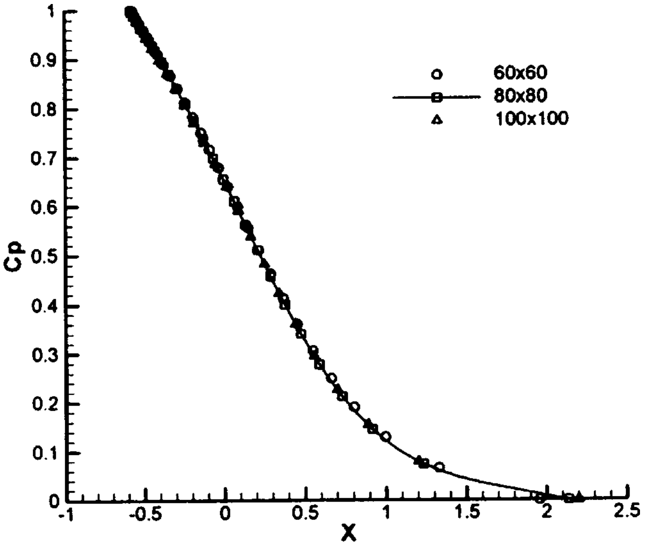

Fig. 10 Pressure coefficient along the lower side of the bend for $\alpha = 60°$ using different grids

this figure. The resulting separation streamline, the flow pattern, and the elbow configuration are shown in Fig. 4.

The velocity distribution along the lower side of the right-angled elbow EC′ is shown in Fig. 5, which is the trend observed by using different numbers of the mesh points along both the upper and lower sides of the bend for a grid-independence study. The pressure distributions along the lower side of the wall are presented in Fig. 6. Also shown in Fig. 6 are the results of Mankbadi and Zaki [1] and the solutions of Lichtarowicz and Markland [2]. The prediction of pressure coefficient distribution by the proposed method is in very good agreement with the solutions of Lichtarowicz and Markland. That is, the same discrepancy between the results of the two referred methods is also encountered between the proposed method and the method of Mankbadi and Zaki. The discrepancies theoretically should not exist, other than possible numerical errors, since these three methods are all classified as exact solution procedures.

For the case where the bend angle is 60 deg, the solution in the physical plane is shown in Fig. 7. Cases with the specified bend angle of 120 and 150 deg are also computed. The corresponding geometry of the separated free streamlines are obtained and plotted in Fig. 8. This also indicates that the solutions produced by the proposed method are more accurate than Mankbadi and Zaki's solution, since the separation streamline should not protrude from the slope of the inner wall AB at the separation point as is shown in their paper for the 90 deg case, [1]. Values of contraction coefficient for different turning angles are shown in Fig. 9, which shows that the contraction coefficient decreases with increasing bend angle.

For typical cases, with a relaxation factor of 1.5 and a 80×80 uniform grid, about 500 iterations were required to obtain the

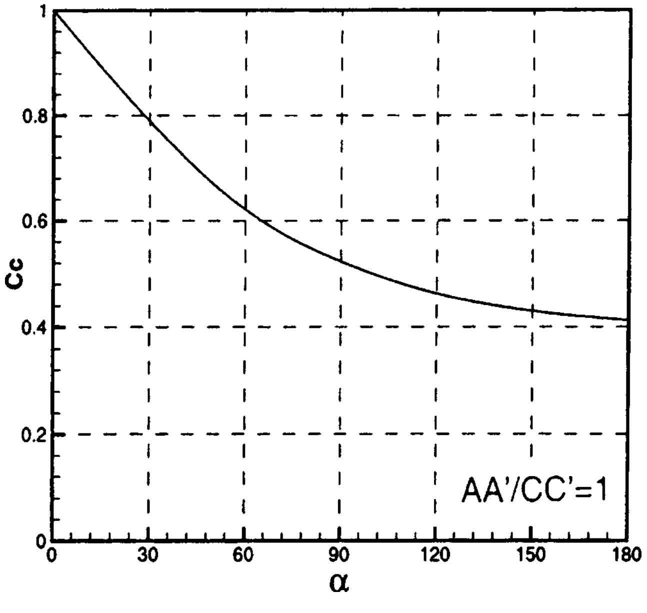

Fig. 9 Contraction coefficients for flow around bends of arbitrary turning angles

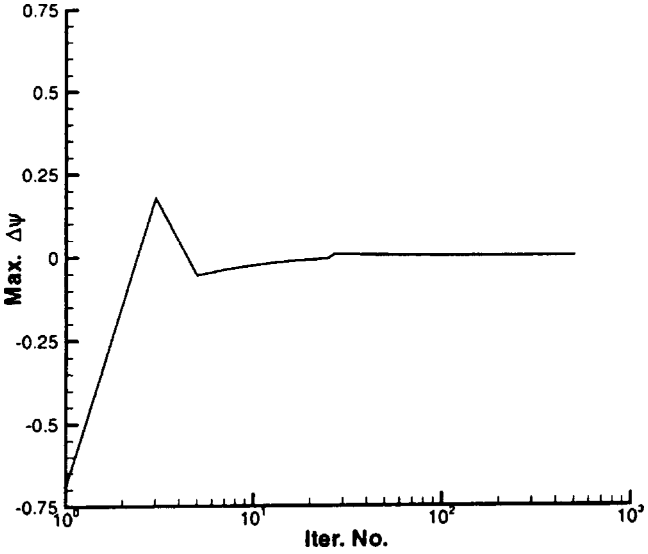

Fig. 11 Maximum correction convergence history for the hodograph solution

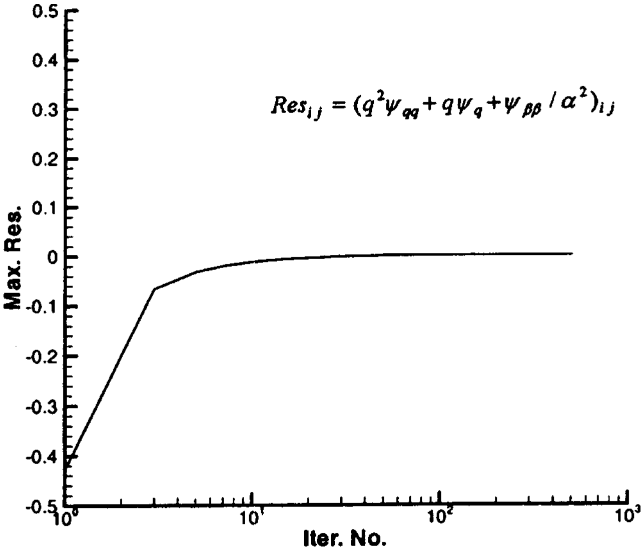

Fig. 12 Maximum residual convergence history for the hodograph solution

converged ψ values for both the variation of ψ and the residual at each grid point to become less than 10^{-6}. Figure 10 shows the pressure coefficient distribution along the lower side of the bend for $\alpha = 60°$ using three different sizes of grid, 60×60, 80×80, 100×100. There is very little difference between the results obtained on the three different grids. A convergence history for the maximum variation of ψ is shown in Fig. 11. The residual history is shown in Fig. 12. About only 15 sec computation time was needed to produce a complete set of results on a Sun Sparc classic workstation.

Conclusions

Separated flow in bends of arbitrary turning angles have been solved through the use of hodograph transformation coupled with numerical computations. With the proposed method, only the upstream uniform velocity and the turning angle need to be specified for the whole flow field calculation. It is found that the present solutions are in very close agreement with Lichtarowicz and Markland's results. The discrepancies between Lichtarowicz and Markland's solutions and the results of Mankbadi and Zaki should not happen theoretically, since these three methods are all classified as an exact solution procedure (other than the possible numerical errors of computation). Hence, the preceding comparison suggests that the solution procedure of Mankbadi and Zaki could be further improved or modified to eliminate the presented discrepancies.

The present work shows that the proposed solution procedure is indeed a simple, fast, and accurate method for the present problem, although it is recognized as an indirect method. A full use of the conformal mapping method for solving a flow problem may be somewhat difficult or complicated, especially in a time when these classical approaches are not mentioned anymore in most text books of fluid dynamics. However, the hodograph formulation of a flow problem coupled with numerical computations will be an attractive way, not only for getting qualitative insight into the flow problems but also for the benefits from the advent of high-speed computers.

The method developed in this paper is not limited to only the flow cases of the present study. It can be extended to many other flow processes, especially when the body has a straight-line profile and/or the flow possesses free boundaries, whether the flow configuration is two-dimensional or axisymmetric. The simplicity in the specification of the boundary conditions in the hodograph plane and the ease of finding solution through iterations make the present approach very effective and economical in dealing with many problems of this nature. Although the present problem was treated by considering the separation occurring only at the inner corner, it is believed that the present method of attack could include separation at the outer corner of the bend. Certainly, more efforts are needed including verification of momentum conservation for each of the solutions of the hodograph equation to single out a physically realistic solution for each flow case. Also, a more practical extension to asymmetric bends can be anticipated.

References

[1] Mankbadi, R. R., and Zaki, S. S., 1986, "Computations of the Contraction Coefficient of Unsymmetrical Bends," AIAA J., **24**, pp. 1285–1289.
[2] Lichtarowicz, A., and Markland, E., 1963, "Calculation of Potential Flow With Separation in a Right-Angled Elbow With Unequal Branches," J. Fluid Mech., **17**, pp. 596–606.
[3] Smith, F. T., 1979, "Laminar Flow of an Incompressible Fluid Past a Bluff Body: The Separation, Reattachment, Eddy Properties and Drag," J. Fluid Mech., **92**, Part 1, pp. 171–205.
[4] Smith, F. T., and Duck, P. W., 1980, "On the Severe Non-symmetric Constriction, Curving or Cornering of Channel Flows," J. Fluid Mech., **98**, Part 4, pp. 727–753.
[5] Heskestad, G., 1971, "Two-Dimensional Miter-Bend Flow," ASME J. Basic Eng., **93**, pp. 433–443.
[6] Roshko, A., 1955, "On the Wake and Drag of Bluff Bodies," J. Aeronaut. Sci., **22**, pp. 124–132.
[7] Liu, S. K., and Chow, W. L., 1978, "Numerical Solutions of the Compressible Hodograph Equation," AIAA J., **16**, pp. 188–189.
[8] Chow, W. L., and Han, T., 1979, "Inviscid Solution for the Problem of Free Overfall," ASME J. Appl. Mech., **46**, pp. 1–5.
[9] Han, T., and Chow, W. L., 1981, "The Study of Sluice Gate and Sharp Crested Weir Through Hodograph Transformation," ASME J. Appl. Mech., **48**, pp. 229–238.
[10] Wu, C., and Chow, W. L., 1985, "Study of an Asymmetric Flap Nozzle as a Vector-Thrust Device," AIAA J. Propul. Power, **1**, pp. 286–291.
[11] Chow, W. L., Chow, W. L., Alice, A. L., and Tsai, P. H., 1987, "Discharge From a Vessel Through an Axisymmetric Control Valve," ASME J. Appl. Mech., **54**, pp. 447–452.
[12] Weng, Z. M., Weng, Z. M., Alice, A. L., and Chow, W. L., 1987, "Discharge of a Compressible Fluid Through a Control Valve," ASME J. Appl. Mech., **54**, pp. 955–960.
[13] Chu, S. S., Miller, S. K., and Chow, W. L., 1990, "Quasi-Steady Discharge of Fluid From a Vessel Through a Poppet Valve," ASME J. Fluids Eng., **112**, pp. 437–440.
[14] Chu, S. S., and Chow, W. L., 1992, "A Hodograph-Based Method for the Solutions of Axisymmetric Orifice Flows," J. CSME, **13**(2), pp. 167–170.
[15] Chu, S. S., and Wei, C. Y., 1996, "Study of the Jet-Plate Interaction Using the Method of Hodograph Transformation," *Proceedings of the 38th Conf. on Aeronautics and Astronautics*, AASRC, Tainan, R.O.C., pp. 191–197.
[16] Chu, S. S., and Chow, W. L., 1997, "Jet-Plate Interaction for Wedge-Shaped Plates of Arbitrary Angles," ASME J. Fluids Eng., **119**, pp. 929–933.
[17] Chu, S. S., and Wu, C. C., 1997, "The Inviscid Interaction Between a Jet and a Flat Plate," *Proceedings of the 39th Conf. on Aeronautics and Astronautics*, AASRC, Tainan, R.O.C., pp. 83–90.
[18] Kirchhoff, G., 1869, "Zur Theorie freir Flussigkeitsstrahlen," J. Reine Angew. Math., **70**, pp. 289–298.
[19] Roshko, A., 1954, "A New Hodograph for Free Streamline Theory," NACA Technical Note No. 3168.
[20] Birkhoff, A., 1950, *Hydrodynamics*, Dover, New York.
[21] Cooke, G. C., 1968, "Peripheral Jets and Plenum Chambers—An Exact Potential Flow Analysis," TRAE 6811, Rensselaer Polytechnic Institute, Troy, NY.
[22] Shapiro, A. H., 1953, *The Dynamics and Thermodynamics of Compressible Fluid Flow*, The Ronald Press Company, New York.

C. Y. Wang
Professor,
Departments of Mathematics and Mechanical Engineering,
Michigan State University,
East Lansing, MI 48824
e-mail: cywang@mth.msu.edu
Mem. ASME

Slip Flow in a Curved Tube

The viscous flow in a curved tube with partial slip on the boundary occurs in many practical situations. The problem is formulated in curved tube coordinates and solved by perturbation for small curvature. The mutual interaction of slip, curvature, and inertia causes changes in the axial flow, surface shear, and secondary flow. It is found that the net flow increases with increased slip and decreased Reynolds numbers.
[DOI: 10.1115/1.1567309]

1 Introduction

The viscous flow in a curved tube is a basic topic in fluid mechanics (e.g., [1]). It was found that, for a Newtonian fluid with no-slip boundary conditions, the curvature of the tube axis causes both a secondary flow and a change in the tube resistance. However, in many instances partial slip may occur on the tube wall. An important example is the hydrodynamic slip regime of for rarefied gasses when the Knudsen number is small, especially in microfluid tubules (e.g., [2]). In this case the gas can be considered as Newtonian fluid with a partial slip boundary condition on the wall. Other instances include a thin lubricant or mucous coating on the tube surface, rough or porous surfaces approximated by partial slip, and particulate fluids with a particle-free wall layer such as that in the microcirculatory blood flow.

In all of these partial slip cases, the no-slip condition is supplanted by the leading order expansion relating the slip velocity with the shear stress

$$\overline{u}=N\overline{\tau} \tag{1}$$

where $\overline{u}$ is the tangential velocity, $\overline{\tau}$ is the shear stress along the surface, and $N>0$ is the slip coefficient. The condition Eq. (1) has been attributed to Beavers and Joseph, but it is more appropriately called the Navier condition since Navier [3] had proposed it more than a century earlier. If $N=0$, it is the same as the no-slip condition and if N is infinite, it is a stress-free condition.

The slip flow solution in a straight circular tube is known, [4], but there is no literature on slip flow in curved tubes. In microfluid systems, curved tubules are needed to change flow direction. Also in the microvasculature there are numerous instances where the blood vessels are curved or tortuous, [5]. It is the aim of this study to investigate the effect of partial slip on the velocity and resistance of the flow through a curved tube.

We shall follow the perturbation method proposed by Dean [6] to treat the flow in a circular tube of small curvature. The fluid is assumed to be Newtonian and the boundary conditions are relaxed to include partial slip.

Formulation

Let the tube be of radius a, and varying curvature $K(s)$, where s is the arc length along the center line. An orthogonal system can then be constructed from the elemental distance squared (Fig. 1)

$$|d\overline{x}|^2=(dr)^2+r^2(d\theta)^2+L^2(ds)^2 \tag{2}$$

where

$$L\equiv 1-K(s)r\cos\theta \tag{3}$$

and (r,θ) are local polar coordinates. Using the scale factors from Eq. (2) the Navier-Stokes equations can be written as (e.g., [7])

$$uu_r+\frac{v}{r}u_0+\frac{w}{L}u_s-\frac{v^2}{r}-w^2\frac{L_r}{L}=-\frac{1}{\rho}p_r-\frac{\nu}{L}\left\{\frac{1}{r}\left[\frac{L}{r}\langle(rv)_r-u_\theta\rangle\right]_\theta +\left[\frac{1}{L}\langle(Lw)_r-u_s\rangle\right]_s\right\} \tag{4}$$

$$uv_r+\frac{v}{r}v_\theta+\frac{w}{L}v_s-\frac{w^2L_\theta}{rL}+\frac{uv}{r}=-\frac{1}{\rho r}p_\theta-\frac{\nu}{L}\left\{\left[\frac{1}{rL}(Lw)_\theta -\frac{1}{L}v_s\right]_s-\left[\frac{L}{r}\langle(rv)_r-u_\theta\rangle\right]_r\right\} \tag{5}$$

$$uw_r+\frac{v}{r}w_0+\frac{w}{L}w_s+uw\frac{L_r}{L}+\frac{vwL_0}{rL} =-\frac{1}{\rho L}p_s+\frac{\nu}{r}\left\{\left[\frac{r}{L}\langle(Lw)_r-u_s\rangle\right]_r+\left[\frac{1}{rL}(Lw)_\theta-\frac{1}{L}v_s\right]_\theta\right\}. \tag{6}$$

Here (u,v,w) are velocity components in (r,θ,s) directions, respectively, p is the pressure, ρ is the density, and ν is the kinematic viscosity. The continuity equation is

$$(rLu)_r+(Lv)_\theta+(rw)_s=0 \tag{7}$$

The boundary conditions are that on the tube wall at $r=a$, the no-slip condition is supplanted, from Eq. (1), by

$$u=0,\quad v+N\rho\nu r\frac{\partial}{\partial r}\left(\frac{v}{r}\right)=0,\quad w+N\rho\nu L\frac{\partial}{\partial r}\left(\frac{w}{L}\right)=0. \tag{8}$$

For a straight tube, curvature is zero and $L=1$. Only the axial velocity component exists. Given a pressure gradient which defines a velocity scale U

$$p_s=-4\rho\nu U/a^2 \tag{9}$$

the solution is

$$w=U[c-(r/a)^2] \tag{10}$$

where $c\equiv 1+2\lambda$ and $\lambda\equiv N\rho\nu/a$ is a normalized slip factor. We shall perturb from this solution for small curvature.

Perturbation Solution

Let the ratio of the tube radius to the radius of curvature of the center line be small, i.e.,

$$aK=\varepsilon k(s) \tag{11}$$

where $\varepsilon \ll 1$ and $k=O(1)$. The other variables are normalized to order unity as follows:

$$\eta\equiv r/a,\quad x=\varepsilon s/a \tag{12}$$

$$p=\frac{\rho\nu U}{\varepsilon a}(-4x+p_0+\varepsilon p_1+\varepsilon^2p_2+\cdots) \tag{13}$$

Contributed by the Fluids Engineering Division for publication in the JOURNAL OF FLUIDS ENGINEERING. Manuscript received by the Fluids Engineering Division January 23, 2002; revised manuscript received December 17, 2002. Associate Editor: J. Marshall.

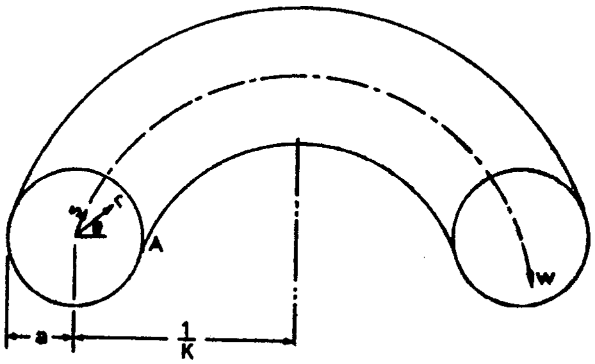

Fig. 1 The curved tube system

$$w = U(w_0 + \varepsilon w_1 + \varepsilon^2 w_2 + \cdots) \tag{14}$$

$$u = U\varepsilon(u_0 + \varepsilon u_1 + \cdots), \qquad v = U\varepsilon(v_0 + \varepsilon v_1 + \cdots). \tag{15}$$

Here p_0 is the pressure at $s=0$ and w_0 is the straight tube solution

$$w_0 = c - \eta^2. \tag{16}$$

Upon substitution into Eqs. (4)–(7) we find $p_1 = 0$ and the first-order equations

$$Rw_0^2 k \cos\theta = -p_{2\eta} - \frac{1}{\eta^2}[(\eta v_0)_\eta - u_{0\theta}]_\theta \tag{17}$$

$$-Rw_0^2 k \sin\theta = -\frac{1}{\eta} p_{2\theta} + \left\{\frac{1}{\eta}[(\eta v_0)_\eta - u_{0\theta}]\right\}_\eta \tag{18}$$

$$\begin{aligned} Ru_0 w_{0\eta} = 4k\eta\cos\theta + \frac{1}{\eta}[\eta(w_1 - k\eta w_0\cos\theta)_\eta \\ + k\eta^2\cos\theta w_{0\eta}]_\eta + \frac{1}{\eta}\left(kw_0\sin\theta + \frac{1}{\eta}w_{1\theta}\right)_\theta \end{aligned} \tag{19}$$

$$(\eta u_0)_\eta + v_{0\theta} = 0 \tag{20}$$

where $R \equiv Ua/\nu$ is a Reynolds number. Without going through the details, the solutions to Eqs. (17), (18), and (20) together with the boundary conditions Eq. (8) are

$$u_0 = Rk\cos\theta f(\eta) \equiv Rk\cos\theta(\eta^6 - 6c\eta^4 + c_1\eta^2 + c_0)/288 \tag{21}$$

$$\begin{aligned} v_0 &= -Rk\sin\theta(\eta f)' \\ &= -Rk\sin\theta(7\eta^6 - 30c\eta^4 + 3c_1\eta^2 + c_0)/288 \end{aligned} \tag{22}$$

$$p_2 = -Rk\cos\theta\eta\left[(c-\eta)^{22} + \frac{1}{288}\left(-\frac{5}{6}\eta^4 + \frac{3c}{2}\eta^2 - \frac{c_1}{36}\right)\right] \tag{23}$$

where

$$c_0 = -\frac{4(1+8\lambda+18\lambda^2)}{1+2\lambda}, \qquad c_1 = \frac{3(3+18\lambda+32\lambda^2)}{1+2\lambda}. \tag{24}$$

Then Eqs. (8) and (19) yield

$$\begin{aligned} w_1 = k\cos\theta l(\eta) \equiv k\cos\theta\left[\frac{\eta^3}{4} + \eta(c-\eta^2) + c_2\eta - \frac{R^2}{144}\left(\frac{\eta^9}{80}\right.\right. \\ \left.\left. - c\frac{\eta^7}{8} + c_1\frac{\eta^s}{24} + c_0\frac{\eta^3}{8}\right)\right] \end{aligned} \tag{25}$$

$$c_2 = -\frac{(1+3\lambda+16\lambda^2)}{4(1+\lambda)} - \frac{R^2(19+171\lambda+420\lambda^2)}{11520(1+\lambda)}. \tag{26}$$

Since w_1 is periodic in θ, it does not contribute to the flow rate, which is of higher order.

The first-order terms of the continuity equation are

$$(\eta u_1 - k\eta^2\cos\theta u_0)_\eta + (v_1 - k\eta\cos\theta\, v_0)_\theta + (\eta w_1)_s = 0. \tag{27}$$

Equation (27) can be separated into products which are periodic in the angle θ and those which are independent of θ. Considering only the latter which affects the second order flow rate, Eq. (27) gives

$$\eta\overline{u_1} - k\eta^2\overline{\cos\theta u_0} = \text{constant} \tag{28}$$

where an overbar denotes the average with respect to the angle θ. The constant is set to zero for boundedness of velocity. Thus

$$\overline{u_1} = k\eta\overline{\cos\theta u_0} = Rk^2 j(\eta) \equiv Rk^2\eta(\eta^6 - 6c\eta^4 + c_1\eta^2 + c_0)/576. \tag{29}$$

The averaging is then applied to the second-order terms of Eq. (6). After some work, the result is

$$\begin{aligned} \overline{u_0 w_{1\eta}} + \overline{u_1 w_{0\eta}} + \frac{1}{\eta}\overline{v_0 w_{1\theta}} - k\overline{\cos\theta u_0 w_0} + k\overline{\sin\theta v_0 w_0} \\ = \frac{2k^2\eta^2}{R} - \frac{1}{R\eta}\left[\eta\left(\frac{k^2}{2}\eta w_0 + k\overline{\cos\theta w_1} - \overline{w_{2\eta}}\right)\right]_\eta. \end{aligned} \tag{30}$$

Using Eqs. (21), (22), (25), and (29), Eq. (30) becomes

$$\overline{w_{2\eta}} = \frac{k^2}{2}\left[l(\eta) + \eta(c-\eta^2) - \eta^3 + \frac{R^2}{\eta}I(\eta)\right] \tag{31}$$

where

$$\begin{aligned} I(\eta) = \eta f(\eta) l(\eta) - \int \{\eta(c-\eta^2)[2f(\eta) + \eta f'(\eta)] \\ + 4\eta^2 j(\eta)\} d\eta. \end{aligned} \tag{32}$$

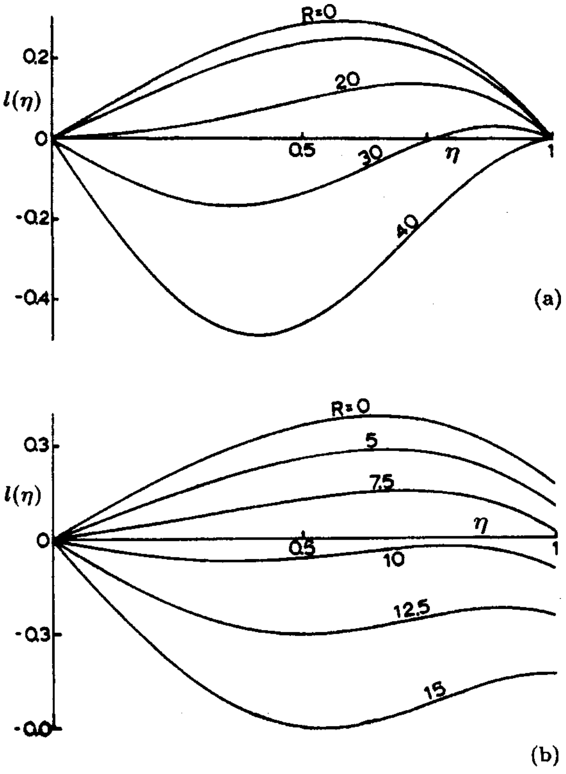

Fig. 2 The function $l(\eta)$ in Eq. (25) (*a*) $\lambda = 0$ (*b*) $\lambda = 1$

Integrating once more and applying the boundary conditions yield

$$
\begin{aligned}
\overline{w_2}=&\frac{k^2}{32(1+\lambda)}\{-3(1+5\lambda+32\lambda^2)+14(1+3\lambda)\eta^2-11(1+\lambda)\eta^4\}\\
&+\frac{k^2R^2}{230400(1+\lambda)(1+2\lambda)}\left\{\begin{array}{c}-(148+1924\lambda+9631\lambda^2+22950\lambda^3+25600\lambda^4)\\ +5(21+231\lambda+1558\lambda^2+6440\lambda^3+11520\lambda^4)\eta^2\\ +25(7+63\lambda+14\lambda^2-864\lambda^3-1536\lambda^4)\eta^4\\ +200(-1-7\lambda-9\lambda^2+22\lambda^3+32\lambda^4)\eta^6\\ +25(3+9\lambda-\lambda^2)(1+2\lambda)\eta^8-7(1+\lambda)(1+2\lambda)^{10}\end{array}\right\}+\frac{k^2R^4}{1147673600(1+\lambda)(1+2\lambda)^2}\\
&\times\left\{\begin{array}{c}-(12357+259497\lambda+2213968\lambda^2+9539220\lambda^3+20628512\lambda^4+17727360\lambda^5)\\ +3360(19+323\lambda+2130\lambda^2+6438\lambda^3+7650\lambda^4)(1+2\lambda)\eta^2\\ -420(331+5627\lambda+38528\lambda^2+130852\lambda^3+216432\lambda^4+132480\lambda^5)\eta^4\\ +560(297+4455\lambda+26782\lambda^2+78972\lambda^3+11704\lambda^4+56160\lambda^5)\eta^6\\ -210(569+7397\lambda+38380\lambda^2+96644\lambda^3+116240\lambda^4+50880\lambda^5)\eta^8\end{array}\right\}\\
&+\frac{k^2R^4}{106168320(1+2\lambda)}\left\{\begin{array}{c}\frac{16}{5}(157+1256\lambda+3456\lambda^2+2880\lambda^3)\eta^{10}\\ -\frac{4}{3}(99+594\lambda+1136\lambda^2+480\lambda^3)\eta^{12}\\ +\frac{128}{7}(1+2\lambda)^2\eta^{14}-(1+2\lambda)\eta^{16}\end{array}\right\}. \qquad (33)
\end{aligned}
$$

The mean flow rate is then integrated

$$F=2\pi\int_0^a wr\,dr=2\pi Ua^2\int_0^1[w_0+\varepsilon^2\overline{w_2}+O(\varepsilon^4)]\eta d\eta=\frac{\pi Ua^2}{2}[1+4\lambda+\varepsilon^2k^2Q+O(\varepsilon^4)] \qquad (34)$$

where

$$Q=\frac{1+7\lambda-288\lambda^2}{48(1+\lambda)}-\frac{11+154\lambda+744\lambda^2+1200\lambda^3}{17280(1+2\lambda)}R^2-\frac{1541+35443\lambda+331990\lambda^2+1577276\lambda^3+3781080\lambda^4+3633120\lambda^5}{4180377600(1+\lambda)(1+2\lambda)^2}R^4. \qquad (35)$$

The above computations are facilitated by a computer program with symbolic capabilities.

Results and Discussions

The zeroth-order axial flow w_0 is the slip flow solution for a straight tube. The effect of slip is to add a constant $2\lambda U$ to the parabolic Poiseuille no-slip profile. The first-order axial flow w_1 is proportional to curvature k, cos θ and the function $l(\eta)$, the latter also depends on slip λ and Reynolds number R. Figure 2(*a*) shows effect of curvature in the no-slip case ($\lambda=0$). We see that for small Reynolds numbers the axial velocity is increased for the inner half of the tube (closer to point A in Fig. 1) and decreased for the outer half of the tube. For higher Reynolds numbers the opposite is true. Fig. 2(*b*) shows the situation when there is slip. We note the velocity ceases to be zero on the boundary. Comparing with Fig. 2(*a*) the effect of slip promotes the switch over (sign change of first order axial flow) at lower Reynolds numbers.

The secondary flow is in a plane normal to the centerline. From Eqs. (21) and (22) one can obtain a stream function

$$\psi=-R\sin\theta(\eta^7-6c\eta^5+c_1\eta^3+c_0\eta)/288. \qquad (36)$$

Figure 3 shows a typical result. The fluid at the center is thrown toward the outer wall due to centrifugal forces and returns (with slip) near the tube wall. This secondary flow is a characteristic of curved tubes, [6]. The location of the center of recirculation is on the vertical axis ($\theta=\pi/2$). Table 1 shows the radius of the center η_c varies somewhat with slip, but the magnitude of the recirculation, indicated by the maximum stream function value ψ_c, increases greatly.

The local shear stress is

$$
\begin{aligned}
\tau&=(\tau_{r0}^2+\tau_{rs}^2)^{1/2}=\frac{\rho\nu}{a}\{[\eta(v/\eta)_\eta]^2+[L(w/L)_\eta]^2\}^{1/2}\big|_{\eta=1}\\
&=\frac{\rho\nu U}{a}[2+\varepsilon k\cos\theta B+O(\varepsilon^2)] \qquad (37)
\end{aligned}
$$

where

$$
\begin{aligned}
B&=1-c-l'(1)\\
&=\frac{3(1440-R^2)+36\lambda(80-R^2)-20\lambda^2(576+5R^2)}{2880(1+\lambda)(1+2\lambda)}. \qquad (38)
\end{aligned}
$$

The increase in shear stress due to curvature is represented by B

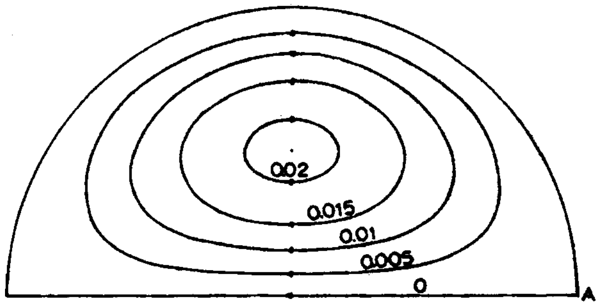

Fig. 3 Secondary flow for λ=0.5, R=1. ψ values are shown

Table 1 Location of center η_c and maximum secondary flow ψ_c

λ	0	0.25	0.5	0.75	1
η_c	0.429	0.485	0.502	0.511	0.515
ψ_c/R	0.00378	0.0118	0.0212	0.0312	0.0415

in Fig. 4. As implied by the axial flow, slip decreases the local shear near the inner wall, and promotes a reversal of shear stress at higher Reynolds numbers.

Equation (34) shows the zeroth-order flow rate is increased by 4λ due to slip. The curvature effect is second order and is represented by Q. If there is no slip

$$Q=\frac{1}{48}-\frac{11}{15(1152)}R^2-\frac{1541}{3150(1152)^2}R^4. \tag{39}$$

This result agrees with Topakoglu [8] and Wang [9] for the no-slip flow in a toroidal tube. Note that Q is positive when $R<5.67$ and negative otherwise. Figure 5 shows the results when slip is present. We see that depending on the Reynolds number and slip, curvature effects may increase or decrease the net flow. In general, higher Reynolds number or higher slip lowers the second-order flow.

The present analysis is not restricted to toroidal tubes since the curvature k can be a function of s. Figure 6 shows some undulating tubes for which $k=\cos(\alpha s)$ while the parameter ε is still small. In these cases the k^2 terms in Eqs. (29)–(34) are replaced by one-half or the mean of $\cos(\alpha s)$. The increases in flow for undulating or curved tubes (as compared to straight tubes of the same centerline length) at low Reynolds numbers is due to the fact that the axial velocity is larger near the inner surface, giving the bulk of the fluid a shorter path. This phenomenon is also observed for undulating channels, [10].

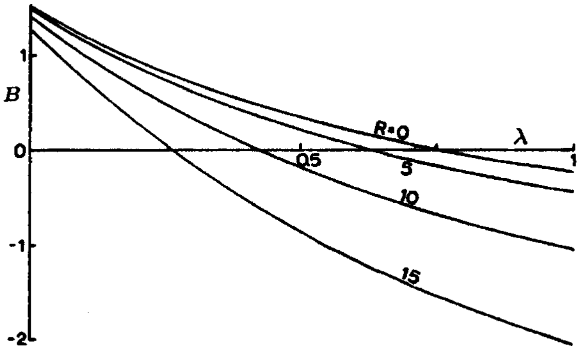

Fig. 4 The function B in Eq. (37)

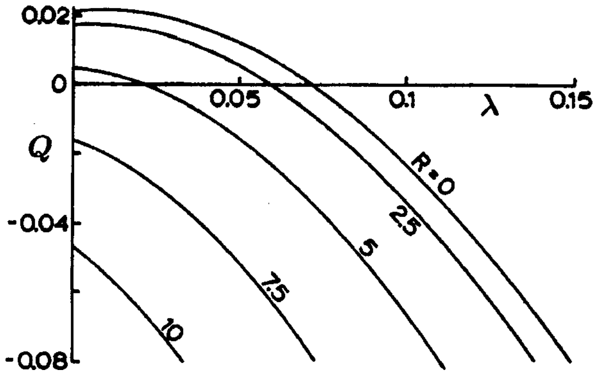

Fig. 5 The function Q in Eq. (34)

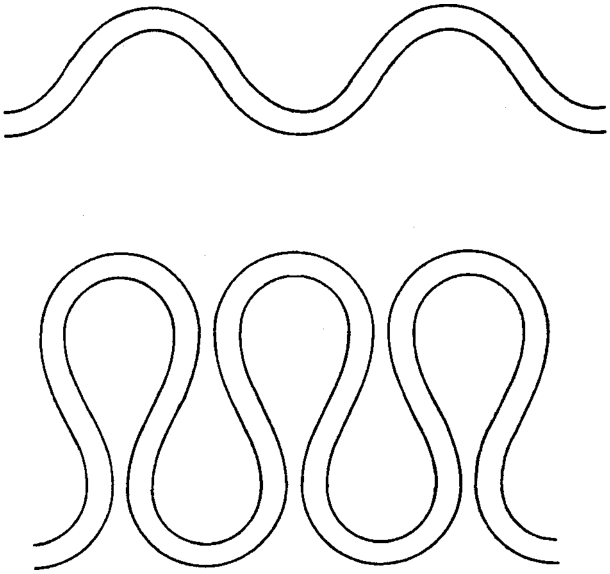

Fig. 6 Some undulating tubes. Top: α=1, ε=0.2. Bottom: α=0.5, ε=0.2.

We considered only the effects of slip and curvature on the flow of an incompressible Newtonian fluid. Other effects, such as compressibility for rarefied gas flow or non-Newtonian effects for blood flow can be included based on the current analysis. Our results do, however, directly apply to viscous flow in rough tubes where the minute roughness can be supplanted by a partial slip condition, [11].

Acknowledgment

This paper is partially supported by NIH Grant RR-01243.

References

[1] Berger, S. A., and Talbot, L., 1983, "Flow in Curved Pipes," Annu. Rev. Fluid Mech., **15**, pp. 461–502.
[2] Sharipov, F., and Seleznev, V., 1998, "Data on Internal Rarefied Gas Flows," J. Phys. Chem. Ref. Data, **27**, pp. 657–706.
[3] Navier, C. L. M., 1827, "Sur les lois du mouvement des fluids," C.R. Acad. Sci., **6**, pp. 389–440.
[4] Kennard, E. H., 1938, *Kinetic Theory of Gases*, MaGraw-Hill, New York, Chap. 8.
[5] Nicola, P. D., Maggi, G., Tassi, G., 1983, *Microcirculation-An Altas*, Schattauer, Stuttgart.
[6] Dean, W. R., 1927, "Note on the Motion of a Fluid in a Curved Pipe," Philos. Mag., **4**, pp. 208–233.
[7] Batchelor, G. K., 1967, *An Introduction to Fluid Dynamics*, Cambridge Univ. Press, Cambridge, UK, Appendix 2.
[8] Topakoglu, H. C., 1967, "Steady Laminar Flows of an Incompressible Viscous Fluid in Curved Pipes," J. Math. Mech., **16**, pp. 1321–1337.
[9] Wang, C. Y., 1981, "On the Low Reynolds Number Flow in a Helical Pipe," J. Fluid Mech., **108**, pp. 185–194.
[10] Wang, C. Y., 1980, "Flow in Narrow Curved Channels," ASME J. Appl. Mech., **47**, pp. 7–10.
[11] Sarkar, K., and Prosperetti, A., 1996, "Effective Boundary Conditions for Stokes Flow Over a Rough Surface," J. Fluid Mech., **316**, pp. 223–240.

Sensitivity Evaluation of a Transport-Based Turbulent Cavitation Model

Rajkumar Vaidyanathan
Inanc Senocak
Jiongyang Wu
Wei Shyy

Department of Mechanical and Aerospace Engineering,
University of Florida,
Gainesville, FL 32611-6250

A sensitivity analysis is done for turbulent cavitating flows using a pressure-based Navier-Stokes solver coupled with a phase volume fraction transport model and nonequilibrium k-ε turbulence closure. Four modeling parameters are assessed, namely, $C_{\varepsilon 1}$ and $C_{\varepsilon 2}$, which directly influence the production and destruction of the dissipation of turbulence kinetic energy, and C_{dest} and C_{prod}, which regulate the evaporation and condensation of the phases. Response surface methodology along with design of experiments is used for the sensitivity studies. The difference between the computational and experimental results is used to judge the model fidelity. Under noncavitating conditions, the best selections of $C_{\varepsilon 1}$ and $C_{\varepsilon 2}$ exhibit a linear combination with multiple optima. Using this information, cavitating flows around an axisymmetric geometry with a hemispherical fore-body and the NACA66(MOD) foil section are assessed. Analysis of the cavitating model has identified favorable combinations of C_{dest} and C_{prod}. The selected model parameters are found to work well for different geometries with different cavitation numbers for attached cavity. It is also confirmed that the cavitation model parameters employed in the literature are within the range identified in the present study. [DOI: 10.1115/1.1566048]

1 Introduction

The inception of cavitation occurs due to the drop in pressure of the flow below the vapor pressure of the liquid. This phenomenon is often encountered in pumps, nozzles, and around underwater bodies. The cavitating flows are typically turbulent and cause structural damage to the body on which it occurs, along with degradation in the performance of the fluid machinery. Various physics and engineering implications related to cavitation can be found in Refs. [1–4].

Recent years have seen a significant progress in computational modeling of cavitation. Single-fluid Navier-Stokes equations have been applied along with physical models to represent the cavitation process. The modeling of cavitation is a complicated task, as one has to address the issues of large density jump across the phase boundaries, interactions between phase change and turbulence, irregularly shaped interfaces, and the stiffness in the numerical model. Among the proposed physical modeling concepts, a transport equation model has been employed by several researchers with different numerical techniques, [5–9]. A volume or mass fraction transport equation, along with appropriate source terms, is solved to establish cavitation inception and as well as to regulate the rate of evaporation and condensation. Different source terms along with empirical constants used to adjust the rate of evaporation and condensation processes have been proposed [5–8]. Physical intuition and geometrical considerations mainly guide the choice of these empirical constants, [9–11]. It has also been shown that in some cases, increasing these constants by an order of magnitude has little effect on the pressure distribution whereas the density level inside the cavity can experience a considerable change, [9–11].

Since cavitation is generally considered as a high Reynolds number phenomenon, turbulence modeling plays a key role and must also be addressed adequately in addition to cavitation modeling and numerical algorithm. Most of the recent research has adopted the original k-ε model, [12], for turbulence closure. The original k-ε turbulence model assumes a balance between the production and dissipation of turbulence kinetic energy. Flows with large streamline curvature and recirculation zones violate this assumption. Hence, in literature, a nonequilibrium k-ε turbulence model has been proposed, [13]. Senocak and Shyy [9] have investigated the effect of turbulence modeling in the context of the nonequilibrium k-ε model. In this study, it has been demonstrated that for cavitating flows with large streamline curvature and recirculation zones, the turbulence model can influence the performance of cavitation modeling and the issue needs an in depth study. A recent review on cavitating flows by Wang et al. [14] provides a detailed outlook.

In the nonequilibrium k-ε model, two parameters, $C_{\varepsilon 1}$ and $C_{\varepsilon 2}$, which control the production and destruction of the dissipation of the turbulence kinetic energy, respectively, are regulated according to the local flow structure, [13]. On the other hand, as will be presented in detail later, in the transport equation-based cavitation model, two empirical parameters, namely C_{dest} and C_{prod}, are devised to regulate the phase change process, [5–8]. The goal of the present effort is to present a systematic sensitivity evaluation method for the empirical parameters arising in the turbulent cavitating flows. The goal is also to probe the interplay and sensitivity of the four modeling parameters associated with turbulence and cavitation closures. The insight gained from this exercise will offer a better foundation to help develop a predictive model capable of accounting for different flow conditions. The tool used for sensitivity evaluation is the response surface methodology (RSM), [15], aided by the design of experiment (DoE), [15], approach. The RSM approach is to conduct a series of well-chosen experiments (empirical, numerical, physical, or some combination of the three), proposed by DoE, and use the resulting information to construct a global approximation (response surface) of the measured quantity (response) over the design space. A standard constrained optimization algorithm is then used to interrogate the response surface for an optimum design.

To facilitate the evaluation of a turbulent cavitation model, we have adopted a two-stage process. First, we evaluate the performance of the nonequilibrium k-ε turbulence model under noncavitating conditions with the aid of a flow over a backward-facing step. The goal is to identify the interdependency of $C_{\varepsilon 1}$ and $C_{\varepsilon 2}$ so as to narrow down the range of variations of these param-

---

Contributed by the Fluids Engineering Division for publication in the JOURNAL OF FLUIDS ENGINEERING. Manuscript received by the Fluids Engineering Division Jan. 31, 2002, revised manuscript received Oct. 30, 2002. Associate Editor: S. Ceccio.

eters. Obviously, there is little use of identifying parameter combinations, which do not work even under noncavitating conditions.

Second, cavitating flow analysis is done for two geometries and different cavitating numbers. The turbulent cavitating flow model introduces two additional empirical parameters arising out of the transport equation. An axisymmetric cylindrical geometry with a hemispherical fore-body and the NACA66(MOD) foil section are adopted for this study. The cavitation number is used to judge the likelihood of the inception of cavitation and is defined as

$$\sigma=\frac{2(p_\infty-p_v)}{\rho U_\infty^2} \tag{1}$$

where p_∞ is the static pressure, p_v is the vapor pressure, ρ is the density and U_∞ is the freestream velocity.

In summary, our goals in this study are:

i. assess the sensitivity of the selected turbulent cavitating flow model to the turbulent and cavitation model parameters.
ii. to investigate how the already proposed values in the literature perform and identify a better combination of these parameters, if any.
iii. probe the impact of the individual and collective behaviors of the modeling parameters. This would help in gaining an insight into the range of predictions that we can expect with these models.
iv. identify suitable combinations of the modeling parameters for different cavitating conditions and for flow around different geometries.

In the following sections, the governing equations are first presented. The turbulence modeling parameters are studied first by computing a single-phase flow over a backward-facing step. Following the outcome of this investigation, cavitating flow computations are done for different geometries and cavitation numbers. The insight obtained on the turbulence modeling parameters is used to reduce the design space for the cavitating flow study. The inclusion of the transport equation for cavitation modeling introduces additional parameters, which are addressed with the aid of the flow over the mentioned geometries. The sensitivity of the modeling parameters, the existence of a single set of parameters for different geometries and cavitation numbers, and the overall capability of the present modeling approach are assessed.

2 Governing Equations and Numerical Techniques

The Favre-averaged Navier-Stokes equations in their conservative form are employed. The equations are presented below in Cartesian coordinates.

$$\frac{\partial\rho_m}{\partial t}+\frac{\partial(\rho_m u_j)}{\partial x_j}=0 \tag{2}$$

$$\frac{\partial}{\partial t}(\rho_m u_i)+\frac{\partial}{\partial x_j}(\rho_m u_i u_j)=-\frac{\partial p}{\partial x_i}+\frac{\partial}{\partial x_j}\left[(\mu+\mu_t)\left(\frac{\partial u_i}{\partial x_j}+\frac{\partial u_j}{\partial x_i}-\frac{2}{3}\frac{\partial u_l}{\partial x_l}\delta_{ij}\right)\right] \tag{3}$$

where ρ_m is the mixture density, u_i is the velocity component in Cartesian coordinates, t is the time, p is the pressure, μ_t is the turbulent viscosity, and μ is the laminar viscosity of the mixture defined as follows:

$$\mu=\mu_l\alpha_l+\mu_v(1-\alpha_l) \tag{4}$$

where α_l is volume fraction of liquid, μ_l is the viscosity of the liquid and μ_v is the viscosity of the vapor.

The volume fraction transport equation is given as

$$\frac{\partial\alpha_l}{\partial t}+\frac{\partial}{\partial x_j}(\alpha_l u_j)=(\dot{m}^+ +\dot{m}^-) \tag{5}$$

where $\dot{m}^+$ is the condensation rate and $\dot{m}^-$ is the evaporation rate.

The mixture density and turbulent viscosity are, respectively, defined as

$$\rho_m=\rho_l\alpha_l+\rho_v(1-\alpha_l) \tag{6}$$

where ρ_l is the density of the liquid and ρ_v is the density of the vapor.

$$\mu_t=\frac{\rho_m C_\mu k^2}{\varepsilon} \tag{7}$$

where C_μ is the turbulence model constant, k is the turbulence kinetic energy and ε is the turbulence dissipation rate.

2.1 Turbulence Model. The k-ε turbulence model used is given by

$$\frac{\partial\rho_m k}{\partial t}+\frac{\partial\rho_m u_j k}{\partial x_j}=P-\rho_m\varepsilon+\frac{\partial\left[\left(\mu+\frac{\mu_t}{\sigma_k}\right)\cdot\frac{\partial k}{\partial x_j}\right]}{\partial x_j} \tag{8}$$

$$\frac{\partial\rho_m\varepsilon}{\partial t}+\frac{\partial\rho_m u_j\varepsilon}{\partial x_j}=C_{\varepsilon1}\frac{\varepsilon}{k}P-C_{\varepsilon2}\rho_m\frac{\varepsilon^2}{k}+\frac{\partial\left[\left(\mu+\frac{\mu_t}{\sigma_\varepsilon}\right)\cdot\frac{\partial\varepsilon}{\partial x_j}\right]}{\partial x_j} \tag{9}$$

where σ_k and σ_ε are the turbulence model constants, $C_{\varepsilon1}$ and $C_{\varepsilon2}$ are the turbulence model parameters that regulate the production and destruction of dissipation of turbulence kinetic energy, respectively. The turbulent production term, P, is defined as

$$P=\frac{\partial u_i}{\partial x_j}\tau_{ij} \tag{10}$$

where the Reynolds stresses are given by

$$\tau_{ij}=-\overline{\rho u_i' u_j'}. \tag{11}$$

The Boussinesq approximation is given by

$$\overline{u_i' u_j'}=\frac{2}{3}k\delta_{ij}-\upsilon_t\left(\frac{\partial u_i}{\partial x_j}+\frac{\partial u_j}{\partial x_i}\right) \tag{12}$$

where u_i' is the fluctuating velocity components in Cartesian coordinates. Wall functions are used to address the effect of wall boundaries along with the $k-\varepsilon$ turbulence model, [12].

2.2 Cavitation Model. Cavitation process is governed by thermodynamics and kinetics of the phase change dynamics in the system. It involves two-phase interaction resulting in high density variations, to the order of 1000. These issues are modeled with the aid of a transport equation with source terms regulating the evaporation and condensation of the phases. Within the homogeneous equilibrium flow theory, two approaches have been pursued to model the cavitation dynamics. The first one is the arbitrary barotropic equation models and the second one is the transport equation-based models. A detailed review is provided in Wang et al. [14]. The transport equation-based models are attractive because of their potential to capture baroclinic vorticity production. Arbitrary barotropic equation models (density is only a function of pressure) do not have this potential because the baroclinic term of the vorticity transport equation yields zero by definition, [11,16]. In agreement with the experimental study of Gopalan and Katz [4], Senocak [11] has demonstrated computationally that the baroclinic vorticity generation is important in the closure region.

For the cases considered Reynolds number is pretty high (around 10^5–10^6), which makes the inertial forces dominate the flow field. Hence, Weber and Froude numbers, which define the ratio of inertial forces over molecular forces and gravitational forces, respectively, are typically large. Therefore, surface tension and buoyancy effects are neglected. The transport equation-based cavitation model source terms, adopted in the present study, are suggested by Kunz et al. [7]. The evaporation of the liquid phase is given by

$$\dot{m}^- = \frac{C_{\text{dest}}\rho_v \alpha_l \text{MIN}[0, p - p_v]}{\rho_l\left(\frac{1}{2}\rho_l U_\infty^2\right) t_\infty} \tag{13}$$

and the condensation of the vapor phase is given by

$$\dot{m}^+ = \frac{C_{\text{prod}}\rho_v \alpha_l^2 (1-\alpha_l)}{\rho_l t_\infty} \tag{14}$$

where C_{dest} and C_{prod} are the empirical parameters to be modeled and t_∞ is the mean flow time scale. A value of 1000 is taken as the nominal density ratio, which is the ratio between thermodynamic values of density of liquid and vapor phases at the given flow conditions. The time scale in the equations is defined as the ratio of the characteristic length scale to the reference velocity scale (l/U).

In a related context, Singhal et al. [17] have recently proposed a model for cavitating flows. In their model the vapor mass fraction is the dependent variable in the transport equation. Both evaporation and mass fraction are functions of pressure.

2.3 Flow Solver. The present Navier-Stokes solver employs a pressure-based algorithm and the finite volume approach, [18,19]. The governing equations are solved on multiblock structured curvilinear grids. To represent the cavitation dynamics, a transport equation model is adopted along with the particular source terms as suggested by Kunz et al. [7]. For turbulent cavitating flow computations the method developed by Senocak and Shyy [9] is used. One of the key features of this method is to reformulate the pressure correction equation to exhibit a convective-diffusive nature. This is achieved through the inclusion of a pressure-velocity-density coupling scheme into the pressure correction equation. This scheme combines the incompressible and compressible formulations, so as to preserve the incompressibility of the liquid phase and it also takes into account the pressure-density dependency in the cavitating regions. Density is also upwinded both in pressure correction and momentum equations in order to improve the mass and momentum conservation in the vicinity of sharp density gradients. The convective terms of momentum and volume fraction transport equations are discretized using the second-order controlled variation scheme (CVS), [20,21]. For more details of the pressure-based method for turbulent cavitating flows, including the numerical accuracy aspects of the cases relevant to those studied here, the reader is referred to Senocak and Shyy [9].

2.4 Sensitivity Analysis. The sensitivity of the objective function to the variation in the design parameters is evaluated with the aid of design of experiments and response surface methodology. Design of experiments is used to select the set of design variables, which are then used for CFD computations. These design variables are selected such that maximum amount of information about the design space can be obtained.

In this study, full factorial design, [22], is used to populate the design space. The range of each design variable is divided into one or more intervals, which mark the number of levels. These intervals are usually evenly spaced. Full factorial design contains all the combinations of the levels of all the design variables.

A response surface (RS) is then generated using the CFD solutions for these design points (i.e., combinations of the modeling parameters). A polynomial-based RSM, in which the design space is represented with a quadratic polynomial, is used in this study. The polynomial coefficients are obtained by linear regression. The maximum or the minimum of the surface is then located using a gradient search method. The RSM is effective in representing the global characteristics of the design space and it filters noise associated with design data. Care has to be taken that the design space is adequately populated and enough information is available to generate the required order of the polynomial. In the present study, the response surfaces were generated using JMP, [22], a statistical analysis software package. The quality of the response surface is estimated by measuring the adjusted root mean square error defined as

$$\sigma_a = \sqrt{\frac{\Sigma e_i^2}{n - n_p}} \tag{15}$$

where e_i is the error at the ith design point, n is the number of design points, n_p is the number of coefficients in the polynomial. This measure accounts for higher-order terms thereby providing an unbiased comparison among polynomial fits of different orders.

Once the response surface is generated it is submitted to an optimization toolbox to maximize/minimize the objective function, which is any quantity of interest obtained from the CFD computations. *Solver*, [23], an optimization tool available as part of Microsoft Excel package, is used in this effort. This tool uses the Generalized Reduced Gradient (GRG2) nonlinear optimization code developed by Lasdon et al. [24].

3 Results and Discussion

3.1 Noncavitating Flow—Backward-Facing Step Flow. In flows with recirculation, the equilibrium between the production and destruction of dissipation of turbulence kinetic energy does not exist. Hence, a nonequilibrium model is used for the present computation where the parameters, $C_{\varepsilon 1}$ and $C_{\varepsilon 2}$, are functions of the production and dissipation of the turbulence kinetic energy. Referring to Eqs. (7) and (8), the constants are defined in Table 1.

To estimate the sensitivities of $C_{\varepsilon 1}$ and $C_{\varepsilon 2}$, turbulent flow over a backward-facing step is considered, which has a large recirculation zone behind the step. Geometry of length-to-step-height ratio of 10 is used. The inlet to step height ratio is 2. A uniformly distributed grid of 121×91 is used. Calculations are carried out for Reynolds number of 10^6. Experimental results, [25], predict the reattachment for such a flow as 7±1 times the step height. The comparison of CFD computations is made with a reattachment length of 7 times the step height.

The design space for the two parameters, β_1 and β_2, constants defining $C_{\varepsilon 1}$ and $C_{\varepsilon 2}$, respectively, in the formulation of the nonequilibrium k-ε turbulence model, is selected based on past experience and the trend noticed in similar situations. According to work done on recirculating flows, it has been suggested by Shyy et al. [13], that the values for $\beta_1 = 1.15$ and $\beta_2 = 1.45$ performs well. Hence, the design space is perturbed about these values of β_1 and β_2, to identify their interdependency and trend. The equilibrium model is excluded since it has been shown by Shyy et al. [13] that it does not perform well for such cases. The design space is represented by black dots in the Fig. 1. To generate a good response surface we need sufficient information over the design space. Increasing the size of the domain leads to the increase in the cost, as more CFD computations have to be carried out. These considerations have led to the compromised design space selected in the present study.

Computations are carried out on the backward-facing step case with different combinations of β_1 and β_2. The reattachment length is obtained by tracking the grid point where the u-velocity

Table 1 Empirical constants used in k-ε turbulence model

Model	C_μ	$C_{\varepsilon 1}$	$C_{\varepsilon 2}$	σ_k	σ_ε
Original k-ε	0.09	1.44	1.92	1.0	1.3
Nonequilibrium k-ε	0.09	$\beta_1 + (1.40 - \beta_1)(P/\varepsilon)$	$\beta_2 + (1.90 - \beta_2)(P/\varepsilon)$	0.8927	1.15

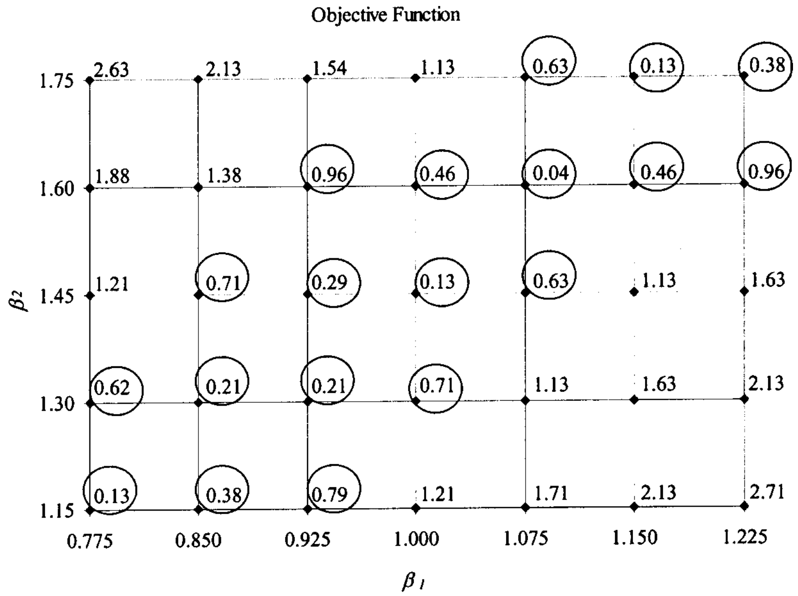

Fig. 1 Design space and objective function for different β_1 and β_2 (black dots represent the design points)

becomes positive. This is done along the grid points closest to the bottom surface. The objective function for the sensitivity analysis is the absolute amount by which the reattachment length differs from a value of seven times the step height. Figure 1 gives the objective function as obtained for the different combination of β_1 and β_2. In the figure, the circled values are for those designs, which have a reattachment length within 7 ± 1 times the step height.

The CFD simulations suggest that the best values of β_1 and β_2 lies within a variation of 10% on either side of the diagonal (left bottom to right top) of the selected design space (Fig. 1). The turbulence model parameters regulate the production and destruction of the dissipation of the turbulence kinetic energy. Hence, the two factors have a balanced dependence on the P/ε and are directly correlated. The solutions also show that there are more than one combination of β_1 and β_2 with identical performance in the mentioned region.

A quadratic response surface is generated using the data obtained from CFD calculations that has the value of the objective function below 1. The response surface has an estimated variance, σ_a, of 0.083. Viewing the plot between the predicted and actual values of the objective function, i.e., the error, it can be seen that the fit is good.

In Fig. 2(*a*), it is clearly seen that the fit is good as most of the points lie close to the perfect fit within a confidence limit of 95%. The obtained response surface is

$$error=0.42-3.50\beta_1+1.93\beta_2+36.11\beta_1^2-46.28\beta_1\beta_2+14.97\beta_2^2 \tag{16}$$

In Fig. 2(*b*), the values in the parenthesis are obtained from the response surface. They agree closely with the CFD solutions. Using this response surface a search for optimum values of β_1 and β_2 is carried out. The optimization problem is set up as follows:

Objective function: $error=|\text{CFD solution}-7|$

Design variables: β_1, β_2

Constraints: $0.775-\beta_1\leqslant 0;$

$$\beta_1-1.225\leqslant 0;$$

$$1.15-\beta_2\leqslant 0;$$

$$\beta_2-1.75\leqslant 0.$$

Goal: Minimize (*error*)

The optimum value of the objective function is obtained for $\beta_1=0.79$ and $\beta_2=1.15$. The value of the objective function, *error*, is equal to 0.16, as predicted by the response surface. CFD computation for the same values of the design parameters, give a value of 0.042 for the *error*, which is the minimum among all the CFD runs made. The same value is also found at a different design point ($\beta_1=1.075$ and $\beta_2=1.60$), suggesting that there are multiple optimum combinations.

It seems that the favorable combination of β_1 and β_2 are those that have equal dependence on the functional part of the factors. Hence, the design space is reduced within a 10% variation on either side of the diagonal running from the bottom left corner to the top right corner of the design space. It would save a lot of computation during the cavitating flow studies by concentrating on the reduced domain. Moreover, there are multiple optimum values available in the domain and hence, different choices of the modeling parameter will lead to the same performance. The existence of multiple optimum combinations of the turbulence parameters is desirable since it allows one to have enough flexibility while assessing the parameters associated with the cavitation model, as will be presented next.

3.2 Cavitating Flows. Computations for turbulent cavitating flow over an axisymmetric geometry and the NACA66(MOD) foil section have been performed. The axisymmetric geometry has a hemispherical fore-body and a cylindrical aft-body. A steady-state computation of cavitating flows is carried out with a Reynolds number of 1.36×10^5, based on the diameter of the body. Sheet cavitation occurs, which is typically a quasi-steady phenomenon. Cavitation number of 0.4 is used for all the cases and 0.3 is used for select few cases to evaluate the effect of cavitation number on the flow.

The performance of the cavitation model is evaluated by comparing the pressure coefficient on the surface of the axisymmetric body obtained from CFD computations with the experimental measurements of Rouse and McNown [26]. In the work done by Reboud et al. [27] for cavitating flows in convergent-divergent nozzles, experimental data of the void fraction and velocity distributions within the cavity are also available. Since the particular study indicates unsteady cavitation, it has not been considered in the present steady-state model. Senocak [11] has considered the aforementioned experimental study in details with time-accurate computations.

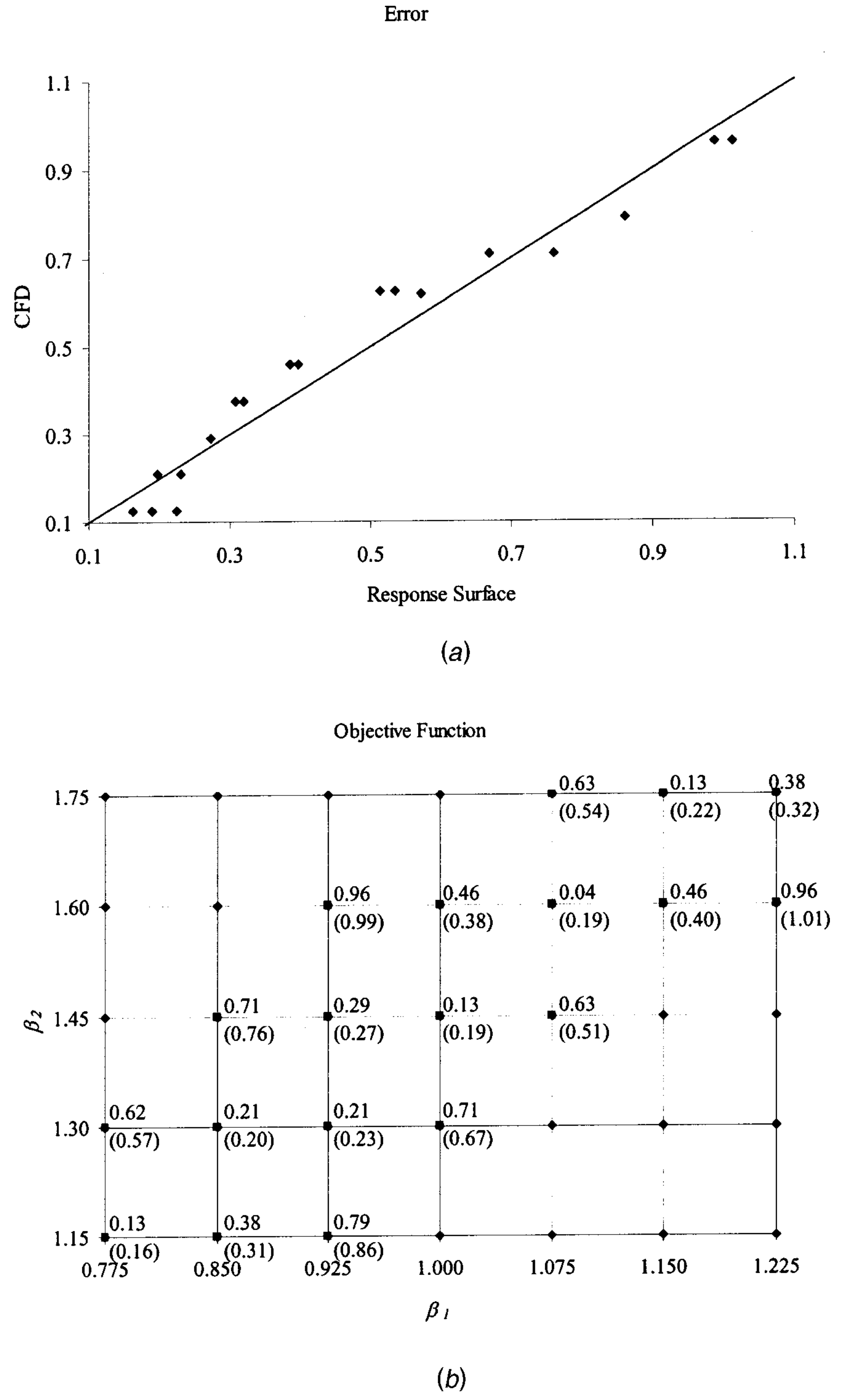

Fig. 2 (*a*) Comparison of response surface prediction of the objective function to the actual values obtained from CFD computations for the flow over a backward-facing step (the values are not normalized), (*b*) comparison between CFD and response surface (in parenthesis) predictions of the objective function

As seen from Eqs. (12) and (13), two modeling parameters, namely, C_{dest} and C_{prod}, are involved. These parameters along with β_1 and β_2 are the design parameters for this study. The sensitivities of the cavitating flow, over the mentioned geometry, to these parameters are estimated. A single-block grid of 119×65 nodes is used for this geometry (Fig. 3(*a*)). A grid sensitivity analysis for this particular case has already been done in Senocak and Shyy [9]. Hence, it is not repeated in the present study.

Computations have also been done for cavitating flows around the NACA66(MOD) foil section (a completely different geometry as compared to the axisymmetric body) with a chord length, *C*, and thickness ratio of 0.09. A six-block grid is constructed around the foil section with a grid distribution of 131×51, 51×41, 191 ×51, 191×31, 41×101, and 131×31 nodes (Fig. 3(*b*)). The grid points are closely clustered nearer to the surface of the foil section along the normal direction and also near the leading edge on the

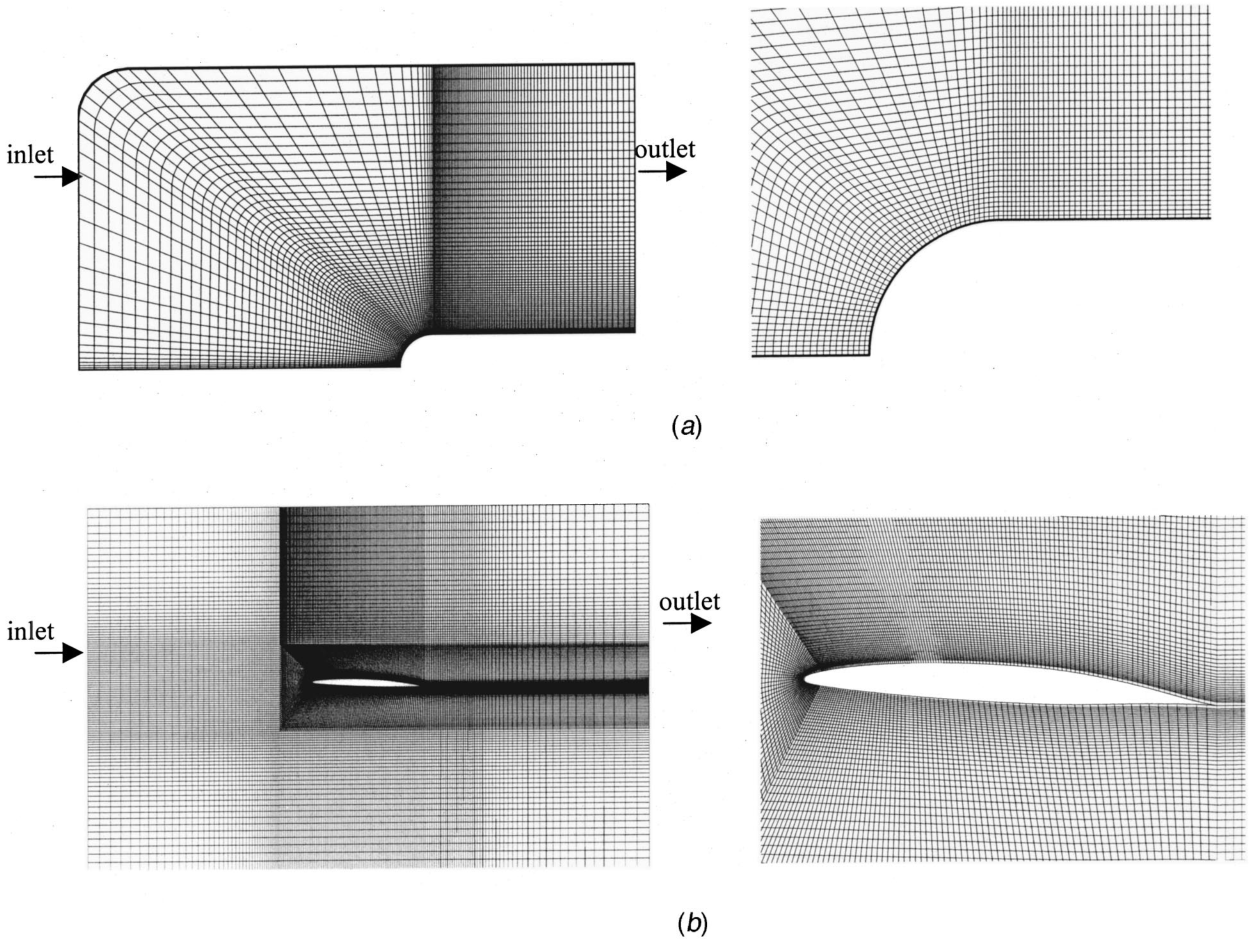

Fig. 3 Grid distribution around (*a*) an axisymmetrical body with a hemispherical fore-body, (*b*) around a NACA66(MOD) foil section

suction side, tangential to the surface of the foil section. A Reynolds number of 2×10^6 based on the chord length, is considered. For this Reynolds number and for an angle of attack of 4°, a leading edge cavitation is expected. Different cavitation numbers are used. Cavitation numbers of 0.84, 0.91, 1.0, and 1.76 are investigated here.

Turbulent flow predictions are affected due to the grid distribution in the near wall region. Depending on the treatment of the near-wall region, care is needed for the y^+ (local Reynolds number) value. In the case of the wall function treatment, the minimum y^+ value should be located in the log-law region to satisfy the equilibrium essence of the wall function formulation, [28]. In single-phase flows, neglecting this issue can cause poor predictions. However, for cavitating flows it is a source of numerical instability as identified in Refs. [11] and [16]. The grid generation can become stiffer and critical if the sheet cavity is thin. One has to satisfy the wall function requirement and also have to provide sufficient numbers of grid points to resolve the thin sheet cavity. Wall function consistent grids, with adequate resolution in the cavity, are adopted in the present study. Senocak [11] provides the corresponding grid sensitivity study for the NACA66MOD foil section case.

3.2.1 Axisymmetrical Geometry. The upper and lower limits of the four model parameters are selected based on experience (Table 2). The range of each design variable is divided into equally spaced intervals as specified by the number of levels in Table 2. Using the full factorial design in the design of experiments, a design space of 144 design points is obtained. The design space is reduced to 81 with the aid of the trend noticed between β_1 and β_2 in the analysis of the backward-facing step case. The CFD computations are carried out for this set of design points. The objective function, *error*, based on the distribution of C_p along the surface of the cavitating body is measured as

$$error(C_p)=\frac{\Sigma_1^{12}|\mathrm{CFD}-\mathrm{Expt}|}{12}. \tag{17}$$

The comparison is done with the C_p values measured at 12 points along the surface of the body during experiments. The solution from the CFD computation using the original k-ε turbulence model along with the cavitation model parameters defined in Senocak and Shyy [9] ($C_{\mathrm{dest}}:9\times10^5$ and $C_{\mathrm{prod}}:3\times10^4$) is considered as the baseline case. The nondimensionalization is done with respect to the mentioned baseline values but in the computations, these parameters are used as they are. Henceforth, nondimensionalized values of C_{dest} and C_{prod} are mentioned. To measure the sensitivity of these parameters, the values of C_{dest} and

Table 2 Design space for the cavitating flow around an axisymmetric geometry with hemispherical fore-body

Variable	Lower Limit	Upper Limit	Number of Levels
β_1	0.775	1.15	4
β_2	1.15	1.75	4
C_{dest} (normalized)	0.89	1.11	3
C_{prod} (normalized)	0.67	1.33	3

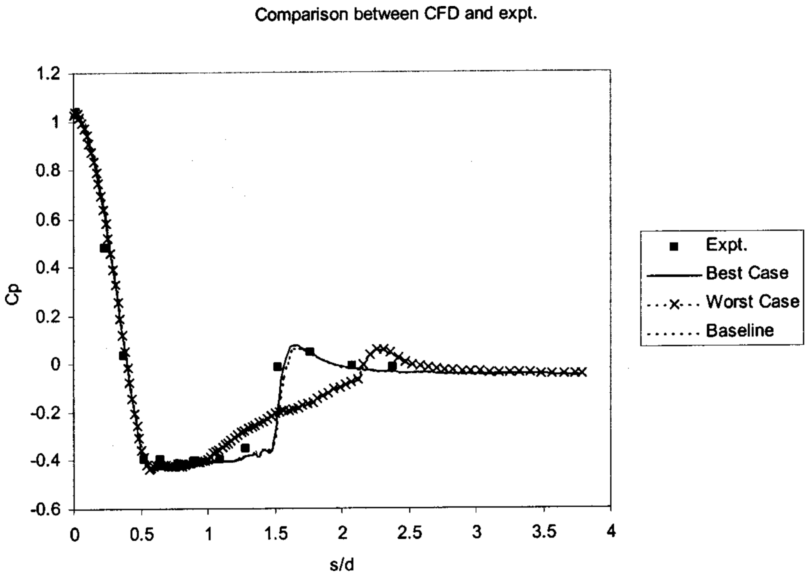

Fig. 4 Comparing the C_p values for the best, the worst and the baseline CFD cases with the experimental results for the axisymmetrical body ($\sigma=0.4$)

Table 3 Cases within 10% variation of *error* as compared to the best case obtained for the axisymmetric body ($\beta_1=0.9$, $\beta_2=1.15$, $C_{\mathrm{dest}}=0.89$, $C_{\mathrm{prod}}=1.33$, *error*=0.039). (i.e. within *error*=0.043).

β_1	β_2	C_{dest} (Normalized)	C_{prod} (Normalized)	Error
0.9	1.15	0.89	1.33	0.039
0.775	1.15	0.89	1.33	0.040
0.9	1.15	0.89	1.0	0.041
0.9	1.15	1.11	1.33	0.041
0.9	1.35	0.89	1.33	0.042
1.025	1.35	0.89	1.33	0.042
0.775	1.15	1.0	0.67	0.043
0.775	1.35	1.0	1.0	0.043
0.9	1.15	1.0	1.33	0.043
1.15	1.75	1.0	1.33	0.043

C_{prod} are perturbed by 11% and 33%, respectively, on either side of the baseline values. The cavitation number adopted here is 0.40.

The best combination of the C_{dest} and C_{prod}, based on CFD computations, is 0.89 and 1.33, respectively, along with $\beta_1=0.9$ and $\beta_2=1.15$. Figure 4 shows the distribution of pressure coefficient as obtained from the CFD computations. The results of the best combination and the baseline case confirms well with the experimental measurements. There is very small difference between the baseline and the best-case results. This confirms that the baseline values selected by trial and error are reasonable. The worst-case obtained within the selected domain is one with $C_{\mathrm{dest}}=1.0$ and $C_{\mathrm{prod}}=0.67$ with $\beta_1=1.15$ and $\beta_2=1.75$.

The *error* for the baseline case is 0.042 and the *errors* for best

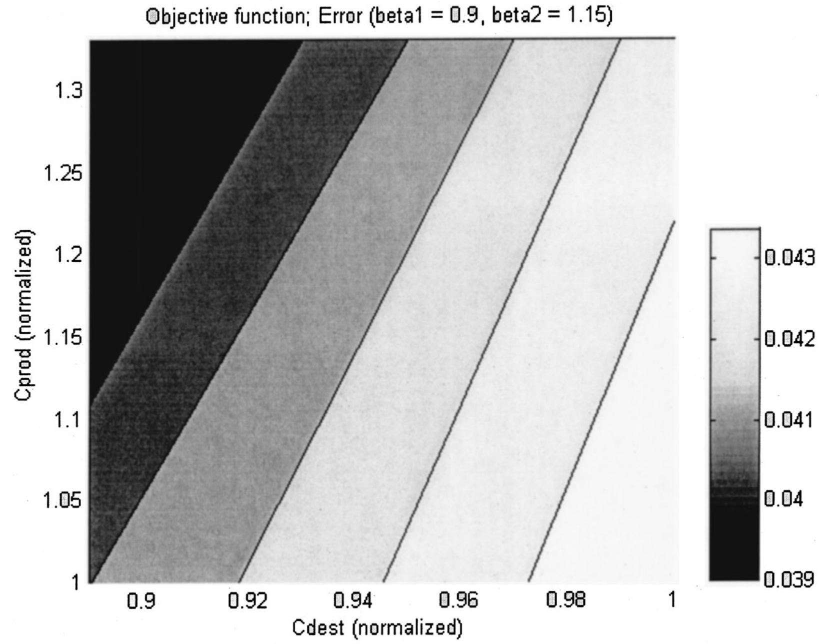

$\beta_1 = 0.9$ and $\beta_2 = 1.15$

Fig. 5 Sensitivity of C_{dest} and C_{prod} for the hemispherical fore-body

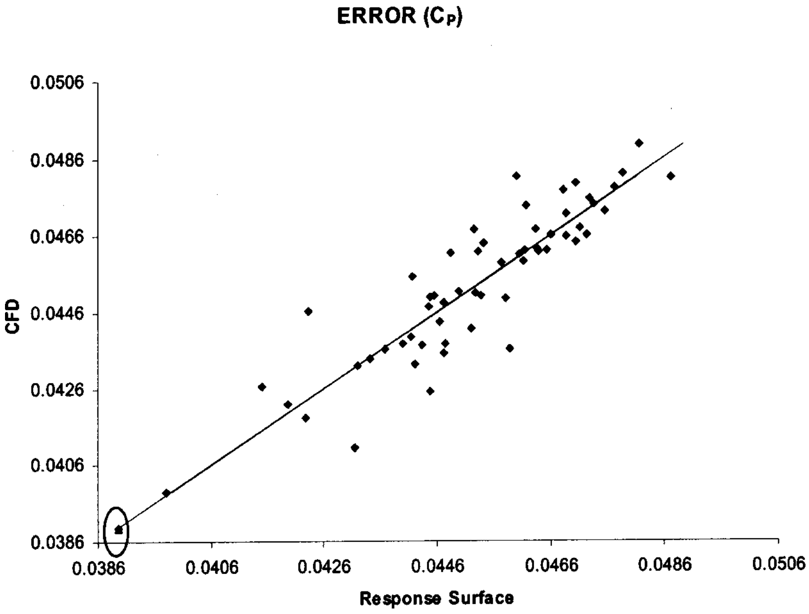

Fig. 6 Comparison of response surface prediction of the objective function to the actual values obtained from CFD computations for the hemispherical object (the values are not normalized)

and worst cases are 0.039 and 0.069, respectively. This shows that the solution can vary drastically within the selected domain if inappropriate combinations of the parameters are selected. Table 3 gives the combinations of the model parameters, which gives *error* values within 10% deviation from the best case obtained for the axisymmetric body. This shows that most of the design points with low values of error are located at $\beta_1=0.9$ and $\beta_2=1.15$ suggesting that this is a good choice for the turbulence model parameters. From the CFD computations it is identified that the best combinations of C_{dest} and C_{prod} are obtained in the upper left quarter of the chosen design space. Figure 5 shows the sensitivity of C_{dest} and C_{prod} in this region for $\beta_1=0.9$ and $\beta_2=1.15$. It shows that the best case is the one with the lower limits of $C_{\text{dest}}(0.89)$ and upper limit of $C_{\text{prod}}(1.33)$ of the chosen domain. The sensitivity of the solution in this design space is marginal for this combination of β_1 and β_2. This suggests that for this combination of the turbulence model factors the variation of the solutions to different combinations of the cavitation model factors are negligible. Hence, extending the domain to look for further improvement will be costly with limited success. Therefore, $\beta_1=0.9$ and $\beta_2=1.15$ are used for the rest of the study on cavitating flows. The sensitivity is modest; hence the optimum combination obtained is accepted even though it lies at the boundary of the chosen design space.

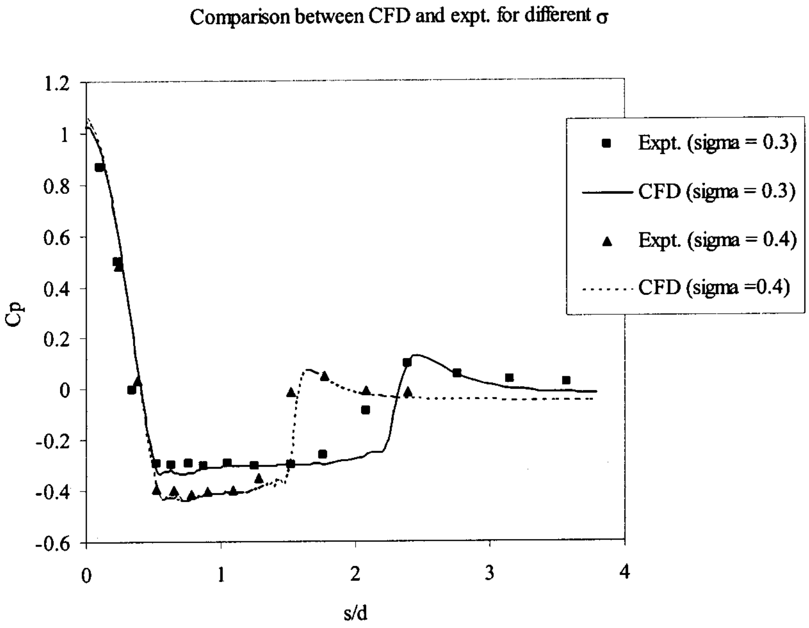

Fig. 7 Comparison of CFD computations with experimental results for different σ for the axisymmetrical object ($\beta_1=0.9$, $\beta_2=1.15$, $C_{\text{dest}}=0.89$ and $C_{\text{prod}}=1.33$)

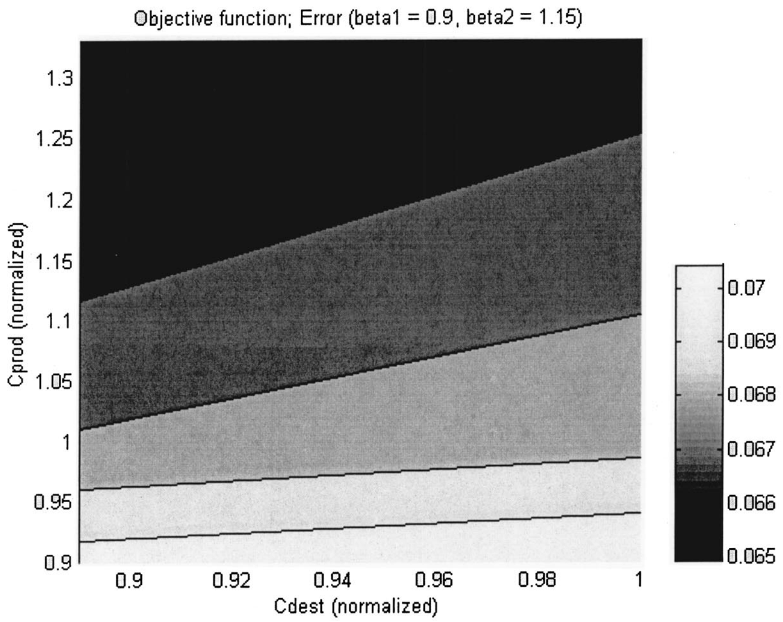

(a) $\sigma = 1.0$, $\beta_1 = 0.9$ and $\beta_2 = 1.15$

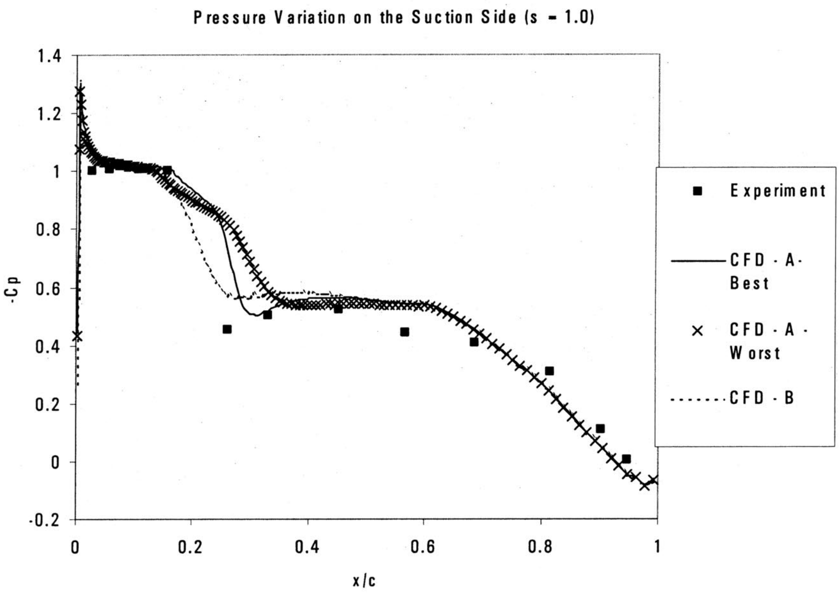

(b) $\sigma = 1.0$

Fig. 8 (*a*) Sensitivity of C_{dest} and C_{prod} for the NACA66(MOD) foil section, (*b*) comparing the C_p values on the suction side. A: Nonequilibrium k-ε turbulence model. B: Original k-ε turbulence model.

Based on the CFD results, a quadratic response surface is generated using the iteratively re-weighted least-square method, [22]. The plot (Fig. 6) between the predicted and the actual value of *error*, suggest a good fit.

In Fig. 6, the solid line indicates the perfect fit. The distribution of data around the perfect fit is well clustered, which suggests a good fit. The best design is circled in Fig. 6. This is identified accurately by both the response surface and CFD computations. The optimum design as predicted by the response surface is with $\beta_1 = 1.01$, $\beta_2 = 1.15$, $C_{\text{dest}} = 0.89$ and $C_{\text{prod}} = 1.33$ whereas that predicted by the CFD run is $\beta_1 = 0.9$, $\beta_2 = 1.15$, $C_{\text{dest}} = 0.89$ and $C_{\text{prod}} = 1.33$. These two identify different optimum combinations of the parameters but in the near vicinity of each other and they agree well with the previous observations.

To check how the sensitivity of these design parameters change with different flow conditions, selected CFD runs were done with a cavitation number of 0.3. The choice of $\beta_1 = 0.9$, $\beta_2 = 1.15$, $C_{\text{dest}} = 0.89$ and $C_{\text{prod}} = 1.33$ gives a good prediction suggesting that this combination is suitable for different flow conditions over this geometry. Figure 7 compares the performance of the CFD computations for $\sigma = 0.3$ and 0.4 for the same combination of the modeling parameters. As the cavitation number decreases, the

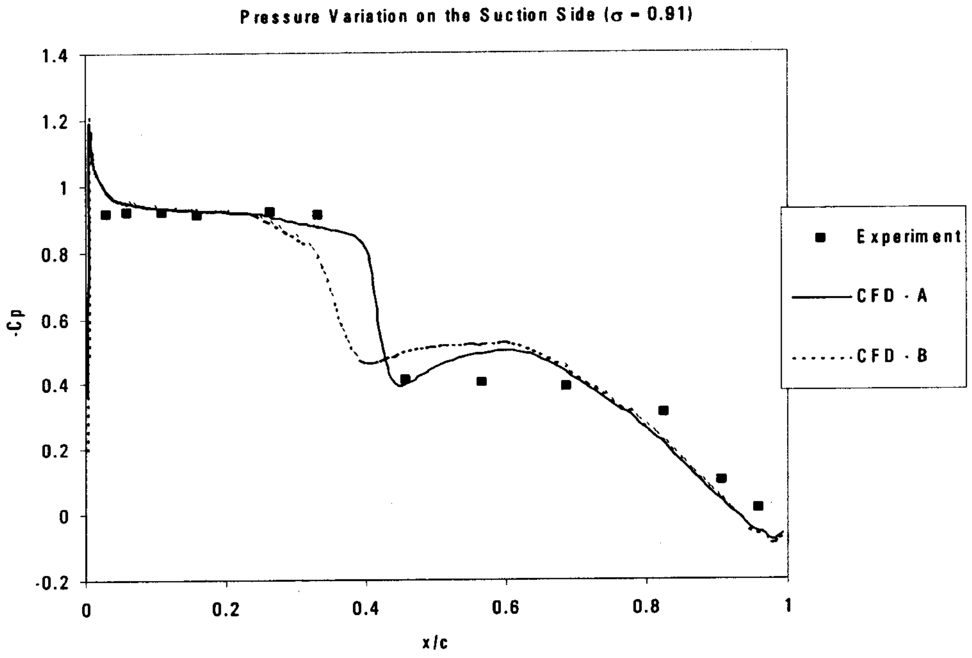

(a) $\sigma = 0.91$

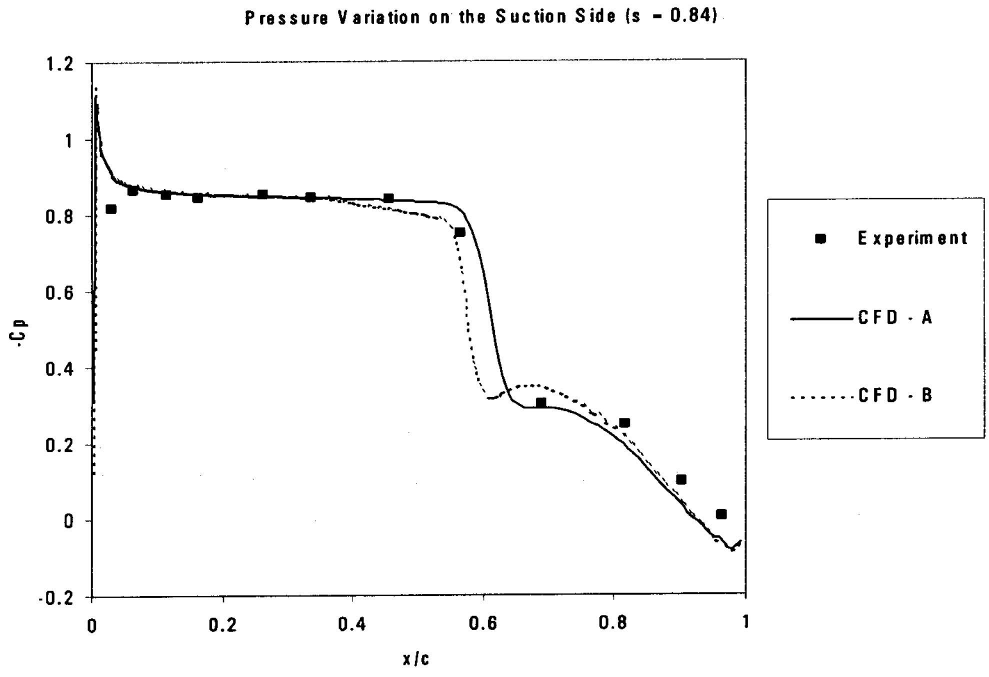

(b) $\sigma = 0.84$

Fig. 9 Comparing the C_p values on the suction side. A: Nonequilibrium k-ε turbulence model.B: Original k-ε turbulence model.

agreement with the experimental results in the closure region worsens. As the cavitation dynamics becomes more complicated, issues such as unsteadiness and compressibility become more pronounced. The present model needs to be further investigated to address these aspects. Nevertheless, the optimized combination of the model parameters perform satisfactorily overall.

3.2.2 NACA66(MOD) Foil Section. For the NACA66(MOD) foil section, the sensitivity analysis is done for the cavitation model parameters alone. The turbulence model parameters are fixed based on the observation made while studying the flow over the axisymmetrical body. The values of β_1 and β_2 are fixed at 0.9 and 1.15, respectively. C_{dest} and C_{prod} are varied between the same range as the range used for the axisymmetrical object. The sensitivity analysis is done for a cavitation number of 1.0. The results are compared with experimental results obtained from Shen and Dimotakis [29]. The error norm used to judge the

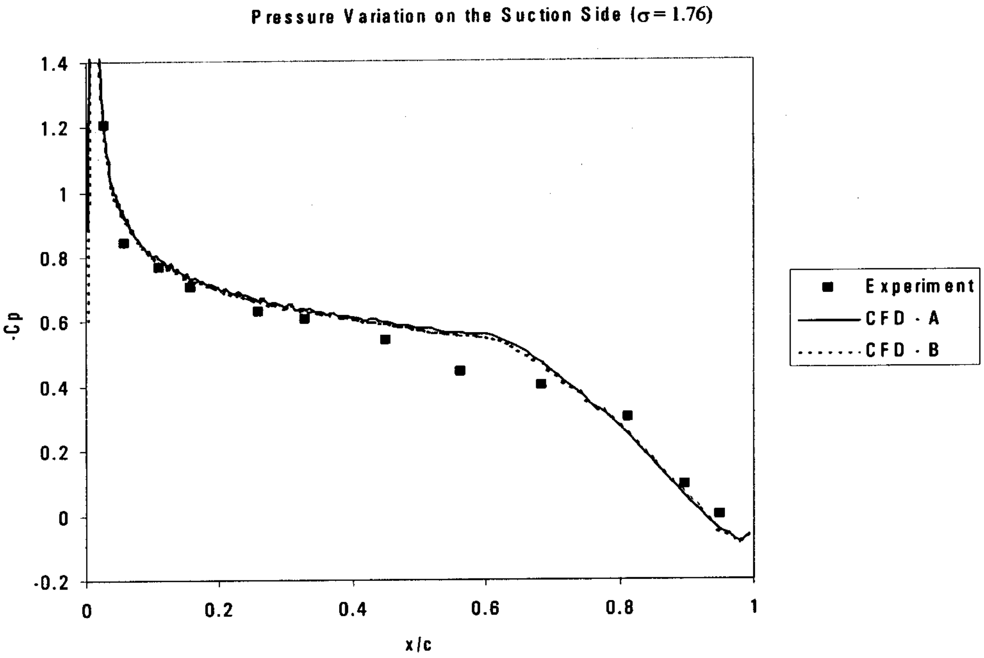

(*c*) $\sigma = 1.76$ (non-cavitating).

Fig. 9 (***continued***)

quality of the CFD solutions is as defined in Eq. (17). The CFD solutions are compared with experimental measurements made at 12 points along the suction side of the foil section. It is found that the best combinations of C_{dest} and C_{prod} are located in the upper left quarter of the chosen domain, just as in the case of the axisymmetrical geometry. It is also found that for this given geometry and flow conditions, the sensitivity of the cavitation model parameters are low (Fig. 8(*a*)). Based on CFD computations, the best combination of C_{dest} and C_{prod} is 0.89 and 1.33, respectively, and the worst combination of C_{dest} and C_{prod} is 1.11 and 0.67, respectively. The solution obtained using former combination captures the closure region of the cavity better than the one using the later combination. (Fig. 8(*b*)). Therefore the combination of C_{dest} and C_{prod}, 0.89 and 1.33, respectively, is used for the computations henceforth. This is identical to the values used for the axisymmetrical object. This shows that the same combination of the model parameters work well for turbulent cavitating flows over different geometries. The prediction with the original k-ε model is also compared in Fig. 8(*b*).

The computations are carried out for different cavitation numbers. For $\sigma=0.91$ and $\sigma=0.84$, the nonequilibrium k-ε turbulence model performs better than the original k-ε turbulence model (Figs. 9(*a*), (*b*)). A noncavitating case ($\sigma=1.76$) is also evaluated to study the efficiency of the model. This is to judge as to how the whole algorithm handles a noncavitating case. For this case, both nonequilibrium and original k-ε turbulence models perform closely (Fig. 9(*c*)).

4 Conclusion

This study offers a systematic approach for assessing the sensitivity of the modeling parameters involved in a transport-equation-based turbulent cavitation model. A single-phase flow over a backward-facing step is analyzed to identify the trend of the turbulence model parameters. The parameters $C_{\varepsilon 1}$ and $C_{\varepsilon 2}$, regulate the production and destruction of the dissipation of turbulent kinetic energy, respectively. Hence, the production and dissipation of turbulence has an equal effect on them. This is clearly seen from the computational results where an almost linear relationship between β_1 and β_2 is noticed. The best combinations of these two parameters are located within 10% variation of the diagonal joining the bottom left corner to the top right corner of the selected domain. Multiple optima are found in the selected design space. Given the fact that multiple optima exist and that the experimental values have an uncertainty, a bandwidth is defined for the turbulent model factors. This defined bandwidth is then adopted for the turbulent cavitating flow study, to reduce the design space.

Analysis of the axisymmetrical projectile geometry indicates that the choice of $\beta_1=0.9$ and $\beta_2=1.15$ is satisfactory, while the sensitivity of the numerical solution to the cavitating model factors is modest. The best combination of the cavitation modeling parameters are located in the upper left quarter of the design space, with the best performance observed for $C_{\mathrm{dest}}=0.89$ and $C_{\mathrm{prod}}=1.33$. The values suggested by the baseline case, [9], are verified to be a good choice too.

The best combinations of the cavitation modeling parameters for the NACA66(MOD) foil section case follows the same trend as that of the axisymmetrical geometry. The best cases are in the same region as that for the axisymmetric geometry and the sensitivity of the CFD solutions to the variations in these parameters is marginal. Same modeling parameters work well for both geometries and different cavitation numbers, suggesting that the present cavitation model does have adequate predictive capabilities.

Inspecting all cases studied, for different geometries and for both single-phase and cavitating flows, one can observe that while the nonequilibrium turbulence modeling approach is not universally superior, it does make useful improvement overall. The combination of $\beta_1=0.9$, $\beta_2=1.15$, $C_{\mathrm{dest}}(\text{nonnormalized})=8\times10^5$ and $C_{\mathrm{prod}}(\text{nonnormalized})=4\times10^4$ performs well for different geometries and flow conditions. Furthermore, the insight gained from the results obtained with the present comprehensive sensitivity evaluations has helped identify not just a single set of values, but also their interplay. As we have discussed, multiple choices of modeling parameters exist within the bandwidth of acceptable solutions. It is also confirmed that the cavitation model parameters employed in the literature, [9], are within the range identified in the present study. In conclusion, for attached cavities, the present turbulent cavitation model and the associated parameter values can perform satisfactorily overall.

Acknowledgments

The work performed here has been partially supported by NASA and Office of Naval Research.

References

[1] Arndt, R. E. A., 1981, ''Cavitation in Fluid Machinery and Hydraulic Structures,'' Annu. Rev. Fluid Mech., **13**, pp. 273–328.

[2] Brennen, C. E., 1995, *Cavitation and Bubble Dynamics*, Oxford University Press, New York.

[3] Knapp, R. T., Daily, J. W., and Hammitt, F. G., 1970, *Cavitation*, McGraw-Hill, New York.

[4] Gopalan, S., and Katz, J., 2000, ''Flow Structure and Modeling Issues in the Closure Region of Attached Cavitation,'' Phys. Fluids, **12**, pp. 895–911.

[5] Singhal, A. K., Vaidyan, N., and Leonard, A. D., 1997, ''Multi-dimensional Simulation of Cavitating Flows Using a PDF Model for Phase Change,'' ASME Paper No. FEDSM97-3272.

[6] Merkle, C. L., Feng, J., and Buelow, P. E. O., 1998, ''Computational Modeling of the Dynamics of Sheet Cavitation,'' 3rd International Symposium on Cavitation, Grenoble, France.

[7] Kunz, R. F., Boger, D. A., Stinebring, D. R., Chyczewski, T. S., Lindua, J. W., Gibeling, H. J., Venkateswaran, S., and Govindan, T. R., 2000, ''A Preconditioned Navier-Stokes Method for Two-Phase Flows With Application to Cavitation Prediction,'' Comput. Fluids, **29**, pp. 849–875.

[8] Ahuja, V., Hosangadi, A., and Arunajatesan, S., 2001, ''Simulations of Cavitating Flows Using Hybrid Unstructured Meshes,'' ASME J. Fluids Eng., **123**, pp. 231–340.

[9] Senocak, I., and Shyy, W., 2002, ''A Pressure-Based Method for Turbulent Cavitating Flow Computations,'' J. Comput. Phys., **176**, pp. 363–383.

[10] Senocak, I., and Shyy, W., 2001, ''Numerical Simulation of Turbulent Flows With Sheet Cavitation,'' CAV2001 4th International Symposium on Cavitation, Paper No. CAV2001A7.002.

[11] Senocak, I., 2002, ''Computational Methodology for the Simulation of Turbulent Cavitating Flows,'' Ph.D. dissertation, University of Florida, Gainesville, FL.

[12] Launder, B. E., and Spalding, D. B., 1974, ''The Numerical Computation of Turbulent Flows,'' Comput. Methods Appl. Mech. Eng., **3**, pp. 269–289.

[13] Shyy, W., Thakur, S. S., Ouyang, H., Liu, J., and Blosch, E., 1997, *Computational Techniques for Complex Transport Phenomena*, Cambridge University Press, New York.

[14] Wang, G., Senocak, I., Shyy, W., Ikohagi, T., and Cao, S., 2001, ''Dynamics of Attached Turbulent Cavitating Flows,'' Prog. Aerosp. Sci., **37**, pp. 551–581.

[15] Myers, R. H., and Montgomery, D. C., 1995, *Response Surface Methodology—Process and Product Optimization Using Designed Experiment*, John Wiley and Sons, New York.

[16] Senocak, I., and Shyy, W. 2002, ''Evaluation of Cavitation Models for Navier-Stokes Computations,'' ASME Paper No: FEDSM2002-31011.

[17] Singhal, A. K., Li, H., Athavale, M. M., and Jiang, Y., 2002, ''Mathematical Basis and Validation of the Full Cavitation Model,'' ASME J. Fluids Eng., **124**, pp. 617–624.

[18] Shyy, W., 1994, *Computational Modeling for Fluid Flow and Interfacial Transport*, Elsevier, Amsterdam (revised printing 1997).

[19] Thakur, S. S., Wright, J. F., Shyy, W., and Udaykumar, H., 1997, ''SEAL: A Computational Fluid Dynamics and Heat Transfer Code for Complex 3-D Geometries,'' Technical Report, University of Florida, Gainesville, FL.

[20] Shyy, W., and Thakur, S. S., 1994, ''A Controlled Variation Scheme in a Sequential Solver for Recirculating Flows. Part I. Theory and Formulation,'' Numer. Heat Transfer, Part B, **25**(3), pp. 245–272.

[21] Shyy, W., and Thakur, S. S., 1994, ''A Controlled Variation Scheme in a Sequential Solver for Recirculating Flows. Part II. Applications,'' Numer. Heat Transfer, Part A, **25**(3), pp. 273–286.

[22] SAS Institute Inc., 1995, JMP Version 3, Cary, NC.

[23] Microsoft Corporation, 1985–1999, Microsoft Excel 2000.

[24] Lasdon, L. S., Waren, A., Jain, A., and Ratner, M., 1978, ''Design and Testing of a Generalized Reduced Gradient Code for Nonlinear Programming,'' ACM Trans. Math. Softw. **4:1**.

[25] Kim, J., Kline, S. J., and Johnston, J. P., 1978, ''Investigation of Separation and Reattachment of a Turbulent Shear Layer: Flow over a Backward-Facing Step,'' Report No. MD-37, Thermosciences Division, Department of Mechanical Engineering, Stanford University, Stanford, CA.

[26] Rouse, H., and McNown, J. S., 1948, ''Cavitation and Pressure Distribution, Head Forms at Zero Angle of Yaw,'' *Studies in Engineering*, Bulletin 32, State University of Iowa.

[27] Reboud, J. L., Stutz, B., and Coutier, O., 1998, ''Two-Phase Flow Structure of Cavitation: Experiment and Modeling of Unsteady Effects,'' 3rd International Symposium on Cavitation, Grenoble, France.

[28] He, X., Senocak, I., Shyy, W., Gangadharan, S. N., and Thakur, S., 2000, ''Evaluation of Laminar-Turbulent Transition and Equilibrium Near-Wall Turbulence Models,'' Numer. Heat Transfer, Part A, **37**, pp. 101–112.

[29] Shen, Y., and Dimotakis, P., 1989, ''The Influence of Surface Cavitation on Hydrodynamic Forces,'' *Proceedings of 22nd ATTC*, St. John, Newfoundland, Canada, Aug., pp. 44–53.

F. M. Owis
Research Associate
e-mail: fowis@vt.edu

Ali H. Nayfeh
Professor,
e-mail: anayfeh@vt.edu

Engineering Science and
Mechanics Department,
Virginia Polytechnic Institute and
State University,
Blacksburg, VA 24061

Computations of the Compressible Multiphase Flow Over the Cavitating High-Speed Torpedo

For high-speed cavitating flows, compressibility becomes significant in the liquid phase as well as in the vapor phase. In addition, the compressible energy equation is required for studying the effects of the propulsive jet on the cavity. Therefore, a numerical method is developed to compute cavitating flows over high-speed torpedoes using the full unsteady compressible Navier-Stokes equations. The multiphase system of equations is preconditioned for low-speed flow computations. Using the mass fraction form, we derive an eigensystem for both the conditioned and the nonconditioned system of equations. This eigensystem provides stability for the numerical discretization of the convective flux and increases the convergence rate. This method can be used to compute single as well as multiphase flows. The governing equations are discretized on a structured grid using an upwind flux difference scheme with flux limits. Single as well as multiphase flows are computed over a cavitating torpedo. The results indicate that the preconditioned system of equations converges rapidly to the required solution at very low speeds. The theoretical results are in good agreement with the measurements. [DOI: 10.1115/1.1568358]

Introduction

Recently, there have been many efforts to develop very high-speed submerged vehicles that travel at hundreds of miles per hour—in some cases, faster than the speed of sound in water. The fastest traditional undersea technologies, in contrast, are limited to a maximum of about 80 mph. The development of such vehicles is based on the physical phenomenon of supercavitation, which reduces the viscous drag drastically. It occurs when bubbles of water vapor form over the submerged bodies that are moving very fast in the water. The formed bubble might occur partially on the body surface or it might grow until it becomes very long compared with the body dimensions; the latter is called supercavitation. The cavity size depends on the body speed, the depth of the water, and the water conditions.

However, supercavitation can cause severe noise, unsteady hydrodynamic forces, structural erosion, and vibration problems. In order to control these problems, it is necessary to predict accurately the extent and behavior of the cavitating flow on the body surface. Accurate prediction of this fluid flow, where sharp interfaces might occur between the different phases, represents a numerical problem of considerable difficulty. In addition, compressibility effects might be significant in this flowfield due to the motion of the vehicle at very high speeds. Therefore, any accurate numerical tool, which might be developed for the prediction of this fluid flow, should take into account the effects of unsteadiness and compressibility. In addition, evaluation of the interaction among the propulsive jet, the body dynamics, the motion of the fins, and the flow around the vehicle is essential for the development of such high-speed vehicles.

Many strategies are adopted to deal with such flows, including volume- and front-tracking methods. In the volume-tracking methods, [1,2], a marker is used to reconstruct the interface and it is advected with the flow. In the front-tracking methods [3–5], a moving interface is described by additional computational elements where the flow properties are interpolated from a fixed grid. The drawbacks of interface-tracking methods are their complexity and inadequacy for more complex problems where the cavity does not have a well-defined interface. Moreover, a moving grid has to be reconstructed as the computations proceed.

Another widely used technique, [6–9], is the interface capturing method where a specified equation for the mixture density is used to close the system. Merkle et al. [10] used separate continuity equations for the different phases. This technique is used also by Kunz et al. [11,12] to model natural and ventilated cavitation over submerged bodies where separate volume fraction equations are used for the condensable and noncondensable gases. We used this technique to develop a multiphase incompressible flow solver for simulating supercavitating flows, [13]. Moreover, other efforts to simulate supercavitating flows are based on the isothermal incompressible equations, [14]. For vehicles moving at very high speeds, compressibility in the vapor cavity has a significant effect on the flow. In addition, the propulsive jet is always compressible. Therefore, it is necessary to solve the full unsteady compressible Navier-Stokes equations in addition to a compressible continuity equation for every phase present in the flow. In some cases, the flow speed might be small compared to the speed of sound in water. In such a case, solving the compressible equations causes numerical problems due to the uncoupling between the pressure field and the density. Therefore, a single algorithm is needed, which is capable of solving incompressible and compressible flows. The key to this algorithm is the preconditioning technique where some of the unsteady terms in the governing equations are modified when the flow becomes incompressible; otherwise, they remain nearly unchanged when the flow is compressible, [15,16].

Our objective is to develop an accurate numerical algorithm for the prediction of supercavitation over submerged bodies. We focus on the numerical problems associated with this type of flow, especially at the interface where high-order accurate numerical methods can cause some oscillations. An upwind flux difference scheme is used for the numerical discretization of the convective fluxes. We control the dissipation in the scheme by using flux limits at the interface, where sharp gradients exist.

Contributed by the Fluids Engineering Division for publication in the JOURNAL OF FLUIDS ENGINEERING. Manuscript received by the Fluids Engineering Division April 4, 2002; revised manuscript received December 17, 2002. Associate Editor: J. Katz.

Predicting cavitation requires a physical understanding of the cavitation process in order to model the mass-transfer rates from water to vapor or from vapor to water where the cavity might be exposed to a pressure higher than the critical pressure. Source terms are added to the governing equations to compute the phase changes. These source terms need to be treated carefully because they could be a major source of numerical instability. We adopted a cavitating model similar to that used by Merkle et al. [10] for the evaporation and condensation processes.

We use a modified two-equation k-ω model to compute the eddy viscosity. This turbulence model is based on the k-ω model developed by Menter [17], which performs very well in case of adverse pressure gradient flows. Rogers [18] used a different formulation of this model to remove the freestream dependency. A zonal approach is implemented in the model, which automatically switches from the Wilcox model, [19], in the near wall region to an equivalent k-ε model, [20], away from the wall. Moreover, we have added density terms to this model to take into consideration the variation of the mixture density in the flowfield, [13].

Governing Equations

Basically, two sets of the field equations are used for the numerical simulation of multiphase flows, namely the multifluid model and the mixture model. The multifluid model assumes that the flow at the interface is generally in thermodynamic equilibrium where the mass, momentum, and energy are exchanged from one phase to the other. As for the mixture model, thermal and dynamic equilibriums are assumed in the different flow regions where the different phases are assumed to be at the same temperature and velocity. This model is generally adequate for bubbly flow. In this model, the momentum and energy equations are used to describe the fluid mixture while a single continuity equation is used for every phase. The mixture model is used in this work and the continuity equations are written in terms of the mass fraction for each fluid component. The mass fraction is defined as

$$y_i=\frac{\rho_i}{\rho_m} \tag{1}$$

where ρ_m is the mixture density and ρ_i is the individual density of fluid element i defined at the partial conditions; that is,

$$\rho_i=\alpha_i\tilde{\rho}_i \tag{2}$$

where $\tilde{\rho}_i$ is the density of fluid element i defined at the mixture conditions and α_i is the volume fraction. Using Eqs. (1) and (2), we define the mass fraction as

$$y_i=\frac{\alpha_i\tilde{\rho}_i}{\rho_m}. \tag{3}$$

The governing equations are described here for a mixture of three fluid elements only. In the computations, the formulation is simply extended for multifluid elements. The governing equations can be written in the following form:

$$\frac{\partial y_l\rho_m}{\partial t}+\frac{\partial y_l\rho_m u_j}{\partial x_j}=S_l \tag{4}$$

$$\frac{\partial \rho_m u_i}{\partial t}+\frac{\partial \rho_m u_i u_j}{\partial x_j}=\frac{\partial p}{\partial x_i}+\frac{\partial \tau_{ij}}{\partial x_j}+\rho_m g_i \tag{5}$$

$$\frac{\partial \rho_m h_t}{\partial t}-\frac{\partial p}{\partial t}+\frac{\partial \rho_m h_t u_j}{\partial x_j}=\frac{\partial u_j\tau_{ij}}{\partial x_j}-\frac{\partial \dot{q}_j}{\partial x_j}+\rho_m g_k u_k+S_e \tag{6}$$

$$\frac{\partial y_v\rho_m}{\partial t}+\frac{\partial y_v\rho_m u_j}{\partial x_j}=S_v \tag{7}$$

$$\frac{\partial y_g\rho_m}{\partial t}+\frac{\partial y_g\rho_m u_j}{\partial x_j}=0 \tag{8}$$

where the shear stresses and the heat flux can be expressed as

$$\tau_{ij}=\frac{2(\mu_m+\mu_t)}{3\ \mathrm{Re}}\left(3\frac{\partial u_i}{\partial x_i}-\frac{\partial u_k}{\partial x_k}\right)\quad \text{for } i=j \tag{9}$$

$$\tau_{ij}=\frac{(\mu_m+\mu_t)}{\mathrm{Re}}\left(\frac{\partial u_i}{\partial x_j}+\frac{\partial u_j}{\partial x_i}\right)\quad \text{for } i\neq j \tag{10}$$

$$\dot{q}=-\left(\frac{\left(\dfrac{k_m}{k_l}\right)}{\mathrm{Pr\,Re}}+\frac{\mu_t}{\mathrm{Pr}_t}\right)\frac{\partial\left[h\left(\dfrac{Cp_l}{Cp_m}\right)\right]}{\partial x_j}. \tag{11}$$

The source terms, which express the phase change, are used as follows:

$$S_l=(\dot{m}_l+\dot{m}_v) \tag{12}$$

$$S_v=-(\dot{m}_l+\dot{m}_v) \tag{13}$$

$$S_e=(\dot{m}_l+\dot{m}_v)\{(h_f^{Ts})_v-(h_f^{Ts})_l\}. \tag{14}$$

The governing equations are normalized with respect to the liquid density, freestream velocity, and the characteristic length of the body. Hence, the Reynolds number is defined as

$$\mathrm{Re}=\frac{U_\infty D\tilde{\rho}_l}{\mu_l}. \tag{15}$$

The mixture density can be calculated using the volume fraction as follows:

$$\rho_m=\sum_{i=2}^{m}\alpha_i\Delta\rho_i+\tilde{\rho}_l \tag{16}$$

where

$$\Delta\rho_i=\tilde{\rho}_l-\tilde{\rho}_i. \tag{17}$$

Using Eq. (3), we express the mixture density as

$$\rho_m=\frac{\tilde{\rho}_l}{1-\sum_{2}^{m}\dfrac{y_i}{\tilde{\rho}_i}(\tilde{\rho}_i-\tilde{\rho}_l)}. \tag{18}$$

In addition, the following equations are used in order to close the system:

$$y_l=1-\sum_{2}^{m}y_i \tag{19}$$

$$h_t=h+\frac{1}{2}(u_1^2+u_2^2+u_3^2) \tag{20}$$

$$h=\sum_{i=1}^{m}y_i\int_{Ts}^{T}Cp_i dT. \tag{21}$$

Finally, an equation of state is used for each phase:

$$\tilde{\rho}_i=f(p,h). \tag{22}$$

The Peng-Robinson equation of state for real fluids is used for both the vapor and liquid, [21]. This equation is a modified form of Van Der Waal equation of state.

The governing equations can be rewritten in the generalized curvilinear coordinates as follows:

$$\Gamma_e\frac{\partial\hat{Q}}{\partial t}+\frac{\partial(F-F_v)}{\partial\xi}+\frac{\partial(G-G_v)}{\partial\eta}+\frac{\partial(H-H_v)}{\partial\zeta}-\hat{S}=0 \tag{23}$$

$$\hat{Q}=\frac{Q}{J}=\frac{1}{J}(p,u_1,u_2,u_3,h,y_v,y_g)^T \tag{24}$$

$$F=\frac{1}{J}(y_l\rho_m U_1,\rho_m u_1 U_1+\xi_{x1}p,\rho_m u_2 U_1+\xi_{x2}p,\rho_m u_3 U_1+\xi_{x3}p,\rho_m htU_1,y_v\rho_m U_1,y_g\rho_m U_1)^T \tag{25}$$

$$G=\frac{1}{J}(y_l\rho_m U_2,\rho_m u_1 U_2+\eta_{x1}p,\rho_m u_2 U_2+\eta_{x2}p,\rho_m u_3 U_2+\eta_{x3}p,\rho_m htU_2,y_v\rho_m U_2,y_g\rho_m U_2)^T \tag{26}$$

$$H=\frac{1}{J}(y_l\rho_m U_3,\rho_m u_1 U_3+\zeta_{x1}p,\rho_m u_2 U_3+\zeta_{x2}p,\rho_m u_3 U_3+\zeta_{x3}p,\rho_m htU_3,y_v\rho_m U_3,y_g\rho_m U_3)^T \tag{27}$$

$$U_1=\xi_{x1}u_1+\xi_{x2}u_2+\xi_{x3}u_3 \tag{28}$$

$$U_2=\eta_{x1}u_1+\eta_{x2}u_2+\eta_{x3}u_3 \tag{29}$$

$$U_3=\zeta_{x1}u_1+\zeta_{x2}u_2+\zeta_{x3}u_3 \tag{30}$$

$$\hat{S}=\frac{1}{J}\{S_l,\rho_m g_1,\rho_m g_2,\rho_m g_3,S_e+\rho_m g_1 u_1+\rho_m g_2 u_2+\rho_m g_3 u_3,S_v,0\}^T \tag{31}$$

where F_v, G_v, and H_v are the viscous fluxes in the generalized curvilinear coordinates. The matrix Γ_e is given in Appendix A.

It can be easily shown that the following derivatives are expressed as

$$\frac{\partial\rho_m}{\partial p}=\rho_m^2\sum_{i=1}^{m}\frac{y_i}{\tilde{\rho}_i^2}\frac{\partial\tilde{\rho}_i}{\partial p} \tag{32}$$

$$\frac{\partial\rho_m}{\partial h}=\rho_m^2\sum_{i=1}^{m}\frac{y_i}{\tilde{\rho}_i^2}\frac{\partial\tilde{\rho}_i}{\partial h} \tag{33}$$

$$\frac{\partial\rho_m}{\partial y_i}=\rho_m^2\left(\frac{1}{\tilde{\rho}_l}-\frac{1}{\tilde{\rho}_i}\right). \tag{34}$$

Turbulence Modeling

A two-equation k-ω model is used for the turbulence closure. The model is a modified version of the model used by Rogers [18] to compute single-phase incompressible flows. This model has different coefficients, depending on the region of solution, to reduce the freestream dependency of the model. The model switches from the k-ω model near the wall to the k-ε model away from the wall. The variation of the mixture density is implemented in the current model. The model is defined as follows:

$$\frac{\partial(\rho_m k)}{\partial t}+\frac{\partial(\rho_m k u_j)}{\partial x_j}=P_k-\beta^*\rho_m\omega k+\frac{\partial}{\partial x_j}\left[(\mu_m+\sigma_k\mu_t)\frac{\partial k}{\partial x_j}\right] \tag{35}$$

$$\frac{\partial(\rho_m\omega)}{\partial t}+\frac{\partial(\rho_m\omega u_j)}{\partial x_j}=\gamma P_\omega-\beta^*\rho_m\omega^2+\frac{\partial}{\partial x_j}\left[(\mu_m+\sigma_\omega\mu_t)\frac{\partial\omega}{\partial x_j}\right]+2(1-F_1)\sigma_{\omega 2}\frac{\mu_t}{k}\frac{\partial k}{\partial x_j}\frac{\partial\omega}{\partial x_j} \tag{36}$$

$$\mu_t=\frac{\rho_m k}{\omega} \tag{37}$$

where P_k and P_ω are the production terms, which are set proportional to the vorticity as explained by Rogers [18]. The constants in the model are blended, depending on the region of solution, to switch from the k-ω model to the k-ε model using the function F_1 as follows:

$$\phi=F_1\phi_1+(1-F_1)\phi_2 \tag{38}$$

where the value of F_1 is zero or one depending on the region, ϕ_1 represents constants for the k-ω Wilcox model, and ϕ_2 represents constants from the Jones-Launder [20] k-ε model.

Cavitation Model

The mass transfer rates $\dot{m}_l$ and $\dot{m}_v$ are required to model the cavitation. A simplified form of the Ginzburg-Landau potential is suggested by Merkle et al. [10]. In this model, the mass transfer rate $\dot{m}_l$ from liquid to vapor is proportional to the volume fraction and the amount by which the local pressure is below the vapor pressure.

The cavitation model is defined as follows:

$$\dot{m}_l=\left(\frac{c_{\text{evap}}}{t_\infty}\right)y_l\rho_m\text{Min}[0,p-p_v]. \tag{39}$$

In the current work, we used the following model for the condensation process:

$$\dot{m}_v=\left(\frac{c_{\text{prod}}}{t_\infty}\right)y_v\rho_m(\tilde{\rho}_l/\tilde{\rho}_v)\text{Max}[0,p-p_v]. \tag{40}$$

Here, t_∞ is the characteristic time of the problem and p_v is the vapor pressure, which is obtained from the thermodynamic tables corresponding to the flow temperature. The constants $(c_{\text{evap}}/t_\infty)$ and $(c_{\text{prod}}/t_\infty)$ are empirical constants, which express the time rate of the evaporation and condensation processes with respect to the flow process. The following values are used in all of the simulations: $c_{\text{evap}}/t_\infty=0.9$ and $c_{\text{prod}}/t_\infty=0.9$.

Linearization of the Flux Vector

An upwind difference scheme is used to discretize the convective flux. Specifically, the flux difference splitting of the Roe scheme [22] is used for the numerical discretization. The details of the numerical scheme are explained in [22–24]. In this section, we review the derivation of the eigensystem for the multiphase flow. The eigenvalues and the eigenvectors are required for the upwind differencing of the convective flux. The convective flux in Eq. (23) can be linearized as follows:

$$\Gamma_e\frac{\partial\hat{Q}}{\partial t}+\Gamma_e\tilde{A}\frac{\partial\hat{Q}}{\partial\xi}+\Gamma_e\tilde{B}\frac{\partial\hat{Q}}{\partial\eta}+\Gamma_e\tilde{C}\frac{\partial\hat{Q}}{\partial\zeta}=\overline{S} \tag{41}$$

$$\tilde{A}=\Gamma_e^{-1}A. \tag{42}$$

The matrices A, $\tilde{A}$, and Γ_e are given in the Appendix.

The eigenvalues of the matrix $\tilde{A}$ are

$$\lambda=\{U_1,U_1,U_1,U_1,U_1,U_1-\overline{c},U_1+\overline{c}\} \tag{43}$$

$$\overline{c}=c\sqrt{\xi_{x1}^2+\xi_{x2}^2+\xi_{x3}^2} \tag{44}$$

where c is the speed of sound for compressible multi-fluid elements, which can be expressed as

$$\frac{1}{c^2}=\frac{\partial\rho_m}{\partial p}+\frac{1}{\rho_m}\frac{\partial\rho_m}{\partial h}. \tag{45}$$

The right eigenvector matrix is given by

$$X_i=\begin{bmatrix} 0 & 0 & \rho_m\overline{c} & \rho_m\overline{c} & 0 & 0 & 0\\ -\xi_{x2} & -\xi_{x1}\xi_{x3} & -\xi_{x1} & \xi_{x1} & 0 & 0 & 0\\ \xi_{x1} & -\xi_{x2}\xi_{x3} & -\xi_{x2} & \xi_{x2} & 0 & 0 & 0\\ 0 & \xi_{x1}^2+\xi_{x2}^2 & -\xi_{x3} & \xi_{x3} & 0 & 0 & 0\\ 0 & 0 & \overline{c} & \overline{c} & 1 & 0 & 0\\ 0 & 0 & 0 & 0 & 0 & 1 & 0\\ 0 & 0 & 0 & 0 & 0 & 0 & 1 \end{bmatrix}. \tag{46}$$

System Preconditioning

As the flow speed becomes very low, the governing equations for the compressible multiphase as well as the single-phase flow tend to be singular. Therefore, the performance of the time-marching schemes becomes very poor because of the large difference between the particle speed and the speed of sound. Many preconditioning techniques have been suggested for the computations of low-speed flows, [15,16], with the aim of solving flow problems that contain compressible and incompressible flows simultaneously. These techniques are based on the introduction of artificial time derivatives to the governing equations such that the system eigenvalues are modified and the disparity in the wave speed is reduced. For multiphase flows, the speed of sound might change significantly from one phase to the other. Therefore, one needs to modify the speed of sound only in certain flow regions where a large disparity between the flow speed and the acoustic wave speed exists. For instance, the acoustic wave speed in water is very large compared with the acoustic wave speed in the cavity. Therefore, we suggest the following preconditioning technique, which alters the mixture speed of sound in the water only while the actual speed of sound in the vapor or gaseous phases remains unchanged.

Equation (41) can be rewritten in the following form after adding the artificial time derivatives:

$$\Gamma_e \frac{\partial \hat{Q}}{\partial t} + \Gamma \frac{\partial \hat{Q}}{\partial \tau} + \Gamma \tilde{A} \frac{\partial \hat{Q}}{\partial \xi} + \Gamma \tilde{B} \frac{\partial \hat{Q}}{\partial \eta} + \Gamma \tilde{C} \frac{\partial \hat{Q}}{\partial \xi} = \overline{S} \tag{47}$$

$$\tilde{A} = \Gamma^{-1} A. \tag{48}$$

The following preconditioning parameter V_P is introduced to the preconditioning matrix Γ:

$$Vp = \left(\frac{\partial \rho'_m}{\partial p} \right) \Bigg/ \left(\frac{\partial \rho_m}{\partial p} \right) \tag{49}$$

where the derivatives in Eq. (43) are defined as

$$\frac{\partial \rho_m}{\partial p} = \rho_m^2 \left(\frac{y_l}{\tilde{\rho}_l^2} \frac{\partial \tilde{\rho}_l}{\partial p} + \frac{y_v}{\tilde{\rho}_v^2} \frac{\partial \tilde{\rho}_v}{\partial p} + \frac{y_g}{\tilde{\rho}_g^2} \frac{\partial \tilde{\rho}_g}{\partial \rho} \right) \tag{50}$$

$$\frac{\partial \rho'_m}{\partial p} = \rho_m^2 \left(\frac{1}{M_p^2} \frac{y_l}{\tilde{\rho}_l^2} \frac{\partial \tilde{\rho}_l}{\partial p} + \frac{y_v}{\tilde{\rho}_v^2} \frac{\partial \tilde{\rho}_v}{\partial p} + \frac{y_g}{\tilde{\rho}_g^2} \frac{\partial \tilde{\rho}_g}{\partial p} \right). \tag{51}$$

M_p is the preconditioning Mach number which is defined in terms of the local Mach number and a cutoff Mach number M_c. The cutoff Mach number is a small value, which is used to avoid the singularity at the stagnation point.

$$M_p = \min[1, \max(M, M_c)] \tag{52}$$

The eigenvalues of the preconditioned system are

$$\lambda_1 = \lambda_2 = \lambda_3 = \lambda_4 = \lambda_5 = U_1 \tag{53}$$

$$\lambda_6, \lambda_7 = \frac{1}{2} \left\{ \left(1 + \frac{c'^2}{c^2} \right) U_1 \pm \sqrt{4 \xi_k c'^2 + \left(1 - \frac{c'^2}{c^2} \right)^2 U_l^2} \right\} \tag{54}$$

$$\xi_k = \xi_{x1}^2 + \xi_{x2}^2 + \xi_{x3}^2 \tag{55}$$

where c' is defined by

$$\frac{1}{c'^2} = \frac{\partial \rho'_m}{\partial p} + \frac{1}{\rho_m} \frac{\partial \rho_m}{\partial h}. \tag{56}$$

It is clear from Eq. (54) that the eigenvalues of the preconditioned system are of the same order as the flow speed. Therefore, the system is well conditioned for single-phase flows as well as for multiphase flows.

Boundary Conditions

Different boundary conditions are used in the simulations, including inflow, outflow, no-slip, and symmetric boundary conditions. All of the boundary conditions are treated implicitly in the code to reduce the restriction on the time step and to increase the stability of the code. At the inflow boundary, flow variables are specified depending on the inlet Mach number. For subsonic inflow, the velocities, the enthalpy, and the mass fractions are specified, whereas the pressure is extrapolated from the interior points. For a subsonic outflow boundary, the pressure is specified, whereas all other variables are extrapolated from the computational domain. For a supersonic outflow, all the flow variables are

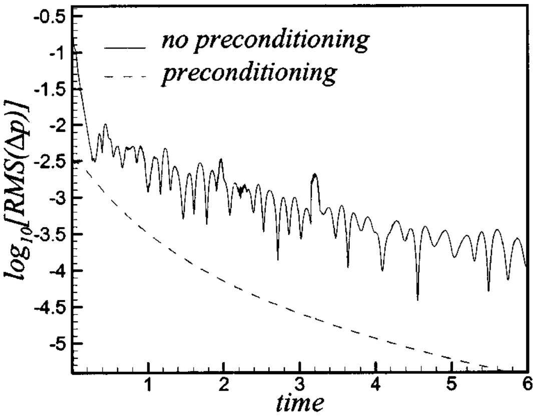

Fig. 1 Convergence history for a single-phase flow over a hemispherical body at Mach number 0.05 with and without preconditioning

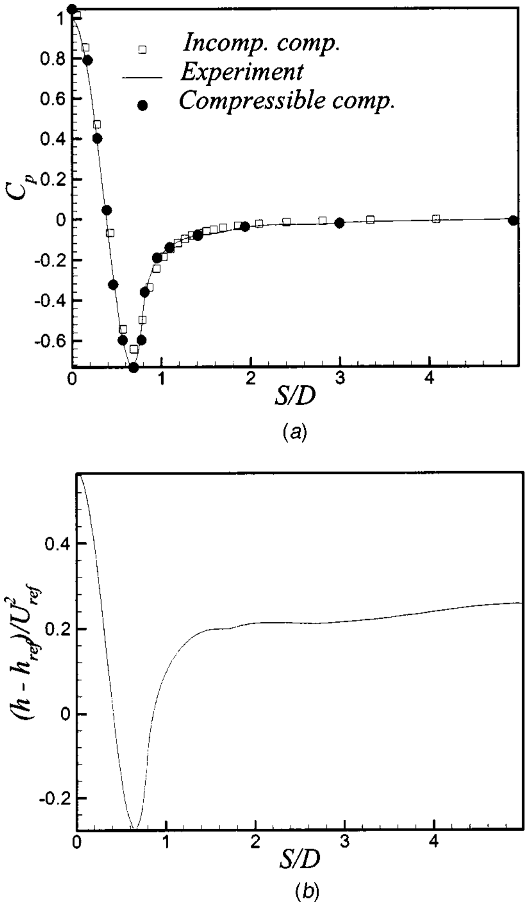

(*a*)

(*b*)

Fig. 2 Single-phase flow over a hemispherical body at Mach number 0.05: (*a*) pressure coefficient, (*b*) enthalpy

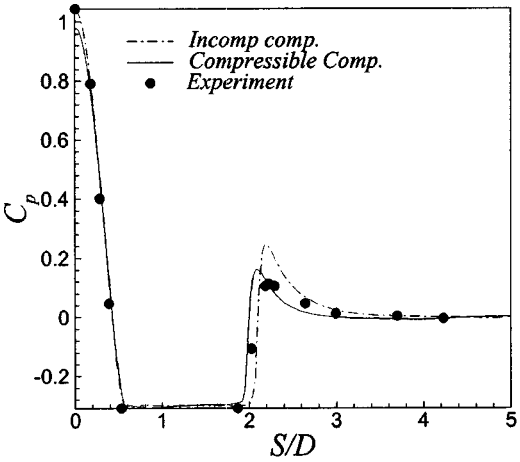

Fig. 3 The pressure coefficient distribution for the cavitating flow over a hemispherical body (U_∞=20 m/s)

extrapolated. At the walls, the velocities are set equal to zero, whereas the mass fraction, the temperature, and the pressure are extrapolated. At the line of symmetry (centerline), the normal velocity to the centerline is set equal to zero, whereas the derivatives of the tangential velocity normal to the line of symmetry, the volume fraction, and the pressure are set equal to zero.

Results

The cavitating flow over hemispherical and conical bodies is computed for different flow speeds and a Reynolds number of 1.4×10^5. Different grid dimensions are used for the different cases and the grid is clustered near the body surface in the normal direction in order to resolve the boundary layer accurately. For the hemispherical body, a grid of dimensions 80 × 32 × 170 is used in the normal, azimuthal and tangential directions, respectively. For the time accurate computations, a physical time step of 0.002 is used in the simulations. At low flow speeds, the results are compared with our incompressible flow computations, [13], and the measurements by Rose and McNown [25]. For the compressible flow computations, the cavitation number can not be specified because the vapor pressure depends on the flow temperature. The vapor pressure is extrapolated from the thermodynamic tables for the different flow temperatures. But, as the flow speed becomes very low, the cavitating flow is nearly isothermal. Therefore, the flow speed is chosen for the compressible flow computations such that the cavitation number is nearly the same as in the incompressible flow computations.

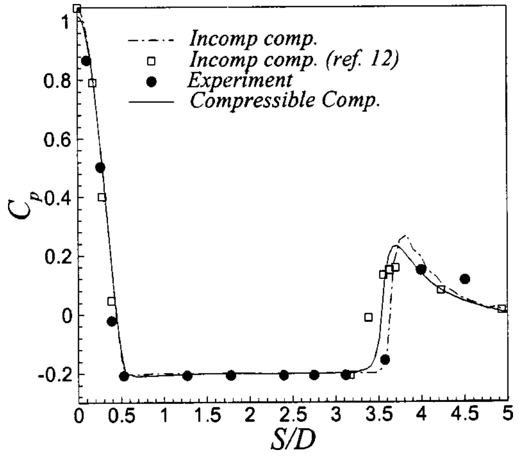

Fig. 4 The pressure coefficient distribution for the cavitating flow over a hemispherical body (U_∞=25 m/s)

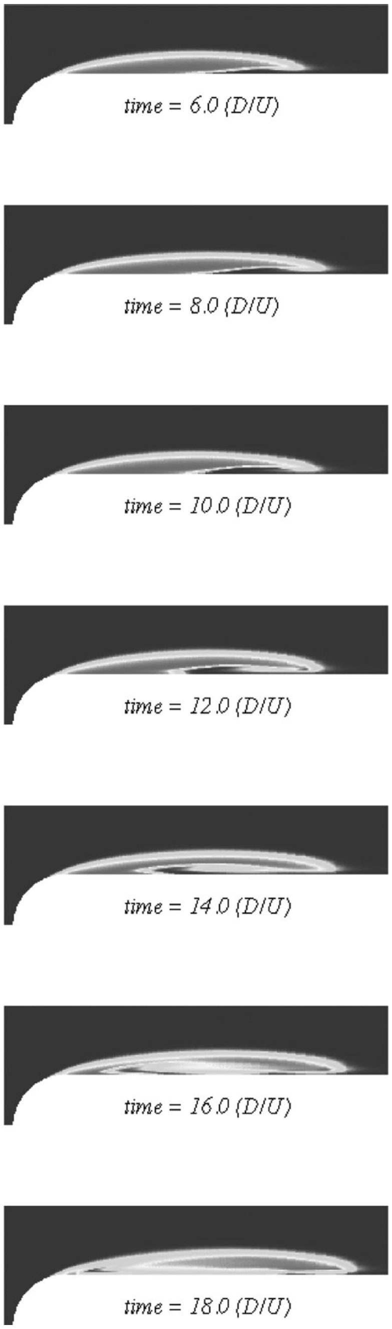

Fig. 5 Time sequence of the cyclic process of the bubble generation, collapse, filling, and break off for the cavitating flow over a hemispherical body (U_∞=25 m/s)

For the cavitating flow at low speeds, it is difficult to obtain convergence without preconditioning the governing equations. Therefore, single-phase flow computations over a hemispherical body are employed to compare the convergence history of the governing equations with and without preconditioning the system as shown in Fig. 1. The results indicate that the pressure field converges rapidly and smoothly for the preconditioned equations. On the other hand, poor convergence is obtained without preconditioning the governing equations, which is attributed to the large difference between the flow speed and the acoustic wave speed. In Fig. 2, the pressure coefficient and the enthalpy for the single-

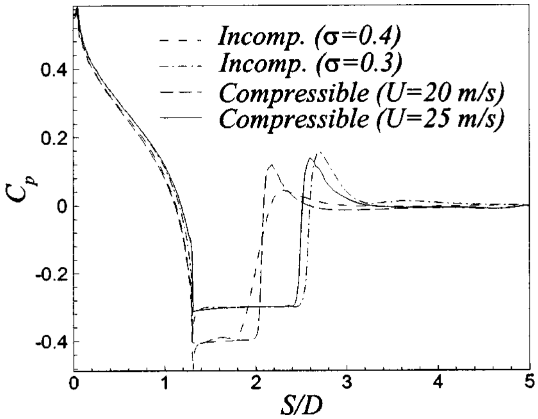

Fig. 6 The pressure coefficient distribution for the cavitating flow over a conical body

phase flow are presented. It is clear from the figure that better results are obtained for the compressible equations compared with the incompressible equations and the data. The difference in the results could be attributed to the difference between the preconditioning techniques of the compressible and incompressible equations since the compressibility effects are very low at this Mach number.

The cavitating flow over an axisymmetric hemispherical body is computed at low speeds using the compressible governing equations. The results are compared with the incompressible computations and the measurements at similar cavitation numbers. The pressure coefficient distribution at the body surface is presented in Figs. 3 and 4. Good results are obtained for the compressible equations compared with the data and the incompressible computations.

The time sequence of the bubble shape for the cavitating flow over a hemispherical body is presented in Fig. 5. As the pressure in the flowfield becomes lower than the vapor pressure, a bubble grows on the projectile surface. Due to the bubble closure on the surface, the pressure increases near the bubble end causing the bubble to collapse. In addition, water is pushed into the bubble due to the large pressure difference near the bubble end and a water jet penetrates deep into the bubble. This water jet reentrance causes the bubble to break off at certain point. As a result, the pressure jump at the bubble end disappears, causing the water jet to slow down until the cycle is repeated.

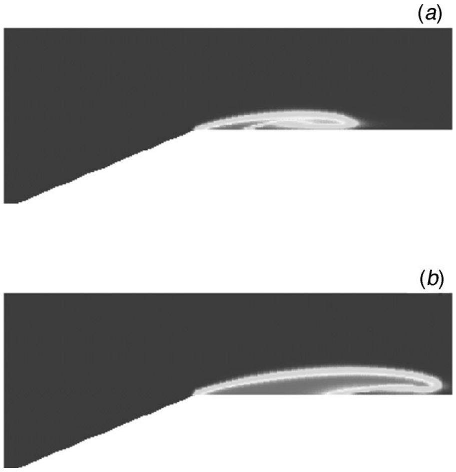

Fig. 7 Instantaneous bubble shape for the cavitating flow over a conical body at different flow speeds: (*a*) $U_\infty = 20$ m/s, (*b*) $U_\infty = 25$ m/s

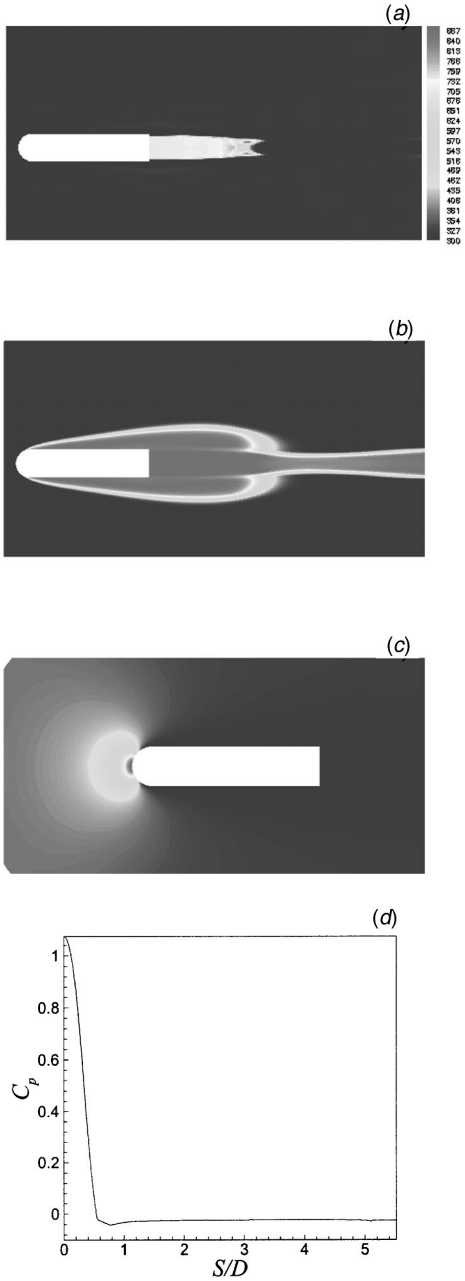

Fig. 8 The cavitating flow over a hemispherical body with the exhaust plume ($U_\infty = 100$ m/s): (*a*) temperature contours, (*b*) density contours, (*c*) pressure contours, (*d*) pressure coefficient distribution along the surface

The cavitating flow over an axisymmetric conical body is computed using the compressible and incompressible equations at low speeds. The time average of the pressure coefficient distribution along the body surface is presented in Fig. 6 for the compressible and incompressible computations. The compressible flow is computed at speeds of 20 m/s and 25 m/s, which are equivalent to cavitation numbers of 0.4 and 0.3 at the specified flow temperature. As expected, the compressible and incompressible results are in close agreement because the density variations in the water and vapor are minimal at these low speeds. The difference between the compressible and incompressible computations might come from

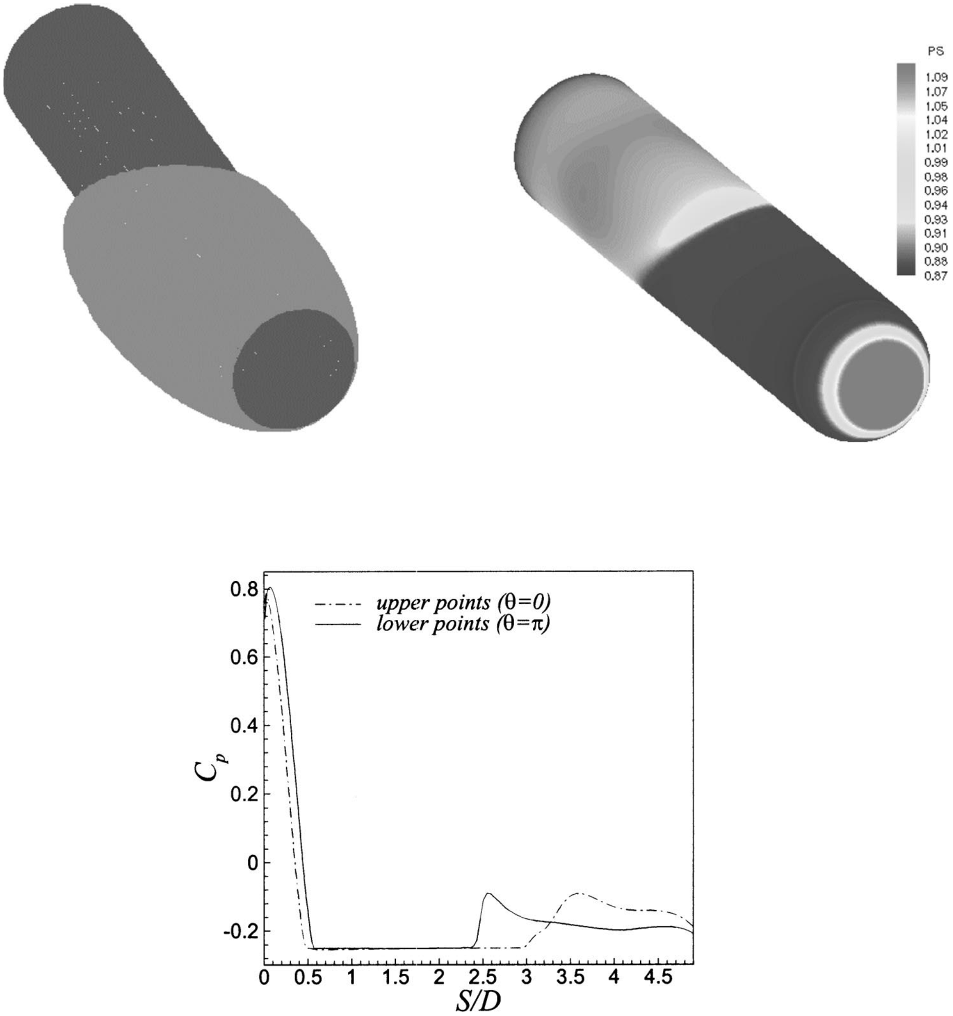

Fig. 9 The cavitating flow over a hemispherical body at an angle of attack ($U_\infty = 20$ m/s, $\alpha = 5$): (*a*) bubble shape, (*b*) surface pressure, (*c*) pressure coefficient distribution at the highest and lowest points of the surface

the addition of all of the shear stress components to the governing equations and the different preconditioning techniques. The bubble shape for the conical flow is presented in Fig. 7 for two different speeds and at a particular time. The figure shows the effect of the flow speed on the bubble size. In addition, the reentrance of a water jet can be noticed in both cases.

The cavitating flow over a hemispherical body at a relatively high speed is investigated in Fig. 8. A supersonic hot propulsive jet is included in the computations. The density of the exhaust gas at the jet inlet conditions is very low compared with the water density and it is of the same order as the vapor density. The jet speed is assumed to be 3.5 the freestream velocity and the jet inlet temperature is assumed to be 700 K. The freestream Mach number is assumed to be 0.075. At this Mach number, the cavity is very long and it covers the whole surface of the body, as can be seen in Fig. 8(*b*), because the cavitation number at these conditions is of the order 0.02. Therefore, the pressure is nearly constant on most of the body surface, which is covered by the cavity as shown in Figs. 8(*c*) and 8(*d*). In this case, the water jet effect on the body surface does not exist and the cavity tends to be less unstable. As most of the body is covered by vapor, the viscous drag is significantly reduced but the total drag is not reduced with the same order. The major part of the drag comes from the nose region where the body is not covered by the bubble, and a high-pressure distribution exists in this region. The drag can be reduced on the nose by using gas injection. Examining the flow of the propulsive jet, compression and expansion waves can be clearly seen behind the cavity in Figs. 8(*a*) and 8(*b*). As a result of the expansion waves, the temperature is highly reduced. A contraction followed by an expansion of the jet plume flow can be also seen in Fig. 8(*b*) due to the underexpansion waves.

To study the effect of the angle of attack on the cavity and the surface pressure distribution, we compute a cavitating flow over a hemispherical body at 5 deg angle of attack and a speed of 20 m/s. As the flow pressure on the upper part of the surface tends to be lower than that on the lower part, the bubble growth is expected to be higher on the upper portion than on the lower portion. Therefore, an asymmetric bubble shape is obtained as clear from Fig. 9(*a*) and stronger water jet effect is expected on the upper part of the body. In addition, unstable waves are generated in the azimuthal direction causing the bubble to oscillate in this direction. The pressure distribution on the surface indicates that a pressure jump occurs at different downstream positions for the different azimuthal positions because of the variation of the bubble length at those positions.

Conclusions

A numerical method is developed to solve the full unsteady compressible Navier-Stokes equations for multiphase flows. In addition, a preconditioning technique is suggested to compute low-speed as well as high-speed multiphase flows. This technique alters the speed of sound only in flow regions where there is a large disparity between the flow speed and the acoustic wave speed. The eigenvalues are derived for both the conditioned and nonconditioned systems of equations. The convective flux vector is discretized using an upwind flux difference splitting scheme on a structured grid. The equations are integrated implicitly in time and the resulting linear system is solved iteratively using the Gauss-Seidel line-relaxation method. All of the boundary conditions are treated implicitly in the code to reduce the restriction on the time step. A zonal turbulence model is employed for the computation of the eddy viscosity and the model is solved separately from the governing equations to alleviate the system stiffness and to reduce the computational time. Cavitating flows over hemispherical and conical bodies are computed at different flow speeds and the propulsive jet is considered in the computations. The results indicate a good convergence history for the preconditioned system. Moreover, the computations at low speeds indicate good agreement with the incompressible flow computations and the measurements, which demonstrate the ability of the method to compute compressible and incompressible multiphase flows simultaneously. In the future, the fins will be included in the computations using the overlap grid and the hydrodynamic forces and moments will be computed at different flow conditions and for different body configurations.

Acknowledgments

The authors would like to thank the Office of Naval Research for supporting this project under the Multidisciplinary University Research Initiative (MURI) on Nonlinear Active Control of Dynamical Systems, Contract Number N00014-96-1-1123.

Nomenclature

c = speed of sound
Cp_i = specific heat for fluid element i
D = body diameter
g_i = gravity vector
h = enthalpy
h_t = total enthalpy
h_f^{Ts} = heat of formation at Ts
k_m = mixture thermal conductivity
$\dot{m}_l$ = mass transfer rate from liquid to vapor
$\dot{m}_v$ = mass transfer rate from vapor to liquid
M = local Mach number
M_p = preconditioning Mach number
p = pressure
Pr_t = turbulent Prandtl number
Re = Reynolds number
t = physical time
T = mixture temperature
Ts = standard temperature ($Ts = 298$ K)
u_i = velocity in the x_i-direction
y_i = mass fraction of phase i
α_i = volume fraction
μ_m = mixture viscosity
μ_t = turbulent eddy viscosity
ρ_v = vapor density
ρ_l = liquid density
τ = artificial time

Appendix

$$\Gamma_e = \begin{bmatrix}
y_l \frac{\partial \rho_m}{\partial p} & 0 & 0 & 0 & y_l \frac{\partial \rho_m}{\partial h} & y_l \frac{\partial \rho_m}{\partial y_v} - \rho_m & y_l \frac{\partial \rho_m}{\partial y_g} - \rho_m \\
u_1 \frac{\partial \rho_m}{\partial p} & \rho_m & 0 & 0 & u_1 \frac{\partial \rho_m}{\partial h} & u_1 \frac{\partial \rho_m}{\partial y_v} & u_1 \frac{\partial \rho_m}{\partial y_g} \\
u_2 \frac{\partial \rho_m}{\partial p} & 0 & \rho_m & 0 & u_2 \frac{\partial \rho_m}{\partial h} & u_2 \frac{\partial \rho_m}{\partial y_v} & u_2 \frac{\partial \rho_m}{\partial y_g} \\
u_3 \frac{\partial \rho_m}{\partial p} & 0 & 0 & \rho_m & u_3 \frac{\partial \rho_m}{\partial h} & u_3 \frac{\partial \rho_m}{\partial y_v} & u_3 \frac{\partial \rho_m}{\partial y_g} \\
ht \frac{\partial \rho_m}{\partial p} - 1 & \rho_m u_1 & \rho_m u_2 & \rho_m u_3 & ht \frac{\partial \rho_m}{\partial h} + \rho_m & ht \frac{\partial \rho_m}{\partial y_v} & ht \frac{\partial \rho_m}{\partial y_g} \\
y_v \frac{\partial \rho_m}{\partial p} & 0 & 0 & 0 & y_v \frac{\partial \rho_m}{\partial h} & y_v \frac{\partial \rho_m}{\partial y_y} + \rho_m & y_v \frac{\partial \rho_m}{\partial y_g} \\
y_g \frac{\partial \rho_m}{\partial p} & 0 & 0 & 0 & y_g \frac{\partial \rho_m}{\partial h} & y_g \frac{\partial \rho_m}{\partial y_v} & y_g \frac{\partial \rho_m}{\partial y_g} + \rho_m
\end{bmatrix}$$

$$A = \begin{bmatrix}
y_l \frac{\partial \rho_m}{\partial p} U_1 & \rho_m \xi_{x1} y_l & \rho_m \xi_{x2} y_l & \rho_m \xi_{x3} y_l & y_l \frac{\partial \rho_m}{\partial h} U_1 & \left(y_l \frac{\partial \rho_m}{\partial y_v} - \rho_m \right) U_1 & \left(y_l \frac{\partial \rho_m}{\partial y_g} - \rho_m \right) U_1 \\
u_1 \frac{\partial \rho_m}{\partial p} U_1 + \xi_{x1} & \rho_m (u_1 \xi_{x1} + U_1) & \rho_m u_1 \xi_{x2} & \rho_m u_1 \xi_{x3} & u_1 \frac{\partial \rho_m}{\partial h} U_1 & u_1 \frac{\partial \rho_m}{\partial y_v} U_1 & u_1 \frac{\partial \rho_m}{\partial y_g} U_1 \\
u_2 \frac{\partial \rho_m}{\partial p} U_1 + \xi_{x2} & \rho_m u_2 \xi_{x1} & \rho_m (u_2 \xi_{x2} + U_1) & \rho_m u_2 \xi_{x3} & u_2 \frac{\partial \rho_m}{\partial h} U_1 & u_2 \frac{\partial \rho_m}{\partial y_v} U_1 & u_2 \frac{\partial \rho_m}{\partial y_g} U_1 \\
u_3 \frac{\partial \rho_m}{\partial p} U_1 + \xi_{x3} & \rho_m u_3 \xi_{x1} & \rho_m u_3 \xi_{x2} & \rho_m (u_3 \xi_{x3} + U_1) & u_3 \frac{\partial \rho_m}{\partial h} U_1 & u_3 \frac{\partial \rho_m}{\partial y_v} U_1 & u_3 \frac{\partial \rho_m}{\partial y_g} U_1 \\
ht \frac{\partial \rho_m}{\partial p} U_1 & \rho_m (ht \xi_{x1} + u_3 U_1) & \rho_m (ht \xi_{x2} + u_3 U_1) & \rho_m (ht \xi_{x3} + u_3 U_1) & \left(ht \frac{\partial \rho_m}{\partial h} + \rho_m \right) U_1 & ht \frac{\partial \rho_m}{\partial y_v} U_1 & ht \frac{\partial \rho_m}{\partial y_g} U_1 \\
y_v \frac{\partial \rho_m}{\partial p} U_1 & \rho_m \xi_{x1} y_v & \rho_m \xi_{x2} y_v & \rho_m \xi_{x3} y_v & y_v \frac{\partial \rho_m}{\partial h} U_1 & \left(y_v \frac{\partial \rho_m}{\partial y_v} + \rho_m \right) U_1 & y_v \frac{\partial \rho_m}{\partial y_g} U_1 \\
y_g \frac{\partial \rho_m}{\partial p} U_1 & \rho_m \xi_{x1} y_g & \rho_m \xi_{x2} y_g & \rho_m \xi_{x3} y_g & y_g \frac{\partial \rho_m}{\partial h} U_1 & y_g \frac{\partial \rho_m}{\partial y_v} U_1 & \left(y_g \frac{\partial \rho_m}{\partial y_g} + \rho_m \right) U_1
\end{bmatrix}$$

$$\tilde{A}=\Gamma_e^{-1}A=\begin{bmatrix} U_1 & \dfrac{\xi_{x1}\rho_m^2}{\dfrac{\partial\rho_m}{\partial h}+\rho_m\dfrac{\partial\rho_m}{\partial p}} & \dfrac{\xi_{x2}\rho_m^2}{\dfrac{\partial\rho_m}{\partial h}+\rho_m\dfrac{\partial\rho_m}{\partial p}} & \dfrac{\xi_{x3}\rho_m^2}{\dfrac{\partial\rho_m}{\partial h}+\rho_m\dfrac{\partial\rho_m}{\partial p}} & 0 & 0 & 0 \\ \dfrac{\xi_{x1}}{\rho_m} & U_1 & 0 & 0 & 0 & 0 & 0 \\ \dfrac{\xi_{x2}}{\rho_m} & 0 & U_1 & 0 & 0 & 0 & 0 \\ \dfrac{\xi_{x3}}{\rho_m} & 0 & 0 & U_1 & 0 & 0 & 0 \\ 0 & \dfrac{\xi_{x1}\rho_m^2}{\dfrac{\partial\rho_m}{\partial h}+\rho_m\dfrac{\partial\rho_m}{\partial p}} & \dfrac{\xi_{x2}\rho_m^2}{\dfrac{\partial\rho_m}{\partial h}+\rho_m\dfrac{\partial\rho_m}{\partial p}} & \dfrac{\xi_{x3}\rho_m^2}{\dfrac{\partial\rho_m}{\partial h}+\rho_m\dfrac{\partial\rho_m}{\partial p}} & U_1 & 0 & 0 \\ 0 & 0 & 0 & 0 & 0 & U_1 & 0 \\ 0 & 0 & 0 & 0 & 0 & 0 & U_1 \end{bmatrix}$$

The preconditioned system:

$$\Gamma=\begin{bmatrix} y_l\dfrac{\partial\rho_m}{\partial p}Vp & 0 & 0 & 0 & y_l\dfrac{\partial\rho_m}{\partial h} & y_l\dfrac{\partial\rho_m}{\partial y_v}-\rho_m & y_l\dfrac{\partial\rho_m}{\partial y_g}-\rho_m \\ u_1\dfrac{\partial\rho_m}{\partial p}Vp & \rho_m & 0 & 0 & u_1\dfrac{\partial\rho_m}{\partial h} & u_1\dfrac{\partial\rho_m}{\partial y_v} & u_1\dfrac{\partial\rho_m}{\partial y_g} \\ u_2\dfrac{\partial\rho_m}{\partial p}Vp & 0 & \rho_m & 0 & u_2\dfrac{\partial\rho_m}{\partial h} & u_2\dfrac{\partial\rho_m}{\partial y_v} & u_2\dfrac{\partial\rho_m}{\partial y_g} \\ u_3\dfrac{\partial\rho_m}{\partial p}Vp & 0 & 0 & \rho_m & u_3\dfrac{\partial\rho_m}{\partial h} & u_3\dfrac{\partial\rho_m}{\partial y_v} & u_3\dfrac{\partial\rho_m}{\partial y_g} \\ ht\,\dfrac{\partial\rho_m}{\partial p}Vp-1 & \rho_m u_1 & \rho_m u_2 & \rho_m u_3 & ht\,\dfrac{\partial\rho_m}{\partial h}+\rho_m & ht\,\dfrac{\partial\rho_m}{\partial y_v} & ht\,\dfrac{\partial\rho_m}{\partial y_g} \\ y_v\dfrac{\partial\rho_m}{\partial p}Vp & 0 & 0 & 0 & y_v\dfrac{\partial\rho_m}{\partial h} & y_v\dfrac{\partial\rho_m}{\partial y_v}+\rho_m & y_v\dfrac{\partial\rho_m}{\partial y_g} \\ y_g\dfrac{\partial\rho_m}{\partial p}Vp & 0 & 0 & 0 & y_g\dfrac{\partial\rho_m}{\partial h} & y_g\dfrac{\partial\rho_m}{\partial y_v} & y_g\dfrac{\partial\rho_m}{\partial y_g}+\rho_m \end{bmatrix}$$

$$\tilde{A}=\Gamma^{-1}A=\begin{bmatrix} \dfrac{U_1\left(\dfrac{\partial\rho_m}{\partial h}+\rho_m\dfrac{\partial\rho_m}{\partial p}\right)}{\dfrac{\partial\rho_m}{\partial h}+\rho_m\dfrac{\partial\rho_m}{\partial p}Vp} & \dfrac{\xi_{x1}\rho_m^2}{\dfrac{\partial\rho_m}{\partial h}+\rho_m\dfrac{\partial\rho_m}{\partial p}Vp} & \dfrac{\xi_{x2}\rho_m^2}{\dfrac{\partial\rho_m}{\partial h}+\rho_m\dfrac{\partial\rho_m}{\partial p}Vp} & \dfrac{\xi_{x3}\rho_m^2}{\dfrac{\partial\rho_m}{\partial h}+\rho_m\dfrac{\partial\rho_m}{\partial p}Vp} & 0 & 0 & 0 \\ \dfrac{\xi_{x1}}{\rho_m} & U_1 & 0 & 0 & 0 & 0 & 0 \\ \dfrac{\xi_{x2}}{\rho_m} & 0 & U_1 & 0 & 0 & 0 & 0 \\ \dfrac{\xi_{x3}}{\rho_m} & 0 & 0 & U_1 & 0 & 0 & 0 \\ \dfrac{\dfrac{\partial\rho_m}{\partial p}(-1+Vp)}{\dfrac{\partial\rho_m}{\partial h}+\rho_m\dfrac{\partial\rho_m}{\partial p}Vp} & \dfrac{\xi_{x1}\rho_m^2}{\dfrac{\partial\rho_m}{\partial h}+\rho_m\dfrac{\partial\rho_m}{\partial p}Vp} & \dfrac{\xi_{x2}\rho_m^2}{\dfrac{\partial\rho_m}{\partial h}+\rho_m\dfrac{\partial\rho_m}{\partial p}Vp} & \dfrac{\xi_{x3}\rho_m^2}{\dfrac{\partial\rho_m}{\partial h}+\rho_m\dfrac{\partial\rho_m}{\partial p}Vp} & U_1 & 0 & 0 \\ 0 & 0 & 0 & 0 & 0 & U_1 & 0 \\ 0 & 0 & 0 & 0 & 0 & 0 & U_1 \end{bmatrix}$$

References

[1] Harlow, F. H., and Welch, J. E., 1965, ‘‘Numerical Calculation of Time-Dependent Viscous Incompressible Flow of Fluid With Free Surface,’’ Phys. Fluids, **8**, p. 2182.

[2] Daly, B. J., 1968, ‘‘Numerical Study of Density-Current Surges,’’ Phys. Fluids, **11**, pp. 15–30.

[3] Peskin, C. S., 1977, ‘‘Numerical Analysis of Blood Flow in the Heart,’’ J. Comput. Phys., **25**, p. 220.

[4] Unverdi, S. O., and Tryggvason, G., 1992, ‘‘A Front-Tracking Method for Viscous, Incompressible Multi-Fluid Flows,’’ J. Comput. Phys., **100**, pp. 25–37.

[5] Unverdi, S. O., and Tryggvason, G., 1992, ‘‘Computations of Multi-Fluid Flows,’’ Physica D, **60**, pp. 70–83.

[6] Kubota, A., Kato, H., and Yamagauchi, H., 1992, ‘‘Cavity Flow Predictions Based on the Euler Equations,’’ J. Fluid Mech., **240**, pp. 59–96.

[7] Lemonnier, H., and Rowe, A., 1988, ‘‘Another Approach in Modeling Cavitating Flows,’’ J. Fluid Mech., **195**, p. 557.

[8] Delannoy, Y., and Kueny, J. L., 1990, ‘‘Cavity Flow Predictions based on the Euler Equations,’’ *ASME Cavitation and Multi-Phase Flow Forum*, **109**, ASME, New York, pp. 153–158.

[9] Jannens, M. E., Hulshoff, S. J., and Hoijmarks, H. W. M., 1997, ‘‘Calculation of Unsteady Attached Cavitation,’’ AIAA Paper No. 97-1936.

[10] Merkle, C. L., Feng, J., and Buelow, 1988, ‘‘Computational Modeling of the Dynamics of Sheet Cavitation,’’ 3rd International Symposium on Cavitation, Grenoble, France.

[11] Kunz, R. F., Boger, D. A., Gibeling, H. J., and Govindan, T. R., 1999, ‘‘A Preconditioning Navier-Stokes Method for Two-Phase Flows,’’ AIAA Paper No. 99-3329.

[12] Kunz, R. F., Boger, D. A., Chyczewski, T. S., Stineberg, D. R., Gibeling, H. J., and Govindan, T. R., 1999, ‘‘Multi-Phase CFD Analysis of Natural and Ventilated Cavitation about Submerged Bodies,’’ Proceedings of 3rd ASME/JSME Joint Fluids Engineering Conference, ASME Paper No. FEDSM99-7364.

[13] Owis, F., and Nayfeh, A. H., 2001, ‘‘Numerical Simulation of Super- and Partially-Cavitating Flows Over an Axisymmetric Projectile,’’ AIAA Paper No. 2001-1042.

[14] Venkateswaran, S., Lindau, J. W., Kunz, R. F., and Merkle, C. L., 2001, ‘‘Preconditioning Algorithms for the Computation of Multi-Phase Mixture Flows,’’ AIAA Paper No. 2001-0279.

[15] Venkateswaran, S., and Merkle, C. L., 1999, ‘‘Analysis of Preconditioning Methods for the Euler and Navier-Stokes Equations,’’ Von Karman Institute Lecture Series, 1999-2003.

[16] Turkel, E., 1993, ‘‘A Review of Preconditioning Methods for Fluid Dynamics,’’ Appl. Numer. Math., **12**, pp. 258–284.

[17] Menter, F. R., 1993, ‘‘Zonal Two-Equation k-ω Turbulence Models For Aerodynamic Flows,’’ AIAA Paper No. 93-1906.

[18] Rogers, S. E., Menter, F., Durbin, P. A., and Mansour, N. N., 1994, ‘‘A Comparison Of Turbulence Models in Computing Multi-Element Airfoil Flows,’’ AIAA Paper No. 94-0291.

[19] Wilcox, D. C., 1988, ‘‘Multiscale Model for Turbulent Flows,’’ AIAA J., **26**(11), pp. 1311–1320.

[20] Jones, W. P., and Launder, P. E., 1973, ‘‘The Calculation of Low Reynolds Number Phenomena With a Two-Equation Model of Turbulence,’’ Int. J. Heat Mass Transf., **16**, pp. 1119–1130.

[21] Peng, D. Y., and Robinson, D. C., 1976, ‘‘A New Two-Constant Equation of State,’’ Ind. Eng. Chem. Fundam., **15**(1), pp. 59–64.

[22] Roe, P. L., 1981, ‘‘Approximate Riemann Solvers, Parameter Vectors, and Difference Schemes,’’ J. Comput. Phys., **43**, pp. 357–372.

[23] Chakravarthy, S. R., Szema, K-Y., Goldberg, U. C., and Gorski, J. J., 1985, ‘‘Application of a New Class of High Accuracy TVD Schemes to the Navier-Stokes Equations,’’ AIAA Paper No. 85-0165.

[24] Rogers, S. E., Kwak, D., and Kiris, C., 1989, ‘‘Numerical Solution of the Incompressible Navier-Stokes Equations for Steady-State and Time-Dependent Problems,’’ AIAA Paper No. 89-0463.

[25] Rouse, H., and McNown, J. S., 1948, ‘‘Cavitation and Pressure Distribution, Head Forms at Zero Angle of Yaw,’’ Studies in Engineering, Bulletin 32, State University of Iowa.

Ranganathan Kumar
Professor,
Department of Mechanical, Materials and
Aerospace Engineering,
University of Central Florida,
Orlando, FL 32816

Thomas A. Trabold
Géneral Motors Corporation,
Honeoye Falls, NY 14612

Charles C. Maneri
Lockheed Martin Corporation,
One River Road,
Schenectady, NY 12301

Experiments and Modeling in Bubbly Flows at Elevated Pressures

Measurements of local void fraction, rise velocity, and bubble diameter have been obtained for cocurrent, wall-heated, upward bubbly flows in a pressurized refrigerant. The instrumentation used are the gamma densitometer and the hot-film anemometer. Departure bubble size is correlated in terms of liquid subcooling and bulk bubble size in terms of void fraction. Flow visualization techniques have also been used to understand the two-phase flow structure and the behavior of the bubbly flow for different bubble shapes and sizes, and to obtain the bubble diameter and rise velocity. The lift model is provided explicitly in terms of Eotvos number which is changed by changing the system pressure. In general, Eotvos number plays a strong role in determining both bubbly lift and drag. Such insight coupled with quantitative local and averaged data on void fraction and bubble size at different pressures has aided in developing bubbly flow models applicable to heated two-phase flows at high pressure. [DOI: 10.1115/1.1567308]

Introduction

Two-phase bubbly flow in a vertical circular tube has been studied by several investigators in air-water, [1–3], and in subcooled boiling flows, [4–8]. There have been relatively few detailed void fraction or bubble size measurements in bubbly flow in noncircular geometries, [7,8], for applications in heat exchangers and microelectronics. Even more scarce are measurements made in noncircular geometries in heated systems at high pressures, [9]. These papers discuss the effect of bubble size on lateral void distribution, and reveal near-wall void peaking due to bubble layers, [1,2], bubble sliding, [2], and center-peaking due to bubble coring, [7]. These flow configurations are known to result from the differences in bubble size and the bubble generation methods. The forces acting on the bubbles are dependent on the bubble size, the bubble shape, and the turbulence in the liquid field.

The present work is undertaken to apply suitable instrumentation to obtain fundamental local data in a modeling refrigerant fluid which simulates boiling systems at high pressures. A rectangular geometry is used to capture desired three-dimensional effects, present improved optical access, and afford simplified instrumentation. The primary objective of this investigation is to perform ‘‘separate effects’’ tests in a modeling fluid, which emphasize the sensitivity of measured results to a specific phenomenon, and to obtain measurements to assist in developing individual closure models required for the analysis of two-phase flow systems. These measurements have been made in a refrigerant fluid, R-134a (SUVA) at elevated temperature and pressure conditions. At 0.9 and 2.4 MPa, R-134a has a liquid-to-vapor density ratio of 27.0 and 7.3, respectively, compared to a ratio of about 850 for atmospheric pressure air-water. Similarly, the surface tension of R-134a is 0.0069 and 0.0021 N/m at 2.4 and 0.9 MPa, respectively, compared with 0.072 N/m for water at atmospheric conditions. These results have been used to develop interfacial drag and bubbly lift models.

Experimental Investigation

Test Facility. Key components of the experimental R-134a loop are a chiller and pressurizer to maintain the liquid phase at the inlet of a circulating canned rotor pump, a large CO_2 heat exchanger, loop heaters, high/low range throttle valves, flow meters, and a vertical test section. Loop conditions are set by programmed logic controllers. Acquired data include mass flow rate, temperature, pressure, and heater power. The loop design pressure ranges from 0.4 to 2.5 MPa, and temperature ranges from 0° to 80°C.

The test section is designed to have flat sides to allow improved optical access and to afford simplified instrumentation measurement capability. In addition, the high aspect ratio of the test section captures three-dimensional effects, which are not normally seen in circular geometries. This test section has a length of 1.2 m, a width of 57.2 mm, and a thickness of 2.5 mm. These dimensions facilitate the use of thin, transparent heater films that enable visual observations and are consistent with the flow and control capabilities of the test loop. Optical access to the flow is provided by eight quartz windows, each 38.1 mm thick by 76.2 mm wide by 0.28 m long. Between each pair of windows are 25.4-mm-diameter unheated instrumentation ports in the side of the test section which permit access to the flow for various instruments. For the reported experiments, rakes of nine thermocouples were located at the inlet and the exit.

The instrument scanning mechanism positions the gamma densitometer system (GDS) along three axes: the *X*-axis (vertical, or streamwise position), the *Y*-axis (horizontal scans along the test section narrow dimension), and the *Z*-axis (horizontal scans across the width of the test section). In order to measure void distributions in either the thickness (*Y*) or the width (*Z*) directions, the gamma densitometer can be rotated 90 deg about the test section. The positioning accuracy of the scanning mechanism is determined to be within ±0.025 mm.

The inlet to the test section is comprised of three independent flow zones which enable the introduction of different flow rates and/or fluid enthalpies. This feature permits the investigation of flows with nonuniform inlet boundary conditions. The bridges between the quartz windows contain brushes to carry current to the window heater films. The triple track window heater design consists of three transparent metallic oxide conductive films, vacuum deposited onto the inside surface, with an antireflective coating on the outside. The three heater film strips occupy a total width of approximately 51 mm. Three silver epoxy buses carry the current around both ends of the windows, and connect with the silver graphite brushes. The instrumentation used in the R-134a experimental program has been extensively discussed in our previous papers, [10–13]. Although the majority of those measurements

---

Contributed by the Fluids Engineering Division for publication in the JOURNAL OF FLUIDS ENGINEERING. Manuscript received by the Fluids Engineering Division December 5, 2001; revised manuscript received November 13, 2002. Editor: S. Ceccio.

pertain to droplets in annular flow, the procedures for measuring bubble signals using various instrumentation are similar, and only the differences will be pointed out here.

A gamma densitometer system was used to determine cross-section-averaged void fraction. The system features a shielded 9 curie Cesium-137 source and a gamma detector. A dual slit, rotating tungsten collimator is incorporated into the source cask to permit two choices for the spatial resolution of the emergent gamma beams. The gamma beam is always normal to the test section X-axis, and its height is 19 mm for the source collimator position. The wide beam, when directed through the edge of the test section, interrogates the entire cross-sectional area of the fluid and, hence, yields a measurement of the cross-sectional average void fraction. Void fraction profiles (averaged over a line parallel to the heated wall) across the narrow dimension are obtained using the narrow beam directed through the test section edge. The effective gamma beam width (full width at half max) at the test section for a narrow beam edge scan is 0.43 mm. For the 0.25 mm steps used, each measurement location overlaps the adjacent one by about 0.18 mm, and the fluid is interrogated to within 0.15 mm of the heated test section walls. The processing of the detected gamma pulses and the conversion of density to void fraction are discussed in detail by Kirouac et al. [10]. For each experimental condition, the average void fraction was established by using a wide gamma beam that interrogated the entire duct cross section at the desired streamwise location.

Two minute counting times were used for both wide beam and narrow beam edge measurements. The total uncertainty, based on the repeatability of an ensemble of measurements at 95% confidence ($\pm 2\sigma$), was determined for each type of GDS measurement. Each wide beam edge measurement was obtained twice and averaged, for a total uncertainty of ± 0.015 in void fraction. For each line-averaged narrow beam measurement, the total uncertainty is ± 0.032. There are no known bias errors in these measurements.

Hot-Film Anemometer (HFA). A constant temperature hot film anemometer (HFA) was primarily used to obtain the local void fraction and bubble diameter. In the current experimental setup, dual sensor probes were installed at $x/L = 0.475$ and $x/L = 0.725$ (in the second and the third windows) at the center of the wall. Some measurements were also made in the fourth window near the exit at $x/L = 0.975$. The probe was positioned in the test section to be parallel to the window surface, and perpendicular to the flow direction. The probe was installed through a hole in a quartz window. This probe had platinum film sensors with a 25-μm diameter and 254-μm active length, and a measured sensor separation distance of 1.44 ± 0.01 mm.

The system consists of a dual sensor HFA probe which was directly exposed to the two-phase flow field, electronic circuitry which controlled the amount of heating current supplied to the probe, an analog-to-digital converter and a PC-based data acquisition system. Voids flowing past the sensor produce a significant decrease in the local heat transfer coefficient and an instantaneous increase in sensor temperature and circuit resistance. To restore balance, the circuit decreases sensor voltage to decrease the current and therefore the sensor temperature. Similarly, as liquid again flows over the sensor, the local heat transfer coefficient increases, resulting in an instantaneous cooling of the sensor and a corresponding increase in output voltage and current to maintain the sensor temperature. A 50 kHz digitizing rate was found to be sufficient to represent the negative voltage pulses for measurements in the current investigation. This digitizing rate was obtained based on a sensitivity study of different rates from 10 to 100 kHz. All measurements documented in this report are based on a 6.4 second data record (i.e., 64,000 discrete voltage samples). Greater details of the complexities and uncertainty of the HFA measurements are provided in [11,12].

In order to account for long rise and fall times of the bubble signal, the analysis method of de Carvalho and Bergles [14] was used, in which level thresholding was used to identify phase changes, and slope thresholding was used to account for the void volume passage time. Once the raw voltage signal is converted into the phase indicator function ($I = 0$ for liquid, -1 for vapor), the number of voltage samples for which the vapor phase is present at the probe divided by the total number of voltage samples gives a measurement of the local ensemble-averaged vapor volume fraction. The passage times of the bubbles are represented by the width of the segments in the phase indicator function which equals -1. The number of negative pulses per unit time provides a measurement of the bubble frequency.

The bubble diameter is calculated by measuring the void fraction and bubble frequency from the upstream sensor, and the bubble velocity through a cross-correlation of signals from both sensors, using the relation

$$d_B = 1.5 \frac{V_B \alpha}{f_B}. \tag{1}$$

The peak in the cross-correlation versus time plot corresponds to the most probable time required for a gas-liquid interface to travel between the HFA sensors, from which the mean interfacial velocity may be calculated.

Measurement Uncertainty. Wherever possible, simultaneous measurements with multiple instruments were performed to confirm data trends, and cross-qualify void fraction and velocity measurements. Kirouac et al. [10] showed that for a system pressure and flow rate of 2.4 MPa and 106 kg/hr, the line-averaged GDS data lie slightly lower than the HFA data as the former averages the void fraction over the entire test section width, and encounters liquid collected along the duct edges. Similar plots will also be shown in the Results Section. They also compared the HFA velocity with the laser Doppler velocimeter (LDV) measurements. The agreement was found to be generally good for all subcooled boiling conditions investigated.

The bubble frequency measurement is complicated by the variable amplitude of the pulses in the output voltage signal. Large bubbles which strike the HFA sensor directly produce large amplitude pulses, while in highly subcooled flows, small bubbles (some of which have a size close to that of the 25 μm diameter sensor) or ‘‘glancing’’ interactions of large bubbles produce smaller voltage signals. These smaller signals are more difficult to resolve due to the inherent noise of the data acquisition system.

The signal-to-noise ratio of the HFA output voltage was very high, and therefore, noise had no perceptible effect on the reported measurements. The spacing between HFA sensors for all probes ranged from 1.2 to 2.5 mm. The main sources of uncertainty considered in void fraction and droplet frequency measurements were repeatability based on pooled standard deviation, and the biases of threshold voltage, small droplets, position and sampling time, and droplet impaction. The uncertainty in void fraction was calculated to be ± 0.025. The uncertainty in frequency was somewhat higher with up to 25% for a mass flow rate of 106 kg/hr and 14% for 532 kg/hr. The sources of uncertainty considered for bubble velocity measurements were repeatability, and the biases of velocity sampling, bubble size, cross-correlation, sensor spacing, and position. This uncertainty was calculated to be 7%.

Flow Visualization. The transparent, conductive indium-tin-oxide coating on the quartz windows provides the distinct advantage of visualizing the high pressure boiling flow. Such high-speed flow visualization gives key information on the bubbly flow topology, bubble size, and shape. The high-speed video system was operated at 250 frames per second to obtain video images of the full duct. Backlighting was used with a strobe light source illuminating a white diffuser. With a 20-μsec strobe flash, the fluid motion could be frozen for most mass flux conditions. The high-speed video zoom optics produced images with approximately four times magnification. (See Fig. 1.)

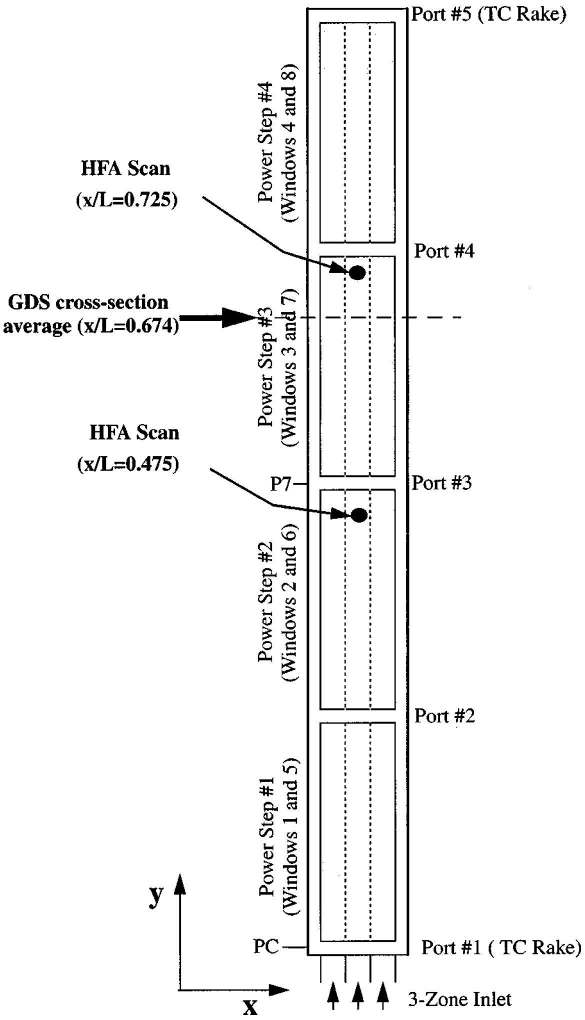

Fig. 1 Schematic of the front view of the test section. Thickness dimension is perpendicular to the paper.

Results and Discussion

The cross-section-averaged void fraction in the axial direction of the test section using a gamma densitometer, and the local void fraction using a hot film anemometer were obtained. The local measurements were used to obtain departure and bulk bubble size. The bubble size measurements have been used to improve the existing models. The test section conditions changed were the inlet subcooling, wall heat flux, and the system pressure so that the force models can be obtained in terms of nondimensional parameters such as Eotvos number.

At high pressures, it is observed that bubbly flow can persist up to high void fractions ($\overline{\alpha}\sim 0.6$). As shown in Fig. 2, for $\overline{\alpha}=0.5$, the bubble frequency is nearly the same for 53 kg/hr and 106 kg/hr at the two system pressures of 0.6 MPa and 1.4 MPa. However, when the pressure is increased to 2.4 MPa with the flow rate maintained constant at 106 kg/hr, the bubble frequency at the duct centerline is nearly 100% greater than that for the lower pressures of 0.6 MPa and 1.4 MPa. This indicates that the flow field is comprised of a greater number of smaller bubbles at higher pressures for roughly the same vapor volume fraction.

The corresponding videotape records of the flow field corroborate the presence of very small bubbles in SUVA at higher void fractions at high pressures. An example of bubbly flow in a thin narrow duct is given in Fig. 3 for $w=532$ kg/hr; $P=1.4$ MPa; $\alpha=0.25$ at a distance of 118 mm from the inlet. Various bubble sizes and shapes are seen to exist for this flow condition. A majority of the bubbles become slightly distorted long before they reach one-third the thickness of the duct (~0.7 mm). Thus, these bubbles continue to be three-dimensional, and tend to become oscillatory since they are distorted until they grow in size to be completely confined between the walls across the duct thickness. In this photograph, a few confined bubbles can be seen near the top right corner. Even though they are confined, they are considered to be bubbles until they reach a certain size proportional to the width of the test section, as discussed later. At a higher pressure of 2.4 MPa (not shown), the bubbly flow regime dominates almost the entire duct at much higher void fractions. This extension of the bubbly flow regime to higher void fractions as the pressure is increased has also been visualized in steam-water systems, [15], in the pressure range from 2.1–13.8 MPa.

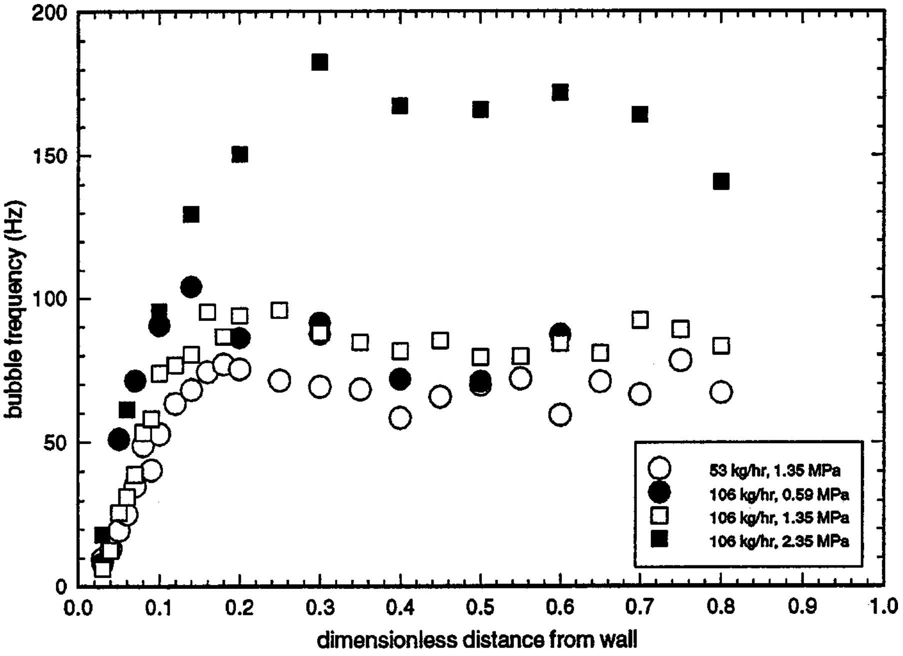

Fig. 2 Bubble frequency at $\alpha=0.5$ for different flow rates and pressure using the hot film anemometer

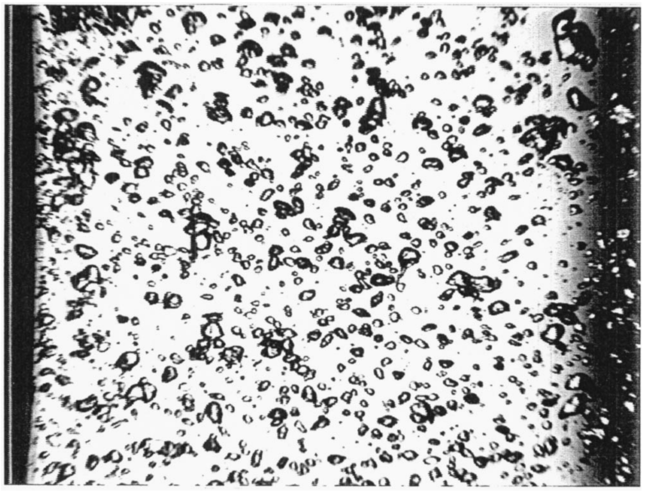

Fig. 3 Photograph of bubbly flow at $\alpha=0.25$; $w=532$ kg/hr; $P=1.4$ MPa. The snapshot captures the entire width of the test section.

Departure Bubble Size. The bubble size at the wall (departure size) is governed by thermal and hydrodynamic mechanisms. It is rather difficult to find a departure diameter model in the literature that would suit high pressure flows. Part of the problem is the bubble formation process itself, which is highly statistical even at the same location under the same conditions, [16–18]. Therefore, a departure bubble size correlation was developed from experimental observations using a relatively simple model derived by Levy, [19], model as the base or kernel. Levy's model was built on the premise that bubble departure is controlled in part by a competition between surface tension, which tends to hold the bubble to the nucleation site, and wall shear stress, which tends to pull the bubble off the nucleation site. When the pressure is increased, the saturation temperature increases, decreasing the surface tension. The decreased surface tension results in a smaller bubble departure diameter. Increasing the flow rate increases the wall shear stress, which similarly reduces the bubble departure diameter. Levy's model is given by

$$d_o=0.0315\left[\frac{\sigma d_H}{\tau_w}\right]^{1/2} \tag{2}$$

where τ_w is the wall shear stress.

Departure bubble size measurements were made in SUVA at 0.83 MPa using a long distance microscope and high-speed video recordings. Accurate measurement of the bubble diameter was affected by three factors: the point of bubble departure was difficult to identify; for very small bubbles (<0.05 mm), magnification was not sufficient to obtain clear images; strong temperature gradients and turbulent mixing led to refractive index variations in the flow which obscured the nucleation sites at large subcooling and high flow rates. In addition to the measurement uncertainty, the bubble departure diameter has considerable variation from site to site and from bubble to bubble at a single site. To account for this, several departure diameters at several nucleation sites were measured for each datapoint.

The departure diameter thus measured is plotted in Fig. 4 as a function of liquid subcooling. The bubble size measurements of Tolubinsky and Kostanchuk [20] in water at atmospheric pressure are also plotted in the same figure for comparison purposes. Both water and SUVA results show a similar trend in that the departure diameter decreases with subcooling. This behavior was incorporated into the Levy model by the following correlation:

$$d_B=\min\left\{\begin{array}{l} d_o e^{-\left(\frac{\Delta T_{\mathrm{sub}}}{45\Delta T_{\mathrm{sonb}}}\right)^{1/2}} \\ d_o \end{array}\right\} \tag{3}$$

where $\Delta T_{\mathrm{sub}}=T_{\mathrm{sat}}-T_1$, and ΔT_{sonb} is the nucleation inception wall superheat. The nucleation inception superheat is given by [21],

$$\Delta T_{\mathrm{sonb}}=\frac{180BH_{DB}}{k_f} \tag{4}$$

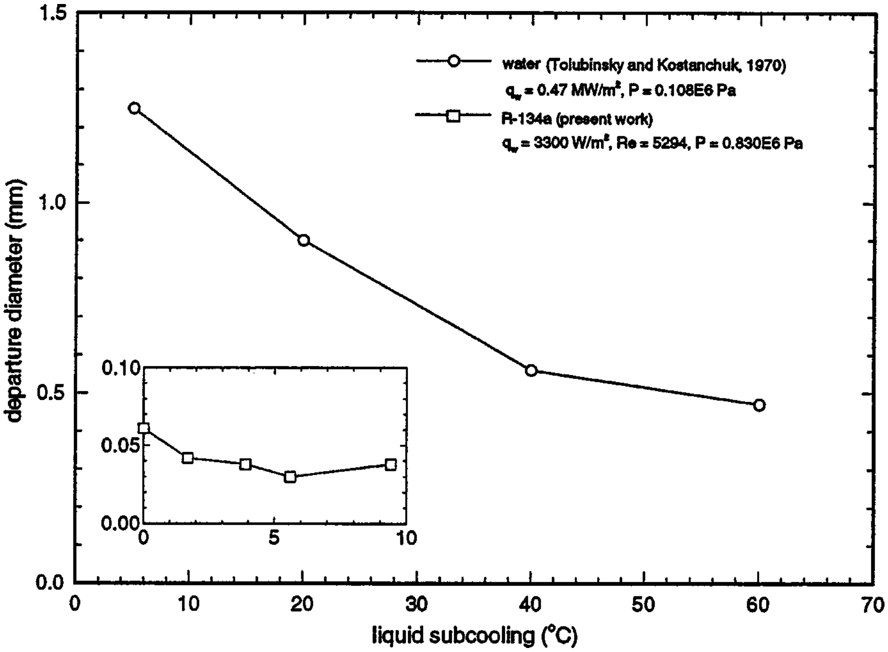

Fig. 4 Relationship between liquid subcooling and bubble departure diameter measured from photographs

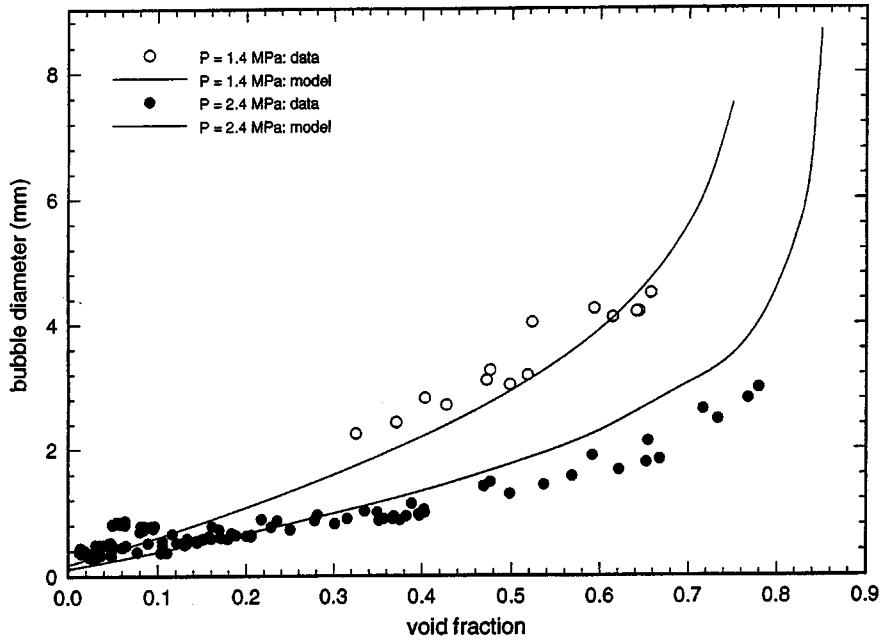

Fig. 5 Relationship between local void fraction and local bubble diameter measured using the hot film anemometer

$$B=\frac{2\sigma T_{\mathrm{sat}}\Delta\rho}{h_{fg}\rho_f\rho_g} \tag{5}$$

$$H_{DB}=0.023\frac{k_f}{d_H}\left[\frac{Gd_H}{\mu_f}\right]^{0.8}\left[\frac{c_{p_f}\mu_f}{k_f}\right]^{1/3} \tag{6}$$

Bulk Bubble Size. Centerline void fraction and bubble size were measured using the hot film probe and plotted in Fig. 5 for two pressures. As further evidence of the extension of the bubbly flow regime as discussed in the previous paragraph, at 2.4 MPa, the bubble diameters are significantly small even at high void fractions. The maximum bubble diameter measured at $\alpha=0.8$ is slightly larger than the thickness of the test section. As the pressure is decreased to 1.4 MPa, the bubble size spans the walls at a much lower void fraction of approximately 0.3. Beyond this void fraction, the bubbles become large enough to be constrained by the walls, but continue to be in the bubbly flow regime.

Similar to the approach used for the departure bubble size, a bulk bubble size model for high pressures was developed using Levy's, [19], d_o as the kernel. Thus the observed void fraction dependence of the bulk flow bubble size was combined with the Levy model by the following correlation:

$$d_B=d_o\left\{1+\frac{21.64\alpha}{(\alpha_o-\alpha)^{0.29}}\right\} \tag{7}$$

where α_o is a critical void fraction which is set at 0.8. This model is compared with data in Fig. 5. Equation (7) is valid up to an incipient slug size which is the minimum cylindrical planar cap bubble size for which the slug terminal rise velocity limit is reached. This size is characterized by a maximum dimension in the width direction that is equal to two-thirds of the duct width.

Bubble Rise Velocity and Drag. The bubble rise velocity measurements are required to develop the drag model for high-pressure boiling flows. These measurements using SUVA and nitrogen (to eliminate condensation effects) bubbles were made in a stagnant liquid using a needle valve of 0.4 mm ID (to generate small bubbles) and 1.6 mm ID (to generate large bubbles). Different size bubbles were generated by controlling the system pressure. The bubble frequency was controlled to less than 1 Hz to prevent the wake interactions between bubbles. Measurements of equivalent bubble size (from the bubble volume) and velocity were obtained directly from magnified (100×) video images, and validated using the hot-film anemometer measurements. Using the single bubble rise velocity measurements as the starting point, an expression for drag coefficient can be developed. The rise velocity is plotted against the spherical equivalent bubble diameter in Fig. 6 where distinct regimes are identified based on the bubble shape and rise behavior. The small bubbles nearly obey Stokes' law in the viscous regime so that the rise velocity can be expressed as

$$U_V=\frac{g\Delta\rho d_B^2}{K_b\mu_1} \tag{8}$$

where $K_b=18$ obtained as the coefficient for the terminal velocity for a sedimenting sphere in a quiescent fluid. In a multiple-bubble environment in a narrow geometry, K_b can be taken to be a bubble size-dependent parameter correlated as a function of Morton number and the diameter ratio to fit the data in the viscous regime.

$$K_b=K_M\left(\frac{d_B}{d_{oo}}\right)^{0.425} \qquad d_{oo}=2\left[\frac{\sigma}{\Delta\rho g}\right]^{1/2} \tag{9}$$

where d_{oo} is the diameter corresponding to the minimum rise velocity, and K_M is given by

$$K_M=60.0(1-e^{-5.32\times10^{10}\mathrm{Mo}_{mb}}) \tag{10}$$

$$\mathrm{Mo}_{mb}=\frac{\mathrm{Mo}}{(1-\alpha)^4}. \tag{11}$$

The value for K_M is provided for organics and is different for steam-water.

At slightly higher bubble diameters, the bubbles become oblate and the rise velocity decreases probably because the wake behind the bubble becomes turbulent. In this distorted-inertial regime, the rise velocity, U_{DI}, is given by, [22], as

$$U_{DI}=\left[g\frac{d_B}{2}\frac{\Delta\rho}{\rho_1}+\frac{2\sigma}{\rho_1 d_B}\right]^{1/2} \tag{12}$$

using the analogy that exists between the propagation velocity of surface waves and rise velocity of bubbles in infinite media. It is noted that Eq. (12) is a direct result of replacing the wavelength

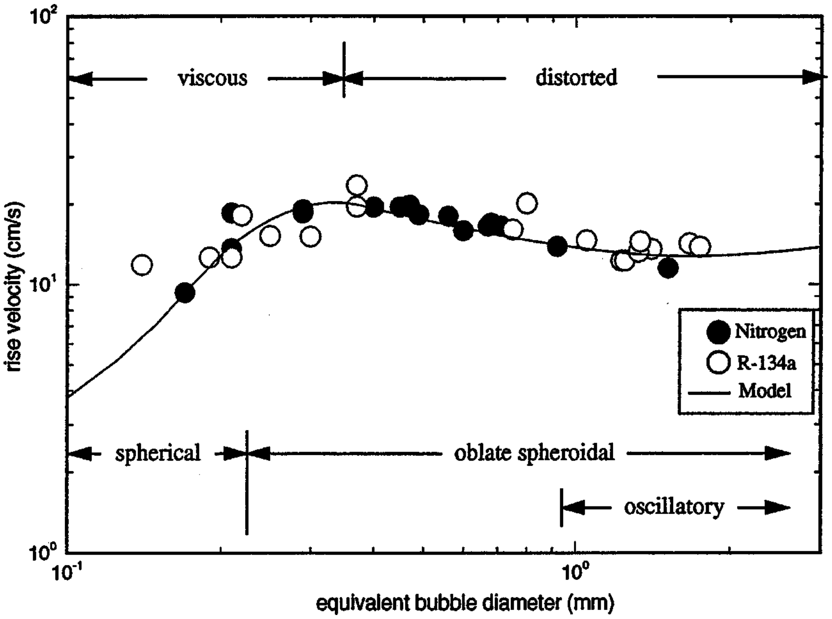

Fig. 6 Relationship between bubble diameter and rise velocity measured using the hot film anemometer and a high-speed video camera

with the bubble perimeter in the critical wave velocity expression obtained from the linear stability theory for large depth surface waves.

The single bubble rise model in infinite media formulated by Fan and Tsuchiya [23],

$$U_B=[U_V^{-\eta}+U_{DI}^{-\eta}]^{-1/\eta} \tag{13}$$

is used as the building block for the proposed model. In a multiple bubble system, the single bubble rise velocity becomes the local drift velocity, V_{gj}^B, where

$$V_{gj}^V=U_V(1-\alpha), \tag{14}$$

$$V_{gj}^{DI}=D_{DI}f_{DI}, \tag{15}$$

and

$$V_{gj}^B=\left\{V_{gj}^{V-\eta}+V_{gj}^{DI-\eta}\right\}^{-1/\eta}. \tag{16}$$

Here, f_{DI}, accounts for the multiple bubble effects in the distorted-inertial regime proposed by Ishii and Zuber [24], and is given by

$$f_{DI}=\frac{(1-\alpha)^{5/2}\left[1+\dfrac{0.46}{\mathrm{Mo}^{1/8}}\right]}{\left[1+\dfrac{0.46}{\mathrm{Mo}^{1/8}}(1-\alpha)^{9/7}\right]}. \tag{17}$$

The combination of Eqs. (14) through (16) yields for the local drift velocity,

$$V_{gj}^B=\{[U_V(1-\alpha)]^{-8}+[U_{DI}f_{DI}]^{-8}\}^{-1/8}, \tag{18}$$

where $\eta=8$ was found to give the best comparison with the experimental data *for bubbles of* different shape that were confined or unconfined. Figure 6 shows that the model is in good agreement with the experimental data.

The above model for V_{gj}^B is useful in developing the interfacial drag model. The drag coefficient for a single bubble may be obtained by equating the drag force for a single bubble to its buoyancy force,

$$C_D=\frac{4}{3}\frac{d_B}{(U_B)^2}\frac{\Delta\rho}{\rho_1}g, \tag{19}$$

where U_B is the rise velocity of a single bubble in a quiescent fluid. In a multiple bubble system, the single bubble rise velocity becomes augmented through interactions with surrounding bubbles so that $U_B\rightarrow V_{gj}^B$, and

$$C_D=\frac{4}{3}\frac{d_B}{V_{gj}^{B^2}}\frac{\Delta\rho}{\rho_1}g. \tag{20}$$

Equation (20) is the expression for the single bubble drag coefficient modified for multiple bubble effects.

Now the drag force per unit volume in a two-phase bubbly flow can be expressed in terms of the multiple bubble-augmented single bubble drag coefficient by

$$F_D=C_D N A_P \rho_l \frac{V_{gj}^2}{2} \tag{21}$$

where V_{gj} is the drift velocity in the multiple bubble system, A_P is the projected area of the single bubble, and N is the bubble number density given by

$$N=\frac{\alpha}{V_B}. \tag{22}$$

Here, V_B is the single bubble volume. Furthermore, the relationship between the relative velocity, V_R and V_{gj} is given by

$$V_{gj}=(1-\alpha)V_R. \tag{23}$$

The substitution of Eqs. (20), (22), and (23) into Eq. (21) yields

$$F_D=\frac{2}{3}d_B\frac{A_P}{V_B}\frac{(1-\alpha)^2}{V_{gj}^{B^2}}\alpha\Delta\rho g V_R^2. \tag{24}$$

For a spherical equivalent bubble,

$$\frac{A_P}{V_B}=\frac{3}{2}\frac{1}{d_B}. \tag{25}$$

Now Eq. (25) becomes

$$F_D=\frac{(1-\alpha)^2}{V_{gj}^{B^2}}\alpha\Delta\rho g V_R^2 \tag{26}$$

Table 1 Experimental flow conditions

Case No.	System Pressure MPa	Flow Rate kg/hr	Net Input Power to the Windows, kW	Inlet Subcooling °C	Exit Quality	Density Ratio ρ_l/ρ_g
1	0.9	283	5.63	36.7	0.13	27.4
2	0.9	283	6.60	36.7	0.19	27.4
3	2.4	53	1.70	29.3	0.39	7.3
4*	1.4	106	1.08	22.0	0.00	16.2

*Only the third window is heated.

The drag force in Eq. (26) can now be expressed in terms of a multiple bubble drag coefficient as

$$F_D = C_{D_{mb}} \rho_l (NA_P) \frac{V_R^2}{2} \tag{27}$$

where

$$C_{D_{mb}} = \frac{4}{3} d_B \frac{(1-\alpha)^2}{V_{gj}^{B^2}} \frac{\Delta\rho}{\rho_l} g, \tag{28}$$

and where (NA_P) is the total projected area of the vapor field.

The drag in Eq. (26) is explicitly independent of the bubble diameter, however, V_{gj}^B, as given by Eqs. (8) through (18) is dependent on the diameter. This expression can be used in the local application of drag force in a multidimensional code.

Vapor Lift. A nondrag force which is significant in bubbly flows is the lift force which appears as a source term in the momentum equation. For laminar shear flows, the lateral lift force is proportional to the vorticity of the liquid phase and the relative velocity. This force captures the influence of the liquid velocity gradient on the bubbles, thereby impacting the transverse distribution of the void fraction. Potential flow theory is used to construct the inviscid flow field around the sphere and the lift force is calculated by integrating the interfacial pressure over the sphere's surface, [25,26],

$$F_L = C_L \rho_l \alpha \;\; v_R \times (\nabla \times v_R). \tag{29}$$

The lift coefficient, C_L, for a single bubble is 0.5 for inviscid flows, but may be very low for highly viscous flows, [27]. In order to determine the lift coefficient, several flow conditions were run at different inlet subcooling, flow rates and system pressure, and the local void fraction profiles were examined. The representative runs are provided in Table 1.

The local distributions of void fraction allow us to identify the flow regime transitions, and are very useful for developing a correlation for the lift coefficient. In Figs. 7–10, the local void profiles from the hot film data are plotted for Cases 1–4 (see Table 1), and the cross-section averaged axial profiles from the gamma densitometer data are provided in the inset. Wherever available, the line-averaged gamma densitometer measurements are also provided. Experimental conditions were chosen such that in Cases 1, 2, and 3 the net vapor generation occurred slightly before the nondimensional axial distance of 0.475 where the hot-film wire was located. Cases 1 and 2 were run at the same flow conditions except with slightly different wall heat. In Fig. 7, at $x/L = 0.475$, a wall-peaked profile can be seen in the low-void bubbly regime as observed by other investigators, [1,2]. This is due to the transverse lift force which drives the small, spherical bubbles toward the walls. When these small bubbles grow in size, they become nonspherical, distorted, and oscillatory, the lift force changes direction and the bubbles move away from the wall. This allows the vapor to concentrate at the center, giving rise to a center-peaked profile, as seen in the figure at $x/L = 0.725$. The effect of increasing the wall heat flux is, as expected, to increase the magnitude of the local void distribution at both streamwise locations (Fig. 8). The shapes of the local void fraction profiles remain similar. In Figs. 7 and 8 (Cases 1 and 2), the line-averaged GDS measurements made at $x/L = 0.674$ are plotted to compare with the HFA measurements. Since the GDS averages the data along a line from edge to edge, it includes the liquid collected near the edges due to the cornering effect. Therefore, these void fraction data are slightly lower than the local measurements made using the HFA. Since the two instruments are located in slightly different axial locations, exact comparisons cannot be made.

The void profiles in Figs. 9 and 10 provide additional evidence of the change in the lift force direction at different pressures. At high pressures, the bubbles produced by wall heating are small and higher in number density, and bubbly flow can persist for void fractions up to and sometimes beyond 0.6. Even so, at higher pressures and lower flow rates, the bubbles ultimately become distorted and oscillatory with additional wall heating downstream, and move away from the wall.

The bubble diameter at which the bubble ceases to be spherical is proportional to $\sqrt{\sigma/(\Delta\rho g)}$. This can also be recast in terms of

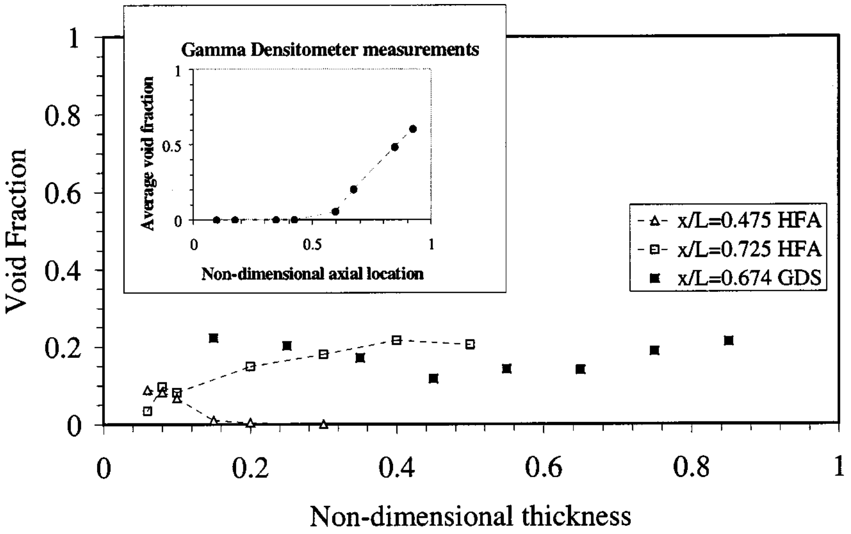

Fig. 7 Local void fraction distribution using the hot film anemometer at two axial locations compared with line-averaged void fraction from the gamma densitometer for Case 1 in Table 1. Cross-section averages from the GDS are provided in the inset.

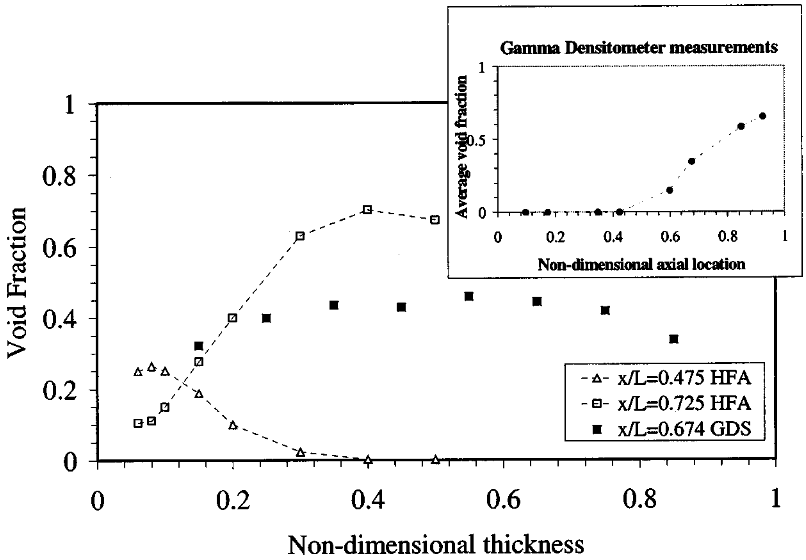

Fig. 8 Local void fraction distribution using the hot film anemometer at two axial locations compared with line-averaged void fraction from the gamma densitometer for Case 2 in Table 1. Cross-section averages from the GDS are provided in the inset.

the parameter, Eotvos number, Eo, defined as $\mathrm{Eo}=g\Delta\rho\overline{d_B^2}/\sigma$. The intrinsic fluctuating bubble motion can be described in terms of Eo [28,29], and the magnitude of the fluctuation increases with Eo. Tomiyama [29] suggests that the function form of the lift given in Eq. (29) is the same for shear-induced lift in small Eo and lift induced by the vortex motion behind the deformed bubble in large Eo. It is also interesting to note that in the formulation of bubbly drag in Eq. (12), the expression for the rise velocity in the distorted inertial regime may be written in terms of Eo. Thus, Eo plays a dominant role in the development of both bubbly lift and drag.

For the current flow situation, the constant of proportionality can be determined by examining the void distributions for multiple flow conditions, and measured spherical-equivalent bubble diameters. This result has been used in conjunction with observations reported in the literature, [28–30], to develop the following lift coefficient which changes signs at a critical bubble diameter.

$$C_L=\begin{array}{ll} 0.1 & \mathrm{Eo}<3 \\ 0.33[1-0.41\sqrt{\mathrm{Eo}}] & 3\leq \mathrm{Eo}\leq 9, \\ -0.075 & \mathrm{Eo}>9 \end{array} \tag{30}$$

where Eo is expressed in terms of $\overline{d_B}$, given by

$$\overline{d_B}=\frac{\int_y \alpha d_B dy}{\int_y \alpha dy}.$$

The three separate regimes that were delineated in terms of Eo in Eq. (30) are very similar to those of [29] in a circular tube, although different functions of Eo was used for the air-water flow in

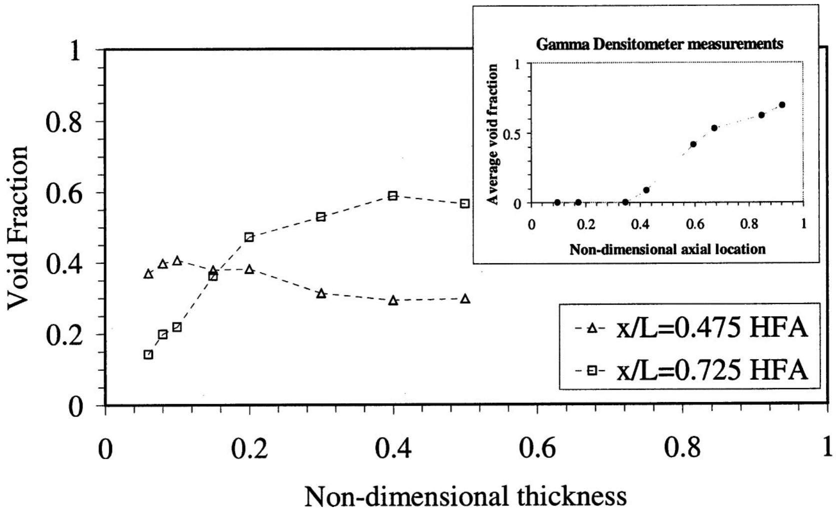

Fig. 9 Local void fraction distribution using the hot film anemometer at two axial locations for Case 3 in Table 1. Cross-section averages from the GDS are provided in the inset.

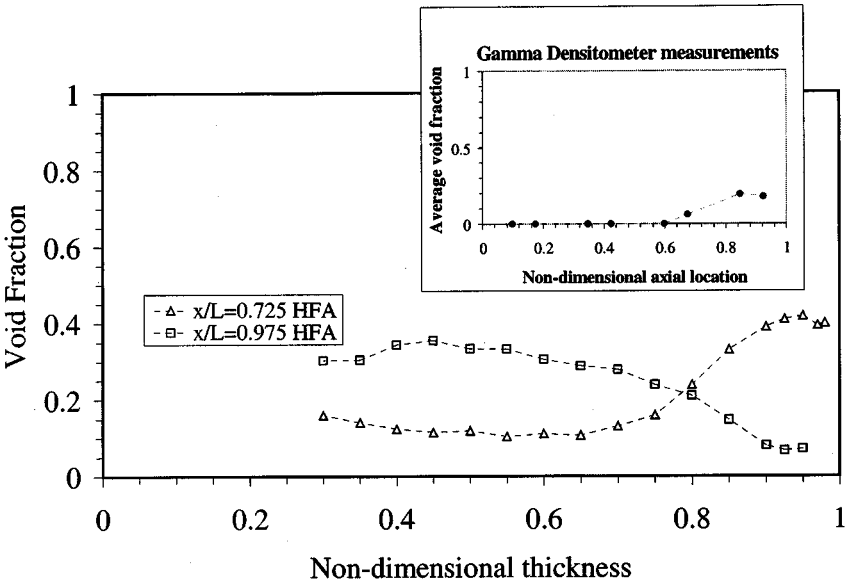

Fig. 10 Local void fraction distribution using the hot film anemometer at two axial locations for Case 4 in Table 1. Cross-section averages from the GDS are provided in the inset.

the circular tube. Note that the lift coefficient used here in R-134a for small bubbles is 0.1, much smaller than the value of 0.3 generally used in air-water systems.

Summary and Conclusions

Detailed measurements of void fraction and bubble size were made in an upward bubbly flow to support model development. A number of cases were run at various heat fluxes, flow rates, inlet subcooling, system pressure in a narrow (very small t/W ratio) duct using a refrigerant (R-134a) as a modeling fluid. The measurements included cross-section-averaged void fraction along the duct using a gamma densitometer; local void fraction and bubble size measurements using a hot film anemometer, and bubble rise velocity using a high-speed camera.

New bubble size correlations for both departure size and bulk size have been proposed with Levy's, [16], model as the base. Separating the bubbly regime into the viscous and the inertial-distorted subregimes, and using Fan-Tsuchiya's, [23], rise velocity in an infinite medium as the building block, a new rise velocity model is proposed. This has been subsequently used to develop a drag model in high pressure flows.

The void profiles in the thickness dimension for many flow conditions (four subcooled inlet conditions are represented in this paper) reveal the presence of both wall peaking and center peaking depending on the bubble size, consistent with the observations in air-water systems in the literature. Such a change in direction in the void gradient near the wall is reflected in the lift coefficient which is developed in terms of the parameter, Eotvos number. This parameter also plays a role in the development of bubbly drag. It seems reasonable to classify the bubbles of different shapes in different groups based on their Eotvos number.

Acknowledgments

We gratefully acknowledge D. M. Considine and K. H. Keller for their experimental support.

Nomenclature

A_P = projected area of a single bubble, m^2
C_D = drag coefficient
d_B = bubble diameter, μm
d_o = bubble diameter corresponding to Levy's model (Eq. (2)), μm
d_{oo} = bubble diameter corresponding to minimum rise velocity, μm
d_H = hydraulic diameter, mm
f_B = bubble frequency, 1/s
F_D = drag force per unit volume, N/m^3
G = mass flux, kg/m^{2}s
L = length of the duct, m
Mo = Morton number, $\mathrm{Mo}=g\mu_1^4\Delta\rho/\rho_1\sigma^3$
N = bubble number density, 1/m^3
P = pressure, MPa
t = thickness of the duct, mm
U_B = single bubble rise velocity, m/s
U_V = rise velocity in the viscous subregime
U_{DI} = rise velocity in the distorted-inertial subregime
V_B = bubble volume, m^3
V_{gj}^B = drift velocity for a single bubble, m/s
V_{gj} = drift velocity in a multiple-bubble system, m/s
V_R = relative velocity, m/s
w = mass flow rate, kg/hr
W = width of the duct, mm
X = flow direction
Y = thickness direction
Z = width direction
α = volume fraction
$\overline{\alpha}$ = line-averaged volume fraction
ρ = density, kg/m^3
$\Delta\rho$ = change in density from liquid to vapor phase, kg/m^3
ΔT_{sub} = $T_{\mathrm{sat}}-T_l$, °C
ΔT_{sonb} = nucleation inception wall superheat (Eq. (4)), °C
μ = dynamic viscosity, kg/m/s
σ = surface tension, N/m
τ_w = wall shear stress, MPa

Subscripts

f = saturation liquid
g = vapor phase
l = liquid phase
sat = saturation

References

[1] Serizawa, A., Kataoka, I., and Michiyoshi, I., 1975, ''Turbulence Structure of Air-Water Bubbly Flow,'' Int. J. Multiphase Flow, **2**, pp. 221–246.

[2] Liu, T. J., and Bankoff, S. G., 1990, ''Structure of Air-Water Bubbly Flow in a Vertical Pipe: I—Liquid Mean Velocity and Turbulence Measurements,'' ASME, New York, Vol. FED-99/HTD-155, pp. 9–17.

[3] Liu, T. J., 1993, ''Bubble Size and Entrance Length Effects on Void Development in a Vertical Channel,'' Int. J. Multiphase Flow, **19**(1), pp. 99–113.

[4] Dix, G. E., 1971, ''Vapor Void Fractions for Forced Convection with Subcooled Boiling at Low Flow Rates,'' Ph.D. thesis, University of California, Berkeley, CA.

[5] Shiralkar, B. S., and Lahey, R. T., Jr., 1972, ''Diabatic Local Void Fraction Measurements in Freon-114 With a Hot-Wire Anemometer,'' ANS Trans., **15**, p. 880.

[6] Delhaye, J. M., Semeria, R., and Flamand, J. C., 1973, ''Void Fraction, Vapor and Liquid Temperatures: Local Measurements in a Two-Phase Flow Using a Microthermocouple,'' ASME J. Heat Transfer, **95**, pp. 363–370.

[7] Jones, O. C., and Zuber, N., 1978, ''Use of a Cylindrical Hot-Film Anemometer for Measurement of Two-Phase Void and Volume Flux Profiles in a Narrow Rectangular Channel. Heat Transfer: Research and Application,'' AIChE Symp. Ser. **74(174)**, pp. 191–204.

[8] Hasan, A., Roy, R. P., and Kalra, S. P., 1991, ''Some Measurements in Subcooled Flow Boiling of Refrigerant-113,'' ASME J. Heat Transfer, **113**, pp. 216–223.

[9] Martin, R., 1972, ''Measurement of the Local Void Fraction at High Pressure in a Heating Channel,'' Nucl. Sci. Eng., **48**, pp. 125–138.

[10] Kirouac, G. J., Trabold, T. A., Vassallo, P. F., Moore, W. E., and Kumar, R., 1999, ''Instrumentation Development in Two-Phase Flow,'' Exp. Therm. Sci., **20**, pp. 79–93.

[11] Trabold, T. A., Kumar, R., and Vassallo, P. F., 1999, ''Experimental Study of Dispersed Droplets in High-Pressure Annular Flow,'' ASME J. Heat Transfer, **121**, pp. 924–933.

[12] Trabold, T. A., and Kumar, R., 2000, ''Vapor Core Turbulence in Annular Two-Phase Flow,'' Exp. Fluids, **28**, pp. 187–194.

[13] Trabold, T. A., and Kumar, R., 2000, ''High Pressure Annular Two-Phase Flow in a Narrow Duct. Part I: Local Measurements in the Droplet Field,'' ASME J. Fluids Eng., **122**, pp. 364–374.

[14] de Carvalho, R., and Bergles, A. E., 1992, ''The Pool Boiling and Critical Heat Flux of Vertically Oriented, Small Heaters Boiling on One Side,'' Rensselaer Polytechnic Institute, Heat Transfer Laboratory Report HTL-12.

[15] Hosler, E. R., 1968, ''Flow Patterns in High Pressure Two-Phase (Steam-Water) Flow With Heat Addition,'' AIChE Symp. Ser., **64**, pp. 54–66.

[16] Abdelmessih, A. H., Hooper, F. C., and Nangia, S., 1972, ''Flow Effects on Bubble Growth and Collapse in Surface Boiling,'' Int. J. Heat Mass Transf., **15**, pp. 115–125.

[17] Mayinger, F., and Bucher, B., 1976, *Proc. NATO Advanced Study Inst. on Two-Phase Flow and Heat Transfer*, Instanbul, August.

[18] Gunther, F. C., 1951, ''Photographic Study of Surface-Boiling Heat Transfer to Water With Forced Convection,'' Trans. ASME, **73**, pp. 115–123.

[19] Levy, S., 1967, ''Forced Convection Subcooled Boiling—Prediction of Vapor Volumetric Fractions,'' Int. J. Heat Mass Transf., **10**, pp. 951–965.

[20] Tolubinsky, V. I., and Kostanchuk, D. M., 1970, ''Vapor Bubbles Growth Rate and Heat Transfer Intensity at Subcooled Water Boiling,'' *Fourth Int. Heat Trans. Conf.*, Paris, Versailles, **5**, p. 132.8.

[21] Davis and Anderson, 1966, AIChE J., **12**, 774–780.

[22] Mendelson, H. D., 1967, ''The Prediction of Bubble Terminal Velocities From Wave Theory,'' AIChE J., **13**, pp. 250–253.

[23] Fan, L. S., and Tsuchiya, K., 1990, *Bubble Wake Dynamics in Liquids and Liquid-Solid Suspensions*, Butterworth-Heinemann, Stoneham, MA.

[24] Ishii, M., and Zuber, N., 1979, ''Drag Coefficient and Relative Velocity in Bubbly, Droplet or Particulate flows,'' AIChE J., **25**, pp. 843–855.

[25] Saffman, P. G., 1965, ''The Lift on a Small Sphere in a Slow Shear Flow,'' J. Fluid Mech., **22**, pp. 385–400.

[26] Drew, D. A., and Lahey, R. T., 1987, ''The Virtual Mass and Lift Force on a Sphere in Rotating and Straining Inviscid Flow,'' Int. J. Multiphase Flow, **13**(1), pp. 113–121.

[27] Eichhorn, R., and Small, S., 1964, ''Experiments on the Lift and Drag of Spheres Suspended in a Poiseuille Flow,'' J. Fluid Mech., **20**(3), p. 513.

[28] Zun, I., 1987, ''Transition From Wall Void Peaking to Core Void Peaking in Turbulent Bubbly Flow,'' *Proc. of ICHMT Conference on Transport Phenomena in Multiphase Flow*, Dubrovnik, Yugoslavia.

[29] Tomiyama, A., 1998, ''Struggle With Computational Bubble Dynamics,'' *Proc of the Int. Conf. on Multiphase Flow*, ICMF'98, Lyon, June 8–12, pp. 1–18.

[30] Kariyasaki, A., 1987, ''Behavior of a Single Gas Bubble in a Liquid Flow With a Linear Velocity Profile,'' *Proc. ASME-JSME Thermal Engineering Joint Conference,* **5**, ASME New York, pp. 261–267.

Measurement of Void Fraction in Magnetic Fluid Using Electromagnetic Induction

S. Shuchi[1]
e-mail: shuchi@akita-pu.ac.jp

H. Yamaguchi

M. Takemura

Department of Mechanical Engineering,
Doshisha University,
Kyoto 610-0321, Japan

A new technique of measuring void fraction in magnetic fluid using electromagnetic induction was proposed. In order to establish the measuring method, a feasibility study was conducted experimentally with an aid of numerical analysis. From the results of static experiment and numerical analysis, it was obtained that there exists a linear relationship between the void fraction and the measured electromotive force, when induction coils were connected in series for Helmholtz excitation coils, regardless of distribution of air bubbles in magnetic fluid. By applying the calibrated linear relationship to actual two-phase situations, it was revealed that the proposed method yielded quite reasonable account for measuring the void fraction, showing excellent agreement with the mechanical measured data in the two-phase flow apparatus, and with the published correlation of the drift flux model. From the results of the present investigation, it was proved that the proposed technique is feasible for the actual measurement of void fraction in two-phase flow of magnetic fluid. [DOI: 10.1115/1.1566049]

1 Introduction

Magnetic fluid behaves as an electrically nonconducting homogeneous media in which single-domain magnetic particles are stabilized even in strong magnetic fields. Since magnetic fluids have magnetic properties along with fluidity, many applications have been proposed such as magnetic seals, dampers, bearings, and so on. Among many promising technological applications, energy conversion devices are another potential area of utility of magnetic fluids. In these devices an attempt [1], was made to utilize the magnetic body force to circulate magnetic fluid with injecting air bubbles or with allowing magnetic fluid itself to boil. To develop or to realize such devices the precise measurement of void fraction in two-phase state of magnetic fluid is necessary. Also it should be noted that the work for the measurement of void fraction in a two-phase state of magnetic fluid would give useful information for those studying the dynamics of magnetic fluid foams [2].

In ordinary two-phase flows there are some measuring techniques for void fraction such as the electrical conductance method [3], with which the void fraction can be obtained by measuring direct electric current through two-phase flow. Similarly by the needle contact method [3–5], void fraction can be obtained by measuring electric current through metal wire, which is inserted in two-phase flow. Among mechanical techniques the valve shutdown method [3], in which a section of flow passage is instantly isolated by closing valves, is often used to measure a void fraction average.

However, for two-phase flow of magnetic fluid, there is a report among very few studies in the literature, i.e., the measurement of void fraction by the ultrasonic echo method [6], which visualizes two-phase flow of magnetic fluid. This measurement method involves heavy-duty equipments with highly sophisticated data acquisition system and is often very limited in a local area of measuring space in two-phase flow. Also this method is strictly limited in dispersed bubble flow regime. Since magnetic fluid is not electrically conductive, the electric current measuring techniques might not be used in general. Furthermore, the magnetic fluid is not transparent, which prevents visualization of two-phase flow. Due to the nature of magnetic fluid, therefore, not being precise and easy measuring techniques for measuring void fraction has not yet been reported in the literature.

In the present study, a focus was given to the magnetization characteristic of magnetic fluid with air bubbles (air void) under the magnetic field, and a new measurement technique is proposed for measuring the void fraction in two-phase flow of magnetic fluid, using the electromagnetic induction. The chief purpose of this work is to establish the measuring method and is to discuss the feasibility of the measurement.

2 Basic Principle and Numerical Prediction

When a container, where magnetic fluid is partially filled, is placed between two excitation coils, as schematically shown in Fig. 1, the magnetic flux density **B** through the induction coils can be expressed by the following formula:

$$\mathbf{B}=\mu_0\{\mathbf{H}+(1-\alpha)\mathbf{M}\} \tag{1}$$

where μ_0 is the permeability of vacuum, **H** is magnetic field, **M** is magnetization of magnetic fluid, and α is void fraction average (the volume rate of gaseous phase in the container). It is noted that the magnetic susceptibility of the gaseous phase (air for example) is in the order of 10^{-7} [7], and can be neglected in Eq. (1). If alternating electric current is applied to the excitation coils, which are situated co-axially along the induction coils, as shown in Fig. 1, the electromotive force is generated in the induction coils (whose winding turn is n) as follows:

$$n\frac{\partial}{\partial t}\int\int_s \mathbf{B}\cdot d\mathbf{S}=-nV \tag{2}$$

where V is the electromotive force for one turn of the induction coils. It is noted further that the magnetic fluid is assumed nonelectrically conductive. Therefore, from Eq. (1) and Eq. (2), the following formula is obtained:

$$n\frac{\partial}{\partial t}\int\int_s [\mu_0\{\mathbf{H}+(1-\alpha)\mathbf{M}\}]\cdot d\mathbf{S}=-nV. \tag{3}$$

According to Eq. (3), for a given volume of magnetic fluid with **M** (at a constant temperature), and by giving **H** from the outside excitation coils, the void fraction average can be principally obtained by measuring output voltage from the induction coils. In

---

[1] To whom correspondence should be addressed.

Contributed by the Fluids Engineering Division for publication in the JOURNAL OF FLUIDS ENGINEERING. Manuscript received by the Fluids Engineering Division January 31, 2001; revised manuscript received October 30, 2002. Editor: S. Ceccio.

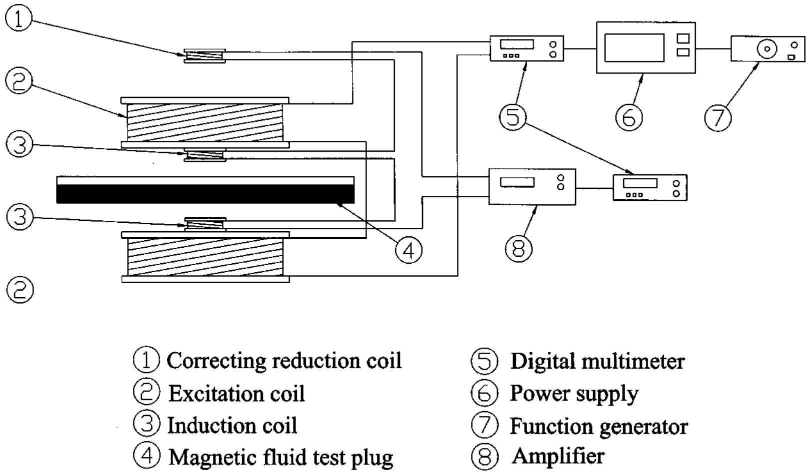

Fig. 1 Schematic diagram of measuring principle and static experimental arrangement

the present study, the excitation coils and induction coils are coaxially aligned and with which symmetric and even magnetic field distribution is generated. It is assumed that there is no magnetizable materials except for the magnetic fluid in the space affected by the magnetic field and no tangential components to the plane defined by either of the induction coils in the space between the induction coils. Thus, from the Gauss' low, the magnetic flux density becomes unique in the space between induction coils as well as in the test plug. Moreover, since the induction current in the induction coil is small (in the order of 10^{-9} A) and the magnetic fluid is nonconductive, the mutual effect of magnetic field intensity by the excitation coils and induction coils is minimal.

In addition, in this work, in order to calculate the amount of relative increase ΔV of the electromotive force which is derived from the magnetization of magnetic fluid by applying magnetic field. ΔV is defined by the following formula:

$$\Delta V = V_\alpha - V_{(\alpha=1.0)} \tag{4}$$

where V_α is the electromotive force at each void fraction, and $V_{(\alpha=1.0)}$ is the electromotive force at $\alpha=1.0$ (without magnetic fluid).

In order to verify the basic measurement principle, a numerical analysis was firstly conducted for (*a*) the situation of the stratified state and (*b*) the bubbly state of two-phase magnetic fluid, as shown in Fig. 2. Particularly, in the present study, the equivalency of measurement for void fraction average α was examined for two-phase modes, typically for (*a*) and (*b*), under the serial arrangement of excitation coils and induction coils, as shown in Fig. 2. In the present study, it should be noted that the numerical analysis was conducted for the two-dimensional situation so as to verify the measuring principle qualitatively for the test arrangement and to obtain the trend of α-ΔV relationship, whereas in the experiment the two-phase state in the test plug is strictly three-dimensional.

In the numerical analysis the following Maxwell equations are solved with Eq. (1).

$$\nabla \cdot \mathbf{B} = 0 \tag{5}$$

$$\nabla \times \mathbf{H} = 0, \quad \mathbf{H} = -\nabla \Psi \tag{6}$$

$$\mathbf{M} = \chi_m \mathbf{H} \tag{7}$$

where χ_m is the magnetic susceptibility and Ψ is the static magnetic potential. The model magnetic fluid is water-based magnetic fluid, from all physical parameters are determined, as shown in Table 1. As the magnetic fluid is linear magnetic material ($\mathbf{M} \| \mathbf{H}$) for very weak magnetic field $|\mathbf{H}|$, χ_m can be treated as constant. Considering Eqs. (1), (5)–(7), the following equation (Laplace equation for the magnetic field potential) is formulated:

$$\frac{\partial \chi}{\partial x} \cdot \frac{\partial \Psi}{\partial x} + (1+\chi_m) \frac{\partial^2 \Psi}{\partial x^2} + \frac{\partial \chi}{\partial y} \cdot \frac{\partial \Psi}{\partial y} + (1+\chi_m) \frac{\partial^2 \Psi}{\partial y^2} = 0. \tag{8}$$

By solving Eq. (8), Ψ is obtained for given cases (*a*) and (*b*). The relationship between α and ΔV can be calculated from Eq. (3) and Eq. (4). The numerical calculation was performed with the finite difference method, using the successive over relaxation (S.O.R) technique. Representative results obtained from the numerical analysis are depicted in Fig. 3, where vector plots of magnetic flux density $\mathbf{B}$ are shown. In both cases the condition of calculation was $\alpha=0.15$ and the excitation frequency was kept constant as $f=100$ Hz, where the applied current to the excitation coils was 0.75 A. As seen in Fig. 3, there observed some deviation of mag-

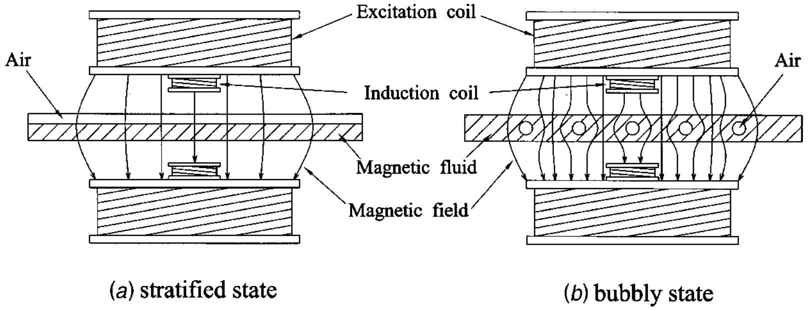

(*a*) stratified state

(*b*) bubbly state

Fig. 2 Distribution pattern of void fraction for numerical analysis

Table 1 Properties of magnetic fluids (at 305K)

Density (10^3 kg/m^3)	1.370
Viscosity (10^{-3} Pa·s)	8.920
Saturation magnetization (10^4 A/m)	3.020
Magnetic susceptibility	22.80
Surface tension (N/m)	0.028

netic flux density adjacent to void area in (*b*), while vertical magnetic flux density persisted in whole space in the case of (*a*). The fact indicates that the configuration of induction coils, i.e., the size of open area and the position of the coils, is an important factor to consider the equivalency of measurements for case (*a*) and (*b*). Namely it was thought that as represented in Fig. 2(*b*) and Fig. 3(*b*), when the void is distributed as bubbles, a fairly large open area of the induction coils with sufficient distance from void positions (the locations of bubbles) is necessary to sense the uniform magnetic flux density. Regarding the requirements of the measuring α, i.e., an appropriate configuration of the induction coils as shown Fig. 3, a representative result of the calibration line (α versus ΔV) is depicted in Fig. 4 resultantly, where the cases of stratified state (*a*) and bubbly state (*b*) were compared. As seen in Fig. 4, the equivalency of measurement, i.e., the independency of two-phase states (*a*) and (*b*) for measuring void fraction average, is obtained. It is mentioned here that the center of the induction coil (the diameter is 20 mm) is 22.5 mm apart from the magnetic fluid test plug (center to center distance). The configuration of induction coils in the numerical analysis was set as the same as the static experimental arrangement (as shown in Fig. 1), which is described in detail in the next section.

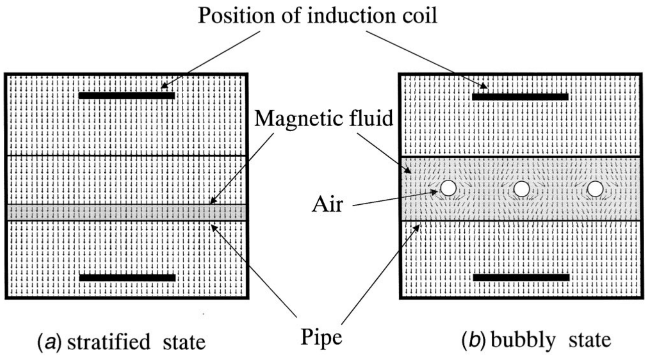

(*a*) stratified state (*b*) bubbly state

Fig. 3 Vector lines of magnetic flux density

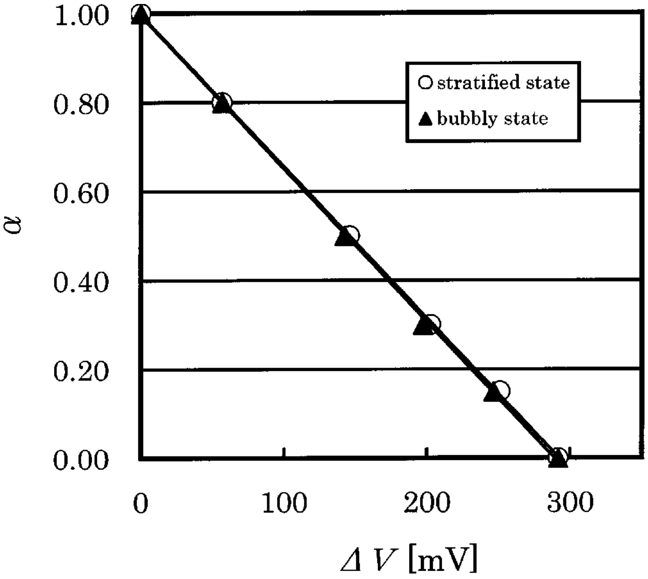

Fig. 4 Calculated results from numerical analysis, α versus ΔV

3 Experimental Arrangements and Results

Based on the measurement principle described in the previous section, experiments were conducted for the static state of two-phase magnetic fluid. The data obtained in the static experiment were then used as a master calibration line for actual flow experiments, where the void fraction measured by means of this electromagnetic induction method is compared with the data obtained by the mechanical valve shutdown method.

3.1 Static Experiment and Results. In Fig. 5(*a*), detailed arrangements of the coils are shown. And the magnetic fluid test plug is depicted schematically in Fig. 5(*b*). In experiment, the test plug was placed in between the induction coils, as shown in Fig. 1 previously. A pair of Helmholtz excitation coils are connected in series, as shown in Fig. 5(*a*) and Fig. 1. In order to excite the coils, a function generator⑦ is connected through a power supply unit⑥ and a digital multimeter⑤ as shown in Fig. 1, and the steady sinusoidal alternative current is applied to the excitation coils. Referring to the numerical results in the previous section, two induction coils (as shown in Fig. 5(*a*)), whose diameters are 20 mm, are connected in series. Therefore, with the configuration arrangement of the induction coils and the excitation coils, linear relationship between output induction voltage and void fraction is possible. The output induction voltage from the induction coils was amplified by ⑧ and displayed on ⑤. And the data were sent to a PC for data acquisition. It is noted that a correcting reduction coil as indicated in Fig. 1 and Fig. 5(*a*) is connected to the induction coil in order to reduce excess induction voltage generated in the induction coils, to keep the voltage less than 8V (the limitation is from the amplifier ⑧). As shown in Fig. 5(*b*) the magnetic fluid test plug, where magnetic fluid is partially filled in, is a cylindrical container whose diameter and length are 12 mm and 300 mm, respectively, which is made of acrylic resin (nonmagnetization material) for visual observation. Fifteen test plugs were prepared with different void fraction from $\alpha = 1.00$ to $\alpha = 0.00$ in the present investigation. Each test plug is placed between the induction coils in the horizontal position statically. Prior to the static experiment, magnetic flux density **B** was measured in the space between the excitation coils without test plug. The magnetic flux density along the X and Z directions indicated in Fig. 5(*a*) are displayed in Fig. 6(*a*) and (*b*), respectively, for a representative input condition of the excitation coils as $I = 0.75$ A and $f = 100$ Hz. It is seen from Fig. 6(*a*) and (*b*) that the magnetic flux density is quite evenly distributed in both the X-direction and Z-direction. The uncertainty associated with measurement of induction voltage is approximately maximum ±0.5%, which was chiefly derived from readings of instrumentation accuracy. And with the initial setting of the void fraction for each test plug, the uncertainty is estimated approximately maximum ±3%, which was mainly derived from the measurement of the weight of the plug including the fluid and air. The void fraction in the plug was determined by measuring magnetic fluid density at the given temperature, 22°C. It is noted that all experiments, including to flow experiment in the next section, were performed at a temperature-controlled room at 22°C±1.

Figure 7 is the final result obtained from the static experiment; the void fraction average α is plotted against the output voltage ΔV from the induction coils. Good linearity was obtained as seen in Fig. 7, and a good agreement between the numerical result (Fig. 4) and the experimentally measured data (Fig. 7) was achieved.

In Fig. 7 the dotted line is the prediction by the Maxwell-Garnett theory along with Volkova et al. [8] and Hale [9] and is as follows:

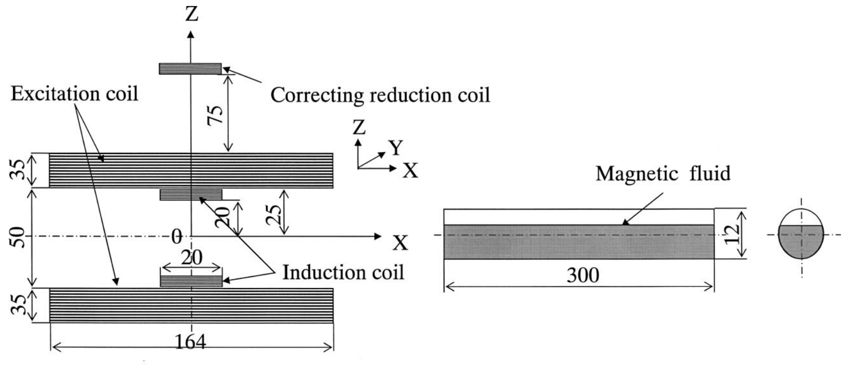

(*a*) Arrangement of coils (*b*) Magnetic fluid test plug

Fig. 5 Arrangement of coils and magnetic fluid test plug

$$\frac{\chi_T/\chi_m - 1}{\chi_T/\chi_m + 2} = \alpha \frac{1/\chi_m - 1}{1/\chi_m + 2} \qquad (9)$$

where χ_m is the magnetic susceptibility of the magnetic fluid and χ_T is the magnetic susceptibility of two-phase state of magnetic fluid. In attempting to compare Eq. (9) with data, χ_T/χ_m is calculated by setting $\chi_T/\chi_m = \Delta V/\Delta V_{\alpha=0}$, where $\Delta V_{\alpha=0}$ is measured induction voltage at $\alpha=0$, since it is reasonable to assume that $\Delta V \propto \chi_T$ for the magnetic field of $\mathbf{M} \| \mathbf{H}$. The theory (Eq. (9)) has been extensively used for calculating bulk dielectric properties of inhomogeneous materials, such as the properties of two-component mixtures in which both the host and the inclusions are isotropic materials with scalar dielectric coefficients. Volkova et al. [8] reported the data for the dependence of magnetic permeability on volume fraction of silica particles in a magnetic fluid and was compared with the Maxwell-Garnett theory. It should be mentioned that although the results presented in Fig. 7 were obtained for the stratified two-phase layers of magnetic fluid in the test plug (as shown in Fig. 5(*b*)), not in the sense of evenly distributed two dispersed component mixture with lattice configuration, it would be worth comparing the data with the Maxwell-Garnett theory [8,9]. As seen in Fig. 7, the prediction has nonlinearity dependence as the theory tends to deviate from data particularly at a high void fraction range. It was understood, therefore, that, although no direct comparison would be possible with the theory, as this point was also mentioned by Volkova et al. [8], there would be some degree of nonlinearity derived from the magnetic dipole although the magnitude is minimal in the present study.

It should be mentioned that there was no dependency on the excitation frequency in measuring void fraction for the frequency range (100~500 Hz). Since the magnetization relaxation time [10], is in the order of 10^{-9} second, so that it can be easily speculated that the independency on frequency for the measure-

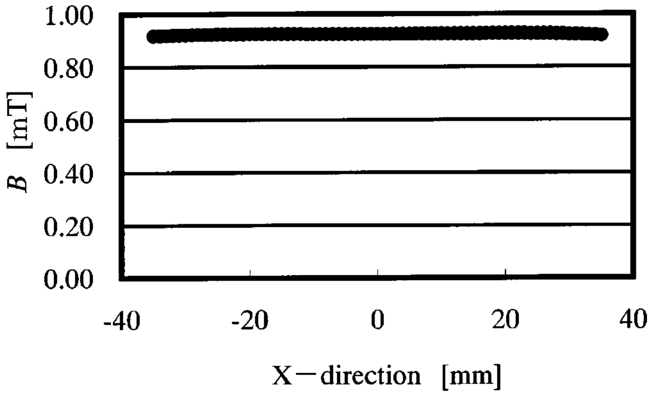

(*a*) distribution at Z = 0

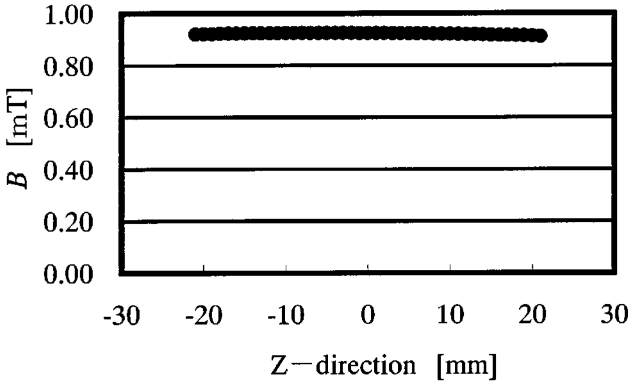

(*b*) distribution at X = 0

Fig. 6 Distribution of magnetic flux density (at $I=0.75$ A, $f=100$ Hz in excitation coils)

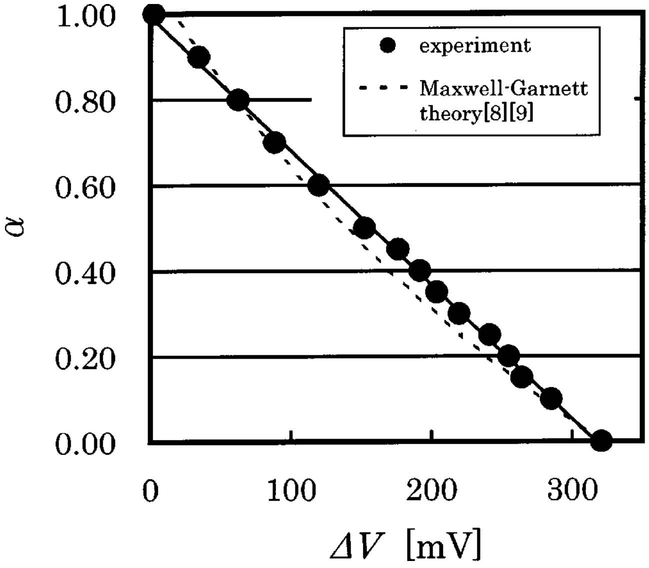

Fig. 7 Measured value in static experiment and comparison with Maxwell-Garnett theory [8,9], α versus ΔV (master line)

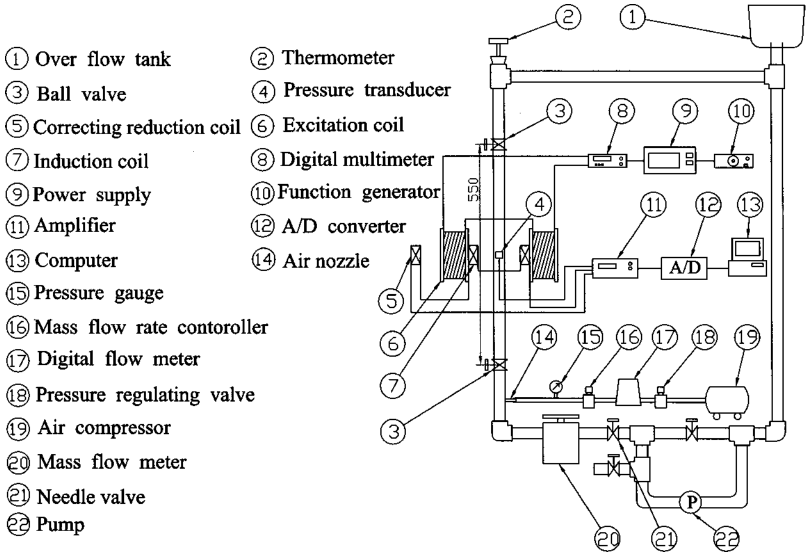

Fig. 8 Schematic diagram of flow experimental apparatus

ment of α in this induction method can be persisted for the order of 10^6 [Hz]. Thus, in the present study, the result obtained in Fig. 7 is determined as the master line (calibration line).

3.2 Flow Experiment and Results. With the result obtained in the static experiment, the proof experiments were then conducted by constructing a flow experimental apparatus as shown in Fig. 8. The apparatus basically consists of the induction void fraction measuring section, excitation coils and the induction coils with attached electronic devices (as explained in Fig. 1 and Fig. 5(*a*)), and a two-phase flow circulation loop with an air bubble injection system. Air bubbles, which are made by compressed air with a compressor ⑲ through a pressure regulator ⑯ and flow meter ⑰, are mixed into a flow of magnetic fluid before the void fraction measuring section. In the present investigation, for the sake of comparison with the induction method, the void fraction average α is also measured mechanically by using the valve shutdown method, [3]. Two ball valves are located between the induction void fraction measuring section (for the induction method) so that the void fraction average contained in the section can be obtained by measuring the height of a liquid column trapped between two valves, when two valves at the two location points in the pipe are instantaneously closed. The inner diameter of the pipe through the measuring section is 12 mm (the same diameter as the test plug in Fig. 5(*b*)), and the total length between two ball valves is 550 mm. The pipe is made of acrylic resin for visual measurement of the height of the liquid column between two ball valves. The pressure transducer is also placed in the measuring section so that the change of the pressure in two-phase flow can be measured for correcting the void fraction. Thus, absolute readings of the pressure transducer enable one to give a correction to the measurement of the void fraction average by the valve shutdown method as follows:

$$\alpha = \frac{P_a}{P_b}\alpha_a \tag{10}$$

where P_a is the mean pressure reading for the transducer after valve closing, P_b is the one before valve closing, α_a is the measured value of the void fraction average by the valve shutdown method, and α is the corrected value. As depicted in Fig. 8, the two-phase flow of magnetic fluid after the measuring section of the void fraction is passed to the overflow tank①, where the gaseous phase is separated, and the liquid phase (magnetic fluid) is forced to circulate in the main loop by the circulation pump. In this apparatus (Fig. 8) the range of the volume flux of the liquid phase j_l is 0.044~0.265 m/s. In the flow experiment, the uncertainty associated with the measurement of induction voltage is the same as in the static experiment (maximum ±0.5%). And with the measurement of the average void fraction in the test section by the valve shutdown method, the uncertainty is chiefly determined by the accuracy of reading the height of the liquid column between the valves. It can be estimated as maximum ±2% at the most, and which is associated with the reading error for the height of the liquid column of 1 mm for $\alpha = 0.5$.

In Fig. 9(*a*), (*b*), and (*c*), the results obtained from the two-phase flow experiments are displayed for the representative volume flux of the liquid phase $j_l = 0.054$, 0.108, and 0.161 m/s, respectively. In each diagram of (*a*), (*b*), and (*c*), the void fraction average α measured by the valve shutdown method (indicated by data points), corresponding to the data obtained by the induction method, is plotted against the master line (the calibration line from the static experiment). It is noted that for higher α the mechanical valve shutdown method tends to lose accuracy due to the intermittent flow mode of two-phase flow; at higher void fraction (lower j_l and higher j_g), the flow mode tends to become the slug flow. As it is seen from each part of Fig. 9, it was confirmed that the induction method proposed in the present study would give adequate accuracy (within ±3% against the mechanical valve shutdown method). And it was proved that the induction method is feasible for measuring the void fraction average in an actual two-phase flow of magnetic fluid. It is noted here that the effect of the magnetic field on the flow was minimal since the pressure change in the measuring section after imposing the magnetic field for void measurement was within 0.4%.

Finally, in consideration of giving an insight to the flow mode of the two-phase flow in the present flow experiments, the data obtained in the flow experiments (in Fig. 9) were compared by a known correlation obtained by the drift flux model, [11–14]; see the Appendix. The correlation was calculated for the bubble flow case, using nominal parameters and the experimental conditions, as representatively described in the Appendix. And the results of the comparison were depicted in Fig. 10. In Fig. 10 ζ is the quality of the two-phase flow defined as follows:

$$\zeta = \frac{G_g}{G} \tag{11}$$

where G_g is mass flow rate of the gas phase and G is total mass flow rate of the two phase. The quality ζ was calculated by values G_g and G measured in the experiment. As seen in Fig. 10, it is understood that the flow mode appearing in the flow experiment

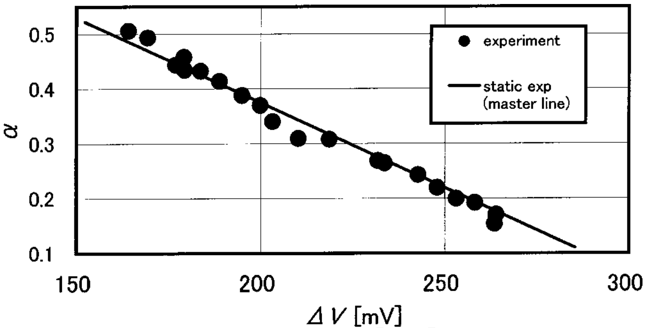

(a) j_l=0.054[m/s]

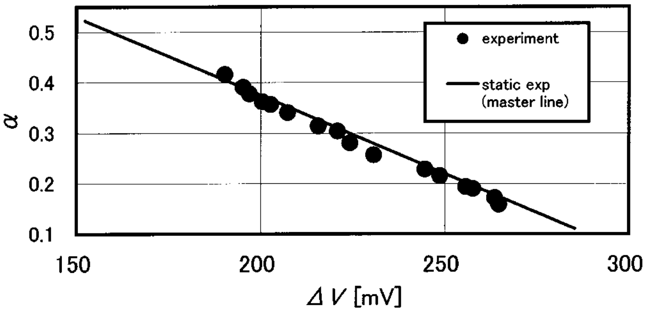

(b) j_l=0.108[m/s]

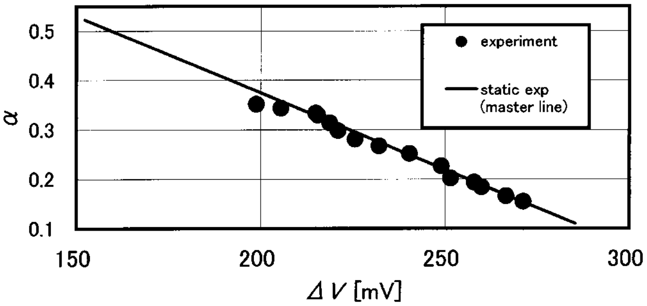

(c) j_l=0.161[m/s]

Fig. 9 Measured value in two-phase flow experiment, α versus ΔV

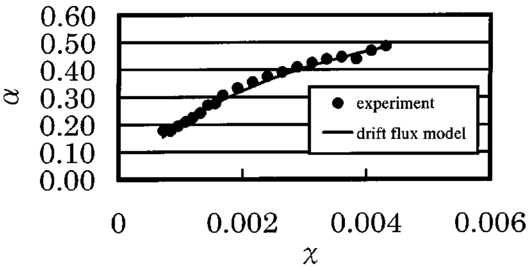

(a) j_l =0.054 [m/s]

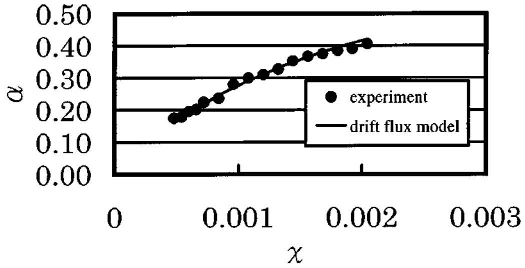

(b) j_l = 0.108 [m/s]

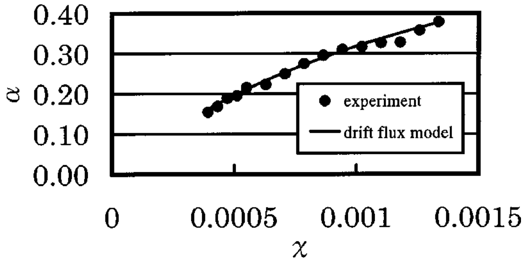

(c) j_l = 0.161 [m/s]

Fig. 10 Comparison between experiment data and the known two-phase flow correlation

was in the bubble flow mode, as the estimated curves (α versus χ) by the correlation shows good agreement with the data obtained in the present study. Thus, the data obtained from the induction method was well correlated by the known correlation formula that gives the certainty of the present method.

Further detailed study would be necessary to verify more extreme cases of two-phase flow modes, such as slug-plug flow or mist flow, etc., whereas no established method is available for these extreme cases at the present stage. It is beyond our scope in the present study. We shall be reporting these cases in our future publications. It is further thought that one extension of the present method would lead to the possibility of measuring the void fraction average for an ordinary liquid-gas two-phase flow, if a magnetic fluid can be resolved into a working fluid, or similarly, if small magnetic particles can be mixed in a two-phase flow.

4 Conclusions

A feasible study was conducted in order to develop a new technique of measuring void fraction average in a two-phase magnetic fluid, using electromotive induction. The void fraction average was measured by voltage readings from the induction coils with applying low frequency and low voltage alternating current to the excitation coils. From the static and flow experiments, the following conclusions were drawn.

1 From the static experiment, it was found that the output voltage from the induction coils is a linear function against the void fraction average. The appropriate connecting configuration of the electromagnetic coils was verified in the present study, and the linear relationship was obtained independent from the local distribution of void fraction.

2 With the results obtained from the static experiment, the proof experiments, using an actual flow experimental apparatus for two-phase flow of magnetic fluid, were conducted. Excellent agreement was reached between the data measured by the mechanical valve shutdown method and the values measured by the proposed induction method, and the feasibility of the method in an actual two-phase flow was indicated.

Acknowledgment

This work was partly supported by warrant-in-aid for Scientific Research (C) from the Ministry of Education, Culture, Sports, Science and Technology, Japan.

Nomenclature

H = magnetic field
B = magnetic flux density

$\mathbf{M}$ = magnetization
μ_0 = permeability of vacuum
χ_m = magnetic susceptibility of magnetic fluid
χ_T = magnetic susceptibility of two-phase state of magnetic fluid
ζ = quality of two-phase state
Ψ = static magnetic potential
V = electromotive force
α = void fraction
j = volume flux
f = frequency
n = turn of secondary coil
C_0 = distribution parameter
v_{gj} = drift velocity
u = flow velocity
P = pressure
G = mass flow rate
ρ = density
σ = surface tension
g = acceleration of gravity

Subscripts

g = gas phase
l = liquid phase
T = sum total of gas phase and liquid phase

Appendix

Drift Flux Model, [11–14]. ⟨ ⟩ symbol expresses a section average and is defined by the following formula for certain quantity of F:

$$\langle F\rangle=\frac{\int_A F\cdot dA}{A}. \tag{A1}$$

⟪ ⟫ symbol expresses a quantity multiplied by void fraction, and can be expressed with the following formula for certain quantity of F:

$$\langle\langle F\rangle\rangle=\frac{\langle\alpha F\rangle}{\langle\alpha\rangle}. \tag{A2}$$

The drift velocity is defined as a quantity that expresses the local speed difference between the gaseous and liquid phase in the drift flux model.

$$v_{gj}=u_g-j_T \tag{A3}$$

The distribution parameter C_0 in the drift flux model is also defined by the following formula:

$$C_0=\frac{\langle\alpha j_T\rangle}{\langle\alpha\rangle\langle j_T\rangle}. \tag{A4}$$

In consideration of Eq. (A2) and Eq. (A3) the average drift velocity can be expressed with the following formula:

$$\langle\langle v_{gj}\rangle\rangle=\frac{\langle\alpha v_{gj}\rangle}{\langle\alpha\rangle}. \tag{A5}$$

Thus, the void fraction average $\langle\alpha\rangle$ in the drift flux model is expressed with the following formula using Eq. (A4) and Eq. (A5):

$$\langle\alpha\rangle=\frac{\zeta/\{\zeta+(1-\zeta)\rho_g/\rho_l\}}{C_0\langle\langle v_{gj}\rangle\rangle/\{(\zeta/\rho_g+(1-\zeta)/\rho_l)G\}} \tag{A6}$$

where in the present investigation the distribution parameter C_0 and average drift speed v_{gj} are determined from the known relation, [13], Eq. (A7) as follows:

$$C_0=1.2-0.2\sqrt{\rho_g/\rho_l},\quad v_{gj}=\sqrt{2}\{\sigma_g(\rho_l-\rho_g)/\rho_l^2\}^{1/4}. \tag{A7}$$

References

[1] Ishimoto, J., Okubo, M., Nisihiyama, N., and Kamiyama, S., 1993, "Basic Study on an Energy Conversion System Using Gas-liquid Two-Phase Flows of Magnetic Fluid," Jpn. Soc. Mech. Eng., Ser. B, **59**(566), pp. 3071–3077 (in Japanese).
[2] Hulzler, S., Weaire, D., Elias, F., and Janiaud, E., 2002, "Juggling with Bubbles in Cylindrical Ferrofluid Foams," Philos. Mag. Lett., **82**(5), pp. 297–301.
[3] Hewitt, G. F., and Hall-Talor, N. S., 1970, *Annular Two-Phase Flow*, Pergamon Press, Oxford, pp. 259–265.
[4] Cummings, P. D., and Chanson, H., 1997, "Air Entrainment in the Developing Flow Region of Plunging," ASME J. Fluids Eng., **119**, pp. 603–608.
[5] Herringe, R. A., and Davis, M. R., 1976, "Structural Development of Gas-Liquid Mixture Flows," J. Fluid Mech., **73**, pp. 97–123.
[6] Ishimoto, J., Okubo, M., and Kamiyama, S., 1995, "Basic Study on an Energy Conversion System Using Boiling Two-Phase Flows of Temperature-Sensitive Magnetic Fluid," Jpn. Soc. Mech. Eng., Ser. B, **61**(581), pp. 157–165 (in Japanese).
[7] Yamada, N., 1996, *Electromagnetic Engineering*, Tokyo, The Institute of Electrical Engineers of Japan, Tokyo p. 215 (in Japanese).
[8] Volkova, O., and Bossis, G., 2000, "Magnetorheolgy of Magnetic Holes Compared to Magnetic Particles," **44**(91), pp. 91–104.
[9] Hale, D. K., 1976, "The Physical Properties of Composite Materials," J. Mater. Sci., **11**, pp. 2105–2141.
[10] Bashtovoy, V. G., Berkovsky, B. M., and Vislovich, A. N., 1988, *Introduction to Thermomechanics of Magnetic Fluids*, Hemisphere Press, Washington, DC, pp. 121–124.
[11] Salomon, L., 1999, *Two-Phase Flow in Complex Systems*, John Wiley and Sons, New York, pp. 118–124.
[12] Graham, B., *One-Dimensional Two-Phase Flow*, McGraw-Hill, New York, pp. 89–103.
[13] Zuber, N., and Findlay, J. A., 1965, "Average Volumetric Concentration in Two-Phase Flow System," ASME J. Heat Transfer, **87**, pp. 453–463.
[14] Ishii, M., 1977, "One-Dimensional Drift-Flux Model and Constitutive Equations for Relative Motion Between Phases in Various Two-Phase Flow Regimes," ANL Rep., **77**, p. 40.

H. S. Yoon
School of Mechanical Engineering,
San 30 Chang Jeon Dong,
Pusan National University,
Kumjung-ku,
Pusan 609–735, Korea

S. Balachandar[1]
Department of Theoretical and
Applied Mechanics,
216 Talbot Laboratory,
University of Illinois,
Urbana, IL 61801
e-mail: s-bala@uiuc.edu

M. Y. Ha
School of Mechanical Engineering,
San 30 Chang Jeon Dong,
Pusan National University,
Kamjung-ku,
Pusan 609-735, Korea

K. Kar
Dow Chemical Company
1776 Dow Center,
Midland, MI 48674

Large Eddy Simulation of Flow in a Stirred Tank

Here we report on results obtained from large eddy simulations of flow inside a stirred tank performed using a spectral multidomain technique. The computations were driven by specifying the impeller-induced flow at the blade tip radius. Stereoscopic PIV measurements along with a theoretical model are used in defining the impeller-induced flow as a superposition of circumferential, jet and tip-vortex pair components. Both time-independent (fixed inflow) and time-dependent (oscillatory inflow) impeller-induced flows were considered. In both cases, the improved impeller-induced inflow allowed for the development of tip-vortex pairs in the interior of the tank. At $Re_m = 4000$ considered here, the flow in the interior of the tank naturally evolves to a time-dependent turbulent state. The jet component of the impeller-induced flow becomes unstable and shows signs of both sinuous and varicose behavior. The vortex pairs are anchored near the blades, but as they extend outwards into the tank their backbones exhibit time-dependent fluctuation. The instability of the jet is intimately connected with the fluctuation of the tip-vortex system. The time-averaged location of the vortex backbone compares well with previous measurements. The radial profile of θ-averaged radial velocity along the midplane is a good sensitive measure for evaluating the computed results. It is observed that computed flow from the 20 deg oscillatory impeller-induced inflow model compares well with the corresponding experimental measurements on the r-z plane. [DOI: 10.1115/1.1566046]

1 Introduction

Under most operating conditions the flow in a stirred tank is fully turbulent over the entire volume. The current standard engineering practice for predicting flow in a stirred tank is based on Reynolds averaged Navier-Stokes (RANS) simulations, [1–5]. In the RANS approach one attempts to compute only the mean quantities and to model the effect of all turbulent fluctuations. A variety of turbulence models are available; however, the scale-up process has been particularly problematic.

The importance of accounting for unsteady flow dynamics has been well recognized, and there are recent attempts at large eddy simulation (LES) of stirred tank flow, [6,7] In LES, not only the mean flow, but also the dynamics of a range of energetic large scales of motion is directly computed. The effect of the unresolved small-scale turbulence needs to be accounted for through subgrid models. LES is particularly appealing for the simulation of the stirred tank flow. There are large and intermediate scale eddies within the tank, which are dictated by the tank and impeller geometries. There are smaller eddies down to the Kolmogorov scale and the range of scales widen with increasing Reynolds number. The smaller scales are driven by the turbulence cascade and are therefore likely to be independent of the specifics of the stirred tank. Thus LES offers a good hope for computing the stirred tank flow from the laboratory scale to the production scale with a universal set of governing equations for the large and intermediate scale eddies.

The development of a reliable computational approach for the design of stirred tank reactors faces an important challenge: incorporation of the effects of the impellers. There have been recent attempts at computing the detailed flow around the impellers using moving/deforming grids and sliding meshes, [8,9]. Instead of a direct computation of the impeller-induced flow, the effect of the impellers can be incorporated into the computations as a distributed momentum source, [6,7] or through an approximate aerodynamic theory for the impeller blades, [10].

There have also been RANS simulations, where the average velocity on a pillbox around the impeller obtained from experimental measurements has been used as inlet boundary condition, [2,5]. The above efforts have assumed the time-averaged impeller-induced flow to be dominated by circumferential and jet flow components and accordingly modeled the impeller-induced flow. However, in the case of a Rushton turbine, the impeller-induced flow in addition consists of pairs of tip vortices induced by the blades, [11–14] which need to be accounted for in the inflow boundary condition.

A simple estimate of the size of the smallest eddy can be obtained from a measurement of turbulent dissipation, [15–17]. For the case of a Rushton turbine of diameter $D = 50$ mm operating at a modest speed of $N = 1.667$ rps in water, Sharp et al. [17] calculated dissipation averaged over the entire tank to be 0.0025 m^3/s^2, which yields a Kolmogorov length scale of about 0.14 mm. The corresponding Reynolds number, defined as $Re_m = ND^2/\nu$, is about 4000, which places the experiment in the transitional regime. The estimated Kolmogorov length scale when compared with the size of the tank (diameter=height=153 mm) clearly illustrates the need for a large eddy simulation even at such transitional Re_m.

Here we report on the results of the corresponding LES performed at $Re_m = 4000$. Phase-locked stereoscopic PIV measurements around the impeller region, [18] are used to obtain the impeller-induced inflow condition for the LES. A detailed theoretical model of the phase-averaged impeller-induced flow is used to incorporate the influence of the tip-vortex component, [14]. Detailed PIV measurements in the interior of the tank, [17], were then used to compare with the computed results of the LES.

The detailed time-dependent three-dimensional flow computed in the interior of the tank is then used to explore the nature of the impeller-induced jet flow and the tip-vortex system in the transitional range of Reynolds number. Particular attention is paid to the extraction and investigation of the tip-vortex pairs in the interior

---

[1] To whom correspondence should be addressed.

Contributed by the Fluids Engineering Division for publication in the JOURNAL OF FLUIDS ENGINEERING. Manuscript received by the Fluids Engineering Division August 17, 2001; revised manuscript received November 12, 2002. Associate Editor: A. K. Prasad.

of the tank. The computed results are compared against the corresponding experimental measurements in the interior of the tank. The nature of instability of the impeller-induced jet flow and the tip-vortex system is investigated. Dissipation at both the large and subgrid scale are measured and compared.

In the frame of reference rotating with the blades, the phase-averaged impeller-induced flow corresponds to a fixed inflow condition, which is time-independent. Nevertheless, the flow in the interior of the tank is time-dependent, owing to the intrinsic unstable nature of the jet flow and the tip vortices. The time-dependent flow, computed based on the *fixed inflow*, qualitatively compares with the experimental observation; however, they differ quantitatively. Most importantly, the computed radial flow is observed to stay focused and decay much slower than its experimental counterpart. The reason for this discrepancy is the time-dependent nature of the impeller-induced inflow. The instantaneous realizations of the phase-locked PIV measurements show considerable variation, even in the region close to the impeller. Therefore, we also consider LES, which incorporate this important behavior through an *oscillatory inflow model*. We also report on the results of a steady RANS simulation, performed in a rotating frame of reference, and compare the results with those of LES and with the experimental measurements.

In Section 2 the LES with dynamic subgrid model is briefly outlined. Section 3 presents the spectral multidomain methodology employed in the LES, with particular attention paid to the implementation of the dynamic subgrid scale model in the context of a nonuniform grid. The fixed and osciallatory models of the impeller-induced flow, which will serve as inflow condition for the LES, are discussed in Section 4. Finally the results are presented in Section 5.

2 Large Eddy Simulation (LES)—Mathematical Formulation

Here we describe briefly the mathematical formulation of LES with the dynamic subgrid scale model, which will be employed here. The basic governing equations are the grid-filtered Navier-Stokes and continuity equations

$$\frac{\partial \overline{u_i}}{\partial t}+\frac{\partial \overline{u_i}\,\overline{u_j}}{\partial x_j}=-\frac{\partial \overline{p}}{\partial x_i}+\frac{1}{\mathrm{Re}}\frac{\partial^2\overline{u_i}}{\partial x_j\partial x_j}-\frac{\partial \tau_{ij}}{\partial x_j}, \tag{1a}$$

$$\frac{\partial \overline{u_i}}{\partial x_i}=0, \tag{1b}$$

where the overbars denote the large (or resolved) scale flow obtained from grid filtering. The effect of the subgrid scale motion on the dynamics of the resolved scale velocity is accounted for by the subgrid scale stress tensor

$$\tau_{ij}=\overline{u_iu_j}-\overline{u_i}\,\overline{u_i}\,, \tag{2}$$

which must be modeled in terms of the resolved scale velocity, $\overline{u_i}$, in order to obtain a closure for Eq. (1). Several closure models for the subgrid scale stress have been proposed. They fall into one of the following general categories: eddy viscosity models, scale similarity models, mixed models, and Lagrangian based models.

In the eddy viscosity model the anisotropic part of the subgrid scale stress tensor is assumed to take the form

$$\tau_{ij}^a=\tau_{ij}-\frac{1}{3}\tau_{kk}\delta_{ij}=-2\nu_T\overline{S}_{ij}\,. \tag{3}$$

The most commonly used eddy viscosity model was originally proposed by Smagorinsky [19] where the eddy viscosity, ν_T, is obtained by assuming that the small scales are in equilibrium. The resulting expression for eddy viscosity is

$$\nu_T=(C_s\Delta)^2|\overline{S}|, \tag{4}$$

where Δ is the filter width, $|\overline{S}|=(2\overline{S}_{ij}\overline{S}_{ij})^{1/2}$ is the magnitude of large-scale strain-rate tensor, S_{ij}. For homogeneous isotropic turbulence with cutoff in the inertial subrange $C_s\approx0.23$. However, in the presence of mean shear C_s is observed to decrease and range from 0.1 to 0.15 (see [20,21]).

The dynamic eddy viscosity approach provides a self-consistent way to internally determine the Smagorinsky coefficient from the current state of the resolved scale motion. Here a second filter (test filter–denoted by a tilde) is defined and applied to the large eddy equation (Eq. (1)). The subgrid scale stress in the new test filter is

$$T_{ij}=\widetilde{\overline{u_i u_j}}-\tilde{\bar{u}}_i\tilde{\bar{u}}_j\,, \tag{5}$$

of which contribution from scales intermediate between the grid and test filters, i.e., the small resolved scales, is given by the resolved turbulent stress

$$L_{ij}=\widetilde{\overline{u_i}\;\overline{u_j}}-\tilde{\bar{u}}_i\tilde{\bar{u}}. \tag{6}$$

The stresses given in Eqs. (2), (6), and (7) are related by the Germano identity

$$L_{ij}^a=T_{ij}^a-\tilde{\tau}_{ij}^a\,, \tag{7}$$

which relates the resolved turbulent stress, which can be calculated explicitly as given in Eq. (6), to the subgrid stresses at the grid and test filters.

The Germano identity can now be exploited to dynamically evaluate the Smagorinsky coefficient. If we assume the Smagorinsky model, with the same Smagorinsky coefficient, to be applicable for the parameterization of both T_{ij} and τ_{ij} (similar to Eqs. (3) and (4)) we now have

$$T_{ij}^a=-2(C_s\tilde{\Delta})^2|\tilde{\bar{S}}|\tilde{\bar{S}}_{ij}\,, \tag{8}$$

where

$$\tilde{\bar{S}}_{ij}=\frac{1}{2}\left(\frac{\partial\tilde{\bar{u}}_i}{\partial x_j}+\frac{\partial\tilde{\bar{u}}_j}{\partial x_i}\right)\quad\text{and}\quad|\tilde{\bar{S}}|=(2\tilde{\bar{S}}_{ij}\tilde{\bar{S}}_{ij})^{1/2}, \tag{9}$$

$\tilde{\Delta}$ is the characteristic filter width associated with the test filter. Eqs (3), (7), and (8) can be combined to obtain the following:

$$(C_s\Delta)^2M_{ij}=L_{ij}^a\quad\text{where}\quad M_{ij}=-2\left(\frac{\tilde{\Delta}}{\Delta}\right)^2|\tilde{\bar{S}}|\tilde{\bar{S}}_{ij}+2\widetilde{|\overline{S}|\overline{S}_{ij}}. \tag{10}$$

The above equation can be used in principle to obtain a space and time-dependent Smagorinsky coefficient. However, such a procedure can be numerically ill-conditioned as M_{ij} locally approaches zero. Furthermore, negative values for the Smagorinsky coefficient can lead to serious numerical difficulty. The past approach to alleviating this problem has been to average along the homogeneous spatial directions or over a short duration in time. Owing to the complex nature of the geometry under consideration, here we simply average over the entire volume and consider the Smagorinsky coefficient to be a function of time. Contracting Eq. (10) with M_{ij} and averaging over the entire computational volume (denoted by $\langle\ \rangle$) we obtain

$$C_s^2=\frac{1}{\Delta^2}\frac{\langle L_{ij}^aM_{ij}\rangle}{\langle M_{ij}M_{ij}\rangle}. \tag{11}$$

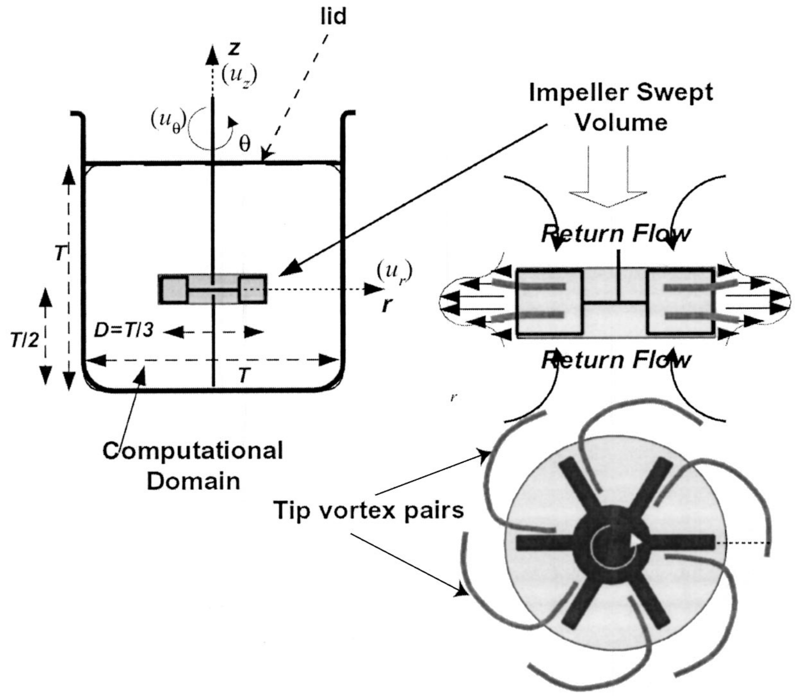

Fig. 1 Schematic of the stirred tank with a typical six-blade Rushton impeller. The plan view shown at the bottom on the right is viewed up from under the tank.

3 Numerical Methodology

The geometry to be considered is a cylindrical vessel of diameter $T = 150$ mm filled with water at room temperature to a height equal to the diameter as shown in Fig. 1. A six-blade Rushton impeller is placed at the center of the tank, halfway between the top and bottom of the fluid. The outer diameter of the impeller is $D = T/3 = 50$ mm and the height of the impeller is $0.4D$. For simplicity no baffles are considered in the tank and the top surface is taken to be flat.

The computational geometry simplifies in a frame of reference rotating with the blades. In this frame of reference, the geometry has a six fold symmetry along the circumferential direction. The present computations assume the geometric periodicity to apply to the flow field as well. Thus the velocity and pressure fields are assumed to be periodic over a 60 deg sector and therefore the computational geometry is confined to this sector. The assumption of periodicity of the flow over the 60 deg sector is valid at low Reynolds numbers in the laminar flow regime, however, the assumption is only approximate when there is feedback of time-dependence to the impeller input. Here we resort to this assumption to maintain the computational cost of the LES manageable.

Owing to periodicity along the θ-direction a Fourier expansion with a corresponding uniform grid is used. A spectral multi-domain technique is used along the r-z plane. The r-z projection of the volume swept by the impeller is shaded gray in Fig. 1. No slip boundary condition is enforced on the top, bottom, and outer boundaries of the tank and along the impeller axis the fluid is assumed to rotate with the axis. Momentum sources are placed along the outflow section of the impeller swept volume, such that the impeller-induced flow, $\mathbf{u}_{\text{imp}}$, is applied as an internal boundary condition. Pressure changes across this interface representing a local momentum source. Thus this approach is similar in spirit to those employed by Eggels [6] and Revstedt et al. [7].

In the computations the tip radius of the impeller ($D/2$) and the blade tip velocity (πND) are chosen as the length and velocity scales, where N is the number of revolutions per second. Following the chemical engineering literature the Reynolds number of the flow is defined as $\text{Re}_m = ND^2/\nu = 2\,\text{Re}/\pi$. Typical computation involves 32 grid points along the circumferential direction and about 72 subdomains in the r-z plane, with each subdomain resolved by up to 13×13 points. The spectral multidomain technique employs Chebyshev expansion within each subdomain and the grid points are accordingly the Gauss-Lobatto points and are therefore nonuniformly distributed, [22] Even at the present Reynolds number of $\text{Re}_m = 4000$ the above grid resolves only a range of large flow scales. A large eddy simulation with an appropriate subgrid model is thus required to account for the unresolved small-scale eddies. The spectral methodology provides an accurate representation for the range of resolved scales. Large eddy simulations at other grid resolutions have also been performed yielding similar results.

Operator split scheme is employed with the advection and diffusion effects taken into account first to obtain an intermediate velocity. The advection terms are treated explicitly using a third-order Adams-Bashforth scheme and the viscous terms are treated semi-implicitly using the Crank-Nicholson scheme. The corresponding pressure field is obtained by solving the pressure Poisson equation, with the divergence of the intermediate velocity as the forcing term. The intermediate velocity is projected back onto the divergence-free space with the pressure correction step. The overall scheme is second-order accurate in time. The three-dimensional Helmholtz and Poisson equations are Fourier transformed in θ to reduce to a set of two-dimensional Helmholtz equations for each circumferential wave number. These two-dimensional Helmholtz equations in the r-z plane are solved efficiently using patching technique.

In the dynamic LES, the test filter along the circumferential direction is chosen to be a sharp cutoff filter, which retains half the total number of circumferential modes (±8 modes for the case of 32 circumferential grid points). Along the radial (r) and axial (z) directions a box-average filter, that essentially projects the flow onto half as many points along these directions, is applied. Thus, for the present nonuniform grid, even though Δ and $\tilde{\Delta}$ vary over the r-z plane, their ratio $(\tilde{\Delta}/\Delta)$ in Eq. (10) can be taken to be 2.

In addition to the LES simulations we also report on a RANS simulation performed using Fluent®. This is a steady simulation performed in a frame of reference moving with the impeller. The boundary conditions applied at the top, bottom, and outer walls of the tank are the same as in the LES. The steady impeller-induced inflow condition enforced is also the same as in the LES.

4 Impeller-Induced Flow

The experimentally measured phase-averaged flow around the impeller swept volume is applied as the boundary condition in the computations. A theoretical model for the impeller-induced flow, [14], is used to cast the experimental measurement into a meaningful velocity boundary condition for the computations. Preliminary results suggest that the impeller-induced flow can be described as a superposition of a circumferential flow, a circular jet and a pair of tip vortices associated with each impeller blade (see Fig. 1). The impeller-induced flow is strongly three-dimensional and as a result a complex theoretical description is necessary to capture all the essential features.

4.1 Theoretical Model. The jet flow from a Rushton turbine slowly changes from a circumferential direction to a more radial direction with increasing radial distance from the axis, [23–25]. Thin shear layer approximation can be applied to obtain an approximate self-similar solution. The jet velocity, $\mathbf{u}_{\text{jet}}$, as a function of the radial (r) and axial (z) distances (see Fig. 1 for coordinate definition) can be expressed in terms, of three parameters: jet momentum, jet thickness, and virtual origin.

The tip vortices are generated from the roll-up of the shear layers as flow accelerates around the rotating impellers, [11–13]. The tip vortices are characterized by the radial and axial position of their backbone and the strength and size (diameter) variation along this backbone. The total influence of the tip vortex system, $\mathbf{u}_{\text{vort}}$, is given by an integration along the backbone of the vortex pair and a summation over all the six tip-vortex pairs.

The flow induced by the impeller, in the neighborhood of the impeller, in the frame of reference rotating with the impeller, can be expressed as, [14],

$$\mathbf{u}_{\text{imp}}(r,\theta,z)=\mathbf{u}_c(r,z)+\mathbf{u}_{\text{jet}}(r,z)+\mathbf{u}_{\text{vort}}(r,\theta,z) \qquad (12)$$

where $\mathbf{u}_c$ is a circumferential flow in the rotating frame of reference. It is important to note that, the above model includes all three components of velocity. Variation along the circumferential direction is also present owing to the presence of the tip vortices. In the laboratory frame of reference this gives rise to time-dependence due to the rotation of the blades. The advantage of the theoretical model is that it reduces the prescription of the boundary condition to a few physically meaningful parameters. This reduction will allow physically meaningful scaling of the impeller-induced flow with impeller size and speed of rotation.

4.2 Fixed (Nonoscillatory) Inflow. The experimental results used in the present study are extensions of those reported in Hill et al. [18]. In the revised experiments, a stationary lid was placed on top of the liquid so as to avoid any free surface effect. Furthermore, the shaft was extended through the impeller to the bottom of the tank, where it was held in place by a small nylon sleeve bearing, to virtually eliminate any wobble of the impeller. The phase-locked velocity measurement from 500 realizations are phase-averaged and owing to the symmetric nature of the experimental setup the phase-averaged flow is further symmetrized about the midplane to obtain the mean flow.

The experimental data is triple-decomposed to obtain the circumferential flow and parameters associated with the circular jet and the tip vortices (for details see [14]). The theoretical description along with these parameter values then provides a *fixed inflow model* for the impeller-induced flow. The nondimensional in-plane and out-of-plane components of the impeller-induced flow at $\text{Re}_m=4000$ are shown in Fig. 2. In particular, the effect of the tip vortices can be seen to be captured near the lower left corner at $\theta\approx0.25$ and $z\approx0.1$. This inflow is steady only in the rotating frame of reference; in the fixed lab frame the above impeller-induced flow is time-dependent, due to the inclusion of the tip vortices, which rotate with the blades.

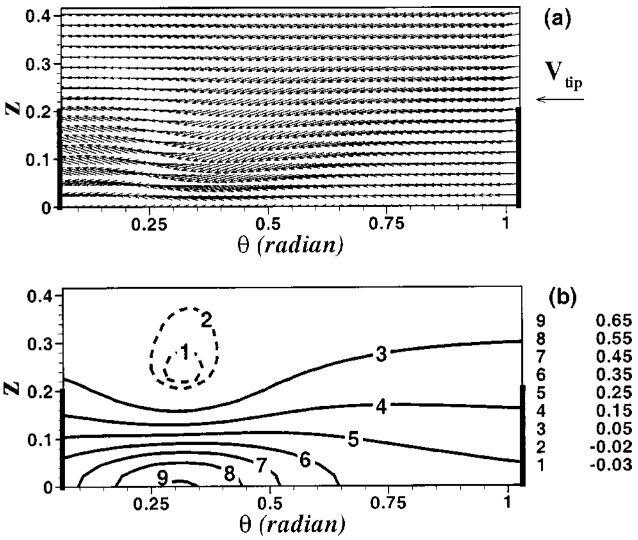

Fig. 2 The velocity field on the curved θ–z surface at (r=1) obtained from the theoretical model of the impeller-induced flow (Yoon et al. [14]). The parameters of the model are obtained such that the model provides the best approximation to the three-component stereo PIV measurement phase-averaged over 500 realizations. (*a*) In-plane velocity vector plot (a reference vector of magnitude equal to the blade tip velocity is provided) and (*b*) out-of-plane radial velocity contour. Only a 60 deg sector above the midplane ($z>0$) is shown and the thick vertical lines indicate the impeller blades.

4.3 Oscillatory Inflow. An accurate theoretical model that accounts for all the essential features of the impeller-induced flow is central for successful computation of the stirred tank flow. The fixed inflow model of the previous subsection is based on the phase-averaged experimental measurement. The instantaneous realizations, however, show considerable variation from instance to instance and as a result they substantially deviate from the phase-average. In particular, the jet flow model assumes that the jet axis lies along the $z=0$ midplane. However, the instantaneous PIV measurements on the r-z plane at varying θ locations show that the jet flow axis deviates up and down from the midplane, [17].

A simple characterization of the jet flow oscillation is attempted here. Each experimental realization of Sharp et al. [17] is examined at $r=1$ (corresponding to the impeller tip); the location and the magnitude of the largest radial velocity are noted. The reason for focusing attention as close to the impeller tip as possible is because we are interested in the nature of the impeller-induced flow just as it exits the impeller swept volume. It should not be confused with any oscillation of the jet that will arise out of inherent instability of the jet as it evolves radially out. If the jet axis were to be perfectly aligned along the midplane, then the maximum velocity is expected to occur at $z=0$. Figure 3(*a*) plots the z-location and the magnitude of the largest radial velocity measured at $\theta=20$ deg and $r=1$ for 100 realizations. Although not perfectly symmetric, considerable scatter about the mean can be observed suggesting up and down motion of the jet axis. Here it must be pointed out that recent experimental results, [26,27], sug-

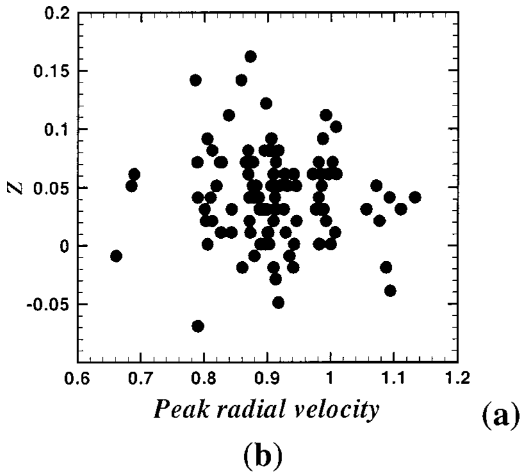

Fig. 3 The *z*-location and the magnitude of the largest radial velocity measured at θ=20 deg and r=1 for the different realizations of the PIV measurement on the *r*-*z* plane, [17]

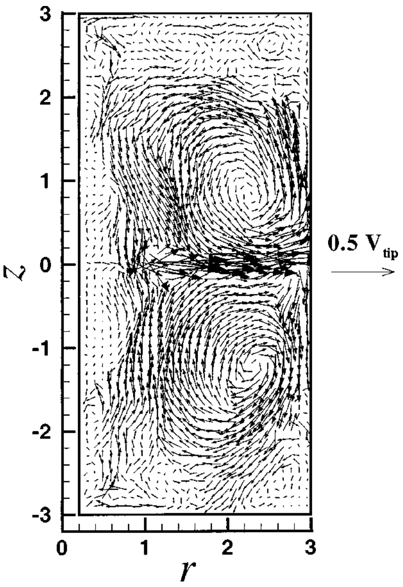

Fig. 4 An instantaneous flow field over the entire *r*-*z* cross section of the tank at θ=30 deg for the fixed inflow model at Re_m=4000. The grid resolution employed in the LES is much finer than what is shown above, where the resolution has been decreased to improve clarity.

gest the low-frequency oscillation to be suppressed at higher Reynolds numbers and also be dependent on the impeller type.

Since the intention of the experiment at that time was not to quantify the degree of oscillation, only an estimate can be obtained. In the computations we have tried three different amplitudes of oscillation, 10 deg, 20 deg, and 30 deg, thus bracketing a range of possible values. As will be shown later in Section 5, the 20-deg oscillation provides a good comparison with the experiments. Detailed information on the nature of oscillation, for example whether it is sinusoidal or not, is not available from the phase-locked measurements of Sharp et al. [17]. Also the frequency of oscillation is not known from the measurements. Here we simply assume the jet to oscillate up and down about the $z=0$ midplane in a sinusoidal manner. The time period of jet oscillation is estimated based on the circulation time of a large eddy around the tank, and in nondimensional terms it is taken to be 20 (since time scale is $1/(2\pi N)$, this corresponds to about 3.2 rotations of the impeller. Support for the oscillatory up and down motion of the jet and the assumed frequency of oscillation comes from the recent cinematographic PIV taken on the *r*-*z* plane close to the impeller, [28]. To contrast from the fixed inflow model, the oscillatory inflow as the boundary condition will henceforth be addressed as the *oscillatory inflow model*.

5 Results

The large eddy simulations were performed over a range of Reynolds number from few hundred to 40,000. However, here the focus will be primarily limited to $\mathrm{Re}_m=4000$, for which experimental data are available, [17,18], and therefore detailed comparisons can be made. For the case of fixed impeller-induced inflow, the stirred tank geometry and all the boundary conditions are symmetric about the axial midplane ($z=0$). At Reynolds numbers of the order considered here, any asymmetry present in the initial condition or arising from the roundoff errors will grow. This asymmetry about the midplane is critical to the time-dependent nature of the flow. In the time-dependent simulations, in order to promote rapid development of time-dependence, the symmetry of the inflow about $z=0$ is artificially disturbed for a short period of time, following which the symmetry of the inflow is restored. As a result there is a transient period where the asymmetry of the flow about the midplane builds up and an unsteady turbulent flow rapidly develops. After the transient, although the flow remains time-dependent, a statistically stationary state can be defined (in the rotating frame of reference). Once fully developed, the flow is computed for 120 nondimensional time units (19 rotations of the impeller). It was ensured that this duration of time integration is more than adequate for the well converged time-averaged statistics to be presented below. In contrast to the LES, in the RANS simulations a steady solution is obtained with the steady inflow model by enforcing the following symmetry on the flow field:

$$u_r(r,\theta,-z)=u_r(r,\theta,z), \quad u_\theta(r,\theta,-z)=u_\theta(r,\theta,z),$$
$$u_z(r,\theta,-z)=-u_z(r,\theta,z). \tag{13}$$

5.1 Fixed Inflow Model.

An instantaneous flow field over the entire *r*-*z* plane at θ=30 deg is shown in Fig. 4. As expected a pair of large-scale cells dominate the flow. However, they do not extend over the entire upper and lower halves of the tank. The flow along the outer wall of the tank separate limiting the size of the large eddies. The overall flow is far more complicated with many intermediate and small-scale components. Careful observation along the top, bottom, and outer walls of the tank reveals what appear to be wall layer vortices, arising from the instability of the boundary layers. Time-resolved movies of the velocity vector field as well as the associated vorticity fields have been made and they display the complex dynamics far more clearly.

Figures 5(*a*) and 5(*b*) show a sequence of two frames each separated by one nondimensional time unit (which corresponds to impeller rotation by approximately 57 deg) obtained from the large eddy simulation. Only the region close to the impeller on the *r*-*z* plane at θ=30 deg is shown. Frames (*a*) and (*b*) show the contours of radial velocity and are for the fixed inflow model at $\mathrm{Re}_m=4000$. In spite of the time-independence of the forcing (fixed impeller-induced inflow) the flow inside the tank is clearly unsteady and complex. The corresponding contours of axial velocity are shown in Figs. 5(*c*) and 5(*d*).

In Fig. 5 by limiting attention to $-1\leqslant z\leqslant 1$ on the *r*-*z* plane we focus attention on the radial evolution of the jet component of the impeller-induced flow. It is known from hydrodynamic stability theory that a simple planar jet has two modes of instability: sinuous and varicose instability, [29]. As shown by the schematic in Fig. 6, the dominant signature of the sinuous instability is the periodic (plus-minus) oscillation of the transverse velocity along the jet centerline. In contrast, the dominant signature of the varicose instability is the fluctuation in the longitudinal velocity about

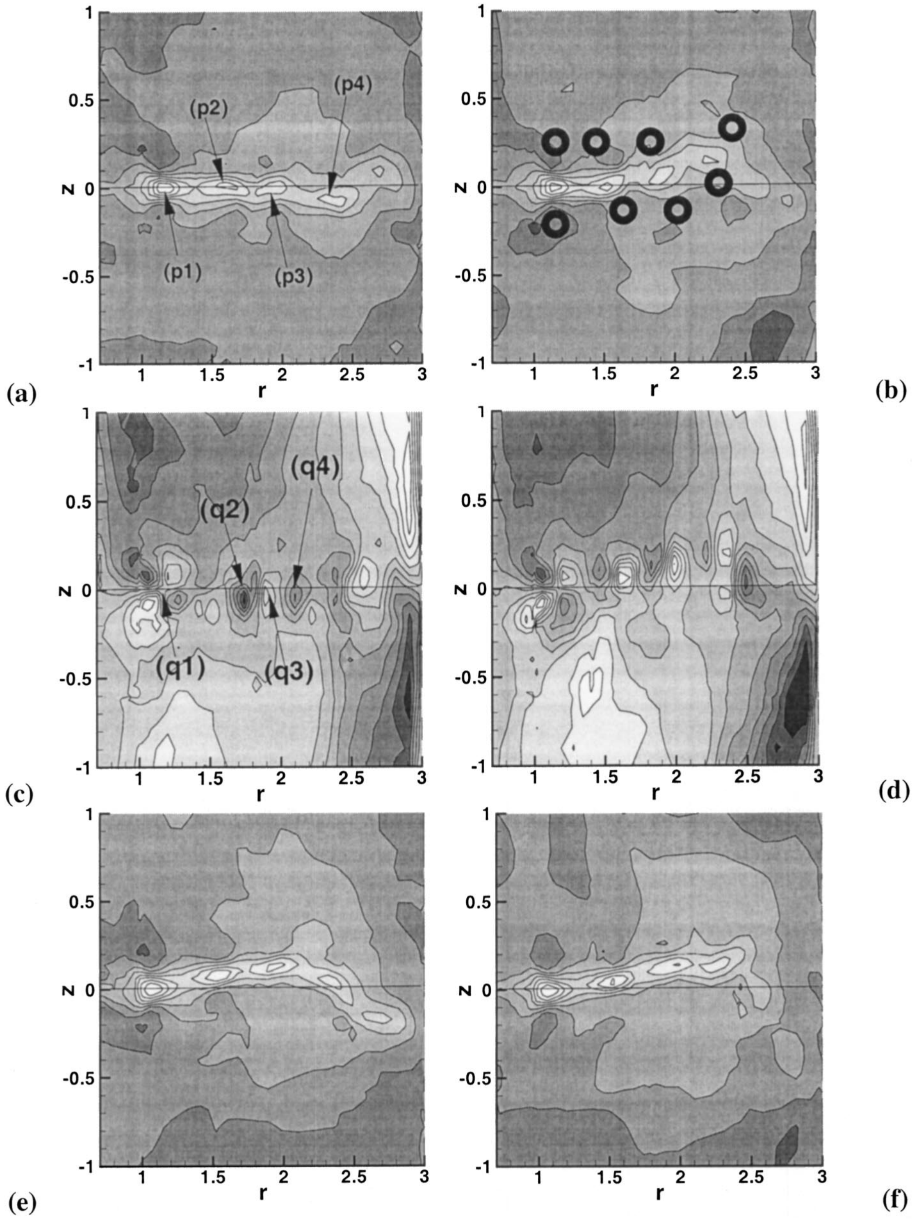

Fig. 5 Frames (*a*) and (*b*) show a sequence of two frames, each separated by 1 nondimensional time unit, showing contours of radial velocity in the region close to the impeller on the *r-z* plane at θ=30 deg for the fixed inflow model. Frames (*c*) and (*d*) show the corresponding contours of axial velocity. Frames (*e*) and (*f*) are the same as frames (*a*) and (*b*), but for the oscillatory inflow model. In frames (*a*), (*b*), (*e*), and (*f*) there are eight contours ranging from −0.1 to 0.6 in steps of 0.1 and in frames (*c*) and (*d*) there are 11 contours ranging from −0.25 to 0.25 in steps of 0.05.

a positive mean. The corresponding signature of the transverse velocity is a quadrapole pattern, similar to that marked **q1** in Fig. 5. The sinuous and varicose disturbances, in a frame of reference moving with the local flow, correspond to different possible eddy patterns as shown in Fig. 6. While a staggered pattern is consistent with the sinuous instability, a tandem arrangement is consistent with the varicose mode.

The peak in the radial velocity (marked **p1** in Fig. 5(*a*) and the quadrapole pattern in the axial velocity (marked **q1** in Fig. 5(*c*)) are due to the primary tip-vortex pair associated with the blade located immediately ahead at θ=0 deg. As we will see belowin Section 5.3, at this circumferential location of θ=30 deg the primary tip vortices are near symmetrically placed about the midplane with their centers located approximately at $r\approx 1.15$ and $z\approx\pm 1.0$. This tandem arrangement of vortices and their position is consistent with the velocity pattern seen in Fig. 5. Similar plots at other times and at the other circumferential locations (not shown here) are qualitatively similar. However, quantitative differences can be observed primarily due to differences in the location of the tip vortices.

In Fig. 5(*a*), downstream of the primary peak a sequence of subsequent peaks in the radial velocity (marked **p2**, **p3**, **p4**) can be seen. Similarly, in Fig. 5(*c*), downstream of the quadrapole pattern (for $r>1.5$) an alternating row of positive and negative axial velocity can be observed (they are marked **q2**, **q3**, **q4**, etc). The simultaneous presence of these two signatures indicates both sinu-

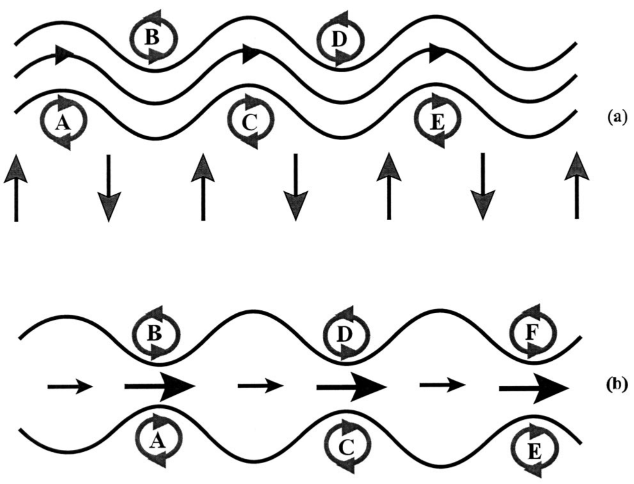

Fig. 6 The schematic of the (*a*) sinuous and (*b*) varicose instability of a jet flow. The dominant signature of the sinuous instability is the periodic (plus-minus) oscillation of the transverse velocity (frame (*a*)). The dominant signature of the varicose instability is the fluctuation in the longitudinal velocity about a positive mean (frame (*b*)). The sinuous and varicose disturbances, in a frame of reference moving with the local flow, correspond to staggered and in-line eddy patterns marked, A, B, etc.

ous and varicose nature of the jet component of the impeller-induced flow. These signatures can also be connected to the presence of vortex pairs as sketched in Fig. 5(*b*), whose presence will later be established in Section 5.3. The secondary and tertiary vortex pairs have their origin at the upstream blades located at $\theta = -60$ deg and $\theta = -120$ deg, respectively. In contrast to the primary vortex pair, the secondary and tertiary pairs are not symmetrically placed about the midplane and are somewhat tilted as schematically shown in Fig. 5(*b*).

The wavelength of the instability is in the range of 0.35 to 0.4 in nondimensional units, which also corresponds to radial spacing between the subsequent vortex pairs. From Fig. 5 it is evident that the location of the secondary peaks and valleys somewhat fluctuate over time. However, based on a sequence of time frames (on a much finer time scale than shown in Fig. 5) the sinuous or varicose oscillation of the jet does not appear to be a traveling mode. In fact, the peaks and valleys in the radial and axial velocity contours can be observed even in the time-averaged flow field. From hydrodynamic stability theory, both the sinuous and varicose instabilities of a jet flow propagate downstream as traveling modes, [29]. Here the jet component of the impeller-induced flow is a nonclassical one with both circumferential and radial components of velocity. Furthermore, the distance from the tip radius to the outer wall of the tank is comparable to the wavelength of the disturbance—only about four or five waves can be accommodated. Thus it appears that the presence of the outer tank wall can have an influence on the nontraveling nature of the disturbance. The stationarity of the disturbance is in agreement with the behavior of the tip-vortex pairs, which are relatively fixed in position in the rotating frame of reference. It is the fluctuations in the tip-vortex position, especially away from the blades in the interior of the tank that contributes to the time variation seen in Fig. 5.

The jet flow as it approaches the outer wall slows down and forms a stagnation point. From Figs. 4 and 5 a long wavelength up and down flapping of the jet flow can be seen. As a result, the stagnation point moves up and down about the midplane and the instantaneous stagnation point flow is asymmetric about $z=0$. At the instance shown in Fig. 4, the stagnation point flow is slightly tilted up with the flow upwards stronger than downwards. At a later time as the jet tilts down the scenario reverses and the circulation on the bottom half of the tank becomes stronger and the cycle goes on. The large-scale circulation advects the smaller vortices present in the tank back towards the midplane of the tank and the interaction of these advected smaller vortices with the jet seems to be responsible for the longer wavelength instability of the jet.

The Smagorinsky coefficient obtained from the dynamic large eddy simulation shows significant time variation. The time-averaged Smagorinsky coefficient of 0.119 compares well with the value of $C_s \approx 0.1$ to 0.15 normally used in the standard Smagorinsky model. The instantaneous Smagorinsky coefficient varies anywhere from about 0.115 to 0.125 thus exhibiting approximately 10% variation about the mean.

The time and θ-averaged radial velocity and vorticity contours, symmetrized about the midplane, are shown over the top half of the tank in Figs. 7(*a*) and 7(*b*). On average a large counterclockwise circulation can be observed in the upper half of the tank, which along with its counterpart in the lower half of the tank forms the primary pair of large-scale circulation. A weaker clockwise circulation can be seen at the top right-hand corner suggesting the presence of a pair of secondary circulation at the outer corners of the tank. Significant vorticity associated with the jet flow can be seen along the midplane of the tank. The boundary layers formed as the jet impinges on the outer wall of the tank can also be identified in the vorticity contours. The return flow along the top wall accelerates as it approaches the axis and develops a strong wall layer, which is visible on the top left corner in Fig. 7(*b*). The peak radial velocity and circumferential vorticity along the midplane near $r=1$ signify the influence of the tip vortex pair.

The corresponding result for the θ-averaged radial velocity and vorticity fields, obtained from the steady RANS simulation is shown in Figs. 7(*c*) and 7(*d*). The flow field is still dominated by the large-scale circulation driven by the impeller-induced jet flow. However, the strength of the circulation is different and the difference can be clearly observed in the vorticity fields. In particular, the RANS simulation predicts the large-scale circulation to extend over the entire tank, without the presence of secondary circulation. This difference may be a consequence of the steady nature of the RANS simulation in the rotating frame of reference and the enhanced diffusion associated with the turbulence model. As a result, the RANS simulation predicts a much broader jet flow induced by the impeller, which remains attached to the outer tank wall forming a single pair of primary circulation.

The time-averaged radial velocity as a function of radial distance from the blade tip at $\theta=0$ deg, 20 deg, 30 deg, and 40 deg are shown in Fig. 8. Along with the experimental results of Sharp et al. [17] also shown are the results of dynamic LES performed with the fixed impeller-induced inflow model and those of the RANS simulation. The experimental measurements show that at $\theta=20$ deg the peak radial velocity is close to the blade-tip location $(r=1)$, however, for larger θ the location of the peak is not at the blade tip, but somewhat radially out. The jet contribution to the radial velocity exhibits a monotonic decay from the blade tip to the outer tank wall. Thus the location of the peak beyond the blade tip is due to the presence of the tip vortices. As shown in the schematic of Fig. 1, the root of the tip-vortex pair lies almost parallel to the blade on the leeward side of the rotating blade and as it extends beyond the blade tip its backbone is curved backwards and its radial location slowly increases with θ. The sense of rotation of the vortex pair is such that fluid is pumped radially out between them and the orientation of the vortex pair is such that a component of this pumping action augments the radial component of velocity.

It should be emphasized that without accounting for the tip vortices the peak velocity will occur at the blade-tip location. Two-dimensional RANS simulations, which employ only the jet component of the impeller-induced flow as the inflow, generally display a monotonic decay of the radial velocity from the blade tip

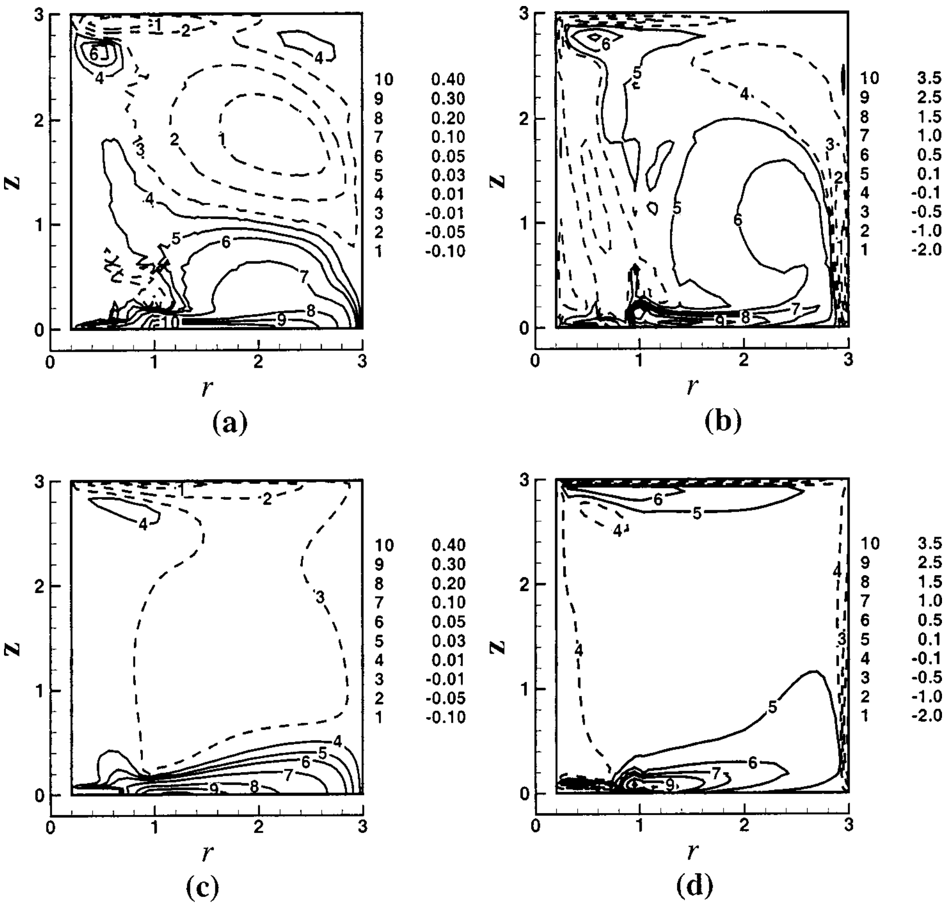

Fig. 7 The time and θ-averaged nondimensional quantities from the dynamic large eddy simulation with fixed inflow model: (*a*) radial velocity contours (*b*) circumferential vorticity contours in the rotating frame of reference. The θ-averaged nondimensional quantities from the RANS simulation: (*c*) radial velocity contours (*d*) circumferential vorticity contours in the rotating frame of reference.

to the outer wall of the tank. It is to be noted that the present three-dimensional RANS simulation shows the peak radial velocity to be located beyond the blade tip, thus illustrating the influence of the tip vortices. However, quantitative comparison with the experimental data in terms of the location and magnitude of the peak is poor. The performance of the (time-dependent) large eddy simulation with the fixed inflow model is no better. The location of the peak radial velocity compares favorably with the experimental measurement; however, the magnitude of the peak is much larger. This suggests that the LES predicts a much stronger influence from the tip vortices. In fact, the secondary and tertiary local peaks observed in the computations with the fixed inflow model are due to the tip vortices from the upstream blades. Their influence persists even upon time-average and remains strong. In contrast, the RANS simulation appears to capture only the effect of the primary vortex pair. This clearly indicates that careful attention must be paid to accurate modeling of the impeller-induced flow. The fixed inflow model captures the effect of tip-vortices qualitatively, however, it appears to overpredict their influence.

5.2 Oscillatory Inflow Model. As described in Section 4.3, an improvement over the fixed inflow model can be obtained by allowing the jet flow component of the impeller-induced flow to oscillate at the blade-tip location. Here the motivation is that the inherent unsteady oscillation of the jet, observed even in the fixed inflow model, would propagate around the tank and feedback to the impeller-induced flow. Thus an oscillatory nature of the impeller-induced flow is fully consistent with its subsequent evolution. Admittedly, this feed back mechanism can be influenced by the assumption of periodicity over a 60 deg sector. Also this feedback mechanism can be quite complex and the nature of impeller-induced flow may be more complicated than a simple sinusoidal oscillation. The present model attempts to incorporate time-dependence of the impeller-induced flow in the simplest possible way, guided in part by the experimental observation, [17,28]. More complete validation of the model requires further experimental verification. In spite of its simplicity, it can be seen below, that the oscillatory inflow model provides substantially improved comparison with the experimental measurements.

Large eddy simulation with the oscillatory inflow model evolves qualitatively similar to the fixed inflow model. Figures 5(*e*) and 5(*f*) show contours of radial velocity on the r-z plane close to the impeller at two different time instances separated by one nondimensional time unit for the 20 deg oscillatory model and thus can be compared with the corresponding plots for the fixed inflow model shown in frames (*a*) and (*b*). The flow field is qualitatively similar and the presence of primary, secondary and tertiary tip-vortex pairs and their influence on the instability of the jet can be observed. The only significant difference is in the long wavelength flapping of the jet, which appears to have strengthened, due to the oscillatory nature of the jet component at inflow.

Figures 9(*a*) and 9(*b*) show the time and θ-averaged radial velocity and vorticity fields on the r-z plane for the dynamic LES with the 20 deg oscillatory inflow model, which can be compared with the corresponding results for the fixed inflow LES and RANS

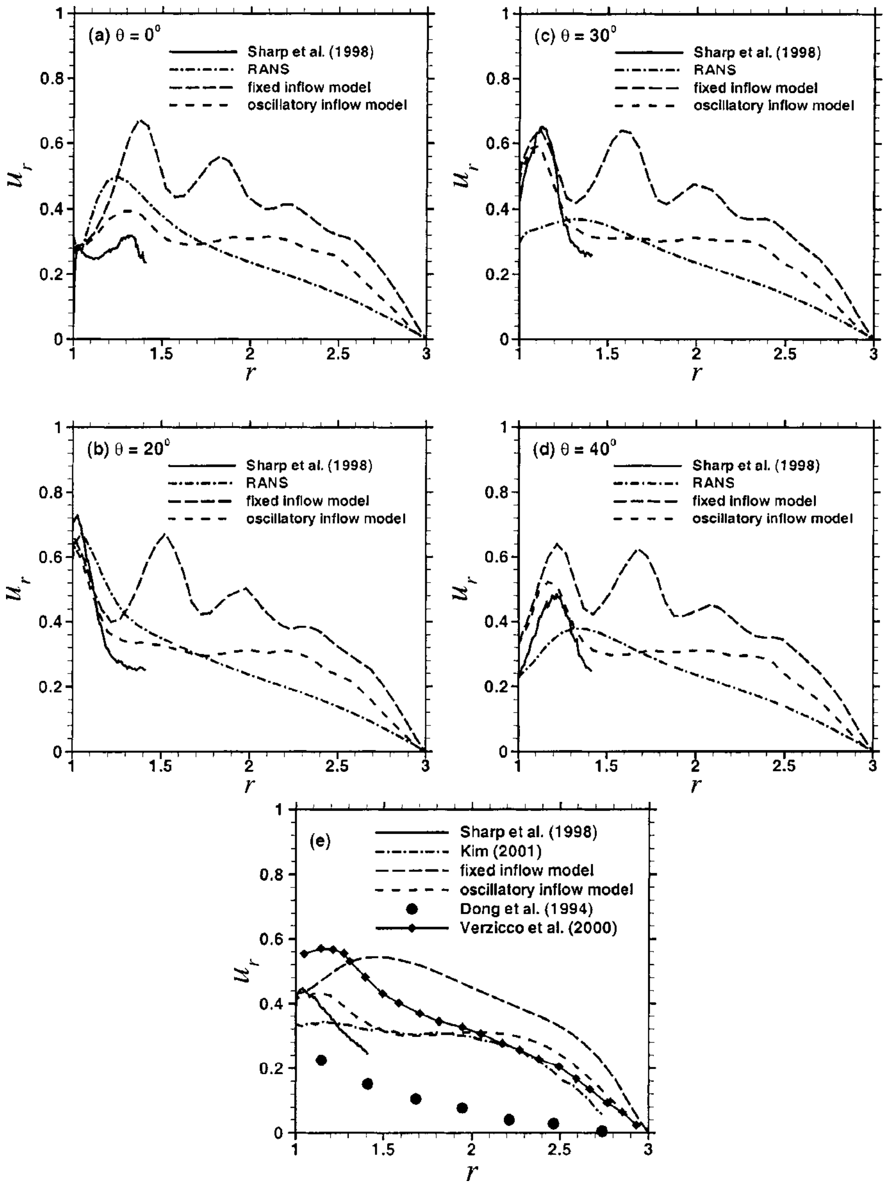

Fig. 8 The time-averaged nondimensional radial velocity as a function of the nondimensional radial distance from the blade tip ($r=1$) to the outer tank wall ($r=3$) along the midplane ($z=0$) at four selected azimuthal locations: (*a*) $\theta=0$ deg, (*b*) 20 deg, (*c*) 30 deg, and (*d*) 40 deg. The LES results of the fixed and oscillatory inflow models are compared with those of RANS and the corresponding experimental measurements by Sharp et al. [17]. Frame (*e*) compares the time and θ-averaged radial velocity from the fixed and oscillatory inflow LES simulations with those of Sharp et al. [17], Kim [28], Dong et al. [3], and Verzicco et al. [30].

shown in Fig. 7. Compared to the fixed inflow, the oscillatory inflow results in a broader mean jet, which results in a reduction in the peak radial as well as circumferential vorticity. This difference is primarily localized close to the midplane of the tank. Over the bulk of the tank, away from the midplane, the flow predicted by the fixed and 20 deg oscillatory models are very similar.

The radial velocity profiles for the 20 deg oscillatory inflow LES are also shown in Fig. 8. The comparison with the experimental result is good. In particular, not only the location of the peak radial velocity, but also the magnitude of the peak is well computed. As in the case of the fixed inflow model, apart from the primary peak, additional local peaks in the radial velocity can be observed. The weaker secondary and tertiary peaks in the radial velocity profile are due to the presence of tip vortices arising from the upstream impeller blades. The effect of the tip-vortex system on the time-averaged radial velocity is far weaker in the case of oscillatory inflow. This reduction in their influence is primarily due to the enhanced up and down wandering of the tip vortices in the case of oscillatory inflow. The peak in the radial velocity profile at $\theta=0$ deg is due to the previous blade located at $\theta=-60$ deg and this peak can be observed in the experimental data as well.

Figure 8(*e*) compares the time and θ-averaged radial velocity along the midplane obtained from the fixed and 20 deg oscillatory large eddy simulations with: (a) the experimental results of Sharp et al. [17] taken over the limited radial range of $1.0<r<1.4$; (b) the PIV measurements of Kim [28] in a stirred tank geometrically similar to the present investigation at a higher Re_m of 6960; and (c) the LDA measurements of Dong et al. [3] in a tank of diameter four times the impeller diameter at $\mathrm{Re}_m=3273$. It must be pointed out that a wealth of velocity measurement exists in the interior of

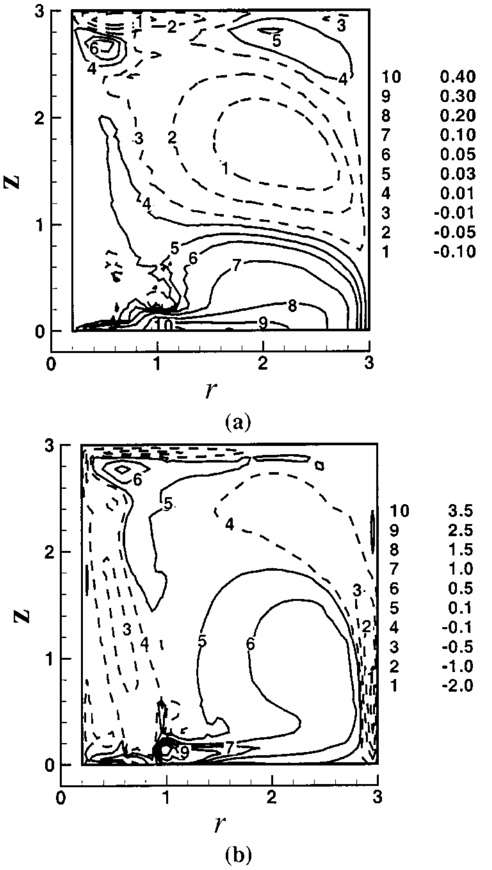

Fig. 9 The contours of the time and θ-averaged nondimensional (*a*) radial velocity and (*b*) vorticity contours from the dynamic large eddy simulation with 20 deg oscillatory inflow model

the stirred tank. The above ones are chosen as they are in an unbaffled tank and better compare with the present computational condition. The oscillatory inflow model better compares with the experimental results of Sharp et al. [17] in terms of the location and magnitude of the primary peak. The measurement of Kim [28] is not adequately resolved near the blade tip, however, satisfactory comparison with the 20 deg oscillatory model can be seen for $r > 1.5$. The present results are consistently higher than the experimentally measured mean radial velocity of Dong et al. [3], over the entire radius range. Apart from the lower Re, Dong et al. [3] used an impeller with eight blades and a relatively larger tank. It can be conjectured that the radial velocity of the resulting jet is much weaker than the present configuration and as a result the persistent difference over the entire tank. It must also be pointed out that the recent LES simulations of Verzicco et al. [30] and the different RANS simulations of Jones et al. [31] performed under conditions similar to the experiments of Dong et al. [3] predict radial velocity significantly larger than those measured by Dong et al. [3] in better comparison with the present simulation results.

5.3 Tip-Vortex Pairs. Here we focus on the vortical nature of the flow within the tank, with particular attention to the presence of the tip-vortex system. Vortex structures will be identified by plotting an isosurface of swirling strength, which is defined as the imaginary portion of the complex eigenvalue of the velocity gradient tensor (see Zhou et al. [32] for the suitability of this quantity in identifying vortices). Swirling strength will be taken to be zero in regions where the eigenvalues are real, indicating lack of vortical motion. Vortex structure thus obtained for the 20 deg oscillatory inflow model at one instance in time is shown in Fig. 10. A perspective view covering the 60 deg sector close to the impeller is shown in frame (*a*) and the corresponding top view of the three-dimensional structure is presented in frame (*b*). In addition to the primary pair (marked **v1**), a secondary and a weaker tertiary vortex pair (marked **v2** and **v3**) can also be seen located radially away from the blade tip. Note that the secondary vortex pair is from the upstream blade and the tertiary pair is from the blade further upstream. The presence of secondary and tertiary vortex pair suggests longterm integrity of the tip-vortex pair. The top and the bottom tip vortices of the pair are of comparable strength. They are nearly symmetric about the midplane close to the impeller swept volume, however, asymmetry naturally sets in as they develop downstream. Vortex structure at other time instances is qualitatively similar. While the primary vortex appears to remain intact and relatively time-independent, the vortex system as it extends away from the blade undergoes strong time-dependence in both its strength and position.

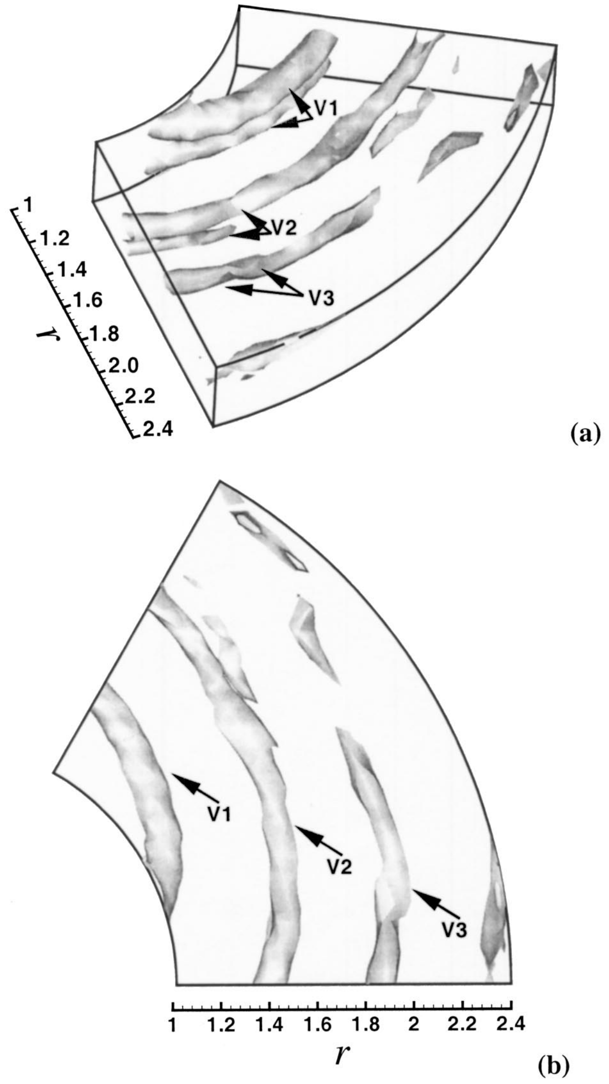

Fig. 10 Tip vortex structure obtained for the θ=20 deg oscillatory inflow model at one instance in time (*a*) perspective view covering the 60 deg sector close to the impeller, (*b*) top view of the three-dimensional structure projected onto a horizontal plane

The correspondence between the tip-vortex system and the sinuous/varicose behavior of the jet is evident. If the flow were to be maintained time-independent by enforcing the symmetry (13), the corresponding tip-vortex system is perfectly symmetric about the midplane and its effect on the jet will appear to be varicose in nature. Thus asymmetry about the midplane is likely to arise from the inherent dominant sinuous instability of the jet. The sinuous

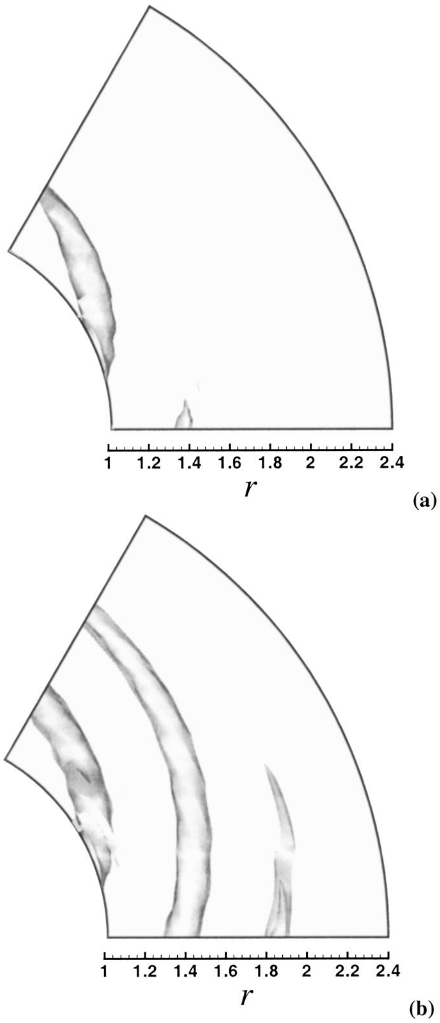

Fig. 11 Top view of the long time-averaged three-dimensional tip vortex structure obtained for the (*a*) 20 deg oscillatory and (*b*) fixed inflow models

instability by breaking symmetry about $z=0$ is the root cause of time-dependence of the flow and introduces time-dependent asymmetry in the tip-vortex system as well. While the heel of the tip-vortex pair is well anchored at the impeller swept volume around $\theta=15$ deg, the vortex tail that extends into the tank oscillates (wags) over time.

The extent of tip vortex oscillation in the interior of the tank can be established by comparing the above instantaneous picture with the corresponding time-averaged view. The difference between the two will be minimal if the tip vortex system is relatively fixed over time, for otherwise, the signature of the tip vortex system will broaden and weaken upon time average. The top view of the time-averaged three-dimensional vortex structure for the 20 deg oscillatory inflow model is shown in Fig. 11(*a*) and the corresponding result for the fixed inflow LES is shown in Fig. 11(*b*). As expected, owing to the time-dependent jitter in the position of the tip vortices, the time-averaged vortex structure appears to decay much faster as it extends into the tank when compared to the instantaneous vortex system. This decay is more rapid for the 20 deg oscillatory inflow model than for the fixed inflow model.

The time-averaged trajectory of the tip-vortex is shown on the r-θ plane in Fig. 12. Also shown are the tip-vortex trajectories measured by van't Riet et al. [11], Sharp et al. [17], and Yianneskis et al. [12]. In the present computations the imprint of the tip-vortex pair is forced at the surface of the impeller swept volume as the inflow condition. The trajectory of the vortex in the interior of the tank compares very well, especially with the experimental measurements of Sharp et al. [17] and Yianneskis et al. [12]. The imprint of the tip vortices can also be seen in the radial and circumferential velocities. In Figs. 13(*a*) and 13(*b*), contours of the time-averaged radial and circumferential velocities are plotted on the r-θ plane at the midplane of the tank. The sense of rotation of the tip-vortex pair is to clearly increase the radial component of velocity. In the rotating frame of reference the effect of the tip-vortex pair appears as a local reduction in the circumferential component of velocity. In the laboratory frame of reference, this will correspond to a local increase in the circumferential velocity (measured in the direction of blade rotation).

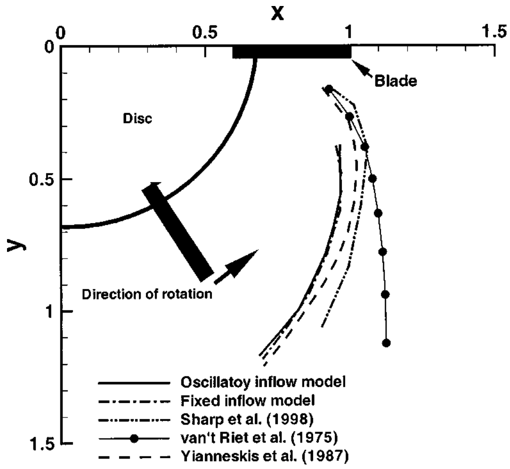

Fig. 12 The top view of the time-averaged backbone of the three-dimensional tip vortex pair projected onto a horizontal plane. The results of the fixed and 20 deg oscillatory model LES are compared with the experimental measurements.

5.4 Dissipation. Dissipation is a quantity of importance in a stirred tank since it provides a direct measure of energy input into the system at the impeller. The efficiency of mixing can then be gauged by evaluating the degree of mixing in relation to total dissipation. In the context of LES, in addition to the resolved scale dissipation, which accounts for the direct loss of energy from the resolved scales to dissipation, there is also subgrid scale dissipation, which accounts for the net transfer of energy from the resolved scales to the subgrid scale and eventually to heat. The resolved scale dissipation in nondimensional form is given by

$$\varepsilon_{\text{res}}=\frac{2}{\text{Re}}\overline{S}_{ij}\overline{S}_{ij}. \tag{14}$$

The corresponding subgrid dissipation in nondimensional form is given by

$$\varepsilon_{\text{sgs}}=-\tau_{ij}^{a}\overline{S}_{ij}. \tag{15}$$

Upon substituting for the subgrid scale stress from Eq. (3) we can see that the ratio of the subgrid to resolved scale dissipation is given by

$$\frac{\varepsilon_{\text{sgs}}}{\varepsilon_{\text{res}}}=\frac{\nu_T}{(1/\text{Re})}. \tag{16}$$

Time histories of volume-averaged ε_{res} and ε_{sgs} are shown in Figs. 14(*a*) and 14(*b*), respectively, for the fixed and oscillatory inflow models. The time and volume-averaged ε_{res} and ε_{sgs} for the fixed inflow model in nondimensional units are 0.0023 and 0.026, while for the oscillatory inflow model they are 0.0022 and 0.025. Dimensional dissipation scales as D^3N^2 and for the present experimental condition of a 50 mm impeller rotating at 1.667 rps the scaling factor for dissipation is $3.47\times10^{-4}\,\text{m}^3/\text{s}^2$. From (16) it

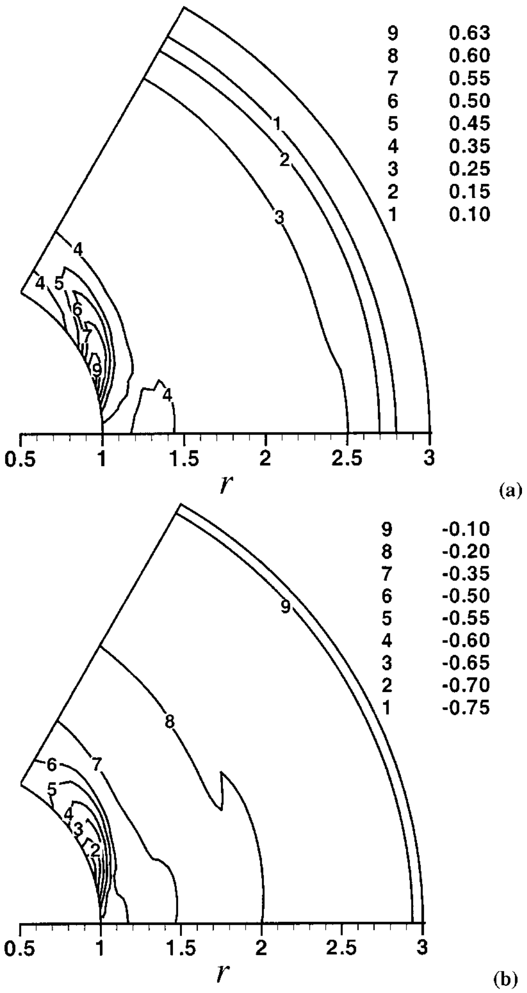

Fig. 13 The contours of time-averaged nondimensional (*a*) radial and (*b*) circumferential velocities on the $z=0$ midplane for the 20 deg oscillatory inflow model

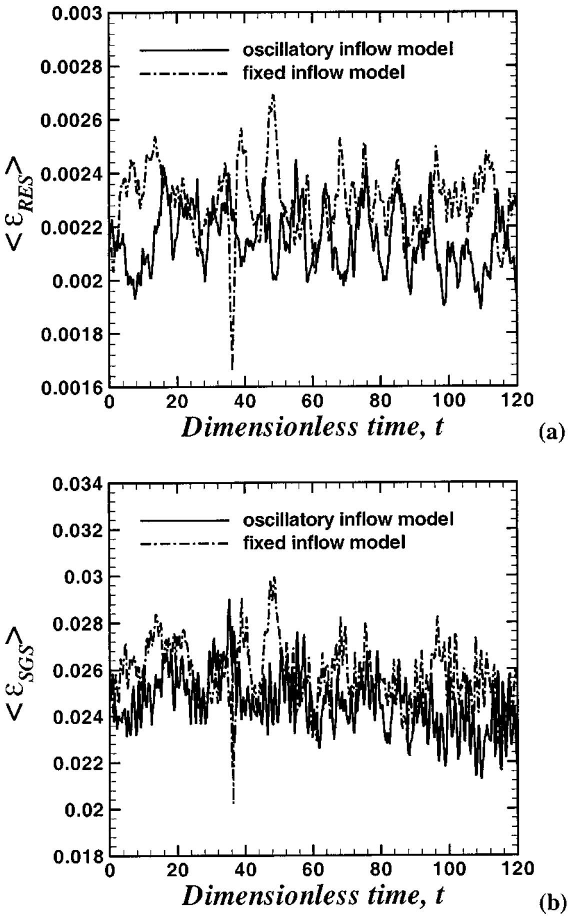

Fig. 14 The time histories of nondimensional volume-averaged (*a*) resolved scale dissipation (ε_{res}), (*b*) subgrid scale dissipation (ε_{sgs}) for the fixed and 20 deg oscillatory inflow models

can be seen that the volume-averaged nondimensional eddy viscosity, ν_T, is about a factor of 10 larger than the nondimensional molecular viscosity of $2\nu/\pi ND^2=1/\text{Re}=1.59\times10^{-4}$. Thus the unresolved small scales account for substantial dissipation. Owing to its spatial variation, the eddy viscosity is likely to be even larger locally. Figure 15 shows the ratio of time and r-z plane averaged ε_{res} and ε_{sgs} as a function of theta. The behavior of fixed and oscillatory models can be observed to be similar with the ratio peaking to a value of about 16 at around $\theta=15$ deg. This could possibly be the effect of the tip-vortex pair, since it is at its peak strength around this circumferential location.

Figure 16(*a*) shows the distribution of time and θ-averaged subgrid scale dissipation for the 20 deg oscillatory model over the entire r-z plane. The dissipation is focused along the shear layers associated with the jet near the midplane of the tank. The enhanced strain field associated with the stagnation point flow also contributes to dissipation. The result for the fixed inflow model is qualitatively similar. Differences begin to emerge only in the neighborhood of the impeller; the time and θ-averaged subgrid scale dissipation in this region for the fixed and oscillatory model are shown in Figs. 16(*b*) and 16(*c*). In the case of the fixed inflow model, the peak dissipation can be observed to occur in the strong shear regions of the focused jet, slightly away on either side of the midplane. In the oscillatory model, however, the location of the shear layers oscillate over time and as a result the peak dissipation occurs along the midplane, thus differently influencing the downstream evolution of jet. But for this subtle difference the behavior of the fixed and oscillatory inflow models are quite similar. The distribution of resolved scale dissipation looks qualitatively similar, but is of a smaller magnitude, and therefore not shown here.

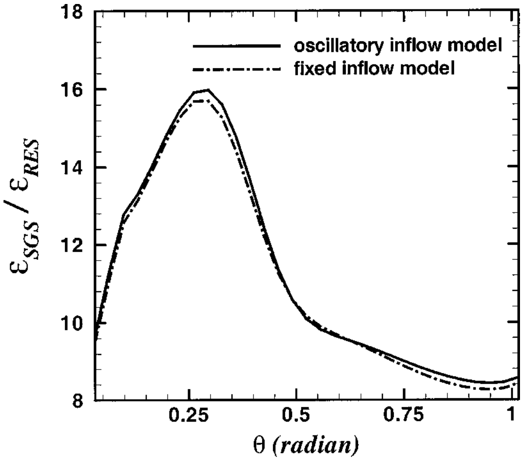

Fig. 15 The ratio of time and r-z plane-averaged nondimensional resolved scale dissipation (ε_{res}) and subgrid scale dissipation (ε_{sgs}) as a function of θ for the fixed and 20 deg oscillatory inflow models

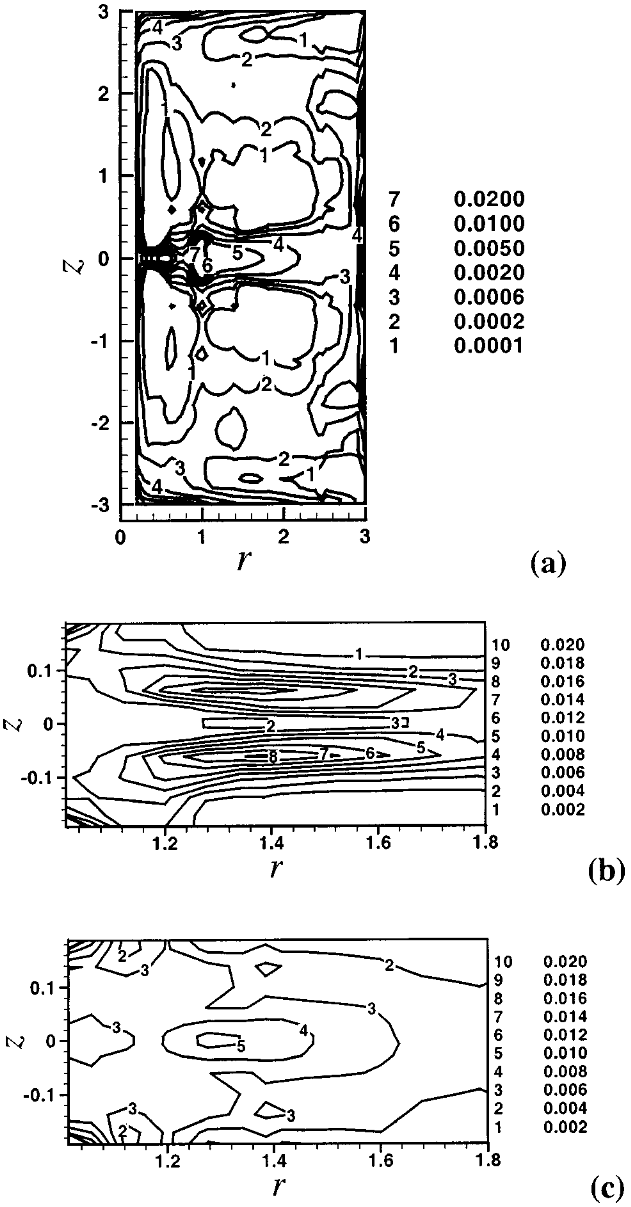

Fig. 16 (*a*) **The distribution of time and θ-averaged nondimensional subgrid scale dissipation for the 20 deg oscillatory model over the entire r-z plane, (*b*) the distribution of time and θ-averaged nondimensional subgrid scale dissipation in the region close to the blade tip for fixed inflow model and (*c*) for the 20 deg oscillatory model**

6 Conclusion

Large eddy and Reynolds-averaged Navier-Stokes simulations of flow in a stirred tank have been performed, with the measurement of the impeller-induced flow applied as inflow in the computations. The stereoscopic PIV measurements provide detailed information on all three components of velocity on the cylindrical surface surrounding the impeller swept volume. The phase-averaged measurements show that the impeller-induced flow needs to be represented as a superposition of circumferential, jet and tip-vortex components. Here we employ the theoretical model of the impeller-induced flow developed in Yoon et al. [14] to extract the computational inflow condition from the experimental measurements.

The inclusion of the tip-vortex pairs in the theoretical model of the impeller-induced flow is important since it accounts for the θ-dependence (three-dimensionality). Two-dimensional simulations that account for only the circumferential and jet flow components of the impeller-induced inflow, thus fail to capture the influence of tip-vortex pairs. The effect of this approximation on the flow is clearly illustrated in the radial distribution of time and θ-averaged radial velocity along the midplane of the tank ($z = 0$). In the absence of tip-vortex influence the computed radial velocity profile peaks at the blade tip radius and monotonically decreases as r increases towards the outer wall. However, the experimental measurements on the r-z plane at varying θ locations show that the peak radial velocity occurs at radial locations larger than the blade tip. Simulations that account for the tip-vortex presence are able to capture this behavior.

At $Re_m = 4000$ considered here, even with a time-independent impeller-induced flow enforced as inflow on the LES (fixed inflow model), the flow in the interior of the tank naturally evolves to a time-dependent turbulent state. The jet component of the impeller-induced flow becomes unstable and shows signs of both sinuous and varicose behavior. The instability of the jet is intimately connected with the tip-vortex system. Instantaneous visualizations of the tip-vortex pairs show that the vortex pairs remain coherent and extend substantially away from the blade into the interior of the tank. On any r-z plane three or more vortex pairs can be observed, with the one closest to the blade tip ($r = 1$) originating from the blade immediately upstream located at $\theta = 0$, and the subsequent ones at larger r corresponding to previous vortex pairs originating from further upstream blades. Due to the rotation of the blades, individual vortex pairs are curved backwards and extend up to about 200 deg. While the vortex pairs are well anchored near the blades, as they extend outwards into the tank their backbone oscillates. From the present simulations it is hard to pinpoint whether the breakdown of the tip-vortex pair is the cause of jet instability or the oscillation in the tip-vortex trajectory is dictated by the jet instability. It is suffice to say that the jet component and the tip-vortex system interact strongly. The time-averaged location of the vortex backbone compares well with previous measurements.

Comparison of the radial velocity profile with the experimental data shows that with the fixed inflow model the jet remains reasonably focused and the effect of the tip-vortex pairs remain strong even upon time-average. This suggests that with the fixed inflow the influence of the tip-vortex system is overpredicted. Careful examination of the experimental data, [17], indicates that the jet component even as it exists the impeller oscillates up and down about the midplane over time. Such undulation will clearly increase the axial spreading of the jet and furthermore amplify the time-dependent wandering of the vortex backbone, thereby somewhat decreasing their influence on the time-averaged flow. Based on such reasoning an oscillatory impeller-induced inflow model was developed where the jet component sinusoidally oscillates about the midplane. Varying amplitudes and frequency of oscillation were considered. A comparison of the time-averaged radial velocity profile along the midplane at varying circumferential locations obtained from the LES with the corresponding experimental measurements shows that the LES with the 20 deg oscillatory inflow model is able to reproduce the experimental result reasonably. However, over the bulk of the tank, away from the midplane, the results for the fixed and oscillatory inflow model are comparable. The above results illustrate the importance of accurate representation of the impeller-induced inflow in the large eddy simulation, especially for extending the present work for higher Reynolds numbers and for other geometries. The effect of the impeller must either be directly simulated accurately, accounting for all the geometric complexities, or accurately modeled based on experimental measurements.

Acknowledgments

This work was supported by a grant from National Science Foundation (CTS-9910543) and a gift from the Dow Chemical

Company. We thank Profs. R. J. Adrian, K. C. Kim, D. F. Hill, and K. V. Sharp for making the experimental results available for appropriate comparison.

References

[1] Middleton, J. C., Pierce, F., and Lynch, P. M., 1986, ''Computations of Flow Fields and Complex Reaction Yield in Turbulent Stirred Reactors, and Comparison With Experimental Data,'' Chem. Eng. Res. Des., **64**, pp. 18–22.

[2] Ranade, V. V., Joshi, J. B., and Marathe, A. G., 1989, ''Flow Generated by Pitched Blade Turbines II: Simulation Using k-e Model,'' Chem. Eng., Commun. **81**, pp. 225–248.

[3] Dong, L., Johansen, S. T., and Engh, T. A., 1994, ''Flow Induced by an Impeller in an Unbaffled Tank—II: Numerical Modeling,'' Chem. Eng. Sci., **49**, pp. 3511–3518.

[4] Gosman, A. D., Lekakou, C., Politis, S., Issa, R. I., and Looney, M. K., 1992, ''Multidimensional Modeling of Turbulent Two-Phase Flows in Stirred Vessels,'' AIChE J., **38**, pp. 1946–1956.

[5] Ju, S. Y., Mulvahill, T. M., and Pike, R. W., 1990, ''Three-Dimensional Turbulent Flow in Agitated Vessels With a Nonisotropic Viscosity Turbulent Model,'' Can. J. Chem. Eng., **68**, p. 3.

[6] Eggels, J. M. G., 1996, ''Direct and Large Eddy Simulation of Turbulent Fluid Flow Using the Lattice-Boltzmann Scheme,'' Int. J. Heat Fluid Flow, **17**, pp. 307–323.

[7] Revstedt, J., Fuchs, L., and Tragardh, C., 1998, ''Large Eddy Simulation of the Turbulent Flow in a Stirred Reactor,'' Chem. Eng. Sci., **53**, pp. 4041–4053.

[8] Luo, J. V., Gosman, A. D., Issa, R. I., Middleton, J. C., and Fitzgerald, M. K., 1993, ''Full Flowfield Computation of Mixing in Baffled Stirred Reactors,'' Trans. Inst. Chem. Eng., **71** Part A, pp. 342–344.

[9] Lee, K. C., Ng, K., and Yianneskis, M., 1996, ''Sliding Mesh Predictions of the Flow Around Rushton Impeller,'' ICHEME Symp. Ser., **140**, pp. 47–58.

[10] Pericleous, K. A., and Patel, M. K., 1987, ''The Source-Sink Approach in the Modeling of Stirred Reactors,'' PhysioChem. Hydrody., **9**, pp. 279–297.

[11] Van't Riet, K., and Smith, J. M., 1975, ''The Trailing Vortex System Produced by Rushton Turbine Agitators,'' Chem. Eng. Sci., **30**, p. 1093.

[12] Yianneskis, M., Popiolek, Z., and Whitelaw, J. H., 1987, ''An Experimental Study of the Steady and Unsteady Flow Characteristics of Stirred Reactors,'' J. Fluid Mech., **175**, p. 537.

[13] Calabrese, R. V., and Stoots, C. M., 1989, ''Flow in the Impeller Region of a Stirred Tank,'' Chem. Eng. Prog., **85**, pp. 43–50.

[14] Yoon, H. S., Sharp, K. V., Hill, D. F., Adrian, R. J., Balachandar, S., Ha, M. Y., and Kar, K., 2001, ''Integrated Experimental and Computational Approach to Simulation of Flow in a Stirred Tank,'' Chem. Eng. Sci., to be published.

[15] Rao, M. A., and Brodkey, R. S., 1972, ''Continuous Flow Stirred Tank Turbulence Parameters in the Impeller Stream,'' Chem. Eng. Sci., **27**, pp. 137–156.

[16] Wu, H., and Patterson, G. K., 1989, ''Laser Doppler Measurements of Turbulent Flow Parameters in a Stirred Mixer,'' Chem. Eng. Sci., **44**, pp. 2207–2221.

[17] Sharp, K. V., Kim, K. S., and Adrian, R. J., 1998, ''A Study of Vorticity and Dissipation Around a Rushton Turbine Using Particle Image Velocimetry,'' *Proc. 9th Int'l Symp. Applications Lasers to Fluid Mechanics*, Lisbon, July 13–16, VKI Publications, Belgium, pp. 14.1.1–10.

[18] Hill, D. F., Sharp, K. V., and Adrian, R. J., 2000, ''Stereoscopic Particle Image Velocimetry Measurements of the Flow Around a Rushton Turbine,'' Exp. Fluids, **29**, pp. 478–485.

[19] Smagorinski, J., 1963, ''General Circulation Experiments With the Primitive Equations. I. The Basic Experiment,'' Mon. Weather Rev., **91**, p. 99.

[20] Germano, M., Piomelli, U., Moin, P., and Cabot, W. H., 1991, ''A Dynamic Subgrid-Scale Eddy Viscosity Model,'' Phys. Fluids A, **A3**, pp. 1760–1765.

[21] Mason, P. J., and Callen, N. S., 1986, ''On the Magnitude of the Subgrid-Scale Eddy Coefficient in Large-Eddy Simulations of Turbulent Channel Flow,'' J. Fluid Mech., **162**, pp. 439–462.

[22] Canuto, C., Hussaini, M. Y., Quarteroni, A., and Zang, T. A. 1988, *Spectral Methods in Fluid Dynamics*, Springer-Verlag, New York.

[23] Kolar, V., Filip, P., and Curev, A. G., 1982, ''The Swirling Radial Jet,'' Appl. Sci. Res., **39**, pp. 329–335.

[24] Kolar, V., Filip, P., and Curev, A. G., 1984, ''Hydrodynamics of a Radially Discharging Impeller Stream in Agitated Vessels,'' Chem. Eng. Commun., **27**, pp. 313–326.

[25] Kresta, S. M., and Wood, P. E., 1991, ''Prediction of the Three-Dimensional Turbulent Flow in Stirred Tanks,'' AIChE J., **37**, pp. 448–460.

[26] Roussinova, V. T., Grgic, B., and Kresta, S. M., 2000, ''Study of Macro-Instabilities in Stirred Tanks Using Velocity Decomposition Technique,'' Trans. Inst. Chem. Eng., **78**, pp. 1040–1052.

[27] Schafer, M., Yianneskis, M., Wachter, P., and Durst, F., 1998, ''Trailing Vortices Around a 45deg Pitched Blade Impeller,'' AIChE J., **44**, pp. 1233–1246.

[28] Kim, K. C., 2002, personal communication.

[29] Drazin, P. G., and Reid, W. H., 1981, *Hydrodynamic Stability*, Cambridge University Press, New York.

[30] Verzicco, R, Iaccarino, G., Fatica, M., and Orlandi, P., 2000, ''Flow in an Impeller Stirred Tank Using an Immersed Boundary Technique,'' *Ann. Res. Briefs*, Center for Turbulence Research, NASA Ames/Stanford University, pp. 251–261.

[31] Jones, R. M., Harvey, A. D., and Acharya, S., 2001, ''Two-Equation Turbulence Modeling for Impeller Stirred Tanks,'' ASME J. Fluids Eng., **123**, pp. 640–648.

[32] Zhou, J., Adrian, R. J., Balachandar, S., and Kendall, T. M., 1999, ''Mechanisms for Generating Coherent Packets of Hairpin Vortices in Near-Wall Turbulence,'' J. Fluid Mech., **387**, pp. 353–396.

Numerical Study of the Flow Around a Bus-Shaped Body

Siniša Krajnović
e-mail: sinisa@tfd.chalmers.se

Lars Davidson

Department of Thermo and Fluid Dynamics,
Chalmers University of Technology,
SE-41296 Gothenburg, Sweden

Flow around a simplified bus is analyzed using large-eddy simulation. At the Reynolds number of 0.21×10^6, based on the model height and the incoming velocity, the flow produces features and aerodynamic forces relevant for the higher (interesting in engineering) Reynolds number. A detailed survey of both instantaneous and time-averaged flows is made and a comparison with previous knowledge on similar flows is presented. Besides the coherent structures observed in experimental and previous numerical studies, new smaller-scale structures were registered here. The mechanisms of formation of flow structures are explained and the difference between instantaneous and time-averaged flow features found in the experimental observations is confirmed. Aerodynamic forces are computed and their time history is used to reveal the characteristic frequencies of the flow motion around the body. A comparison is made of pressure and velocity results with experimental data and shows fairly good agreement. [DOI: 10.1115/1.1567305]

1 Introduction

The time-averaged flow around cars is fairly well known and understood, [1]. In contrast, the instantaneous flow has until recently been unstudied and still remains unexplored. The aerodynamic properties of the vehicles, such as drag, lift, stability, wind noise, and the accumulation of water and dirt on the surface of vehicles are result of transient motions of the flow. Understanding of these processes could lead to better design of the aerodynamics and thus improved performance of vehicles. Thus Volvo Car Corporation is working together with Chalmers to develop an unsteady numerical method and to gain a deeper understanding of the unsteady flow around a car.

Shapes of real cars are too complex to be used for detailed flow studies in experiments and numerical simulations. Although these shapes are used in the automotive industry to determine global quantities such as drag or lift, they are not amenable to learning about the interaction of the flow features around the car responsible for its aerodynamic properties. Therefore engineers often study simplified car-like shapes, [2–5], that can produce flow similar to that around a real car.

Most studies of these flows were made only in the wake region and it was found that the wake consists of a near wake (separation bubble) and a pair of counterrotating longitudinal vortices. These longitudinal vortices were first visualized by Ahmed [6], who studied the wake structures behind three vehicle shapes with different rear-end geometries. Bearman et al. [2] studied time-averaged flow structures in the flow behind a simplified vehicle body shape and found that the longitudinal vortices are important features of the vehicle wakes. The same body was used in the study of the influence of the moving floor on aerodynamic forces and the near-wake flow, [7].

A near-wake region behind Ahmed's body, [3], with variable base slant angle (the angle between the roof and the rear face) was studied by Ahmed et al. [3]. They found that the time-averaged wake consists of a pair of horseshoe vortices, situated one above another in the separation bubble, and of trailing vortices coming off the slant side edges. Han [8] used Reynolds-averaged Navier-Stokes equations (RANS) to simulate the flow around the body from [3] and reported that the flow structures are in agreement with those found in experiments, [3]. The computed pressure at the rear vertical face of the body was (for a base slant angle smaller than 20°) underpredicted, resulting in the computed drag being 30% higher than the measured drag, [1,8]. He also found that a flow at the slant angle of the body larger than 30° becomes highly unsteady and cannot be predicted using steady-state RANS simulations.

Duell and George [5,9] made measurements in the wake of a bus-like body based on Ahmed's body, [3], with a rear slant angle of 90°. They reported two periodic processes in the wake corresponding to the dimensionless frequencies at Strouhal numbers 0.069 and 1.16. The lower value was attributed to the periodic interaction of the upper and lower partitions of the ring vortex in the near wake. The higher value was found to be associated to the vortex shedding process in the shear layer. The flow around a similar body was measured by Barlow et al. [4,10] who studied the influence of the aspect ratio (model width/model height) on the aerodynamic forces.

Bearman [11] presented velocity measurements of the wake of a car model. Although he reported a pair of time-averaged counterrotating vortices similar to those found in [6] and [2], he showed that these vortices are formed by a substantial number of instantaneous vortex structures that move randomly in time and space. He thus raised the question of whether the wake flow behind a car can be accurately simulated using RANS equations.

Some early attempts to use transient simulations for this kind of flow are presented in [12–14]. Although the authors of these papers denoted their simulations direct numerical simulations (DNS), [12,13], or large-eddy simulation (LES), [14], we would classify these simulations as very unresolved LES and thus the accuracy of predicted flows is doubtful.

This paper aims to present a LES of the flow studied in [9] and [5]. Being a three-dimensional time-dependent technique, LES should be better suited for this unsteady flow than RANS. It has already been applied to various bluff body flows, [15–17] where it proved to be successful. Our intention is to gain a good understanding of the instantaneous and time-averaged flows around this body. This paper presents not only the drag and lift coefficients that describe the aerodynamic properties of the body, but also the flow structures responsible for these properties.

The paper is organized as follows. Section 2 presents the LES equations and the model representing the influence of the small turbulence scales on the large resolved ones. The numerical method used in this work is summarized in Section 3. Section 4 describes the body, the computational domain, and the boundary conditions used in the simulations and compares them with the ones used in the experiment, [9,5]. Section 5.1 presents the time-averaged and instantaneous flow around the body that resulted

---

Contributed by the Fluids Engineering Division for publication in the JOURNAL OF FLUIDS ENGINEERING. Manuscript received by the Fluids Engineering Division April 9, 2002; revised manuscript received October 30, 2002. Associate Editor: J. Marshall.

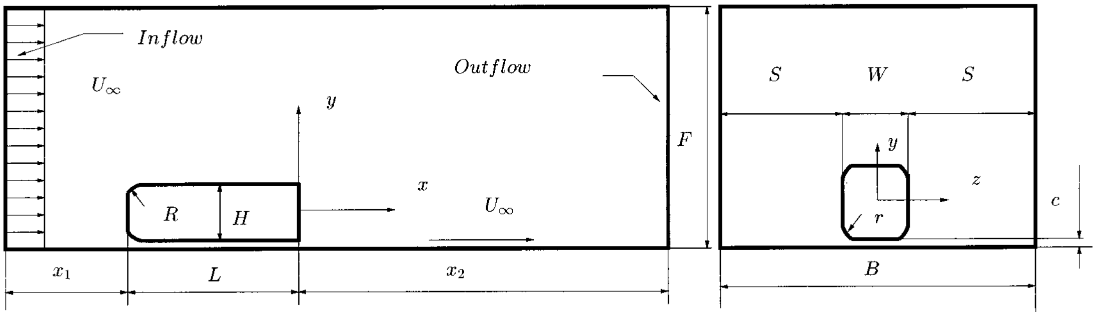

Fig. 1 Geometry of the vehicle body and computational domain

from the simulations and compares them with previous knowledge of this flow. The influence of the flow on the body through the aerodynamic forces is considered in Section 5.2. Section 5.3 presents a comparison of the velocity field in the near wake from the simulations with the one from hot-wire measurements [5,9]. The numerical accuracy is discussed in Section 6. Finally, some concluding remarks are made in Section 7 and some problems with the simulations are discussed.

2 Governing Equations and Subgrid-Scale Modeling

The governing large-eddy simulation (LES) equations are the filtered incompressible Navier-Stokes and the continuity equations filtered with the spatial filter of characteristic width Δ (Δ is the grid resolution in this work):

$$\frac{\partial \overline{u_i}}{\partial t}+\frac{\partial}{\partial x_j}\left(\overline{\overline{u_i}\,\overline{u_j}}\right)=-\frac{1}{\rho}\frac{\partial \overline{p}}{\partial x_i}+\nu\frac{\partial^2 \overline{u_i}}{\partial x_j \partial x_j}-\frac{\partial \tau_{ij}}{\partial x_j} \tag{1}$$

and

$$\frac{\partial \overline{u_i}}{\partial x_i}=0. \tag{2}$$

Here, $\overline{u_i}$ and $\overline{p_i}$ are the resolved velocity and pressure, respectively, and the bar over the variable denotes filtering.

These equations are derived applying a filtering operation

$$\overline{f}(x_i)=\int_\Omega f(x_i')G(x_i,x_i')dx_i' \tag{3}$$

on the Navier-Stokes and the continuity equations, [18]. Here G is a top hat filter function and Ω represents the entire flow domain. The filtered variables in the governing Eqs. (1) and (2) are obtained implicitly through the spatial discretization.

The derivation of Eqs. (1) and (2) from the Navier-Stokes equations, the continuity equation and Eq. (3) requires that the differentiation operations commute with the filtering operator, i.e.,

$$\overline{\frac{\partial f}{\partial x_i}}=\frac{\partial \overline{f}}{\partial x_i}. \tag{4}$$

The commutation property in Eq. (4) is valid if the filter width Δ is constant. However, a variable filter width is used in inhomogeneous flow (including the flow studied in this paper). That results in a violation of Eq. (4). An analysis of the commutation error, [19], shows that the error is of order $\mathcal{O}(\Delta^2)$, and it is thus in this work of the same order as the discretization error.

The goal of the filtering is to decompose the fluid motion into a large-scale component that can be computed exactly and the small subgrid scale (SGS). The influence of the small scales of the turbulence on the large energy carrying scales in Eq. (1) appears in the SGS stress tensor, $\tau_{ij}=\overline{u_i u_j}-\overline{u_i}\,\overline{u_j}$, which must be modeled. A large number of models for the SGS stress tensor have been proposed in the past four decades (see [20] for a review), most of them built on the algebraic eddy viscosity model originally proposed by Smagorinsky [21]. Although the original Smagorinsky model has some drawbacks, [20], it is used in this paper for its simplicity and low computational cost. The Smagorinsky model represents the anisotropic part of the SGS stress tensor, τ_{ij}, as

$$\tau_{ij}-\frac{1}{3}\delta_{ij}\tau_{kk}=-2\nu_{\mathrm{sgs}}\overline{S}_{ij} \tag{5}$$

where $\nu_{\mathrm{sgs}}=(C_s\Delta)^2|\overline{S}|$ is the SGS viscosity,

$$\overline{S}_{ij}=\frac{1}{2}\left(\frac{\partial \overline{u_i}}{\partial x_j}+\frac{\partial \overline{u_j}}{\partial x_i}\right) \tag{6}$$

is the resolved rate-of-strain tensor and $|\overline{S}|=(2\overline{S}_{ij}\overline{S}_{ij})^{1/2}$. The Smagorinsky constant, C_s, must be adjusted for different flows. The value of $C_s=0.1$ previously used for bluff-body flows, [15–17], is used in this work. This value of C_s is inappropriate in the laminar shear flows since the SGS stresses are zero here, and thus the Smagorinsky coefficient of $C_s=0$ should be used in this region, [22]. The formation of a turbulent boundary layer in the experiment was ensured with boundary layer trip wires mounted at the front of the model. Because of this there is no laminar boundary layer on the body and the assumption of nonzero SGS stresses (i.e., $C_s=0.1$) used in our LES is thus correct. The filter width, Δ, is defined in this work as $\Delta=(\Delta_1\Delta_2\Delta_3)^{1/3}$, where Δ_i are the computational cell sizes in three coordinate directions.

3 Numerical Method

Large-eddy simulation (LES) Eqs. (1) and (2) are discretized using a three-dimensional finite volume method for solving the incompressible Navier-Stokes equations using a collocated grid arrangement, [23]. Both convective and viscous plus subgrid fluxes are approximated by central differences of second-order accuracy. The time integration is done using the Crank-Nicolson second-order scheme. The SIMPLEC algorithm is used for the pressure-velocity coupling. The code is parallelized using block decomposition and the PVM and MPI message passing systems, [24]. Additional details on this code can be found in [23] and [24].

4 Description of the Test Case and Numerical Details

A flow around a bus-shaped body studied in [9] and [5] was computed. The geometry of the computational domain is given in Fig. 1. All the geometric quantities are normalized with the body height, H, equal to 0.125 m. A domain with an upstream length of $x_1/H=8$, a downstream length of $x_2/H=21$, and a spanwise width of $B=5.92H$ was used for the simulation. Similar values for upstream and downstream lengths were found sufficient by Sohankar et al. [25] in large-eddy simulations (LES) of the flow around a square cylinder. Although experimental studies, [5,9], were carried out for several different aspect ratios (W/H), we chose $W/H=1$, for which the drag and lift data exist from another experiment, [4,10] using a similar body. The values of the other geometrical quantities are $L/H=3.68$, $S/H=2.46$, $R/H=0.152$,

$r/H = 0.1016$, and $F/H = 4$. As can be seen from the radii R/H and r/H the roundness of this model is exaggerated compared to full-scale bus. This is common practice in the experimental studies of reduced scale models, [1]. The ground clearance of $c/H = 0.08$ is similar to the clearance ratio of buses. The Reynolds number $\mathrm{Re} = U_\infty H/\nu$ was 0.21×10^6. As it will be shown later in the paper, the choice of such a low Reynolds number (low from vehicle aerodynamics perspective) will have some implications on the flow around the fore-body of the bus but the LES of the higher Reynolds number flow was not feasible at the time of this work.

In the experimental setup, the location of the front side relative to the inlet was $4.512H$ and the distance from the test section exit to the back wall perpendicular to the flow was $14.832H$. A moving ground belt and boundary layer scoop were used to simulate the floor boundary condition and to minimize boundary layer effects. The cross section of the tunnel test section, the ground clearance, and the position of the model's cross section with respect to the tunnel were identical in LES and the experimental setup.

In the experiments of Duell and George [5,9], the inlet mean velocity was uniform within 1% and the average turbulent intensity was 0.3%. A uniform velocity profile constant in time was thus used as the inlet boundary condition in this work. The convective boundary condition $\partial \overline{u}_i/\partial t + U_c\,(\partial \overline{u}_i/\partial x) = 0$ was used at the downstream boundary. Here, U_c was set equal to the incoming mean velocity, U_∞. To simulate the moving ground, the velocity of the lower wall was set equal to U_∞. The lateral surfaces were treated as slip surfaces using symmetry conditions, $\partial \overline{u}/\partial z = \partial \overline{v}/\partial z = \overline{w} = 0$. No-slip boundary conditions were used on the wall in fine and medium-grid simulations, while the wall functions based on the "instantaneous logarithmic law" are used in the coarse-grid simulation. The implementation of the wall functions in the coarse-grid simulation is as follows: The instantaneous logarithmic law of the form

$$\overline{u}^+ = \frac{\ln y^+}{0.4} + 5.2 \tag{7}$$

is used in the logarithmic region ($y^+ \geqslant 11.63$ where $y^+ = y\overline{u}_\tau/\nu$). Here, $\overline{u}^+ = \overline{u}/\overline{u}_\tau$ and the friction velocity is defined as $\overline{u}_\tau = (\tau_{\mathrm{wall}}/\rho)^{1/2}$. Point $y^+ = 11.63$ is defined as the intersection point between the near wall linear law and the logarithmic law. The linear law ($y^+ \leqslant 11.63$) is of the form

$$\overline{u}^+ = y^+. \tag{8}$$

The approximate boundary condition when $y^+ \geqslant 11.63$ is implemented in the code by adding the artificial viscosity, ν_{bc}, resulting from the approximate wall boundary condition (7) to the laminar viscosity on the wall. The friction velocity, $\overline{u}_\tau$, is first computed from (7). The wall shear stress is then modeled as

$$\tau_{\mathrm{wall}}/\rho \equiv \left(\nu \frac{\partial \overline{u}}{\partial y}\right)_{\mathrm{wall}} = \nu_{bc}\frac{\overline{u}}{y} \tag{9}$$

where τ_{wall} is the wall shear stress. The artificial viscosity is now determined from the definition of the friction velocity and Eq. (9) as

$$\nu_{bc} = \frac{\overline{u}_\tau^2 y}{\overline{u}} = \frac{\overline{u}_\tau y}{\overline{u}^+} \tag{10}$$

where $\overline{u}^+$ is obtained from (7). The homogeneous Neumann condition was used for the pressure at all boundaries.

To investigate the influence of the near-wall resolution on the results and to establish the results' grid independence, we made computations on three different computational grids. The topology of the grid consists of 24 (coarse and medium grids) and 40 (fine grid) blocks where 6 (coarse and medium grids) and 18 (fine grid) blocks form an O grid. An additional larger bus surface was made for the outer surface of the O grid. The O grid, with a thickness of $0.04H$, was created between this surface and the surface of the vehicle body (see Fig. 2). The total number of cells was 1.8, 2.1, and 4.5 million in the coarse, medium, and fine grids, respectively, resulting in the resolution presented in Table 1.

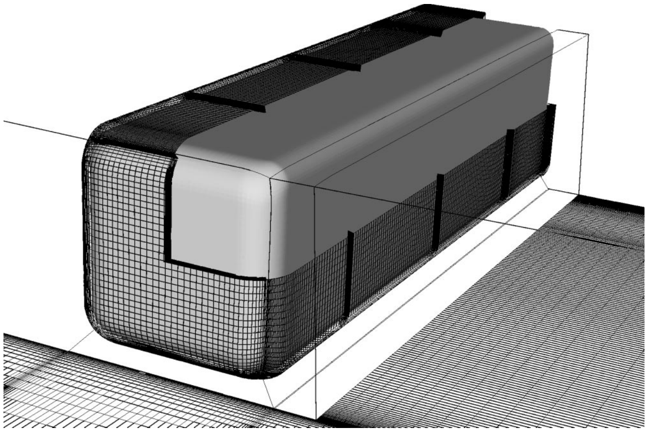

Fig. 2 The topology of the fine grid. Note that only *O* grid and few blocks around it are shown. One-fourth of the *O* grid is removed in this figure.

The time step was 2×10^{-4} in the coarse-grid simulation and 1×10^{-4} in the medium and fine-grid simulations, giving a maximal CFL number of approximately 6.5. The CFL number was smaller than one in 98% of the cells during the entire simulation. The averaging time, tU_∞/H, in the simulation was 94.4 (59,000 time steps), 48 (60,000 time steps), and 62.4 (78,000 time steps) in the coarse, medium, and fine-grid simulations, respectively. The time-averaged streamlines projected onto plane $y = 0$ downstream the bus were found to be approximately symmetric with respect to the plane $z = 0$ (not shown in the paper) which indicates that the number of averaging samples and the averaging times were sufficient.

5 Results and Discussion

5.1 Description of the Flow. As we will see in this section, the instantaneous coherent structures distinguish themselves from the time-averaged ones. Following the flow along and behind the body, we present these differences below and also fill in the information on the vortices that were not observed in the experiments. All results presented in this section are from the fine-grid computation unless otherwise stated.

Front-End Flow. Although the body has rounded leading edges, the flow separates at the front lateral and roof edges of the body (Figs. 3 and 4). The character of the leading-edge flow (i.e., attached or detached) is dependent of the leading-edge radii and the Reynolds number, [26]. As the Reynolds number is decreased, a more rounded leading edge is needed to avoid separation. The influence of the Reynolds number on the optimum radius (radius that eliminates the flow separation at the front edges) for the edge of a cubic bodies is discussed in [27] and [26]. For example,

Table 1 Spatial resolution expressed in the wall units (e.g., $\Delta s^+ = \Delta s \overline{u}_\tau/\nu$, where $\overline{u}_\tau$ is the friction velocity). *s* is the streamwise direction, *n* is the wall-normal direction, and *l* is the direction parallel with the surface of the body and normal to the streamwise direction. Values in parentheses are for the separation bubbles close to the front end. $\langle . \rangle_t$ denotes time averaging.

Case	$\langle \Delta s^+ \rangle_t$	$\langle \Delta n^+ \rangle_t$	$\langle \Delta l^+ \rangle_t$
Coarse	15–580	11.8–18.8	14–217
Medium	15–580 (30–500)	0.8–1.2 (0.5)	14–217 (21–224)
Fine	5–164 (44–153)	0.5–0.8 (0.3)	14–142 (21–100)

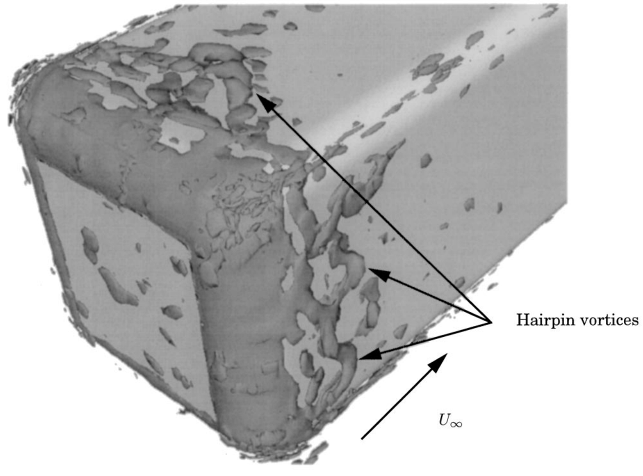

Fig. 3 The isosurface of the instantaneous second invariant of the velocity gradient, [35], $Q = 11000$

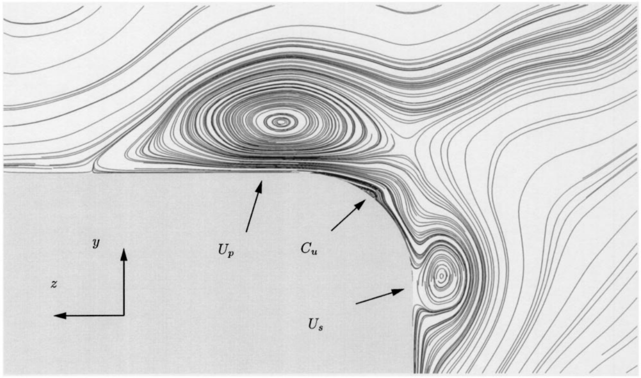

Fig. 5 Time-averaged streamlines projected onto plane $x = -0.8H$. The rotation of U_p and U_s is counterclockwise and clockwise, respectively. View from behind of the upper-right edge of the body.

Hucho et al. [27] found that these radii for $\mathrm{Re} < 10^6$ must be $r/H > 0.17$, [27], and applying Cooper's, [26], study to the present geometry, with $R/H = 0.152$ and $r/H = 0.102$, leads to $\mathrm{Re} > 0.8 \times 10^6$ and $\mathrm{Re} > 1.3 \times 10^6$, respectively, to avoid the separation. We thus conclude that the separated flow on the leading edge observed in our simulation is accurately predicted and in agreement with previous knowledge.

The contribution of the fore-body pressure drag to total drag of trucks and buses is small but the generation of the separation regions with recirculating flow close to the leading edges influences the wind generated noise and the accumulation of water and dirt on the surface of vehicle. Therefore the extrapolation of the results from the low-Reynolds study in this paper to high Reynolds number vehicles on the road is of interest. Unfortunately this is not a trivial task owing to the variation in the level of roundedness of the fore-body and the operating Reynolds number. For example for a city bus at operating Reynolds number of 2.2×10^6 (speed of 40 km/h and height of $H = 3$ meters), the leading edge radii must be larger than 0.15 meter ($r/H = 0.05$, [26]) to avoid separation. The radii on city buses are smaller than this value and the flow after the leading edges is probably detached. On the other hand there are busses and trucks operating on the highway where the fore-body is formed to maintain attached flow. We argue that although the flow is detached on leading edges of the vehicles at lower Reynolds number, the flow is probably attached (if the leading-edge radii are large enough) at higher Reynolds numbers when the aerodynamics is of greater importance. For additional details on the influence of the fore-body radii and the Reynolds number on the flow after leading edges, we refer the reader to [27] and [26].

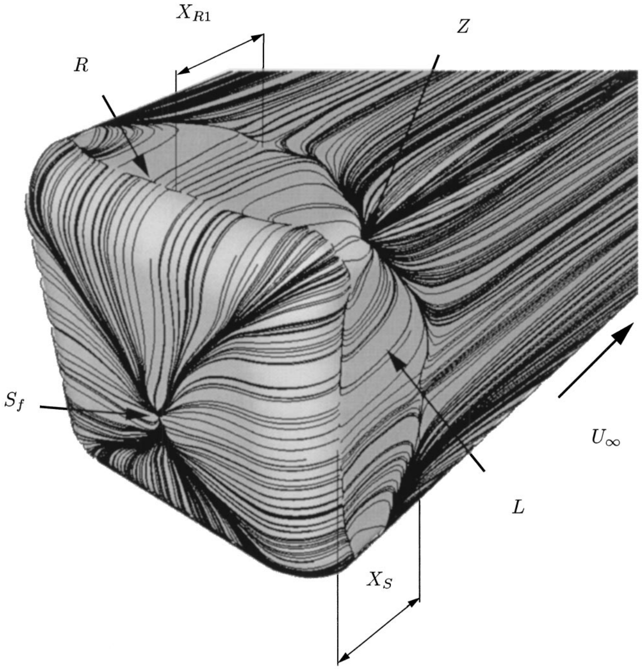

Fig. 4 Time-averaged trace lines on the surface of the body showing the roof vortex, R, the lateral vortex, L, and the stagnation point, S_f. View of the front face of the body.

Vortices parallel with the line of separation are formed in the separation region and transported downstream. They are lifted further back, forming hairpin vortices attached with their two legs to the surface of the body (Fig. 3). They break down shortly after their birth, indicating the reattachment to the body. When time-averaged, they form lateral vortices, L (one on each side of the body), and one vortex on the roof of the body, R (Fig. 4). The positions of these vortices are visualized in Fig. 4, and the reattachment lengths of the lateral vortices and the roof vortex, X_{R1} and X_S, respectively, (Fig. 4) are presented in Table 2. The stagnation point, S_f, located at $y = -0.13H$, $-0.10H$, and $-0.10H$ in the coarse, medium, and fine-grid simulations is shown in Fig. 4.

Trailing Vortices. Close to the upper lateral edges, we find four trailing vortices (two on each side of the bus). Figure 5 shows these vortices for one side of the bus. It can be seen that there is one vortex on each side of the edge (U_p and U_s) and one very thin separation bubble in the middle (C_u). These vortices originate at approximately point Z in Fig. 4 and exist along the entire bus. Their foci have approximately same position in the $y-z$ plane along the body (see [28]).

Similar to the trailing vortices at the upper lateral edges, a pair of trailing vortices is formed around each lower lateral edge of the bus. The size of the vortices on the underbody side is diminished by the small ground clearance, and they are much smaller than those on the lateral side of the edge (T vortices in Fig. 6). These vortices are very thin and are visible only after a very long averaging time as a result of the three-dimensional and unsteady flow underneath the body.

Here we concentrate on the strong trailing vortices on the lateral side of the lower edge of the body (Fig. 6). The right (shown in Fig. 6) and the left vortices rotate counterclockwise and clockwise, respectively. These vortices are present from the reattach-

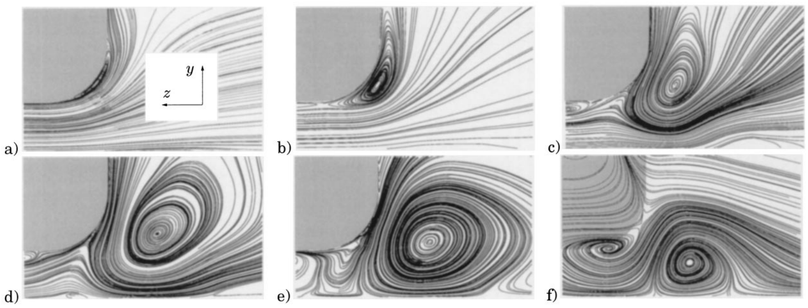

Fig. 6 Time-averaged streamlines projected onto planes: (*a*) $x=-3.36H$, (*b*) $x=-2.88H$, (*c*) $x=-1.68H$, (*d*) $x=-0.48H$, (*e*) $x=0$, and (*f*) $x=0.32H$. The direction of the rotation of this vortex (*T*) is counterclockwise. View from behind of the lower-right edge of the body.

ment of the lateral vortices, L (Fig. 4), at $x=-3.36H$ to approximately $x=0.4H$. They are much stronger than the vortices at the upper edges of the body. On their way downstream the T vortices first grow in diameter, reaching their maximum in the vicinity of the rear face of the body $(x=0)$, and then shrink further downstream (Fig. 6). Although they form at the surface near the reattachment line, they move away from the body in the lateral direction and towards the channel floor as they pass the body (Fig. 6). This motion of the vortices can be explained with their direction of the rotation shown in Fig. 7 and according to reasoning similar to that in potential theory. As they are formed very close to the body surface, they move towards the channel floor in a way similar to the potential vortex and its image replacing the body. Close to the floor, the vortex image in the floor takes over resulting in a sideward deflection. Han [8] found these vortices near the lower lateral edges of the Ahmed's body and concluded that they were formed due to the viscous interaction between the body and the ground-plane boundary layer.

The trailing vortices found in the time-averaged field (Fig. 6) are no longer present in the instantaneous velocity field (Fig. 8). The instantaneous flow is composed of a number of vortex structures that move randomly in time and space (Fig. 8).

Flow Underneath a Bus. It is well known that the flow underneath a passenger car has a three-dimensional character, [1], similar to what is valid for our simplified bus, see Fig. 7. Although the boundary layer is not formed on the moving floor, it is formed along the underbody of the bus. The boundary layer retards the fluid in the streamwise direction and, to satisfy continuity, fluid must either spread outwards to lateral sides or accelerate in the lower part of the channel, and it takes less energy to do the former. This outward motion forms the trailing vortices, *T*, which pump out the fluid from the flow underneath. At the same time, there is a thin region close to the underbody of the bus (see Fig. 7) where the flow moves towards the center plane of the body $(z=0)$.

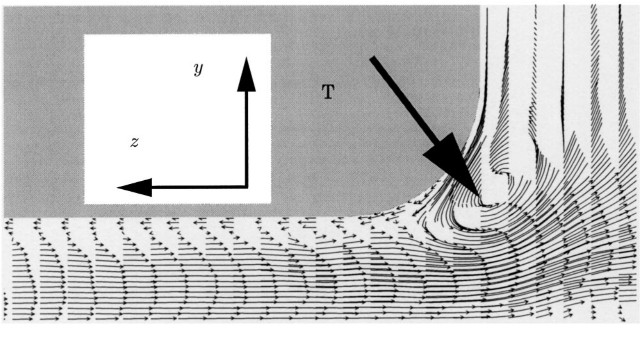

Fig. 7 Time-averaged velocity vectors in plane $x=-1.68H$. View from behind of the lower-right edge of the bus.

Near-Wake Region With Separation Bubble. The flow separates on the rear edges of the body and forms four secondary vortices, B (top, bottom and one on each side, see Figs. 9 and 10), each with its axes parallel to its separation edge. Velocities near the rear edge of the bus are small and difficult to measure, and these structures were therefore not observed in the experiments. Our simulations show that these vortices are very unsteady and thus cannot be studied in RANS simulations, [8]. These vortices have approximately the same size except for the one close to the underbody edge, which is much thinner than the other three vortices. Figure 9 shows that the fine and the medium simulations

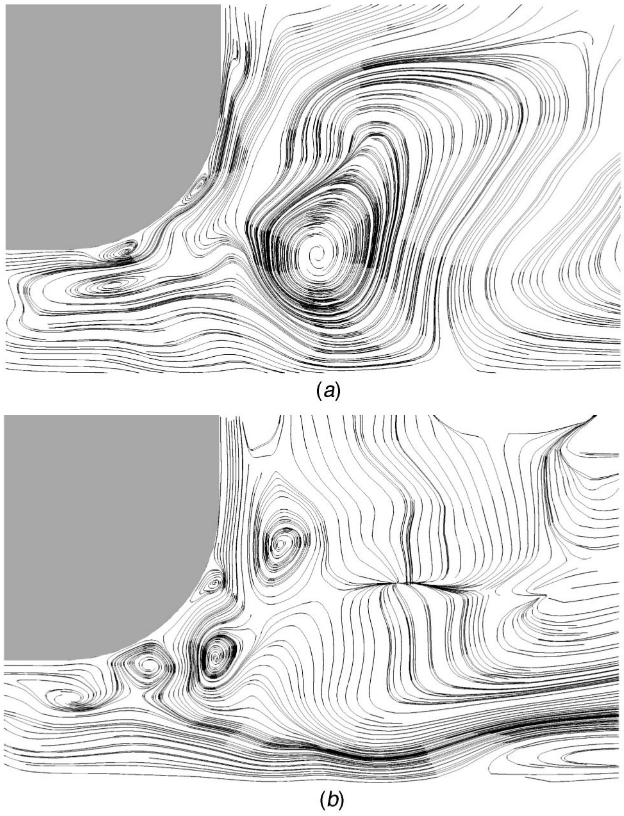
(*a*)

(*b*)

Fig. 8 Instantaneous streamlines at $x=-0.48H$. The time difference between two pictures is $tU_\infty/H=3.2$. View from behind of the lower-right edge of the bus.

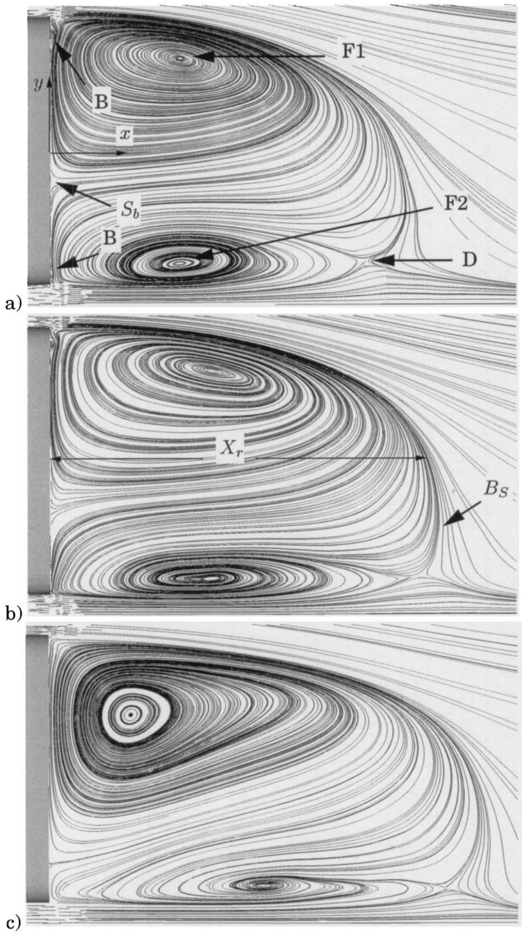

Fig. 9 Time-averaged streamlines projected onto symmetry plane $z=0$ of the bus. (*a*) Fine grid, (*b*) medium grid, (*c*) coarse grid.

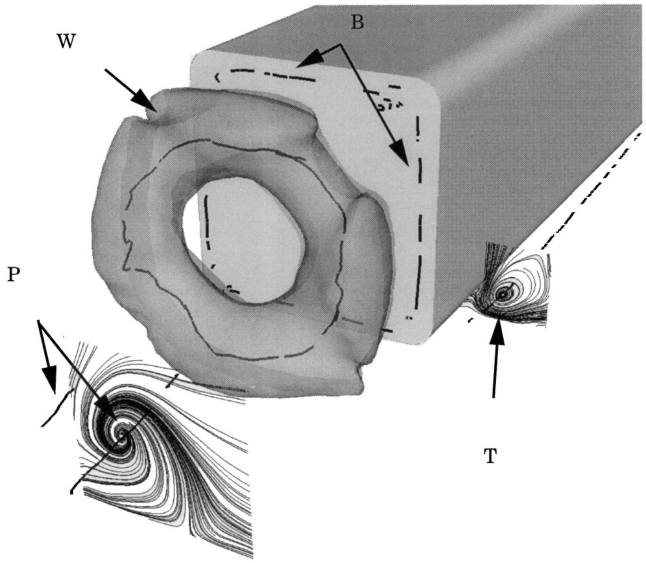

Fig. 10 The isosurface of time-averaged pressure $p=-0.20$. The black curves represent the vortex cores of the thin edge vortices *B*, the ring vortex *W*, and the longitudinal vortices behind the separation bubble *P*. Vortices on the right side ($z<0$), *P* and *T*, are visualized using streamlines in planes $x=1.4H$ and $x=-0.48H$, respectively (note that the mirror image vortices on the left side, i.e., $z>0$, are not shown in this figure). View of the rear face of the body.

predicted these vortices and that the coarse simulation failed to predict them. Two larger counterrotating vortices with foci $F1$ and $F2$ roll up and form a separation bubble (Fig. 9). Although all simulations show these two vortices, there are evident differences in their size and position in the three simulations (Fig. 9).

The first impression in Fig. 9 is that the resolution of the boundary layer on the body is directly responsible for the size of the wake. The free stagnation point (B_s) downstream of the separation bubble is found to be below the center of the rear face of the model, i.e., below $y=0$ (Fig. 9 and Table 2). In the experiments, [5,9], the free stagnation point was assumed to be at $y=0$, where the recirculation length X_r (Fig. 9) was measured. A comparison of this length from our LES with the experimental value is shown in Table 2. Only the fine grid simulation predicted this length close to the experimental value of $1.1H$, and we conclude that the spanwise and streamwise resolution is important for capturing the correct size of the wake.

In agreement with the experiments [5,9] the lower vortex with focus $F2$ is smaller than the upper one (focus $F1$). This is a consequence of the small ground clearance, which reduces the amount of fluid entering the lower vortex. The lower vortex is very unsteady and is averaged from a number of instantaneous vortices (Fig. 11) whereas the upper vortex is also present, slightly modified, in the instantaneous flow. The lower vortex contains approximately the same amount of fluid in the three simulations but the shape is changed (Fig. 9) and the extension of the vortex in x and y directions is decreased and increased, respectively, with the grid refinement. The position of the stagnation point, S_b (Fig. 9), on the rear of the body moves in the positive y-direction while the position of the saddle point, D, moves towards the body with the grid refinement.

Another pair of vortices is formed in the $x-z$ plane, in agreement with results in [9] and [5], and these together with the vortices in the $x-y$ plane form a ring vortex, W (Fig. 10). The cores of ring vortex W, edge vortices B, trailing vortex T, and longitudinal vortices P are visualized in this figure using the critical point theory, [29,30], i.e., we plotted the points whose rate-of-deformation tensor has one real and a pair of complex-conjugate eigenvalues and whose velocity is zero. The formation of a ring vortex was also observed in the experimental study of Ahmed's body but only when the strength of upper and lower horseshoe vortices in the separation bubble was approximately equal, [3]. According to Ahmed [3], the equal strength of these vortices can lead to a merging process of the upper and lower vortices, resulting in a ring vortex. Han [8] confirmed the existence of this coherent structure in the near wake of Ahmed's body, and Duell and George [5,9] found this structure in the near wake of the body. The ring vortex was time-averaged from the instantaneous coherent structure, W_i, shown in Fig. 11. This structure moves back and forth, and its weak periodic pumping motion is correlated with the shedding of the vortices from the end of the separation bubble (Fig. 11). A similar flow structure was found in the experiments [5,9].

Table 2 Lengths for reattachment on the roof (X_{R1}), lateral walls (X_S) and behind the bus (X_r). X_{free} and Y_{free} are coordinates of the free stagnation point at the closure of the separation bubble.

Contribution	X_{R1}/H	X_S/H	X_r/H	X_{free}/H	Y_{free}/H
Duell and George [5]	-	-	1.1	-	-
Coarse	0	0	1.44	1.6	−0.17
Medium	0.41	0.41	1.42	1.42	−0.23
Fine	0.33	0.33	1.18	1.3	−0.2

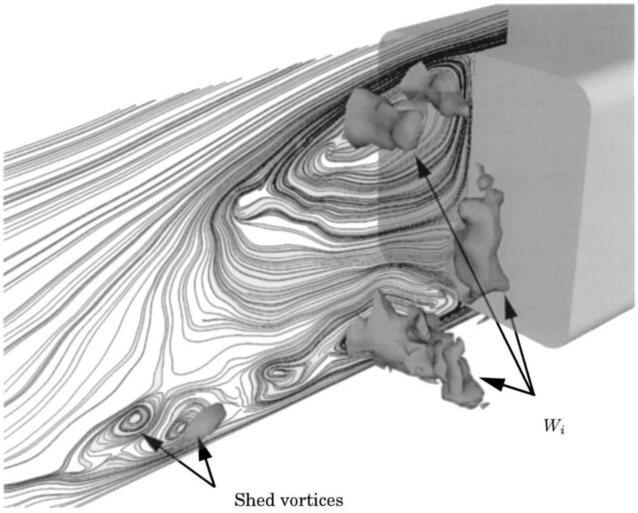

Fig. 11 The instantaneous streamlines projected onto symmetry plane $z=0$ of the bus and the isosurface of the instantaneous pressure, $p=-0.20$. Note that only half of the pressure surface (for $z \leqslant 0$) is shown.

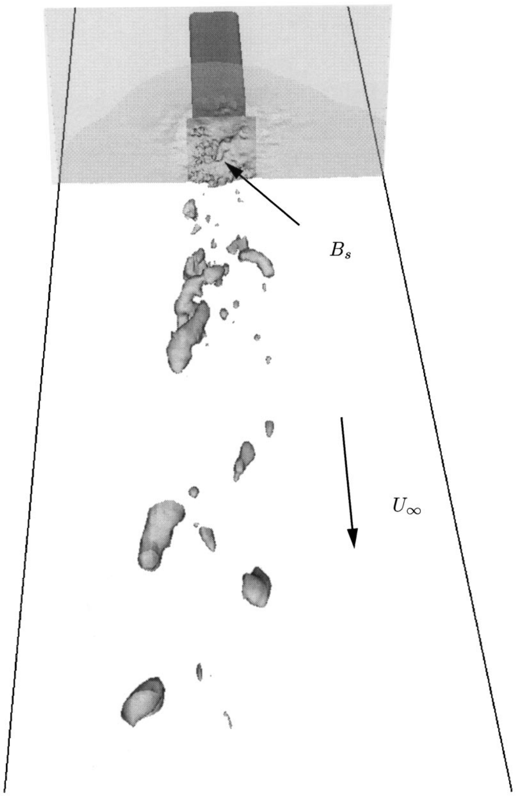

Fig. 13 Instantaneous coherent structures in the far wake visualized with isosurface of pressure $p=-0.035$. B_s is the free stagnation point at the closure of the separation bubble. View of the rear face of the bus.

Longitudinal Vortices Behind the Separation Bubble. The main flow in the streamwise direction interacts with the separation bubble in the wake, resulting in the transverse (i.e., in the y and z-directions) flow. The transverse flow restricts the length of the bubble in the wake and forms a pair of counterrotating longitudinal vortices after the bubble closure (see Fig. 12). One of these vortices ($z<0$) is shown in the plane close to the bubble closure in Fig. 10. Similar vortices were found in the study of the wake structures of different vehicle shapes in [3,4,6] and behind a car model in [11]. The rotation of these vortices is in an inward direction (Fig. 12), transporting the fluid in the space between vortices towards the floor (Fig. 12). This is in agreement with the direction of rotation of vortices in the far wake of a similar body in [4]. The position of these vortices lies about $0.1H$ away from the center plane $z=0$ at their origin ($x=1.3H$). As a result of their inward direction of rotation, their position first moves towards the floor and against each other, similar to a pair of counterrotating potential vortices. As the downwards motion of these vortices is slowed by the presence of the floor, their mutual interaction results in their deflection sideways, away from the symmetry plane $z=0$. This is similar to the interaction of the pair of counterrotating potential vortices and their mirror images replacing the floor. They spread outward with increasing distance from the rear of the bus. They extend far downstream and were detected as far as at the outlet ($x=21H$), where their spanwise position is about $0.85H$ away from plane $z=0$. These results are in agreement with the findings in [6]. The instantaneous wake is different from the time-averaged one and contains not only two longitudinal vortices but a larger number of vortices that move randomly in time and space (Fig. 13). This is in agreement with [11].

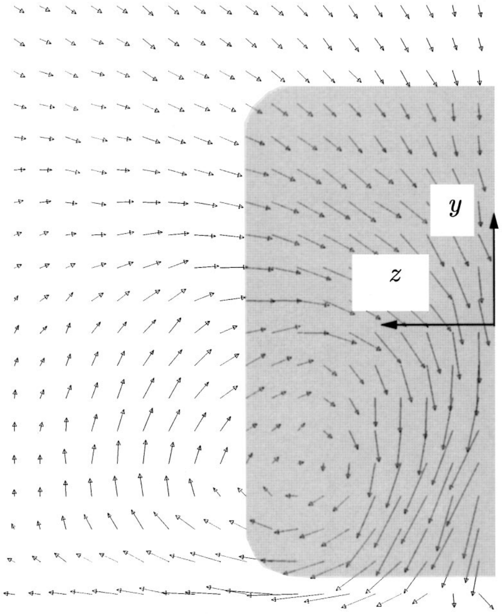

Fig. 12 The time-averaged longitudinal vortex in the far wake in plane $x=3.52H$. View of the rear face of the bus.

The time-averaged flow structures around the rear part of the body and in the wake are summarized in the schematic sketch in Fig. 14. One-fourth of the separation bubble is removed in this sketch to show the flow pattern and the direction of the rotation of the vortices. The direction of the rotation of the longitudinal vortices in this figure is indicated with a positive (ω_x^+) or negative (ω_x^-) streamwise vorticity component.

5.2 Aerodynamic Forces. The forces acting on the surface of the body as a result of the surface pressure were studied both time-averaged and instantaneously. The drag $\langle C_D \rangle_t$ and lift $\langle C_L \rangle_t$ coefficients that are interesting in engineering are presented in Table 3. Drag coefficient $\langle C_D \rangle_t = 0.33$ in the fine-grid simulation is equal to the value measured for an almost identical body in [10]. The aspect ratio ($AR=W/H$) and the ground clearance for the body in [10] are equal to the ones for the body studied here. Although the Reynolds number was higher in [10] (1.6×10^6

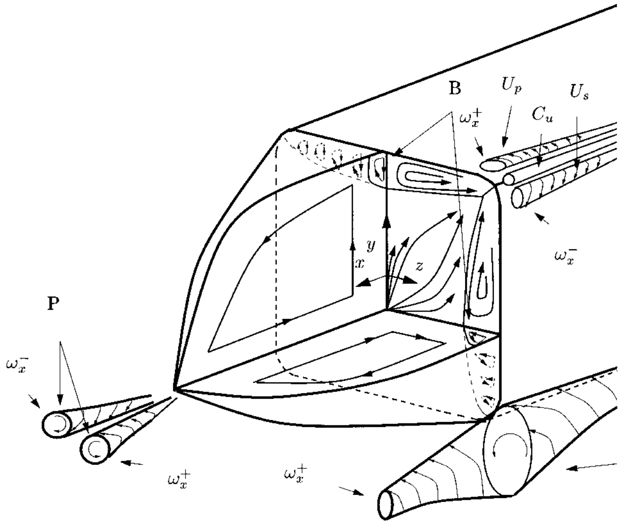

Fig. 14 Schematic representation of the time-averaged wake flow.

based on the body height and incoming velocity), it is probably a good assumption that the wake flow, responsible for the chief part of the total drag, becomes Reynolds-number independent at Re $=0.21\times10^6$. Table 3 shows that 69% of the pressure drag comes from the rear face.

As can be seen in Table 3, the bus is exposed to a negative lift (down force). The values of the time-averaged lift coefficient in Table 3 are close to the value of -0.06 measured in [10].

The r.m.s. values of the drag and lift coefficients were $C_{D_{\mathrm{rms}}}=0.0075$ and $C_{L_{\mathrm{rms}}}=0.0033$, respectively, in the fine-grid simulation. In addition to these design-relevant quantities, we studied the side force coefficient, C_S, and found that it varied with $C_{S_{\mathrm{rms}}}=0.0039$ in the fine-grid simulation. The time history of these coefficients was paid special attention and the coefficient signals were Fourier transformed, resolving their dominating frequencies. Four dominating peaks are found in the Fourier transform of C_D at the Strouhal numbers of $\mathrm{St}=fH/U_\infty=0.061$, 0.14, 0.43, and 0.73 in the fine-grid simulation. The periodic motion containing the most energy is St=0.061, but the reliability of this frequency is weak owing to the short time history (averaging time corresponds to approximately four periods of the signal). There were no peaks in the Fourier transform of C_L, and two main frequencies at St=0.22 and St=0.6 were observed in the side-force signal. The main frequency of the spanwise motion, St=0.22, is close to the shedding frequency of transverse vortices of St =0.23 found in Bearman's study of the wake behind a car model, [11]. The similarity of the spanwise motions behind these two different vehicle bodies raises the possibility that a similar vortex shedding exists behind other vehicle bodies.

Unfortunately, only the pressure coefficient $C_p=(p-p_\infty)/(0.5\rho U_\infty^2)$ at the rear face of the body was measured in the experiments of Duell and George [5,9]. The integrated value of C_p over the rear surface, $\langle\overline{C_p}\rangle_t$, measured in the experiment is -0.286 and is lower than the values resulting from our simulations (Table 3). One explanation for the discrepancy between LES and experimental data is that, in our LES, we could not afford to resolve the boundary layer on the lateral walls of the channel, thereby reducing the blockage of the cross section. A simple estimation of the displacement thickness at the position of the rear surface of the body gives a 5% decrease in the dynamic pressure, which is exactly the difference between our LES results and the experimental data.

Table 3 Time-averaged pressure drag, lift, and rear pressure coefficients and dominating frequency (St_p) of the $\overline{C_p}$ signal (note that $\overline{C_p}$ means the integrated C_p over the rear surface)

Case	$\langle C_D\rangle_t$	$\langle C_L\rangle_t$	$\langle\overline{C_p}\rangle_t$	St_p
Coarse	0.206	−0.066	−0.216	0.073
Medium	0.318	−0.066	−0.224	0.055
Fine	0.33	−0.071	−0.229	0.059

The $\overline{C_p}$ signal was also Fourier transformed, revealing a dominating frequency presented in Table 3 that is very close to the frequency of C_D (St=0.061) presented above. The characteristic frequency of the $\overline{C_p}$ signal (Table 3) compares well with the experimental value, [5,9] of St=0.069 (note that this value is measured with static and not moving ground, [5]). Baker [31] discussed the characteristic oscillation frequency for a wide range of different ground vehicle bodies and noted that the frequency of St=0.05, which is close to the values in Table 3, is dominant for at least some of these bodies. He concluded that this oscillation can be, as in the case of the bus studied in this paper, due to a pumping of the reverse flow region immediately behind the vehicle (see [5]) or a characteristic frequency of the entire wake.

5.3 Comparison of the Velocities With the Experimental Data. Duell and George [5,9] used hot-wire anemometry for velocity measurements. The near-wake flow is highly turbulent, with regions of reversed flow, and hence velocity measurements cannot be made accurately using single nonpulsed hot wire, [5,7]. Since there are no other velocity data except those in [5], we used these data for comparison with our LES results.

The velocity reported by Duell and George [5,9] was $\overline{V}_{\mathrm{eff}}=(\overline{U}^2+\overline{V}^2)^{1/2}$ where $\overline{U}$ and $\overline{V}$ are the time-averaged velocity components in the x and y-directions, respectively. We computed $\overline{V}_{\mathrm{LES}}=(\langle\overline{u}\rangle_t^2+\langle\overline{v}\rangle_t^2)^{1/2}$ and compared it with their experimental data in Fig. 15. Here, $\langle\overline{u}\rangle_t$ and $\langle\overline{v}\rangle_t$ are the time-averaged resolved velocity components in the x and y-directions, respectively, obtained from LES.

Although the shapes of the computed profiles in the separation bubble ($x/H=0.32$ and $x/H=0.98$) are similar to those of the experiments, there are some differences in the core of the bubble (Fig. 15). The agreement of the experimental data inside the separation bubble with LES results becomes worse with grid refinement (Fig. 15). To explain this behavior we computed the r.m.s. velocity intensity in the separation bubble and found that these were locally higher than 55% of the time-averaged velocity. Duell [5] found that these intensities varied between 32% and 70%. According to Chandrsuda and Brashaw [32], the hot-wire measurements are reliable only if the r.m.s. velocity intensity is less than about 30%. Chandrsuda and Brashaw [32] also found that, when the turbulence intensity exceeds 50%, hot-wire results become highly unreliable. From this we conclude that the experimental data are not accurate in this region. Position $x/H=1.63$ is downstream of the separation bubble, but the local turbulence intensity is still in excess by some 30% of the time-averaged velocity. Figure 15 shows that, at $x/H=1.63$, agreement between computed and measured profiles becomes better with better spatial resolution.

6 Comparison of the Three Simulations

The accuracy of the numerical results in this paper is judged from the grid refinement study. There is a 24% difference in reattachment lengths X_{R1} and X_S between the fine and medium-grid simulations (Table 2). The corresponding difference in the reattachment length, X_r, measured at $y=0$ was 20%, but the difference in the position of the free stagnation point, X_{free}, was only 9%. The value of X_r from the coarse-grid simulation differed by only 1% from the medium-grid value (Table 2). There is a 6% difference in the time-averaged drag coefficient $\langle C_D\rangle_t$ between the fine and the medium-grid simulations and a 54% difference

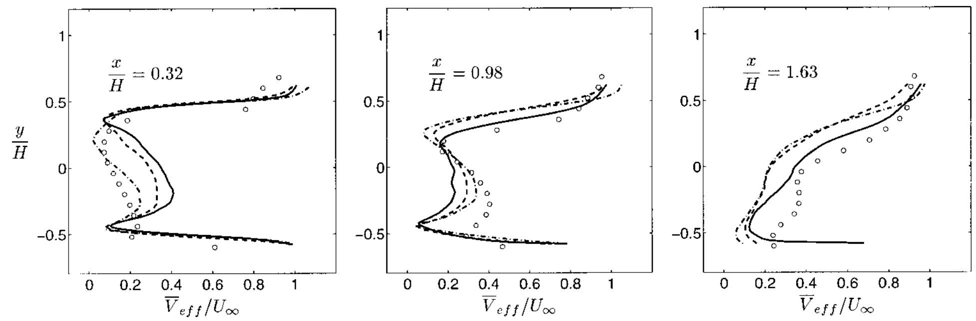

Fig. 15 Time-averaged velocity profiles at three downstream locations at $z=0$. Fine grid (solid curve); medium grid (dashed curve); coarse grid (dashed-dotted curve); experiment (symbols).

between the medium and the coarse-grid simulations (see Table 3). The great difference in $\langle C_D \rangle_t$ between the medium and the coarse-grid simulations is caused by the failure of the coarse-grid simulation to predict separation regions *R* and *L* in Fig. 4, thus producing too low a surface pressure at the front edges of the body. The time-averaged lift coefficient $\langle C_L \rangle_t$ remained unchanged between the coarse and medium-grid simulations and decreased by some 6% from the medium to the fine-grid simulations. The time-averaged pressure coefficient at the rear face of the body $\langle C_p \rangle_t$ changed by 3–4% with different spatial resolutions (Table 3). The velocity profiles changed most in the wake region (Fig. 15), but the trend is consistent with grid refinement.

None of the three grids was sufficient for accurate representation of the coherent structures in the boundary layer which are responsible for the maintenance of turbulence. Thus we constructed such a grid with the resolution on the body expressed in the wall units $\langle \Delta s^+ \rangle_t = 30-145$, $\langle \Delta n^+ \rangle_t = 0.5-0.8$ and $\langle \Delta l^+ \rangle_t = 14-35$. Here $\Delta f^+ = \Delta f \overline{u_\tau}/\nu$, $\overline{u_\tau}$ is the friction velocity and $\langle \cdot \rangle_t$ denotes time averaging, *s* is the streamwise direction, *n* is the wall-normal direction, and *l* is the spanwise direction. The resulting structured grid contains 9.8×10^6 cells, of which approximately 2×10^6 cells are located in the near-wall region ($y^+ < 20$). Note that the resolution of the boundary layers on the lateral walls and the ceiling of the wind tunnel was not considered here. If the refinement of the grid was made also on the tunnel walls the size of the grid would be very large. Thus the simulation was not performed on this grid. Additional details on the estimation of the spatial resolution and its extension to the high Reynolds number flow can be found in [33].

7 Concluding Remarks

While the flow around car-like bodies is highly unsteady, our knowledge of this flow is based primarily on experimental and numerical studies of the time-averaged flow. This has been the main obstacle in the development of accurate models for this flow. The large-eddy simulation used in this study predicted not only large-scale coherent structures that agree with previous knowledge but also some new, smaller structures. The latter were either too close to the wall to be observed in experiments or too unsteady to be predicted using RANS simulations. This study has shown that the instantaneous flow is very different from the time-averaged one, not only in the wake but also along the entire body. This suggests revision of the established picture of this flow. The instantaneous coherent structures can either appear randomly in time and space, such as those in the far wake, or in a periodic motion such as those shed from the rear edges. The three-dimensional picture of the flow underneath the body has been confirmed and explained by the growth of the boundary layer on the underbody. It has been shown that the flow near the lower lateral edges is highly unsteady, with a substantial number of instantaneous longitudinal vortices that average to two strong and two weak time-averaged vortices. These instantaneous vortices, together with the lateral vortices, close to the front face of the body, and the longitudinal vortices in the far wake are responsible for the variation of the side force on the body. Prediction of these vortices is thus important for traffic safety and comfort.

Very fine spatial resolution ($\langle \Delta n^+ \rangle_t \leqslant 1$, $\langle \Delta l^+ \rangle_t = 14$, where *n* is the wall-normal direction and *l* is the direction parallel with the surface of the body and normal to the streamwise direction) close to the edges of the body used in two of the simulations resolved two pairs of the time-averaged longitudinal vortices along the upper lateral edges of the body. These were also averaged from a number of unsteady instantaneous vortices.

The existence of the time-averaged vortex ring in the near wake suggested by previous studies, [3,5,8,9], was confirmed, and the pumping frequency of the instantaneous structures was found to be responsible for the periodic variation of the drag on the body.

The resolution of the low-frequency change in the pressure on the rear face of the bus requires very long time-averaging. This together with the costly grid refinement studies needed to prove the numerical accuracy are the main problems to overcome in large-eddy simulations of this kind of flow. These will be solved to some extent by increases in computer power.

The results from this study cannot be directly translated to the high Reynolds number flow owing to possible differences in the region around the fore-body of the bus. Still, we believe that the rest of the flow does not change much with the increase in Reynolds number. We motivate this with findings by Rodi et al. [34]. These authors presented results from the simulations of flow around a surface-mounted cube at two different Reynolds numbers, 3000 and 40,000, based on the incoming velocity and cube height. They found a great similarity in the results for these two flows. Time-averaged coherent structures had almost identical shapes and sizes in the two flows. Thus it seems likely that the qualitative knowledge about the flow around three-dimensional bluff bodies (such as a car) can be extracted from the flow at lower Reynolds number. This observation is not new and has long been used for experimental studies, [2–5]. Note, however, that the choice of the lower Reynolds number, which is high enough to produce a flow similar to that around a full-scale vehicle, is not trivial.

The knowledge gained in this work will hopefully help engineers to understand the flow around similar bodies at higher Reynolds number and to develop better turbulence models for RANS equations.

Acknowledgments

This work was supported by National Swedish Board for Technical Development (NUTEK), the Swedish Agency for Innovation Systems (VINNOVA), and Volvo Car Corporation. Computer time on the SGI ORIGIN 2000 machines, provided by UNICC at Chalmers, is gratefully acknowledged. The authors wish to thank Gunnar Johansson for helpful discussions.

References

[1] Hucho, W-H., 1998, *Aerodynamics of Road Vehicles*, 4th Ed., Society of Automotive Engineers, Warrendale, PA.

[2] Bearman, P. W., Davis, J. P., and Harvey, J. K., 1983, ''Measurement of the Structure of Road Vehicle Wakes,'' *International Journal of Vehicle Design* (Technological Advances in Vehicle Design Series, SP3, Impact of Aerodynamics on Vehicle Design), pp. 493–499.

[3] Ahmed, S. R., Ramm, G., and Faltin, G., 1984, ''Some Salient Features of the Time Averaged Ground Vehicle Wake,'' SAE Paper No. 840300.

[4] Barlow, J., Guterres, R., Ranzenbach, R., and Williams, J., 1999, ''Wake Structures of Rectangular Bodies With Radiused Edges Near a Plane Surface,'' SAE Paper No. 1999-01-0648.

[5] Duell, E. G., and George, A. R., 1999, ''Experimental Study of a Ground Vehicle Body Unsteady Near Wake,'' SAE Paper No. 1999-01-0812.

[6] Ahmed, S. R., 1981, ''Wake Structures of Typical Automobile Shapes,'' ASME J. Fluids Eng., **103**, pp. 162–169.

[7] Bearman, P. W., De Beer, D., Hamidy, E., and Harvey, J. K., 1989, ''The Effect of a Moving Floor on Wind-Tunnel Simulation of Road Vehicles,'' SAE Paper No. 880245.

[8] Han, T., 1989, ''Computational Analysis of Three-Dimensional Turbulent Flow Around a Bluff Body in Ground Proximity,'' AIAA J., **27**(9), pp. 1213–1219.

[9] Duell, E. G., 1994, ''Experimental Investigation of Unsteady Near Wakes of Ground Vehicle Bodies,'' Ph.D. thesis, Cornell University, Ithaca, NY.

[10] Barlow, J. B., Guterres, R., and Ranzenbach, R., 1999, ''Rectangular Bodies With Radiused Edges in Ground Effect,'' AIAA Paper No. 99-3153.

[11] Bearman, P. W., 1997, ''Near Wake Flows Behind Two- and Three-Dimensional Bluff Bodies,'' J. Wind. Eng. Ind. Aerodyn., **69–71**, pp. 33–54.

[12] Kataoka, T., China, H., Nakagawa, K., Yanagimoto, K., and Yoshida, M., 1991, ''Numerical Simulation of Road Vehicle Aerodynamics and Effect of Aerodynamic Devices,'' SAE Paper No. 910597.

[13] Hashiguchi, M., Kawaguchi, K., Yamasake, R., and Kuwahara, K., 1989, ''Computational Study of the Wake Structure of a Simplified Ground-Vehicle Shape With Base Slant,'' SAE Paper No. 890597.

[14] Aoki, K., Ohbayashi, T., Zhu, M., and Miyata, H., 1993, ''Finite-Volume Simulation of 3D Vortical Flow-Fields About Road Vehicles With Various After-Body Configuration,'' SAE Paper No. 931896.

[15] Sohankar, A., Davidson, L., and Norberg, C., 2000, ''Large Eddy Simulation of Flow Past a Square Cylinder: Comparison of Different Subgrid Scale Models,'' ASME J. Fluids Eng., **122**(1), pp. 39–47.

[16] Sohankar, A., Davidson, L., and Norberg, C., 2000, erratum, ASME J. Fluids Eng., **122**(3), p. 643.

[17] Krajnović, S., and Davidson, L., 2002, ''Large Eddy Simulation of the Flow Around a Bluff Body,'' AIAA J., **40**(5), pp. 927–936.

[18] Ghosal, S., 1999, ''Mathematical and Physical Constraint on Large-Eddy Simulations of Turbulence,'' AIAA J., **37**(2), pp. 425–433.

[19] Ghosal, S., and Moin, P., 1995, ''The Basic Equations for the Large Eddy Simulation of Turbulent Flows in Complex Geometry,'' J. Comput. Phys., **118**(1), pp. 24–37.

[20] Meneveau, C., and Katz, J., 2000, ''Scale-Invariance and Turbulence Models for Large-Eddy Simulation,'' Annu. Rev. Fluid Mech., **32**, pp. 1–32.

[21] Smagorinsky, J., 1963, ''General Circulation Experiments With the Primitive Equations,'' Mon. Weather Rev., **91**(3), pp. 99–165.

[22] Pope, S. B., 2000, *Turbulent Flows*, 1st Ed., Cambridge University Press, Cambridge, UK.

[23] Davidson, L., and Farhanieh, B., 1995, ''CALC-BFC: A Finite-Volume Code Employing Collocated Variable Arrangement and Cartesian Velocity Components for Computation of Fluid Flow and Heat Transfer in Complex Three-Dimensional Geometries,'' Report 95/11, Department of Thermo and Fluid Dynamics, Chalmers University of Technology, Gothenburg.

[24] Nilsson, H., and Davidson, L., 1998, ''CALC-PVM: A Parallel SIMPLEC Multiblock Solver for Turbulent Flow in Complex Domains.'' Internal Report 98/12, Department of Thermo and Fluid Dynamics, Chalmers University of Technology, Gothenburg.

[25] Sohankar, A., 1998, ''Numerical Investigation of Vortex Shedding Around Square Cylinders at Low Reynolds Number,'' Ph.D. thesis, Department of Thermo and Fluid Dynamics, Chalmers University of Technology, Gothenburg.

[26] Cooper, K. R., 1985, ''The Effect of Front-Edge Rounding and Rear Edge Shaping on the Aerodynamic Drag of Bluff Vehicles in Ground Proximity,'' SAE Paper No. 850288.

[27] Hucho, W. H., Janssen, L. J., and Emmelmann, H. J., 1976, ''The Optimization of Body Details–A Method for Reducing the Aerodynamic Drag of Road Vehicles,'' SAE Paper No. 760185.

[28] Krajnović, S., and Davidson, L., 2002, ''A Test Case for Large-Eddy Simulation in Vehicle Aerodynamics,'' *Proceedings of the 5th International Symposium on Engineering Turbulence Modelling and Measurements*, W. Rodi and N. Fueyo, eds., Mallorca, Spain, Elsevier, New York, pp. 647–656.

[29] Chong, M. S., Perry, A. E., and Cantwell, B. J., 1990, ''A General Classification of Three-Dimensional Flow Fields,'' Phys. Fluids, **5**(2), pp. 765–777.

[30] Sujudi, D., and Haimes, R., 1995, ''Identification of Swirling Flow in 3-D Vector Fields,'' AIAA Paper No. AIAA 95-1715.

[31] Baker, C. J., 2001, ''Flow and Dispersion in Ground Vehicle Wakes,'' J. Fluids Struct., **15**(7), pp. 1031–1060.

[32] Chandrsuda, C., and Bradshaw, P., 1981, ''Turbulence Structures of Reattaching Mixing Layer,'' J. Fluid Mech., **110**, pp. 171–194.

[33] Krajnović, S., 2002, ''Large Eddy Simulations for Computing the Flow Around Vehicles,'' Ph.D. thesis, Department of Thermo and Fluid Dynamics, Chalmers University of Technology, Gothenburg.

[34] Rodi, W., Ferziger, J. H., Breuer, M., and Pourquié, M., 1997, ''Status of Large-Eddy Simulations: Results of a Workshop,'' ASME J. Fluids Eng., **119**, pp. 248–262.

[35] Jeong, J., and Hussain, F., 1995, ''On the Identification of a Vortex,'' J. Fluid Mech., **285**, pp. 69–94.

O. Igra

G. Hu

Pearlstone Center for Aeronautical
Engineering Studies,
Department of Mechanical Engineering,
Ben-Gurion University of the Negev,
Beer Sheva, Israel

J. Falcovitz

Institute of Mathematics,
Hebrew University of Jerusalem,
Jerusalem, Israel

W. Heilig

Ernst Mach Institute,
Eckerstr. 4,
79108 Freiburg, Germany

Blast Wave Reflection From Wedges

While a lot of attention was given to shock wave reflections from wedges during the past four decades, only little work was published regarding the similar case of blast wave reflection from wedges. In the present paper this subject is studied experimentally and theoretically/numerically. The obtained results show that the geometry of the reflected wave pattern is similar in the two cases when both incident waves have the same initial pressure jump across their fronts. However, different reflected pressure signatures (history) are observed in these two cases. The pressures obtained behind a reflected shock wave are always higher than those obtained behind the corresponding similar blast wave. In the present case differences as high as 17% were observed. [DOI: 10.1115/1.1567310]

Introduction

Shock wave reflection from wedges has been thoroughly investigated in the past four decades and by now it is well known and documented, e.g., in [1]. Shock waves are readily generated in shock tubes or shock tunnels. Such facilities were widely employed for experimentally studying shock wave reflection from wedges. However, most shocks encountered in nature are actually blast waves. They result from a very rapid release of energy such as in lightning, volcanic eruptions, or explosions. In a blast wave a rapid pressure decline follows immediately behind the pressure jump across the wave front. As a result, unlike the case of shock wave reflection, in the case of blast wave reflection the reflected wave is propagating into a nonuniform state. This affects the reflection process. Kobayashi et al. [2] studied numerically the reflection patterns of blast waves. First, waves over a two-dimensional wedge were investigated and compared with results obtained for similar pseudo-stationary shock waves. Thereafter, stronger blast waves were considered; strong enough to excite internal degrees of freedom in the gas. Heilig [3] reported on the usage of a shock tube for generating blast waves, the proposed technique is employed in the present research work.

In the present investigation, blast wave reflection is studied experimentally and numerically. In the experimental part, a shock tube equipped with a very short driver is employed. Due to the very short driver the expansion wave, generated upon rupturing the diaphragm separating the driver and the driven sections of the shock tube, is quickly reflected from the driver's end wall and catches up with the incident shock wave, altering the original incident shock wave into a blast wave. The process of altering the shock wave into a blast wave was calculated numerically, modeling the flow as one-dimensional. Typical results are shown in Fig. 1. This figure shows pressure distributions in the driven section of the shock tube at different times; from $t=1\ \mu$s after the diaphragm rupture and up to $t=3300\ \mu$s. In the used shock tube three different driver's length could be employed; they were 15 mm, 30 mm, or 45 mm. The length of the driven section was about 3000 mm. It is apparent from this calculation (Fig. 1) that while at early times at ($t\leqslant 10\ \mu$s) the expected shock wave pressure signature is obtained, at late times ($t\geqslant 100\ \mu$s) a clear blast wave pressure signature has evolved. In the experimental and numerical results shown subsequently, the reflection from a wedge placed in the shock tube test section takes place when the incident wave has decayed into a blast wave. The reflection process of the blast wave from a wedge placed inside the test section is studied using shadowgraph diagnostics (for recording the resulting wave pattern) and pressure measurements. In the numerical study, the Eulerian equations of motion are solved numerically using a Godonuv based, second-order accurate scheme—the GRP. A detailed description of the GRP scheme is available in [4].

Theoretical Background and Numerical Scheme

The considered flow is modeled as a two-dimensional inviscid flow of an ideal gas. This is justified since during the short duration of the considered flow, the effects due to viscosity and heat conduction are small enough to be neglected. The conservation of mass, momentum, and energy for such flows expressed in a vector form, are

$$\frac{\partial U}{\partial t}+\frac{\partial F(U)}{\partial x}+\frac{\partial G(U)}{\partial y}=0 \qquad (1a)$$

$$U(x,y,t)=\begin{pmatrix}\rho\\ \rho u\\ \rho v\\ \rho E\end{pmatrix};\quad F(x,y,t)=\begin{pmatrix}\rho u\\ \rho u^2+p\\ \rho uv\\ u(\rho E+p)\end{pmatrix};$$

$$G(x,y,t)=\begin{pmatrix}\rho v\\ \rho uv\\ \rho v^2+p\\ v(\rho E+p)\end{pmatrix} \qquad (1b)$$

$$e=E-\frac{1}{2}(u^2+v^2),\quad p=(\gamma-1)\rho e \qquad (1c)$$

Contributed by the Fluids Engineering Division for publication in the JOURNAL OF FLUIDS ENGINEERING. Manuscript received by the Fluids Engineering Division March 29, 2002; revised manuscript received December 4, 2002. Associate Editor: W. W. Copenhaver.

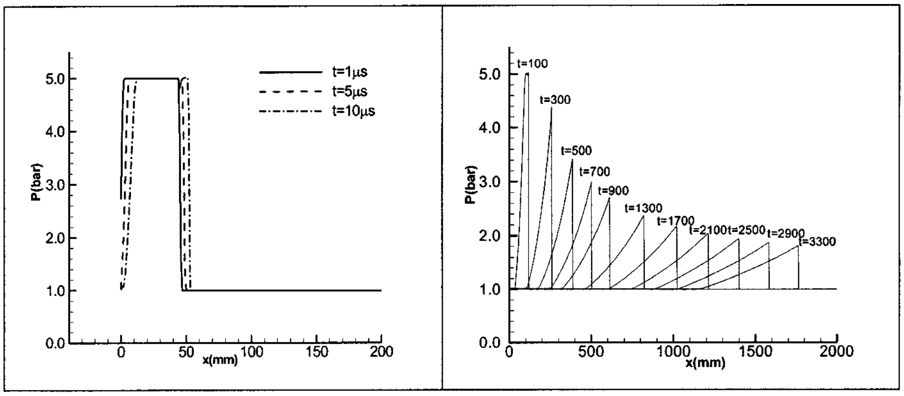

Fig. 1 Blast wave generation in a short driver shock tube. The driver length is 45 mm $P_4=5$ bars, $P_1=748$ torr, and $T_1=20.1°C$.

where ρ, p, and (u,v) are the density, pressure, and (x,y) velocity components, respectively. E and e are the total and internal specific energies and x, y, and t are the Cartesian coordinates and time.

The finite difference approximation to (1*a*) is formulated as a Strang-type operator splitting, using the GRP scheme as the one-dimensional finite difference operator. The splitting consists in replacing the system (1*a*) by the following pair of one-dimensional conservation laws:

$$\frac{\partial}{\partial t}U+\frac{\partial}{\partial x}F(U)=0, \tag{2a}$$

$$\frac{\partial}{\partial t}U+\frac{\partial}{\partial y}G(U)=0 \tag{2b}$$

where system (2) is taken to mean that an integration by an infinitesimal time step dt of (1*a*) is obtained as an integration of U by dt according to (2*a*), followed by a dt integration of U according to (2*b*). Assume that a one-dimensional second-order-accurate finite difference scheme is available and denote its integration operator for time step Δt by $L_x(\Delta t)$, $L_y(\Delta t)$ corresponding to (2*a*) and (2*b*), respectively. It was shown by Strang [5] that the operator $L(\Delta t)$ given by

$$L(\Delta t)=L_x(\Delta t/2)L_y(\Delta t)L_x(\Delta t/2) \tag{3}$$

is a second-order finite difference approximation to (1*a*).

In a series of computations of shock wave phenomena, it was found out that the simplified sequence

$$L(\Delta t)=L_x(\Delta t)L_y(\Delta t) \tag{4}$$

provided results that were virtually indistinguishable from those obtained by (3) [4,6]. We thus generally employ the more efficient splitting, i.e., (4).

The one-dimensional GRP scheme for (2*a*) is briefly outlined in the following. Let the computational domain be divided into a grid of equally spaced points $x_{i+1/2}=(i+1/2)\Delta x$, where Δx is the grid spacing and the ith cell is the interval $x_{i-1/2}<x<x_{i+1/2}$. The conservative second-order difference scheme for the time integration of the conservation laws, (2*a*), is

$$U_i^{n+1}=U_i^n-\frac{\Delta t}{\Delta x}\left[F(U)_{i+1/2}^{n+1/2}-F(U)_{i-1/2}^{n+1/2}\right],\qquad \Delta t=t^{n+1}-t^n \tag{5}$$

where U_i^n denotes the average value of U in cell i at time $t=t_n=n\Delta t$, and where the time-centered fluxes $F(U)_{i+1/2}^{n+1/2}$ are ob-

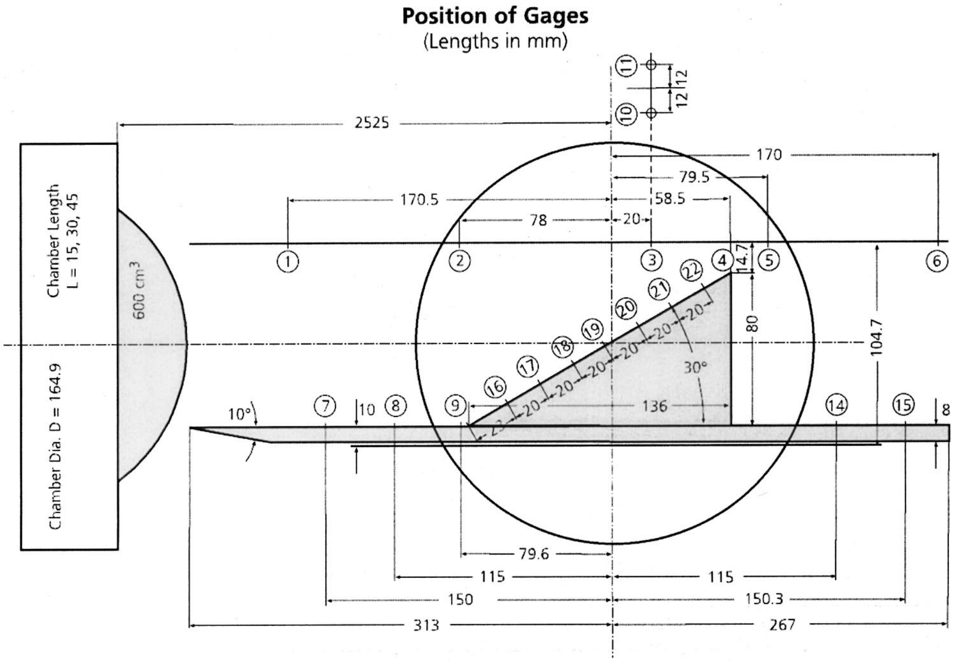

Fig. 2 Schematic description of the wedge location in the shock tube test section

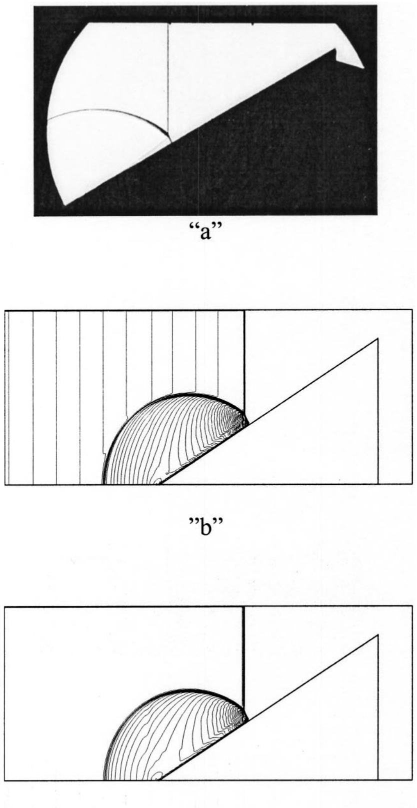

Fig. 3 Wave pattern evolved over the wedge 132 μs after the incident blast wave passed the wedge leading edge. Initial conditions are: the driver length is 45 mm $P_4 = 5$ bars, $P_1 = 748$ torr, and $T_1 = 20.1°C$. The driver and the driven gases are air.

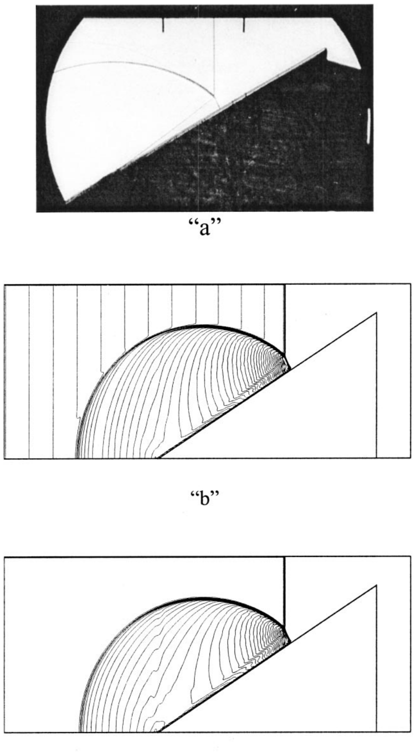

Fig. 4 Wave pattern evolved over the wedge 192 μs after the incident blast wave passed the wedge leading edge. Initial conditions as indicated in Fig. 3.

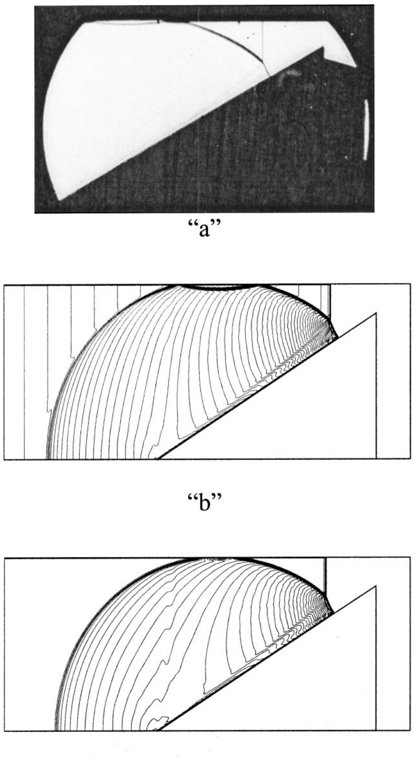

Fig. 5 Wave pattern evolved over the wedge 252 μs after the incident blast wave passed the wedge leading edge. Initial conditions as indicated in Fig. 3.

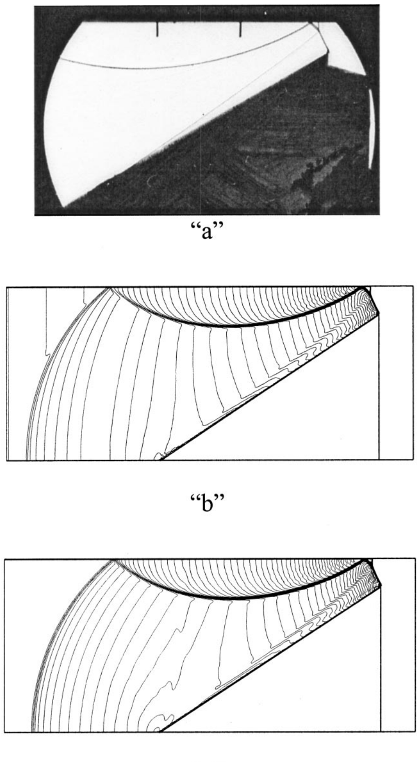

Fig. 6 Wave pattern evolved over the wedge 312 μs after the incident blast wave passed the wedge leading edge. Initial conditions as indicated in Fig. 3.

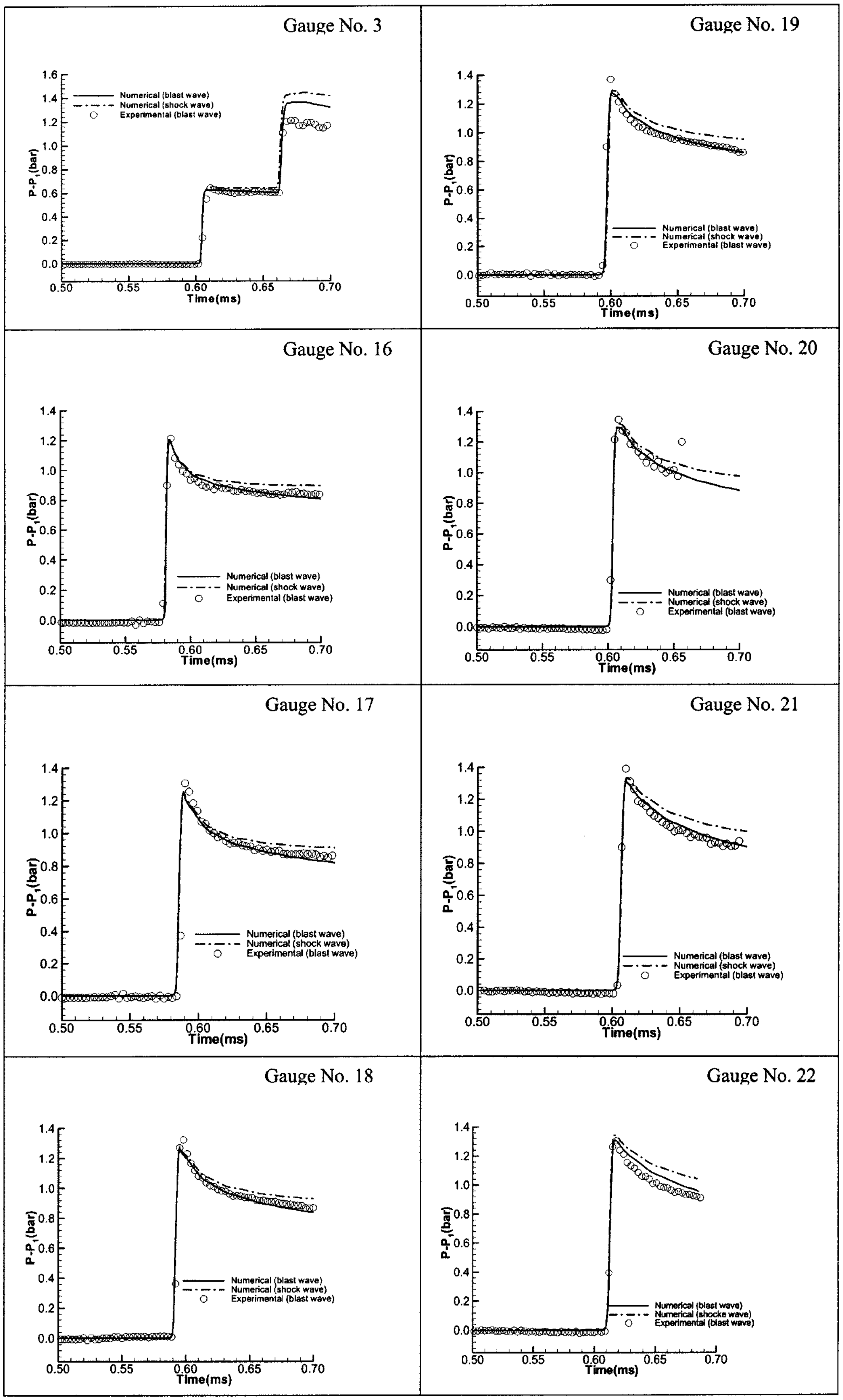

Fig. 7 Recorded and computed pressure signatures over the wedge and at the shock tube top wall. Initial conditions are given in Fig. 3. o=measured results, solid line=computed for blast wave, dashed line=computed for a similar shock wave.

tained analytically from solutions to generalized Riemann problems that arise at cell interfaces $x_{i+1/2}$ as a result of the piecewise

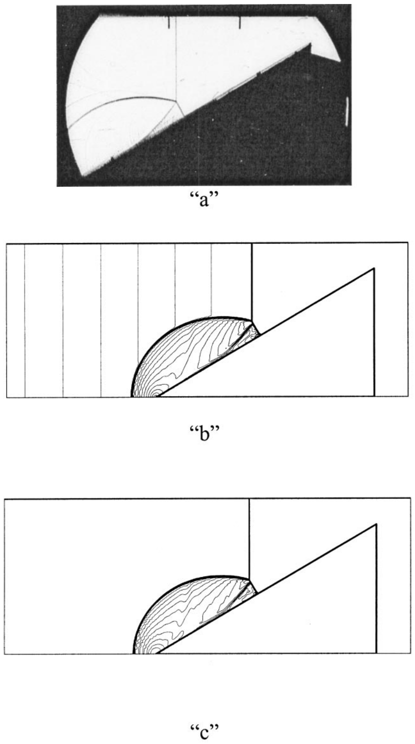

Fig. 8 Wave pattern evolved over the wedge 106 μs after the incident blast wave passed the wedge leading edge. The driver length is 45 mm, $P_4=30$ bar, $P_1=748.7$ torr, and $T_1=20.4°C$. Both the driver and the driven gases are air.

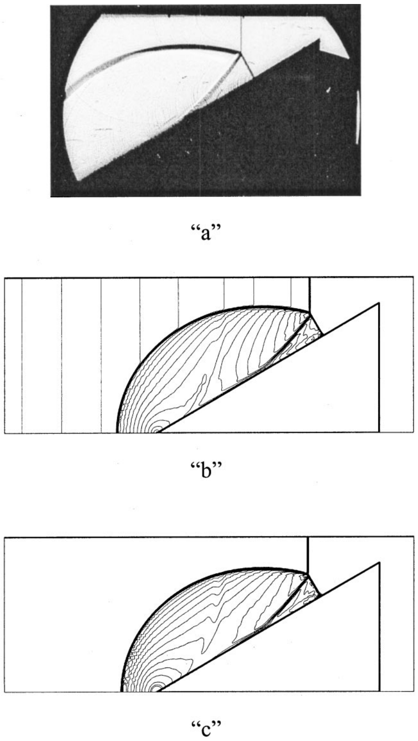

Fig. 9 Wave pattern evolved over the wedge 163 μs after the incident blast wave passed the wedge leading edge. Initial conditions as indicated in Fig. 8.

linear approximation to $U(x,y,t_n)$ in cell i. The unique feature of the GRP scheme is that fluxes are calculated from closed-form expressions obtained from an analytical solution to each generalized Riemann problem. For details regarding the GRP scheme the reader is referred to [4].

In the experimental part, a shock tube equipped with a very short driver section is employed. In the numerical part the entire flow generated inside the shock tube is studied, from its initiation upon the diaphragm rupture until the incident blast wave has passed the wedge.

In order to save computing time we separated the calculation into two steps. In the first step, the flow of the incident blast wave before its arrival at the wedge is computed using one-dimensional flow modeling of the entire shock tube. The process of altering the shock wave into a blast wave is shown in Fig. 1. This figure shows pressure distributions from $t=1$ μs after the diaphragm rupture and up to $t=3.3$ ms. In the second step, where the two-dimensional flow is solved, results obtained from the first step are inserted as the initial flow conditions just before the wedge leading edge. The computational domain is a 550 mm×95 mm rectangle that is divided into a grid of 1100×190 equal-size (square) cells. Such grid ensures high resolution in the numerical reconstruction of the investigated flow field.

The oblique wedge boundary is implemented in two space dimensions by treating it as a straight line that cuts a regular Cartesian grid. We apply a two-dimensional moving boundary tracking (MBT) scheme to the irregular cut-cells embedded in a regular mesh, as described in [7]. In that method, the boundary may be moving, but here it is stationary.

Results and Discussion

For the experimental part, the 80 mm×110 mm shock tube of the Ernst Mach Institute in Freiburg, Germany was used. The required blast waves were obtained by employing a very short driver. The wedge (having a deflection angle of 30.5 deg) was placed inside the shock tube test section; its leading edge was located 2447.5 mm from the diaphragm separating the driven and

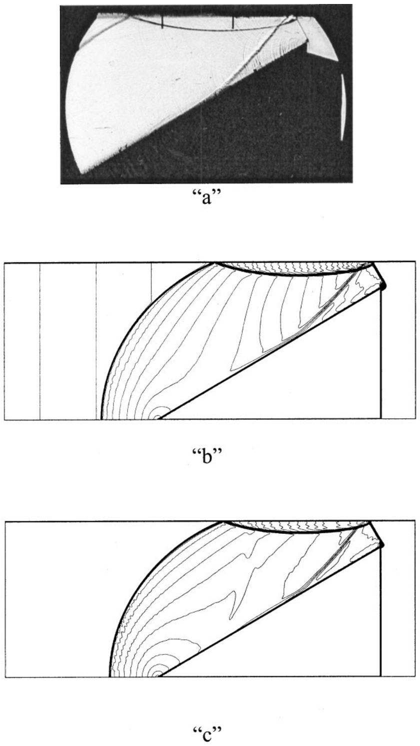

Fig. 10 Wave pattern evolved over the wedge 221 μs after the incident blast wave passed the wedge leading edge. Initial conditions as indicated in Fig. 8.

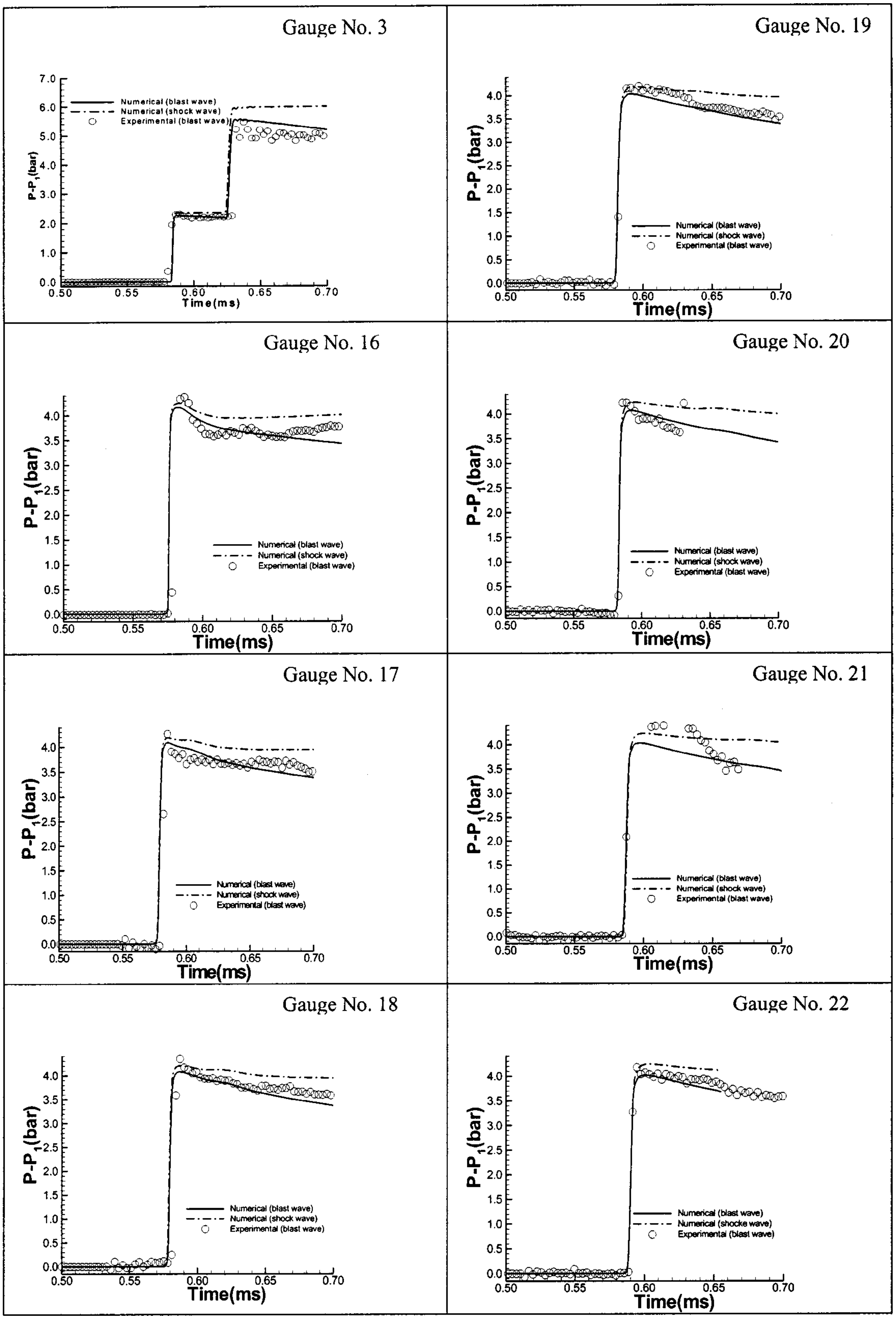

Fig. 11 Recorded and computed pressure signatures over the wedge and at the shock tube upper wall. Initial conditions are given in Fig. 8. o=measured results, solid line=computed blast wave, dashed line =computed shock wave.

the driver sections of the shock tube. For each experiment the following was recorded: The wave pattern developed over the wedge using shadowgraph photography, and pressures at various places on and around the wedge. Locations of the various pressure gauges employed in the present experiments are shown in Fig. 2. For recording the wave pattern developed over the wedge the Cranz-Schardin spark camera of the Ernst Mach Institute was used. This camera provides 24 photos during each experiment.

As described in the previous section, the GRP scheme was used for simulating the experimentally generated flow. In the first step the flow developed inside the shock tube was calculated using a one-dimensional version of the GRP code. A typical result is shown in Fig. 1. The blast wave pressure signature obtained near the wedge leading edge was used as the initial condition for the two-dimensional GRP scheme, which is used to compute the flow around the wedge. For comparison with a similar shock wave reflection, a similar two-dimensional computation with a shock wave having the same pressure jump as that experienced across the blast front (as it reaches the wedge leading edge) was performed.

In the following a sample of the obtained results is discussed. Results, shown in Figs. 3 to 6, contain experimental and numerical findings obtained for the case where the driver length was 45 mm and the driver pressure (at the diaphragm rupture time) was 5 bar. The initial conditions in the driven section were: $P_0 = 748$ torr and $T_0 = 20.1°\mathrm{C}$. Accuracies in reading the initial conditions are: the driver pressure is recorded to within ±0.01 bar, the initial pressure in the driven section is read to within ±10 torr, and the ambient temperature to within ±0.1°C. Figures 3 to 6 show the wave pattern evolved over the wedge at various times during the passage of the incident blast wave. Frames marked ''a'' show shadowgraph photos taken during the interaction process. As mentioned, during each experiment 24 photos were taken, the time gap between successive photos in the present case was 10 μs. Only a few of the 24 photos are shown in Figs. 3–6. Frames marked ''b'' are simulations showing isopycnics (lines of constant density). For comparison simulations obtained for a similar shock wave case are also shown, these are labeled as ''c.'' The shock and the blast waves at the leading edge of the wedge are ''matched'' by having the same pressure jump. It is apparent from the results shown in Figs. 3–6 that the present numerical simulations accurately reproduce the experimentally obtained wave pattern over the wedge. Only small differences can be detected between the blast (''b'') and the shock (''c'') wave cases. In the case of a shock wave reflection from the wedge, the reflected wave propagates into a uniform flow field. Therefore, no lines of constant density appear outside of the area engulfed by the reflected shock wave. This is not the case for the reflected blast wave since it is reflected into a field in which the pressure (and the density) monotonically decreases. As a result, one notices density changes outside of the area engulfed by the reflected blast wave, frame ''b'' in Figs. 3–6. Although the wave pattern observed in the case of reflected blast wave is very similar to that shown in a similar shock wave reflection, compare frames ''b'' and ''c,'' some small differences can be detected. The isopycnics geometry behind the reflected blast wave (inside the region engulfed by the reflected wave) is different from that observed behind a similar shock wave reflection. The difference becomes clearer with increasing time, see in Figs. 5 and 6. This difference in the isopycnics' geometry is an indication that different density and pressure, prevail behind these reflected waves. Results shown in Fig. 7 show pressure histories at different places along the wedge (gauges 16 to 22) and on the wall above the wedge (gauge 3); for gauges location see Fig. 2. Each graph contains three sets of data, circles shows pressures recorded by a piezoelectric gauge, a solid line represents numerical simulation obtained for blast wave reflection from the wedge, while the dashed line stands for simulations obtained for a similar shock wave reflection. Kistler pressure gauges (Kistler 603B) were used during the present investigation. These gauges are pre-calibrated by the manufacturer. At the beginning of each experimental series the gauges calibration is confirmed by testing the output reading from the gauges while they are attached to a pressure chamber in which a known pressure is kept. The pressure is being recorded during the pressure release process toward atmospheric level. In almost all checked cases the obtained electrical output was in good agreement with the values suggested by the manufacture's calibration. The used gauges have a response time of 1 μs and the uncertainty in the pressure reading is at most ±5%. It is clear from Fig. 7 that the numerical results obtained for a blast wave agree well with the recorded pressures. The numerical pressure history obtained for the corresponding shock wave is normally higher than either the recorded or the corresponding pressure in the blast wave case. The difference can reach 15% (see, for example, Gauge No. 21 in Fig. 7).

In Fig. 5 one observes the secondary reflection of the wedge-reflected wave from the shock tube upper wall. It is apparent that the wedge-reflected wave moves faster in the case of blast reflection (see frames ''b'' and ''c'' in Fig. 5). Pressure gauge number 3 is located at the shock tube upper wall and its pressure-record is shown on the top of Fig. 7. Watching this figure one can easily follow the reflection process shown in Fig. 5. Until about $t = 0.605$ ms the incident blast wave has not reached the location of pressure gauge No. 3, and the recorded pressure is the ambient value. The arrival of the incident blast wave is marked by the first pressure jump (at about $t \approx 0.605$ ms). This is followed by a region of a mild pressure decline, which lasts until the arrival of the wave reflected from the wedge at the position where gauge number 3 is located. Until about $t \approx 0.655$ ms. Thereafter a monotonous pressure decline takes place while the wave reflected from the shock tube ceiling propagates downward, towards the wedge; see also Figs. 5 and 6. It should be noted that different time counting is used in Figs. 3–6 and in Fig. 7. While in Figs. 3–6 the time $t = 0$ is the time when the incident blast wave reached the wedge leading edge, in Fig. 7 $t = 0$ is the time at which computation is initiated.

Results obtained for a similar geometry (driver's length of 45 mm and the same wedge), but with a significantly higher driver's pressure ($P_4 = 30$ bar) are shown in Figs. 8–11. As expected, the incident blast wave is stronger in the present case and therefore the blast wave reaches the wedge end much faster than in the previous case; at $t = 221$ μs in Fig. 10 as compared with 312 μs in Fig. 6. (In both cases the time $t = 0$ was taken when the blast wave reached the wedge leading edge.) As before, similar wave patterns are observed during the blast and shock reflection from the wedge. Again, small differences can be observed in the isopycnics at late times in the reflection process. The difference between blast and shock reflection is more pronounced in the pressure history shown in Fig. 11. Here too the measured pressures are close to those calculated for a blast wave. In the present case the measured and/or computed pressures for the blast wave are up to 17% lower than those calculated for a similar shock wave, see for example results obtained for gauge No. 17 in Fig. 11 at $\mathrm{t} = 0.7$ ms. Throughout most of the investigated time pressures computed for the blast wave case agree well with the measured values. The pressures obtained for a similar shock wave are always higher than the measured values. It should be noted that although the used piezoelectric pressure gauges are most suitable for measuring shock and blast waves pressure signatures (they have very fast response time and fairly accurate readings), they are not immune from random/side effects. These effects could be seen when comparing the pre-blast wave readings (ambient pressure) from gauges number 16 and 18 shown in Fig. 11. While in the reading from gauge number 16 the expected, constant value of P_1 is recorded, in gauge number 18 significant ''noise'' is recorded in the second half of the pre-blast readings. The possibility that such nonphysical pressure fluctuations/noise are included in the post-blast pressure readings could not be ignored. However, as stated

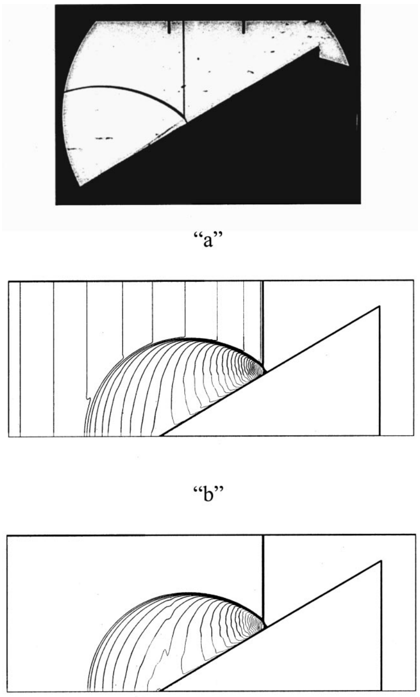

"a"

"b"

"c"

Fig. 12 Wave pattern evolved over the wedge 197 μs after the transmitted blast wave passed the wedge leading edge. Initial conditions are: driver's length 15 mm, $P_4=5$ bar, $P_1=738.6$ torr, and $T_1=20.9°$C. Both the driver and the driven gases are air.

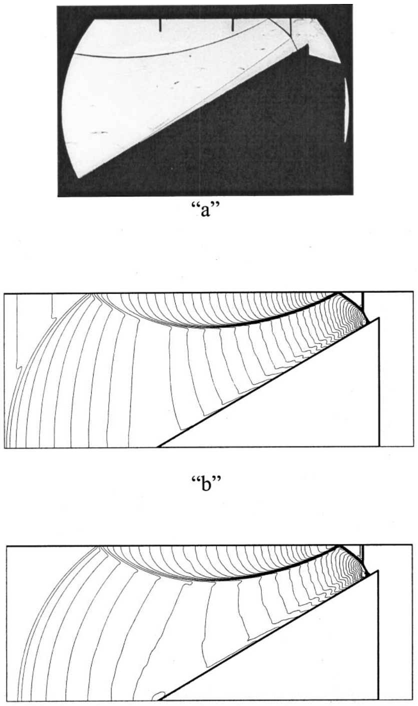

"a"

"b"

"c"

Fig. 13 Wave pattern evolved over the wedge 343 μs after the incident blast wave passed the wedge leading edge. Initial conditions as indicated in Fig. 12.

before, readings from most of the gauges are in good agreement with calculated pressures obtained for the blast wave case.

The last case to be discussed is the case when the driver length is extremely short (driver length of 15 mm), and the driver pressure is 5 bar. Obtained results for this case are shown in Figs. 12 to 15. Here the initial conditions in the driven section are very similar to those employed in the previously discussed case, i.e., in Figs. 1 and 3 to 7. However, due to the fact that the shock tube driver in the present case is three times shorter than the one used previously, the initially generated shock wave decays faster into a blast wave, and the resulted blast is weaker than that obtained with a longer driver. Comparing the results obtained in the present case for the pressure jump across the blast wave front at $x=1755$ mm (Fig. 15) with those obtained for the same place ($x=1755$ mm) in Fig. 1 shows that the pressure jump in the present case is 20% smaller than what is obtained for the longer driver, shown in Fig. 1. Due to this weakening of the incident blast wave it takes a longer time for the wave to reach the trailing edge of the wedge; 343 μs in Fig. 13 as compared with 312 μs in Fig. 6, where the blast wave already started its diffraction down the wedge rear wall.

As observed before, here too the same wave reflection pattern is observed when comparing the blast wave reflection with a similar shock wave reflection; see frames ''b'' and ''c''in Figs. 12 and 13. While the waves geometry is practically identical, differences are noticed in the isopycnics shown in Figs. 12 and 13 indicating different density distribution behind the reflected waves. As could be expected differences also exist, between the two cases, regarding pressure histories calculated along the wedge (see Fig. 14). It should be noted that all pressures shown in Fig. 14 are significantly lower than those shown in Fig. 7. As mentioned this is due to the quick decay of the incident blast wave in the case of a very short driver. Again, pressure computations obtained for the blast wave case are closer to the measured values than those computed for a similar shock wave.

Kobayashi et al. [2] claimed that in blast wave reflection the resulting slipstream is barely observable for weak to moderate blast waves and the attachment point of the reflected blast wave on the shock tube lower wall (floor) is located further upstream than that in a similar shock wave reflection from the considered wedge. While present results support the second claim (although the difference between the two cases is very small), the statement regarding the slipstream seems to be a result of the used numerical scheme. In our results the slipstream is equally noticed in both, the blast and shock reflection isopycnics. The difference in the obtained attachment point for the reflected blast or shock waves is very small. However, the reflected blast wave is always attached a little bit further upstream than a similar reflected shock wave.

In summary the reflected wave pattern which developed above the wedge depends mostly on the discontinuous jump across the front of the incident wave. Therefore, no real difference is observed in the wave pattern obtained from incident shock or blast waves collision with a given wedge, when both waves have the same pressure jump across their fronts. On the other hand, the pressures acting on the wedge depend on both the initial pressure jump through the wave front (which is the same, for the shock and the blast waves in the considered study) and on the pressure decay rate behind the wave front (which vanishes in the case of a shock wave). Due to this difference, the experimentally recorded pressures are lower than those predicted for a similar shock wave reflection. In the present investigation the difference can easily reach 17%.

It should be noted that the GRP scheme used for the present numerical simulations of the reflection process was also used for solving similar, and for more complex flows, e.g., Igra et al.

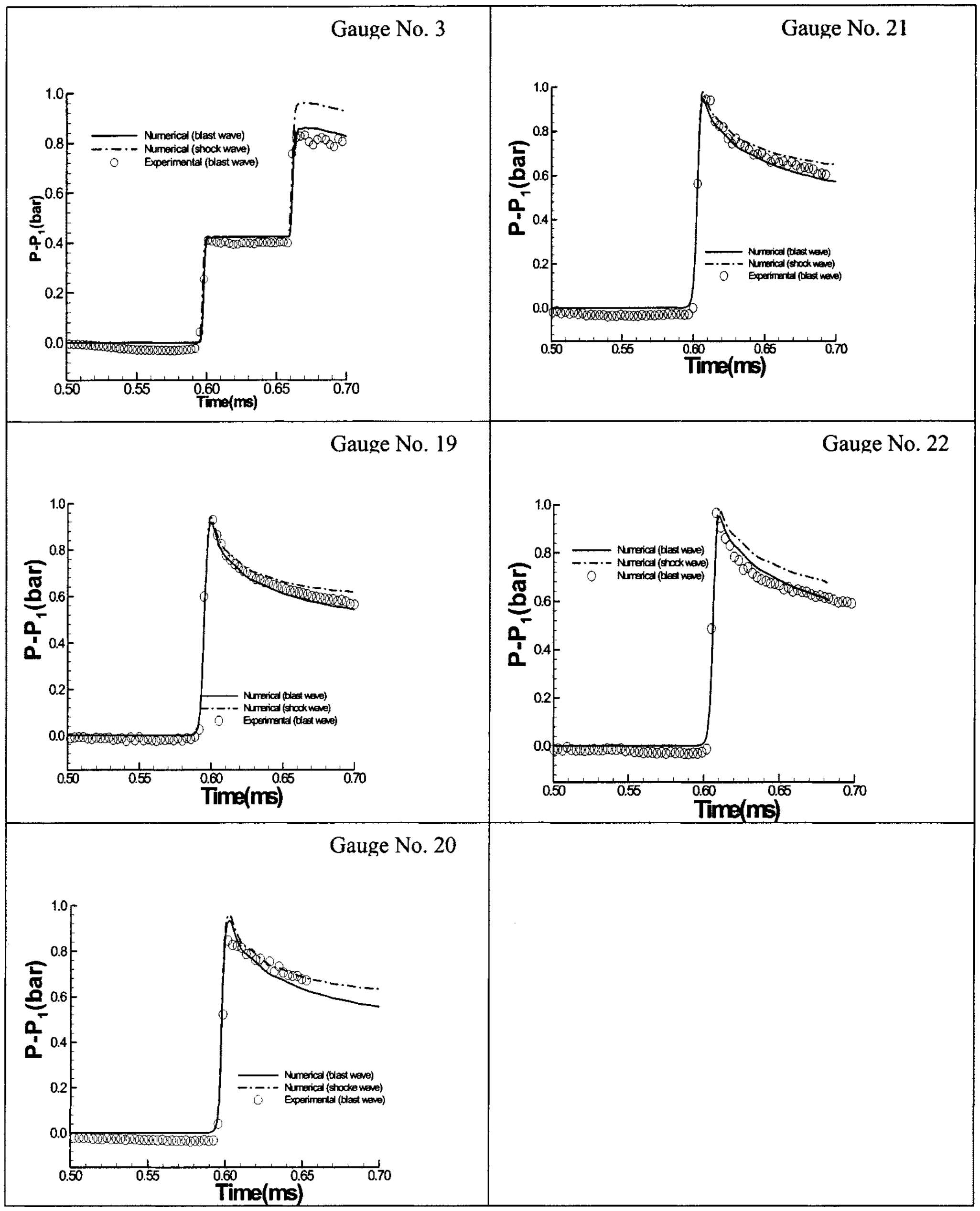

Fig. 14 Recorded and computed pressure signatures over a wedge and at the shock tube top wall. Initial conditions as indicated in Fig. 12. o=measured results, solid line=blast wave and dashed line=similar shock wave.

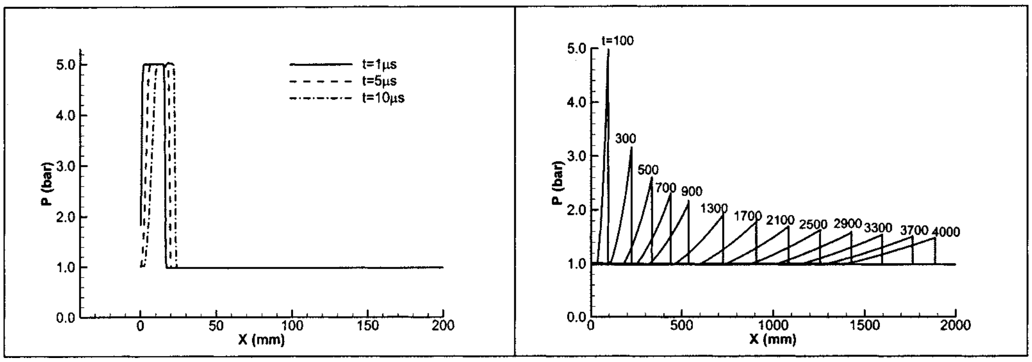

Fig. 15 Blast wave generation in a very short driver shock tube. The driver length is 15 mm, $P_4=5$, $P_1=738.6$ torr, and $T_1=20.9°C$.

[6,8,9]. It was shown there that doubling the number of grid points has practically no effect on the obtained wave pattern and/or pressures. This is also the case in the present study.

Conclusions

- Planar blast waves can be generated using a shock tube having a very short driver, relative to the length of the driven section.
- The used physical model and its numerical solution simulate accurately the obtained experimental findings. It could therefore be safely employed for studying blast and shock wave interaction with obstacles.
- It is shown that while the wave pattern resulting from the interaction of a blast wave with a wedge is very similar to that obtained for a similar shock wave reflection, the resulting pressure field is different. In the investigated case differences as large as 17% are found.
- In past shock tube studies of wave reflection from wedges, or other obstacles, attention was given to limit the test time to a period in which the pressure behind the shock wave is almost constant, i.e., the pressure history through the shock wave looks like a step function. Obviously these are normally very short times. The present study indicates that as long as the pressure decay rate behind the pressure jump across the shock front is small both, the resulting wave pattern in the reflection process, and the pressures acting on the reflecting body will be practically the same as in a similar 'pure' shock wave reflection.

Acknowledgment

This work was supported by the German-Israeli Foundation for Research and Development. Their support is acknowledged with thanks.

References

[1] Ben-Dor, G., 1991, *Shock Wave Reflection Phenomena*, Springer, New York.
[2] Kobayashi, Y., Takakura, Y., and Higashino, F., 1999, ''On Reflection Patterns of Blast Waves and the Real Gas Effect,'' G. J. Ball, R. Hillier, and G. T. Roberts, eds., *Shock Waves*, Proceedings of the 22nd International Symposium on Shock Waves, London, UK.
[3] Heilig, W., 2000 ''Use of the Shock Tube for Generating Blast Waves,'' *Proceedings of the 16th International Symposium on Military Aspects of Blast and Shock*, Cranfield University, Oxford, UK.
[4] Falcovitz, J., and Ben-Artzi, M., 1995, ''Recent Developments of the GRP Method,'' Japan Soc. Mech. Engrs. Int. J. Ser. B, **38**, pp. 497–517.
[5] Strang, G., 1968, ''On the Construction and Comparison of Difference Schemes,'' SIAM (Soc. Ind. Appl. Math.) J. Numer. Anal., **5**, pp. 506–517.
[6] Igra, O., Falcovitz, J., Reichenbach, H., and Heilig, W., 1996, ''Experimental and Numerical Study of the Interaction Between a Planar Shock Wave and a Square Cavity,'' J. Fluid Mech., **313**, pp. 105–130.
[7] Falcovitz, J., Alfandary, G., and Hanoch, G., 1997, ''A Two-Dimensional Conservation Laws Scheme for Compressible Flows With Moving Boundaries,'' J. Comput. Phys., **138**, pp. 83–102.
[8] Igra, O., Wu, X., Falcovitz, J., Meguro, T., Takayama, K., and Heilig, W., 2001, ''Experimental and Numerical Study of Shock Wave Propagation Through Double-Bend Ducts,'' J. Fluid Mech., **437**, pp. 255–282.
[9] Igra, O., Wu, X., Hu, G., and Falcovitz, J., 2002, ''Shock Wave Propagation Into a Dust-Gas Suspension Inside a Double-Bend Conduit,'' ASME J. Fluids Eng., **124**, pp. 483–491.

Modeling of Combustion in Gasoline Direct Injection Engines for the Optimization of Engine Management System Through Reduction of Three-Dimensional Models to ($n \times$ One-Dimensional) Models

P. Emery
Renault–Direction de la Recherche API,
TCR RUC T 80,
1, avenue du Golf,
78288 Guyancourt Cedex, France

F. Maroteaux[1]
Laboratoire de Mécanique Physique
Université P. et M. Curie,
2, place de la Gare de Ceinture,
78210 St. Cyr l'Ecole, France
e-mail: maroteau@ccr.jussieu.fr

M. Sorine
INRIA–Rocquencourt, BP 105,
78153 Le Chesnay Cedex, France

Gasoline direct injection (GDI) spark ignition engines may be able to run over a wide range of operating conditions. The GDI process allows combustion with lean mixtures which may lead to improved fuel economy and emissions relative to homogeneous spark ignition (SI) engines. To satisfy the different modes of operation, the tuning of GDI engines requires a large number of engine tests which are time-consuming and very expensive. To reduce the number of tests, a model with a very short computational time to simulate the engines in the whole operating range is needed; therefore the objective of this paper is to present a reduced model to analyze the combustion process in GDI engines, applied to a homogeneous stoichiometric mode. The objective of the model is to reproduce the same tendencies as those obtained by three-dimensional models, but with a reduced computational time. The one-dimensional model is obtained thanks to a reduction methodology based on the geometry of the combustion front computed with three-dimensional models of the KIVA-GSM code, a modified version of KIVA-II code including a CFM combustion model. The model is a set of n one-dimensional equations (i.e., for n rays), taking into account a thin flame front, described with the flamelet assumption. It includes a CFM combustion model and a (k,ε)-model including the mean air motions (swirl and tumble). The results of the one-dimensional model are compared to those obtained by the KIVA IIGSM under different engine conditions. The comparison shows that the one-dimensional model overestimates the maximum cylinder pressure, which has an insignificant effect on the net indicated work per cycle. The results obtained by the numerical simulations are close to those given by the three-dimensional model, with a much reduced computation time. [DOI: 10.1115/1.1570859]

1 Introduction

The gasoline direct injection (GDI) engine offers a multitude of potential advantages which may lead to improved emissions and fuel economy relative to port injected spark ignition (SI) engines. Especially at part load conditions, the GDI engines are able to run in a stratified charge mode which combines the benefits of lean combustion with a nearly throttle free operation. This is the major step in overcoming the principal disadvantages of SI engines compared to diesel engines. Furthermore, the GDI process has no delay in fuel transport during cold start, warm up, and transient mode, which leads to combustion with lean mixtures and reduced HC and CO emissions. At full load operation, the combustion system is switched to the homogeneous stoichiometric mode, and to purge the NO_x catalyst the combustion system is switched to a rich mode (equivalence ratio greater than one, generally fixed around 1.3). The gasoline direct injection engines are thus able to run over a wide range of operating conditions (homogeneous stoichiometric, homogeneous lean, stratified lean).

Generally, three-dimensional models are used to understand different phenomena and to analyze the in-cylinder processes for the optimization of the combustion chamber design. These three-dimensional models implemented in different codes (KIVA or Star-CD for example) require many hours on a high end computer, to compute a combustion phase for one cycle and are not suited to assist the engine tuning. Today, the car manufacturers need models with a very short computational time to simulate the engine in the whole operating range; this step is very important for the engine tuning, to reduce the number of engine experiments on the engine test bench, which are very expensive.

The objective of this study is to provide the car manufacturers with a simple physical combustion model to assist engine tuning and engine management system optimization, with the aim of air-fuel ratio and performance control over the whole engine operating range. It has to be calibrated on a few operating points, using

---

[1] To whom correspondence should be addressed.

Contributed by the Fluids Engineering Division for publication in the JOURNAL OF FLUIDS ENGINEERING. Manuscript received by the Fluids Engineering Division June 13, 2002; revised manuscript received November 1, 2002. Associate Editor: G. E. Karniadakis.

a three-dimensional model. Furthermore, the model must have the same calculation times (few minutes on a workstation) and ease of use as a zero-dimensional model, keeping as much as possible the structure and physical properties of the three-dimensional models (KIVA II, [1]).

In the literature, we can find many zero-dimensional models which can be used to control the performance, [2–7]. These models need the adjustment of many coefficients for each operating condition, leading to many lookup tables, and are not suited to describe correctly the stratified charge mode for the GDI engine.

To represent the effect of nonhomogeneous fuel-air mixture in the chamber by another way than three-dimensional models, and to avoid the need of too many lookup tables, we have opted for a one-dimensional model to describe the combustion. The model proposed here is a one-dimensional model taking into account a thin flame front, described with the flamelet assumption. It includes a CFM (coherent flame model) similar to the one implemented in the KIVA-GSM code. The turbulence is taken into account with a (κ,ε)-model, which includes the effects of swirl and tumble in the combustion chamber. This model is a set of n one-dimensional equations (i.e., n for rays) obtained with a methodology of reduction of three-dimensional space to a one-dimensional space, followed by a calibration step. The model has been applied to a homogeneous stoichiometric mode at first and is still in progress for the stratified mode, which is not developed in this paper.

2 Methodology

2.1 Introduction. The objective of the reduced model is to reproduce the same tendencies as those obtained by three-dimensional models, here a KIVA-GSM code. The main idea of the reduction methology is to find a one-dimensional model, as close as possible to a given three-dimensional model. The model construction proceeds in three steps: one-dimensional space-domain determination, model-equations determination, and model parameters identification.

The one-dimensional space domain is the intersection of the moving chamber volume with the union of a finite number (n) of rays representative of the propagation of the flame surface density. These fixed rays can be extracted from the three-dimensional computations: by hand when n is small (one or two, which is the case here), or automatically for a large values of n. Each ray is associated with a fraction of the total volume: its control volume, a measure of its importance. Automatic extraction of rays is still under current research and will be published later. It consists in extracting from the three-dimensional computation pictures (temperature or flame surface density or the reaction rate) a numerical front to get a simple geometrical model for the propagation phenomena. This front is extracted from computed data with an image-processing technique: an adaptation of the level set method, [8–9]. Finally, the desired rays are the trajectories of some particular points of the extracted front.

When a set of representative rays is chosen, the equations for the one-dimensional model are simply, on each ray, a one-space variable version of the three-dimensional equations. Some added terms account for exchanges of mass, heat, and surface density between adjacent control volumes. The one-dimensional model is complete at this step.

The parameter values of the three-dimensional model are taken as initial values for the identification of the one-dimensional model parameters. These parameters and the new exchange-term parameters of the reduced model are identified by comparison of the three-dimensional and one-dimensional models on some representative operating conditions: They are tuned in order to recover as precisely as possible the cylinder pressure, heat release, and turbulence (ε and κ) during the combustion phase.

Note that each parameter of this reduced model has a clear physical meaning, making the identification easier. This would not be the case if we had used a more standard reduction methodology, like a nonlinear Galerkin approximation with a coarse basis, for example, the popular POD (proper orthogonal decomposition) technique for computational fluid dynamics, [10].

2.2 Propagating Fronts Theory. A large number of physical systems are written in the form of propagating fronts; if we observe the three-dimensional model equations (KIVA-GSM) which describe the combustion process, we can note that their structure is close to the propagating fronts equations. This remark is qualitatively important since it means that some states of the three-dimensional equations follow the behavior of a front which propagates in the combustion chamber. This remark is also important in the case of the model reduction (three-dimensional to one-dimensional and one-dimensional to zero-dimensional) thematic which is the objective of this work. The propagating fronts equations are very widely studied in the mathematical literature, [11], and the way to reduce them is well known, [12].

As a reminder the equations of the propagating fronts have a general form (here written, for example, in one-dimension):

$$\frac{\partial C}{\partial t}=\frac{\partial}{\partial x}\left(D\frac{\partial C}{\partial x}\right)+f(C) \tag{1}$$

where the first term of the right-hand side of the equation is the diffusion term and the second term represents the reaction term (modeling the chemistry process for example). The most important property of the Eq. (1) is its solution in the form of a progressive wave as (for example for a one-dimensional case):

$$C(x,t)=\tilde{C}(x-at) \tag{2}$$

where a represents the wave velocity.

For example, when the term D (Eq. (1)) is constant and with a boundary conditions $(\partial C/\partial x)=0$, finding C (in Eq. (2)) is similar to determining $\tilde{C}$ and a, which verify (Eq. (3)):

$$D\tilde{C}''+a\tilde{C}'+f(\tilde{C})=0 \tag{3}$$

$$\lim_{\zeta\to-\infty}\tilde{C}(\zeta)=C_0;\quad \lim_{\zeta\to+\infty}\tilde{C}(\zeta)=0;\quad f(C_0)=f(0)=0.$$

The closest case to the physical situation of interest here is the case of monostable equations, which correspond to one stable equilibrium and one unstable equilibrium. Then, we can deduce from the Eq. (3) a value a_0 such as for every $a\geqslant a_0$, there exists a solution in the form of Eq. (2). The most classical situation is to choose the following monostable equation:

$$f(C)=C(C_0-C). \tag{4}$$

These monostable equations have been studied by many authors in different fields, [13–14]. Their behavior can be applied to combustion:

1. The system starts from a stable or slowly varying state: for example, fresh charge.
2. A trigger mechanism occurs: spark ignition (SI engines) or self ignition (diesel engines) which creates a new stable state (burned gas).
3. The newly created state is separated from the first one by a front which delimits the two zones: burned gas (stable state) and fresh charge, and which spreads (the combustion front propagates).

2.3 Similarity With the Three-Dimensional Equations When we observe the three-dimensional equations which describe the turbulent combustion process, we can notice that the equation of the flame surface density and the equation of the dissipation rate of turbulent kinetic energy comply with the criteria of the propagating fronts equations.

The equation of the flame surface density (from KIVA-GSM)

Table 1 Engine geometry

Bore	82.7 mm
Stroke	93 mm
Connecting rod length	144 mm
Displaced volume	1998 cm^3
Compression ratio	10

$$\frac{\partial\Sigma}{\partial t}+\mathrm{div}(\vec{\tilde{u}}\Sigma)=\mathrm{div}\left[\left(\lambda_{\Sigma}\overline{\rho}\tilde{\kappa}\frac{\tilde{\kappa}}{\tilde{\varepsilon}}+\frac{\mu_t}{S_c}\right)\overrightarrow{\mathrm{grad}}\left(\frac{\Sigma}{\overline{\rho}}\right)\right]+\alpha_{\Sigma}(\overline{\kappa_t}+\overline{\kappa_L})\Sigma$$

$$-\beta S_L\frac{\Sigma^2}{(1-\overline{c})}+\phi_{\Sigma}$$

has a nonlinear term on the right-hand side written as follows:

$$f(\Sigma)=\Sigma\left(\alpha_{\Sigma}(\overline{\kappa_t}+\overline{\kappa_L})-\beta S_L\frac{\Sigma}{(1-\overline{c})}\right)$$

which has the same structure as the general form of Eq. (4) (Fisher-KPP equations, [15]). Then the equation for Σ takes into account the propagating front in the combustion chamber and more precisely a thin flame front which delimits the fresh gas zone and the burned gas zone.

The equation of the dissipation rate of the turbulent kinetic energy written as follows (from KIVA-GSM):

$$\frac{\partial\overline{\rho}\tilde{\varepsilon}}{\partial t}=\mathrm{div}(\overline{\rho}\vec{\tilde{u}}\tilde{\varepsilon})=\mathrm{div}\left[\left(\lambda_{\varepsilon}\overline{\rho}\tilde{\kappa}\frac{\tilde{\kappa}}{\tilde{\varepsilon}}+\frac{\mu_t}{S_c}\right)\overrightarrow{\mathrm{grad}}\,(\tilde{\varepsilon})\right]$$

$$+(C_1G_k-C_2\overline{\rho}\tilde{\varepsilon})\frac{\tilde{\varepsilon}}{\tilde{\kappa}}-C_3\overline{\rho}\tilde{\varepsilon}\,\mathrm{div}(\vec{\tilde{u}})$$

has also on the right-hand side a nonlinear term which can be written as

$$f(\tilde{\varepsilon})=(C_1G_k-C_2\overline{\rho}\tilde{\varepsilon})\frac{\tilde{\varepsilon}}{\tilde{\kappa}},$$

the latter also has a structure similar to the Eq. (4). We can note here that there is a second front in the combustion chamber. Consequently, we observe two fronts: the first one which we called the «chemical front» or «combustion front» due to the equation for Σ and the second one the «turbulent front» due to the equation for ε. We can find here an analogy with the zero-dimensional models of Keck [16] and Tabaczynski [17], which take into account a chemical front in the form of a volume of burned gas, and a turbulent front in the form of gas carried by the flame.

2.4 Numerical Observations. We have used the results obtained from the KIVA-GSM code applied to the Renault F5R direct injection gasoline engine to observe the trace of the two fronts extracted with the level set method. The engine geometry is described in Table 1 and the combustion chamber is shown on Figure 1.

Two operating conditions have been chosen, in order to be representative of the engine conditions in the vehicle:

- part load at 2000 rpm, equivalence ratio 1, ignition timing 18 deg CA (BTDC).
- full load at 5000 rpm, equivalence ratio 1.11, ignition timing 18 deg CA (BTDC).

The observation of the different fronts has been set up from the different plots along one ray, from the spark plug to the piston.

Chemical Front. The Fig. 2 shows the evolution of the flame surface density obtained at 2000 rpm along one ray. Here from the spark plug to the piston center we observe then the trace of the front. On this figure, at the abscissa 0 (spark plug), we see that there is no longer a flame (only burned gas in this region) and when we follow the ray the front is reached close to the piston shown by the increase of the flame surface density.

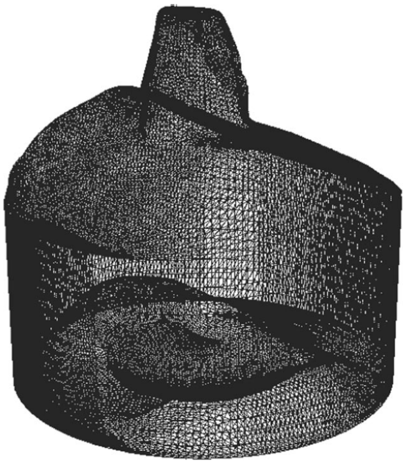

Fig. 1 Geometry of the combustion chamber

We observe the same kind of evolution at 5000 rpm full load. Figures 3–4 show the evolution of the flame surface density for this point and at different times (TDC, 3 deg ATDC); we see on these figures a progress of the flame front with time from the spark plug to the piston along the ray.

Turbulent Front. In order to verify that the behavior is similar for the turbulent kinetic energy dissipation rate, we have plotted on Figs. 5–6 on the same graph at 5000 rpm (TDC, 3 deg ATDC), the chemical front and the turbulent front. A propagating front with time can also be observed for the dissipation rate. The turbulent front is ahead of the chemical front, but both fronts progress at the same speed. This conclusion is independent from the ray orientation; Figs. 7–8 show the progress of both fronts along a different ray, from the spark plug to the cylinder periphery. There also both fronts progress with the same speed, with the

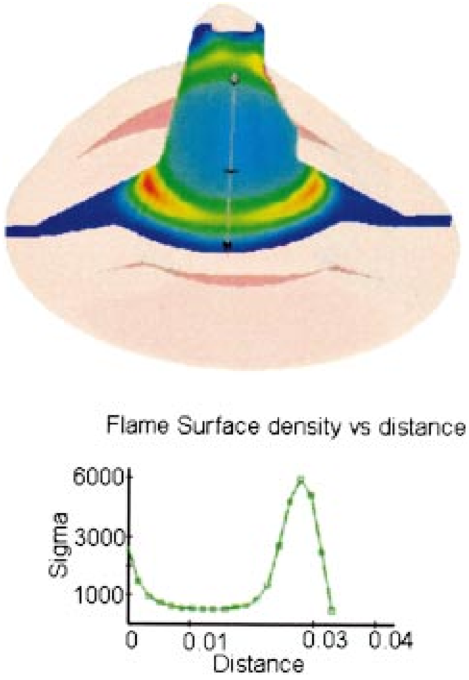

Fig. 2 Reaction rate and flame surface density at part load and 2000 rpm—0 deg crank angle (TDC)

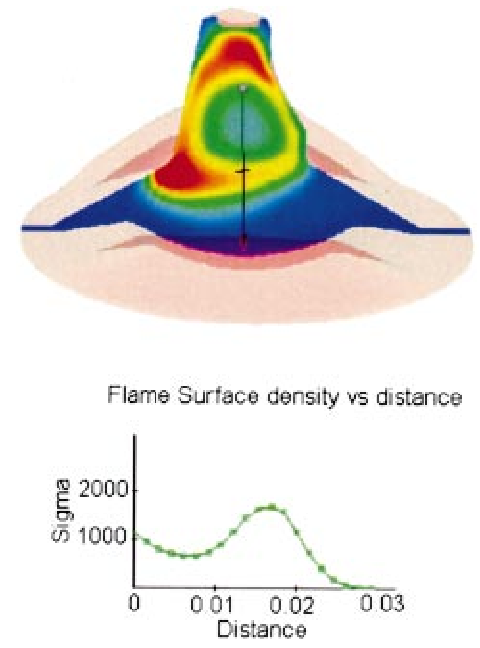

Fig. 3 Reaction rate and flame surface density at full load and 5000 rpm—0 deg crank angle (TDC)

turbulent front in advance. These conclusions are in agreement with the assumption of the zero-dimensional models, [2,16], according to which a volume of gas carried by the flame (function of turbulence) is in advance with respect to a volume of burned gas (representative of chemistry).

The main idea to reduce the three-dimensional models has been found by the observation of the properties of three-dimensional equations, among which two equations have a behavior of fronts propagating, as already seen above. Consequently, the three-dimensional space can be represented by (*n*) times a one-dimensional space; where the number of rays (*n*) is extracted from the three-dimensional computation pictures. To reproduce the same combustion process as the three-dimensional models, we just have to build a one-dimensional model as close as possible to a given three-dimensional model, and to solve the one-dimensional equations on each ray.

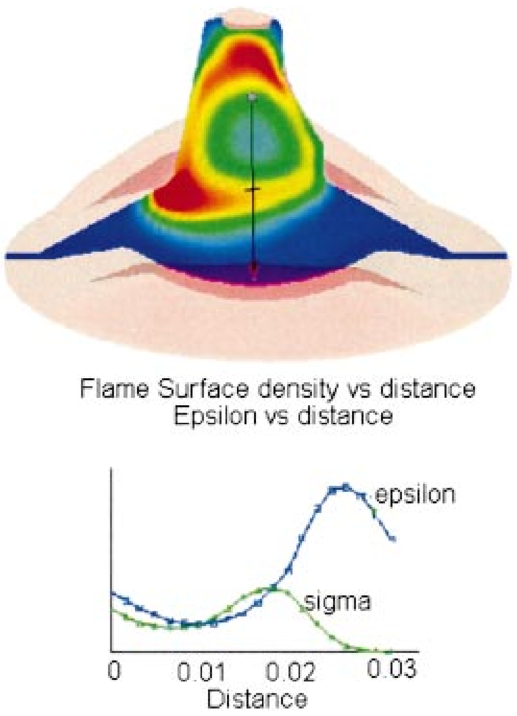

Fig. 5 Reaction rate and flame surface density and epsilon at full load and 5000 rpm—0 deg crank angle (TDC)

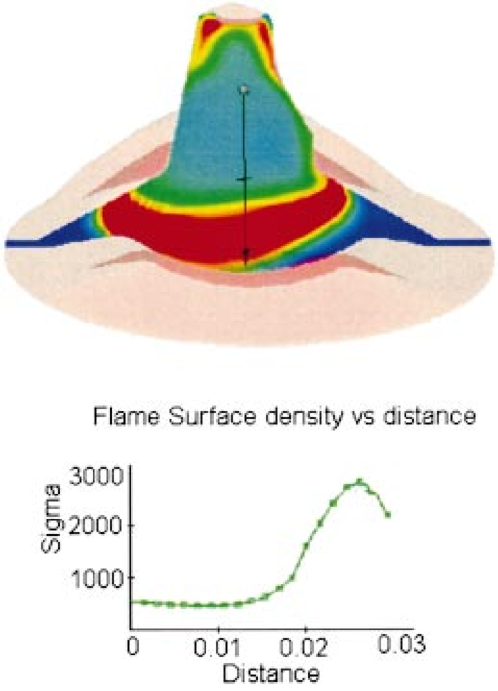

Fig. 4 Reaction rate and flame surface density at full load and 5000 rpm—3 deg crank angle (ATDC)

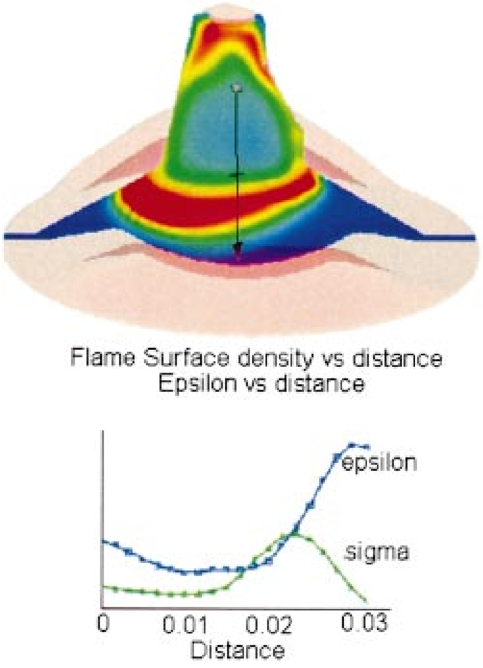

Fig. 6 Reaction rate and flame surface density and epsilon at full load and 5000 rpm—3 deg crank angle (ATDC)

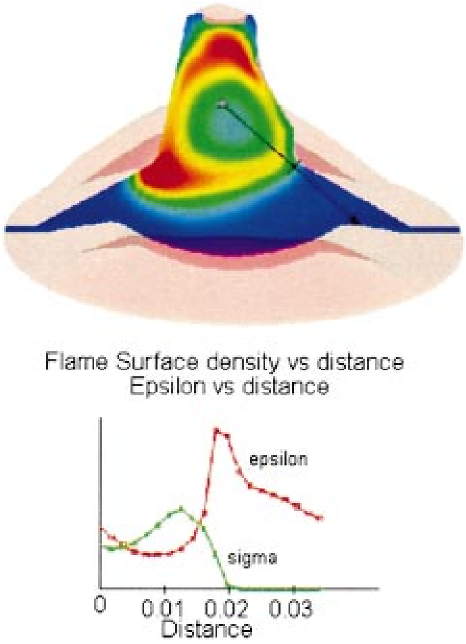

Fig. 7 Reaction rate and flame surface density and epsilon at full load and 5000 rpm (TDC) along a ray from the spark plug to the cylinder periphery

3 One-Dimensional Model Presentation

3.1 Assumptions. The assumptions used for this model are mostly identical to the assumptions used in the three-dimensional models:

- combustion occurs in a premixed flame regime and there are no fuel molecules left in the burned gas,
- the gases are assumed to behave as perfect gases,
- the gas mixture is ideal,

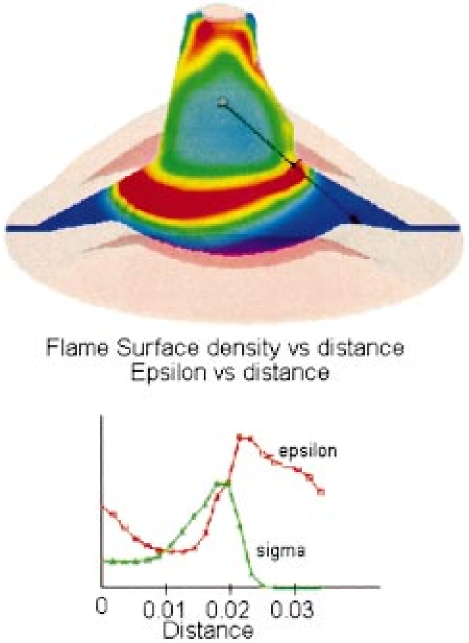

Fig. 8 Reaction rate and flame surface density and epsilon at full load and 5000 rpm—3 deg crank angle (ATDC) along a ray from the spark plug to the cylinder periphery

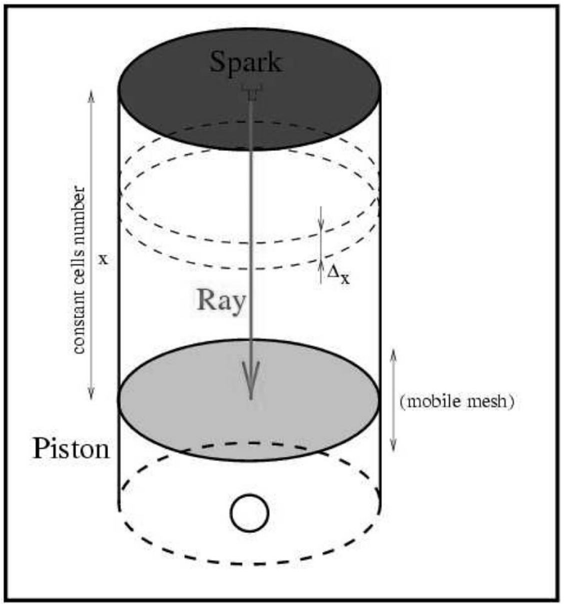

Fig. 9 Model's geometry

- the flamelet assumption is used. It means that the flame is a combination of convex laminar flames, [18]; the combustion chemical reactions take place in a thin sheet which divides the fresh gases and the burned gases,
- the Lewis number characterizing the diffusion of energy with respect to the diffusion of species is equal to 1,
- the gas thermodynamical characteristics $(h, Cp, Cv \ldots)$ are calculated as a function of composition and temperature with a chemical kinetics model,
- the heat release per mass unit is only function of the fuel. It depends on the equivalence ratio and on the rate of residual burned gas,
- the fresh gases are a mixture of fuel, oxygen, nitrogen, carbon dioxide, and water, and
- the laminar and turbulent Schmidt numbers characterizing the diffusion of momentum with respect to the diffusion of species are assumed to be equal to 1.

3.2 Combustion Model. The combustion model used here is a coherent flame model, [18–20], consisting of a thin flame sheet dividing the fresh gases and the burned gases. This flame propagates from the spark plug towards the piston (see Fig. 9). Its shape is modeled by turbulence.

The average fuel consumption rate is given by

$$\overline{\dot{\omega}_F}=\gamma\tau\tilde{T}_u\overline{\rho_u}S_L\Sigma$$

where

$\overline{\rho_u}$ = average local density of the fresh charge,
$\tilde{Y}_{F_u}$ = average mass fraction of fuel in the fresh charge,
S_L = laminar flame velocity,
γ = rate between the specific heats at constant pressure and at constant volume,
τ = rate of thermal expansion (function of fuel), and
Σ = flame area volume density.

The laminar flame velocity is estimated with the Metgalghi and Keck model, [21]. It is described as a function of the fresh charge temperature, of the pressure, and of the rate of residual gas:

$$S_L=S_{L_0}\left(\frac{\tilde{T}_u}{T_0}\right)^{\alpha}\left(\frac{\overline{p}}{p_0}\right)^{\beta}(1-2.07x_{\text{res}}^{0.77})$$

$$S_{L_0}=0.01(30.5-54.9(\phi-\phi_m)^2)$$

$$\alpha=2.4-0.27\phi^{3.51}$$

$$\beta=-0.357+0.14\phi^{2.77}$$

with

$\widetilde{T}_u$ = average fresh charge temperature,
T_0 = a reference temperature,
$\overline{p}$ = average pressure,
p_0 = a reference pressure,
x_{res} = residual gas molar fraction,
ϕ = mixture equivalence ratio, and
ϕ_m = reference equivalence ratio ($\phi_m=1.21$, given by [22]).

The average fuel mass fraction in the fresh charge is given by the following transport equation:

$$\frac{\partial\overline{\rho}\widetilde{Y}_F}{\partial t}+\frac{\partial\widetilde{u}\overline{\rho}\widetilde{Y}_F}{\partial x}=\frac{\partial}{\partial x}\left[\lambda_{YF}\overline{\rho}\widetilde{k}\frac{\widetilde{k}}{\widetilde{\varepsilon}}\frac{\partial\widetilde{Y}_F}{\partial x}\right]-\overline{\rho}Y_{Fu}S_L\Sigma$$

where

$\overline{\rho}$ = average local density,
$\widetilde{Y}_F$ = fuel average mass fraction (in the Favre meaning),
$\widetilde{u}$ = local average velocity,
λ_{YF} = 0.09, and
Y_{Fu} = fuel average mass fraction in the fresh gas (this value is constant because the mixture is homogeneous).

The above equation is coupled through $\overline{\dot{\omega}}_F$ with the equation of transport which gives the flame surface density:

$$\frac{\partial\Sigma}{\partial t}+\frac{\partial\widetilde{u}\Sigma}{\partial x}=\frac{\partial}{\partial x}\left[\lambda_\Sigma\overline{\rho_u}\widetilde{k}\frac{\widetilde{k}}{\widetilde{\varepsilon}}\frac{\partial(\Sigma/\overline{\rho})}{\partial x}\right]+K\alpha_\Sigma\frac{\widetilde{\varepsilon}}{\widetilde{\kappa}}\Sigma+\frac{2}{3}\frac{\partial\widetilde{u}}{\partial x}\Sigma$$

$$-\frac{\beta_\Sigma\Sigma}{(1-\overline{c})}\widetilde{S}_L\Sigma,$$

where K represents the turbulent stretching of the flame front calculated from the ITFNS (intermittent turbulence net flame stretch) model, [23]. $\overline{c}$ is the variable which characterizes the combustion progress, given by

$$\overline{c}=1-\frac{\overline{\rho}\widetilde{Y}_F}{\overline{\rho_u}Y_{F_u}}.$$

The flame kernel ϕ_Σ which represents the initial condition (function of time) for the flame surface density is described as following:

$$\phi_\Sigma(x)=\frac{C}{\Omega}\left(1-\mathrm{erf}\left(\frac{|r(x)-R_1|}{2l_e}\right)\right)$$

where Ω is such as

$$\int_V\phi_\Sigma dV=4\pi R_1^2=C$$

with

R_l = the flame radius core,
l_e = the representative length of the fluctuating position of the spark center, and
l_e = $l_0+u't_1$ (l_0: constant; u': fluctuation of the velocity field; t_1: ignition delay).

The mass balance equation and the momentum balance equation are written:

$$\frac{\partial\overline{\rho}}{\partial t}+\frac{\partial\overline{\rho}\widetilde{u}}{\partial x}=0$$

$$\frac{\partial\overline{\rho}\widetilde{u}}{\partial t}+\frac{\partial\overline{\rho}\widetilde{u}\widetilde{u}}{\partial x}=\frac{\partial}{\partial x}\left[\frac{4}{3}\lambda_u\overline{\rho}\widetilde{\kappa}\frac{\widetilde{\kappa}}{\widetilde{\varepsilon}}\frac{\partial\widetilde{u}}{\partial x}-\frac{2}{3}\overline{\rho}\widetilde{\kappa}\right]-\frac{\partial\overline{p}}{\partial x}.$$

The energy balance is then written in the following way:

$$\frac{\partial\overline{\rho}\widetilde{T}}{\partial t}+\frac{\partial\overline{\rho}\widetilde{u}\widetilde{T}}{\partial x}=\gamma\frac{\partial}{\partial x}\left[\lambda_t\overline{\rho}\widetilde{k}\frac{\widetilde{k}}{\widetilde{\varepsilon}}\frac{\partial\widetilde{T}}{\partial x}\right]-\frac{\overline{p}}{c_v}\frac{\partial\widetilde{u}}{\partial x}+\gamma\tau\widetilde{T}_u\overline{\rho_u}S_L\Sigma+\phi_{tt}\,.$$

The fresh charge energy balance is solved to find the average temperature and average density of the fresh charge which is a closing equation. It is written

$$\frac{\partial\overline{\rho}\widetilde{T}_u}{\partial t}+\frac{\partial\overline{\rho}\widetilde{u}\widetilde{T}_u}{\partial x}=\gamma_u\frac{\partial}{\partial x}\left[\lambda_{tu}\overline{\rho}\widetilde{k}\frac{\widetilde{k}}{\widetilde{\varepsilon}}\frac{\partial\widetilde{T}_u}{\partial x}\right]-\frac{\overline{\rho}}{\overline{\rho_u}}\frac{\overline{p}}{c_v}\frac{\partial\widetilde{u}}{\partial x}$$

$$+\frac{(\gamma_u-1)}{\gamma_u}\frac{\widetilde{T}_u}{\widetilde{T}}\gamma\tau\widetilde{T}_u\overline{\rho_u}S_L\Sigma+\phi_{nu}\,.$$

The term ϕ_{tt} represents the heat exchange between the gas and the cylinder wall and the term ϕ_{ttu} represents the heat exchange between the fresh gas and the cylinder wall.

3.3 Turbulence Model Including the Swirl and Tumble Motion Effects. The turbulence model used here is a model of the type (k,ε), [24–26], written for our case in a one-dimensional form.

The mean motions of the swirl and the tumble are generally used in the engines to increase the turbulence levels which have a beneficial effect on the air-fuel mixture preparation. In the GDI engines the tumble is also used to carry the fuel near the spark plug for the improvement of the stratification.

The velocity field of the one-dimensional model converges naturally to a linear solution between the zero velocity at the cylinder head and the piston velocity. Consequently, the tumble or the swirl motions cannot be described by a one-dimensional velocity field because those motions are not one dimensional. However, their mean motion acts on the combustion by the turbulence. Therefore, to take into account the influence of turbulent kinetic energy generated by the swirl and tumble motion, their effect is introduced in the turbulence model by a source term obtained from the equation of the vorticity:

$$\frac{d(I\omega)}{dt}=\dot{J}_i-\dot{J}_e-\tau_f$$

where
I is the inertial momentum for the gas mass,
ω is the angular velocity of the fluid,
$\dot{J}_i$ and $\dot{J}_e$ are the angular momentum flux at the intake and the exhaust, and
τ_f is the wall shear stress.

With the assumption that all the energy dissipated by the wall friction (from the swirl and tumble) is transformed completely in turbulent kinetic energy, the above equation becomes

$$-V\frac{d(\overline{\rho}\widetilde{\kappa})}{dt}-\overline{\rho}\widetilde{\kappa}\frac{dV}{dt}=I\omega\frac{d\omega}{dt}$$

where V is the chamber volume.

The turbulent kinetic energy and the dissipation rate are described by the equations of this turbulence model where the effect of swirl and tumble has been added as following:

$$\frac{\partial(\overline{\rho}\widetilde{k})}{\partial t}+\frac{\partial(\widetilde{u}\overline{\rho}\widetilde{k})}{\partial x}=\frac{\partial}{\partial x}\left[(\mu_L+\mu_T)\frac{\partial\widetilde{k}}{\partial x}\right]+\left[\frac{4}{3}(\mu_L+\mu_T)\frac{\partial\widetilde{u}}{\partial x}\right.$$

$$\left.-\frac{2}{3}\overline{\rho}\widetilde{k}\right]\frac{\partial\widetilde{u}}{\partial x}-\overline{\rho}\widetilde{\varepsilon}-\frac{I\omega}{V}\frac{d\omega}{dt}-\frac{\overline{\rho}\widetilde{k}}{V}\frac{dV}{dt}$$

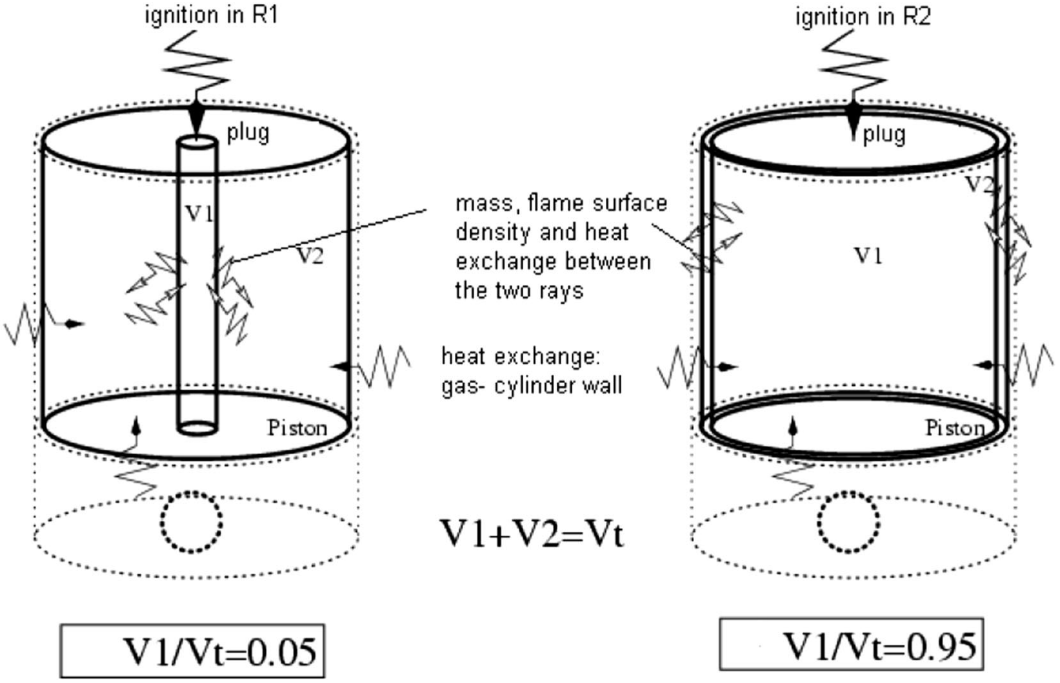

Fig. 10 Control volume for the two rays model

$$\frac{\partial(\overline{\rho}\tilde{\varepsilon})}{\partial t}+\frac{\partial(\tilde{u}\overline{\rho}\tilde{\varepsilon})}{\partial x}=\frac{\partial}{\partial x}\left[(\mu_L+\mu_T)\frac{\partial\tilde{\varepsilon}}{\partial x}\right]+C_{\varepsilon_1}\frac{\tilde{\varepsilon}}{\tilde{k}}\left[\frac{4}{3}(\mu_L+\mu_T)\frac{\partial\tilde{u}}{\partial x}\right.$$

$$\left.-\frac{2}{3}\overline{\rho}\tilde{k}\right]\frac{\partial\tilde{u}}{\partial x}-C_{\varepsilon_2}\overline{\rho}\frac{\tilde{\varepsilon}^2}{\tilde{k}}-C_{\varepsilon_3}\overline{\rho}\tilde{\varepsilon}\frac{\partial\tilde{u}}{\partial x}$$

$$-\frac{\tilde{\varepsilon}}{\tilde{k}}\left(\frac{I\omega}{V}\frac{d\omega}{dt}+\frac{\overline{\rho}\tilde{k}}{V}\frac{dV}{dt}\right)$$

where C_{ε_1}, C_{ε_2}, and C_{ε_3} are three constants, respectively, equal to 1.44, 1.92, and 1 (values usually given to these constants).

4 Two Rays Model

The one-dimensional model equations presented in Section 3 have been solved over two parallel rays (chosen by hand). The first one R_1 is directed in the center of the combustion chamber, from the spark plug towards the piston center (see Fig. 10). The second one R_2 is directed towards the cylinder wall in order to take into account the development of the flame in the transverse direction and the heat exchange between the gas and the cylinder wall.

Each ray is associated with a fraction of total volume: its control volume, a measure of its importance. We have then defined a ratio between the two volumes (see Fig. 10) as

$$\Upsilon=V_1/V_t$$

where V_1 is the volume corresponding to the ray R_1 and V_t represents the total volume (V_1+V_2). When Υ tends towards one, the volume V_1 tends towards the total volume.

The two adjacent volumes exchange mass, heat, and surface density between them through their common surface. The volume V_1 exchanges heat with the cylinder wall. The exchange terms are necessarily zero-dimensional because the objective here is to build a model (n) times one dimension.

The exchanges between the rays take place with a transverse velocity function of the thermodynamic conditions in the upstream cell. This velocity is modeled by the Barré-St-Venant formula as follows:

$$w=\frac{\overline{p}_{\text{upstream}}}{\overline{\rho}_{\text{upstream}}}\sqrt{\frac{2\gamma_{\text{upstream}}}{(\gamma_{\text{upstream}}-1)r_{\text{upstream}}\tilde{T}_{\text{upstream}}}(\chi^{2/\gamma_{\text{upstream}}}-\chi^{1+\gamma_{\text{upstream}}/\gamma_{\text{upstream}}})}$$

where w represents the exchange velocity and the subscript upstream refers to the upstream conditions (see Fig. 11).

The one-dimensional model presented in the section above, is written with the exchanges terms in the following way:

$$\frac{\partial\overline{\rho_i}\tilde{\Lambda}_i}{\partial t}+\frac{\partial\overline{\rho_i}\tilde{u}_i\tilde{\Lambda}_i}{\partial x_i}=\cdots+(-1)^i\frac{S_{\text{exch}}}{\overleftrightarrow{V}_{x_i}}w_{(x_i)}[(\tilde{\Lambda}_1-\tilde{\Lambda}_0)\overline{\rho}_{\text{conv}}$$

$$+(\overline{\rho_2}-\overline{\rho_1})\tilde{\Lambda}_{\text{conv}}]$$

where

S_{exch} = is the common surface exchange (function of Υ),
$\overleftrightarrow{V}_{(x_i)}$ = is the volume of the cell receiving the exchange (function of Υ),
$\overline{\rho}_{\text{conv}}$ = is the convected density,
$\tilde{\Lambda}_{\text{conv}}$ = is the convected quantity $(\Sigma,\tilde{T},\tilde{T}_u,\tilde{Y}_F,\overline{\rho})$,
i = is equal to zero for the ray R_1 and equal to 1 for the ray R_2, and

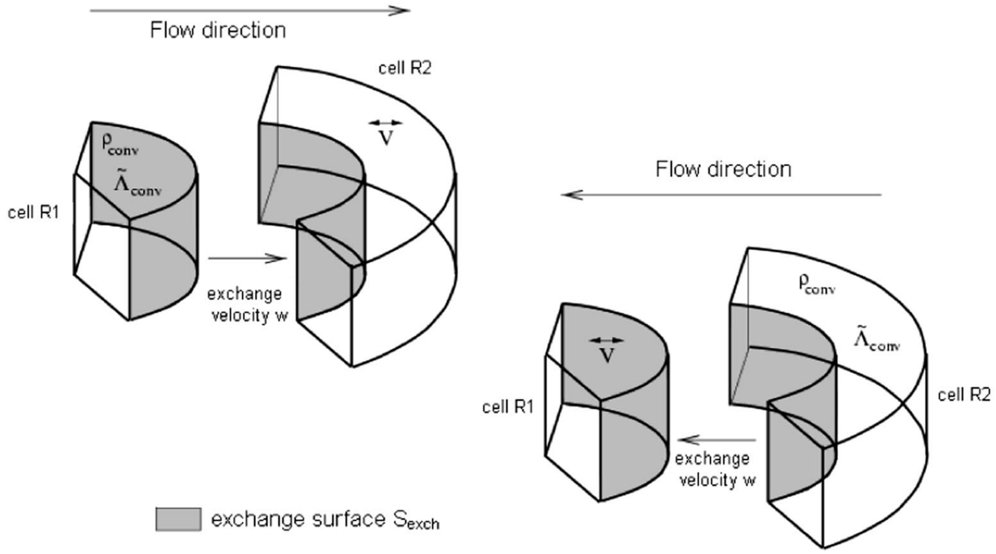

Fig. 11 Exchanges terms between the two connected cells function of the velocity direction

$\tilde{\Lambda}$ = corresponds to the different variables $(\Sigma,\tilde{T},\tilde{T}_u,\tilde{Y}_F,\overline{\rho})$.

5 Numerical Methods

The model presented here has been written with Matlab Simulink, in order to make its use easier for industrial applications. A numerical scheme which is second order in space has been used for the spatial resolution. The time integration is managed by Matlab and the solver used a Runge-Kutta scheme of the fourth order. The boundary conditions for density are written with the NSCBC formalism (Navier-Stokes characteristic boundary conditions), [27], in order to make the numerical scheme more conservative. The one-dimensional mesh is mobile and takes into account the motion of the piston with time. The change in ray length is made at constant mesh numbers. The mesh size is changing with time.

6 Results

6.1 Results for the One Ray Model and the Two Rays Model. The two-rays model has been built in order to show the feasibility of the *n*-rays modeling of combustion in homogeneous mode. The one-dimensional model developed here has been solved also over one ray from the spark plug to the piston center (in this case the exchanges terms become equal to zero and only the equations presented in Section 3 are solved over one ray). As we have seen before, the choice of the value for the ratio Υ (for the two rays model) has a consequence on

- the heat transfer between the gas and the cylinder wall and
- the size of the cell where the spark ignition occurs.

The ratio Υ varies between zero (the volume V_2 is more important) and one (the volume V_1 is more important), we have then fixed two values for this ratio (0.95 and 0.05) in order to cover the whole variation domain.

Figure 12 shows the evolution of the gas temperature during the compression stroke for the one-ray model and the two-rays model ($\Upsilon=0.05$ and $\Upsilon=0.95$). We can observe from this figure that when the volume V_2 is smaller (i.e., $\Upsilon=0.95$), the mean temperature of the gas is higher during the compression stroke (the gas temperature is lower than the wall temperature). This means that when the external volume is small, the heat transfer is amplified from the cylinder wall to the gas.

We observe the same tendencies for the evolution of the mean temperature during the expansion stroke (Fig. 13). We observe the effect of Υ on the heat transfer during this phase, when the value of Υ is high the mean temperature of the gas is high. These observations are in agreement with the conclusion above, when the external volume is small (here the gas temperature is greater than the wall temperature) the heat exchange is higher from the gas to the wall and the mean temperature of the gas is smaller.

The effect of Υ on the flame kernel is to modify the size of the cell where the ignition occurs. The burned mass fraction at the beginning of combustion is shown in Fig. 14, where we observe that when Υ is high the burning volume is important and the combustion is slightly faster.

6.2 Comparison of the Three-Dimensional Model With the One-Dimensional Model. The results of the one-dimensional model have been validated with those given by the complex three-dimensional computation code. As a matter of fact, the objective of this study being the reduction of multidimensional models, it seemed more appropriate to compare the results of the one-dimensional model to the results of the three-dimensional model from which it was derived. Of course, only data integrated on the whole combustion chamber can be compared. We show here the evolution of burned mass fraction and average cylinder pressure. The two operating conditions were tested on the mesh of the Renault F5R engine: one full load operating condition at 5000 rpm, a second one at 2000 rpm part load. The two models were initialized with the same values coming from three-dimensional intake computations and the simulations were done from 130 deg CA (BTDC) to 100 deg CA (ATDC).

At 2000 rpm the evolutions of the pressure (Fig. 15) from the two models are close. The one-dimensional model overestimates the maximum pressure, in this case the combustion is slightly faster (Fig. 16). This difference is mostly due to the fact that for the one-dimensional model we describe the combustion for the whole combustion chamber over two rays. Consequently, the

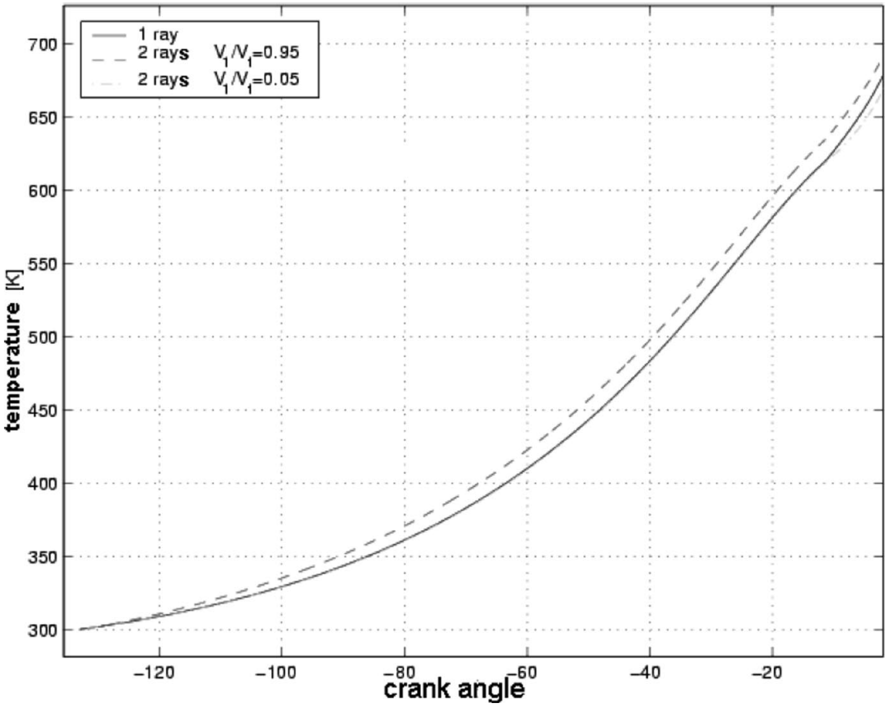

Fig. 12 Evolution of the temperature during the compression stroke for the one ray model and the two rays model versus crank angle at 2000 rpm part load

flame propagation occurs slightly faster due to the size of the cell which is function of the parameter Y. This parameter has an important effect on the flame kernel. The improvement of these results is in progress by building a geometrical model for the propagating phenomena.

At 5000 rpm, we observe the same tendencies as for 2000 rpm, the pressure calculated by the one-dimensional model is higher than the pressure given by the three-dimensional model (Fig. 17) and the combustion is faster (Fig. 18). The differences for this engine speed and load are more important.

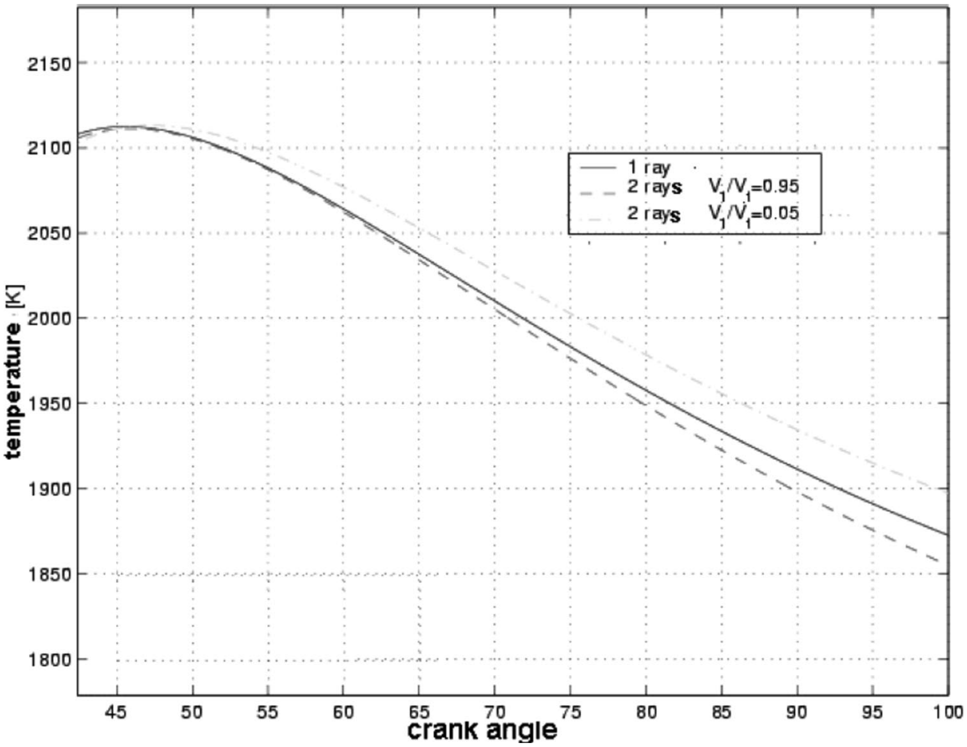

Fig. 13 Evolution of the temperature during the expansion stroke for the one ray model and the two rays model versus crank angle at 2000 rpm part load

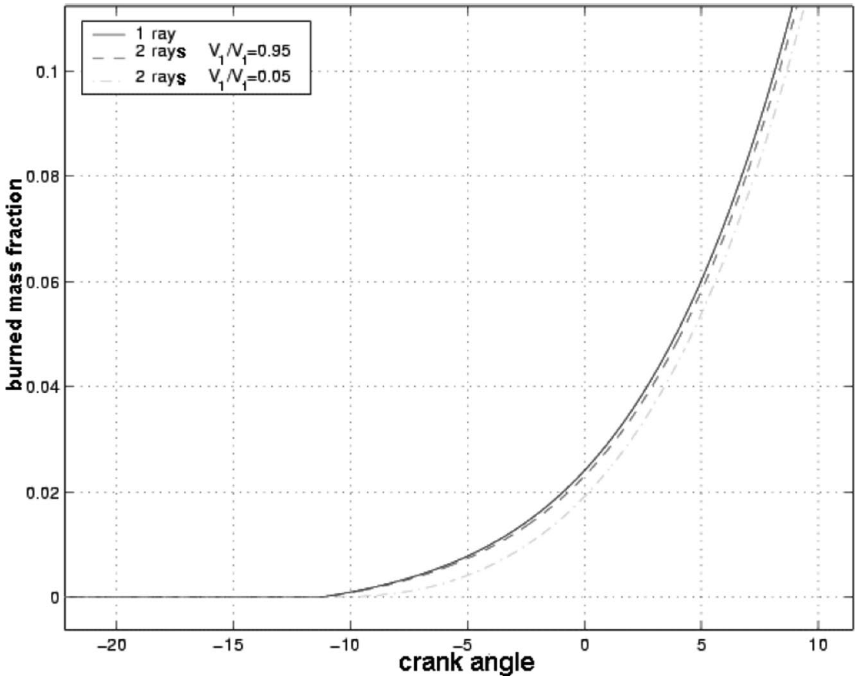

Fig. 14 Evolution of the burned mass fraction at the beginning of combustion for the one ray and the two rays models versus crank angle at 2000 rpm part load

It can be noticed that for the two parameters above, on the chosen operating conditions, the one-dimensional model gives very close results to those given by the three-dimensional model, with a much reduced computation time. In Table 2 the computation times for the one-dimensional model and the two operating conditions are compared to those required by KIVA-GSM. It can be noticed that for the two-rays model the computation time is higher than for the one-ray model, which is due to the increase in number of the cells. However, those computation times are around a few minutes instead of several hours for the KIVA code.

The differences observed between the pressure simulated by the one-dimensional model and the three-dimensional model corre-

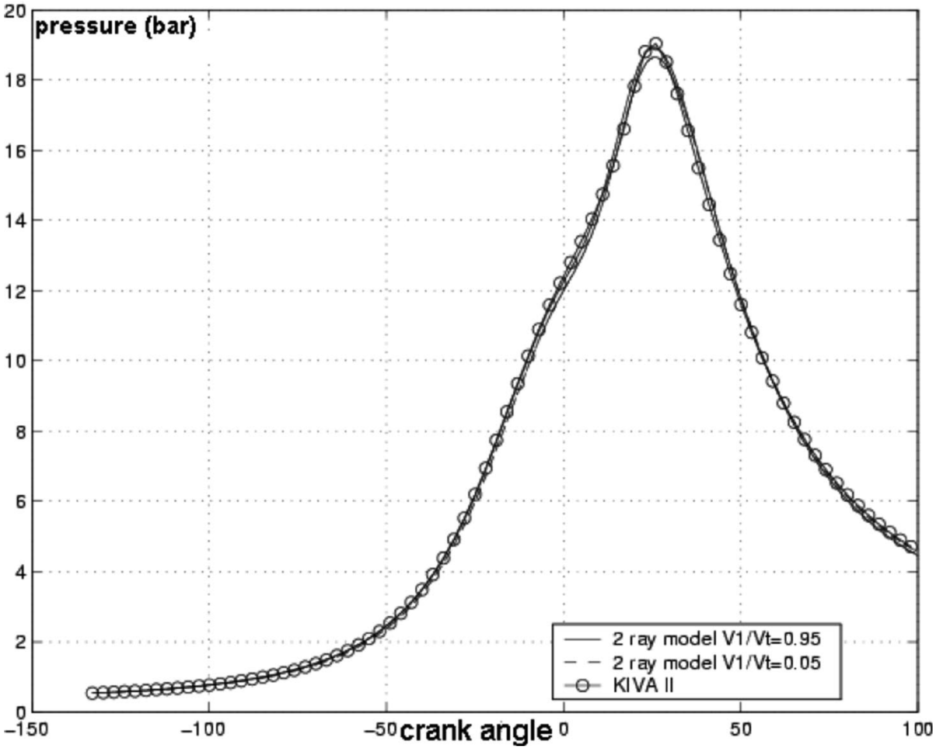

Fig. 15 Comparison 2 rays one-dimensional model/KIVA. Cylinder pressure versus crank angle at 2000 rpm.

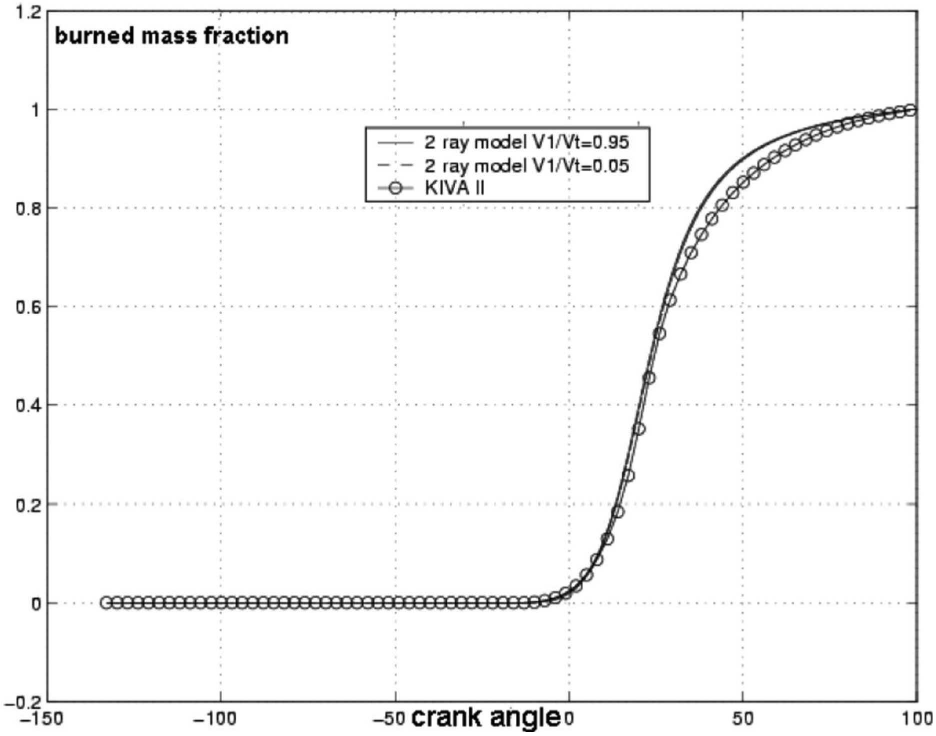

Fig. 16 Comparison 2 rays one-dimensional model/KIVA. Burned mass fraction versus crank angle at 2000 rpm.

spond to the maximum cycle pressure. The one-dimensional model will be used for the engine tuning and in this case, the output parameter is the work transferred from the gas to the piston. Consequently, these maximum pressure differences have an insignificant effect on the net indicated work per cycle (or the mean effective pressure). In Tables 3 (2000 rpm) and 4 (5000 rpm), the comparison between the different models (one-dimensional and three-dimensional) and engine measurements shows that the relative error is smaller than 5% in terms of engine torque and mean effective pressure. In the same tables, the results

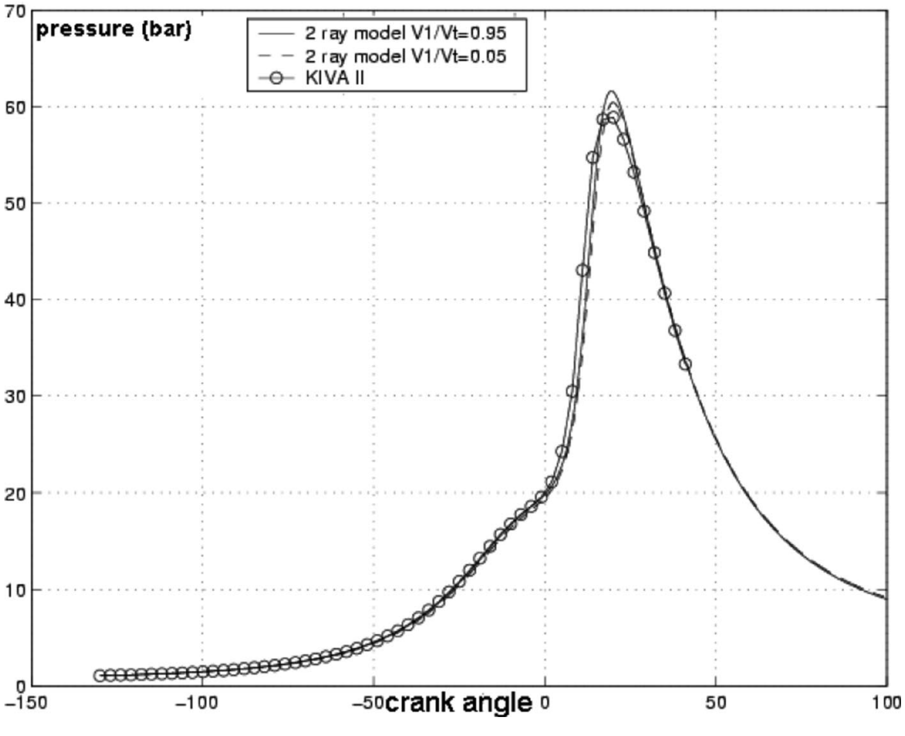

Fig. 17 Comparison 2 rays one-dimensional model/KIVA. Cylinder pressure versus crank angle at 5000 rpm.

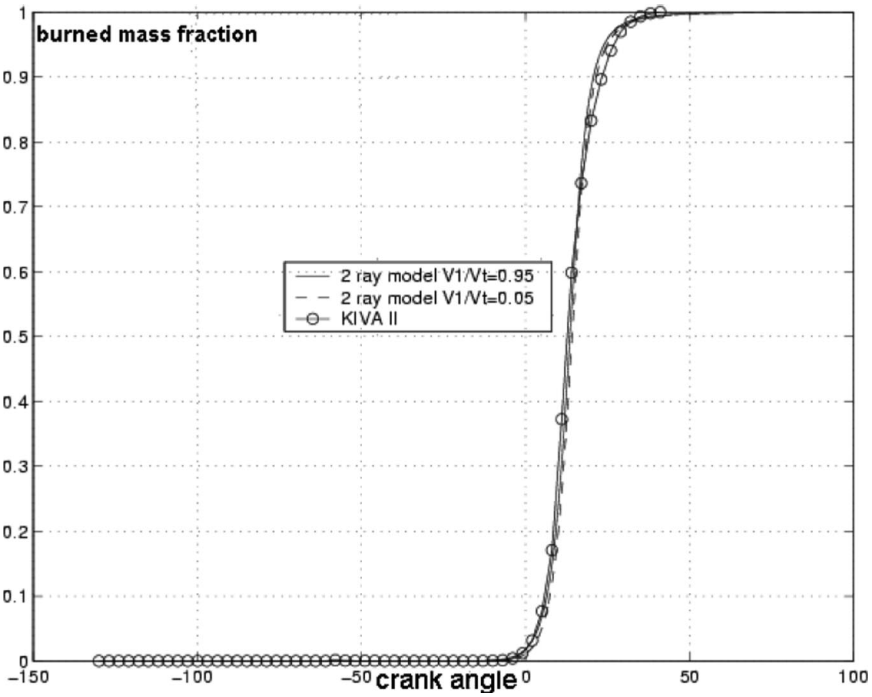

Fig. 18 Comparison 2 rays one-dimensional model/KIVA. Burned mass fraction versus crank angle at 5000 rpm.

obtained with the one-dimensional model over two rays are improved compared to the results obtained with the one-dimensional model over one ray.

Conclusion and Perspectives

In this study, a one-dimensional model has been developed to describe the combustion process in the gasoline direct injection engine. The equations of this one-dimensional model have the same mathematical structure as the equations of the three-dimensional model (KIVA-GSM). Furthermore, the combustion, turbulence, and ignition models applied in one-dimensional are derived from those used in KIVA-GSM. The numerical platform used in Matlab Simulink, since this model is aimed at industrial use and has to be user friendly.

The objective of this one-dimensional model is to reproduce the same tendencies as those obtained by KIVA-GSM with a short computational time. Consequently, this model has been built from the observations of the evolution of the flame surface density obtained from the three-dimensional simulation, which has an evolution similar to the propagation fronts. The one-dimensional model is a set of *n* one-dimensional equations (i.e., for *n* rays). For the present study, one or two rays have been chosen manually. At first, the model has been applied to a homogeneous charge because in this case the combustion occurs in premixed flames, which are more simple to describe, and it is easier to verify if this approach gives good tendencies.

The comparison of the results between the one-dimensional model and the three-dimensional model has shown that the one-dimensional model overestimates the maximum pressure, which has an insignificant effect on the output parameters required for the engine tuning phase. The model needs a few minutes to simu-

Table 2 Comparison of computation times for the one-dimensional and KIVA code at 2000 rpm and at 5000 rpm. Simulations from 130 deg CA (BTDC) to 100 CA (ATDC).

Computation Times From 130 deg (BTDC) to 100 deg (ATDC)	2000 rpm	5000 rpm
1 ray model (50 cells) SUN ULTRA 10	2 m 53 s	1 m 6 s
2 rays model SUN ULTRA 10 (2×50 cells)	11 m 49 s	3 m 21 s
KIVA-GSM (117306 cells) high end computer NEC SX-5S	Greater than 48 h	24 h

Table 3 Comparison of the mean effective pressure and the engine torque for the one-dimensional model, engine measurements and the KIVA code at 2000 rpm

2000 rpm (Part Load)	Imep+ (Bar)	CMI+ (N.m)	Relative Error/ KIVA-GSM
Engine	4.8	191.4	
KIVA-GSM	4.77	189.67	
1 ray model	4.92	195.61	3.14%
2 rays model ($\Upsilon=0.95$)	4.85	192.98	1.68%
2 rays model ($\Upsilon=0.05$)	4.91	195.21	2.94%

Table 4 Comparison of the mean effective pressure and the engine torque for the one-dimensional model, engine measurements and the KIVA code at 5000 rpm

5000 rpm (Full Load)	Imep+ (Bar)	CMI+ (N.m)	Relative Error/ KIVA
Engine	4.1	163.2	
KIVA-GSM	4.07	161.73	
1-ray model	4.27	170.10	4.91%
2-rays model ($\Upsilon=0.95$)	4.20	166.82	3.19%
2-ray model ($\Upsilon=0.05$)	4.19	166.41	2.95%

late the combustion process, instead of several hours required by KIVA-GSM code, for a relative error lower than 5% in term of mean effective pressure and engine torque.

In the further steps of this study, we will improve the model described in this paper by increasing the number of representative rays. The level set method will be used to represent the numerical front, which will lead to extract the *n* representative rays. For the heterogeneous mode, the model presented here can reproduce the premixed flames but the methodology needs further improvements, to take into account the diffusion flames which occur also when the air-fuel mixture is not homogeneous. Furthermore, to control the pollutant emissions a chemical kinetic reaction mechanism model will be added to the one-dimensional model to evaluate emissions for different engine operations.

Acknowledgments

This research was funded by Renault Automobiles. The authors wish to thank this company.

References

[1] Amsden, A. A., O'Rourke, P. J., and Butler, T. D., 1989, ''KIVA II: A Computer Program for Chemically Reactive Flows With Sprays,'' Paper No. LA-11560-MS, Los Alamos National laboratory, Albuquerque, NM.

[2] Tabaczyski, R. J., 1977, ''A Turbulent Entrainment Model for Spark Ignition Engine Combustion,'' SAE Technical Paper No. 770647.

[3] Tabaczynski, R. J., Novak, J. M., and Hires, S. D., 1978, ''The Prediction of Ignition Delay and Combustion Intervals for a Homogeneous Charge Spark Ignition Engine,'' SAE Technical Paper No. 780232.

[4] Heywood, J. B., and Poulos, S. G., 1983, ''The Effect of Chamber Geometry on Spark Ignition Engine Combustion,'' SAE Technical Paper No. 830334.

[5] Rashidi, M., Beretta, G. P., and Keck, J. C., 1983, ''Turbulent Flame Propagation and Combustion in Spark Ignition Engines,'' Combust. Flame, **52**, pp. 217–245.

[6] Borgnakke, C., Arpaci, V. S., and Tabaczynski, R. J., 1980, ''A Model for the Intantaneous Heat Transfer and Turbulence in a Spark Ignition Engine,'' SAE Technical Paper No. 800287.

[7] Heywood, J. B., 1998, *Internal Combustion Engine Fundamentals*, McGraw-Hill, New York.

[8] Osher, S., and Sethian, J. A., 1988, ''Fronts Propagating Curvature-Dependent Speed: Algorithms Based on Hamilton-Jacobi Formulations,'' J. Comput. Phys., **78**, pp. 12–49.

[9] Sethian, J. A., 1999, *Level Set Methods and Fast Marching Methods*, Cambridge University Press, Cambridge, UK.

[10] Berkooz, G., Holmes, P., and Lumley, J. L., 1993, ''The Proper Orthogonal Decomposition in the Analysis of Turbulent Flows,'' Annu. Rev. Fluid Mech., **25**(5), pp. 539–575.

[11] Berestycki, H., Nicolaenko, B., and Sheurer, S., 1985, ''Traveling Wave Solutions to Combustion Models and Their Singular Limits,'' SIAM (Soc. Ind. Appl. Math.) J. Math. Anal., **6**(6) .

[12] Berestycki, H., Larrouturrou, B., and Lions, P. L., 1990, ''Multi-Dimensional Traveling Wave Solutions of a Flame Propagation Model,'' Arch. Ration. Mech. Anal., **1**, pp. 33–49.

[13] Ketfi-Cherif, A., 1999, ''Modélisation mathématique d'organes de véhicules automobiles à basse consommation. Application en simulation, estimation et commande,'' Ph.D. thesis, Université Paris IX Dauphine.

[14] Fisher, R. A., 1937, ''The Wave of Advance of Advantageous Genes,'' Ann. Eugenics, **7**

[15] Kolmogoroff, A., Petrovskii, I., and Piscounoff, N., 1937, ''Etude de l'équation de diffusion avec croissance de quantité de matière et son application à un problème biologique,'' *Bulletin of Mathematics*, **1**, Moscou University.

[16] Blizard, N. C., and Keck, J. C., 1974, ''Experimental and Theorical Investigation of Turbulent Burning Model for Internal Combustion Engines,'' SAE Technical Paper No. 740191.

[17] Tabacsynski, R. J., 1977, ''A Turbulent Entrainment Model for Spark Ignition Engine Combustion,'' SAE Technical Paper No. 770647.

[18] Duclos, J. M., Veynante, D., and Poinsot, T., 1993, ''A Comparison of Flamelet Models for Premixed Turbulent Combustion,'' Combust. Flame, **95**, pp. 101–117.

[19] Boudier, P., Henriot, S., Poinsot, T., and Baritaud, T., 1992, ''A Model for Turbulent Flame Ignition and Propagation in Piston Engines,'' The Combustion Institute, Pittsburgh, 24th Symposium on Combustion, Sydney, Australia, PA, p. 503.

[20] Duclos, J. M., Zolver, M., and Baritaud, T., 1999, ''three-dimensional Modeling of Combustion for DI-SI Engines,'' Rev. Inst. Fr. Pet., **54**, pp. 259–264.

[21] Metghalchi, M., and Keck, J. C., 1982, ''Burning Velocities of Mixture of Air With Methanol, Isooctane and Indolene at High Pressure and Temperature,'' Combust. Flame, **48**, pp. 191–210.

[22] Rodhes, D. B., and Keck, J. C., 1985, ''Laminar Burning Speed Measurements of Indolene-Air Diluent Mixtures at High Pressure and Temperature,'' SAE Technical Paper No. 850047.

[23] Meneveau, C., and Poinsot, T., 1991, ''Stretching and Quenching of Flamelets in Premixed Turbulent Combustion,'' Combust. Flame, **86**, pp. 311–332.

[24] Lumley, J. L., and Tennekes, H., 1972, ''A First Course in Turbulence,'' M.I.T. Press, Cambridge, MA.

[25] Hinze, J. O., 1975, *Turbulence*, McGraw-Hill, New York.

[26] Landau, L., and Lifchitz, E., 1986, *Physique Théorique—Mécanique des Fluides*, MIR.

[27] Poinsot, T. J., and Lele, S. K., 1992, ''Boundary Conditions for Direct Simulations of Compressible Viscous Flows,'' J. Comput. Phys., **101**, pp. 104–130.

Analysis of a Turbulent Propeller Inflow

Stephen A. Huyer
e-mail: huyersa@npt.nuwc.navy.mil

Stephen R. Snarski

Naval Undersea Warfare Center,
Hydrodynamics Branch,
Code 8233, Building 1302,
Newport RI 02874

The unsteady turbulent inflow into a swirl-inducing stator upstream of propeller (SISUP) propeller is presented. The upstream stators and hull boundary layer generate a complex, three-dimensional inflow that was measured using x-wire anemometry. High resolution measurements consisting of 12 locations in the radial direction and 600 in the circumferential direction yielded mean velocity and rms turbulent quantities for a total of 7200 points. The axial, radial, and circumferential velocity fields were thus measured. This enabled the induced velocity due to the stator wakes, the induced velocity due to the propeller, and the turbulent hull boundary layer to be characterized. To assist in decoupling the effects on the velocity field due to the stator and propeller, a potential flow computation of the swirl component was used. Spectra and autocorrelation analysis of the inflow velocity field were used to estimate the integral length scale and lend further insight into the turbulent flow structure. These data can be used to validate computational fluid dynamics codes and assist in developing of turbulent inflow models.

[DOI: 10.1115/1.1570860]

Introduction

Propellers that operate on actual vehicles ingest a complex unsteady inflow, which greatly affects the unsteady forces and radiated noise. This unsteady inflow is generated by the wakes and boundary layers produced by upstream surfaces. On submarines, the sail, bow planes, stern planes, and rudders all produce wakes in addition to the hull boundary layer. Similarly, on undersea weapons and unmanned undersea vehicles, upstream control surfaces and stators produce wakes, which combine with the hull boundary layer to produce a very complex spatially and temporally varying inflow. In turn, the inflow is modified due to the thrust produced by the propeller. Understanding the unsteady characteristics of the inflow and subsequent modification due to the propeller is key to understanding the response and radiated noise. A detailed description of the upstream inflow into an actual integrated propeller on an axisymmetric body during operation would facilitate an understanding of the underlying physical mechanisms.

There are several reports of the unsteady flow fields downstream of propellers or cascades. Measurements by Satyanarayana [1] characterized the unsteady wakes produced by airfoils and cascades undergoing sinusoidal gusts. The purpose was to validate the assumptions made by theory (Sears [2] strip theory, for example). He measured the instantaneous and time-averaged wake velocities characterizing the velocity defects and noted the cascade effect. He also demonstrated using pressure measurements at the trailing edge that the Kutta condition assumption was essentially valid for low frequencies. Inoue and Kuroumaru [3] measured the three-dimensional structure in the wake of a propeller and characterized the wake vorticity shed from the hull, the propeller blades, and the tip vortices. Some very recent thesis work by Lynch [4] characterized the modification of a grid-generated turbulent inflow by the propeller. Measurements downstream of the propeller highlighted the alterations in the turbulent structure as well as modification of the propeller flow due to the turbulence. Scharpf and Mueller [5] also examined the turbulence ingestion noise problem. These measurements are vital to understand how propeller wakes impact downstream surfaces, such as stators and propeller blade rows, to produce noise.

There have also been some reports that characterize the unsteady turbulent inflow into a propeller with varying degrees of resolution. Wojno et al. [6] reports measurements of the grid-generated turbulence and characterized the mean and spectral content of the propeller inflow. Subramanium and Mueller [7] and Jessup [8] measured a sinusoidally generated distorted axial inflow. Cyclic velocity defects were produced by a series of screens and open spaces placed in the wind tunnel test section and could be viewed as a model for upstream control surface wakes. They then examined the effect of the cyclic inflow on unsteady propulsor forces and radiated noise. Chiu et al. [9] conducted five-hole probe measurements of the steady-state inflow velocity on an axial fan with and without upstream obstructions. They then measured the noise and unsteady rotor force. Aravamudan and Harris [10] measured near-field fluctuating velocities produced by a rotor ingesting turbulence. These measurements were correlated with the far-field radiated noise measurements. Chandrashekhara [11] measured the turbulent inflow into a propulsor and computed the velocity spectra and integral length scales. The inflow data were then used to predict the radiated fan noise. Manoha [12] presented some inflow velocity measurements for a propeller operating on an axisymmetric body. He presented cross correlations for various spacing in the axial, radial and tangential directions. Experimental data were used to adjust an analytical model of the velocity cross-correlation and spectra to be used for radiated noise predictions. Many other examples in the literature present axisymmetric boundary layer inflow measurements as a means to establish boundary conditions for computer codes utilized in propulsor design and flow simulation (for example, Kerwin et al. [13,14] and Mautner et al. [15]). While this work addresses various types of inflow, it does not treat the detailed inflow produced by a typical vehicle configuration during propeller operation.

Typical inflow into a propeller on an actual vehicle is very complex. The wakes produced by upstream control surfaces contain the shed vorticity producing a wake deficit. These wakes are characteristically narrow and highly unsteady. As the propeller encounters these wakes, there is a subsequent unsteady response resulting in periodic, narrowband forces resulting in an acoustic signature that may be used to characterize the vehicle. The turbulence in the wake can further excite the narrowband forces. The hull boundary layer contains turbulent eddies of various length scales that are ingested into the propeller. This results in a broadband type of response function that increases the overall noise. The spectral characteristics of the response will be dependent on the spectral character of the inflow. Since the propeller will directly modify the inflow, including the advection of upstream

---

Contributed by the Fluids Engineering Division for publication in the JOURNAL OF FLUIDS ENGINEERING. Manuscript received by the Fluids Engineering Division July 8, 2002; revised manuscript received December 16, 2002. Associate Editor: Y. Tsujimoto.

wakes and boundary layer eddies, measurement of the full three-dimensional, unsteady, inflow velocity field during operation will provide a wealth of data to increase our understanding of the underlying mechanisms responsible for unsteady propeller forces and radiated noise. This type of database would also provide a wealth of information to establish predictive models.

To this end, detailed measurements of the three-dimensional turbulent inflow have been made for a full-scale prototype swirl-inducing, stator upstream of propeller concept (SISUP) propeller. Experiments were conducted at the Naval Undersea Warfare Center (NUWC) in the acoustic wind tunnel (AWT) facility to characterize the three-dimensional turbulent inflow into a propeller simulating full operating conditions. A full-scale model of an unmanned undersea vehicle (UUV) was sting mounted in the AWT and the SISUP propeller mounted to the afterbody. Detailed x-film anemometry inflow measurements permitted resolution of the hull boundary layer and the thin wakes shed from the stators and will be presented to gain a better understanding of the three-dimensional structure of the stator wakes and perturbed inflow boundary layer. The objectives of this article are to (a) characterize the global flow field induced by the stators and propeller; (b) highlight the influence of the propeller on the inflow; (c) quantify the turbulence in the hull boundary layer and stator wakes; and (d) provide relevant data that can be used to validate computational fluid dynamic algorithms and develop turbulent inflow models. Meeting these objectives will lead to a better understanding of the underlying physics.

Methodology

Experiments were previously conducted at the Naval Undersea Warfare Center, Division Newport (NUWC) in the open jet wind tunnel facility. Further information on the facility and its features may be found in Gedney et al. [16]. The wind tunnel has a circular exit 1.22 m (4 ft.) in diameter, maximum speed of 61 m/sec (200 ft/sec) and average turbulence level of 0.3%, and spatial uniformity of 0.5% at 36.5 m/sec (120 ft/sec). The test area is also located in a large anechoic chamber so radiated noise measurements may be made. A 35.6 cm diameter, 7.62 m cantilever sting mount is anchored to a foundation upstream in the tunnel settling chamber. Full-scale unmanned undersea vehicle (UUV) models can then be mounted to the sting and the boundary layer allowed to fully develop. There is then no additional interference from model support guy wires.

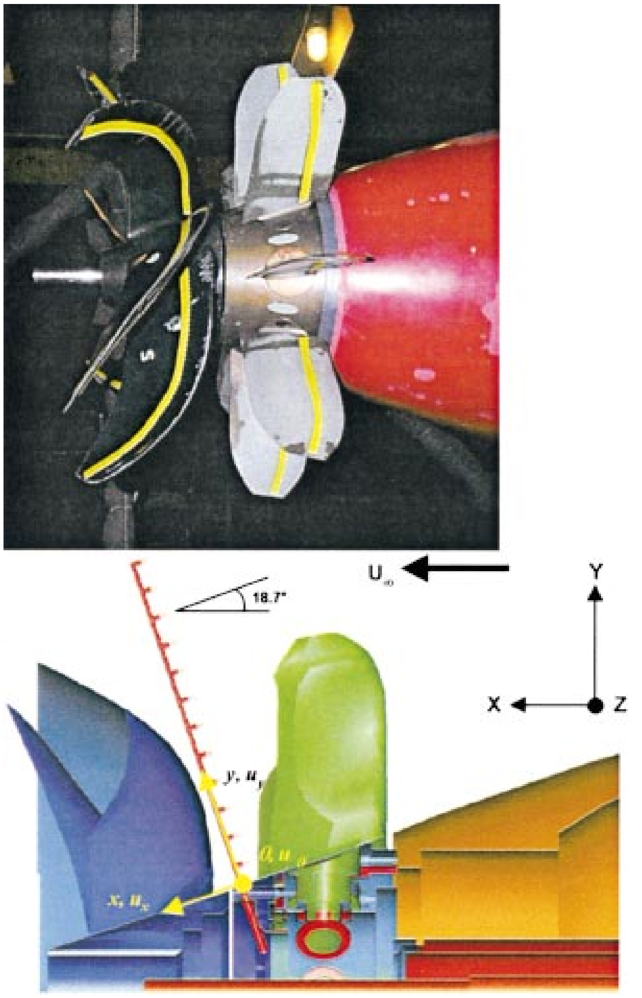

Fig. 1 Solid model of SISUP stator and propeller blade and actual experimental configuration with Hama boundary layer trips. The local and global coordinate system is displayed. From Muench [18].

Coordinate System. The global and local coordinate system is illustrated in Fig. 1 displaying the SISUP geometry. The x-coordinate is defined positive in the direction of the freestream. The y-coordinate is positive vertical and the z-coordinate is positive to port. The local cylindrical coordinate system, x, r, θ, for definition of the inflow measurement plane is also shown. x is positive in the direction of the freestream and parallel with the hull; r is positive normal to the hull surface; θ is positive in the counter-clockwise direction (looking upstream) and is 0 at an angle of 83.41 deg relative to top dead center of the wind tunnel. At the point of inflow measurement, the hull converges at an 18.7° angle relative to the tunnel centerline. The origin of the local coordinate system (x-r) is at the propeller mid-chord at the root chord location.

Swirl-Inducing, Stator Upstream of Propeller (SISUP) Geometry. The SISUP propeller was developed by the Naval Ocean Systems Center as an alternative to counter-rotating propulsors for undersea vehicles (see Mautner et al. [16]). It is an open (no-duct) propeller with complex geometry incorporating rake, twist and skew. The stators are located upstream of the propeller and are set at an angle of attack to counterbalance the torque generated by the propeller. There are a total of eight stators, equally spaced along the perimeter of the hull in 45-deg increments with the first stator located at 38.59 deg. The propeller consists of six blades equally spaced at 60-deg intervals. At the hub, the distance between the trailing edge of the stator row and leading edge of the rotor is 3.9 cm. This particular configuration theoretically results in an initial blade rate tonal of 24-x shaft rate (Uhlman [17]). The SISUP propeller was designed to be deployed on a 53.34 cm (21 in.) torpedo type UUV. The overall propeller radius is 45.72 cm (18 in.) located downstream of a 49.53 cm (19 $^1/_2$ in.) stator. The blade section profiles were developed from the NACA 0010-64 sections and the thickness/chord ratio varies from 0.16 at the root to 0.08 at the blade tip. For a design advance ratio, $J=2.343$, the experimentally determined thrust coefficient, $C_T=0.12$ (Mautner et al. [16], scaled to the current six-blade test configuration). The SISUP propulsor configuration is shown in Fig. 1.

The SISUP configuration was mounted on a 53.34 cm (21 in.) UUV and sting mounted at the centerline of the wind tunnel (Fig. 2). The SISUP propeller was mounted on the UUV afterbody and connected to a quiet electric spinner assembly. Boundary layer trips were attached to the stator and propeller blades to ensure turbulent boundary layer flow. The height of Hama trips was calculated to establish turbulent flow at 18.3 m/sec and was 0.8 mm high for the stator blades and 0.7 mm high for the propeller blades. The trips were placed at $\frac{1}{4}$ chord along the entire span of the blades to insure an adverse pressure gradient downstream of the trips.

Figure 3 shows a two-dimensional slice of the SISUP stator/

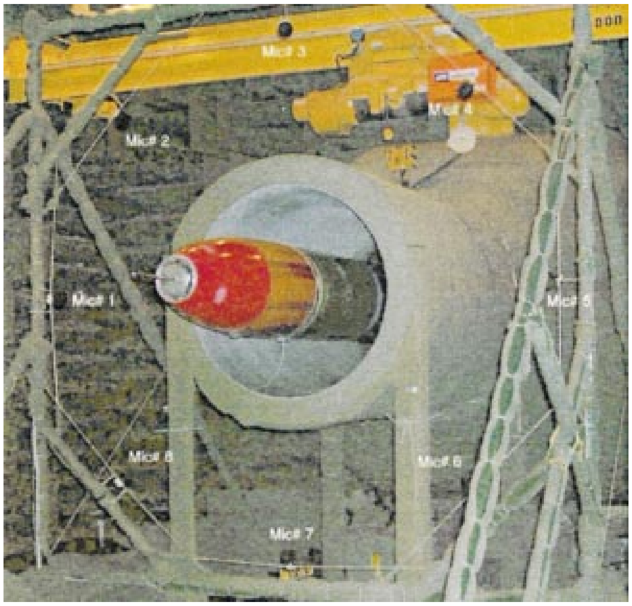

Fig. 2 UUV afterbody and wind tunnel configuration. From Muench [18].

propeller geometry in the global coordinate system. All length scales are nondimensionalized by the propeller radius and the origin is at the afterbody centerline (radial coordinate) at the propeller root mid-chord (axial coordinate). The stator trailing edge is shown to originate at $x/R_{\text{prop}} = -0.41$ and demonstrates little variation with r/R_{prop}. The propeller leading edge, however, shows a tremendous variation in x/R_{prop} with r/R_{prop} due to the rake and skew of the propeller. The measurement plane is situated normal to the surface and forms an angle of 18.7 deg perpendicular with the tunnel centerline. The symbols display the actual measurement points. As can be seen, the distance from the stator trailing edge to the inflow measurement plane increases linearly.

Inflow Measurements. Inflow measurements were conducted for freestream velocities of 18.3, 29.3, and 36.6 m/sec with measurements at 29.3 m/sec presented here. Velocities were chosen so that the boundary layer thickness in air at 36.6 m/sec was the same as that for equivalent Reynolds numbers in water (20.57 m/sec). At the end of the cylindrical UUV section (before the afterbody), the Reynolds number was approximately 120 million and the measured boundary layer thickness was approximately 4.3 cm. The in-water boundary layer thickness was approximately 5% less compared with in-air measurements (Muench [18]).

Cylindrical hot-film anemometry was used to measure the unsteady, three-dimensional velocity field. TSI Incorporated constructed customized $u_x - u_r$ (Model 1246AI-20) and $u_x - u_\theta$ (1246C-20) x-wire probes with probe lengths of 3.05 cm. The cylindrical hot-films had diameters of 50 μm, were 1 mm in length, and had a frequency response of 50 kHz. Another set of similar probes had probe lengths of 5.08 cm. The probes were connected to a TSI IFA100 bridge circuit and digitally acquired using a TSI IFA200 system. Data were sampled at 10 kHz for 8192 samples and low-pass filtered at 3 kHz using −15 dB/decade anti-aliasing filters. A temperature sensor was also used to measure the instantaneous flow temperature so corrections to the velocity could be made during post-processing. By utilizing the wind tunnel cooling system a constant flow temperature of 70°F ±1.0°F was maintained for all test speeds. Data were stored on a PC computer and post-processed using MATLAB software to provide analysis of mean and rms velocities for all three directions.

A rotating hub mechanism contained six probe sockets spaced 60 deg apart which were situated normal to the body between the stator and propeller blades. This resulted in a measurement angle of 18.7 deg relative to the centerline perpendicular. A stepper motor was designed to rotate the mechanism in 0.6-deg increments with an error of 0.01 deg. Measurements were taken at 12 stations in the radial direction above the body surface in approximately 2-cm increments. Actual measurement locations normal to the hull surface correspond to nondimensional radii (relative to propulsor radius) of 0.39, 0.47, 0.57, 0.65, 0.73, 0.82, 0.9, 1.06, 1.15, 1.23, and 1.32. Error in the radial measurements was 0.05 cm. Radial measurements were taken simultaneously at six locations—three $u_x - u_r$ measurements and three $u_x - u_\theta$ measurements so that for each azimuthal survey, three different radial locations could be measured. A total of four surveys completed the 12 radial measurements of the inflow for each test condition. While axial-radial and axial-tangential velocities could be correlated, the method did not allow for correlation between radial and tangential velocities. Figure 3 shows the measurement inflow plane. At the hub surface, the measurement plane begins 2.3 cm upstream from the propulsor root leading edge (20 mm downstream of the stator trailing edge). Since the stators are vertical, the measurement array forms an 18.7-deg angle with the stator trailing edge as r increase. For the outward radial measurement location corresponding the stator tip, the hot-film probe is approximately 6.6 cm downstream of the stator trailing edge.

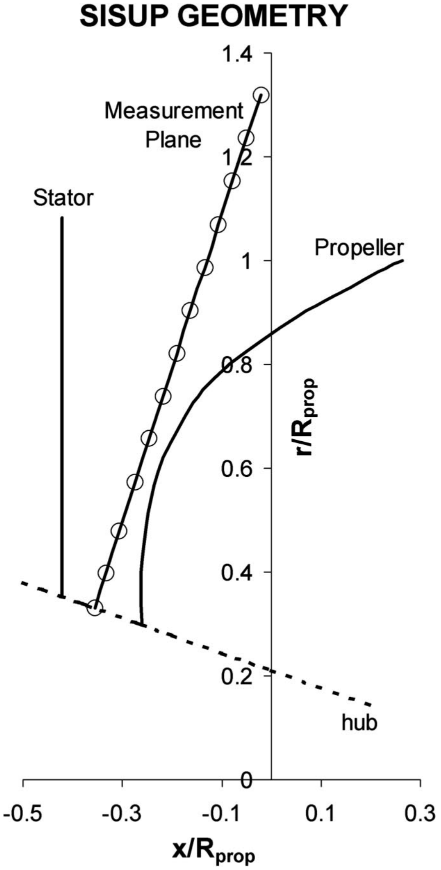

Fig. 3 SISUP geometrical configuration displaying the stator trailing edge, rotor leading edge and measurement locations (symbols mark the specific locations)

Probe Calibration and Error. The x-wire probes were calibrated in both yaw and pitch directions using a TSI model 1128 air velocity calibrator over a speed range from 0.05 m/sec to 50 m/sec and yaw and pitch of ±30 deg in 6 deg increments. To minimize errors in the velocity data, probes were calibrated before and after each data run and the average of the calibration coefficients used. The maximum error due to the fourth-order equations is on the order of 2%. The error in the freestream velocity due to fan acceleration/deceleration can be kept low on the order of 0.5%. The largest error is due to the fact that two-dimensional x-wire probes are used in a fully three-dimensional velocity field. This could not be avoided since the standard three-dimensional hot-film probes would not fit into the limited space. Since u-v and u-w measurements are made, this error can be estimated by examining the difference in mean u-values for the different probes used. The maximum errors in u-velocity were on the order of 5%. As a result, analysis showed the corresponding maximum errors in the radial and circumferential direction were approximately 10%. Therefore, the root sum square of errors for velocity in the u-direction was 5.5%, and 10.2% for r and θ velocity components.

Results

For all results presented, unless otherwise noted, the velocities are nondimensionalized by the freestream velocity and all length scales are nondimensionalized by the propeller radius. The experimental data presented here are taken for the 29.3 m/sec freestream velocity case. The propeller is a right-hand screw that rotates counterclockwise $(+\theta$ direction).

Qualitative Description of the Inflow. The axial velocity and turbulent intensity $(|u'|)$ of the inflow is shown in Fig. 4. The color plots were created using FIELDVIEW® graphical visualization package and qualitatively highlights the hull boundary layer and stator wakes. Red colors display velocities approaching freestream and blue highlights the lower velocities. Arrows showing θ angles of 0 deg and 90 deg are plotted to display the circumferential coordinate and may be used as a reference for the plots presented layer. The stator wakes are very well defined. They begin at the hull surface and bow out at increased radial directions in the negative θ-direction. Near the tips, they again extend in the positive θ-direction. The hull boundary layer effect can clearly be recognized by the green region and appears to extend from the surface to approximately one-third up the stator wakes.

The turbulent intensity further highlights the extent of the hull boundary layer and stator wake structure. The stator wakes appear thicker by comparison in the turbulence plots compared with the velocity plots. Also, the red region in the lower hull boundary layer corresponds with the green region in the velocity plots and extends approximately half way up the stator wakes. A region of lesser turbulence, indicated by the green region, extends from approximately one-half to two-thirds the way up the stator wake. The light blue region is indicative of the freestream turbulence in the wind tunnel.

Figure 5 shows velocity vector plots in the r-θ plane with the turbulent magnitude highlighted in the background. Streamlines were created using the intrinsic functions in FIELDVIEW® to highlight the tip vortices and were computed based on the radial and circumferential velocities only. The wedge encompasses two of the stator wakes. The velocity vectors show significant circumferential and radial velocities due to the stator wakes. The swirl induced by the stators directs the flow in the clockwise direction. In the hub region, as the stator wake is approached on the $-\theta$ side, the vectors show that circumferential velocities are reduced and a peak in radial velocity toward the hull is seen. On the other side of the wake $(+\theta$ side), the radial velocity is reversed in the $+r$ direction and the circumferential velocities then increase (clockwise direction) away from the stator. At outboard locations, the circumferential velocities are diminished and the radial velocities become increasingly directed away from the hull. Quantitative characterization of the flow follows in the next subsection.

Circumferential Surveys. Mean axial inflow velocities are plotted in Fig. 6 at select radial locations focusing on just two of the stator wakes. θ varies from 0 deg to 90 deg in the counterclockwise direction. The stator wake velocity defects can clearly be seen in both plots. The overall mean values increase at outward radial locations due to the hull boundary layer effect. At the radial location nearest the hull $(r/R_{\text{prop}}=0.39)$, following the velocity defect $(+\theta$ side of the wake), the velocity gradually increases reaching a peak just before the stator wake defect on the $-\theta$ side of the wake for the next stator. Similar behavior is seen until $r/R_{\text{prop}}=0.65$ where the velocity on each side of the stator wakes appears to be comparable. From $r/R_{\text{prop}}=0.72$ to $r/R_{\text{prop}}=0.98$, the opposite trend is seen. The velocity gradually decreases from the $+\theta$ side of the wake to the $-\theta$ side of the next wake. At the outer radial locations, the probes are outside the stator wake, but an imprint of the stator induced velocities can still be seen. Also notice, the variation in circumferential location of the stator wake velocity defects resulting from the pitch variation of the stator.

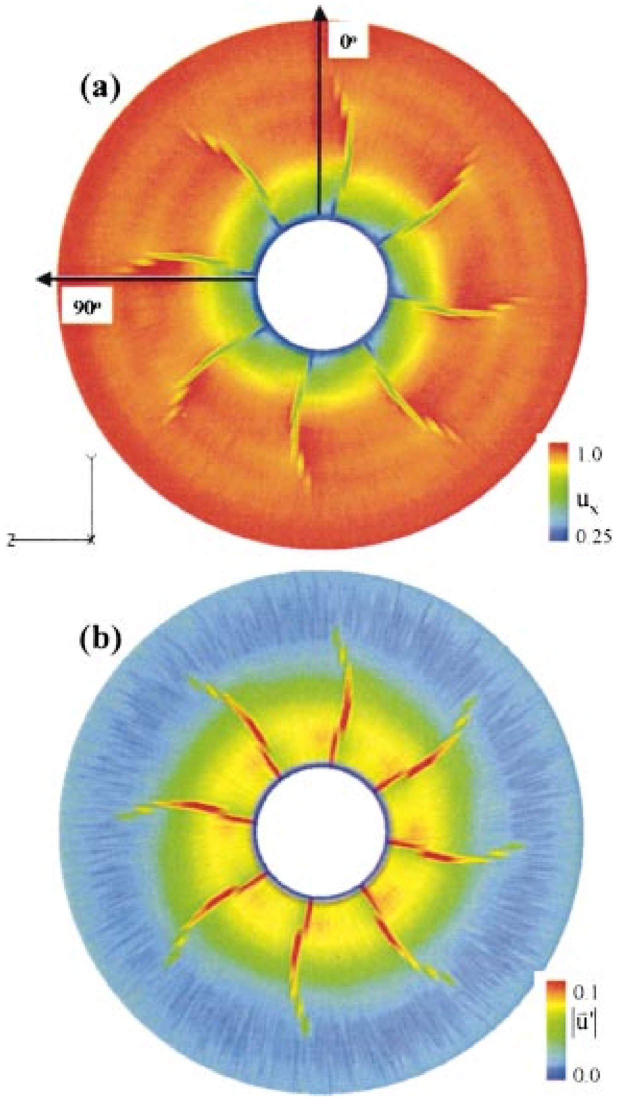

Fig. 4 Axial velocity component of the mean inflow scaled by the freestream velocity (*a*) and magnitude of the rms turbulence scaled by the freestream velocity (*b*). Inflow plane begins 1 cm upstream of propulsor root leading edge. $U_\infty=29.3$ m/sec. View is looking upstream.

Circumferential mean velocity surveys at the same radial locations as in Fig. 6 are plotted in Fig. 7. The stator wakes are clearly visible. The direction of the velocity is consistently opposite the direction of propeller rotation for all radial locations, except at the tip. Near the surface at $r/R_{\text{prop}}=0.39$, u_θ reaches a minimum midway between two stators, exhibiting a hump in the velocity profile. At successive stations outboard, however, u_θ reaches a maximum exhibiting a velocity defect between the stators. Average u_θ

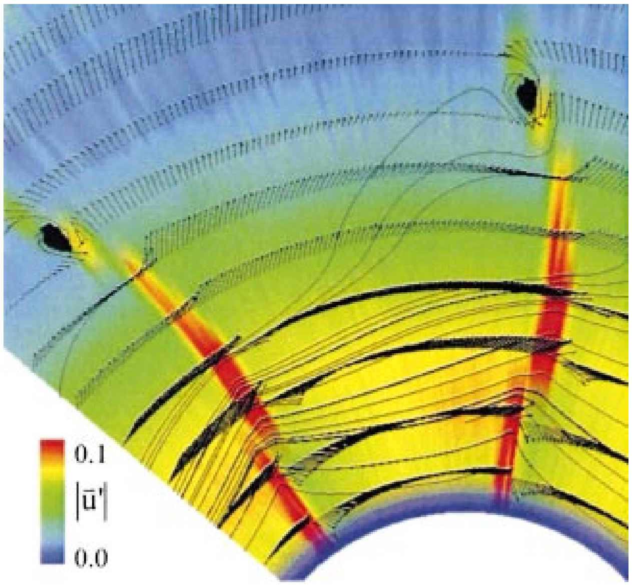

Fig. 5 Total inflow *r*-*θ* plane velocity vectors with background colored by the turbulent magnitude. Scale is the same as in Fig. 4.

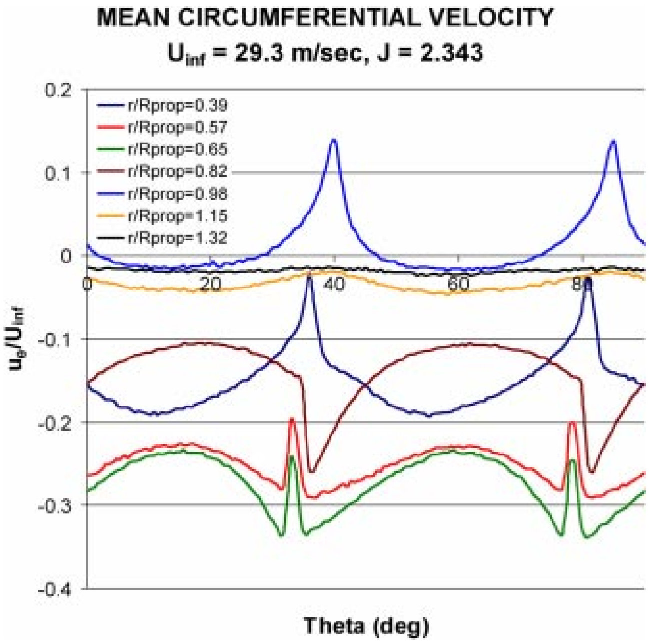

Fig. 7 Circumferential survey of the mean circumferential velocity component

appear approximately the same for $r/R_{\text{prop}}=0.57$ and 0.65, with $u_\theta=-0.25$ then increase for $r/R_{\text{prop}}=0.82$ to $u_\theta=-0.15$. At the remaining radial locations, the mean circumferential velocity appears zero with a stator tip vortex imprint still seen for $r/R_{\text{prop}}=0.98$ resulting in positive u_θ values.

Turbulent intensities were computed as the root sum square of the rms velocities and are plotted in Fig. 8. The surveys and selected radial locations are identical to those presented in Fig. 6. The stator wakes can clearly be seen by the peaks in turbulent intensity. The width of the wakes can be defined by width of the turbulent intensity "pulse" and are used to approximate the edges of the stator wakes. At the inboard radial locations, the turbulent intensity is relatively constant between the stators at a level of 0.05 from $r/R_{\text{prop}}=0.39$ to $r/R_{\text{prop}}=0.65$. At the outer radial locations, turbulent intensity decreases to 0.02 by $r/R_{\text{prop}}=0.82$. At the outermost radial locations, it appears that the freestream axial turbulence is on the order of 0.015. Based on the axial velocity profile and turbulent intensity, the hull boundary layer thickness, δ/R_{prop}, was estimated to be 0.43 and extends to $r/R_{\text{prop}}=0.82$.

Figure 9 shows the stator wake geometry by plotting the location of the center of the wake and the edges as a function of radial position and circumferential angle. The center of the wake was defined as the point where the axial velocity was a minimum. Each wake edge was defined based on the peaks in turbulent magnitude of the stator wakes. The first local minima, before and after the sharp decrease in turbulence, is defined as the wake edge. As can be seen, the wake position undulates from the hub to the tip.

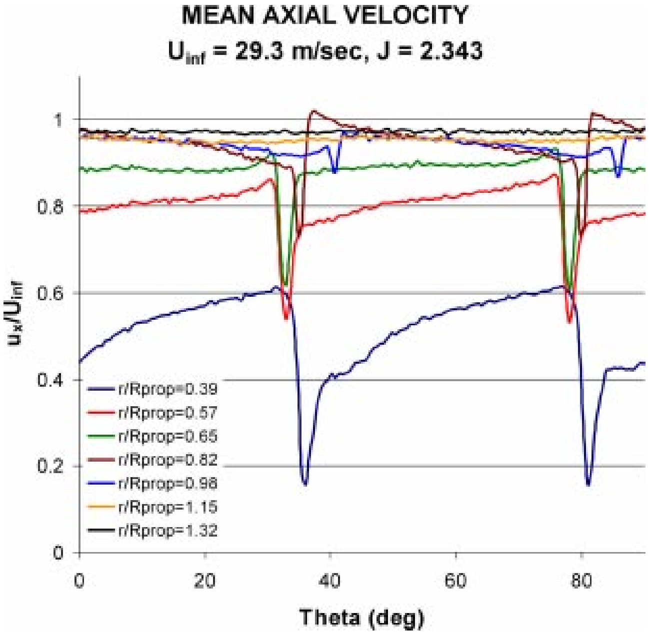

Fig. 6 Circumferential survey of the mean axial inflow velocity

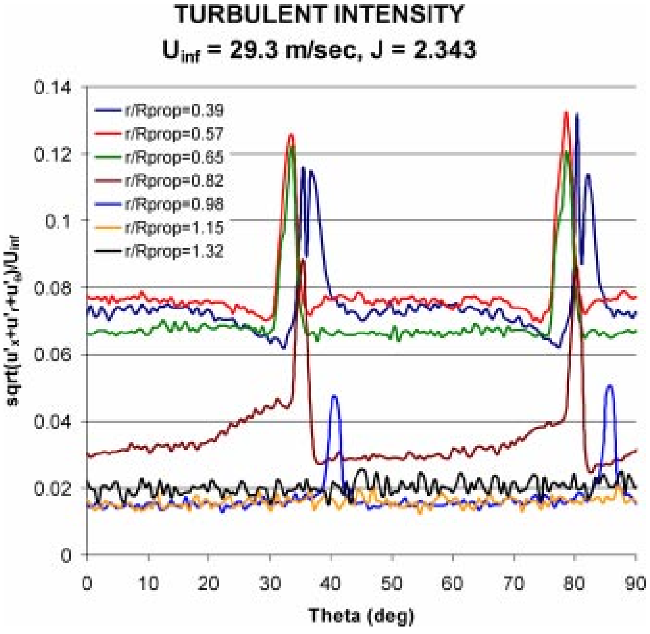

Fig. 8 Circumferential survey of the turbulent intensity

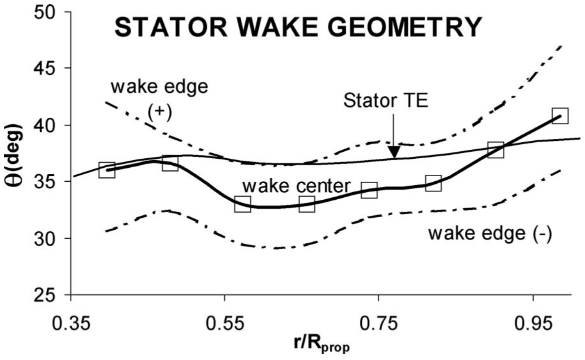

Fig. 9 Stator wake geometry

It remains approximately constant from $r/R_{\mathrm{prop}}=0.38-0.45$, shifts clockwise from $r/R_{\mathrm{prop}}=0.45$ to 0.6 and then shifts counterclockwise from $r/R_{\mathrm{prop}}=0.6$ to 0.95. The wake thickness (as a function of θ) appears thicker close to the hub ($r/R_{\mathrm{prop}}<0.45$), appears to remain relatively constant along the span before becoming thicker at the tip due to the tip vortex. The linear wake thickness increases with increased radius since actual thickness is the product of the differential θ angle and radius. Wake thickness increases radially since the measurement plane is located increasingly downstream relative to the stator trailing edge (see Fig. 3).

Radial Profiles. Axial velocity profiles are plotted as a function of radius in Fig. 10 at the wake center, wake edges, and at the geometric center between the first two stator wakes. As a reference, a profile for a flat-plate turbulent boundary layer is plotted as well. All velocity profiles presented that are associated with the wakes follow the wake geometry (Fig. 9) and are therefore not at a constant θ angle. This highlights the extent of the velocity defect and velocities at the wake edges. The velocity defect is clearly evidenced for the wake center velocity profile. The hull boundary layer effect can be seen from the velocity profile between the stator wakes. Notice the smooth transition for this case up to $r/R_{\mathrm{prop}}=0.95$ where some fluctuation is evidenced out to $r/R_{\mathrm{prop}}=1.2$. Some interesting behavior is noted comparing the axial velocities at the wake edges. From $r/R_{\mathrm{prop}}=0.4$ to 0.7 the axial velocity is less on the $+\theta$ side of the wake and from 0.7 to 1.0 the velocity is less on the $-\theta$ side of the wake. In the remainder of the wake, the velocities are equivalent. The reference flat-plate profile is fuller near the surface, but follows the profile between the stator wakes from $r/R_{\mathrm{prop}}=0.65$ outboard.

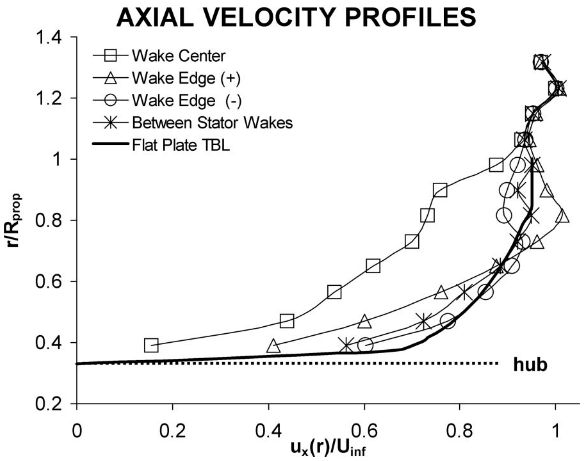

Fig. 10 Axial velocity profiles along the wake edge (+ and −), wake center, and between the stator wakes. Flat-plate turbulent boundary layer profile is provided as a reference.

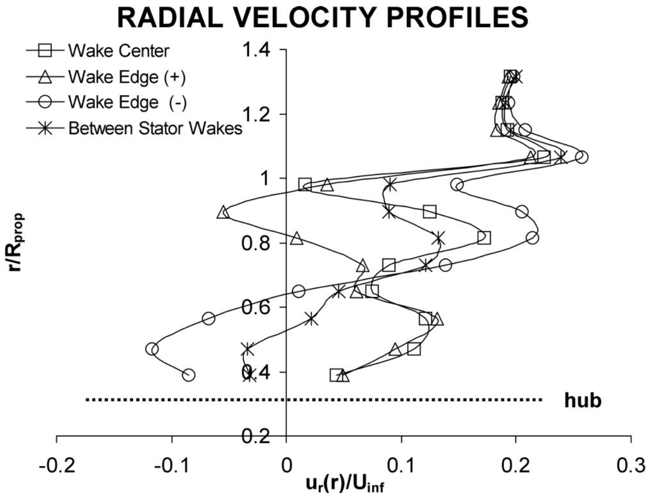

Fig. 11 Radial velocity profiles along the wake edge (+ and −), wake center, and between the stator wakes

Figures 11 and 12 show the radial and circumferential velocity profiles for the same conditions presented in Fig. 10. In the case of the circumferential velocity, the stator-induced circumferential velocity obtained from potential flow calculations is plotted as a reference. Potential flow calculations are based on the method presented by Kerwin et al. [13,14], which may be referenced for the complete formulation. In these calculations, lifting line theory is used to compute the induced velocity field due to the stator. The assumptions include inviscid flow, an infinitely thin stator blade, and the vorticity confined to infinitely thin filaments in the blade and wake. The implicit Kutta condition is satisfied at the trailing edge. The no-flux boundary conditions are enforced at the lattice control points and the linear set of equations solved for the vortex circulations. At each time step in the calculation, the vorticity is shed at the trailing edge into the wake. The solution converges as the wake is formed downstream.

For the radial and circumferential velocity profiles there appears to be significantly more fluctuations compared with the axial velocity profiles. Between the stator wakes, the low radial velocities in the hull boundary layer suggest the flow is parallel with the hull. After $r/R_{\mathrm{prop}}=0.6$, the flow begins to be directed more in the

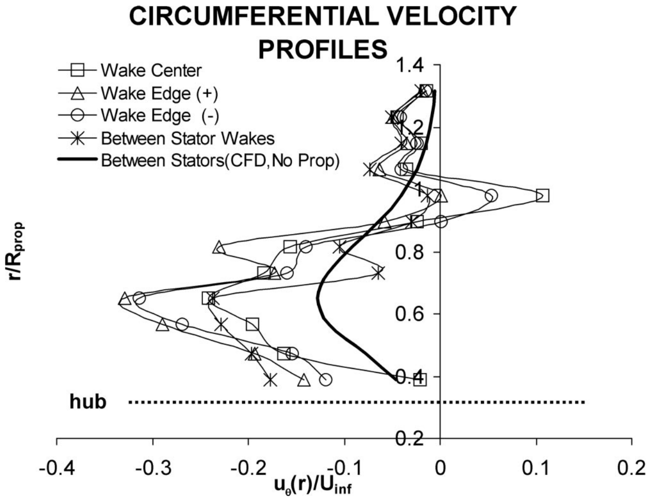

Fig. 12 Circumferential velocity profiles along the wake edge (+ and −), wake center, and between the stator wakes. Potential flow calculations for the stator only are provided as a reference.

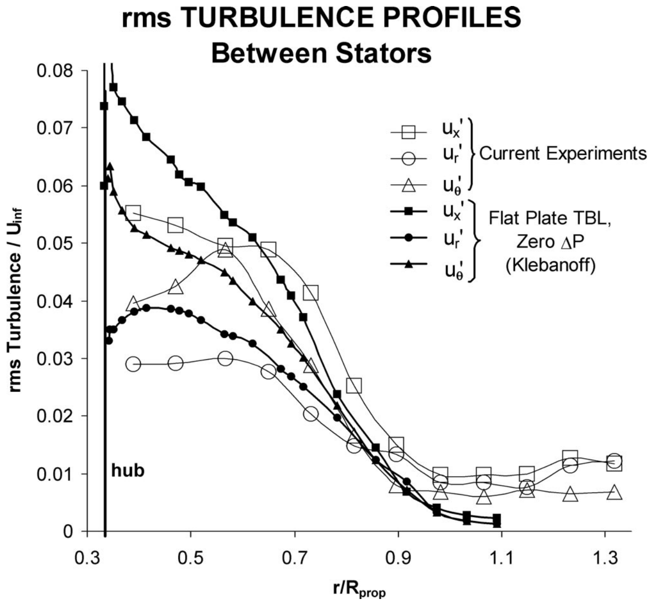

Fig. 13 rms turbulence profiles between the stator wakes for u_x', u_r', and u_θ'. Experimental flat-plate data by Klebanoff (Hinze [19]) are provided as a reference.

direction of the freestream. There does appear to be a fluctuation from $r/R_{prop}=0.8$ to 1.0 before near freestream conditions are reached at $r/R_{prop}=1.3$. Comparing the wake edge profiles, the radial velocities are negative on the $-\theta$ side of the wake out to $r/R_{prop}=0.65$. The two traces then cross over before negative radial velocities are seen at $r/R_{prop}=0.9$ for the $+\theta$ profile. Wake center radial velocities are consistently positive.

The circumferential velocity profiles show that u_θ is consistently less in magnitude on the $-\theta$ side of the wake compared with the $+\theta$ side. The velocity differential is less near the hub and becomes greatest at $r/R_{prop}=0.8$. The shapes of the two profiles are quite similar. Minimum circumferential velocities of -0.35 are seen at $r/R_{prop}=0.6$ for the wake edge profiles. Minimum circumferential velocities of -0.25 are seen for the profile between the stator wakes. Near $r/R_{prop}=1.0$, there are positive θ velocities at the wake center and $-\theta$ wake edge. At further outboard stations, u_θ diminish to near zero.

Figure 13 shows the rms turbulent profiles of u_x', u_r', and u_θ' with flat-plate zero pressure gradient experimental data from Klebanoff (from Hinze [19]) shown as a reference. The reference turbulent profiles show a sharp peak near the surface and decrease throughout the boundary layer. In contrast, the measured turbulent profiles appear flat as they approach the surface. u_x' and u_r' exhibit a plateau $r/R_{prop}=0.67$ before decreasing. u_θ' exhibits a peak at $r/R_{prop}=0.6$ before decreasing. In all cases, the measured turbulent intensities are less at the wall and greater at mid to outer boundary layer locations. This behavior is consistent with the presence of an adverse pressure gradient.

Velocity Spectra. Figure 14 plots the axial velocity power spectra to illustrate the frequency component of the turbulent inflow more clearly. Separate plots are shown at $r/R_{prop}=0.39$ and 0.98 corresponding to the near hull turbulent boundary layer region and the outer flow region. Velocity spectra are shown for the wake center, wake edge and between stators. In both plots, power is plotted in logarithmic scale. At $r/R_{prop}=0.39$, frequency is plotted on a logarithmic scale and the power spectra for all three cases exhibit a turbulent broadband type of power decay with increased frequency (all appear to follow the $-5/3$ exponential decay seen for turbulent flow). A peak in the power spectra at $f/f_{prop}=6$ (corresponding to the blade rate) can be identified. The blade rate effect is clearer at $r/R_{prop}=0.98$ where frequency is plotted on a linear scale. Here the blade rates and second harmonic can clearly be seen for the power spectra between the stators. At the wake center and wake edge the second harmonic cannot be seen.

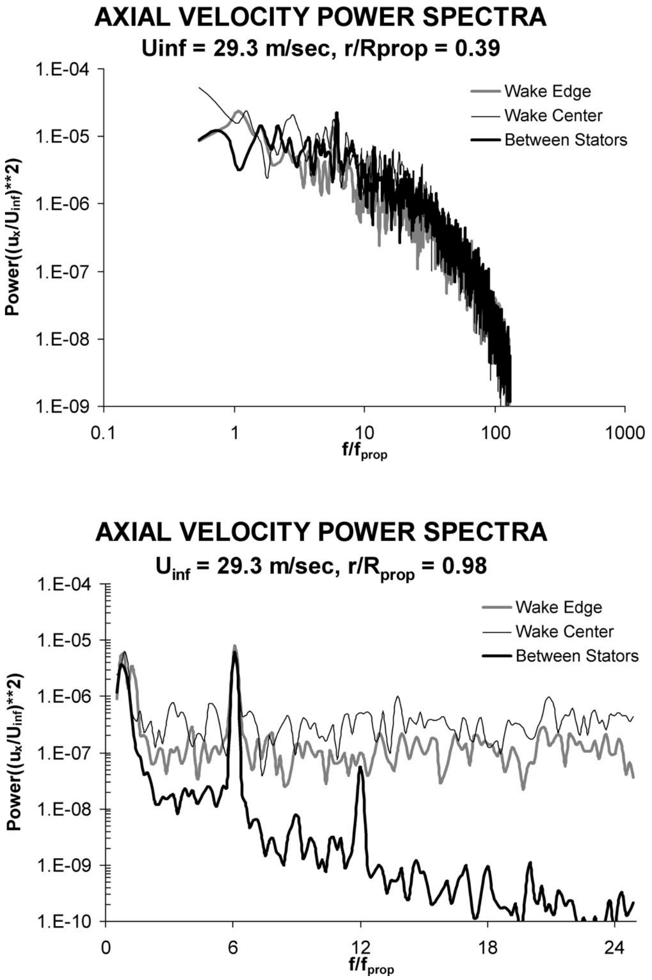

Fig. 14 Power spectra of the unsteady axial velocities taken at the wake edge, wake center and between stators for $r/R_{prop}=0.39$ and 0.98

Table 1 lists the integral length scales in the axial direction computed from the unsteady time series axial velocity. Although not shown, the values for radial and circumferential components were found to be similar. L_{11} were computed based on the standard definition (e.g., Pope [20]) using the autocorrelation of the unsteady velocity to obtain the integral time scale, then using Taylor's hypothesis (using uniform freestream velocity) to obtain the length scale. All length scales are assumed to be normalized by R_{prop}. Also, as could be seen in the spectral data, a significant component of the velocity field was due to the influence of the propulsor producing a defined frequency, $f/f_{prop}=6$. Prior to computing L_{11}, the velocity was high-pass filtered with a lower fre-

Table 1 Wake and boundary layer integral length scales

R/R_{prop}	Wake Center, L_{11}	Wake Edge, L_{11}	Between Stators, L_{11}	Wake Thickness
0.3889	0.0641	0.0513	0.0513	0.0774
0.4711	0.0513	0.0513	0.0641	0.0543
0.6500	0.0385	0.0513	0.0513	0.0817
0.8157	0.0385	0.0513	0.0513	0.0854
0.9815	0.0256	0.0385	0.1538	0.1850

quency bound of $f/f_{\mathrm{prop}}=9$ to effectively eliminate the blade rate harmonic. This allowed for the length scale of the turbulence to be better computed. As can be seen, L_{11} for both the stator wakes and hull boundary layer (between stators) are equivalent and the values compare with the local wake thickness. For the test case located at the tip between the stators, the velocity data were not filtered and the value of $L_{11}=0.1538$ corresponds to the length scale of the $f/f_{\mathrm{prop}}=6$ disturbance produced by the propulsor.

Discussion

Influence of the Stator and Its Wakes. The stators were designed to provide a lift force to counterbalance the torque generated by the rotor. Since the propeller rotates counterclockwise when viewed aft (in the positive θ-direction), the propeller generates an opposite torque in the clockwise direction. The stator must produce an opposing force in the counterclockwise (positive θ) direction. At the same time, the stators produce a swirl component from the downwash produced by the lift that will generally be in the negative θ-direction. Potential flow computations shown in Fig. 12 highlight the stator induced circumferential velocity. In order to minimize the unsteady forces, the stators need to produce as smooth and steady flow as possible. Near the tip, the lift decreases to minimize the formation of the tip vortex. For that reason, the stators have a component of twist. Near the hub, the local pitch angle is set to produce no lift. As r/R_{prop} is increased, the twist increases to obtain positive angles of attack. At outboard span locations, the stator blade is twisted back to reduce the local angle of attack so zero lift is achieved near the tip. This design is to spread out the tip vorticity to minimize coherence of the tip vortex. Potential flow analysis of the stator force shows zero lift at the hub increasing outboard for maximum lift force at $r/R_{\mathrm{prop}}=0.7$. The lift then declines sharply so effectively zero lift is produced from $r/R_{\mathrm{prop}}=1.04$ to 1.083 (location of stator tip).

Analysis of the inflow velocity data reveals the resulting flow structure produced by the lifting stators. When the stators produce lift in the $+\theta$ direction, there will be a suction force on the $+\theta$ side of the stator and pressure force on the $-\theta$ side. The magnitude of suction force will be a maximum at the point of maximum lift ($r/R_{\mathrm{prop}}=0.7$). Similarly, on the pressure side, the point of maximum pressure force will be at the point of maximum lift. This effectively sets up a local flow in the radial direction so that on the suction side, the flow is directed from the hub to $r/R_{\mathrm{prop}}=0.7$ ($+u_r$) and from the tip to $r/R_{\mathrm{prop}}=0.7$ ($-u_r$). The opposite effect occurs on the pressure side so the flow is from $r/R_{\mathrm{prop}}=0.7$ to the hub ($-u_r$) and from $r/R_{\mathrm{prop}}=0.7$ to the tip ($+u_r$). This flow is also coupled with the local axial flow. As flow is directed inward toward the hub, the axial flow is decelerated. When the radial flow is directed outward, the axial flow is accelerated. This was clearly seen in the axial and radial velocity profiles. On the $+\theta$ wake edge, the radial velocity near the hub is increased on the corresponding axial velocity decreased. At the point of maximum lift, the velocities on opposite sides of the wake are comparable and as the tip is approached on the $+\theta$ wake edge, the radial velocity is decreased and axial velocity increased. The exact opposite occurs for the $-\theta$ wake edge.

The circumferential velocity profiles demonstrate the lifting effect of the stators as well. The velocities on the $+\theta$ side of the wake are greater in magnitude (increased $-u_\theta$) compared with the $-\theta$ wake side. For a lifting surface, the shed vorticity will induce a velocity on the suction side in the direction of the local flow, and a velocity opposite to the direction of the local flow on the negative side. For the present geometric configuration, higher negative u_θ would be expected on the $+\theta$ side of the wake as were observed. Also, the increase in velocity differential will increase at the point of maximum lift, which was observed as well. Near the tip, the large velocity differential and positive u_θ may be attributed to the effect of the tip vortex. The stators also generate a mean swirl velocity as indicated from the potential flow analysis presented in Fig. 12. The swirl velocities start out small near the hub and reach a maximum just before the point of maximum stator lift. Swirl velocities then decrease near the tip, but are still evident outside the tip.

The turbulence plots demonstrate the persistence of the stator wake from the root to the tip since the measurement plane geometry resulted in increasing linear distance from the probe to the stator trailing edge. At the hub, the distance to the stator trailing edge (normalized by R_{prop}) is 0.03 and at the stator tip it is approximately 0.25. The average nondimensional stator chord length is 0.4. At the hub, the turbulent intensity is 0.1 at the center of the wake. At $r/R_{\mathrm{prop}}=0.65$ the intensity is reduced to 0.095 and the downstream distance is 0.12. At $r/R_{\mathrm{prop}}=0.9$ the turbulence is reduced to 0.06 and the downstream distance is 0.2 (half the stator chord length). The turbulent data demonstrates that the wake maintains its strength as it is advected far downstream and will significantly impact the propeller.

Induced Flow due to the Propeller. Since the inflow velocity measurements were taken while the propeller was operating it is important to realize that there will be an induced velocity component due to the thrust produced by the propeller. The propeller will tend to accelerate the axial inflow and reduce the radial component so the flow is parallel to the body. The circumferential velocity component upstream due to the propeller was found to be small from potential flow analysis. To estimate the effect of the propeller on the inflow it is best to examine the inflow directly between the stators for both the mean circumferential velocities and unsteady axial velocities. Although not shown, potential flow analysis showed that the computed stator induced velocities in the axial direction are small (on the order of 0.01 near to hub and 0.005 near the tip). In the radial direction the computed velocities are consistent with the measured velocities.

Near the hub, u_θ is decreased by approximately -0.15 (factor of 2.0) compared with the potential flow results and the level of that decrease appears consistent out to $r/R_{\mathrm{prop}}=0.65$. After this point the difference between the measured u_θ between the stators and the potential flow results are small. The fact that the measurement plane is further away from the propeller will certainly influence the reduced difference. It is also expected that the induced velocity from the propeller is felt closest to the hub and the effects diminish further away. The reason for the increased $-u_\theta$ is that increased local axial flow near the hub must be generating additional lift on the stators and corresponding increased swirl. Assuming the swirl varies linearly with the inflow velocity, the measured velocities in the lower boundary layer should be on the order of twice the expected velocities without the propeller. Based on the axial velocity profiles, the propeller-induced velocities are on the order of 0.25 in the lower boundary layer region ($r/R_{\mathrm{prop}}<0.65$) and decay in some fashion away from the hub.

Hull Boundary Layer and Wake Turbulence. The hull boundary layer extended to $r/R_{\mathrm{prop}}=0.82$, or almost two-thirds the effective propeller span. Therefore, the boundary layer will have a significant effect on the operating regime of the propeller. The relatively thick boundary layer may be attributable to the adverse pressure gradient due to surface curvature as well as the added disturbances from the stators. Interestingly, the turbulence in the boundary layer and the stator wakes exhibited qualitatively similar behavior. In both cases there were no coherent frequencies (except for blade rate effects) that could be attributed to vortex shedding. With regard to the stator wakes, the lack of vortex shedding is probably due to the use of the Hama boundary layer trips to ensure turbulent flow over the stators. There would be no narrowband shedding frequencies expected from the hull boundary layer since it is fully developed turbulence. For the most part, the integral scale of the turbulence was approximately 0.05 at the wake edge and hull boundary layer and 0.03 at the wake center. The stator wake thickness is on the order of 0.08, so the integral scale correlates well with the wake thickness. Spectral data also exhibited broadband characteristics with no evidence of narrowband effects (except, of course, the blade rates).

Analysis of the turbulent intensities in the axial, radial, and circumferential directions also revealed, to some extent, the structure of the boundary layer. Flat-plate zero-pressure-gradient data provided a baseline to compare the present results. For zero-pressure gradient, the turbulence and vorticity are concentrated near the wall. In the outer layer, the velocity fluctuations due to the advecting vortical eddies are relatively small. The adverse pressure gradient causes a redistribution of the boundary layer vorticity. As suggested by the turbulent intensity plots, the vorticity becomes more uniformly distributed in a larger region of the boundary layer. The present data show this region to extend out to $r/R_{\text{prop}}=0.65$. The turbulent intensities outboard are higher than the flat plate data as expected to conserve total energy. The slope of the decay in turbulence after the plateau compares well with the flat-plate data. This increases the confidence level of the current results.

Conclusions

Experimental data characterizing the unsteady three-dimensional inflow into a SISUP propeller has been presented and discussed. x-wire anemometry was used to simultaneously measure two velocity components at a time. Axial, radial, and circumferential mean velocity and rms were reduced from the x-wire signals. Time series and spectral data were presented to provide insight into the turbulent frequency content of the flow. Integral time-scale calculations provided effective length scales of the turbulent flow. High-resolution measurements in the azimuthal direction allowed for characterization of the upstream stator wakes as well as the hull boundary layer. Derived quantities such as integral length scale and detailed wake geometry could then be presented to highlight the physical mechanisms.

The stator wakes exhibited a sharp decrease in mean velocity and increase in turbulence. Immediately aft of the stator wakes, this decrease in mean velocity was on the order of 30% of the freestream velocity. This wake deficit was evident from the root out to 90% of the tip. The correlated turbulent magnitude in the center of the wake was on the order of 12% near the root, diminishing to 8% near the tip. This decrease was attributed to the fact that the measurement plane was at an angle relative to the stator trailing edge so that at the root measurements were proximal to the trailing edge and at the tip were on the order of half a chord length downstream. Still, these levels are significant and will be ingested into the propeller. Turbulence measurements also showed a relatively thick hull boundary layer at the inflow plane. The hull boundary layer influenced the flow out to 82% of the propeller radius.

Analysis of the inflow highlighted some of the flow structure present. Since the stators were designed to produce a maximum lift at approximately 70% of the propeller radius, an induced radial flow was established that influenced the axial flow as well. On the pressure side of the stator the radial flow was directed away from the point of maximum lift resulting in radial flow toward the hull at inboard locations and away from the hull at outboard locations. This had the tendency to decelerate the axial flow inboard and accelerate it outboard. The opposite effect was seen on the suction side of the stator wake. These lifting effects due to shed vorticity could also be seen in the circumferential velocity field with increased velocities on the suction side of the wake.

The influence of the propeller on the inflow was established as well. Potential flow calculations showing the induced circumferential velocity due to the stator wakes assisted in decoupling the effects of the stators and the propeller on the measured inflow. Increased swirl velocities near the hub were shown to be due to the increased axial flow producing increased stator lift and corresponding swirl. The magnitude of the swirl was greatest near the hub (on the order of 15% of the freestream velocity) becoming less at outboard stations. The propeller-induced axial velocity was estimated to be on the order of 25% of freestream based on axial velocity profiles.

Turbulent intensities revealed a redistribution of the boundary layer vorticity due to the adverse pressure gradient on the afterbody. Data showed that the turbulent intensities were flat from the surface out to two-thirds of the boundary layer thickness suggesting a uniform vorticity distribution. The following decay in turbulence followed closely classical flat-plate boundary layer data adding an increased confidence level in the current results.

Spectral analysis and autocorrelation of the time series data yielded the basic length scales of the turbulent flow as well as the spectral content. In all cases, the blade rate frequency was dominant so high-pass filtering was used to remove this component for integral length scale calculations. At higher frequencies, the inflow exhibited broadband characteristics. The nondimensional length scales of the turbulent flow were mostly on the order of 0.05 and were effectively similar for the stator wakes and hull boundary layer. Lack of defined vortex shedding frequencies as well as the broadband character of the stator wakes may be attributed to the boundary layer trips used.

The turbulent inflow presented here provides a wealth of information that may be used to construct models of the inflow for use in propulsor unsteady force and radiated noise calculations. Efforts are currently underway to compute the tonal characteristics of the unsteady forces based on the mean inflow. In addition, various turbulence models may be developed based on the spectral and statistical information presented here. These models can then form a basis to compute the narrow and broadband hydrodynamic forcing functions responsible for propeller radiated noise.

Acknowledgments

This work was funded by the Office of Naval Research under Contract N0001402WX20474, Dr. Kam Ng, program manager, and the NUWC Internal Research Program, Mr. Richard Philips, program manager. The experimental data used in this work was collected during SISUP experiments, supervised by Dr. John Muench for this thesis work and funded by the Office of Naval Research under Dr. Patrick Purtell.

Nomenclature

c = blade chord
D_{prop} = propeller diameter
R_{prop} = propeller radius
J = advance ratio $=U_\infty/(nD_{\text{prop}})$
l = length scale (e.g., chord or body length)
n = propeller rotational frequency (Hz)
ρ = fluid density
x = axial coordinate
r = radial coordinate
θ = circumferential coordinate
Re = Reynolds number $=U_\infty l/\nu$
ν = kinematic viscosity
U_∞ = freestream velocity
u_x = axial velocity (parallel to hull)
u_r = radial velocity (perpendicular to hull)
u_θ = circumferential velocity
u_x' = rms axial velocity
u_r' = rms radial velocity
u_θ' = rms circumferential velocity
$|u'|$ = turbulent intensity $=\sqrt{u_x'^2+u_r'^2+u_\theta'^2}$

References

[1] Satyanarayana, B., 1977, ''Unsteady Wake Measurements of Airfoils and Cascades,'' AIAA J., **15**(5), pp. 613–618.
[2] Sears, W. R., 1941, ''Some Aspects of Non-stationary Airfoil Theory and Its Practical Application,'' J. Aeronaut. Sci., **8**(3), pp. 104–108.
[3] Inoue, M., and Kuroumaru, M., 1984, ''Three-Dimensional Structure and De-

cay of Vortices Behind an Axial Flow Rotating Blade Row,'' ASME J. Eng. Gas Turbines Power, **106**, pp. 561–568.
[4] Lynch, D. A., III, 2001, ''An Experimental Investigation of the Unsteady Response of a Stator Located Downstream of a Propeller Ingesting Broadband Turbulence,'' Ph.D. thesis, Department of Aerospace and Mechanical Engineering, University of Notre Dame.
[5] Scharpf, D. F., Mueller, T. J., 1995, ''An Experimental Investigation of the Sources of Propeller Noise due to the Ingestion of Turbulence at Low Speeds,'' Exp. Fluids, **18**, pp. 277–287.
[6] Wojno, J. P., Mueller, T. J., and Blake, W. K., 2002, ''Turbulence Ingestion Noise, Part I: Experimental Characterization of Grid-Generated Turbulence,'' AIAA J., **40**(1), pp. 16–26.
[7] Subramanian, S., and Mueller, T. J., 1995, ''An Experimental Study of Propeller Noise due to Cyclic Flow Distortion,'' J. Sound Vib., **183**(5), pp. 907–923.
[8] Jessup, S. D., 1990, ''Measurement of Multiple Blade Rate Unsteady Propeller Forces,'' David Taylor Research Center Report DTRC-90/015.
[9] Chiu, W.-S., Lauchle, G. C., and Thompson, D. E., 1989, ''Subsonic Axial Flow Fan Noise and Unsteady Rotor Force,'' J. Acoust. Soc. Am., **85**(2), pp. 641–647.
[10] Aravamudan, K. S., and Harris, W. L., 1979, ''Low-Frequency Broadband Noise Generated by a Model Rotor,'' J. Acoust. Soc. Am., **6**(2), pp. 522–533.
[11] Chandrashekhara, N., 1971, ''Sound Radiation From Inflow Turbulence in Axial flow Fans,'' J. Sound Vib., **19**(2), pp. 133–146.
[12] Manoha, E., 1998, ''Broadband Noise From a Propeller in Turbulent Flow,'' *Proceedings of the ASME Noise Control and Acoustics Division*, ASME, New York, NCA-Vol. 25, pp. 137–148.
[13] Kerwin, J. E., and Lee, C. S., 1978, ''Prediction of Steady and Unsteady Marine Propeller Performance by Numerical Lifting Surface Theory,'' Trans Soc Nav. Arch. Marine Eng., **86**, pp. 218–253.
[14] Kerwin, J. E., 1986, ''Marine Propellers,'' Annu. Rev. Fluid Mech., **18**, pp. 367–403.
[15] Mautner, T. S., Nelson, D. M., and Gillcrist, M. C., 1988, ''Investigation of the SISUP (Swirl Inducing Stator Upstream of Propeller) Concept for Marine Propulsion,'' *Naval Ocean Systems Center, Proceedings: Propellers '88*.
[16] Gedney, C. J., Abbot, P. A., and Corriveau, P. J., 1998, ''Inferring Blade Rate Forces From Wind Tunnel Sound Power Measurements,'' ASME Winter Annual Meeting, *Symposium on Flow Noise Modeling, Measurement and Control*.
[17] Uhlman, J. S., 1995, ''An Examination of the Frequencies of the Unsteady Harmonic Forces Generated by Propulsors,'' NUWC-NPT Technical Report 10,470, Naval Undersea Warfare Center.
[18] Muench, J. D., 2001, ''Periodic Acoustic Radiation From a Low Aspect Ratio Propeller,'' Ph.D. thesis, Department of Mechanical Engineering and Applied Mechanics, University of Rhode Island.
[19] Hinze, J. O., 1975, *Turbulence*, 2nd Ed. McGraw-Hill, New York.
[20] Pope, S. B., 2000, *Turbulent Flows*, Cambridge University Press, New York.

Yong Cho
Ph.D. student

Young J. Moon[1]
Professor
e-mail: yjmoon@korea.ac.kr

Department of Mechanical Engineering,
Korea University,
Seoul 136-701, Korea

Discrete Noise Prediction of Variable Pitch Cross-Flow Fans by Unsteady Navier-Stokes Computations

The unsteady viscous flow fields of a cross-flow fan are computed by time-accurately solving the two-dimensional incompressible Navier-Stokes equations with the unstructured triangular mesh solver algorithms. Based on pressure fluctuation data acquired at the surfaces of 35 rotating blades and stabilizer, acoustic pressures are predicted by the Ffowcs Williams-Hawkings equation. The aerodynamic noise sources of the cross-flow fan are also identified by correlating the acoustic pressure fluctuations with the unsteady flow characteristics during one revolution of the impeller. The present method is applied to the uniform and random pitch fans to investigate their performance and aeroacoustic noise characteristics, especially the frequency modulation of the tonal noise at the blade passing frequency (BPF). [DOI: 10.1115/1.1568356]

1 Introduction

Cross-flow fans are widely used for air conditioners, air curtains, car ventilators, household heaters, etc., due to their large capacity of mass flow and size compactness. Since fan geometry and flow structures are complex, the aerodynamic modeling, [1–5], of the cross-flow fan has been pursued with some limits. Figure 1 shows a cross-sectional view of the cross-flow fan with the measured internal velocity field, [6].

Recently, the aeroacoustic noise reduction of the cross-flow fan has become an important issue besides its energy savings and size compactness, since they are mainly used in closed spaces. The aerodynamic noise of the cross-flow fan can be divided into a discrete tonal noise induced by the periodic interactions between the rotating blades and the fan casing and a broadband noise due to the turbulent fluctuations. The BPF (blade passing frequency) tonal noise in particular is known as the most annoying component to the human ear. Research effort has been pursued in various aspects for reducing the BPF tonal noise: (i) modifying the stabilizer shape and location by Fukano et al. [7], Chen and Lee [8], Lee et al. [9], and Koo [10], (ii) employing the impeller with irregular blade pitches by Lee et al. [9] and Hayashi et al. [11], and (iii) dividing the impeller into a number of blocks and introducing a phase shift of blade pitch in the spanwise direction by Kobayashi and Konno [12] and Hayashi et al. [13]. The aeroacoustic noise modeling has also been attempted by Hayashi et al. [11], Kobayashi and Konno [12], and Hayashi et al. [13]. They proposed a simple sinusoidal model for the acoustic pressure generated by the periodic interactions between the rotating blades and the stabilizer, but this model was only useful in qualitative prediction of the random pitch fan characteristics.

In the present study, a computational method is proposed for the aerodynamic and aeroacoustic modeling of the cross-flow fan. The unsteady flow solutions of the cross-flow fan are directly calculated by time-accurately solving the two-dimensional incompressible Navier-Stokes equations in moving coordinates. The unstructured triangular meshes are used to model the rotating impeller blades and a sliding mesh technique, [14], is employed to allow the unsteady interactions through the interface between the rotating meshes and the stationary ones. The sound pressure at any specified position is then predicted by the Ffowcs Williams-Hawkings equation, [15], based on unsteady pressure data acquired at the surfaces of 35 rotating blades and stabilizer. The aerodynamic noise sources of the cross-flow fan are identified and the performance and aeroacoustic noise characteristics of the uniform and random pitch fans are investigated.

2 Numerical Methodology

2.1 Unsteady Viscous Flow Computation. To consider the unsteady interactions between the rotating impeller blades and the stationary fan casing, the two-dimensional incompressible Navier-Stokes equations in moving coordinates are time-accurately solved. The governing equations are written in a nondimensional form as

$$\frac{\partial(u-w_x)}{\partial x}+\frac{\partial(v-w_y)}{\partial y}=0, \tag{1}$$

$$\frac{\partial u}{\partial t}+(u-w_x)\frac{\partial u}{\partial x}+(v-w_y)\frac{\partial u}{\partial y}=-\frac{\partial p}{\partial x}+\frac{1}{\mathrm{Re}}\left(\frac{\partial^2 u}{\partial x^2}+\frac{\partial^2 u}{\partial y^2}\right), \tag{2}$$

$$\frac{\partial v}{\partial t}+(u-w_x)\frac{\partial v}{\partial x}+(v-w_y)\frac{\partial v}{\partial y}=-\frac{\partial p}{\partial y}+\frac{1}{\mathrm{Re}}\left(\frac{\partial^2 v}{\partial x^2}+\frac{\partial^2 v}{\partial y^2}\right), \tag{3}$$

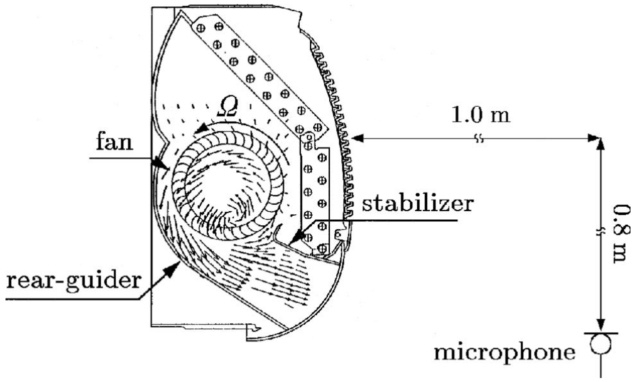

Fig. 1 A cross-flow fan configuration and the measured internal velocity field, [6]

---

[1] To whom correspondence should be addressed.

Contributed by the Fluids Engineering Division for publication in the JOURNAL OF FLUIDS ENGINEERING. Manuscript received by the Fluids Engineering Division May 8, 2001; revised manuscript received Nov. 27, 2002. Associate Editor: T. Gatski.

where $\mathbf{w}=(w_x,w_y)=(-\omega y,\omega x)$ is a velocity vector of the moving coordinate (ω: angular speed) and Re is the Reynolds number.

The velocity and pressure fields are solved in a coupled manner by following a projection method-based algorithm, [16,17], and the time-accuracy of the method is retained by enforcing the continuity at each time step. The momentum equations, Eqs. (2)–(3), are spatially discretized on the triangular meshes by a cell-center based unstructured finite volume method. The x-direction equation is, for example, expressed as

$$\Omega_i\frac{\Delta u_i}{\Delta t}=-\sum_{j=\chi(i)}\left[\left(u(u-w_x)+p-\frac{1}{\mathrm{Re}}\frac{\partial u}{\partial x}\right)\Delta y-\left(u(v-w_y)-\frac{1}{\mathrm{Re}}\frac{\partial u}{\partial y}\right)\Delta x\right]_{i,j}^{n},\tag{4}$$

where i is a center-cell index, j is a neighboring cell index, χ is a mapping relation between i and j, and Ω_i is a cell area.

A second-order upwind scheme is applied to the nonlinear convective flux terms in Eq. (4) by following a MUSCL approach, [18]. An upwind cell is first determined by evaluating the relative velocity vector at the cell face and then the upwind-directed transported quantities $q_l^{\pm}=(u,v)$ are obtained by

$$\begin{cases} q_l^-=q_i+\nabla q_i\cdot\mathbf{r}_l & \text{if } \mathbf{v}_l^r\cdot\mathbf{n}_l>0\\ q_l^+=q_j+\nabla q_j\cdot\mathbf{r}_l & \text{if } \mathbf{v}_l^r\cdot\mathbf{n}_l<0\end{cases},\tag{5}$$

where l is a cell face index between two adjacent cells i and j, $\mathbf{v}_l^r$ is a relative velocity vector in the moving frame of reference, $\mathbf{n}_l$ is an outward normal vector at the cell face, and $\mathbf{r}_l$ is a distance vector from the upwind cell center to the cell face. The gradient vector ∇q_i in Eq. (5) is evaluated by a discrete surface integral along the cell faces, based on the divergence theorem. The terms related to the viscous fluxes are treated by a centered scheme, and Eq. (4) is advanced in time by a four-stage Runge-Kutta method.

A Poisson equation derived for the pressure field is spatially discretized on the unstructured triangular meshes and solved iteratively by a pointwise Gauss-Seidal method. Due to the collocated arrangement of the variables, a checkerboard pressure field may appear and the velocities at the cell face are redefined by the momentum interpolation technique proposed by Rhie and Chow [19]. At the sliding mesh interface between the rotating zone including impeller and the stationary zone, the function values and their gradients are linearly interpolated by determining the coefficients of a shape function for the triangle composed by three adjacent cells. The accuracy assessment of the sliding mesh interface treatment was verified in Ref. [14] for a simplified unsteady flow model: a cross paddle oscillating in a circular enclosure and generating vortices that time-periodically cross the sliding mesh interface. Details of the numerical schemes and interpolation procedures are fully described in Refs. [14], [20].

2.2 Aeroacoustic Noise Prediction.

The present cross-flow fan (blade count, $Z=35$) rotates at 1000 rpm with the impeller blade tip velocity of 5.55 m/s (or $M=0.016$). Thereby the BPF noise ($f=1000\,\mathrm{rpm}/60\,\mathrm{sec}\times35=583\,\mathrm{Hz}$) of the cross-flow fan has an acoustic wave length ($\lambda=c_0/f=343\,\mathrm{m/s}/583\,\mathrm{Hz}=588\,\mathrm{mm}$) far exceeding the fan characteristic dimensions: fan outer diameter ($D=106$ mm), exit height ($=63$ mm), blade chord ($=14.2$ mm), and blade spacing ($=9.5$ mm). For this reason, the effects of fan casing and interblade acoustic interference such as reflection, diffraction, and scattering are neglected in the present aeroacoustic modeling. Also, the quadrupole noise associated with flow turbulences, [9–11], are excluded, because the flow Mach number of the cross-flow fan is quite low.

The sound pressure generated from the rotating blades and stabilizer is predicted by the Ffowcs Williams-Hawkings equation, [15], assuming that flow is uniform in the spanwise direction. Also, the noise sources are assumed compact, since the compact noise source conditions suggested by Farassat [21] are satisfied. For example, the maximum length of the noise source (corresponding to a grid section along the blades and stabilizer), $l_{\max}$ ($=5.37\times10^{-3}$ m) is much smaller than the minimum distance between the noise source and the observer, $r_{\min}(=1.23\,\mathrm{m})$, and the time step that takes for a sound wave to cross $l_{\max}$, $\Delta\tau$ ($=1.910\times10^{-5}$ sec) is also much smaller than the period of BPF noise, $T(=1.714\times10^{-3}$ sec). Using the compact noise source formula given by Succi [22], contributions of noise sources n_s are summed as

$$p'(\mathbf{x},t)=\sum_{i=1}^{n_s}\,[p'_{t,i}(\mathbf{x},t)+p'_{\mathrm{ln},i}(\mathbf{x},t)+p'_{lf,i}(\mathbf{x},t)],\tag{6}$$

where $\mathbf{x}$ is a position vector to the observer and t is an observer time. Among the three terms, the first term represents the monopole noise related to the blade moving volume (i.e., blade thickness) and the second and third terms are the near and far-field dipole noises related to the forces (pressures) exerted on the surface.

Each term is written as

$$p'_{t,i}(\mathbf{x},t)=\frac{\rho_0V_0}{4\pi}\left[\frac{1}{1-M_r}\frac{\partial}{\partial\tau}\left(\frac{1}{1-M_r}\frac{\partial}{\partial\tau}\left(\frac{1}{r_i|1-M_r|}\right)\right)\right]_{\mathrm{ret}},\tag{7a}$$

$$p'_{\mathrm{ln},i}(\mathbf{x},t)=\frac{1}{4\pi}\left[\frac{1}{r_i^2}\frac{1}{(1-M_r)^2}\left(\mathbf{r}_i\cdot\mathbf{f}_i\frac{1-\mathbf{M}_i\cdot\mathbf{M}_i}{1-M_r}-\mathbf{f}_i\cdot\mathbf{M}_i\right)\right]_{\mathrm{ret}},\tag{7b}$$

$$p'_{lf,i}(t)=\frac{1}{4\pi}\left[\frac{1}{r_i}\frac{1}{(1-M_r)^2}\left(\frac{\mathbf{r}_i}{c_0}\cdot\frac{\partial\mathbf{f}_i}{\partial\tau}+\frac{\mathbf{r}_i\cdot\mathbf{f}_i}{1-M_r}\left(\frac{\mathbf{r}_i}{c_0}\cdot\frac{\partial\mathbf{M}_i}{\partial\tau}\right)\right)\right]_{\mathrm{ret}},\tag{7c}$$

where ρ_0 is the density of the undisturbed medium, c_0 is the speed of sound, V_0 is the blade volume, $\mathbf{r}_i(=(\mathbf{x}-\mathbf{y}_i)/r_i)$ is a unit vector from the noise source i to the observer ($r_i=|\mathbf{x}-\mathbf{y}_i|$), and $\mathbf{f}_i$ is the force vector acting onto the fluid.

The local source Mach number vector, its first time derivative, and the relative Mach number are also defined as

$$\mathbf{M}_i=\frac{1}{c_0}\frac{\partial\mathbf{y}_i}{\partial\tau},\quad\frac{\partial\mathbf{M}_i}{\partial\tau}=\frac{1}{c_0}\frac{\partial^2\mathbf{y}_i}{\partial\tau^2},\quad M_r=\mathbf{r}_i\cdot\mathbf{M}_i=\frac{\mathbf{x}-\mathbf{y}_i}{r_i}\cdot\frac{1}{c_0}\frac{\partial\mathbf{y}_i}{\partial\tau},\tag{8}$$

where $\mathbf{y}_i$ is a position vector to the noise source i.

The terms in the square brackets of Eq. (7) are evaluated at a retarded time (τ), where

$$\tau=t-\frac{r_i(\tau)}{c_0},\tag{9}$$

and the acoustic pressure $p'(\mathbf{x},t)$ at the observer time is calculated by the following procedure; (i) calculate the thickness and loading noises generated at the retarded time τ, (ii) determine the distance $r_i(\tau)$ between the source and the observer and calculate the observer time t, and (iii) after the acoustic pressures are known at each instant of retarded time τ, sort the acoustic pressures according to their arrival times at the observer.

A sound pressure level is then determined by

$$L_p=10\log_{10}(p'_{\mathrm{rms}}/p_{\mathrm{ref}})^2,\tag{10}$$

where p'_{rms} is a root mean square of the acoustic pressure and $p_{\mathrm{ref}}(=2\times10^{-5}\,\mathrm{Pa})$ is a standard reference pressure. The SPL spectrum is obtained by a fast-Fourier transform (FFT) algorithm using MATLAB V.5.1.

3 Computational Results and Discussion

3.1 Cross-Flow Fan Impellers.

In the present study, the performance and aeroacoustic noise characteristics of the uniform and random pitch fans (type A and B) are investigated. All three impellers consist of 35 blades, and the uniform pitch fan has a

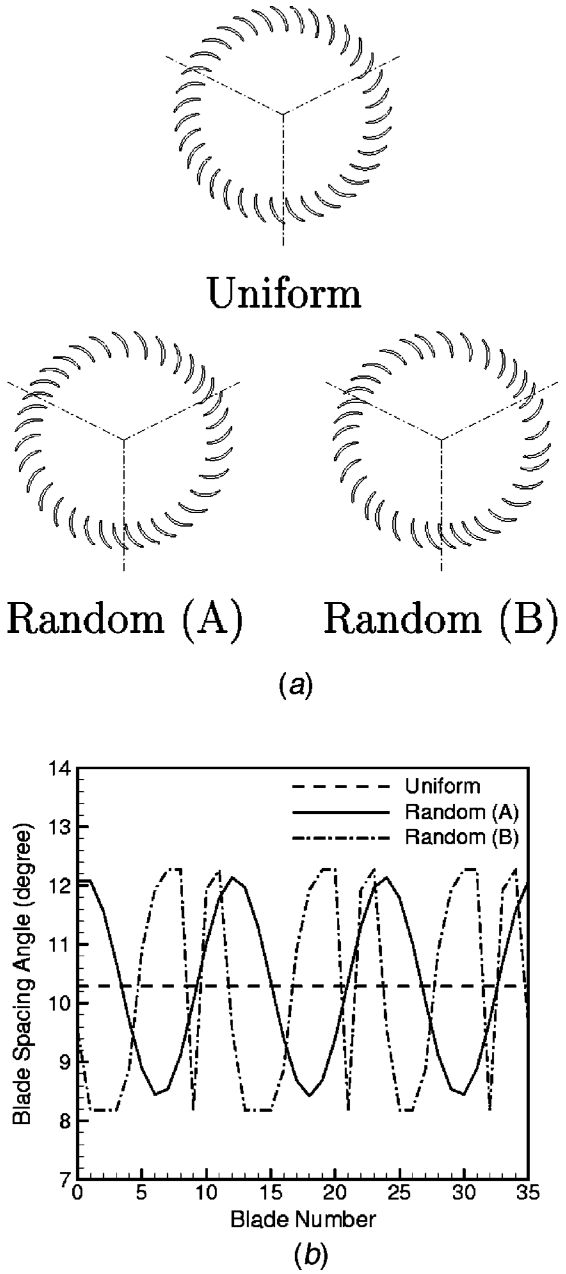

Fig. 2 Cross-flow fan impellers, (*a*) impeller cross-sections ($Z=35$), (*b*) blade pitch angle distributions

constant blade pitch angle of 10.286 deg. Figure 2 shows the cross-section profiles and pitch distributions of these impellers. The type A random pitch impeller has a sinusoidal pitch variation, i.e., $\Delta\theta_i=[360/35+\{35/(3\times 2\pi)\}\times\cos(3\times 2\pi/35\times(i-0.5))]\times\pi/180$ (i=blade number), while the type B impeller has an irregular blade pitch profile such that a small blade pitch angle is abruptly added to the largest blade pitch angle position. Similar random pitch profiles have also been tested for the axial and radial fans by Mellin and Sovran [23] and Boltezar et al. [24].

3.2 Unsteady Viscous Flow Computations. A generic-type cross-flow fan as shown in Fig. 3 is considered in the computation. It only consists of basic components such as impeller, stabilizer, and rear-guider, excluding heat exchanger and entrance grille. The impeller blade has inner, outer, and setting angles of 79.6 deg, 161.6 deg, and 33.4 deg, respectively, and the chord length is 14.24 mm with a maximum thickness of 1.2 mm. The impeller inner and outer diameters are 81.62 mm and 106 mm (D) and its span is 340 mm (L). Since the aspect ratio (L/D) of the impeller is 3.2, the flow three-dimensionality effect is expected to be minimal. This was also confirmed by Chen [25] that the flow 5 mm away from the side walls is nearly two-dimensional. The present cross-flow fan operates at a rotational speed of 1000 rpm, and the Reynolds number ($\mathrm{Re}=V_{\mathrm{tip}}c/\nu$) based on the impeller blade tip velocity (5.55 m/s) and the chord length (c) is 5300. According to the pre-calculated flow field solutions, the Reynolds number based on the local velocity and the blade pitch ranges from 1690 to 2680 within most of the blade passages, except for a flow exit region where it is locally 4000 at the maximum flow rate case. Therefore, the internal flow of the cross-flow fan is assumed two-dimensional, incompressible, and laminar in the present computations.

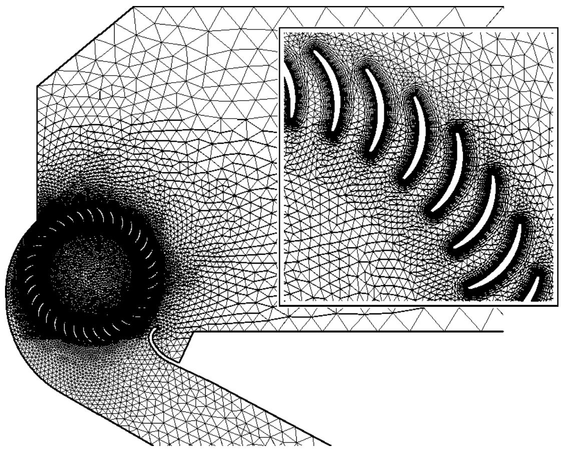

Fig. 3 Triangular meshes for the present test model: uniform pitch, 60743 cells (rotating part), 28345 cells (stationary part)

The computational domain is divided into two zones, a rotating zone including impeller and a stationary zone, and a sliding mesh technique, [14], is applied at the interface in order to allow the unsteady interactions between two zones. Figure 3 shows the triangular meshes of the cross-flow fan generated by the advancing front method, [26], and also the mesh details near the blades. As visualized in Yamafuji's experiment, [27], the fan performance is closely related to the small-scale vortices shed from the blades, because they will eventually form a large-scale eccentric vortex and the fan performance will be determined by it. Therefore, properly resolving the viscous flow effects near the blades is essential in order to accurately predict the location and strength of the eccentric vortex. In the present computation, 60,743 and 28,345 cells are used for the rotating and stationary zones, respectively.

A time-accurate computation starts with the impeller rotating from a quiescent flow condition. The computational boundaries of the inflow and the outflow are set to a distance five times the impeller outer diameter from the fan entrance and the exit. A uniform velocity is imposed at the inflow boundary, while a constant static pressure is prescribed at the outflow boundary. The inlet velocity is gradually increased following an arc-tangent function from zero to a given mass flow rate during two cycles of impeller rotation. This procedure smoothly develops a through flow and an eccentric vortex inside the fan and finally leads to a quasi-steady state with a pressure rise subject to the given mean flow rate. During computations, a constant time step of $\Delta t=1\times 10^{-4}$ is used, which corresponds to approximately 1/900 of the blade passing period.

A fully developed internal flow field is established after approximately six impeller revolutions. The time-averaged streamlines inside the uniform pitch fan ($\phi=0.602$) are presented in Fig. 4(a), where the size and location of the eccentric vortex developed near the stabilizer are clearly discernible. The instantaneous vor-

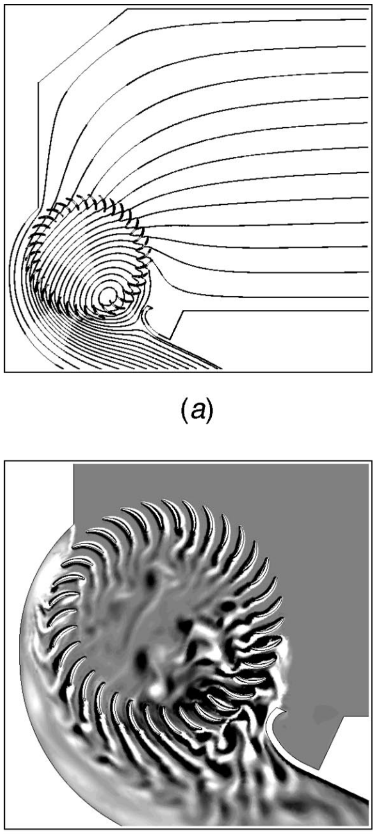

(*a*)

(*b*)

Fig. 4 Time-averaged streamlines patterns and instantaneous vorticity contours: 1000 rpm, ϕ=0.602, (*a*) streamlines, (*b*) vorticity

ticity field contours shown in Fig. 4(*b*) also visualize the vortical flow structures inside the fan, such as eccentric vortex, blade wakes, vortex sheet emanated from the stabilizer, and separated flows within the blade passages. Among these, unsteady interactions between the rotating blade wake and the stabilizer will cause the pressure to fluctuate and generate aeroacoustic noise of the cross-flow fan. This issue will further be discussed in Section 3.3.

Table 1 Mesh sizes of three different grids

	Impeller	Casing	Total
Grid A	12418	7241	19659
Grid B	41196	6996	48192
Grid C	60743	28345	89088

First, the fan performance is compared with experiments in Fig. 5, where the static pressure coefficient $\psi_s(=\Delta P_s/(0.5\rho_0 V_{\text{tip}}^2))$ is plotted against the flow coefficient $\phi(=Q/(V_{\text{tip}}DL))$. Here $\Delta P_s(=P_{s,\text{exit}}-P_{s,\text{inlet}})$ is the pressure difference between the exit and the inlet and Q is the flow rate. The static pressure rise of the cross-flow fan is obtained by time-averaging the unsteady flow solutions for ten impeller revolutions. Accuracy assessment is made by performing the grid-dependent test with three different mesh sizes for the uniform pitch fan (summarized in Table 1). It is indicated in Fig. 5 that the fan performance of Grid B and C agrees quite well with experiments, [28], except for $\phi<0.35$, while the performance is substantially underpredicted by Grid A. Since the casing part of Grid B has similar grid resolution of Grid A, this underprediction is largely due to the lack of grid resolution in the impeller part. The fan performance is a global quantity and may have attributions from many other factors, but it seems closely related to the mesh resolution near the blades for resolving the viscous flow effects. The discrepancy at the lower flow rates ($\phi<0.35$) may result from unstable flow developments near the rear-guider. This is an off-design condition similar to the stall in the turbomachinery. In this case, the eccentric vortex noticeably oscillates due to the increased mismatch of blade incidence angles and the flow separations around the blades. This unsteady flow effect may also be caused by the manifestations of flow three-dimensionality and turbulence. In Fig. 6, the fan performances of the uniform and two random pitch (type A and B) impellers are also compared. The figure indicates that the type A and B fan performances are not significantly affected by the random distributions of their pitch profiles at $0.4<\phi<0.6$ (a typical fan operation range).

3.3 Aeroacoustic Noise Characteristics. The aeroacoustic noise generated from the cross-flow fan can be divided into a discrete tonal noise at BPF and a broadband noise in the range of 300~3000 Hz. For low-speed fans, the dipole-type discrete noise is commonly known as a major noise source compared to the broadband noise.

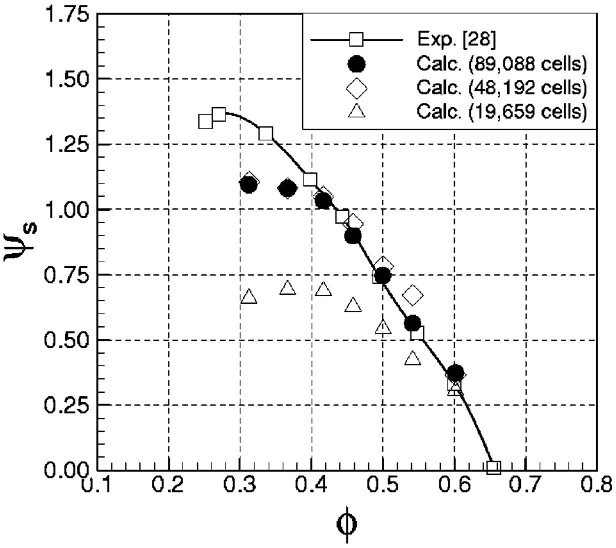

Fig. 5 Grid-dependent test for fan performance prediction

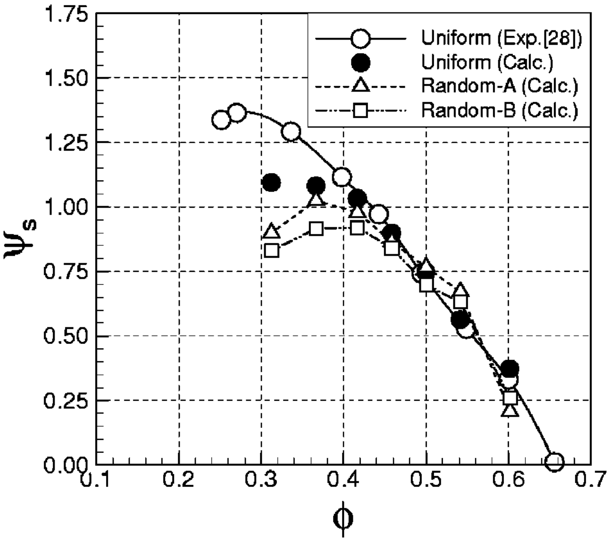

Fig. 6 Comparison of the cross-flow fan performance

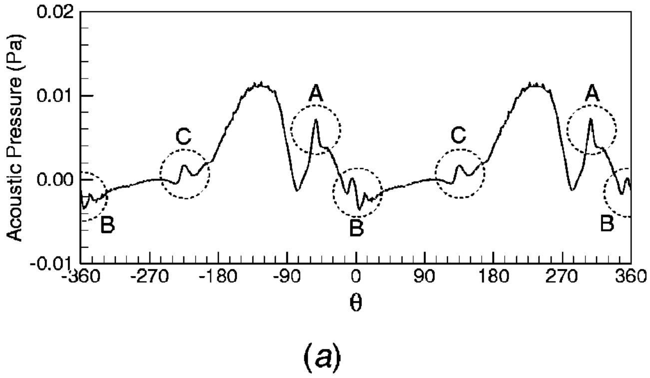

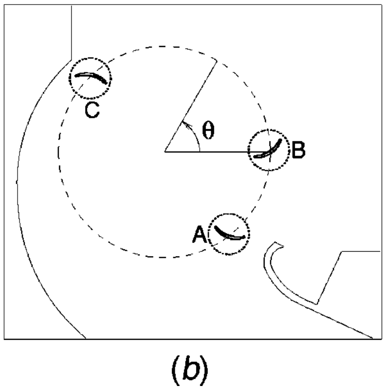

Fig. 7 Aerodynamic noise source identification: uniform pitch, ϕ=0.602, (*a*) acoustic pressure fluctuations along the blade rotation angle (θ), (*b*) identified noise source positions

To identify the discrete noise sources of the cross-flow fan, a sound pressure signature generated from a blade is first investigated for the uniform pitch fan case. The acoustic pressure is calculated by the Ffowcs Williams-Hawkings equation, applied to the unsteady flow solution at the highest flow rate case ($\phi = 0.602$). This is the case where the BPF noise and its modulations by the variable pitch fans are most discernible, since the noise level increases as the flow rate increases. Figure 7(*a*) shows the acoustic pressure variations along the blade rotation angle (θ) for an observer positioned at 1 m horizontally away from the fan entrance and 0.8 m vertically below. This observer position is based on KS (Korean Standard) B 6361, [29], or JIS (Japanese Industrial Standard) B 8346, [30]. One can clearly notice that the acoustic pressure gradually varies except for the positions at A $(=307\ \text{deg})$, $B(=0\ \text{deg})$, and $C(=133\ \text{deg})$. The gradually varying components do not contribute much to the peak noise generation, since the total noise generated from all 35 blades is just a summation of the acoustic pressures whose phases are only shifted by a pitch angle of 10.286 deg (uniform pitch case). Therefore, only components with acoustic pressure variation less than or close to the blade pitch angle will attribute to the BPF noise generation at the observer position. The graphical locations of the identified noise sources are also presented in Fig. 7(*b*). The fluctuations at A (stabilizer) and C (rear-guider) are due to the interactions between the rotating blade wakes and the stationary fan casing, while the fluctuation at B is caused by the interaction of the rotating blades with the vortex sheet emanated from the stabilizer (see Fig. 4(*b*)). The noise source at A may be considered as the dominant one, since it has steepest acoustic pressure variation.

In order to estimate the total noise generated from the cross-flow fan, the Ffowcs Williams-Hawkings equation is now applied to the surfaces of 35 impeller blades and stabilizer shown in Fig. 8. The acoustic pressure is calculated using the unsteady pressure data saved every ten aerodynamic time steps ($\Delta t = 1 \times 10^{-3}$) for 111 periods of blade passing. Although the sampling time is ten times larger than the aerodynamic time step, it is sufficiently small enough to accurately predict the acoustic pressure. Figure 9 shows the monopole and dipole components generated from the rotating blades. The dipole noise clearly exhibits the acoustic pressure fluctuations at BPF with the amplitude of 1.2×10^{-3} Pa, while the monopole noise is almost negligible as expected. Figure 10 also shows the near and far-field dipole noises generated from the blades and stabilizer. The BPF noise clearly appears at both the rotating blades and the stabilizer, and some near-field noise effect is also exhibited by the rotating blades.

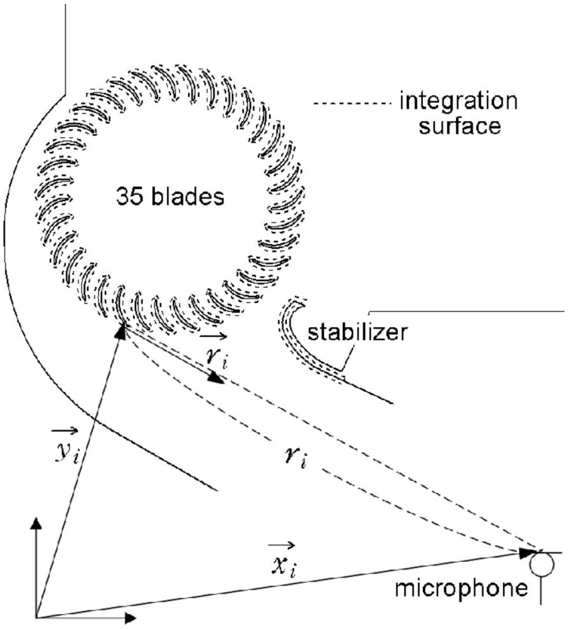

Fig. 8 Integration surfaces and geometric parameters used in the FW-H equation

The BPF tonal noise can be modulated by fans with random pitch variations, since the blade wake intensity varies according to the impeller blade pitch. In the present study, the random pitch fans of type A and B are considered to examine their discrete noise characteristics at ϕ=0.602. Figure 11 shows the time histories of acoustic pressure generated from the rotating blades and stabilizer for all three impellers. The type A and B random pitch impellers exhibit not only the high-frequency irregular acoustic

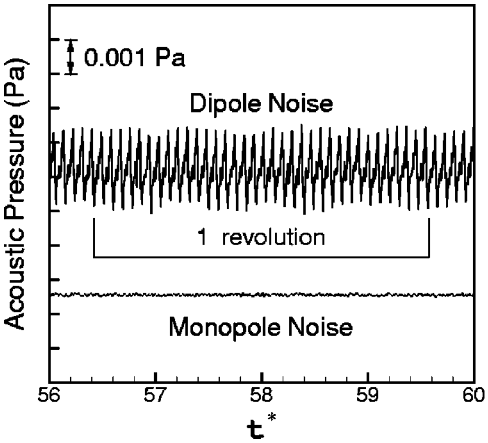

Fig. 9 Monopole and dipole noises generated from the blades: uniform pitch, ϕ=0.602

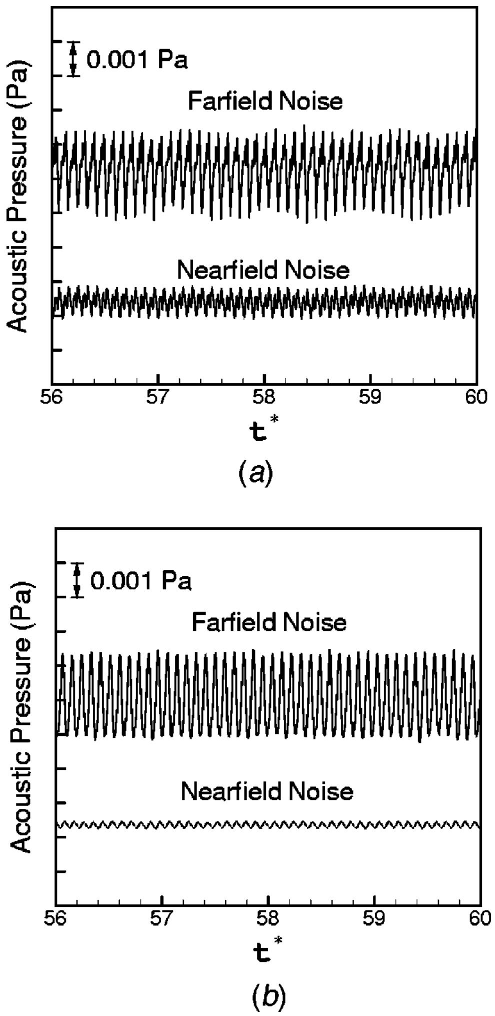

Fig. 10 Near and far-field dipole noises generated from the blades and stabilizer, (*a*) rotating blades, (*b*) stabilizer

pressure fluctuations corresponding to their own blade passing but also the low-frequency large-scale fluctuations caused by three-cycle pitch variations (near-field noise effect).

The sound pressure level (SPL) spectra of these three impellers are presented in Fig. 12. A tonal noise clearly appears at BPF (583 Hz=1000 rpm/60 sec×35) for the uniform pitch fan, while the

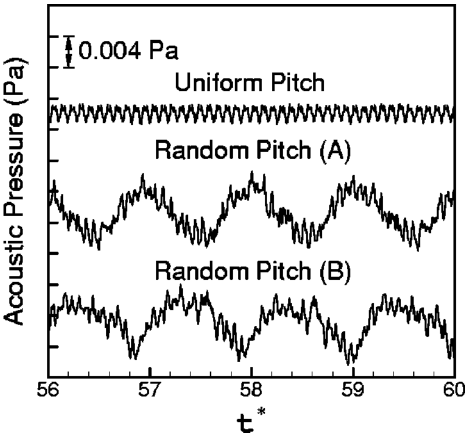

Fig. 11 Time histories of acoustic pressure generated from the blades and stabilizer

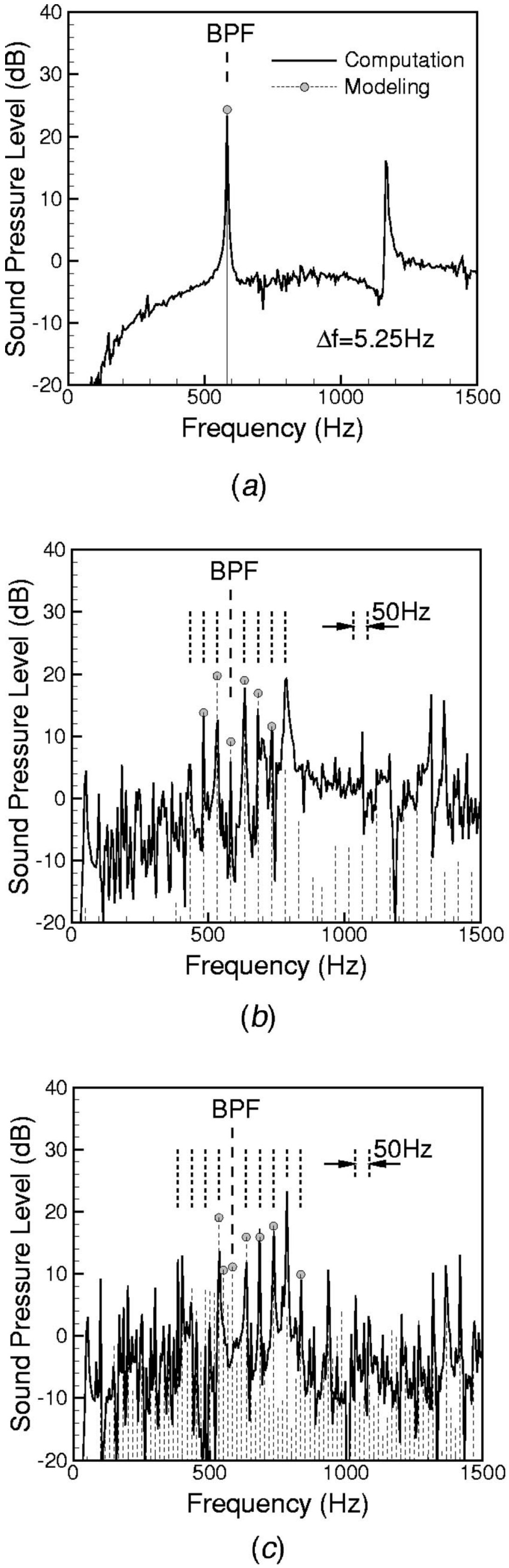

Fig. 12 Sound pressure level (SPL) spectra: —— (NS/FW-H), - - - (Modeling/FW-H, ○: 9 dB or above), (*a*) uniform (*b*) random A (*c*) random B

random pitch impellers show the modulated frequency characteristics. The split discrete frequencies are separated by multiples of 50 Hz (=1000 rpm/60 sec×3) from the BPF due to the near-field noise effect. The type A impeller shows the nearly symmetric spreading of the BPF noise, while the type B exhibits an uneven spreading characteristic toward the higher frequencies. This seems due to the increased irregularities in the type B pitch variations. Mellin and Sovran's experiment, [23], also showed a similar result of uneven spreading characteristic by increasing the randomness in the blade pitch distribution of the axial fan. The type A and B random pitch fans also generate a low-frequency component at 50 Hz due to the three-cyclic pitch variations, which is filtered by A weighting. Even though the overall sound pressure levels (OASPL) of these random pitch fans are slightly increased by 2.7 dB for the type A and 1.1 dB for the type B, the BPF tonal noise, most annoying component to the human ear, is considerably reduced by 5.7 dB for the type A (1.6 dB for the type B), without much loss of fan performance.

The modulated frequencies of random pitch fans predicted by the present method are now validated with those calculated by a theoretical model. The model estimates the static pressure fluctuations at the stabilizer, assuming that (i) the pressure fluctuations vary as a sinusoidal function, (ii) the fluctuation period is proportional to the blade pitch, and (iii) the fluctuation amplitude is also proportional to the blade pitch as well as its change of ratio. The static pressure fluctuations at the stabilizer are written as

$$p(t)=a_i+cs_i\cos\left[2\pi\left(\omega t-\sum_{n=1}^{i-1}b_n\right)\Big/ b_i\right],\quad (0\leqslant\omega t<2\pi) \tag{11}$$

where ω (rad/sec) is the rotational speed of the impeller and i is the blade number in relation with $\Sigma_{n=1}^{i-1}b_n\leqslant\omega t<\Sigma_{n=1}^{i}b_n$. Also, a_i is a constant for function continuity and s_i is the amplitude of the pressure fluctuations generated by the ith blade;

(i) $\Sigma_{n=1}^{i-1}b_n\leqslant\omega t<\Sigma_{n=1}^{i-1}b_n+b_i/2$,

$$a_i=\frac{-kb_{i+1}-(3k+1)b_i}{\bar{b}}+(4k+1),\quad s_i=\frac{b_i}{\bar{b}}+k\frac{b_{i+1}-b_i}{\bar{b}} \tag{12}$$

(ii) $\Sigma_{n=1}^{i-1}b_n+b_i/2\leqslant\omega t<\Sigma_{n=1}^{i}b_n$,

$$a_i=\frac{-3kb_{i+1}-(k+1)b_i}{\bar{b}}+(4k+1),\quad s_i=\frac{b_i}{\bar{b}}-k\frac{b_{i+1}-b_i}{\bar{b}} \tag{13}$$

and $\bar{b}$ is the uniform blade pitch angle (=10.286 deg). In the present modeling, k is chosen as 3 and c in Eq. (11) is determined by the direct computation of the uniform pitch case $(=0.009\rho_0V_{\text{tip}}^2\ \text{Pa})$. The SPL spectra predicted by the model equation with the Ffowcs Williams-Hawkings equation are plotted in Fig. 12 for the uniform and random pitch impellers. Both results by the direct computation and the modeling are reasonably close in prediction of the BPF noise (uniform pitch) and its modulated discrete frequencies (type A and B random pitch). This model has also been tested in Ref. [14] for predicting the modulated frequencies of the axial and radial random pitch fans [23,24].

4 Conclusions

A computational method is proposed for the aerodynamic and aeroacoustic modeling of the cross-flow fan. The performance and aeroacoustic noise characteristics of the uniform and random pitch (type A and B) fans are predicted by the unsteady Navier-Stokes computations with the Ffowcs Williams-Hawkings equation.

(1) The time-averaged solutions indicate that the fan performance is quite favorably compared with experiments (uniform pitch fan) and is not substantially affected by the random pitch fans at $0.4<\phi<0.6$ (a typical fan operation range).

(2) The discrete noise sources of the cross-flow fan are identified at $A(=307\text{ deg})$, $B(=0\text{ deg})$, and $C(=133\text{ deg})$ positions and the noise source at A is found a dominant one among them. A visualization of the instantaneous vortical flow field around the impeller shows that the noise at B in particular is caused by the periodic interactions of the rotating blades with the vortex sheet emanated from the stabilizer.

(3) The SPL spectra of the tested impellers indicate that a tonal noise clearly appears at BPF (=583 Hz) for the uniform pitch fan, while the BPF noise is split into several discrete frequencies by random pitch fans (type A and B), each separated by multiples of 50 Hz due to the three-cycle pitch variations. The symmetric spreading of frequencies in the type A changes to an uneven spreading toward the higher frequencies in the type B, due to the increased irregularities in the pitch variations. The computational result also indicates that, without much loss of performance, the BPF tonal noise of the uniform pitch fan can be reduced by 5.7 dB using the type A random pitch impeller.

Acknowledgments

The authors wish to thank Mr. Jin, Sim-Won of the LG Digital Appliance Laboratory for providing the fan performance data. This work was partially supported by the Korea Research Foundation (97-005-E00199), and the Korea Science and Engineering Foundation (2000-08) through the Regional Research Center for Advanced Climate Control Technology at the SunMoon University.

References

[1] Ilberg, H., and Sadeh, W. Z., 1965–1966, "Flow Theory and Performance of Tangential Fans," Proc. Inst. Mech. Eng., **180**, Part 1, (19), pp. 481–491.
[2] Yamafuji, K., 1975, "Studies on the Flow of Cross-Flow Impellers (2nd Report, Analytical Study)," Bull. JSME, **18**(126), pp. 1425–1431.
[3] Fukano, T., Chen, C., and Hara, Y., 1995, "A Numerical Analysis of Flow in a Cross-Flow Fan," *Numerical Simulations in Turbomachinery*, ASME, New York, FED-227, pp. 53–58.
[4] Bert, P. F., Pessiani, M., Combes, J. F., and Kueny, J. L., 1996, "Unsteady Flow Calculation in a Cross-Flow Fan Using a Finite Element Method," ASME Paper No. 96-GT-443.
[5] Tsurusaki, H., Tsujimoto, Y., Yoshida, Y., and Kitagawa, K., 1997, "Visualization Measurement and Numerical Analysis of Internal Flow in Cross-Flow Fan," ASME J. Fluids Eng., **119**, pp. 633–638.
[6] Jin, S. W., and Lee, N. Y., 1998, "An Experimental Study on Applications of Cross Flow Fan," *Proceedings of SAREK'98 Winter Annual Conference*, pp. 544–549 (in Korean).
[7] Fukano, T., Hara, Y., Yamashita, Y., and Kinoshita, K., 1993, "Study of Noise Reduction of a Cross-Flow Fan (2nd Report, Effect of the Stabilizer Clearance)," Turbomach. J., **21**(6), pp. 350–357 (in Japanese).
[8] Chen, P. H., and Lee, D. S., 1995, "Effect of Tongue Shape on the Performance Curve and the Acoustic Noise of Cross-Flow Fan," J. Chin. Soc. Mech. Eng., **16**(5), pp. 445–455.
[9] Lee, D. S., Chen, P. H., and Miao, J. M., 1997, "Noise Reduction of a Cross-Flow Fan," J. Chin. Inst. Eng., **20**(3), pp. 265–273.
[10] Koo, H. M., 2000, "Discrete Frequency Noise Reduction of the Cross-Flow Fan of the Split Type Room Air-Conditioners Using the Skewed Stabilizers," JSME Int. J., Ser. C, **43**(1), pp. 104–109.
[11] Hayashi, T., Kobayashi, Y., Nagamori, A., and Horino, H., 1996, "Low-Noise Design of Cross-Flow Fan Based on Frequency Modulation," Trans. Jpn. Soc. Mech. Eng., **62**(601), pp. 3446–3451 (in Japanese).
[12] Kobayashi, Y., and Konno, S., 1993, "A Study of High Quality Cross Flow Fan for Room Air Condition," Refrigeration, **68**(794), pp. 1287–1292 (in Japanese).
[13] Hayashi, T., Kobayashi, Y., Nagamori, A., and Horino, H., 1998, "Low-Noise Design for Cross-Flow Fans (Reduction of Blade Passing Tones by Noise Source Interference)," Trans. Jpn. Soc. Mech. Eng., **64**(617), pp. 218–223 (in Japanese).
[14] Moon, Y. J., Cho, Y., and Nam, H. S., 2003, "Computation of Unsteady Viscous Flow and Aeroacoustic Noise of Cross Flow Fans," Comput. Fluids, **32**, pp. 995–1015.
[15] Ffowcs Williams, J. E., and Hawkings, D. L., 1969, "Sound Generation by Turbulence and Surfaces in Arbitrary Motion," Philos. Trans. R. Soc. London, Ser. A, **A264**, pp. 321–342.
[16] Chorin, A. J., 1968, "Numerical Solution of the Navier-Stokes Equations," Math. Comput., **22**, pp. 745–762.
[17] Hirt, C. W., and Cook, J. L., 1972, "Calculating Three-Dimensional Flows Around Structures and Over Rough Terrain," J. Comput. Phys., **10**, pp. 324–340.
[18] Van Leer, B., 1979, "Towards the Ultimate Conservative Difference Schemes

V—A Second Order Sequel to Godunov's Method,'' J. Comput. Phys., **32**, pp. 101–136.

[19] Rhie, C. M., and Chow, W. L., 1983, ''Numerical Study of the Turbulent Flow Past an Airfoil With Trailing Edge Separation,'' AIAA J., **21**(11), pp. 1525–1532.

[20] Cho, Y., 1999, ''Numerical Prediction of the Cross-Flow Fan Performance and Noise Characteristics by an Unstructured Flow Solver Algorithm,'' M.S. thesis, Department of Mechanical Engineering, Korea University, Seoul, Korea.

[21] Farassat, F., 1981, ''Linear Acoustic Formulas for Calculation of Rotating Blade Noise,'' AIAA J., **19**(9), pp. 1122–1130.

[22] Succi, G. P., 1980, ''Design of Quiet Efficient Propellers,'' SAE Paper No. 790584, pp. 2039–2052.

[23] Mellin, R. C., and Sovran, G., 1970, ''Controlling the Tonal Characteristics of the Aerodynamic Noise Generated by Fan Rotors,'' ASME J. Basic Eng., **92**, pp. 143–154.

[24] Boltezar, M., Mesaric, M., and Kuhelj, A., 1998, ''The Influence of Uneven Blade Spacing on the SPL and Noise Spectra Radiated From Radial Fans,'' J. Sound Vib., **216**(4), pp. 697–711.

[25] Chen, C., 1997, ''On Similitude of Cross-Flow Fan in Dynamic Performance and Noise Character,'' Chin. J. Mech. Eng., **10**, No. 3, pp. 203–208.

[26] Peraire, J., Vahdati, M., Morgan, K., and Zienkiewicz, O. C., 1987, ''Adaptive Remeshing for Compressible Flow Computations,'' J. Comput. Phys., **77**, pp. 449–466.

[27] Yamafuji, K., 1975, ''Studies on the Flow of Cross-Flow Impellers (1st Report, Experimental Study),'' Bull. JSME, **18**(123), pp. 1018–1025.

[28] Cho, Y., Moon, Y. J., and Jin, S. W., 1999, ''Numerical Prediction of Cross-Flow Fan Performance and Noise Characteristics by Unsteady Flow Computations,'' *Proceedings of the Korean Society of Mechanical Engineers B*, Spring Annual Conference, pp. 417–422 (in Korean).

[29] Korean Standards, 1987, KS B 6361 Methods of A-Weighted Sound Pressure Level Measurement for Fans, Blowers and Compressors.

[30] Japanese Industrial Standards, 1991, JIS B 8346 Fans, Blowers and Compressors—Determination of A-Weighted Sound Pressure Level.

Vortex-Induced Vibration Characteristics of Two Fixed-Supported Elastic Cylinders

Z. J. Wang

Y. Zhou[1]
e-mail: mmyzhou@polyu.edu.hk

R. M. C. So

Department of Mechanical Engineering,
The Hong Kong Polytechnic University,
Hung Hom, Kowloon, Hong Kong

Interference effects on vortex-induced vibrations of two side-by-side elastic cylinders, fixed at both ends (with no deflection and displacement) in a cross-flow, were experimentally investigated. The dynamic responses of the cylinders were measured using two fiber-optic Bragg grating (FBG) sensors. Simultaneously, a single hot wire was used to measure the velocity in the wake. It has been previously observed that violent resonance occurs when transverse cylinder spacing ratio, T/d, is either large (>2.0) or small (<1.2), but not for intermediate cylinder spacing, i.e., $T/d=1.2\sim 2.0$. This work aims to improve the understanding of the physics behind this observation, and mostly focuses on the fluid-structure interaction in the flow regime of intermediate cylinder spacing. It is well known that in this flow regime the fluid dynamics around one cylinder is totally different from that around the other; the vortical structures are characterized by different dominant frequencies, i.e., about 0.1 and 0.3 (normalized), respectively. The present data indicates that the vortical structures at these frequencies are either weak or different in the formation process from the case of $T/d>2.0$ or $T/d<1.2$, thus resulting in a weak excitation and subsequently an absence of violent resonance. The interrelationship between the vortical structures generated by the two cylinders is also investigated and interpreted in terms of different vortex generation mechanisms. The different fluid dynamics around each cylinder is further found to be responsible for a deviation between the natural frequencies of the combined fluid-cylinder system associated with each cylinder.

[DOI: 10.1115/1.1568360]

1 Introduction

Flow-induced unsteady forces are of common occurrence in turbomachines, offshore pilings, large buildings, etc. Generally they are created by vortices shed from the structures exposed to a cross flow. These flow-induced forces could cause structural fatigue and, under certain unfavorable conditions, may lead to drastic failure of the structures. Consequently, interest in understanding the associated physics and predicting the structural motions is rapidly growing, [1,2]. The flow-induced vibration of a two-dimensional bluff body in a cross-flow is a simple version of this class of fluid-structure interaction problems. Even then, it is governed by a number of major parameters, such as the reduced velocity, the reduced damping, and mass ratio, [3]. Each of these parameters plays a different role in the dynamic response of the cylinder.

The flow-induced vibration problem of two side-by-side elastic cylinders in a cross flow is further complicated by the ratio T over d. Varying T/d may lead to the formation of a single or multiple wakes. When T/d is beyond 2, two distinct vortex streets have been observed, [4]. The two streets are coupled, with a definite phase relationship. Williamson [5] showed that, at $\mathrm{Re}\equiv U_\infty d/\nu=100\sim 200$, the two streets might occur in phase or in antiphase. The vortex centers and the saddle points of the two in-phase streets are antisymmetrical about the flow centerline, but symmetrical for the antiphase case. For $1.5<T/d<2.0$, the base pressure on one cylinder is smaller than that measured on its neighbor. The gap flow between the cylinders is deflected towards the cylinder with the lower base pressure, resulting in one narrow wake. Meanwhile, one wide wake develops behind the neighboring cylinder. The deflected gap flow is bi-stable and randomly changes over from one side to the other, [6,7]. The timescale for the changeover is several orders of magnitude longer than that of vortex shedding and of the instability of the separated shear flows, [8]. The nature of the deflected gap flow is nominally independent of Re. At $T/d<1.2$, the two cylinders behave like one structure, generating a single vortex street, [9]. The variation in fluid dynamics with T/d naturally influences the dynamic response of the cylinders and their resonance (or synchronization) behavior.

Most previous studies were concerned with the flow-induced vibrations on rigid cylinders. Even in the free vibration case, the cylinders, flexibly mounted at both ends, were relatively rigid, [10]. Here, a rigid cylinder is defined as one having infinite structural stiffness. The dynamic characteristics of an elastic cylinder, defined as one with finite structural stiffness, fix-supported at both ends (no deflection), can be quite different from a rigid one. For example, there is only one natural frequency for a rigid cylinder system but more than one associated with an elastic cylinder system, [11]. Understanding of the interaction between fluid and elastic structures as a fully coupled problem is far from complete.

There have been relatively few studies on two side-by-side elastic cylinders in a cross-flow. Zhou et al. [12] recently carried out a fairly detailed investigation of the fluid-structure interaction of this particular problem. They found that the natural frequencies of the combined fluid-structure system vary slowly with U_r but sharply, up to about 10%, near resonance. The sharp variation is dictated by the vortex shedding frequency, in distinct contrast with the lock-in phenomenon, where the forced vibration of a structure modifies the vortex shedding frequency. They further observed violent vibrations, associated with resonance, for $T/d=1.13$ and 3.00, but not for $T/d=1.70$. It is well known that, in the asymmetrical flow regime such as at $T/d=1.70$, the narrow and wide wakes are characterized by a dominant frequency of $f_s^*=f_s d/U_\infty\approx 0.3$ and 0.1, respectively. One issue naturally arises is why the violent vibration is absent at this cylinder spacing. Furthermore, how are the dominant vortical structures related in the two wakes? Evidently, the fluid dynamics around each cylinder is

---

[1] To whom correspondence should be addressed.

Contributed by the Fluids Engineering Division for publication in the JOURNAL OF FLUIDS ENGINEERING. Manuscript received by the Fluids Engineering Division March 13, 2002; revised manuscript received September 15, 2002. Associate Editor: M. Plesniak.

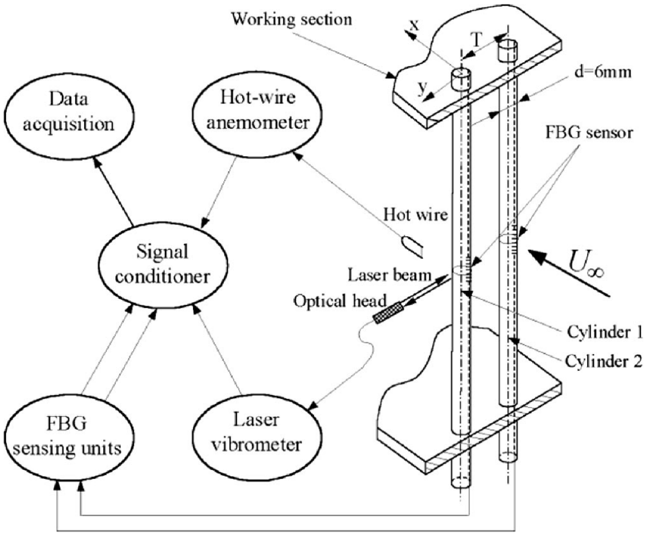

Fig. 1 Experimental arrangement

quite different from that around its neighbor. How would this difference impact upon the fluid-structure interactions? None of these issues has been adequately addressed in the literature.

In engineering problems, the vibration amplitudes are usually large relative to their respective characteristic length scales. However, the physics of the fluid-structure interaction can also be acquired by studying flow-induced vibration phenomenon with small to moderate vibration amplitudes, [13]. The present study aims to examine the physics of fluid-structure interaction in a simple flow-induced vibration problem of two side-by-side cylinders with relatively small vibration amplitude. The focus is on the asymmetrical flow regime associated with $T/d = 1.70$. The wake fluctuating velocity and the structural vibrations of the two cylinders were simultaneously measured using one single hot wire and two fiber-optic Bragg grating (FBG) sensors, [11,14]. Flow visualization was also conducted. The measurements shed light on the absence of violent vibrations in the asymmetrical flow regime. The interrelationship between vortical structures generated by the two cylinders is examined based on the phase spectra between the simultaneously measured vibration signals. Finally, the effects of interference between the cylinders on the natural frequencies of the combined fluid-structure system are discussed.

2 Experimental Details

Figure 1 shows a schematic mounting of two acrylic cylinders symmetrically placed about the midplane of the tunnel working section, which is 0.5 m long with a cross section of 0.35 m $\times$0.35 m. In this experiment, the origin of the coordinate system is chosen at the center of Cylinder 1. The other cylinder is labeled as Cylinder 2. Both cylinders were fix-supported at the ends, and their structural characteristic properties, as summarized in Table 1, are identical. Experiments were mostly conducted for $T/d = 1.7$. For the purpose of comparison, measurements were also obtained for $T/d = 3.0$ and 1.13. The three different T/d values represent three distinct flow regimes. In order to minimize the variation of $f_0^{(1)}$ due to mounting and remounting, only Cylinder 2 was moved to effect a T/d change. In this paper, $f_0^{(n)}$ $(n = 1,2,3, \ldots)$ denotes the nth mode structural natural frequency of the test cylinder, while $f_x^{(n)}$ and $f_y^{(n)}$ $(n = 1,2,3, \ldots)$ stand for the nth mode in-line and cross-flow natural frequencies, respectively, of the fluid-cylinder system. The values of $f_0^{(1)}$ determined for Cylinder 1 were 104 Hz for the lift (or y) direction and 98.6 Hz for the drag (or x) direction. Similarly, $f_0^{(1)}$ for Cylinder 2 was found to be 94, 95, and 101 Hz for the lift direction and 96, 101, and 101 Hz for the drag direction for $T/d = 1.13$, 1.70, and 3.00, respectively. Since the difference in $f_0^{(1)}$ was very small, its effect on fluid-structure interaction can be considered negligible.

Table 1 Structural characteristic properties of the cylinders

Material	End Conditions	L (m)	d (m)	EI (Nm^2)	M^*	$\zeta_0^{(1)}$
Acrylic	Built-in	0.35	0.006	0.224	565	0.026

In the present investigation, it was important to minimize tunnel vibrations, which were caused by the fan and motor. The frequency of the wind tunnel vibration was estimated to be 20–30 Hz, [11]. Care was taken to isolate the working section from the vibration sources through the use of vibration absorbers. The maximum effect of the tunnel vibration on the spectral energy distribution associated with the first-mode natural frequency was about 1.1%, indicating a negligible tunnel vibration effect on the measurements.

A total blockage to the flow due to the two cylinders was calculated to be 3.4%, and the aspect ratio was 58. The Reynolds number Re investigated varied from 800 to 11,000, giving a corresponding reduced velocity U_r range of 3–48. For the present aspect ratio, it has been verified that the mean velocity and turbulence intensities are reasonably uniform across most of the wake for the current Re range. No attempt was made to manipulate the end boundary conditions, although Williamson [15] and Prasad and Williamson [16] showed that it was possible to control oblique and parallel shedding at Re as large as 5000. In the freestream, the longitudinal turbulence intensity was less than 0.2%. Three spacing ratios were investigated, i.e., $T/d = 3.00$, 1.70, and 1.13. These ratios were chosen because the resulting flow regimes were representative of the different proximity effects for two side-by-side cylinders, [17].

A single hot wire (Tungsten) was located at $x/d = 2$ and $y/d = 1.5$ throughout the entire experiments to measure the instantaneous velocity at that location. The wire was operated at an overheat ratio of 1.8 with a constant temperature anemometer to monitor the streamwise fluctuation velocity u in the wake. This measurement provided a check on the vortex shedding frequency determined from the strain signals.

The dynamic strains of the two cylinders along the x or y direction were measured simultaneously using two FBG sensors. An optical silicon fiber of diameter 125 μm built with an FBG sensor was buried in a groove along the span of cylinder. The FBG sensor was located at mid span of the cylinder and at 90° from the leading stagnation line. This arrangement was used to measure the y-direction strain. Since the sensor grating has a finite length of about 10 mm, the measurement represents the average strain over this length. The strain thus measured is designated as ε_y. In principle, ε_y is independent of the vibration of the structure along the x-direction. However, nonlinear fluid-structure interactions could create cross-talk between the x and y direction, thus x-direction vibration might affect ε_y and vice versa. In order to measure the x-direction strain ε_x, the cylinder was rotated so that the FBG sensor was located at the rear stagnation line. A major contribution to error came from nonlinearity effects when calibrating the relation between the output voltage and strain [11,14].

The signals u, ε_{y1} and ε_{y2} or u, ε_{x1} and ε_{x2}, where the subscripts 1 and 2 represent the cylinder number, were offset, amplified and digitized using a 12 bit A/D board and a personal computer at a sampling frequency of 6.0 kHz per channel. The record length was about 20s. This record length was sufficiently long for the root mean square (rms) values $\varepsilon_{x,\mathrm{rms}}$ of ε_x and $\varepsilon_{y,\mathrm{rms}}$ of ε_y to reach their stationary state, with a variation smaller than 1.0%.

The uncertainties of the measured or calculated quantities are summarized in Table 2.

Table 2 Uncertainties

Mean Velocity Measured by Pitot Tube	Bending Displacement Measured by Laser Vibrometer	Dynamic Strain Measured Using the FBG Sensing System	Natural Frequencies Calculated From the Strain or Displacement Signal Using FFT
±3.0%	±7.5%	±8.0%	±0.35 Hz

3 Absence of Resonance at Intermediate Cylinder Spacing

When the vortex shedding frequency f_s approaches the natural frequencies of the combined fluid-structure system, synchronization or resonance occurs. In general, this leads to violent structural vibrations. Indeed, violent resonance is observed as f_s approximately coincides with the first-mode ($f_y^{(1)}$) or third-mode natural frequency ($f_y^{(3)}$) of the combined fluid-structure system for $T/d = 3.0$ and 1.13, but not for $T/d = 1.7$. The absence of resonance at this T/d could be of engineering significance. The issue was, however, not adequately addressed and the physics behind it is unclear.

Figure 2 presents the dependence of $\varepsilon_{y,\mathrm{rms}}$ and $\varepsilon_{x,\mathrm{rms}}$ on U_r. Evidently, $\varepsilon_{y,\mathrm{rms}}$ and $\varepsilon_{x,\mathrm{rms}}$ of Cylinder 1 is in general agreement with those of Cylinder 2. At $T/d = 3.00$, $\varepsilon_{y,\mathrm{rms}}$ displays three peaks at $U_r \approx 4.2$, 12.0, and 26.0, respectively, while $\varepsilon_{x,\mathrm{rms}}$ shows only one tiny peak at $U_r \approx 26.0$. These peaks result from the occurrence of the first-mode, second-mode, and third-mode resonance, respectively, [12]. The third-mode resonance at $U_r \approx 26$ is most prominent because the resonance of higher mode is associated with greater flow excitation energy. The second-mode resonance at $U_r \approx 12$ is barely discernible because the measurement was conducted at the midspan of the cylinder, which is insensitive to the second-mode vibration. If the shedding of vortex rolls is spanwise in-phase, the second-mode vibration should not be excited at the measurement point. However, the separation point over a circular cylinder oscillates over a range of 75°∼85°, [18]. The oscillation is unlikely to be spanwise in phase, thus partially responsible for the three-dimensional nature of the shed vortices. The vortex cell has a typical spanwise extent of $1 \sim 3d$, [19–21], thus inducing the spanwise asymmetrical excitation force and subsequently exciting the second mode of vibration. At $T/d = 1.13$, $\varepsilon_{y,\mathrm{rms}}$ and $\varepsilon_{x,\mathrm{rms}}$ display only one peak at $U_r \approx 11$, which is ascribed to the first-mode resonance. Based on Chen [3], the third-mode resonance may be predicted to occur at $U_r \approx 54$, which is beyond the present measurement range. Nevertheless, the data around $U_r = 49$ appear to shoot up rapidly, probably signaling an approach to a third-mode resonance. On the other hand, there is no noticeable peak for the case of $T/d = 1.70$. The question then is why the structure could not be excited.

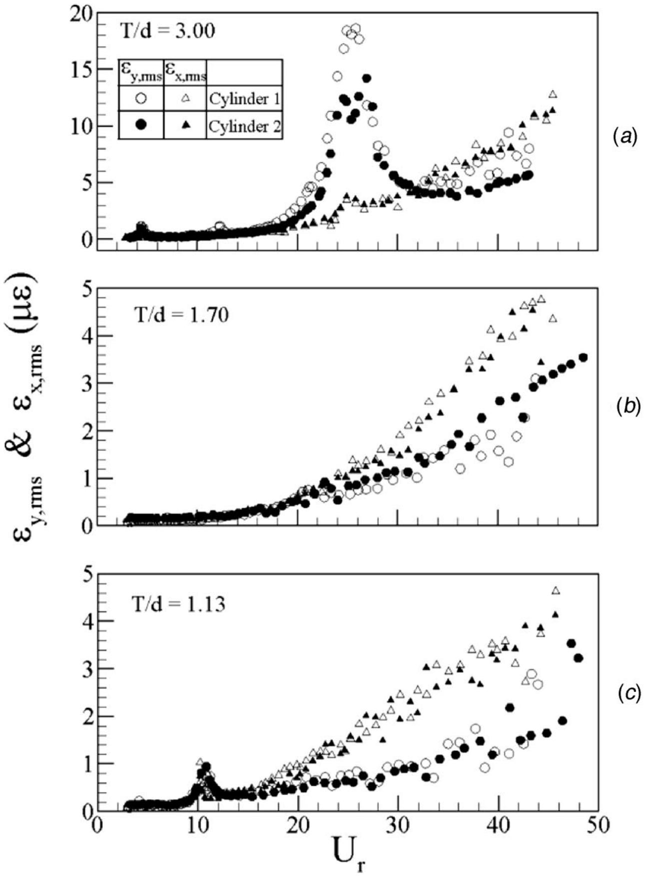

Fig. 2 Variation of $\varepsilon_{y,\mathrm{rms}}$ and $\varepsilon_{x,\mathrm{rms}}$ with U_r: (*a*) $T/d=3.00$; (*b*) $T/d=1.70$; (*c*) $T/d=1.13$. ○, $\varepsilon_{y,\mathrm{rms}}$, Cylinder 1; ●, $\varepsilon_{y,\mathrm{rms}}$, Cylinder 2; △, $\varepsilon_{x,\mathrm{rms}}$, Cylinder 1; ▲, $\varepsilon_{x,\mathrm{rms}}$, Cylinder 2.

It is well documented that two dominant frequencies, i.e., $f_s^* = f_s d/U_\infty \approx 0.1$ and 0.3, occur in the near-wake of two side-by-side cylinders at $T/d = 1.7$. Figure 3(*a*) presents the spectra of signals u and ε_y at $U_r \approx 16$, where $f_s^* (\approx 0.3) \approx f_y^{(3)*}$. Note that the flow behind the two cylinders at $T/d = 1.7$ is nonstationary since the gap flow between the cylinders is stably deflected and may change its deflection from time to time, [8]. Therefore, a test was conducted to estimate the time interval for the gap flow to change its deflection from one side to the other at $T/d = 1.7$. During a sampling period of five minutes, only one change was recorded for Re=5900. The result is consistent with the measurement of Kim and Durbin [8], who found that the switching interval of the gap flow deflection was in the vicinity of minutes for $\mathrm{Re} = 3.5 \times 10^3$, which was several orders larger than the vortex shedding frequency. On the other hand, the present sampling duration was only 20 sec. It would be unlikely that one signal included both modes of gap flow deflection. Although $E_{\varepsilon y}$ exhibits a peak at $f_y^{(3)*}$ as well as at $f_y^{(1)*}$ and $f_y^{(2)*}$, the peak is by far less pronounced than its counterpart at $T/d = 3.0$ (Fig. 4) or 1.13 (Fig. 5). Similarly, the peak at $U_r \approx 48$ (Fig. 3(*b*)), where $f_s^* (\approx 0.1) \approx f_y^{(3)*}$, is not so pronounced for either of the cylinders. The most likely reason is the weak excitation force, implying weak vortical structures generated by the two cylinders. This is indeed evidenced by the less pronounced peak in E_u in Fig. 3 (c.f. Figs. 4 and 5).

In order to gain a thorough understanding of the weak vortex excitation, the typical flow structures at $T/d = 1.7$ obtained from flow visualization are compared with those at $T/d = 3.0$ and 1.13 in Fig. 6. As expected, at $T/d = 1.7$ the gap flow (Fig. 6(*b*)) between the two cylinders is deflected towards one (upper) cylinder, forming one narrow and one wide wake. Vortex shedding in the narrow wake is evident. A few observations could be made from these visualization photos. Firstly, both the size and the strength of the vortices in the narrow wake ($T/d = 1.7$), which correspond to the dominant frequency $f_s^* \approx 0.3$, appear significantly smaller than the other two cases. Secondly, the vortex formation length in the narrow wake has substantially increased; it was estimated to be about 5d for Re=450, compared with about 4d (Figure 6(*a*)) for the $T/d = 3.0$ case. This increase, likely a result of the gap flow effect, may further impair the vortex excitation force on the cyl-

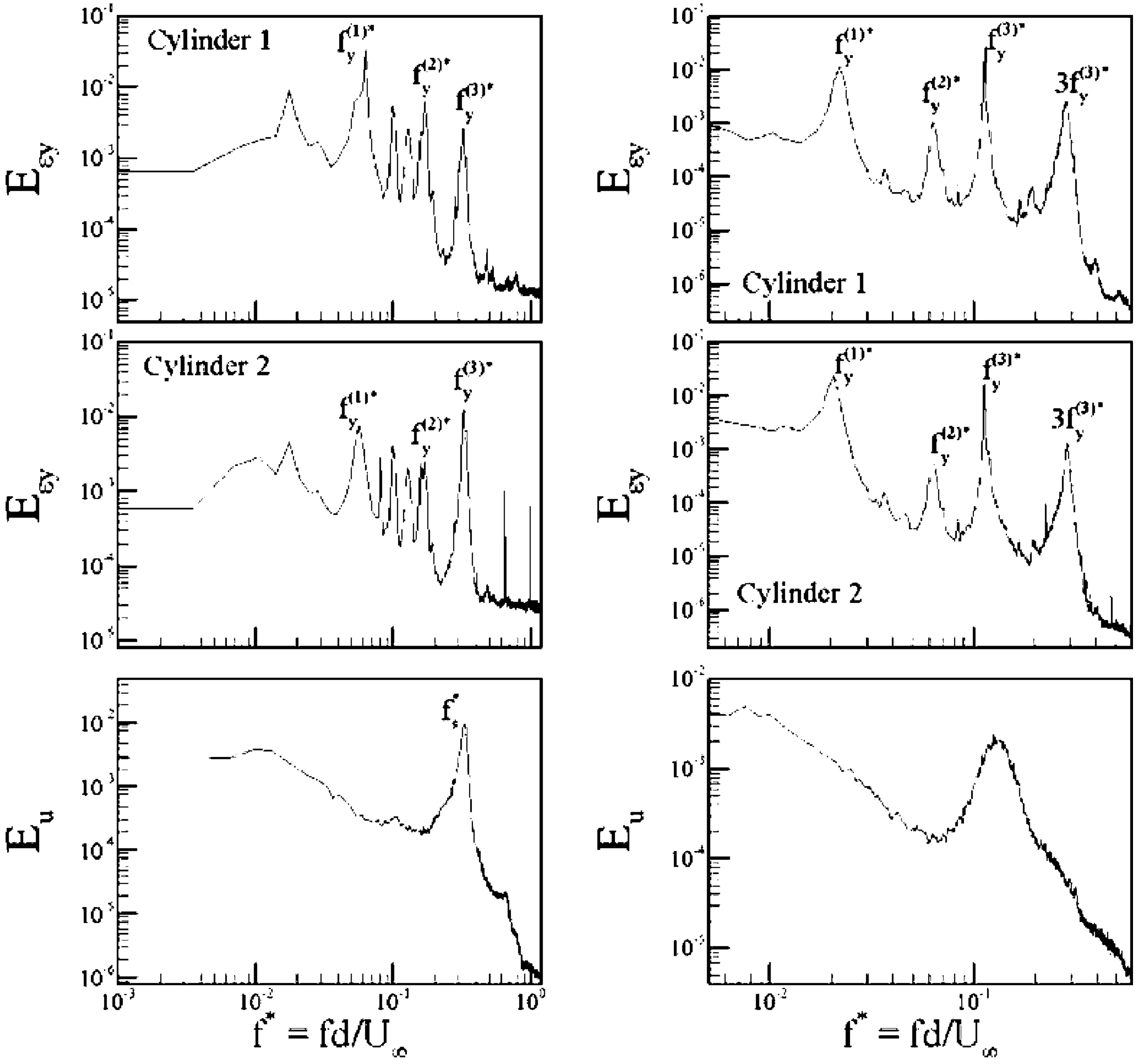

(*a*) (*b*)

Fig. 3 Power spectra $E_{\varepsilon y}$ (upper plate: Cylinder 1; middle plate: Cylinder 2) of the strain ε_y and E_u (lower plate) of the streamwise velocity u at $T/d=1.7$. (*a*) $U_r \approx 16$, Re=3900, where $f_s^*(\approx 0.3) \approx f_y^{(3)*}$; (*b*) $U_r \approx 48$, Re=11000, where $f_s^*(\approx 0.1) \approx f_y^{(3)*}$. The hot wire was located at $x/d=2$ and $y/d=1.5$.

inder. Note that the vortex formation length also exhibits an increase at $T/d=1.13$ (Fig. 6(*c*)), consistent with the observation by Sumner et al. [9]. But the vortex strength probably increases in this case, thus compensating the reduction in the excitation force on the cylinder due to the prolonged formation length. Thirdly, Zhou et al. [12] observed that the two counterrotating vortices in the narrow wake approached each other, possibly generating a low-pressure region between them, thus drawing in the gap vortex in the wide wake. Since the vortex shedding frequency in the narrow wake was about 0.1 and the three merging vortices were associated with small lateral spacing between them, the hot wire could measure a frequency tripling that (≈ 0.1) in the wide wake. Meanwhile, the interaction between the merging vortices will weaken the coherence of vortical structures and consequently the excitation force on the cylinder. Combination of these three factors could contribute to the considerably weakened structural vibration at $T/d=1.7$ even when $f_s^*(\approx 0.3)=f_y^{(3)*}$.

In the wide wake, the vortical structures, which are responsible for the peak at $f_s^* \approx 0.1$ in E_u, roll up even further downstream. Furthermore, their formation mechanism could be different from those in the narrow wake. Zhang and Zhou [22] recently measured the flow up to $x/d=10$ behind three side-by-side cylinders ($T/d=1.5$) using both hot-wire and laser-illuminated flow visualization techniques. They observed a wide wake behind the central cylinder and a narrow wake on each side of the wide wake. It was found that the vortical structures in the narrow wakes were shed from the cylinder and vanished at $x/d \approx 5$. On the other hand, the vortical structures in the wide wake started to roll up at $x/d \approx 5$ (Re>450). They were very weak initially but grew in strength

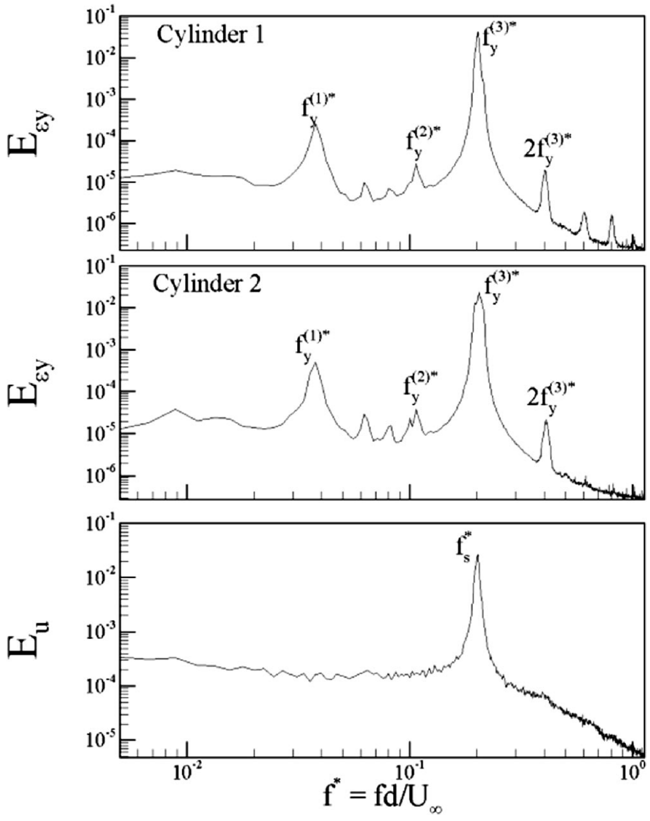

Fig. 4 Power spectra $E_{\varepsilon y}$ (upper plate: Cylinder 1; middle plate: Cylinder 2) of the strain ε_y and E_u (lower plate) of the streamwise velocity u at $T/d=3.0$. $U_r \approx 26$, Re=6200, where $f_s^*(\approx 0.2) \approx f_y^{(3)*}$. The hot wire was located at $x/d=2$ and $y/d=1.5$.

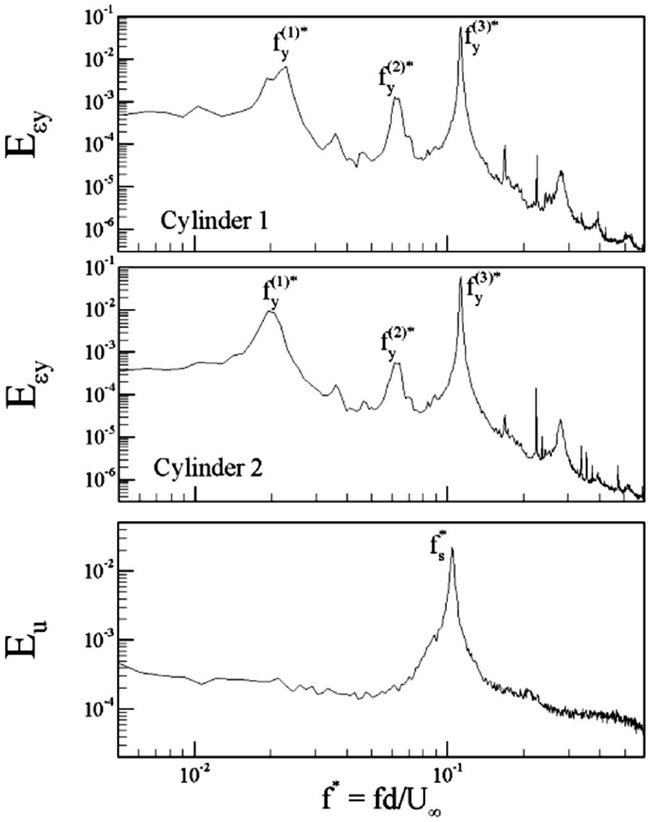

Fig. 5 Power spectra $E_{\varepsilon y}$ (upper plate: Cylinder 1; middle plate: Cylinder 2) of the strain ε_y and E_u (lower plate) of the streamwise velocity u at $T/d=1.13$. $U_r \approx 48$, Re=11000, where $f_s^*(\approx 0.1) \approx f_y^{(3)*}$. The hot wire was located at $x/d=2$ and $y/d=1.5$.

with increasing x/d, resembling those in a screen near-wake, which were ascribed to the shear layer instability of the developing wake, [21,23]. This instability differs from that responsible for vortices shed from a cylinder, which decay as x/d increases. The two-cylinder case may bear a resemblance to that of three cylinders. The vortices seen in the wide wake (Fig. 6(*b*)) may be generated from the shear layer instability in the developing wake, whereas those in the narrow wake originate from the boundary layer separation from the cylinder, probably disappearing before $x/d=10$. This speculation is corroborated by the observation (Fig. 3) that the peak at $f^* \approx 0.1$ in E_u is rather broad, in contrast with the sharp peak at $f^* \approx 0.3$, implying a stronger periodicity of vortices in the narrow wake than that in the wide wake. The vortices generated due to the shear layer instability in the developing wake are unlikely to cause a strong excitation force on the cylinder.

One question has yet to be answered: why is the dominant frequency about 0.1 in the wide wake? Roshko [24] proposed a universal Strouhal number $\mathrm{St}_u = f_s d_w / U_w$, where d_w is the wake width, $U_w = U_\infty (1 - C_{pw})^{1/2}$, and C_{pw} is the pressure coefficient in the wake. The Strouhal number, St_u, is a constant, about 0.16 in a single cylinder wake. The Strouhal number $\mathrm{St} = f_s d / U_\infty$ could then be written as $\mathrm{St} = \mathrm{St}_u (d/d_w)(1 - C_{pw})^{1/2}$. Evidently, d_w or the shear layer thickness and St are inversely related. Presumably, this relationship is also valid in the wide wake, where the vortical structures are probably generated by the shear layer instability in the developing wake. This implies that the vortical structure frequency $f^* \approx 0.1$ might be dictated by the shear layer thickness.

It can be seen that $\varepsilon_{x,\mathrm{rms}}$ becomes larger than $\varepsilon_{y,\mathrm{rms}}$ as U_r increases (Fig. 2). This is more significant for cases with smaller T/d. For example, $\varepsilon_{x,\mathrm{rms}}$ exceeds $\varepsilon_{y,\mathrm{rms}}$ at $U_r \approx 33$, 23 and 15, respectively, for $T/d = 3.0$, 1.7, and 1.13. Bearman and Wadcock [7] measured the mean drag and mean lift on two side-by-side cylinders, which indicated an increasing repulsive force as the two cylinders approach each other. The increased repulsive force may lead to an increase in fluid rigidity between the two cylinders, which may be partially responsible for the suppressed transverse vibrations of the two cylinders. The increased repulsive force, however, has little effect on the drag direction vibration in the present investigation. Consequently, $\varepsilon_{x,\mathrm{rms}}$ tends to overwhelm $\varepsilon_{y,\mathrm{rms}}$ as T/d reduces.

It is pertinent to comment that at $T/d = 1.13$ the peak in $\varepsilon_{x,\mathrm{rms}}$ (Fig. 2(*c*)) at $U_r \approx 11$ is quite prominent, comparable to that in $\varepsilon_{y,\mathrm{rms}}$. This is in distinct contrast with the case of $T/d = 3.0$ (Fig. 2(*a*)). Two reasons may be responsible for this observation. First, when resonance occurs at $U_r \approx 11$, the spectral phase shift $\Phi_{\varepsilon_1 \varepsilon_2}$ ($\equiv \tan^{-1} Q_{\varepsilon_1 \varepsilon_2} / Co_{\varepsilon_1 \varepsilon_2}$, where $Co_{\varepsilon_1 \varepsilon_2}$ and $Q_{\varepsilon_1 \varepsilon_2}$ are the co-spectrum and quadrature spectrum of ε_1 and ε_2, respectively, and the cross-spectrum is computed from the Fourier transform of the correlation $\overline{\varepsilon_1(t+\tau)\varepsilon_2(t)}$) between ε_{y1} and ε_{y2} at the vortex shedding frequency is near 0.5π, indicating that the two cylinders do not vibrate in phase. This impairs the vibration in the lift direction, and accounts for the observation that the $\varepsilon_{y,\mathrm{rms}}$ magnitude at the first-mode resonance ($U_r \approx 11$) for $T/d = 1.13$ is rather comparable with that ($U_r \approx 4.2$) for $T/d = 3.0$, in spite of the fact that the former occurs at a higher U_r. Secondly, for an isolated cylinder or two side-by-side cylinders at $T/d = 3.0$, the drag fluctuates twice as fast as the lift, implying that resonance does not occur simultaneously in the drag and lift directions. The hump or mild peak in $\varepsilon_{x,\mathrm{rms}}$ at $U_r \approx 4.2$, 12, and 26, where resonance occurs in the lift direction, is either due to cross talk between lift and drag

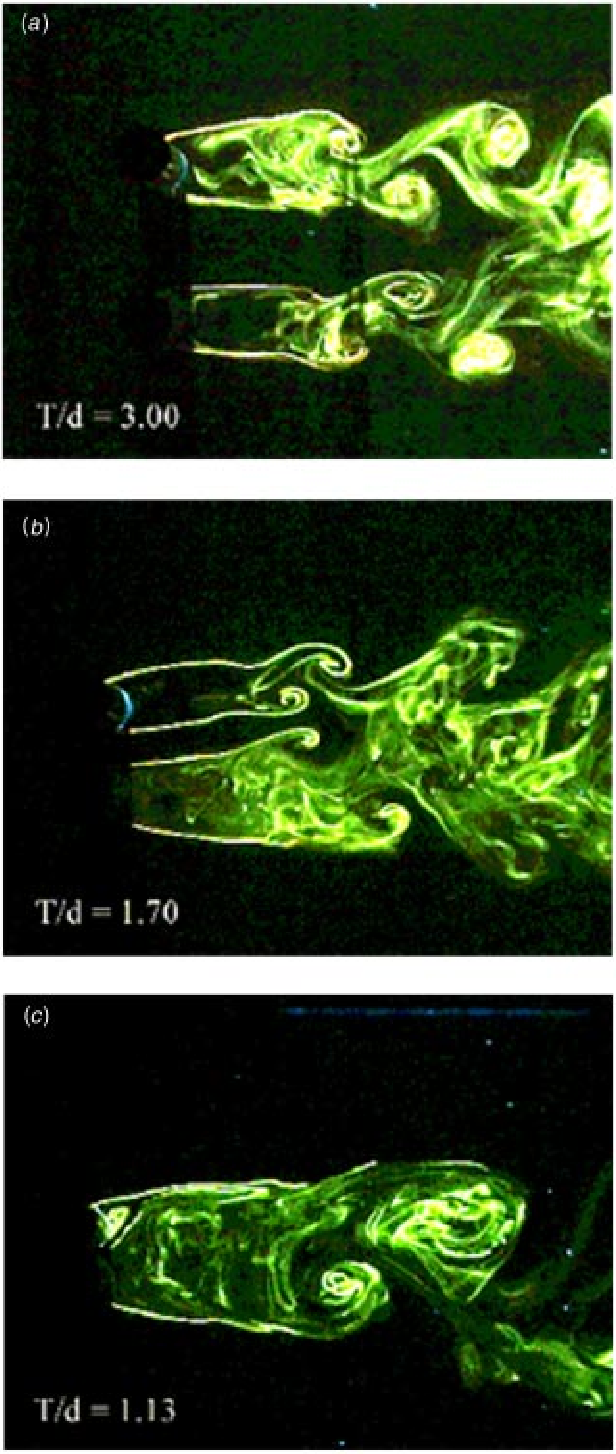

Fig. 6 Laser-illuminated flow visualization in the water tunnel behind two side-by-side cylinders. (*a*) $T/d=3.0$; (*b*) 1.7; (*c*) 1.13. Re=450. Flow is from left to right.

or due to the nonlinear effect created by the violent vibration in the lift direction. At $T/d=1.13$, however, vortices are shed from the outer side of the cylinders only (Fig. 6(*c*)), i.e., the drag fluctuates at the same frequency as the lift. Therefore, resonance occurs simultaneously in both directions. This explains the pronounced peak in $\varepsilon_{x,\mathrm{rms}}$ at $U_r\approx 11$.

4 Interrelation Between Vortex Streets

The interrelation between vortices generated by the two cylinders is examined based on the spectral phase Φ_{12} between the

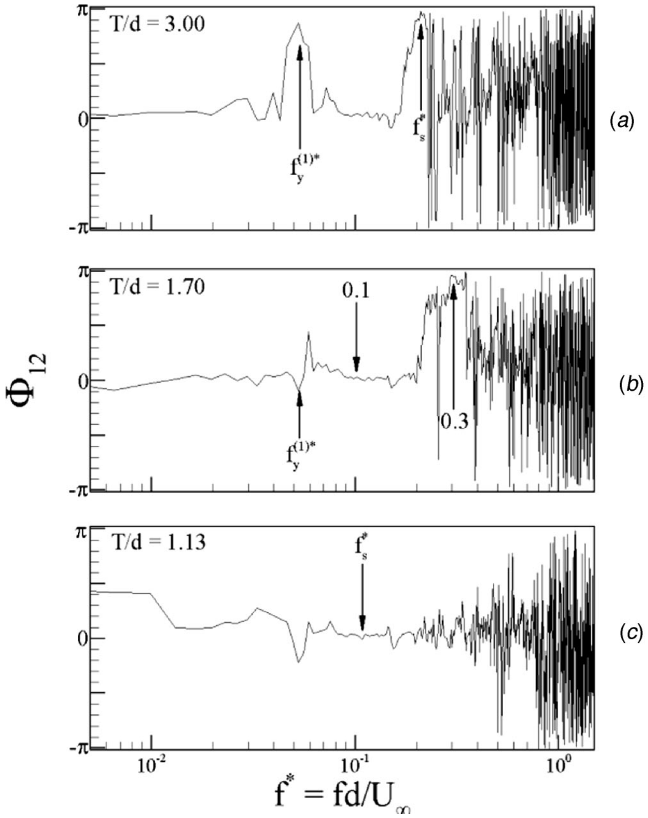

Fig. 7 Spectral phase Φ_{12} between ε_{y1} and ε_{y2} ($U_r=16$, Re $=3900$): (*a*) $T/d=3.00$, (*b*) 1.70, (*c*) 1.13

simultaneously obtained ε_y signals from the two cylinders. For $T/d=3.0$, Φ_{12} (Fig. 7(*a*)) at $f_s^*\approx 0.2$ approaches π, indicating a dominant symmetric vortex shedding from the two cylinders, as previously reported, [6,7]. With symmetrical vortex excitation, Φ_{12} at $f_y^{(1)*}$ also approaches π.

At $T/d=1.13$, Φ_{12} (Fig. 7(*c*)) at $f_s^*\approx 0.1$ is zero, consistent with flow visualization (Fig. 6(*c*)) that vortices are alternately shed from the outer or free stream side only of the two cylinders to form a single vortex street, as observed by Sumner et al. [9]. With the vortex excitation force acting alternately on each, the two cylinders behave like a single structure vibrating in phase.

The $T/d=1.7$ case is more complicated; Φ_{12} is approximately zero at $f^*\approx 0.1$ but approaches π or $-\pi$ at $f^*\approx 0.3$ (Fig. 7(*b*)). In order to understand the observation, it is useful to find the possible connection, if any, between the instabilities in the boundary layer of the cylinders and the dominant frequencies in the wake.

One supplementary experiment was conducted to measure simultaneously the outer shear layers of the two cylinders using two single hot wires. The hot wires were placed at $x/d=0$ and $0.2d$ away from the surface of each cylinder (Re=5900). The spectra of the hot-wire signals (Fig. 8) display peaks at $f^*\approx 0.1$ and 0.3 for both cylinders, identical to those predominant in the downstream vortex streets. This may not be coincidental.

Prasad and Williamson [25] obtained an empirical correlation, i.e., $f_{SL}/f_S=0.0235\ \mathrm{Re}^{0.67}$, between Re and the shear layer instability frequency for a single cylinder in a cross-flow based on published data, [26–31], and their own measurements. This correlation would predict $f_{SL}^*=0.789$ for the present Re, significantly higher than the measurement, 0.1 or 0.3. Although strong interactions between shear layers associated with different cylinders may possibly cause the deviation, the upstream influence from the downstream vorticity dynamics is more likely. This influence may have an impact upon the initial evolution of the shear layer insta-

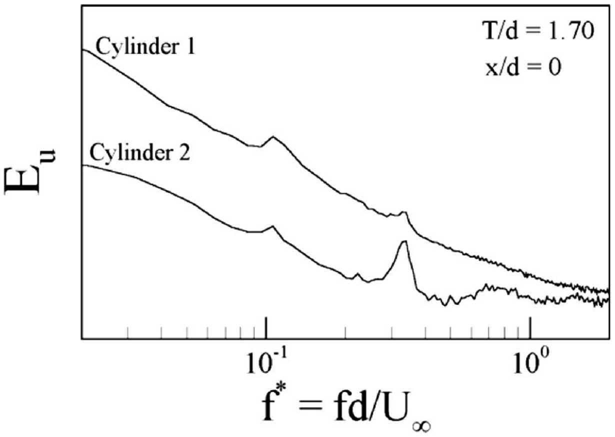

Fig. 8 Power spectrum E_u of the hot-wire signals simultaneously measured in the two outer shear layers associated with the two cylinders. $T/d=1.7$, Re=5900. Two hot-wires were placed at $x/d=0$ and 0.2d away from the surface of each cylinder.

bility, [32,33]. Michalke [34] further suggested that the initial shear layer instability was controlled by downstream vorticity dynamics.

It was discussed in Section 3 that the dominant frequency $f^* \approx 0.3$ in the narrow wake could have a connection with the merging of the two cross-stream vortices in the narrow wake with the gap vortex in the wide wake. The dominant frequencies developed in the wakes may feed back upstream and excites the instabilities of shear layers around the cylinders. Since one single source, i.e., the three merging vortices, could be responsible for the instability at $f^* \approx 0.3$ in the shear layers associated with both cylinders, the vortical structures at $f^* \approx 0.3$ may be induced simultaneously in the outer shear layers of the two cylinders. This is consistent with the observation that the structural responses of the cylinders are antiphased, namely, $\Phi_{12} \approx \pi$ at $f^* \approx 0.3$. Note that the peak at $f^* \approx 0.3$ is stronger for Cylinder 2 (Fig. 8) than for Cylinder 1, probably because Cylinder 2 is responsible for the narrow wake, thus nearer to the three merging vortices than Cylinder 1.

Presumably, the vortices in the wide wake are generated from the shear layer instability in the developing wake (Section 3). Again, this frequency could feed upstream and excite that in the boundary layer of the cylinder. Given that Cylinder 2 is responsible for the narrow wake, the instability at $f^* \approx 0.1$ in the shear layers around this cylinder is more likely to be influenced by the vortical structures of the inner row in the wide wake, whereas that associated with Cylinder 1 could be connected to the vortical structures of the outer row. As the two rows of vortical structures in the wide wake occur alternately, [22], the induced instabilities are characterized by a phase relationship of π. Accordingly the two cylinders will be alternately excited, giving rise to $\Phi_{12} \approx 0$, as the $T/d=1.13$ case.

5 Fluid Dynamics Effects on System Natural Frequencies

Zhou et al. [12] studied the effect of the flow on the natural frequencies of the combined fluid-cylinder system and found that $f_y^{(1)}$, $f_y^{(3)}$, $f_x^{(1)}$, and $f_x^{(3)}$ may depend on U_r and T/d. Primarily, they focused on the natural frequencies of the fluid-cylinder system associated with Cylinder 1. In the present investigation, an examination is carried out on whether the flow has the same effect on the system natural frequencies associated with each of the two cylinders.

Comparisons between the first-mode natural frequencies, $f_y^{(1)}$ and $f_x^{(1)}$, associated with Cylinder 1 and 2 are shown in Figs. 9 and 10. At $T/d=3.0$ and 1.13, the behavior of $f_y^{(1)}$ or $f_x^{(1)}$ is rather similar for the two cylinders. The frequencies decrease slowly with U_r but experience an abrupt change when resonance occurs. This behavior has been observed and discussed in detail by Zhou et al. [12]. Interested readers should refer to this paper for details. At $T/d=1.7$, however, there is an appreciable difference, up to 5%, in $f_y^{(1)}/f_0^{(1)}$ or $f_x^{(1)}/f_0^{(1)}$ between the two fluid-cylinder systems. The natural frequencies are determined from the fluctuating strain spectra, which were calculated using a conventional FFT algorithm. The frequency resolution Δf, fixed by the sampling rate and the record length used in the FFT calculation, is estimated to be 0.35 Hz. The corresponding uncertainty in $f_y^{(1)}/f_0^{(1)}$ or $f_x^{(1)}/f_0^{(1)}$ is less than 0.4%. Therefore, the difference in $f_y^{(1)}/f_0^{(1)}$ or $f_x^{(1)}/f_0^{(1)}$ between the two fluid-cylinder systems cannot be attributed to experimental errors.

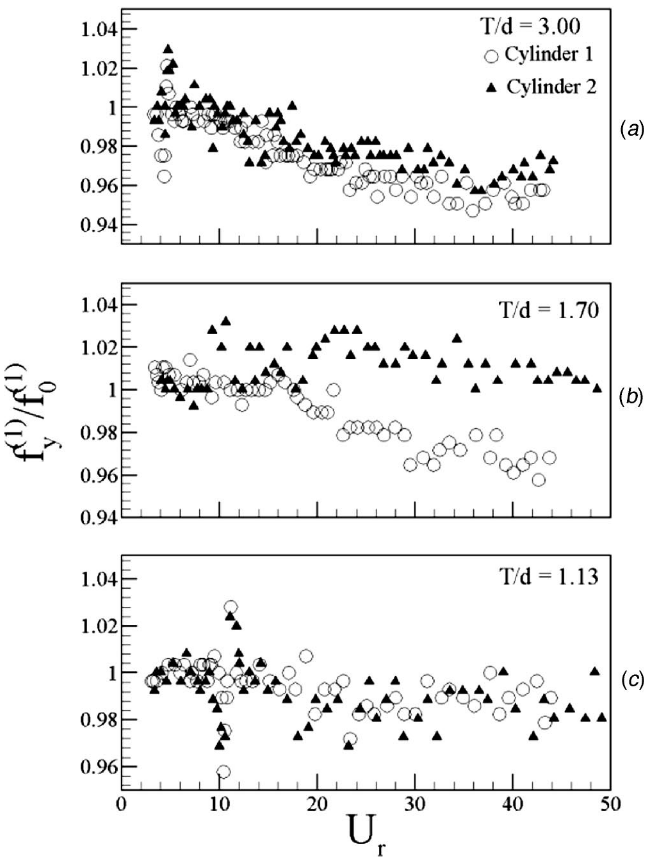

Fig. 9 Variation of the cross-flow $f_y^{(1)}$ with T/d and U_r: ○, Cylinder 1; ▲, Cylinder 2. (*a*) $T/d=3.00$, (*b*) 1.70, (*c*) 1.13.

Considering the fluid-cylinder system as a spring-damper-mass model, both fluid and structure contribute to the system mass, stiffness, and the effective damping ratio. A number of factors could alter the natural frequency of the system. One is the fluid force on the cylinder. For example, as the two cylinders approach each other, the repulsive force increases. This is equivalent to an increase in fluid rigidity. Furthermore, the increasing repulsive force between the cylinders gives rise to an increase in the tensile axial loading on the cylinder, which is fix-supported at both ends, and subsequently increases the structural rigidity, [35]. As a result, the system natural frequency might increase. Added mass is another factor that may change the natural frequency of the system. Chen [3] calculated the added mass on two side-by-side cylinders in a cross flow and found that, in the range of $1.13<T/d<4$, the added mass increases as T/d decreases, thus contributing to a decrease in the system natural frequency. Nonlinear fluid damping

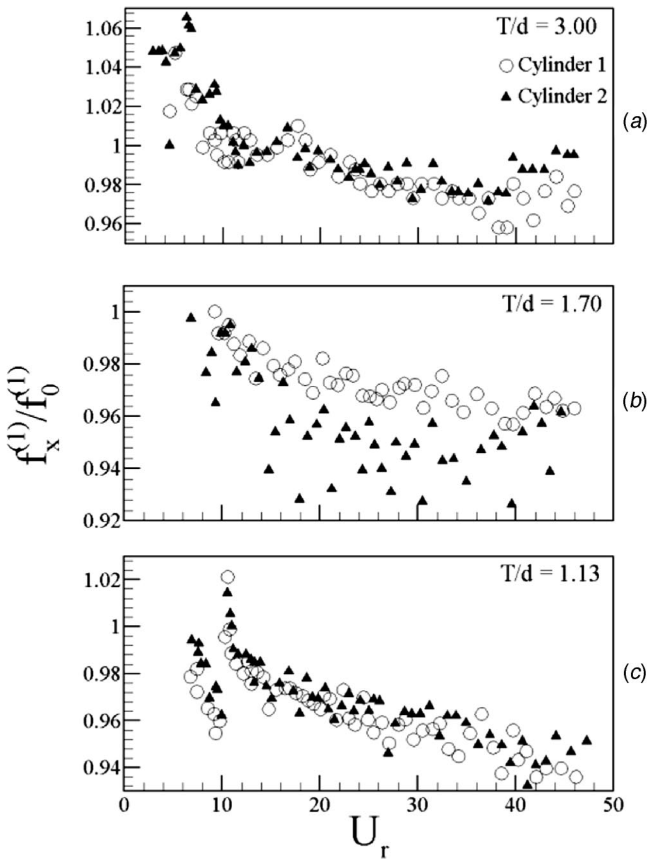

Fig. 10 Variation of the inline $f_x^{(1)}$ with T/d and U_r: ○, Cylinder 1; ▲, Cylinder 2. (*a*) $T/d=3.00$, (*b*) 1.70, (*c*) 1.13.

may also affect the system natural frequency, which has yet to be better understood. The behavior of the system natural frequency is the combined effect of varying system mass, stiffness and damping ratios with T/d. All of these factors are related to fluid dynamics, which is quite different around each cylinder for the range of $T/d=1.5\sim2.0$, [7]. For example, at $T/d=1.7$, the base pressure on one cylinder is smaller than that measured on its neighbor. The gap flow is deflected towards the cylinder with the lower base pressure, resulting in a narrow wake. Meanwhile a wide wake develops behind the neighboring cylinder. Correspondingly, the mean drags and lifts on the two cylinders also differ considerably. It is then not surprising to see an appreciable deviation in $f_y^{(1)}/f_0^{(1)}$ or $f_x^{(1)}/f_0^{(1)}$ between the two fluid-cylinder systems.

6 Conclusions

The free vibration of two side-by-side cylinders, fixed at both ends, in a cross-flow has been experimentally investigated using fiber-optic Bragg grating sensors. The investigation is largely focused on the asymmetrical flow regime, i.e., $T/d=1.7$. The following conclusions can then be drawn.

1. Resonance may occur violently at $T/d=1.13$ and 3.0 but not at $T/d=1.7$. At intermediate spacing, the gap flow between the cylinders is deflected, forming one narrow and one wide vortex street. The vortical structures are likely to be drastically weakened in strength and coherence due to interactions between the two streets such as the merging of the two cross-stream vortices in the narrow street and the gap vortex in the wide street. Consequently, resonance is suppressed. This suggests an enhanced structural stability.

2. Interrelationship between the vortical structures generated by the two cylinders is examined. At $T/d=3.0$, each cylinder is associated with one Karman vortex street. The two streets are predominantly antiphased. At $T/d=1.13$, the vortices are shed alternately from the outer side only of the two cylinders. At $T/d=1.7$, two prominent frequencies at $f^*\approx0.1$ and 0.3 are identified in the boundary layers of both cylinders as well as in the wakes. It is proposed that while the frequency at $f^*\approx0.1$ is likely due to the shear layer instability in the developing wide wake, that at $f^*\approx0.3$ may be connected to the merging of the gap vortex in the wide wake and the two cross-stream vortices in the narrow wake. Both frequencies feed back upstream and are possibly responsible for the observed instabilities in the boundary layers. This proposition predicts that the vortical structures at $f^*\approx0.3$ in the outer shear layers of the two cylinders tend to occur simultaneously and those at $f^*\approx0.1$ may be antiphased, which is consistent with the observation of $\Phi_{12}\approx0$ at $f^*\approx0.1$ and π at $f^*\approx0.3$.

3. As T/d reduces to 1.7, the fluid dynamics, such as fluid forces, base pressure and vortex formation, around one cylinder is very different from that around its neighbor. Consequently, the natural frequencies of the combined fluid-cylinder systems, associated with each individual cylinder, may exhibit appreciable differences, up to 5%.

Acknowledgments

The authors wish to acknowledge support given to them by the Central Research Grant of The Hong Kong Polytechnic University through Grant G-V529 and the Research Grants Council of the Government of the HKSAR through Grants PolyU5125/98E and PolyU5128/98E.

Appendix

Strain-Displacement Relations. The strain-displacement relationship of a beam may be written as, based on three-dimensional elastic theory, [36],

$$\varepsilon_x=\frac{\partial X}{\partial x}+\frac{1}{2}\left(\frac{\partial X}{\partial x}\right)^2+\frac{1}{2}\left(\frac{\partial Y}{\partial x}\right)^2+\frac{1}{2}\left(\frac{\partial Z}{\partial x}\right)^2+\cdots \qquad (A1)$$

where X and Y are the bending displacement in the longitudinal and lateral direction, respectively, and Z is the spanwise displacement. If the beam is an elastic circular cylinder, fixed-supported at both ends, the strain-displacement relationship is reduced to

$$\varepsilon_z=\frac{\partial Z}{\partial z}-\left(\frac{\partial Z}{\partial z}\right)^2+\frac{1}{2}\left(\frac{\partial X}{\partial z}\right)^2+\frac{1}{2}\left(\frac{\partial Y}{\partial z}\right)^2+O(Z^2), \qquad (A2)$$

[37]. In (A2), $Z=(d/2)(\partial Y/\partial z)$. Under the small deformation assumption, the strain due to the drag at the midspan of the cylinder along the stagnation line is approximately linear, [36], viz.

$$\varepsilon_X=\frac{d}{2}\left(\frac{\partial^2 X}{\partial z^2}\right)_{z=0}. \qquad (A3)$$

Similarly, the strain at $\pi/2$ away from the stagnation line due to the lift is given by

$$\varepsilon_Y=\frac{d}{2}\left(\frac{\partial^2 Y}{\partial z^2}\right)_{z=0}. \qquad (A4)$$

If the vibration of a cylinder follows one mode, for example, the first mode, the strain-displacement relationship may be described exactly by the elastic theory. However, in the present investigation, the free vibration of the elastic cylinders includes multiple modes; the first, second, and third mode are evident in Figs. 4 and 5. The displacement functions corresponding to each mode are different, [35]. Therefore, we do not expect the measured strain-displacement relationship is consistent with the elastic theory. Nevertheless, for the case of a single cylinder, Zhou et al. [11] and Jin et al. [14] found an empirical relation between Y_{rms} and $\varepsilon_{y,\mathrm{rms}}$, which was approximately linear for small dis-

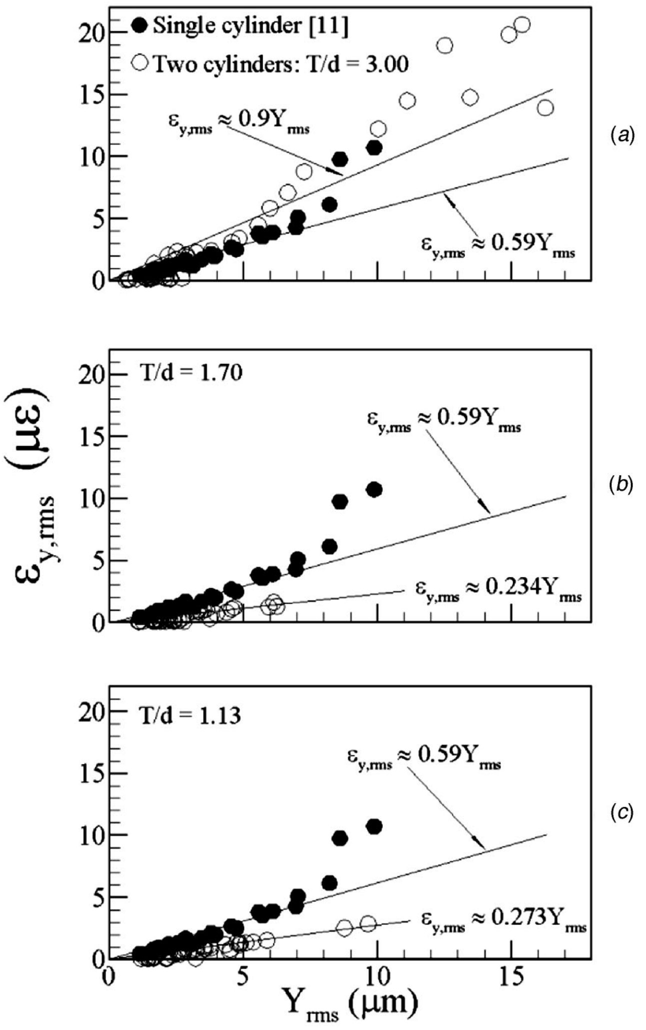

Fig. 11 Relation between Y_{rms} and $\varepsilon_{y,rms}$ of the same cylinder for different T/d ratios: ○, present data; ●, single cylinder, [11]

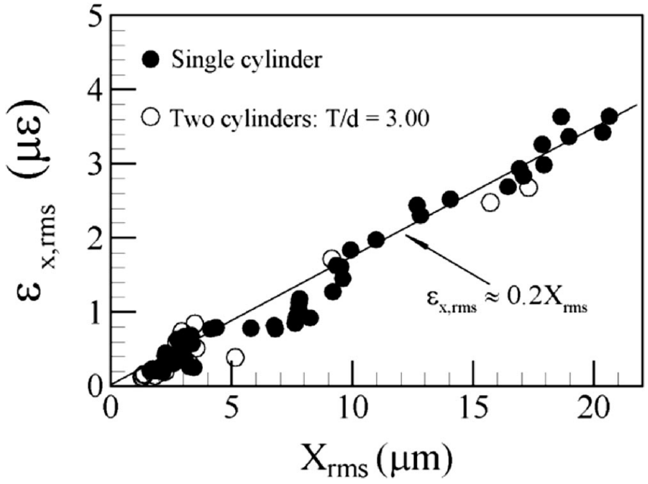

Fig. 12 Relation between $\varepsilon_{x,rms}$ and X_{rms}: ○, two cylinders at $T/d=3.00$; ●, single cylinder. Solid line indicates a best fit to the experimental data.

placement. The strain-displacement relation was presently quantified for two side-by-side cylinders. The relation could change as the interference from the neighboring cylinder intensifies.

The bending displacement Y (or X) along the y (or x) direction was measured, simultaneously with ε_y (or ε_x) using a Polytec Series 3000 Dual Laser Beam Vibrometer. The use of the laser vibrometer to measure Y has been discussed in detail, [13]. One laser beam was used to measure the displacement at the midspan of the cylinder; the other was employed to monitor the tunnel vibration at the same cross section. The differential signal from the two beams significantly reduced contamination from tunnel vibrations. The experimental uncertainty in the Y measurement was about ±7.5%. X was very difficult to measure using a laser vibrometer, as discussed in So et al. [13]. There were three reasons for this difficulty. First, the signal-to-noise ratio was relatively weak. Secondly, it was quite difficult to get an accurate measurement of X due to the small curvature of the cylinder and tunnel vibration. Thirdly, the method used to position the optical head of the laser vibrometer was not very reliable and was easily affected by tunnel wall vibration. Since then, a great part of the difficulties had been overcome and it was possible to measure X with fair accuracy. The optical head of the laser vibrometer was introduced into the tunnel at $x/d \approx 50$ downstream of the cylinder and the laser beam was directed towards the cylinder surface along the x-axis. The overall measurement uncertainty was estimated to be ±8%. This uncertainty depends on the signal-to-noise ratio, which in turn was affected by the wind speed. For example, the signal-to-noise ratio varied between 1 and 4 in the speed range 5 m/s to 15 m/s for the two side-by-side cylinders. Even though this measurement accuracy was not as good as that deduced for Y, the result could be used to establish an approximate strain-displacement relation in the x-direction.

Plots of $\varepsilon_{y,\mathrm{rms}}$ versus Y_{rms} measured from Cylinder 1 are presented in Fig. 11. The $Y_{\mathrm{rms}}-\varepsilon_{y,\mathrm{rms}}$ relation is generally linear for small Y_{rms}, consistent with the elastic theory. It is likely that the first mode vibration is dominant. But the slope changes at different T/d, which could be attributed to a different combination of vibration modes. When $U_r<20$, $Y_{\mathrm{rms}}<6\ \mu\mathrm{m}$, the relation between $\varepsilon_{y,\mathrm{rms}}$ and Y_{rms} (Figure 11(*a*)) is approximately linear for the $T/d=3.00$ case, in reasonably good agreement with that reported by Zhou et al. [11] and Jin et al. [14] for a single cylinder. The result suggests a small interference effect in this case. When $U_r>20$, $Y_{\mathrm{rms}}>6\ \mu\mathrm{m}$, $\varepsilon_{y,\mathrm{rms}}$ increases faster and the $\varepsilon_{y,\mathrm{rms}}-Y_{\mathrm{rms}}$ relation starts to deviate from linearity. This deviation is not surprising. The third-mode resonance occurs near $U_r\approx 26$ where f_s coincides with the third-mode natural frequency of the fluid-cylinder system (Fig. 2). At a higher mode of vibration, Y experiences a faster spanwise variation for given amplitude. Consequently, the strain, a second derivative of Y with respect to the spanwise variation, will increase faster than the displacement. As T/d decreases, ε_y reduces for the same Y, thus the ε_y-Y relation varying. This may be attributed to a different mixture of vibration modes when interference between the cylinders intensifies.

The measurements of ε_x and X were conducted for a single cylinder. The variations of $\varepsilon_{x,\mathrm{rms}}$ with X_{rms} are shown in Fig. 12. Again, the relation between $\varepsilon_{x,\mathrm{rms}}$ and X_{rms} is linear and can be approximated by $\varepsilon_{x,\mathrm{rms}}=0.2X_{\mathrm{rms}}$. Since the displacement in the drag direction is much smaller than that in the lift direction, the linear relation between $\varepsilon_{x,\mathrm{rms}}$ and X_{rms} is expected to extend beyond that ($U_r\approx 26$) in the lift direction. These results, together with those given by Zhou et al. [11] for the lift direction, show that the trend of the dynamic response of the cylinder along the drag and lift direction is quite similar for the range of U_r investigated. There is one difference between the results for the drag and lift direction though. While the ε_y-Y relation is only linear for $Y_{\mathrm{rms}}<8$, the ε_x-X relation remains linear for the range of X_{rms} tested, which is greater than 20. The reason could be attributed to the much smaller fluctuating drag compared to the lift. As a result, the strain ε_x and the vibration amplitude X are much smaller and non-linear effects have not yet been established.

The measurement of X using the laser vibrometer proved to be difficult for the two-cylinder case, especially at high freestream velocities. Therefore, only a few data points at these velocities were obtained. Nevertheless, the limited data indicates an approximately linear $\varepsilon_{x,\mathrm{rms}} - X_{\mathrm{rms}}$ relation (Fig. 12) at $T/d = 3.00$, in good agreement with the single cylinder case. For $T/d < 3.00$, the drag direction vibration was weak, therefore, the signal-to-noise ratio was poor and the measurements were not successful.

Nomenclature

A = cross-section area of a cylinder (m^2)
d = diameter of circular cylinder (mm)
E = Young's modulus of the cylinders (N/m^2)
$E_\alpha(f)$ = spectrum of fluctuation α (α represents either ε_x, ε_y or u), normalized so that $\int_0^\infty E_\alpha(f)\,df = 1$
f = frequency in spectrum analysis (Hz)
f_s = vortex shedding frequency of a stationary cylinder (Hz)
f_{SL} = frequency of the shear layer instability (Hz)
$f_0^{(n)}$ = nth mode structural natural frequency (Hz), $n = 1,2,3,\ldots$
$f_x^{(n)}$, $f_y^{(n)}$ = nth mode inline and cross-flow natural frequencies, respectively, of the fluid-cylinder system (Hz), $n = 1,2,3,\ldots$
I = area moment of inertia (m^4)
L = spanwise length of the test cylinder (mm)
m = cylinder mass per unit length $= \rho_s A$
M = sum of added mass and the cylinder unit length mass
M^* = mass ratio $= M/\rho d^2$
Re = Reynolds number $\equiv U_\infty d/\nu$
St = Strouhal number $= f_s d/U_\infty$
T = Center-to-center cylinder spacing (mm)
u = streamwise fluctuation velocity (m/sec)
U_∞ = freestream velocity (m/sec)
U_r = reduced velocity $\equiv U_\infty / f_0^{(1)} d$
x,y = coordinates in streamwise and lateral directions, respectively
X,Y = displacements of the cylinder in the x and y directions, respectively, measured at midspan of the cylinder (μm)
X_{rms}, Y_{rms} = root mean square values of X and Y, respectively (μm)

Greek Symbols

ρ = fluid density
ρ_s = structural density
ε_x, ε_y = dynamic strains due to drag and lift, respectively, measured by fiber-optic Bragg grating (FBG) sensors ($\mu\varepsilon$)
$\varepsilon_{x,\mathrm{rms}}$, $\varepsilon_{y,\mathrm{rms}}$ = root mean square values of ε_x and ε_y, respectively ($\mu\varepsilon$)
ν = fluid kinematic viscosity
Φ_{12} = spectral phase shift between the ε_y signals obtained from the two cylinders
$\zeta_0^{(1)}$ = first-mode structural damping ratio

Superscript

$*$ = dimensionless parameter normalized by d and U_∞ unless otherwise stated

Subscript

1, 2 = represent the cylinder number

References

[1] Blevins, R. D., 1994, *Flow-Induced Vibration*, Krieger Publishing Company, Malabar, Florida, p. 313.
[2] Ziada, S., and Staubli, T., eds., 2000, *Flow-Induced Vibration*, A. A. Balkema, Rotterdam, Netherlands.
[3] Chen, S. S., 1987, *Flow-Induced Vibration of Circular Cylindrical Structures*, Hemisphere Publishing Corporation, Washington, DC, pp. 52–55; 457–461.
[4] Landweber, L., 1942, ''Flow About a Pair of Adjacent, Parallel Cylinders Normal to a Stream,'' D. W. Taylor Model Basin, Department of the Navy, Report 485, Washington, DC.
[5] Williamson, C. H. K., 1985, ''Evolution of a Single Wake Behind a Pair of Bluff Bodies,'' J. Fluid Mech., **159**, pp. 1–18.
[6] Ishigai, S., Nishikawa, E., Nishmura, K., and Cho, K., 1972, ''Experimental Study on Structure of Gas Flow in Tube Banks With Tube Axes Normal to Flow—Part 1: Karman Vortex Flow Around Two Tubes at Various Spacings,'' Bull. JSME, **15**, pp. 949–956.
[7] Bearman, P. W., and Wadcock, A. J., 1973, ''The Interference Between a Pair of Circular Cylinders Normal to a Stream,'' J. Fluid Mech., **61**, pp. 499–511.
[8] Kim, H. J., and Durbin, P. A., 1988, ''Investigation of the Flow Between a Pair of Circular Cylinders in the Flopping Regime,'' J. Fluid Mech., **196**, pp. 431–448.
[9] Sumner, D., Wong, S. S. T., Price, S. J., and Paidoussis, M. P., 1999, ''Fluid Behavior of Side-by-Side Circular Cylinders in Steady Cross-Flow,'' J. Fluids Struct., **13**, pp. 309–338.
[10] Mahir, N., and Rockwell, D., 1996, ''Vortex Formation From a Forced System of Two Cylinders, Part 2: Side-by-Side Arrangement,'' J. Fluids Struct., **10**, pp. 491–500.
[11] Zhou, Y., So, R. M. C., Jin, W., Xu, H. G., and Chan, P. K. C., 1999, ''Dynamic Strain Measurements of a Circular Cylinder in a Cross Flow Using a Fibre Bragg Grating Sensor,'' Exp. Fluids, **27**, pp. 359–367.
[12] Zhou, Y., Wang, Z. J., So, R. M. C., Xu, S. J., and Jin, W., 2001, ''Free Vibrations of Two Side-by-Side Cylinders in a Cross Flow,'' J. Fluid Mech., **443**, pp. 197–229.
[13] So, R. M. C., Zhou, Y., and Liu, M. H., 2000, ''Free Vibrations of an Elastic Cylinder in a Cross Flow and Their Effects on the Near Wake,'' Exp. Fluids, **29**, pp. 130–144.
[14] Jin, W., Zhou, Y., Chan, P. K. C., and Xu, H. G., 2000, ''An Optical Fibre Bragg Grating Sensor for Flow-Induced Structural Vibration Measurement,'' Sens. Actuators, **79**, pp. 36–45.
[15] Williamson, C. H. K., 1996, ''Vortex Dynamics in the Cylinder Wake,'' Annu. Rev. Fluid Mech., **28**, p. 477.
[16] Prasad, A., and Williamson, C. H. K., 1997, ''Three-Dimensional Effects in Turbulent Bluff-Body Wakes,'' J. Fluid Mech., **343**, pp. 235–265.
[17] Zdravkovich, M. M., 1985, ''Flow-Induced Oscillations of Two Interfering Circular Cylinders,'' J. Sound Vib., **101**, pp. 511–521.
[18] Dwyer, H. A., and Mccroskey, W. J., 1973, ''Oscillating Flow Over a Cylinder at Large Reynolds Number,'' J. Fluid Mech., **61**(4), pp. 753–767.
[19] King, R., 1977, ''A Review of Vortex Shedding Research and Its Application,'' Ocean Eng., **4**, pp. 141–171.
[20] Higuchi, H., Kim, H. J., and Farell, C., 1989, ''On Flow Separation and Reattachment Around a Circular Cylinder at Critical Reynolds Numbers,'' J. Fluid Mech., **200**, pp. 149–171.
[21] Zhou, Y., and Antonia, R. A., 1994, ''Effect of Initial Conditions on Structures in a Turbulent Near-Wake,'' AIAA J., **32**, pp. 1207–1213.
[22] Zhang, H. J., and Zhou, Y., 2001, ''Effect of Unequal Cylinder Spacing on Vortex Streets Behind Three Side-by-Side Cylinders,'' Phys. Fluids, **13**, pp. 3675–3686.
[23] Zhou, Y., and Antonia, R. A., 1995, ''Memory Effects in Turbulent Plane Wakes,'' Exp. Fluids, **19**, pp. 112–120.
[24] Roshko, A., 1954, ''On the Drag and Shedding Frequency of Bluff Cylinders,'' Nat. Adv. Comm. Aero., Wash., Tech. Note 3169.
[25] Prasad, A., and Williamson, C. H. K., 1997, ''The Instability of the Shear Layer Separating From a Bluff Body,'' J. Fluid Mech., **333**, pp. 375–402.
[26] Norberg, C., 1987, ''Effect of Reynolds Number and a Low-Intensity Freestream Turbulence on the Flow Around a Circular Cylinder,'' Dept. Applied Thermodynamics and Fluid Mechanics, Chalmers University of Technology, Publ. 87/2.
[27] Bloor, M. S., 1964, ''The Transition to Turbulence in the Wake of a Circular Cylinder,'' J. Fluid Mech., **19**, pp. 290–304.
[28] Okamoto, S., Hirose, T., and Adachi, T., 1981, ''The Effect of Sound on the Vortex-Shedding From a Circular Cylinder,'' Bull. JSME, **24**, pp. 45–53.
[29] Kourta, A., Boisson, H. C., Chassaing, P., and Ha Minh, H., 1987, ''Nonlinear Interaction and the Transition to Turbulence in the Wake of a Circular Cylinder,'' J. Fluid Mech., **181**, pp. 141–161.
[30] Wei, T., and Smith, C. R., 1986, ''Secondary Vortices in the Wake of Circular Cylinders,'' J. Fluid Mech., **169**, pp. 513–533.
[31] Maekawa, T., and Mizuno, S., 1967, ''Flow Around the Separation Point and in the Near-Wake of a Circular Cylinder,'' Phys. Fluids Suppl. S184.
[32] Rockwell, D., 1983, Invited lecture: ''Oscillations of Impinging Shear Layer,'' AIAA J., **21**, pp. 645–664.
[33] Ho, C. M., and Huerre, P., 1984, ''Perturbed Free-Shear Layers,'' Annu. Rev. Fluid Mech., **16**, pp. 365–424.
[34] Michalke, A., 1984, ''Survey on Jet Instability Theory,'' Prog. Aerosp. Sci., **21**, pp. 159–199.
[35] Weaver, W., Timoshenko, S. P., and Young, D. H., 1989, *Vibration Problems in Engineering*, 5th Ed., John Wiley and Sons, New York, pp. 54–55, 366, 416–466.
[36] Donnell, L. H., 1976, *Beams, Plates, and Shells*, McGraw-Hill, New York, pp. 84–85.
[37] Nayfeh, A. H., and Mook, D. T., 1995, *Nonlinear Oscillations*, John Wiley and Sons, New York, pp. 96–97.

Measurements Within Vortex Cores in a Turbulent Jet

Amit Agrawal
e-mail: agrawaa@me.udel.edu

Ajay K. Prasad
e-mail: prasad@me.udel.edu

Department of Mechanical Engineering,
University of Delaware,
Newark, DE 19716

High-pass filtering of instantaneous two-dimensional PIV data is employed to educe vortices occurring in the axial plane of a self-similar turbulent axisymmetric jet. An automated method is used to identify the vortices and to measure circulation, tangential velocity, vorticity, and centrifugal force within their cores (defined here as the region within the largest closed streamline). Results include radial variation of these quantities within vortex cores, and the energy of vortices. We find that the vorticity is maximum at the vortex center and decreases monotonically with the radial coordinate. Results indicate that the center of a larger vortex spins faster than a smaller vortex (in an ensemble averaged sense); however, the trend reverses to give the expected result at the core edge. Vorticity results for different vortex radii collapse upon normalization. The average energy of vortices is seen to increase as the square of the vortex radius. In addition, three possible regimes of vortex number versus vortex size are suggested by our data.
[DOI: 10.1115/1.1568357]

Introduction

Turbulent flows are characterized by vortices ranging in size from the integral length scale down to the Kolmogorov scale. The two ends of the range of vortex scales are associated with different properties. For example, large-scale vortices account for most of the turbulent energy, while the small scales carry almost the entire vorticity. Even for a given vortex size, the range of their associated properties is expected to be large. These notions have proved extremely useful in understanding the nature of turbulence. In this paper, we provide direct measurement of vortex properties to substantiate these ideas.

To date, researchers have found it rather difficult to educe instantaneous structures from turbulence data. By their very nature, pointwise techniques lack spatial resolution which is imperative for visualizing and measuring the properties of these structures; at best, pointwise techniques must rely on conditional averaging to expose only the dominant structures. Consequently, experimental data about properties of vortical structures in different flow fields is rather scarce, and especially the nature of the vortex core is virtually unexplored.

PIV can provide velocity information with substantially greater spatial resolution. Further, high-pass filtering can be employed to educe vortical structures from instantaneous two-dimensional PIV frames (Adrian et al. [1], and Agrawal and Prasad [2]). Agrawal and Prasad [2] applied high-pass filtering to PIV data of a turbulent jet, and presented statistical distributions of vortex radius, circulation, vorticity, and energy as a function of Reynolds number and radial position. In [3], we applied low-pass filtering to examine the various organizational modes of large vortices in a turbulent jet. In this paper, we use the same high-pass filtering technique to focus on the detailed properties *within* vortex cores.

Three types of vortex cores are commonly described in the literature—potential, Rankine and Lamb. A potential vortex possesses a $1/r$ tangential velocity (v_θ) distribution within its core; however, due to a singularity at the origin, it clearly cannot exist in nature. The singularity is removed in a Rankine vortex which has a core with a solid-body like rotation (constant angular velocity), while the flow outside the core is irrotational. Therefore, $v_\theta \sim r$ inside the core, and $v_\theta \sim 1/r$ beyond it (Fig. 1, adapted from Kundu [4]). It should be noted that for a real vortex, the presence of viscosity will smooth out the abrupt change in slope of v_θ at the core edge. For Lamb vortices vorticity within the core decays exponentially with the radial coordinate. Both Rankine and Lamb vortices are expected to better resemble a real vortex. However, Rankine vortices are somewhat easier to model, and so we will compare and contrast our results with them wherever appropriate.

Some theoretical studies of viscous vortex cores have been conducted in the past. For example, Mayer and Powell [5] derived the distribution of angular, axial, and radial velocities for a viscous core starting from the Navier-Stokes equations. They assumed the flow quantities to be self-similar within the core, and that the

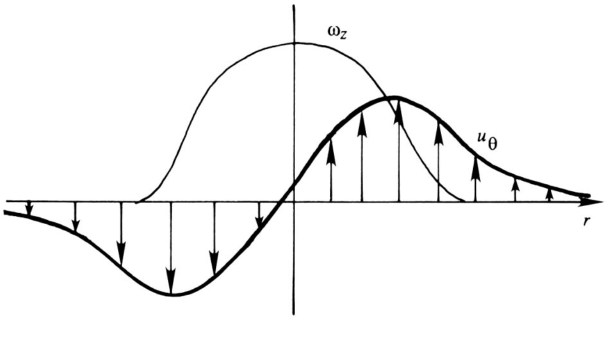

(*a*) Real vortex

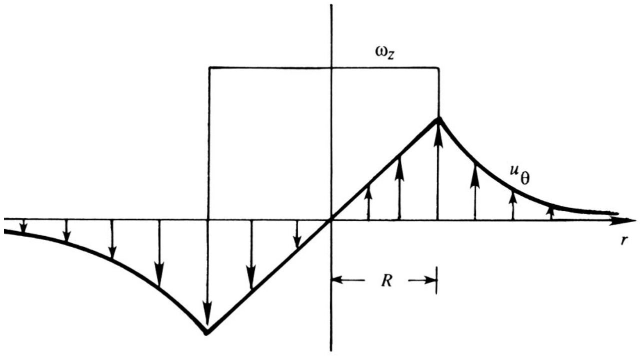

(*b*) Rankine vortex

Fig. 1 Velocity and vorticity distributions in (*a*) a real and (*b*) a Rankine vortex (adapted from Kundu [4])

Contributed by the Fluids Engineering Division for publication in the JOURNAL OF FLUIDS ENGINEERING. Manuscript received by the Fluids Engineering Division March 13, 2002; revised manuscript received September 15, 2002. Associate Editor: M. Plesniak.

carrier fluid had a simple algebraic velocity distribution. From their angular velocity result they report a solid-body rotation near the vortex axis, and an inviscid solution outside the core. On the experimental side, measurements have been made for a tip vortex of an airfoil, and vortex rings. For example, Desabrais and Johari [6] used an ultrasound method to measure the circulation of a tip vortex, and found that the circulation is maximized when the entire vortex core is enclosed within the measurement path. Maxworthy [7] obtained LDA measurements inside the cores of laminar and turbulent vortex rings and found that the change from a constant ω to radially varying ω is much sharper for turbulent vortex rings.

The situation for Mayer and Powell [5], Desabrais and Johari [6], and Maxworthy [7] is simpler because a single vortex was treated in isolation. Additionally, these studies considered a carrier fluid that was laminar. Our situation is more complicated in that our goal is to examine a large population of vortex cores occurring naturally in turbulent flows. These myriad of vortices interact amongst themselves and affect their neighbors, warranting measurements for a general class of turbulent flows. The present work is intended to address these needs. Specifically, we report results for the radial variation of circulation, tangential velocity, and vorticity within the core of vortices present in the axial plane of a self-similar turbulent axisymmetric jet. We also present results for centrifugal force and energy associated with vortices of different sizes.

Experimental Setup and Eduction Technique

PIV measurements were conducted in a 1.2-m-tall glass tank with a 0.5-m-square cross section, which houses a nozzle at the bottom (orifice diameter, $d=2$ mm). Twin Nd-YAG pulsed lasers (350 mJ/pulse at 532 nm) provided illumination for PIV with a pulse separation of 12 ms. 8-μm hollow spherical glass particles were used as tracers for PIV with water as the working fluid. Recording was done using a Kodak 1.0 ES camera with a 1026 $\times 1000$ pixels array. The view frame at $110 \leqslant z/d \leqslant 175$ was centered on the jet axis, with the edges of the frame extending to $\pm 1.5b$ (b is defined as the radial location at which the mean streamwise velocity reduces to e^{-1} of the mean centerline velocity). Measurements were conducted for jet Reynolds number, Re (based on d and the exit velocity) of 3000. See Agrawal and Prasad [2] for additional details.

The definition of Robinson et al. [8]—"A vortex exists when instantaneous streamlines mapped on to a plane normal to the core exhibit a roughly circular or spiral pattern, when viewed in a reference frame moving with the center of the vortex core," is used here for the definition of a vortex. Vortices were educed using the high-pass filtering technique (Adrian et al. [1], and Agrawal and Prasad [2]) in which the instantaneous field is first smoothed using a Gaussian kernel. Next, the resulting low-pass field (with the higher frequencies suppressed) is subtracted from the original velocity field, exposing the vortices which represent the high-frequency content in the velocity signal. The standard deviation of the Gaussian kernel was three grid units, and the filter was truncated at five grid units. These parameters were chosen carefully to expose all vortices. An illustration of the high-pass filtering operation on a small subset of the total PIV frame is provided in Fig. 2. It was verified that all the vortices in the high-pass field could also be identified by an alternate technique, viz. Galilean transformation, [1–3].

An automated method was employed to identify the vortices. A vortex center was located if the high-pass filtered velocity vectors displayed a monotonic variation in angular orientation from 0 to 2π while moving in a closed path around it. A point was accepted as a vortex center, r_0, if seven out of eight neighboring points satisfied the above criterion. The outermost radial position enclosed by a closed streamline determined the radius of the vortex, R. It should be noted that we are using the concept of "closed streamline" to mean that in the instantaneous, two-dimensional PIV vector field, the integration of the velocity data will produce streamlines which are closed around the vortex center. In reality, because our flow field is turbulent (three-dimensional, dissipative, and unsteady (albeit stationary)) the streamlines that we identify for our eduction process need not coincide with the actual streamlines in the flow. Our usage of the term merely provides a simple way to identify a vortex center, and to measure the size of the vortex. An example of a high-pass filtered field with the identified vortices can be found in [2].

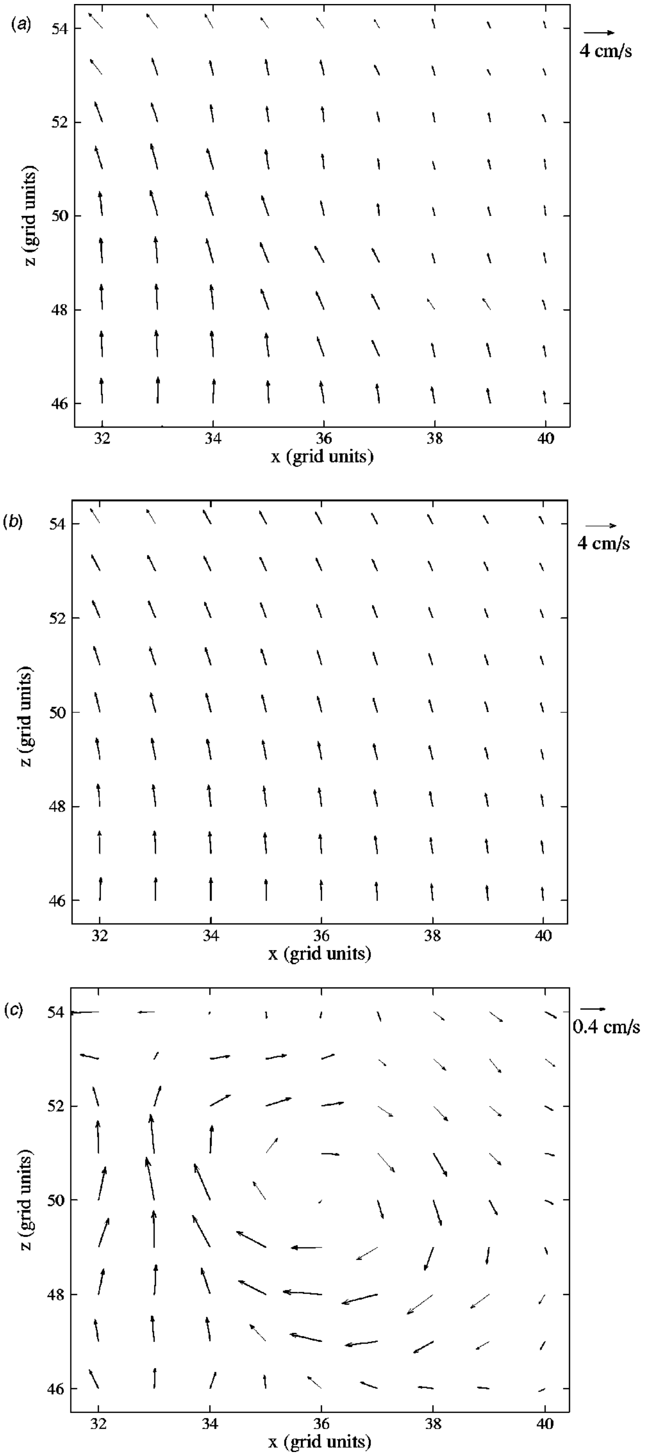

Fig. 2 (*a*) Instantaneous, (*b*) low-pass filtered, and (*c*) high-pass filtered vector fields (1 grid unit=2 mm)

Agrawal and Prasad [2] employed an automated procedure with the above criteria to identify vortices with radii equal to *integer* grid units. This procedure has been extended here to also identify vortices with non-integer radii and obtain improved resolution. The modified algorithm is thus able to resolve two new radii at $\sqrt{5}$ and $\sqrt{8}$ grid units between vortices of radii 2 and 3 grid units, and so on. Thus, we can now distinguish vortices of sizes 1, $\sqrt{2}$, 2, $\sqrt{5}$, $\sqrt{8}$, 3, $\sqrt{10}$, $\sqrt{13}$, and 4 grid units (note, each number is the square root of the sum of the squares of two integers), increasing the resolution from four to nine levels. The increased resolution provides sufficient datapoints to probe the vortex core with confidence. It was verified that the results from the current enhanced eduction program match that of [2], validating the robustness of the new method.

Vortex radius (R), rotational sense, and circulation (Γ) were measured directly here whereas tangential velocity (v_θ), vorticity (ω), centrifugal force (F_c), and energy (E) were derived. Circulation is calculated by integrating along a circular path centered at r_0:

$$\Gamma = \oint \mathbf{u}' \cdot d\mathbf{s},$$

where, $\mathbf{u}'$ denotes the high-pass filtered velocity field. The derived quantities are expressed as follows:

$$v_\theta(r) = \text{tangential velocity at } r = \frac{\Gamma(r)}{\pi r},$$

$$\omega(r) = \text{vorticity at } r = \frac{\Gamma(r)}{\pi r^2},$$

$$F_c(r) = \text{centrifugal force at } r = r\omega^2(r) = \frac{\Gamma^2(r)}{\pi^2 r^3},$$

where r is the distance from the vortex center, r_0. The energy of the vortex was obtained as

$$E = c_1 \Gamma^2(R),$$

where c_1 is a constant. (We set $c_1 = 1$ for the energy plots presented herein.)

Experimental Uncertainty. The rms value of any vortex property (such as circulation, tangential velocity, or vorticity) can be determined directly from the large population of vortices that we have educed for each value of R. As evident in Table 1, we have a sizable population of vortices from which we can draw reliable statistical results. We will focus on Γ in this section, because tangential velocity and vorticity are derived directly from Γ, therefore the relative uncertainty in their mean values would be the same as that of $\overline{\Gamma}$. Table 2 lists the normalized value of rms of circulation, $\sigma_\Gamma/\overline{\Gamma}$ for each value of R ranging from one to four grid units. Two sets of rms values are listed in Table 2, one corresponding to the center of the vortex (actually $r = 1$) and the other corresponding to its edge ($r = R$). These rms values include the true variability in Γ, [2], as well as the errors accruing from the measurement process.

Table 1 Sample size for different vortex radii (based on a total of 10140 vortices from 222 PIV frames). (1 grid unit=2 mm.)

R (Grid Units)	Sample Size
1	3813
$\sqrt{2}$	2182
2	1253
$\sqrt{5}$	1204
$\sqrt{8}$	848
3	222
$\sqrt{10}$	58
$\sqrt{13}$	75
4	49

Table 2 Normalized rms, and the fractional uncertainty in the mean value of Γ for vortices of all R at the vortex center and vortex edge. Note that the uncertainties in v_θ and ω are identical to Γ as these quantities are derived from Γ. (1 grid unit =2 mm.)

R (Grid Units)	At $r=1$		At $r=R$	
	$\sigma_\Gamma/\overline{\Gamma}$	$\Delta\overline{\Gamma}/\overline{\Gamma}$ (%)	$\sigma_\Gamma/\overline{\Gamma}$	$\Delta\overline{\Gamma}/\overline{\Gamma}$ (%)
1	0.60	1.9	0.60	1.9
$\sqrt{2}$	0.56	2.3	0.54	2.3
2	0.57	3.2	0.55	3.1
$\sqrt{5}$	0.48	2.7	0.42	2.4
$\sqrt{8}$	0.47	3.2	0.41	2.8
3	0.44	5.8	0.42	5.5
$\sqrt{10}$	0.39	10	0.33	8.5
$\sqrt{13}$	0.47	10.6	0.49	11.1
4	0.45	12.6	0.44	12.3

The rms values listed in Table 2 are sufficient to place uncertainty bounds (using the standard expression for 20 to 1 odds) on the mean quantities listed subsequently in this paper, such as $\overline{\Gamma}$, $\overline{v_\theta}$, $\overline{\omega}$. We will provide these results towards the end of this section. However, we will first show that the errors that arise from the measurement process amount to only a small fraction of the true variability in circulation.

The definition of Γ indicates that errors in measuring velocity and r will contribute to the error in Γ. For PIV measurements, the error associated with the measured velocity is determined primarily by the error in locating the correlation peak to subpixel accuracy. Our estimated value is about 1/10th of a pixel, which is a more or less standard value quoted by most PIV practitioners (Prasad [9]). The characteristic velocity scale in our flow (centerline velocity) corresponds to a displacement of about six pixels; consequently, the relative error in the characteristic velocity measurement is about 1.5%. In the current paper, we are interested in the high-pass filtered field which is obtained by subtracting the local mean velocity from the instantaneous velocity field. As seen by comparing Fig. 2(a) with Fig. 2(c), the characteristic velocity of the high-pass filtered field decreases by about one order of magnitude, therefore the *relative* error of the high-pass filtered field is amplified to about 15%.

The measurement of r is affected by the fact that the vortex center may not lie exactly on a grid point. In addition, not all closed streamlines are perfectly circular or even perfectly closed due to the nature of our eduction process and the criteria employed therein. Further, due to the discretizing nature of the eduction process, the true vortex radius may be slightly smaller or larger than the measured value. These effects can produce an additional random error in the value of Γ. It is not apparent that one can accurately quantify these errors without extensive modeling and simulations. However, we have roughly estimated that these sources will contribute an error of about 15% to 20%. Adding to this the uncertainty in velocity measurements, we obtain a cumulative (in a root-sum-square sense) measurement error in Γ of about 25%.

The rms values ($\sigma_\Gamma/\overline{\Gamma}$) listed in Table 2 can approach 40% to 60%. It is therefore apparent that the measurement error contributes only a small fraction to the total rms (note that the rms values must be combined in a root-sum-square sense). In fact, it is easily shown that the rms due to measurement error is only about 15% of the total rms. Most of the rms is therefore contributed by the genuine variability in Γ for a given R.

Finally, the uncertainty in the *average* value of Γ can be estimated using the standard expression (for 20 to 1 odds):

$$\Delta\overline{\Gamma} = \frac{1.96\sigma_\Gamma}{\sqrt{N}}$$

where N is the number of contributing vortices in the given ensemble. For example, from Table 1 $\sqrt{N}\approx 62$ for $R=1$ and 7 for $R=4$. Therefore, $\Delta\overline{\Gamma}/\overline{\Gamma}\approx 2\%$ for $R=1$ and 13% for $R=4$. $\Delta\overline{\Gamma}/\overline{\Gamma}$ values for vortices of all R are listed in Table 2 (at the center and at the edge).

Results and Discussion

Results presented in this paper pertain to a jet Reynolds number of 3000, with the view frame located between $110\leqslant z/d\leqslant 175$. Each PIV frame contains 60×60 vectors on a square grid (grid spacing = 2 mm). Therefore the radius of the smallest resolved vortex is 2 mm, and the range of spatial scales that can be resolved here is about 30. The corresponding Kolmogorov length scale is approximately 0.2 mm, therefore the data is not fully resolved at the small scales. As noted in [2], the unresolved vortices will, however, not affect the results presented herein.

Results in this paper are based on a total of 10,140 vortices, corresponding to 222 PIV frames (average of about 46 vortices per frame). These vortices correspond to the self-similar regime of jets. Due to the turbulent nature of the flow, the distribution of vortices over space and time is somewhat random, implying that a different number of vortices will be captured in each frame. Figure 3 depicts the variations in the number of vortices in successive PIV frames. No noticeable trend is apparent, which confirms that the flow conditions are stationary.

A breakdown of the number total of vortices of different radii is shown in Table 1. The number of vortices present in the flow decreases monotonically with increasing R. Nevertheless, even for the largest vortices, the sample size is large enough to compute useful statistics. Figure 4 suggests that the number of vortices drops drastically beyond a certain size; therefore, two distinct curves are needed to fit the data. The expressions for the two curves are indicated in Fig. 4. Figure 4 helps to infer the presence of yet another regime for vortices smaller than 1 grid unit. Although these vortices are too small to be resolved from our current dataset, it should be obvious that the curve that fits vortices of size 1 to 2.8 grid units cannot be sustained indefinitely owing to a singularity as $R\rightarrow 0.5$. Eventually, viscosity will begin to dominate as the Kolmogorov scale is approached and a different curve fit will apply there. More detailed measurements at the smallest scales are required to confirm this extrapolation.

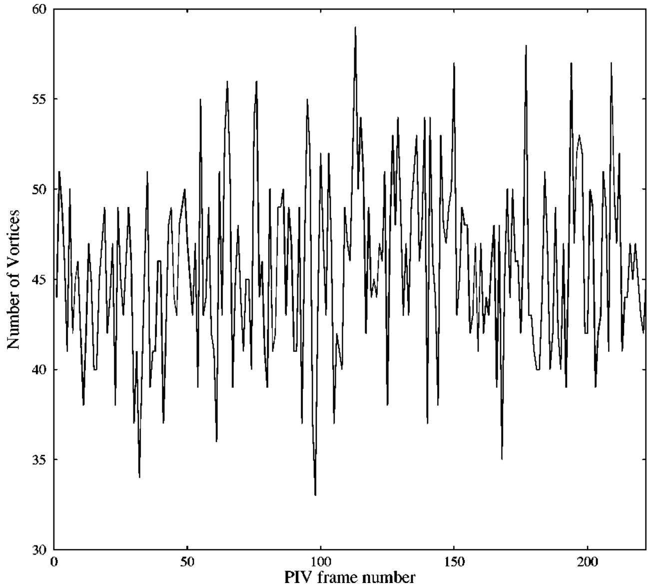

Fig. 3 Variation in the number of vortices in successive PIV frames for a typical run

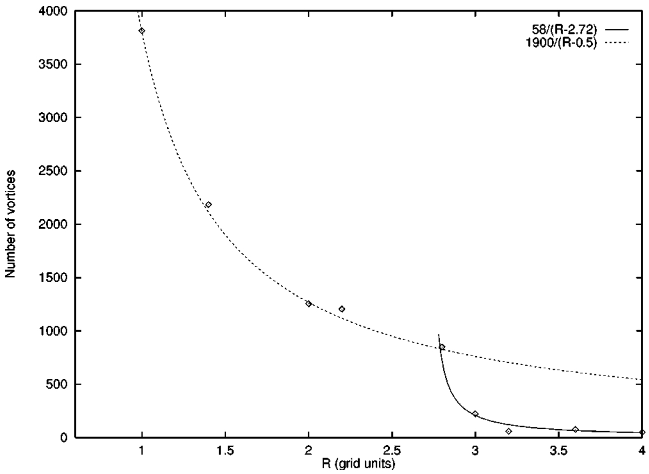

Fig. 4 Curve fits to number of vortices of different sizes (1 grid unit=2 mm)

Vorticity obtained by differentiating the instantaneous velocity map is qualitatively similar to that obtained by differentiating the high-pass filtered field (Figs. 5(*a*) and 5(*b*), respectively) indicating that the high-pass filtered field accurately represents the instantaneous vorticity field. The quantitative difference between Figs. 5(*a*) and 5(*b*) is because Fig. 5(*a*) represents the *total* vorticity, whereas Fig. 5(*b*) represents only the high-pass filtered vorticity. While Fig. 5 validates our education technique, the use of high-pass filtering in the first place warrants justification. The reason for employing the filtering technique is that our vortex identification and measurement scheme described above specifically looks for closed streamlines which are only seen in the high-pass filtered field.

Does the Largest Closed Streamline Represent the Core Size? As mentioned above, we denote the radius of the largest closed streamline as the vortex radius, making it important to understand the relation between them. A single vortex in a quiescent environment will present closed streamlines for all r. However, in a turbulent field, the presence of additional vortices with random circulations in the neighborhood will disturb the closed streamline pattern around any vortex. It can be expected that a given vortex will feel the presence of its neighbors more strongly beyond its edge corresponding to regions of small ω, whereas regions of high ω corresponding to the vortex core are less likely to be affected. Based on this qualitative argument, it is plausible that the region of high-vorticity concentration bounded by the largest closed streamline $(r<R)$ would correspond to the vortex core.

The above conjecture was tested with a simulation using Rankine vortices. 44 Rankine vortices were placed on a 60×60 grid such that their number, center locations, rotational sense, and circulations corresponded to the vortices in a real (randomly chosen) PIV frame. Each Rankine vortex core size was assigned as R, the radius of the largest corresponding closed streamline. Therefore, $v_\theta\sim r$ for $r\leqslant R$, and as $1/r$ for $r>R$. While streamlines for an individual Rankine vortex are closed for all r, this is no longer true after superposing the velocity fields from all 44 vortices. This superposed velocity field was high-pass filtered and input into our vortex education program. It was found that for 50% of the resulting vortices, the vortex core size corresponded *exactly* to R. For the remaining vortices the largest closed streamline was *larger* than their prescribed cores (more so for isolated vortices compared to vortices occurring in close proximity). In no case did we find streamlines closing inside the prescribed core. This simulation supports our belief that the largest closed streamline encompasses the vortex core in its entirety.

The criterion of using the largest closed streamline to determine the vortex core size is also consistent from the point of view of

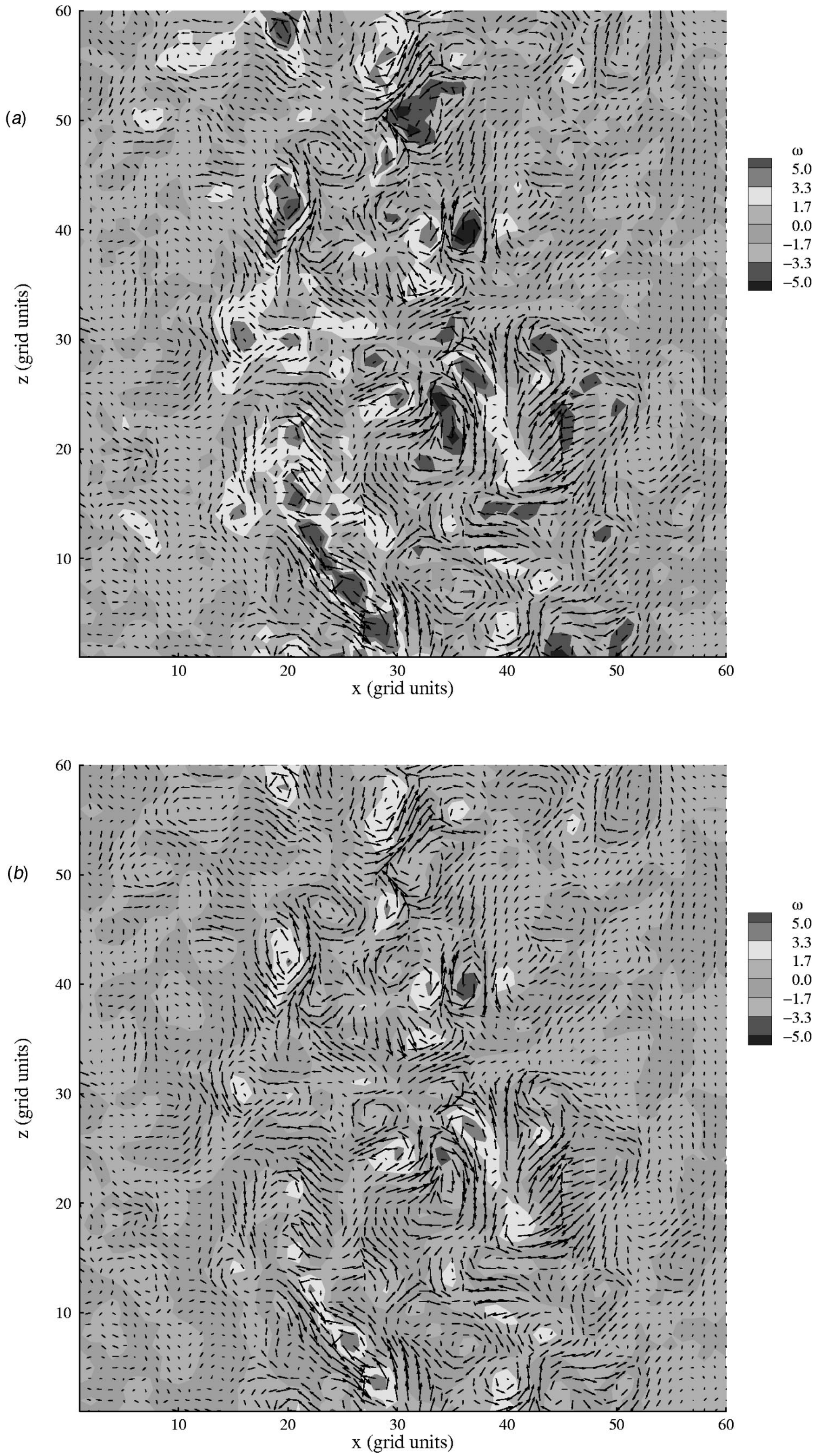

Fig. 5 Vorticity obtained by differentiating (*a*) instantaneous and (*b*) high-pass filtered field with overlaid high-pass field vectors

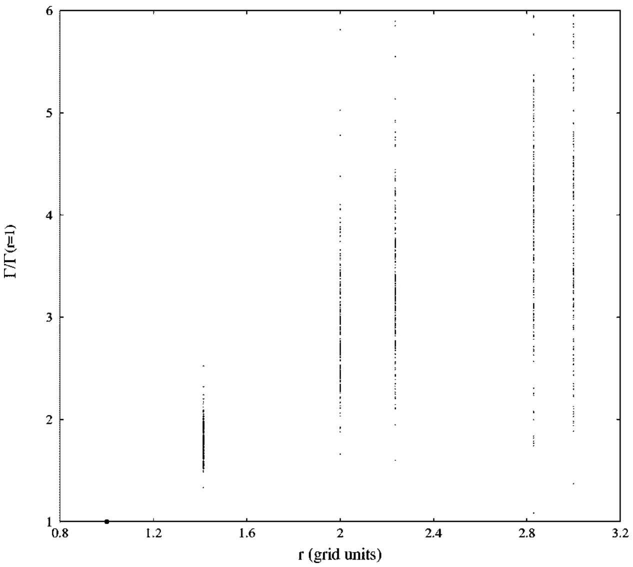

Fig. 6 Normalized circulation within vortices of radii $R=3$ grid units (total 222 vortices)

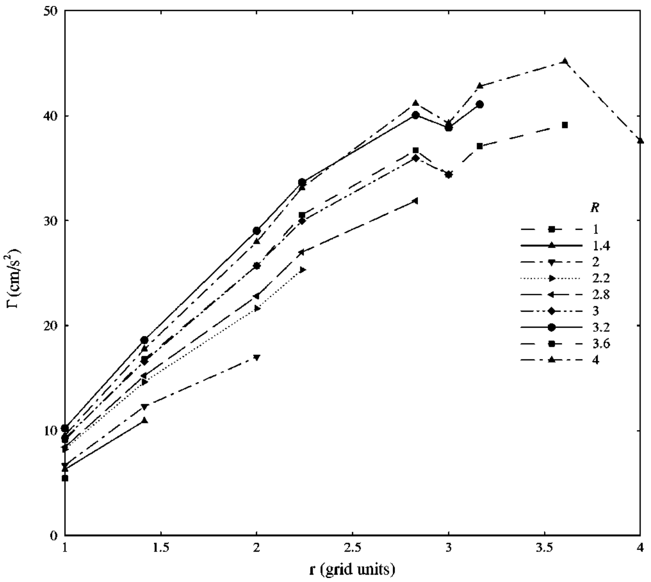

Fig. 7 Variation of average circulation within vortex cores for vortices of varying radii (1 grid unit=2 mm). See Table 2 for the values of the relative uncertainty in Γ.

circulation. For a Rankine vortex, Γ increases as r^2 within the core, and reaches a constant path-independent value once the entire core is encompassed within the path. Agrawal and Prasad [2] have demonstrated that for vortices in a turbulent jet flow, circulation does increase with r within the region of closed streamlines, and may increase or decrease beyond it depending for example on the presence and circulation of vortices in the neighborhood. This again indicates that the entire region where vorticity is present (the vortex core) is encompassed by the largest closed streamline, while no useful information about circulation or other properties can be extracted outside it.

Variation Within Vortex Cores

Circulation and Tangential Velocity. The radial variation of circulation within vortex cores is plotted in Fig. 6. For illustration purposes we chose circulation and $R=3$ grid units; however similar observations can be made for other properties and within vortex cores of other radii. For an easier comparison between vortices of different circulations, the results are normalized by the circulation at $r=1$. The scatter in the figure must be viewed in light of the fact that Fig. 6 includes data from 222 vortices (see Table 1), i.e., 222 data points exist for each r. The scatter in the circulation data is consistent with our expectation (see the earlier section on experimental uncertainty) that even vortices of a given size can exhibit a wide range in properties. The scatter increases monotonically with r, for example, the normalized rms is 0.19 and 0.39, respectively for $r=2$ and 3. However, the increase is scatter with r is simply an artifact of the normalization with respect to $\Gamma(r=1)$. As listed in Table 2, the value of $\sigma_\Gamma/\overline{\Gamma}$ is about 0.4 for all $r\leqslant 3$.

Figure 7 reveals that the ensemble averaged circulation increases with r inside the core, and tends to plateau near the core edge. As noted earlier, circulation is expected to display such a behavior within vortex cores. Moreover, for a given r, larger vortices have larger Γ associated with them.

Figure 8 shows polynomial fits to the ensemble averaged data for circulation for vortices of $R=3$ grid units. Figure 8 reveals that for real vortices, $\Gamma\sim r^2$ is valid only for a very small subregion inside the vortex core ($r<1.4$). $\Gamma\sim r$ for $1.4\leqslant r\leqslant 2.4$. Finally for $r>2.4$, Γ is seen to vary as $r^{0.8}$. The different polynomial fits to the data reveal that a real $R=3$ vortex is similar to a Rankine vortex only for $r<1.4$, and differs substantially from it beyond $r=1.4$. In fact, the latter fits help to identify possible alternate regimes (for example, constant v_θ region, see below), and to characterize the deviation of a real vortex from a Rankine vortex.

Figure 9 shows that the radial variation of ensemble averaged v_θ is nonmonotonic in nature. For most R it is seen to increase and then decrease, with maximum v_θ lying within the vortex core. Based on the fit in Fig. 8, it can be concluded that on an average v_θ varies almost linearly deep inside the core, remains constant for a large part, and then decreases as $r^{-0.2}$ towards the edge. The somewhat linear increase in v_θ indicates that the flow very close to the vortex center undergoes a solid-body-like rotation. It should be noted that while this subregion of solid-body-like rotation is a small part of the entire vortex core, it assures that the dissipation remains bounded.

Vorticity. Figure 10 shows the ensemble averaged vorticity for various vortex sizes. Describing ω as a constant within the vortex core is clearly not apt, indicating that the approximation to a

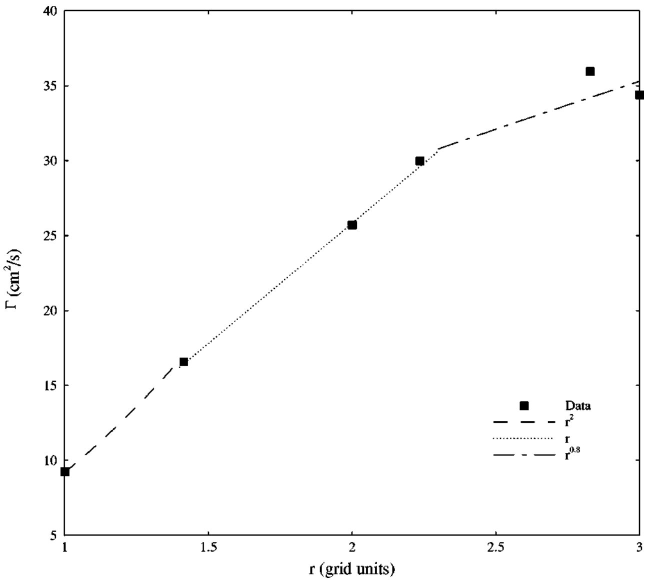

Fig. 8 Polynomial fits to average circulation for vortex radius =three grid units

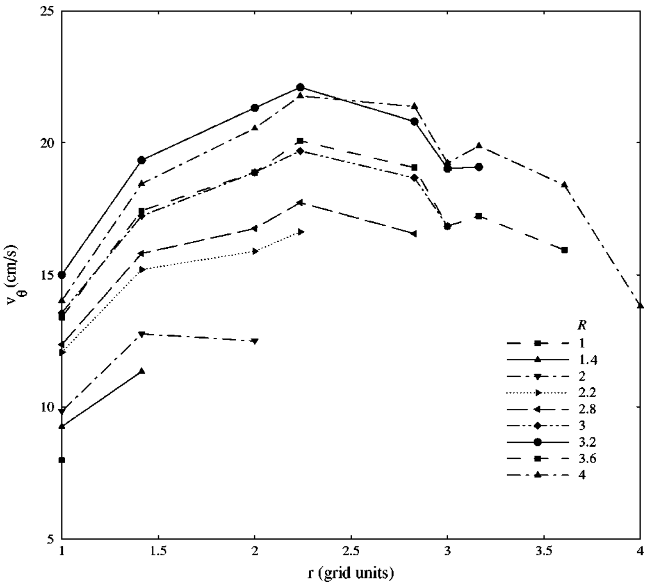

Fig. 9 Variation of average tangential velocity within vortex cores for vortices of varying radii. See Table 2 for the values of the relative uncertainty in v_θ.

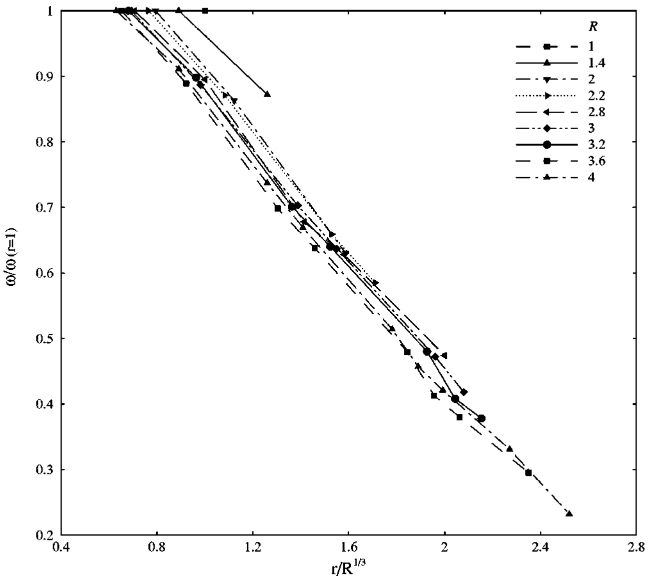

Fig. 11 Normalized vorticity within vortices of different radii

Rankine vortex is not perfect. The maximum value of ω occurs at $r=1$, and decreases monotonically with r. The plot (Fig. 10) looks qualitatively similar to Fig. 1. Thus we have verified experimentally the trend depicted in Kundu's [4] schematic drawing (Fig. 1).

Another interesting observation can be gleaned from the plot by carefully following the vorticity values from different vortex radii. It is commonly assumed that most of the vorticity in turbulent flow is associated with small scales which is consistent with the belief that on average a large vortex will overturn slower compared to a small vortex. However, Fig. 10 reveals that at least for the range of vortices investigated herein this is *not* necessarily true. Compared to their smaller counterparts large vortices exhibit a larger ω at the center. The list of vortices with highest to lowest vorticity at the core reads as $R=3.2$, 4, 3, 3.6, 2.8, 2.2, 2, 1.4, 1. Although two (out of a total of nine) vortices occur out of sequence, the general trend is from the largest to the smallest R, and the outliers may be attributed to experimental jitter resulting from a combination of measurement error and the true variability in ω. As stated in the earlier section on experimental uncertainty, the uncertainty in mean vorticity can approach about 13% in the worst case. This uncertainty could account for the nonmonotonic behavior of the list.

As one progresses towards the edges of these larger vortices, ω drops to a value smaller than the corresponding value at the core-edge of smaller vortices, i.e., the terminal value of ω decreases as R increases. This is highlighted in Fig. 10 by the use of a special symbol (heavy circles). The list of vortices with highest to lowest vorticity at the edge reads as $R=1.4$, 1, 2.2, 2, 3.2, 2.8, 3, 3.6, 4. Although the variation is not perfectly monotonic (three outliers out of a total of nine) a downward trend in ω with increasing R is quite apparent. Figure 10 supports the contention that the classical picture only applies at the core edge, and *not* throughout the core of the vortex. Again, experimental uncertainty could account for the outliers in the list.

Additional insights about vortices can be obtained if a suitable scaling is available by which data can be collapsed. This motivated us to find appropriate ways to normalize the results. Dimensionally homogeneous relationships were sought initially, but these did not lead to a successful collapse of the data. Instead, it was found that a dimensionally inhomogeneous expression of the form

$$\frac{\omega}{\omega_c}=f\left(\frac{Br}{R^n}\right),$$

showed promise. Here ω_c denotes the value of vorticity at the vortex center; however, because of our inability to measure it we used $\omega(r=1)$, and B denotes a constant. $n=1/3$ gave the most satisfactory collapse of the vorticity values from different vortex-radii (see Fig. 11). While the lack of dimensional homogeneity is somewhat unsatisfactory, it should be noted that the collapse is not dependent on the units that are used for the length scales as the differences can be absorbed in the constant B. Results are particularly good for $R\geqslant 2$. Vortices with $R\leqslant\sqrt{2}$ lying above the normalized curve are explained as follows.

$\omega(r=1)$ underestimates the vorticity at the center, with the difference between ω_c and $\omega(r=1)$ increasing with decreasing R. The difference becomes substantial for small vortices ($R\leqslant\sqrt{2}$). Therefore, the vorticity value does not fall on the normalized curve, rather it falls above it. A direct advantage of normalization is that the correct value of ω_c can be estimated from the normal-

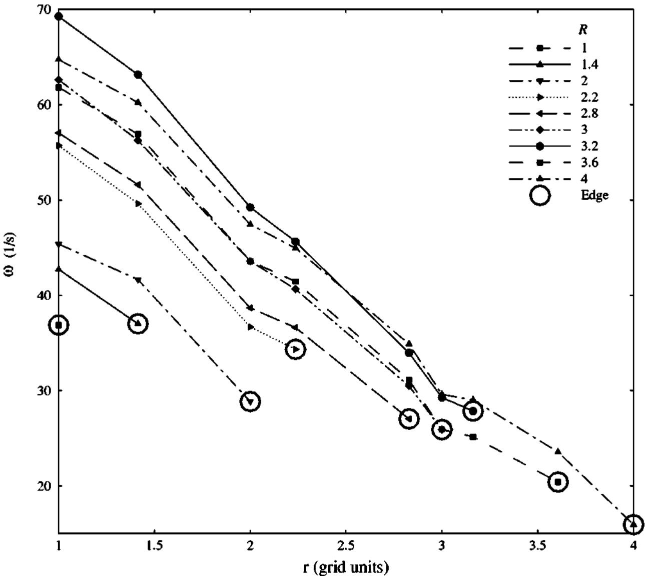

Fig. 10 Variation of average vorticity within vortex cores for vortices of varying radii. See Table 2 for the values of the relative uncertainty in ω.

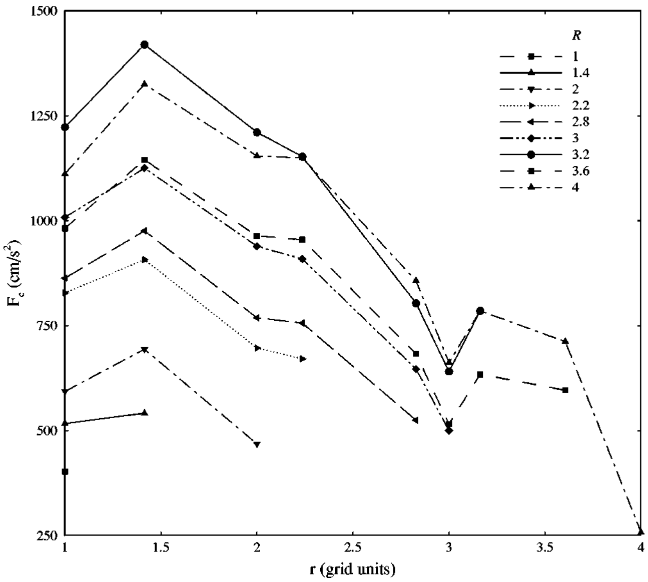

Fig. 12 Variation of average centrifugal force within vortex cores for vortices of varying radii

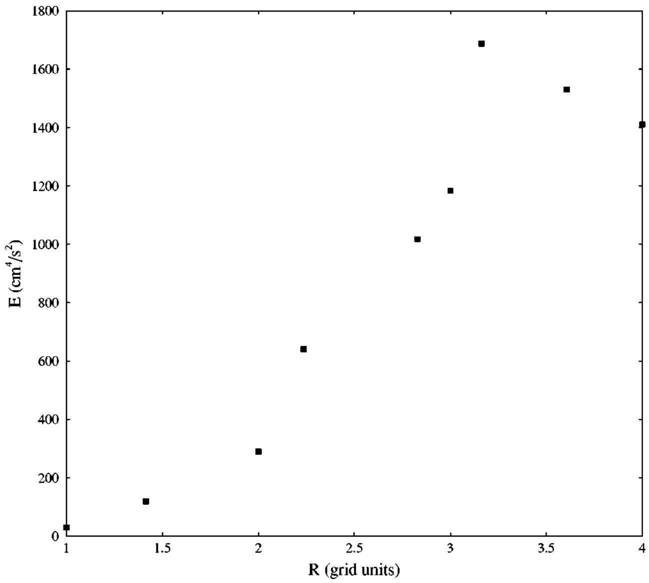

Fig. 13 Average energy associated with different vortex radii

ized curve. This is all the more useful for vortices of smaller radii. For example ω_c for $R=1$ is estimated as $53s^{-1}$ corresponding to a difference of about 30% from $\omega(r=1)$.

Centrifugal Force and Energy. Knowledge of the centrifugal force, F_c within vortex cores is important because like other body forces it can induce relaminarization. From a purely practical viewpoint, radial variation of F_c is relevant in planning PIV measurements. If the density of the fluid and seeding particles are mismatched, particles may not track the flow well. Regions of large vorticity are particularly susceptible to errors. It is expected that particles (with density greater than the fluid) will be centrifuged out of the vortex core, resulting in a poor particle concentration near the vortex center and an increased concentration near the core edge (our measurements are not affected by this because the density of particles was matched to that of the carrier fluid). This makes it important to know the radial variation of F_c within the vortex core.

For a Rankine vortex, F_c increases linearly in the core, and decreases as $1/r^3$ beyond it. Therefore, F_c can be expected to be a maximum at the core edge. The plot for a real vortex core is, however, nonmonotonic (Fig. 12), increasing slightly followed by a monotonic decrease. The increase corresponds to the solid-body-like rotation subregion (constant ω but increasing r). The subsequent decrease is consistent with the fact that ω decays faster than $r^{-1/2}$. Interestingly, the plot reveals that the maximum centrifugal force occurs between the vortex center and the edge (and not at the core edge).

Energy of the vortices for different radii is depicted in Fig. 13. It can be seen that the average energy associated with a given vortex radius increases as R^2 for the range of vortex sizes investigated. Therefore, the qualitative nature of the curve for energy versus vortex radius is in accordance with the classical theory of turbulence, i.e., average energy of vortices should increase with their size.

Conclusions

Measurements inside vortex cores have provided new insights into the nature of vortices in a turbulent field. The criterion of closed streamlines was used to identify vortices in a turbulent jet, and methods were developed to measure the properties within the vortex core. It is argued here that for turbulent flows with a myriad of underlying vortices, the largest closed streamline bounds the vortex core. Three possible regimes of vortex number versus vortex size are suggested by our data. The vortex-core has a small solid-body rotation like subregion (constant vorticity). However for a large part of the vortex core, the tangential velocity remains a constant. Subsequently near the core edge the tangential velocity decreases as $r^{-0.2}$.

There is substantial evidence to support that the centers of smaller vortices rotate slower than those of large vortices (although the variation is not perfect due to experimental uncertainty); however, the trend reverses near the core edge. Therefore, it can be concluded that the classical picture is only applicable for the core edge, and *not* throughout the core of the vortex and that the general understanding of turbulence implicitly refers to the vorticity at the core edge. An expression to normalize the vorticity from different vortex radii can be utilized to estimate the correct value of vorticity at the vortex-center for smaller vortices. In accordance with the turbulence theory, the average energy of the vortices is seen to increase with the vortex radius. In fact, the average energy appears to increase as the square of the vortex radius for the range of vortex sizes investigated here.

Acknowledgments

This work was supported by National Science Foundation, under grant NSF-ATM-9714810.

References

[1] Adrian, R. J., Christensen, K. T., and Liu, Z.-C., 2000, "Analysis and Interpretation of Instantaneous Turbulent Velocity Fields," Exp. Fluids, **29**, pp. 275–290.

[2] Agrawal, A., and Prasad, A. K., 2002, "Properties of Vortices in the Self-Similar Turbulent Jet," Exp. Fluids, **33**, pp. 565–577.

[3] Agrawal, A., and Prasad, A. K., 2003, "Organizational Modes of Large-Scale Vortices in an Axisymmetric Turbulent Jet," Flow, Turbul. Combust., **68**, pp. 359–377.

[4] Kundu, P., 1990, *Fluid Mechanics*, Academic Press, San Diego, CA.

[5] Mayer, E. W., and Powell, K. G., 1992, "Similarity Solutions of Viscous Vortex Cores," J. Fluid Mech., **238**, pp. 487–507.

[6] Desabrais, K. J., and Johari, H., 2000, "Direct Circulation Measurement of a Tip Vortex," AIAA J., **38**, pp. 2189–2191.

[7] Maxworthy, T., 1977, "Some Experimental Studies of Vortex Rings," J. Fluid Mech., **81**, pp. 465–495.

[8] Robinson, S. K., Kline, S. J., and Spalart, P. R., 1989, "Quasi-Coherent Structures in the Turbulent Boundary Layer. Part II: Verification and New Information From a Numerically Simulated Flat-Plate Boundary Layer," *Near Wall Turbulence. Proceedings of Zaric Memorial Conference*, edited by S. J. Kline and N. H. Afgan, eds., Hemisphere, New York, pp. 218–247.

[9] Prasad, A. K., 2000, "Particle Image Velocimetry," Curr. Sci., **79**, pp. 101–110.

Momentum Thickness Measurements for Thick Axisymmetric Turbulent Boundary Layers

Kimberly M. Cipolla
Mechanical Engineer

William L. Keith
Mechanical Engineer

Naval Undersea Warfare Center,
Code 2141, 1176 Howell Street,
Newport, RI 02841-1708

Experimental measurements of the mean wall shear stress and boundary layer momentum thickness on long, thin cylindrical bodies are presented. To date, the spatial growth of the boundary layer and the related boundary layer parameters have not been measured for cases where δ/a *(a=cylinder radius) is much greater than one. Moderate Reynolds numbers* ($10^4<Re_\theta<10^5$) *encountered in hydrodynamic applications are considered. Tow tests of cylinders with diameters of 0.61, 0.89, and 2.5 mm and lengths ranging from approximately 30 meters to 150 meters were performed. The total drag (axial force) was measured at tow speeds up to 17.4 m/sec. These data were used to determine the tangential drag coefficients on each test specimen, which were found to be two to three times greater than the values for the corresponding hypothetical flat-plate cases. Using the drag measurements, the turbulent boundary layer momentum thickness at the downstream end of the cylindrical bodies is determined, using a control volume analysis. The results show that for the smallest diameter cylinders, there is no indication of relaminarization, and a fully developed turbulent boundary layer exists. A scaling law for the momentum thickness versus length Reynolds number is determined from the data. The results indicate that the spatial growth of the boundary layers over the entire length is less than for a comparable flat-plate case.* [DOI: 10.1115/1.1568359]

Introduction

The case of a large aspect ratio cylinder in axial flow is encountered in many engineering applications, such as towed array sonar systems, towed antennas, and the fishing and seismic industries. Of particular interest here is the case for which the cylinder is constant density and neutrally buoyant, such that it tows in a horizontal plane without sagging or drooping. At high Reynolds numbers, this configuration will result in the formation of an axisymmetric turbulent boundary layer, free from the effects of crossflow.

A review of axisymmetric turbulent boundary layers is given by Lueptow [1]. Although the range of experimental data is limited, the results indicate that axisymmetric turbulent boundary layers have a fuller mean velocity profile and higher wall shear stress than their flat-plate counterparts. This is true even for cases of mild curvature ($\delta/a\approx1$). Furthermore, the lack of data over a systematically varied range of parameters has made it difficult to identify the appropriate scaling laws. To date, there have been no measurements of the spatial growth of axisymmetric turbulent boundary layers. This is largely due to laboratory constraints, and the difficulty of making measurements of this type during sea trials. Here, we are interested in cases where $\delta(x)/a$ is much greater than one. The details of the turbulent boundary layer when δ/r approaches 100 remains to be investigated. While there have been a few experimental studies of the axisymmetric boundary layer on cylinders, they have been limited to cases for which $\delta/r<40$ and the Reynolds number $\mathrm{Re}_\theta\approx10^3$. In general, these measurements, [2,3], were performed in a wind tunnel at streamwise locations $x/r<10^3$. In addition, a number of theoretical studies, including [4,5], have assumed a similarity with flat-plate boundary layers and simply incorporated transverse curvature terms into the equations. The resulting expressions for the velocity profile have not been fully validated. However, comparison with the limited experimental results indicate that the effects of transverse curvature have not been characterized sufficiently.

Some investigators, [6,7], have hypothesized that for a fixed freestream velocity, as the radius a decreases, the surface area becomes too small to support a turbulent boundary layer. The similarity of the full velocity profile on the cylinder to that of a flat plate in a favorable pressure gradient leads to the conclusion that their behavior with respect to relaminarization will be similar. However, the fullness of the velocity profiles are due to different physical effects, and there is no freestream acceleration in the case of the cylindrical boundary layer. Nonetheless, if relaminarization were possible, one would expect a marked reduction in the wall shear. In contrast, the data presented here for diameters as small as 0.61 mm and aspect ratios up to 3.5×10^5 show an increase in the mean wall shear stress when compared to a flat plate. This result agrees with the findings of Willmarth et al. [2], in which there was no evidence of relaminarization for cylinders as small as 0.5 mm in diameter.

Neves et al. [8] investigated axisymmetric cylindrical boundary layers with mild curvature ($\delta/a=5$ and 11) using DNS simulations. However, the calculations were performed for very low Reynolds number flow between concentric cylinders. The results, therefore, do not accurately represent the outer region of the boundary layer. In the near wall region, they found the slope of the mean velocity profile decreased and the skin friction coefficient increased with increasing curvature.

The approach here encompasses data analysis of full-scale experiments conducted at the National Aeronautics and Space Administration (NASA) Langley Research Center in Hampton, VA, using the high-speed seawater tow tank (HSSTT). These experiments demonstrated the viability of making integrated mean wall shear stress measurements with ±0.1-lb accuracy at tow speeds of 2.0 to 17.0 m/s, typical of actual applications. The total axial force was measured with an in-line load cell mounted at the tow point for cylinders of 0.89 mm and 2.5 mm in diameter. Sample lengths

---

Contributed by the Fluids Engineering Division for publication in the JOURNAL OF FLUIDS ENGINEERING. Manuscript received by the Fluids Engineering Division Apr. 18, 2002, revised manuscript received Dec. 3, 2002. Associate Editor: T. Gatski.

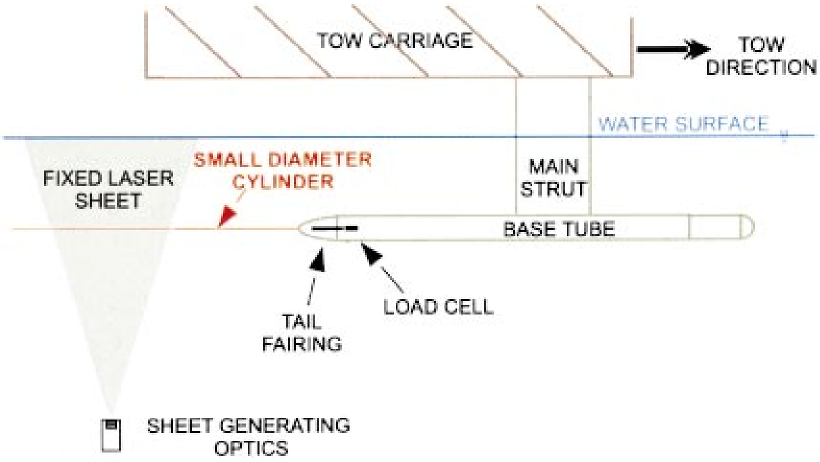

Fig. 1 Schematic of experimental setup using the high-speed seawater tow tank (HSSTT)

were 30.5, 91, and 152 meters when not under load. At least three runs were made for each configuration and speed to reduce uncertainty. Results for the 0.61-mm-diameter case, which provide supplemental data at low tow speeds, are also presented in this report. In addition, laser measurements showed no large-scale transverse motions (snaking) existed during the tows, and the tow angle was less than 1° for all cases, confirming that the cylinders were approximately neutrally buoyant.

Experimental Facility and Test Setup

Tow tests were performed using the HSSTT, a concrete tank that is 878 m long, 3.66 m deep, and 7.32 m wide, with a total volume of approximately 20,000 m^3, [9]. The HSSTT was located at NASA's Langley Research Center in Hampton, VA. The unique aspects of this hydrodynamic test facility include its high-speed carriage and the ability to vary the salinity of the ambient water, leading to variable density. Specifically, the carriage can be operated from 1.0 to 18.0 m/s with a maximum acceleration of 1.1 m/s^2 and a maximum deceleration of 2.0 m/s^2. An automatic controller maintains the carriage speed to within ± 0.01 m/s. No measurable change in the water density and salinity was measured throughout the depth and length of the tank over the course of these experiments. Values of 20°C and 18 parts per thousand salinity were recorded, with kinematic viscosity $1.03\times10^{-6}\ m^2/s$ and density 1013 kg/m^3.

The tow carriage rides above the tank, and a streamlined strut pierces the water surface to hold a base tube at the centerline of the tank. The carriage is designed for easy access to the tow strut, and includes a climate-controlled laboratory space for operation of electronics and other equipment. The facility includes a drydock, a 24-m-long section located at the downstream end of the tow tank, which enables rapid installation and reconfiguration of test models. Also, the tow tank contains wave suppressors mounted on the side walls at the air-water interface that dampen out standing surface waves generated by the strut.

In this set of experiments, nylon cylinders with diameters of 0.61, 0.89, and 2.5 mm and lengths ranging from 30.5 to 152 meters, were towed. The cylinders are neutrally buoyant, so that they tow in a horizontal plane. A typical record length (per run) is 1 minute of data for a tow speed of 5 m/s. Figure 1 shows a schematic of the experimental setup. Each cylinder was attached to a load cell mounted within the main towing strut/base tube of the tow carriage. The base tube is approximately at the centerline of the tow tank cross section (underwater), therefore, the cylindrical boundary layers grew spatially without obstruction from the walls or the free surface. A 50 ft leader line was used to separate the cylinder under test from any wake from the base tube. A small connector at the aft end of the leader line served as the origin of the boundary layer. For each time series of load cell data, the ensemble averaged force represents the spatial average of the mean wall shear stress over the surface of the cylinder.

A laser sheet was used to visualize the two-dimensional flow field at a fixed location approximately two-thirds down the length of the tank. For these tests, the laser sheet was located at the centerline and was aligned with the axis of the cylinder. Observations were recorded with a stationary, underwater camera. The cylinders were clearly visible as they passed through this laser sheet, enabling direct measurements of the tow angle over the entire length of the bodies. In all cases, the cylinders towed linearly, with no large or small-scale motion observed. The mean wall shear stress on the cylinders resulted in no motions due to instabilities of the cylinders under tow. At the start of each run, there were no visible standing waves on the water surface. It is therefore assumed that the level of ambient turbulence is negligible.

Analysis and Results

The measured load D is used to infer the average tangential drag coefficient C_d on each cylinder tested, where

$$C_d = \frac{D}{\frac{1}{2}\rho A_s U_o^2}.$$

Based on the uncertainties of the measured quantities, the maximum experimental uncertainty of C_d is 2%.

Figure 2 shows the total drag force D measured with the load cell, versus time, during a typical test run. The tow tank was long enough to enable the acquisition of data at two different tow speeds in a single run, as indicated in Fig. 2. The load values are seen to reach equilibrium in a very short time (5–10 seconds). The tangential drag coefficients C_d versus tow speed U_o for the 0.89-mm-diameter cylinders are shown in Fig. 3. Two different lengths of this diameter were towed, with values $L_1 = 96.93$ meters and $L_2 = 155.91$ meters ($L/a = 2.2\times10^5$ and 3.5×10^5, respectively). Elongation of the cylinders due to the applied drag load is accounted for in the calculations. As expected, the average drag coefficient decreases with increasing speed. No dependence on cylinder length is immediately apparent.

Also shown in Fig. 3 are the drag coefficients for hypothetical smooth flat plates, with lengths the same as the cylinders tested. In this approximate comparison, edge effects due to the finite flat

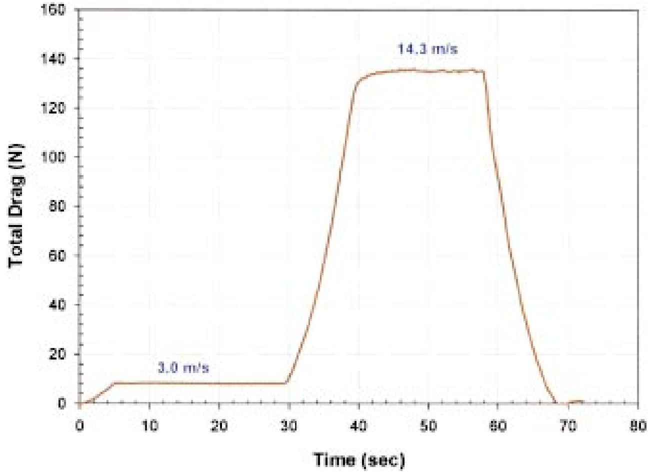

Fig. 2 Total drag versus time measured during a typical run

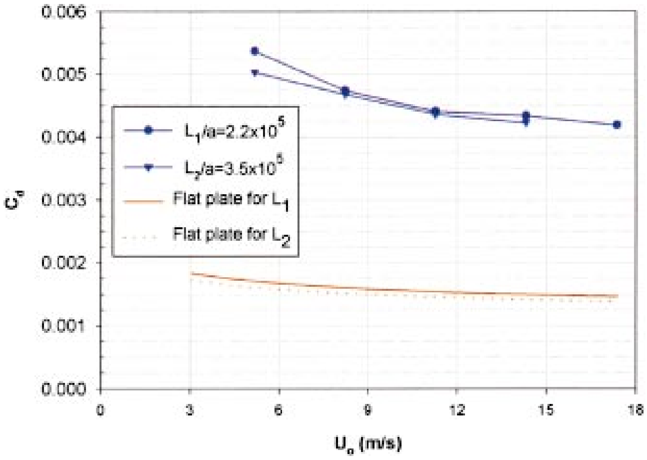

Fig. 3 Measured tangential drag coefficient versus tow speed for 0.8-mm-diameter cylinders compared to predicted flat-plate values

plate span are not taken into account. The values are calculated from the basic Prandtl-Schlichting equation for a flat plate with a turbulent boundary layer at zero pressure gradient, [10]. The predicted flat-plate values are approximately 30% of the values measured for the long cylinders. For these cases of high values of length and Reynolds number, the fully developed turbulent boundary layer dominates the measurements, with the transition zone having a negligible effect on the measurements. We therefore conclude that, on average, there is a higher wall shear stress on a small-diameter cylinder than a flat plate. The result is a higher total drag when integrated over the cylinder length.

Following Ackroyd [4], the measured data for all cylinders tested are plotted in Fig. 4. Here, $C_d(L/a)$ versus $\mathrm{Re}_a(a/L)$ is shown, where Re_a is the Reynolds number based on radius a, which was used by Ackroyd. The symbols are the measured data, with the black, blue, and green colors corresponding to the three diameters, 0.61 mm ($L/a=2\times10^5$), 0.89 mm ($L/a=2.2\times10^5$ and 3.5×10^5), and 2.5 mm ($L/a=2.8\times10^4$), respectively. The solid curves are the analytical values for different aspect ratios L/a from Ackroyd. In general, there is good agreement between the measured data and the theory for all of the cylinders tested. This agreement supports the existence of a turbulent boundary layer on the cylinders tested, since Ackroyd's analysis is developed for turbulent flow. We note that Ackroyd's theory is compared to a very limited amount of data available for aspect ratios $L/a<10^5$. While the comparison shows reasonable agreement, Ackroyd points out that the range of experimental data is too limited to fully validate his theory over the entire turbulent flow regime.

The vertical tow angle of each cylinder was determined from an underwater video camera mounted on the side of the HSSTT at the location of the laser sheet. In each case, the measured angle was less than 1 deg over the entire length. This is expected, as the cylinders are approximately neutrally buoyant. Previous results, [11], have shown that boundary layer separation and vortex shedding do not occur at angles below 5 deg. Also, no large-scale transverse motions of the cylinders were observed during the present experiments. Note that the presence of ambient turbulence or unsteady motion of the tow point, with wavelengths much greater than the boundary layer length scales, would be required to cause large-scale transverse motions of the cylinder. This test facility is designed to eliminate these sources of perturbation. Furthermore, as the aft end of the cylinders passed through the laser sheet, they did not exhibit a "whipping" or flapping motion.

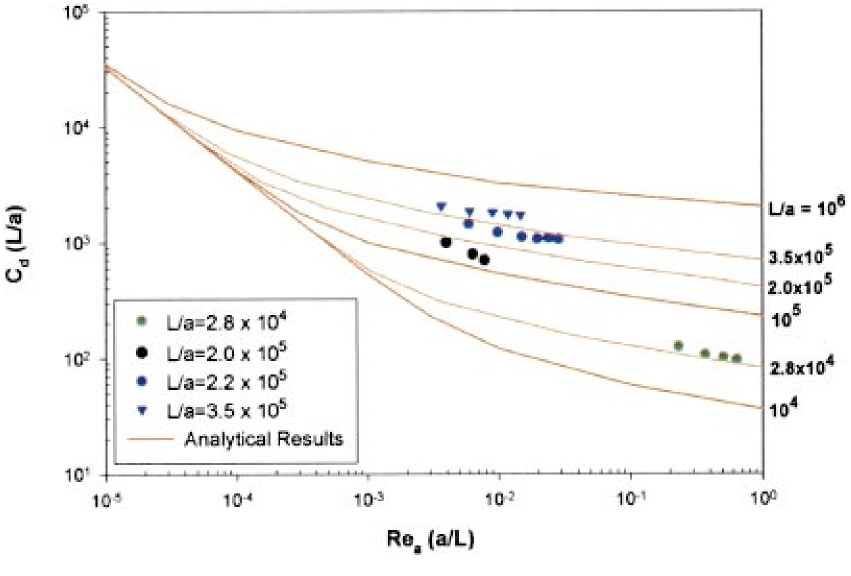

Fig. 4 $C_d(L/a)$ versus $\mathrm{Re}_a(a/L)$ analytical results from Ackroyd [4]

Displacement and Momentum Thickness

Using cylindrical coordinates, as shown in Fig. 5, expressions for the displacement thickness and the momentum thickness are derived. For convenience, the radius of the cylindrical control volume is chosen to be equal to the value of δ at the end of the cylinder, and the length is the total length of the cylinder. The origin is the centerline of the cylinder, such that the surface of the cylinder is at $r=a$. In the following analysis, all quantities represent the temporal mean values.

The displacement thickness δ^* is defined as the amount by which streamlines are displaced due to the presence of the boundary layer. The corresponding reduction in the mass flow rate can be expressed as

$$2\pi\rho U_o\int_a^{\delta+a}\left(1-\frac{u(r)}{U_o}\right)r\,dr. \tag{1}$$

Taking a ring annulus with thickness such that it produces an equivalent mass flow rate with the freestream velocity yields

$$\dot{m}=2\pi\rho\int_a^{\delta^*+a}U_o r\,dr=\pi\rho U_o(\delta^{*2}+2a\delta^*). \tag{2}$$

Equating Eqs. (1) and (2) leads to a quadratic equation for δ^* given by Eq. (3) below, which can be solved directly if the velocity distribution $u(r)$ is known.

$$\delta^{*2}+2a\delta^*=2\int_a^{\delta+a}\left(1-\frac{u(r)}{U_o}\right)r\,dr \tag{3}$$

The definition of momentum thickness θ is derived in an analogous manner. Equating the momentum flux through an annulus in the freestream, to the momentum flux defect in the boundary layer, leads to

$$\theta^2+2a\theta=2\int_a^{\delta+a}\frac{u(r)}{U_o}\left(1-\frac{u(r)}{U_o}\right)r\,dr \tag{4}$$

which again can only be evaluated for θ if $u(r)$ is known. However, the momentum thickness may also be derived using a control volume analysis. A cylindrical control volume is used, as shown in Fig. 5, and steady-state conditions are imposed. Conservation of mass for the control volume yields

$$\int_{CS}\rho\overline{V}(r,\theta,x)\cdot d\overline{A}=0 \tag{5}$$

where vector $\overline{V}$ is the temporal mean velocity at the location of the control volume surfaces. Conservation of momentum applied to the control volume can be written as

$$\int_{CS}\overline{V}\rho\overline{V}\cdot d\overline{A}=\sum\overline{F}. \tag{6}$$

Note that the only applied force $\overline{F}$ on the cylindrical control volume of fluid is the shear force at the wall of the cylinder. This force is equal to the streamwise component of the mean wall shear stress averaged over the surface area of the entire cylinder multiplied by the total surface area $A_s=2\pi aL$. Evaluating the integral at each control surface, and making use of Eq. (5), yields

$$\frac{\tau_{\text{ave}}A_s}{\rho U_o^2}=\int_{A_2}\frac{u(r)}{U_o}\left(1-\frac{u(r)}{U_o}\right)dA \tag{7}$$

where $dA=r\,dr\,d\theta$. The quantity τ_{ave}, which is inferred from the drag measurements, is related to the spatially varying wall shear stress through the relation

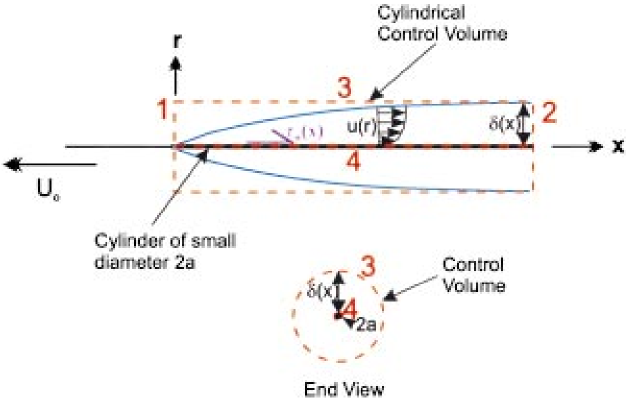

Fig. 5 Sketch of control volume for cylindrical coordinates

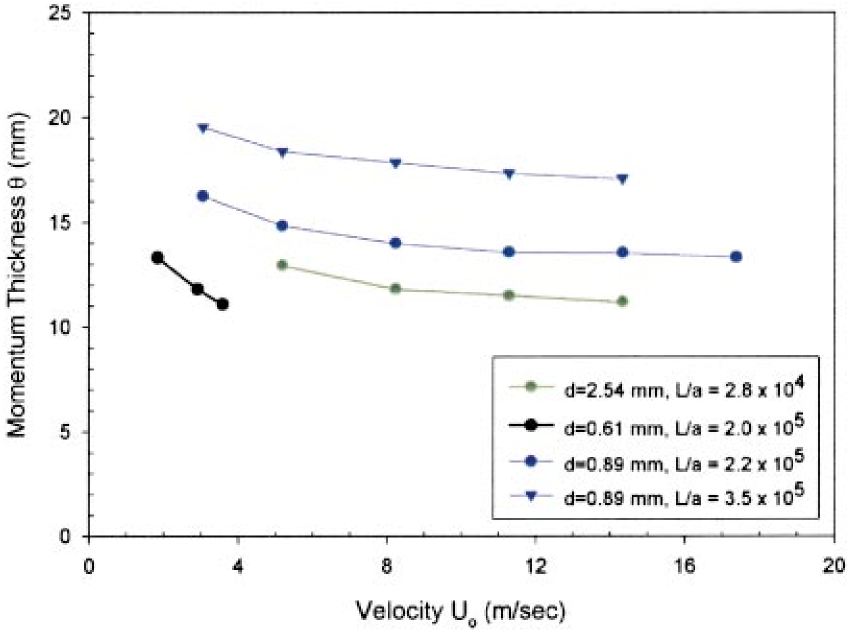

Fig. 6 Momentum thickness θ at the end of the cylinder as a function of tow speed

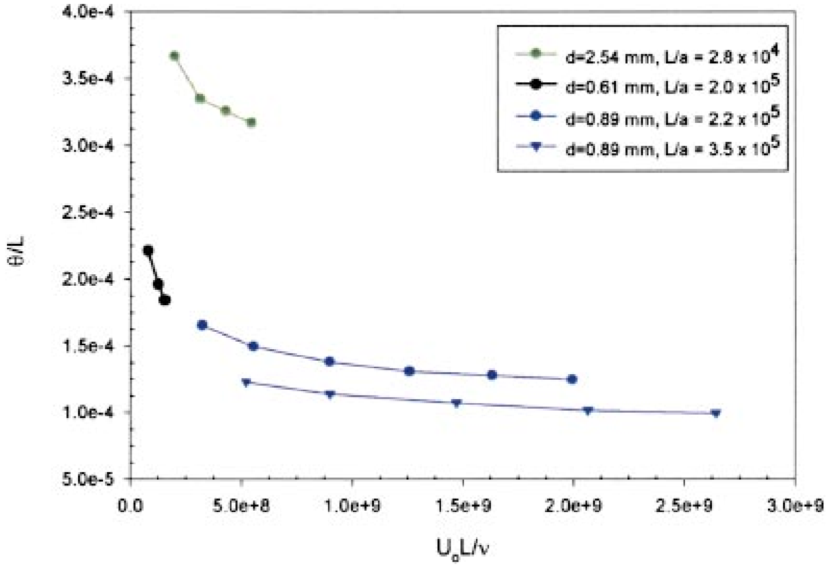

Fig. 7 Ratio of momentum thickness to length, $\theta(L)/L$ versus nondimensional velocity U_oL/ν

$$\tau_{\text{ave}}=\frac{1}{L}\int_0^L \tau_w(x)dx. \tag{8}$$

Equation (7) can be simplified to

$$\frac{\tau_{\text{ave}}}{\rho U_o^2}=\frac{1}{L}\int_a^{a+\delta}\frac{u(r)}{U_o}\left(1-\frac{u(r)}{U_o}\right)\frac{r}{a}dr=\frac{1}{2}C_d \tag{9}$$

where C_d is the total tangential drag coefficient over the cylinder length L. Using Eq. (4) for the definition of momentum thickness, the following relationship is obtained between θ evaluated at $x=L$ and C_d for the case of a cylinder in a steady, uniform flow:

$$\theta^2+2a\theta-aLC_d=0 \tag{10}$$

In summary, an expression has been derived relating the tangential drag coefficient to the momentum thickness for the case of a fully developed axisymmetric turbulent boundary on a cylinder of length L, using a cylindrical control volume. Note that for a typical laboratory experiment, a local measurement of C_d is generally difficult to obtain directly because it requires measurements of the velocity profile in the viscous sublayer. An accurate measurement of the spatially averaged C_d is also difficult because it requires the use of a calibrated drag balance. However, the momentum thickness is readily determined from measurements of the velocity profile in the log-law and outer regions. In contrast, in this set of experiments very accurate measurements of the tangential drag coefficients have been obtained, but measurements of the velocity profiles were not possible. Therefore, Eq. (10) can be used to obtain the momentum thickness at the end of the cylinder from the measured total drag on the towed cylinder. By towing cylinders of various lengths, an estimate of the spatial growth of the momentum thickness can effectively be determined. The maximum value of the associated experimental uncertainty for the momentum thickness is 1%.

Figure 6 shows data values calculated for the momentum thick-

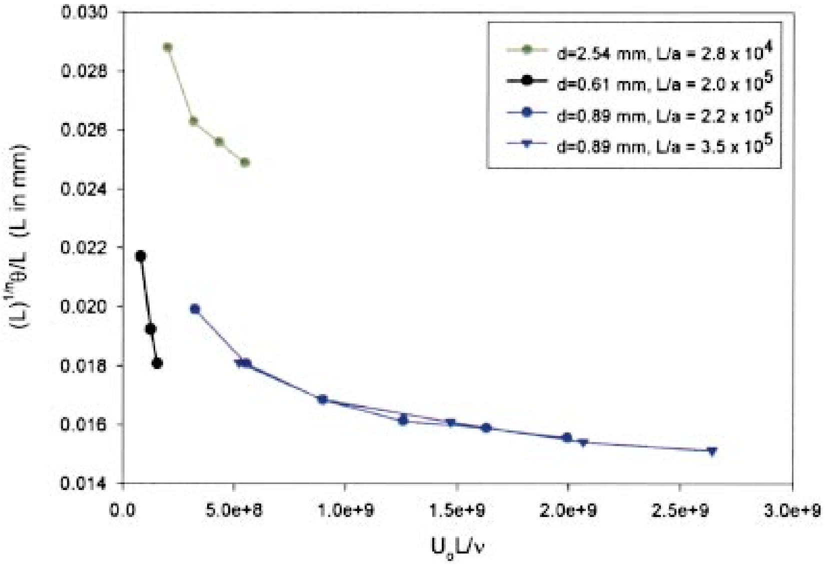

Fig. 8 Dimensional scaling of momentum thickness versus nondimensional velocity U_oL/ν

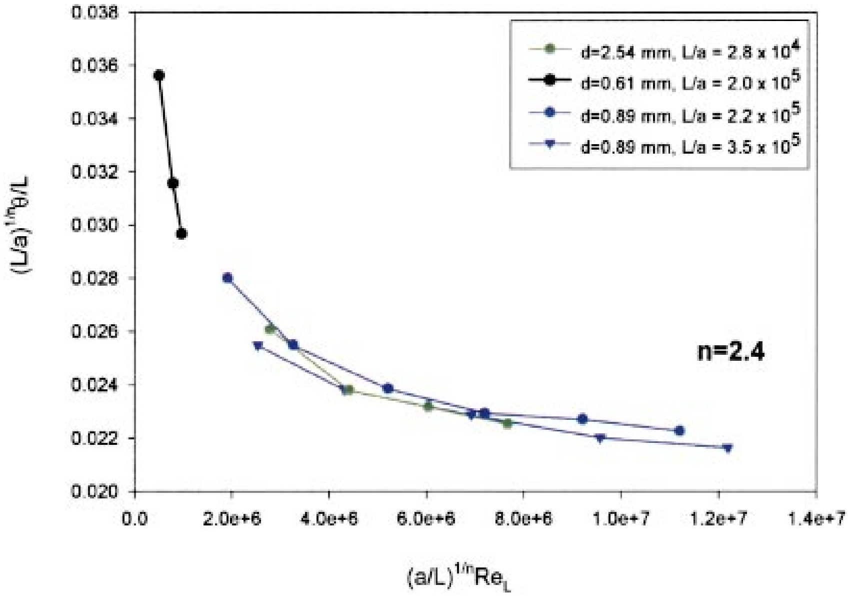

Fig. 9 Nondimensional momentum thickness, scaled for $2.8\times10^4<L/a<3.5\times10^5$

ness at the end of each cylinder, $\theta(L)$, versus the tow speed U_o. The trend of decreasing momentum thickness with increasing velocity for a given cylinder is apparent, as one would expect from flat-plate theory. For the case of $d=0.89$ mm, for a fixed U_o, one can also see that $\theta(L)$ increases with increasing length, as expected. In order to nondimensionalize the results of Fig. 6, L and ν/L are chosen as the primary length and velocity scales, respectively. The nondimensional velocity U_oL/ν may be interpreted alternatively as a Reynolds number based on the length L. The results of applying this simple scaling are shown in Fig. 7 as $\theta(L)/L$ versus U_oL/ν. Clearly, this scaling does not collapse the data for the various cylinders tested. In order to improve the data collapse for the case of $d=0.89$ mm, the additional factor $L^{1/n}$, where n is an empirically determined constant, is introduced to the scaling for $\theta(L)$. However, note that this scaling does not result in a nondimensional quantity. The results are shown in Fig. 8, where the length L is in millimeters. The use of this scaling clearly collapses the data for the two lengths of 0.89-mm-diameter cylinder; however, no collapse is observed for cylinders of different diameters, as the length scale a has not been utilized. The results of incorporating the cylinder radius a into the scaling are presented in Fig. 9, with $\theta(L)/L$ scaled with the quantity $(a/L)^{1/n}$ and U_oL/ν scaled with the quantity $(L/a)^{1/n}$.

This scaling described above produces a good collapse of the data for all cases presented here. Although the parameter a/L is a ratio of the major length scales of the body under tow, it can be viewed as incorporating the effect of the relative transverse curvature on the growth of the boundary layer. While the momentum thickness is known to increase with length, the radius a is shown to have a secondary effect on its growth. Since this data includes measurements on cylinders of various L/a, it provides a preliminary estimate of $\theta(L)$. By systematically varying the length of a fixed diameter cylinder under tow, a more accurate measurement

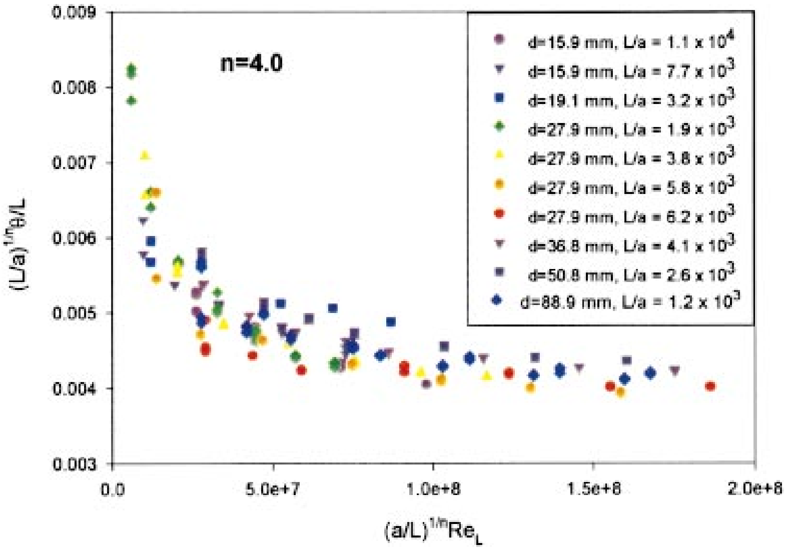

Fig. 10 Nondimensional momentum thickness, scaled for $1.2\times10^3<L/a<1.1\times10^4$

of the spatial growth of the momentum thickness could be determined. This data has been acquired in a subsequent tow test and will be presented in a future publication.

Similarly, Fig. 10 shows a plot using the same scaling for momentum thickness data obtained for $1.2\times10^3 < L/a < 1.1\times10^4$ during an independent series of tow tests, [12]. For this range of aspect ratios, a value of $n = 4.0$ was found to effectively collapse the data. The results in Figs. 9 and 10 demonstrate that a scaling law of this form is appropriate for this class of flows. However, data at intermediate values of aspect ratio L/a are required to determine a universal scaling law.

Summary

Direct drag measurements on long, small-diameter towed cylinders were performed, and the average mean wall shear stress over the wetted surface was computed for each case. These values were approximately two to three times higher than values for a flat-plate case, with comparable length and freestream velocity. This effect is readily explained by considering the wetted area of the cylinders, which must support a wall shear sufficient for a fully developed turbulent boundary layer to exist and grow over the length of the cylinder. While previous studies have measured a higher wall shear stress in an axisymmetric boundary layer, these are the first measurements at Reynolds number values $\mathrm{Re}_\theta > 2\times10^4$. The angle of the cylinders during tow was measured using a laser light sheet, and found to be less than 1 deg. In each case, the cylinders towed straight and demonstrated no evidence of hydrodynamic instabilities, which led to the conclusion that no shedding of the boundary layer occurred, as discussed by Wei [11], and the boundary layers grew to the maximum possible thickness. In addition, the ambient turbulence intensity was negligible, and no standing waves were observed in the tow tank during testing.

Using a control volume analysis, an expression for the momentum thickness at the end of the cylinders is derived which enables calculation of $\theta(L)$ from a simple measurement of the total tangential drag. This is of interest when velocity profile measurements are not possible, such as during tow tank tests and sea trials. Cylinders of the dimensions tested here can only be studied in these types of test environments, as typical laboratory facilities cannot accommodate them. A scaling law for the momentum thickness versus length Reynolds number is determined from the data. Assuming the boundary layer thickness is an order of magnitude greater than the momentum thickness, ratios of δ/a as great as 430 were achieved. This is two orders of magnitude greater than values previously achieved in laboratory test facilities. The results also indicate that the spatial growth of the boundary layers over the entire length is less than for a comparable flat-plate case.

Acknowledgments

The authors would like to thank the Office of Naval Research (Code 321SS) and the Naval Undersea Warfare Center Division Newport In-House Laboratory Independent Research Program for their support of this research.

Nomenclature

a = cylinder radius (mm)
A_s = total cylindrical surface area (m^2)
C_d = tangential drag coefficient
D = drag force (Newtons)
F = force (vector quantity) (Newtons)
δ = boundary layer thickness (mm)
δ^* = displacement thickness (mm)
L = cylinder length (m)
ν = kinematic viscosity (m^2/s)
θ = momentum thickness (mm)
ρ = fluid density (kg/m^3)
r = radial coordinate
τ_{ave} = mean wall shear stress (Newtons/m^2)
$u(r)$ = mean streamwise velocity (m/s)
U_o = tow speed (m/s)
V = mean velocity (vector quantity) (m/s)
x = streamwise coordinate

References

[1] Lueptow, R. M., 1988, ''Turbulent Boundary Layer on a Cylinder in Axial Flow,'' NUSC Technical Report 8389, Naval Underwater Systems Center, New London, CT, Sept. 29.

[2] Willmarth, W. W., Winkel, R. E., Sharma, L. K., and Bogar, T. J., 1976, ''Axially Symmetric Turbulent Boundary Layers on Cylinders: Mean Velocity Profiles and Wall Pressure Fluctuations,'' ASME J. Fluids Eng., **76**, Part 1, pp. 35–64.

[3] Luxton, R. E., Bull, M. K., and Rajagopalan, S., 1984, ''The Thick Axisymmetric Boundary Layer on a Long Fine Cylinder in Axial Flow,'' Aeronaut. J., **88**, pp. 186–199.

[4] Ackroyd, J. A. D., 1982, ''On the Analysis of Turbulent Boundary Layers on Slender Cylinders,'' ASME J. Fluids Eng., **104**, pp. 185–190.

[5] Rao, G. N. V., 1967, ''The Law of the Wall in a Thick Axisymmetric Turbulent Boundary Layer,'' ASME J. Appl. Mech., **34**, pp. 237–238.

[6] Patel, V. C., 1973, ''A Unified View of the Law of the Wall Using Mixing-Length Theory,'' Aeronaut. Q., **24**, pp. 55–70.

[7] Piquet, J., and Patel, V. C., 1999, ''Transverse Curvature Effects in Turbulent Boundary Layer,'' Prog. Aerosp. Sci., **35**, pp. 661–672.

[8] Neves, J. C., Moin, P., and Moser, R. D., 1994, ''Effects of Convex Transverse Curvature on Wall-Bounded Turbulence. Part 1. The Velocity and Vorticity,'' J. Fluid Mech., **272**, pp. 349–381.

[9] Brown, D. A., 1985, ''Langley Seawater Tow Tank Facility: Description and Operation,'' NUSC Technical Document 6392, Naval Underwater Systems Center, New London, CT, June 17 (unclassified).

[10] Schlichting, H., 1979, *Boundary-Layer Theory*, 7th Ed., McGraw-Hill, New York, pp. 635–667.

[11] Wei, T., 1983, ''Static Pressure Distribution on Long Cylinders as a Function of Yaw and Reynolds Number,'' Report 014439-1-T, Department of Aerospace Engineering, University of Michigan, Ann Arbor, MI.

[12] Cipolla, K. M., and Williams, M. R., 2001, ''Drag Measurements of Long Cylinders in Axial Tow,'' *Proceedings of the Undersea Defense Technology Hawaii Conference*, Waikiki, HI, Paper No. 6B.3.

Analysis for the Effect of Inverter Ripple Current on Fuel Cell Operating Condition

Randall S. Gemmen
Gas Energy Systems Dynamics Division,
National Energy Technology Center,
Morgantown, WV 26507
e-mail: randall.gemmen@netl.doe.gov

The effect of inverter ripple current on fuel cell stack performance and stack lifetime remains uncertain. This paper provides a first attempt to examine the impact of inverter load dynamics on the fuel cell. Since reactant utilization is known to impact the mechanical nature of a fuel cell, it is suggested that the varying reactant conditions surrounding the cell govern, at least in part, the lifetime of the cells. This paper investigates these conditions through the use of a dynamic model for the bulk conditions within the stack, as well as a one-dimensional model for the detailed mass transport occurring within the electrode of a cell. These two independent modeling approaches are used to verify their respective numerical procedures. In this work, the inverter load is imposed as a boundary condition to the models. Results show the transient behavior of the reactant concentrations within the stack, and of the mass diffusion within the electrode under inverter loads with frequencies between 30 Hz and 1250 Hz. [DOI: 10.1115/1.1567307]

Introduction

The demand for on-site power is expected to increase in the coming years. The drivers for this increased demand are, in part

- a need for improved power quality which itself is driven by the need for improved product quality; e.g., computer industry,
- a need for improved power reliability as uncertainties due to deregulation result in market disruptions,
- an expectation that some consumers will be able to produce power on-site more cheaply than what can be purchased through the grid,
- demand for increased efficiency through integrated heat/electricity (cogeneration) systems, and
- the increased difficulties in obtaining permits for large power plants and their associated need for an extensive network of power distribution hardware.

Fuel cell technology is expected to play a significant role in helping to meet these upcoming demands for distributed generation (DG), Rastler [1]. While it is not clear what the optimal near-term size will be for these systems, it is expected that there will be opportunities across the entire spectrum, from residential to large industrial. Several companies have already expressed interest in these various markets; e.g., Schmidt [2], Foger and Godfrey [3], and Susai et al. [4]. Fuel cell systems have already been demonstrated to provide high-quality power output. They are also potentially simpler (involve fewer moving parts) enabling them to be more reliable than conventional power generation technology. They are presently being developed for mass production (Surdoval et al. [5]) thereby helping to reduce their present high capital cost from ~$1000–$5000 per kW to less than $500 per kW. Finally, because of their superior emissions performance, the environmental permit process will be relatively easy. As a result, they can be readily applied as new options for such applications as grid support (Acquavia et al. [6]).

In spite of the aforementioned drivers and beneficial features of fuel cell technology, certain challenges remain before they can be applied to real-world applications (Rastler [1]). One of these challenges is technology risk, which includes the issue of durability—a subject that has not been sufficiently examined (Fowler et al. [7]). It is important that fuel cell technology be demonstrated to achieve long life (>40,000 hours), so that mass-market adopters, such as residential owners, will accept the technology. Many parameters can impact durability: operating pressure fluctuations, operating temperature, and load variations, to name just a few. For DG applications, fuel cells will provide DC power to an inverter, which converts the DC power to standard AC power. By its nature, an inverter will impose its own time varying load on a fuel cell, apart from that due to any load variations. As discussed below, a danger exists if peak current levels from these loads lead to undesirable conditions within the cell—in particular low reactant conditions. To guard against improper conditions, inverters are often, and perhaps arbitrarily, given specifications by fuel cell developers, such as *maximum ripple current*, without fully understanding the impact to the system cost or actual fuel cell durability (Mauch [8]).

To begin to examine this issue, this paper presents a model for the unsteady bulk conditions within the stack, and a model for the transport (diffusion) of reactants through porous fuel cell electrodes. While the effect of inverter loads on performance needs to be considered for all fuel cell types, this study is limited to polymer electrolyte membrane (PEM) fuel cells. Based on the results from this study, an understanding for the effect of inverter loads on conditions near the electrolyte surface is achieved. These results will allow future investigations examining the issue of durability a method for delineating when unsteady loads begin to significantly impact the fuel cell reactant conditions.

The paper begins by describing some technical issues related to time varying fuel cell loads. The paper continues by describing a zero-dimensional model that was originally developed to investigate fuel cell control strategies. In the present work, the zero-dimensional model is used to investigate the bulk behavior of the fuel cell conditions when the system is subjected to an inverter-type load. Subsequently, a description of a one-dimensional electrode model is provided. The latter model provides the detailed conditions near the electrolyte-electrode interface. Results are then presented for both models, followed by a discussion of the critical conditions resulting from an inverter load. The paper concludes with a summary of the work, and a discussion of needed future work.

Contributed by the Fluids Engineering Division for publication in the JOURNAL OF FLUIDS ENGINEERING. Manuscript received by the Fluids Engineering Division November 6, 2001, revised manuscript received November 26, 2002. Associate Editor: J. Katz.

Technical Issues With Time Varying Fuel Cell Loads

For the application considered here (DG), maximizing fuel efficiency is a primary consideration. For this to occur, it would seem that the fuel cell should operate at zero excess fuel. However, it is already well understood that to produce a useful output voltage, a minimal amount of excess fuel is necessary. (Pure hydrogen fuel cells have a *potential* for zero or near zero excess fuel; however, these require special techniques, which are not considered here.) Further, as indicated previously, safe fuel cell operation requires that some level of reactant concentration be maintained within the fuel cell in order to sustain the desired mechanical state of a fuel cell. If not enough excess fuel is supplied to support the voltage potential across the entire cell, internal damage to the cell can result, such as oxidation of the cell materials. Hence, there is a tradeoff between fuel cell integrity (i.e., lifetime) and fuel cell performance (i.e., efficiency.) As a consequence, when designing for *steady-state conditions*, selection for the optimal fuel input and air input for a given load are required. These fuel and air requirements are often specified via ''fuel utilization'' and ''air utilization'' parameters—the fraction of fuel/air used at a given load. The method by which these values is best determined, even in the analysis for steady-state conditions, is not well understood largely because the issues impacting durability are themselves not well understood, although progress is being made (Taniguchi et al. [9], Hsiao and Selman [10], Ioselevich et al. [11,12], Gulzow et al. [13], Mattsson et al. [14], and Costamagna [15]).

Because fuel utilization and current production are directly linked, when addressing the practical situation of *variable loads*, the designer needs to specify a current tolerance, i.e., ''ripple current,'' around a time-average design point, giving attention to the aforementioned issues. This also means that the designer is required to accept a lower fuel utilization (fuel efficiency) in order to provide a certain level of ''chemical capacitance'' which can absorb these sometimes unpredictable current variations. Since the success of many commercial fuel cell programs depends on maximizing efficiency, it becomes important to understand the impact of ripple current, and, where necessary, find ways to minimize it.

A *standard (practical) definition* of ripple current for fuel cell technology has not yet been proposed. The definition for ripple current used here is ''any current deviation from a specified average current.'' This definition is convenient for modeling; since the parameters can be directly and independently specified. However, before leaving this topic, other definitions are proposed for purposes of initiating the development of a more useful definition that will allow a fuel cell developer to communicate effectively to an inverter developer, and vice versa. The problem with the above definition in practice lies in the assessment of a meaningful ''average value'' (what is the meaningful integration time?).

Perhaps an improved definition for ripple is the variation of current from the instantaneous fuel cell theoretical current. The theoretical current for a fuel cell is that maximum current possible as dictated by the instantaneous flow rate of the limiting reactant (with a proper discount due to any fuel utilization limitations). The benefit of this definition is that ripple is then related directly to the degradation issues described above—if ripple is too strong, overdepletion of the reactants will occur, which may result in cell failure. This definition is a conservative definition, since it does not consider the temporal nature of ripple, and the internal capacitance of reactants within the stack that can adsorb the ''shock'' of any sudden load change. A further improved definition (that can be derived from Eq. (5)), is

$$I_{\mathrm{Rip}_{\mathrm{Max}}}=K_{\mathrm{Flw}}I_{\mathrm{th}}+K_{\mathrm{Cap}}\omega \tag{1}$$

where K_{Flw} is a constant proportional to the fuel utilization tolerance (the tolerance being minimized in order to maximize fuel efficiency), K_{Cap} is a constant proportional to the accepted reactant capacitance tolerance, I_{th} is the theoretical fuel cell current, and ω is the frequency of the ripple. K_{Flw} and K_{Cap} are related—higher values of K_{Flw} provide higher values for K_{Cap} due to the increased fuel concentration that results as increased excess fuel is supplied. As the equation indicates, higher ripple frequencies allow higher ripple currents.

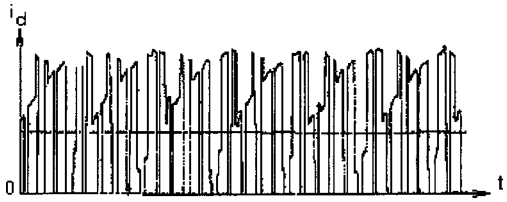

Fig. 1 Character of ripple current for a three-phase DC to AC inverter. Reference: Mohan et al. [16].

While the above formula is relatively simple, if multiple frequencies exist, as is often the case, then the designer also needs to consider phase variations between these frequencies which can lead to instantaneously high values of current when all ripple waves are in-phase. The only way to treat these cases in a general manner, however, is to do an on-line analysis of the conservation of species within the stack. Such an analysis, while certainly possible with modern control technology, is more complicated than the previous two proposals, and may not achieve the stated goal of improving the communication between inverter designer and fuel cell developer.

Model

The model for the ripple current, and the two models for the fuel cell are presented in detail in the following subsections.

Ripple Current Model. An inverter load applied to a fuel cell has several transient features (Lesster [16]). There is a current ripple related to the frequency of the fundamental output waveform (e.g., 120 Hz ripple for a 60 Hz single-phase output for certain inverter topologies). In addition, there may be a high-frequency ripple related to a DC/DC converter switching frequency and the carrier frequency for a pulse-width-modulated output stage. The character of ripple is shown in Fig. 1 (Mohan et al. [17] and Famouri [18]).

At present there is little endurance data to show how such loads can affect the fuel cell over extended periods of time (e.g., greater than several thousands of hours). Short-term studies at our lab at fuel and air utilizations below 70% and 20% and negligible diffusion limits show that a PEM fuel cell can withstand significant load changes without noticeable degradation. Even so, to ensure minimal impact to the performance of the fuel cell, as well as its durability, fuel cell developers would prefer to specify as little ripple as possible, e.g., below 2% of the theoretical fuel cell current (Allen [19]). However, to filter out ripple via electrical capacitors requires very large values of electrical capacitance when specifications below 1% ripple are given (Lesster [16]). (Alternatively, certain advanced inverter topologies can achieve lower ripple without capacitors, albeit at greater costs.) This paper will examine how an imposed ripple current, simulated as a constant frequency square-wave, affects the conditions of the reactants within the stack and electrode of the fuel cell. The parameters in the ripple model are

$$I_{\mathrm{Rip}}(t)=AS[1+x*\mathrm{sqwv}(t)] \tag{2}$$

where A is the current-density amplitude factor, S is the active area of the cell where electrochemistry occurs, x is the ripple factor, which is the ratio of the oscillation to steady amplitudes, and $\mathrm{sqwv}(t)$ is a square wave function with unity amplitude and zero average. This form of ripple model is sufficient for a first-order analysis, since the ripple current is often nearly proportional to load at low (120 Hz) frequency. In this work, a range of frequencies and amplitudes are examined to show the impact of these variables on the reactant conditions surrounding the cell.

Zero-Dimensional Bulk Stack Model. A variety of fuel cell models have been developed and exercised to accomplish focused studies into PEM operation, e.g., Wang et al. [20], Wang et al. [21], Baschuk and Li [22], Springer et al. [23], and Springer et al. [24]. For PEM fuel cells, much of the focus is on water management, and, as these references show, various levels of models are employed to examine such effects (depending on the submodel used or application water issues may also be ignored). For the present study, Matlab (Simulink) was used to provide an assessment for the overall conditions occurring within the fuel cell when loaded by an inverter. For the cathode flow rates, humidity conditions, and current densities examined in the present model, Wang et al. [21] indicate that water buildup in the fuel cell will be minimal (their model shows two-phase flow to be incipient at 7000 amp/m^2 whereas the present results reach 4400 amp/m^2). As such, for this introductory investigation on ripple no water management issues are examined at this time.

A high-level view of the Simulink model is shown in Fig. 2. Fixed fuel and air supplies are delivered to their respective humidifier volumes. The gases are humidified to saturation at a prescribed temperature, and are then passed on to the fuel cell. The calculated outputs from the fuel cell module are stack voltage, fuel utilization, and anode H_2 partial pressure. If desired, a simple fuel utilization control scheme can be applied as shown in Fig. 2. In addition, various types of loads can be employed using the Multiport Switch; e.g., a resistive load, or various prescribed current loads. The model assumes constant stack operating pressure (101 kPa). The instantaneous reactant input flow rates to the cell are controlled by a pressure-flow relationship, with the upstream pressure source taken from reactant humidifier volumes, and the downstream pressure being the prescribed stack operating pressure. The model assesses the transient pressure within the humidifiers as part of the analysis. The fuel cell submodel is shown in Fig. 3(*a*), where the conservation of hydrogen moles within the anode passage is analyzed as shown in Fig. 3(*b*). The cathode has similar analysis, but conserves both oxygen and water vapor, consumed and produced, respectively, by the electrochemical reactions. The electrochemical model shown in Fig. 3(*c*) accounts for the principle loss mechanisms in fuel cells; i.e., resistance, diffusion, and activation. The resistance and electrical capacitance (i.e., ''double-layer capacitance'') of a fuel cell is accounted for by a first-order R-C circuit, as shown in Fig. 3(*c*). At this time only approximate values for the resistance and electrical capacitance are provided based in part on some recent studies (Eikerling and Kornyshev [25] and Kötz and Carlen [26]).

The above model description is detailed more precisely with the following mathematical formulations. For pressure within the humidifiers we have

$$\frac{dP_h}{dt}=\frac{RT}{V}(n_{ih}-n_{oh}) \tag{3}$$

where P_h is the humidifier pressure, R is the universal gas constant, T is the prescribed humidifier temperature, n_{ih} is the prescribed humidifier molar input flow rate, and n_o is the humidifier molar exit flow rate. The molar output flow rate is given by the pressure-flow relationship

$$n_{oh}=K(P_h-P_s) \tag{4}$$

where K is a flow constant determined by a laminar flow relationship, and P_s is the stack pressure.

The partial pressures of the reactants in the anode and cathode are provided by

$$\frac{dP_j}{dt}=\frac{RT_s}{V_s}\left(n_iY_{j\_i}-n_oY_{j\_o}-\frac{I(t)N}{Z_jF}\right) \tag{5}$$

where P_j is the partial pressure of reactant ''j,'' T_s is the prescribed stack temperature, V_s is the volume of the stack anode or cathode passages, Y_j is the mole fractions of reactant ''j'' within the anode or cathode (subscript j_I for inlet conditions, and j_o for outlet conditions), $I(t)$ is the stack current having a prescribed current ripple, N is the number of cells in a stack, Z_j is the number of electrons per molecule of reactant ''j,'' and F is the Faraday constant having a value of 96439.0 coulomb/gm-mole of electrons. The stack exit flow, n_o, is evaluated from

$$n_o=n_i-n_I \tag{6}$$

where n_I is the net instantaneous mole loss in a stack passage, anode, or cathode, due to the instantaneous electrochemical reactions occurring within the passage. That is, n_I is directly proportional to the current through the stack. For the anode in a PEM fuel cell, there is a net loss of moles due to the consumption of one molecule of hydrogen per two electrons processed through a single cell of the stack. For the cathode, there is a net gain of moles, because two water molecules replace each oxygen molecule for every four electrons processed through a cell. As is evident with this approach, we presently ignore the net electro-osmotic drag of water across a PEM membrane (Futerko and Hsing [27]). Other fuel cell technologies may have different behavior depending on what charge (proton or electrons) are transported across the electrolyte.

Finally, the stack voltage is evaluated using the Nernst equation, which provides the ideal cell voltage. In addition, as indicated above, various loss mechanisms are taken into account, such as internal resistance, diffusion through the electrode, and electrochemical activation. The Nernst voltage potential is

$$E_N=Eo+\frac{RT}{Z'F}\ln\left(\frac{P_{H_2}P_{O_2}^{1/2}}{P_{H_2O}P_o^{1/2}}\right) \tag{7}$$

where Eo is the standard state potential which is evaluated from the change in standard state Gibbs free energy of the overall chemical reaction, Z' is the number of electrons occurring in the overall reaction (e.g., 2 when hydrogen is selected as the basis for the overall electrochemical reaction equation), and P_x is a partial pressure of the given reactant within the cell anode/cathode.

Under steady-state current loads, the actual operating voltage of the cell is given by

$$E=E_N-IR-\eta_D-\eta_{ec} \tag{8}$$

where R is the cell resistance, η_D is the cell diffusion loss, and η_{ec} is the cell electrochemical loss. These latter loss mechanisms are evaluated by

$$\eta_D=\frac{-RT}{Z'F}\ln\left(1-\frac{I}{I_D}\right) \tag{9}$$

$$\eta_{ec}=\frac{RT}{\alpha Z'F}\ln\left(\frac{I}{I_{ex}}\right) \tag{10}$$

where I_D is the diffusion limiting current density, α is the transfer coefficient, and I_{ex} is the exchange current density. The parameter I_D is calculated based on a one-dimensional (quasi-steady) Fikian-diffusion analysis through the diffusion layer given the instantaneous freestream conditions and zero concentration of reactant at the active layer. Finally, to evaluate the stack voltage, the cell voltage, E, is multiplied by the number of cells in the stack, N.

Under dynamic loads, the reactance of the fuel cell electrical capacitance also needs to be considered, as we have attempted to do for the present work—again, see Fig. 3(*c*).

One-Dimensional Electrode Model. The zero-dimensional system/stack model provides information on the bulk behavior of the fuel cell system due to transient inverter loads, $I(t)$, but it

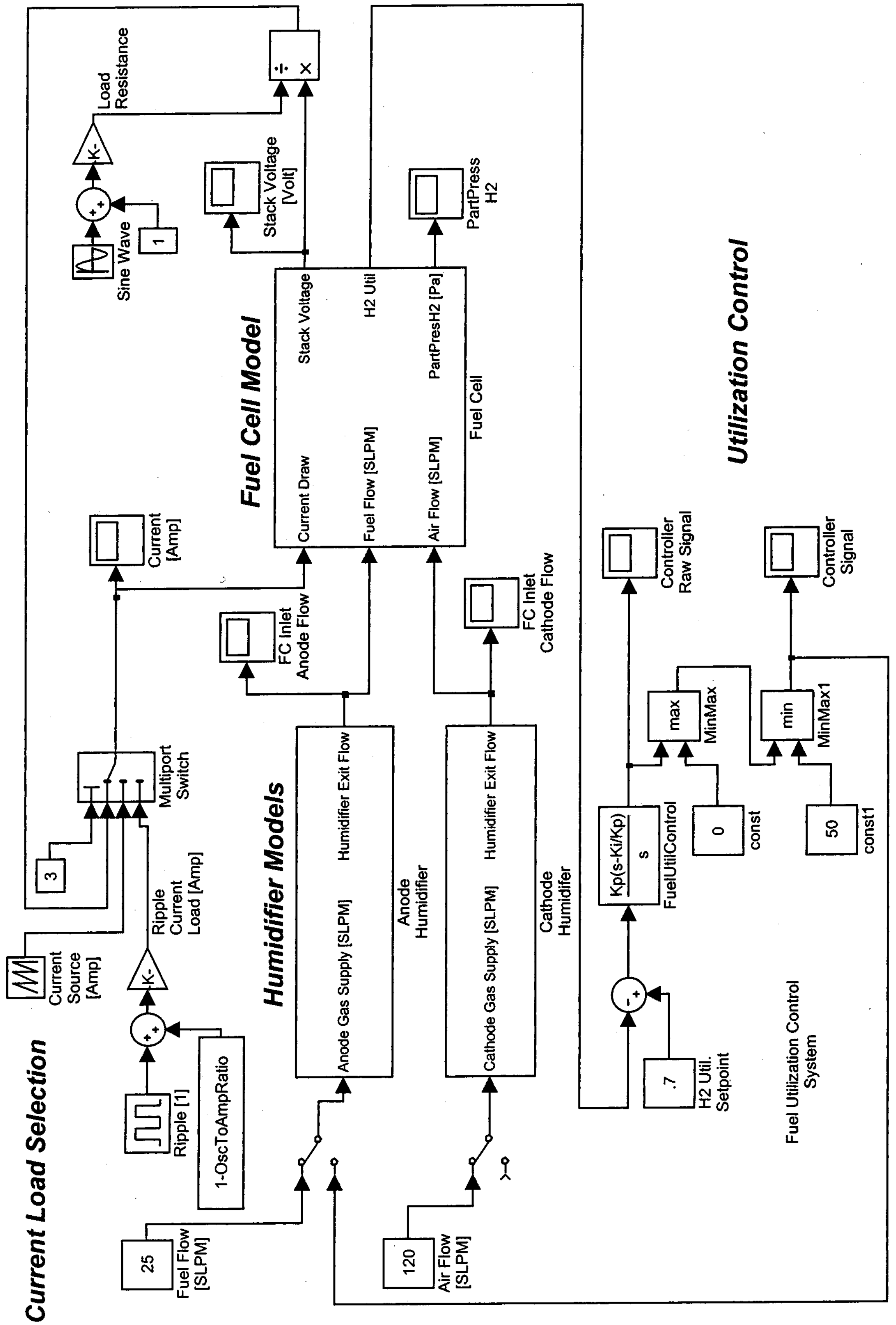

Fig. 2 Simulink model overview.

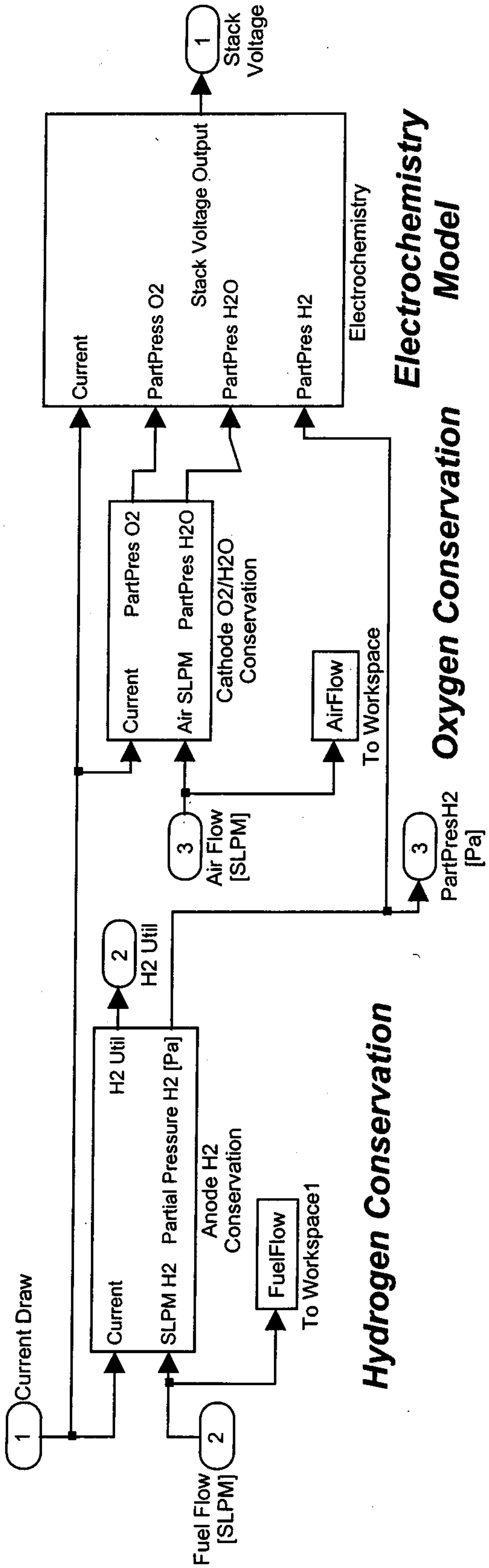

(*a*)

Fig. 3 (*a*) **Fuel cell submodel overview,** (*b*) **anode hydrogen conservation model,** (*c*) **electrochemical model**

cannot describe the precise conditions within the electrodes, which are known, albeit poorly, to impact the degradation of the cell materials.

A simplified analysis was assumed for the transport through the electrode. Because the typical membrane-electrode assembly (MEA) is thin, on the order of 0.040 in. or less, it is assumed that the temperature remains constant through the MEA. In addition, it is also assumed that the pressure remains constant in the diffusion layer—that is, pressure driven flow is much less than transport due to molecular diffusion. The prediction for the molecular diffusion though an electrode is analyzed by

$$\varepsilon \frac{dY_j}{dt} + u \frac{dY_j}{dx} = D' \nabla^2 Y_j \tag{11}$$

where Y_j is the specie, "j" and mole fraction, D' is the effective diffusion coefficient, which takes into account tortuosity and porosity of the electrode via

$$D' = D \frac{\varepsilon}{\tau} \tag{12}$$

where D is the molecular binary diffusion coefficient, ε is the porosity, and τ is the tortuosity of the electrode. Similar treatments have been employed in more detailed fuel cell analyses work (Arnost and Schneider [28], Dutta et al. [29], and Drescher et al. [30]). In Eq. (11), the convection velocity, u, is evaluated by the identity, $\rho \varepsilon^{2/3} u = n''$, where ρ is the molar density and n'' is the flux of moles at the surface which is proportional to the current density. Here, $\varepsilon^{2/3}$ is assumed to correlate with the effective flow area (normal to the MEA) provided by the pores in the diffusion layer, which assumes isotropic pore geometry. Finally, while it is well known that water management is critical to the optimal performance of a PEM, at this time concerns for water condensation/evaporation are ignored.

A zero-dimensional conservation equation for the moles in the anode/cathode gas-volumes is also analyzed, similar to Eq. (5), but with a specified constant input reactant flow rate. The result is provided as a mole fraction boundary condition on the gas side of the electrode in the above one-dimensional diffusion model. Because the current and consumption of reactive species are directly related, the transient flux-type boundary condition at the electrolyte surface is

$$\frac{dY_j}{dx} = \frac{I(t)}{\rho D' Z_j F} \tag{13}$$

where ρ is the gas density, and $I(t)$ is the time varying current flow through the cell dictated by the imposed inverter load.

An implicit finite difference scheme was employed for the analysis. The time step was governed by the frequency of the inverter load (0.3% of period), and the spatial resolution was given by the relation

$$l = 3.0\sqrt{D' \tau'} \tag{14}$$

where l is the spatial resolution and τ' is the time step. If the number of nodes resulting from the above relation were less than 20, then the model imposed 20 nodes for the analysis, and used the above relation to give the time step.

Results

The focus of this analysis is on the effect of inverter load on cell reactant concentrations. Because the hydrogen flow is normally the limiting reactant (excess hydrogen may only be 20% while excess oxygen may be 200% and higher), the bulk model is used to analyze the conservation of hydrogen in the anode volume, and provide information on the general character of the bulk hydrogen fluctuations over a wide range of load frequencies and fluctuations. However, hydrogen is more diffusive than oxygen,

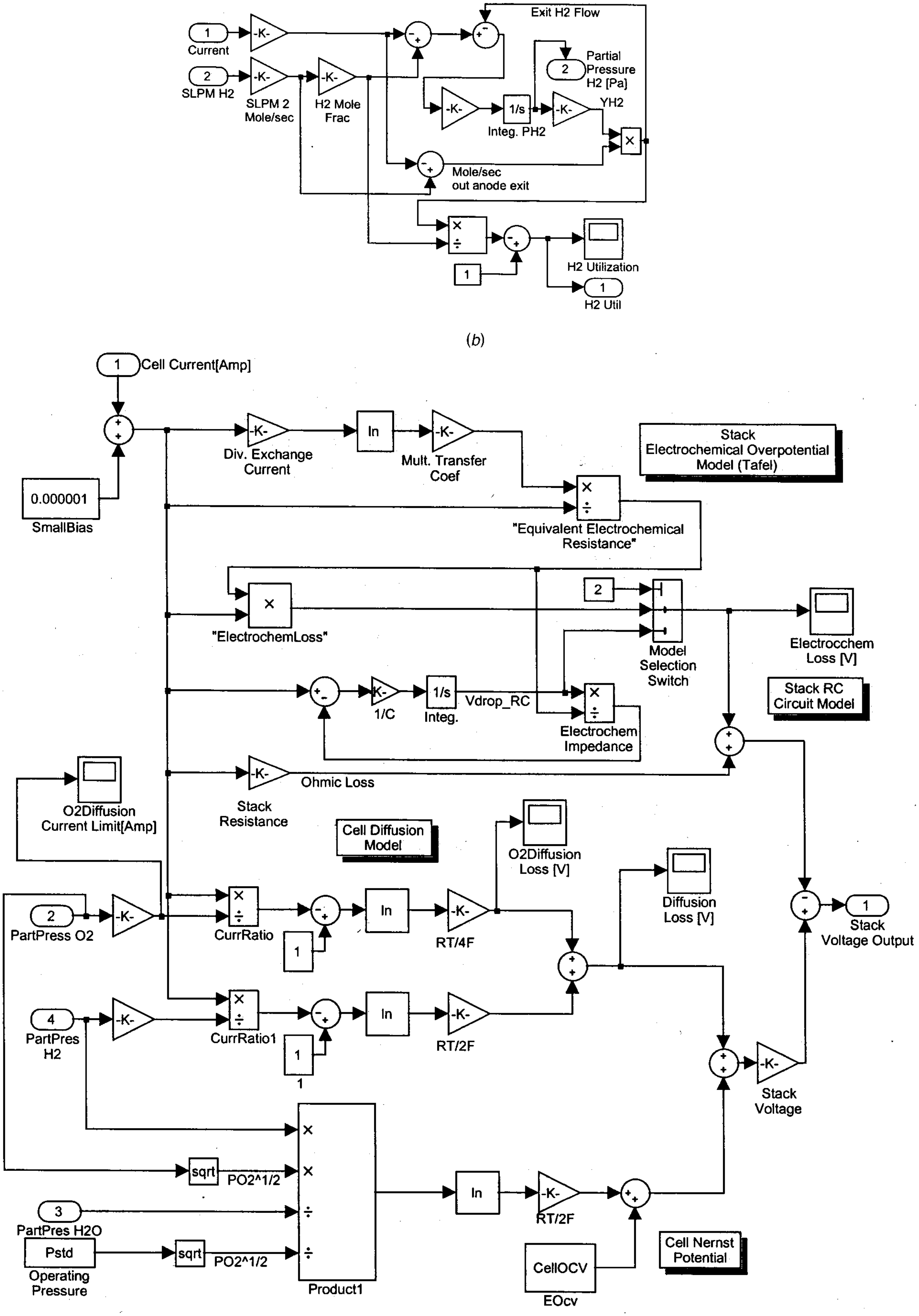

(b)

(c)

FIG. 3. (*continued.*)

Table 1 Simulink problem definition and operating conditions. (The "assumed" values come from an NETL-designed fuel cell.)

VARIABLE	VALUE	Ref.
Number Of Cells In Stack	60	Assumed
Cell Active Width (m)	0.1	Assumed
Cell Active Length (m)	0.1	Assumed
Operating Pressure (Pa)	101000	Assumed
Operating Temperature (K)	353	Wang et al. [20]
Anode Flow Rate (slpm)	25	Assumed
Cathode Flow Rate (slpm)	120	Assumed
Specific Cell Capacitance (farad/cm2)	0.077	See paper
Specific Cell Resistance (ohm-cm2)	0.48	Assumed
Exchange Current Density (amp/cm2)	0.03	Springer [23]
Transfer Coefficient	0.5	Wang et al. (2001) ($\alpha_c/Z' = 2/4$)
Anode Relative Humidity	0.9	Assumed
Cathode Relative Humidity	0.03	Wang et al. [20]
Anode Channel Width (m)	0.002	Assumed
Anode Channel Height (m)	0.0003	Assumed
Anode Channel Length (m)	0.1	Assumed
Cathode Channel Width (m)	0.003	Assumed
Cathode Channel Height (m)	0.001	Assumed
Cathode Channel Length (m)	0.1	Assumed
Diffusion Layer Tortuosity	4	Assumed
Diffusion Layer Porosity	0.4	Baschuk and Li [21]
Number Of Anode Channels	13	Assumed
Number Of Cathode Channels	17	Assumed
Anode Humidifier Gas Volume (m3)	0.0141	Assumed
Anode Inlet Manifold Width (m)	0.1	Assumed
Anode Inlet Manifold Height (m)	0.0003	Assumed
Anode Inlet Manifold Depth (m)	0.015	Assumed
Cathode Humidifier Gas Volume (m3)	0.0212	Assumed
Cathode Inlet Manifold Width (m)	0.1	Assumed
Cathode Inlet Manifold Height (m)	0.001	Assumed
Cathode Inlet Manifold Depth (m)	0.015	Assumed
Anode Flow Constant (slpm/Pa)	0.00183	Assumed
Cathode Flow Constant (slpm/Pa)	0.00104	Assumed

meaning that oxygen may impose a limiting condition before that of hydrogen. Such conditions are assessed through the use of the one-dimensional diffusion electrode model.

Zero-Dimensional Bulk Stack Model. The Simulink model employed the parameters shown in Table 1. The main data presented are for a frequency range between 30 Hz and 240 Hz, and a current amplitude factor, "A," between 346 and 4400 amp/m^2. For all cases the ripple factor "*x*" remained constant at 0.3. The 30 Hz case is selected for presenting time-history results, which are shown in Fig. 4(*a*). The figure shows the fluctuation (about the average) of hydrogen partial pressure for several different magnitudes of "A." The partial pressure for each case is normalized by the average partial pressure for that case. It is found that significant variations in hydrogen concentration result only at large current amplitudes—9% at 44 amp=4400 amp/m^2 load, corresponding to nearly 98% hydrogen utilization. At frequencies above 30 Hz, where inverters produce more ripple (e.g., 60 Hz and 120 Hz), these variations can be shown to be less than 4% of the mean. As evident in Fig. 4(*a*), the variations in partial pressure never reach a steady state. Not until frequencies reach as low as 0.1 Hz, will the system reach equilibration within each half-cycle as is evident with the data shown if Fig. 4(*b*).

Figure 5 shows a response curve for the hydrogen variations due to transient loads. Shown in Fig. 5 is the ratio of minimum hydrogen concentration achieved by a ripple load to that achieved by a steady state load ($x=0$) of equivalent average current. If the ratio is significantly less than one for a given inverter load, then the inverter load will negatively impact the performance of the cell relative to the equivalent steady state load. As can be seen, for the given conditions, significant deviations from the steady-state conditions only occur for frequencies below 120 Hz, and for current amplitude factors at 4400 amp/m^2 (440 mA/cm^2). As indicated previously, this magnitude of current corresponds to very high fuel utilizations that are not typically employed in fuel cell

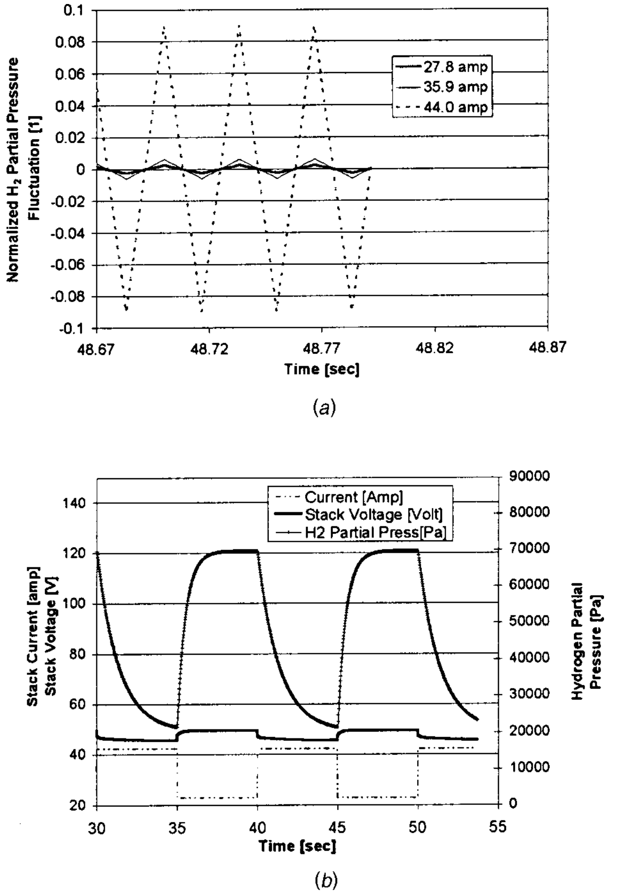

(*a*)

(*b*)

Fig. 4 (*a*) Simulink results of hydrogen partial pressure time history for 30 Hz and selected current amplitude factors, (*b*) Simulink results of hydrogen partial pressure time history for 0.1 Hz and 3250 amp/m^2 current amplitude factor

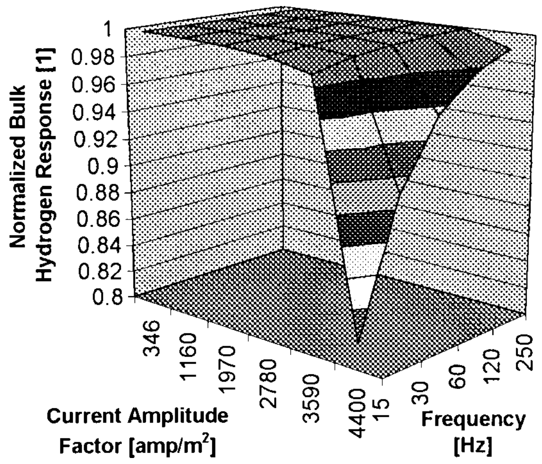

Fig. 5 Hydrogen concentration response curve from simulink model. Because hydrogen diffusion is fast, this response curve is very comparable to that predicted by the Diffusion Model for current <3500 amp/cm^2. See Fig. 7.

applications. In summary, it is clear that typical inverter loads do not significantly impact the *bulk* conditions within the fuel cell analyzed here.

One-Dimensional Electrode Diffusion Model. Data on the normalized minimum *oxygen* concentration at the electrode surface was generated via the one-dimensional model. This time ripple factors ranged from $x=0.01$ to 0.3, and frequency ranged from 30 Hz to 1250 Hz. The same geometric analysis was considered as in the zero-dimensional bulk model. Values for oxygen diffusion, tortuosity, and porosity were 0.000284 m^2/sec (Wang et al. [21]), 4.0, and 0.4, respectively. Results from this analysis are shown in Figs. 6(*a*) to 6(*d*). As can be seen, significant deviations from steady state conditions occur for frequencies 120 Hz and less, provided current amplitude factors are greater than 1960 amp/m^2 (196 mA/cm^2), and ripple factors are 0.3. For the given conditions, this amplitude factor corresponds to only about 21% oxygen utilization, and 44% hydrogen utilization. Hence, it can already be concluded that diffusion plays an important part in the behavior of these systems to transient loads. Finally, to avoid significant deviations regardless of the current amplitude level, ripple factors need to be less than 4%. Again, for most fuel cell applications the dominant ripple current is usually 120 Hz, and as the figures show, greater than 1% deviations from the steady-state conditions can occur for ripple factors greater than 3%. Frequencies greater than 1250 Hz do not impact the conditions to any significant degree except at very high utilizations and ripple factors.

A comparison of the results from both models for the oxygen and hydrogen concentration is shown in Fig. 7 for the 60 Hz case. As the figure shows, when the current amplitude factor, "A," increases, so does the deviation from the steady-state reactant concentration, i.e., $x=0$. The diffusion model shows a greater variation from the steady state, as may be expected due to the transport

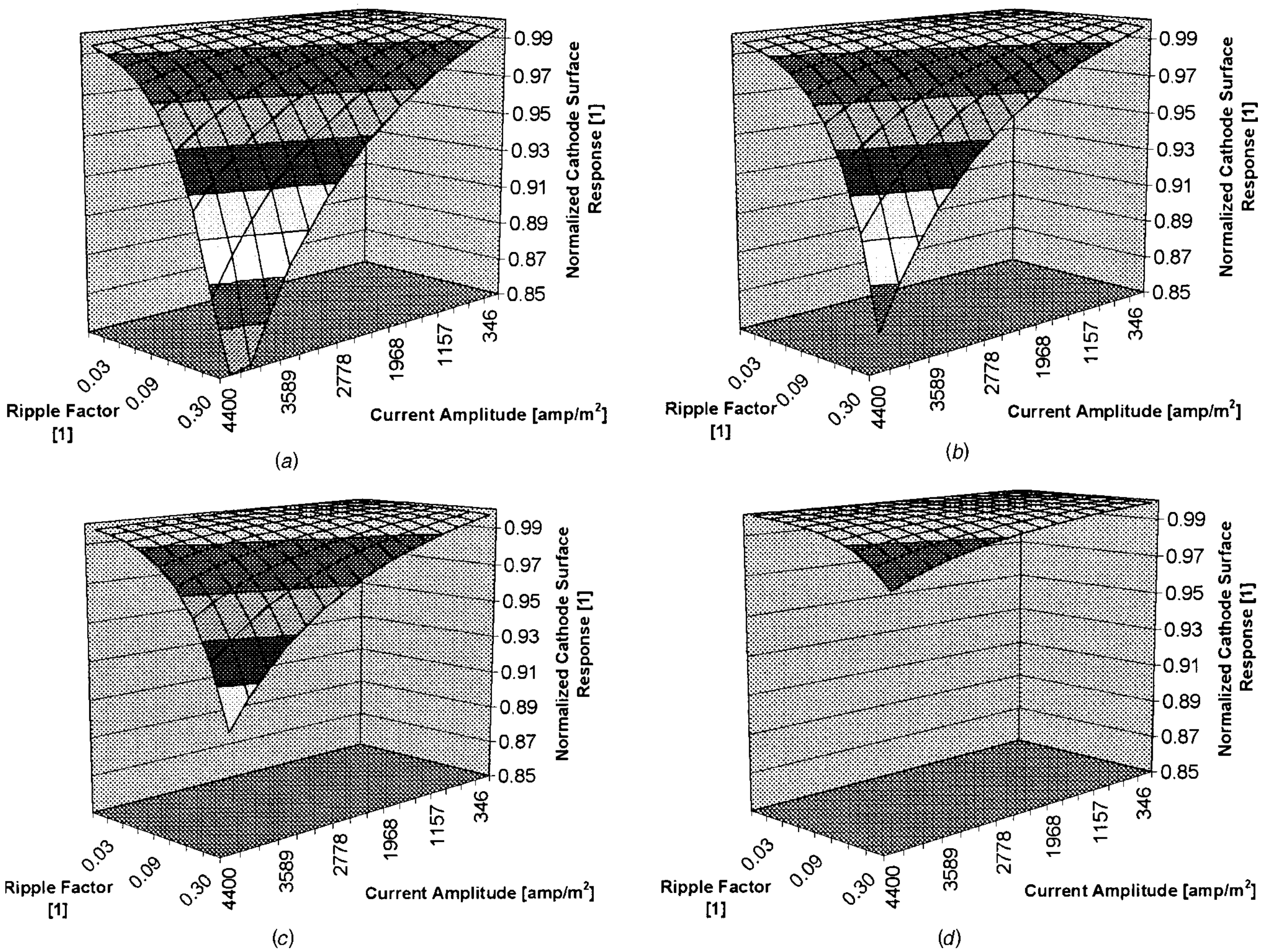

Fig. 6 (*a*) Oxygen concentration response curve from diffusion Model—30 Hz case, (*b*) oxygen concentration response curve from diffusion model—60 Hz case, (*c*) oxygen concentration response curve from diffusion model—120 Hz case, (*d*) oxygen concentration response curve from diffusion model—1250 Hz case

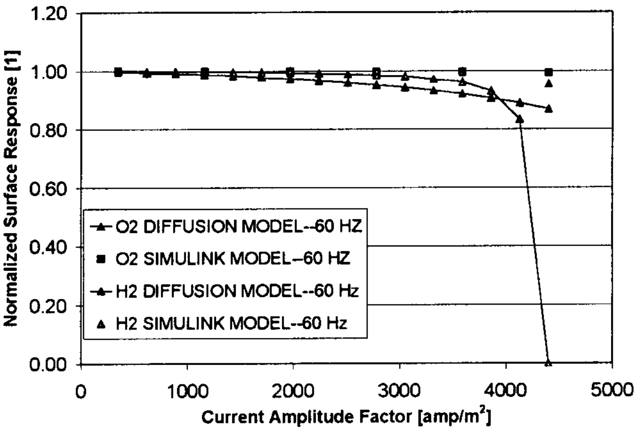

Fig. 7 Model comparisons for oxygen and hydrogen normalized surface responses. Data connected by lines come from the diffusion model. Data shown are for $x=0.3$, 60 Hz.

impedance caused by the porous electrode. The figure also confirms the expectation that the oxygen response is impacted the most by diffusion, up to a point where hydrogen utilization becomes severe (high current amplitude factors). From these results it can be concluded that accurate modeling of the diffusion behavior is critical if reliable transient behavior predictions are to be achieved. Finally, the two models were further compared by examining their respective gas-stream hydrogen concentrations (not shown here). The two models predicted the same hydrogen response to ripple variations to within 0.5%, which verifies the numerical approach employed in each of the models.

Summary

This paper serves to initiate discussion in what appears to be a neglected topic in the fuel cell literature. It is shown that for the fuel cell geometry considered here unsteady fuel cell loads, such as those imposed by an inverter, can have significant impact on the conditions within the fuel cell diffusion layer. The main cause for the deviation in conditions from equivalent steady load conditions is the oxygen molecular diffusion through the cathode electrode—consumption of gas within the channels of the fuel cell appears to be less of concern. Before these results are considered general, however, other fuel cell geometries and inverter load conditions may need to be investigated. For the cell/stack configuration considered here, oxygen experienced the greatest variation. Preliminary results indicate that to ensure negligible inverter ripple impact, inverter frequencies need to be above 120 Hz, or have ripple factors less than 4%.

Many challenges remain in this research area. One specific need is to develop more quantitative information on the exact chemical and mechanical changes that may occur within an electrode and electrolyte, as well as at their interface, due to conditions that result from various levels of ripple current. With such information, improved fuel cell technology will be possible, thereby enabling the necessary stack lifetimes for achieving commercial success.

Nomenclature

A = current amplitude factor (amp/m^2)
D' = effective diffusion coefficient (m^2/sec)
E_N = Nernst voltage (V)
Eo = standard state voltage (V)
F = Faraday constant (see text)
I_{Rip} = ripple current (amp/m^2)
I_D = diffusion limit current (amp)
I_{ex} = exchange current (amp)
I = cell current (amp)
K = flow constant (gm-mol/sec/Pa)
l = spatial resolution in one-dimensional model (m)
n = molar flow rate (gm-mol/sec)
N = number of cells in stack (l)
P_j = reactant partial pressure (Pa)
P_h = humidifier pressure (Pa)
P_s = stack pressure (Pa)
t = time (sec)
T = operating temperature (K)
R = cell resistance (ohm)
V = humidifier volume (m^3)
V_s = stack anode/cathode volume (m^3)
x = ripple factor (l)
Y = mole fraction (l)
Z = electrons per reactant molecule (l)

Greek

ρ = gas density (gm-mol/m^3)
ε = electrode porosity (l)
α = transfer coefficient (l)
τ' = time step in one-dimensional model (sec)
τ = electrode tortuosity (1)

References

[1] Rastler, D., 2000, ‘‘Challenges for Fuel Cells as Stationary Power Resource in the Evolving Energy Enterprise,’’ J. Power Sources, **86**, pp. 34–39.
[2] Schmidt, M., ‘‘The Hexis Project,’’ Fuel Cells Bulletin No. 1.
[3] Foger, K., and Godfrey, B., 2000, ‘‘System Demonstration Program at Ceramic Fuel Cells Ltd.—In Australia,’’ Fuel Cell 2000, Lucerne, Switzerland, July 10–14.
[4] Susai, T., Kawakami, A., Hamada, A., Miyake, Y., and Azegami, Y., 2001, ‘‘Development of a 1 kW Polymer Electrolyte Fuel Cell Power Source,’’ J. Power Sources, **92**, pp. 131–138.
[5] Surdoval, W. A., Singhal, S. C., and McVay, G. L., 2001, ‘‘The Solid State Energy Conversion Alliance (SECA)—A U.S. Department of Energy Initiative to Promote the Development of Mass Customized Solid Oxide Fuel Cells for Low-Cost Power,’’ presented at the 7th International Symposium on Solid Oxide Fuel Cells, June 3–8, Tsukuba, Japan.
[6] Acquaviva, V., Poggi, P., Muselli, M., and Louche, A., 2000, ‘‘Grid-Connected Rooftop PV Systems for Reducing Voltage Drops at End of the Feeder—A Case Study in Corsica Island,’’ Energy, **25**, pp. 741–756.
[7] Fowler, M. W., Mann, R. F., Amphlett, J. C., Peppley, B. A., and Roberge, P. R., 2002, ‘‘Incorporation of Voltage Degradation into a Generalized Steady State Electrochemical Model for a PEM Fuel Cell,’’ J. Power Sources, **106**, pp. 274–283.
[8] Mauch, K., 2001, Xantrex Technology, Inc., private communication, Feb.
[9] Taniguchi, S., Kadowaki, M., Kawamura, H., Yasuo, T., Akiyama, Y., Miyake, Y., and Saitoh, T., 1995, ‘‘Degradation Phenomena in the Cathode of a Solid Oxide Fuel Cell With an Alloy Separator,’’ J. Power Sources, **55**, pp. 73–79.
[10] Hsiao, Y. C., and Selman, R., 1997, ‘‘The Degradation of SOFC Electrodes,’’ Solid State Ionics, **98**, pp. 33–98.
[11] Ianiguchi, S., Kadowaki, M., Kawamura, H., Yasuo, T., Akiyama, Y., and Miyake, Y., 1995, ‘‘Degradation Phenomina in the Cathode of a Solid Oxide Fuel Cell with an Alloy Separator,’’ J. Power Sources, **55**, pp. 73–79.
[12] Ioselevich, A., Kornyshev, A., and Lehnert, W., 1999, ‘‘Statistical Geometry of Reaction Space in Porous Cermet Anodes Based on Ion-Conducting Electrolytes—Patterns of Degradation,’’ Solid State Ionics, **124**, pp. 221–237.
[13] Gulzow, E., Schulze, M., Wagner, N., Kaz, T., Reissner, R., Steinhilber, G., and Schneider, A., 2000, ‘‘Dry Layer Preparation and Characterization of Polymer Electrolyte Fuel Cell Components,’’ J. Power Sources, **86**, pp. 352–362.
[14] Mattsson, B., Ericson, H., Torell, L., and Sundholm, F., 2000, ‘‘Degradation of a Fuel Cell Membrane, as Revealed by Micro-Raman Spectroscopy,’’ Electrochim. Acta, **45**, pp. 1405–1408.
[15] Costamagna, P., 2001, ‘‘Transport Phenomena in Polymeric Membrane Fuel Cells,’’ Chem. Eng. Sci., **56**, pp. 323–332.
[16] Lesster, L. E., 2000, ‘‘Fuel Cell Power Electronics: Managing a Variable-Voltage DC Source in a Fixed-Voltage AC World,’’ Fuel Cells Bulletin, **3**(25), pp. 5–9.
[17] Mohan, N., Undeland, T. M., and Robbins, W. P., 1995, *Power Electronics: Converters, Applications, and Design*, 2nd Ed., John Wiley and Sons, New York.
[18] Famouri, P., 2002, private communication. Aug.
[19] Allen, G., 2002, ‘‘Equipment Design and Interface Specifications for 10 kWe Inverter,’’ inverter specification data provided by Fuel Cell Technologies, Ltd. for the Future Energy Inverter Competition.
[20] Wang, C. Y., Wang, Z. H., and Pan, Y., 1999, ‘‘Two-Phase Transport in Proton Exchange Membrane Fuel Cells,’’ HTD-Vol. 364-1, *Proceedings of the ASME Heat Transfer Division*, **1**, HTD-Vol. 364-1, ASME, New York.
[21] Wang, Z. H., Wang, C. Y., and Chen, K. S., 2001, ‘‘Two-Phase Flow and

Transport in the Air Cathode of Proton Exchange Membrane Fuel Cells,'' J. Power Sources, **94**, pp. 40–50.

[22] Baschuk, J. J., and Li, X., 2000, ''Modeling of Polymer Electrolyte Membrane Fuel Cells With Variable Degrees of Water Flooding,'' J. Power Sources, **86**, pp. 181–196.

[23] Springer, T. E., Zawodzinski, T. A., and Gottesfeld, S., 1991, ''Polymer Electrolyte Fuel Cell Model,'' J. Electrochem. Soc., **138**(8), pp. 2334–2342.

[24] Springer, T. E., Wilson, M. S., and Gottesfeld, S., 1993, ''Modeling and Experimental Diagnostics in Polymer Electrolyte Fuel Cells,'' J. Electrochem. Soc., **140**(12), pp. 3513–3526.

[25] Eikerling, M., and Kornyshev, A. A., 1999, ''Electrochemical Impedance of the Cathode Catalyst Layer in Polymer Electrolyte Fuel Cells,'' J. Electroanal. Chem., **475**, pp. 107–123.

[26] Kötz, R., and Carlen, M., 2000, ''Principles and Applications of Electrochemical Capacitors,'' Electrochim. Acta, **45**, pp. 2483–2498.

[27] Futerko, P., and Hsing, I-Ming, 2000, ''Two-Dimensional Finite Element Method Study of the Resistance of Membranes in Polymer Electrolyte Fuel Cells,'' Electrochim. Acta, **45**, pp. 1741–1751.

[28] Anost, D., and Schneider, P., 1995, ''Dynamic Transport of Multicomponent Mixtures of Gases in Porous Solids,'' Chem. Eng. J., **57**, pp. 91–99.

[29] Dutta, S., Shimpalee, S., and Van Zee, J. W., 2000, ''Three-Dimensional Numerical Simulation of Straight Channel PEM Fuel Cells,'' J. Appl. Electrochem., **30**, pp. 135–146.

[30] Drescher, I., Lehnert, W., and Meusinger, J., 1998, ''Structural Properties of SOFC Anodes and Cathodes,'' Electrochim. Acta, **43(19–20)**, pp. 3059–3068.

Journal of Fluids Engineering

Technical Briefs

Computational Fluid Dynamics Performance Estimation of Turbo Booster Vacuum Pump

H.-P. Cheng[1]
Assistant Professor, Department of Air Conditioning
and Refrigeration Engineering, National Taipei University
of Technology, 1 Sec. 3., Chung-Hsiao E. Road,
Taipei 106, Taiwan, R.O.C.
e-mail: hpcheng@ntut.edu.tw

C.-J. Chen
Director General, Precision Instrument Development
Center, National Science Council, 20 R&D Road VI,
Science-Based Industrial Park, Hsinchu 300, Taiwan
R.O.C.

P.-W. Cheng
Graduate Student, Department of Air Conditioning
and Refrigeration Engineering, National Taipei University
of Technology, Taipei 106, Taiwan R.O.C.

The CFD performance estimation of a turbo booster vacuum pump shows the axial vortex and back flow is evident when the mass flow rate is increased. The pressure is increased from the pump inlet to the outlet for the low mass flow rate cases. But for high mass flow rate cases, the pressure is increased until the region near the end of the rotor is then decreased. The calculated inlet pressure, compression ratio, and pumping speed is increased, decreased, and decreased, respectively, when the mass flow rate is increased. The pumping speed is increased when the rotor speed is increased. [DOI: 10.1115/1.1566042]

Introduction

The turbo molecular pump (TMP) is a very important high vacuum pump of semiconductor and TFT–LCD (thin film transistor–liquid crystal display) manufacturing equipment, and it is widely used in the etching, LPCVD (low pressure chemical vapor deposition), MOCVD (metal-organic chemical vapor deposition), ion implantation, and sputtering machines. The main characteristics of the TMP are that its pumping volume flow rate is near constant for free molecular flow, and is decreased dramatically for the continuum and slip flow, [1]. Because more and more semiconductor and TFT-LCD manufacturing processes are carried out in the continuum and slip flow regions, there are many workers using the hybrid rotors which are equipped with turbo blade rotors and molecular drag mechanism, [2], to improve the pumping performance of TMP in the regions of continuum and slip flow, [3]. But only a few papers deal with the continuum flow mechanism using numerical methods, [4–6].

In this paper, a commercial CFD code, [7], is used to investigate the detailed three-dimensional flow field of a new type turbo molecular pump, TBP (turbo booster pump), which was designed with a goal to enhance the pumping performance of the pump in continuum and slip flow regions. The detailed pressure and velocity fields for ten mass flow rates and four rotor rotational speeds are examined and discussed.

Mathematical Analysis

Governing Equations. The schematic diagram for the cross section of the TBP is shown in Fig. 1. The gas flows into the pump from the inlet port of the casing, then through the grooves of the rotor, and out the exit port of the casing. Figure 2 illustrates the outer peripheral surface of the rotor. The outer diameter (D) of the rotor is 206.8 mm, and the axial length (L) is 201 mm. The rotor is equipped with five spiral blades. Each blade consists of three

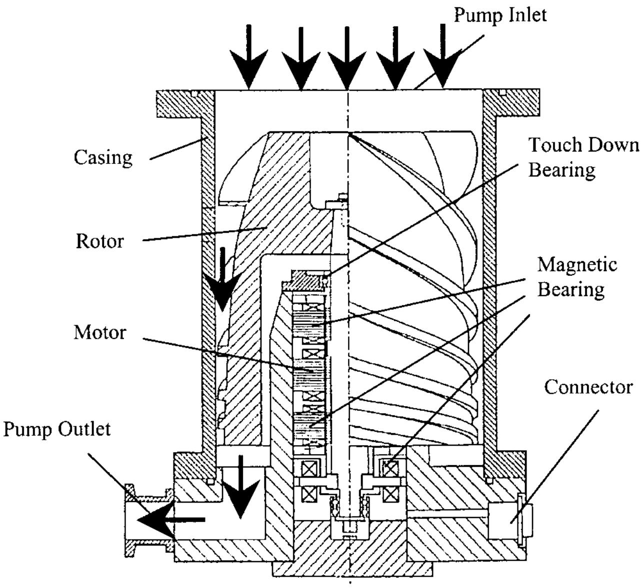

Fig. 1 Schematic diagram for the cross section of the turbo molecular pump

---

[1] To whom correspondence should be addressed.

Contributed by the Fluids Engineering Division for publication in the JOURNAL OF FLUIDS ENGINEERING. Manuscript received by the Fluids Engineering Division Dec. 15, 1999; revised manuscript received July 5, 2002. Associate Editor: B. Schiavello.

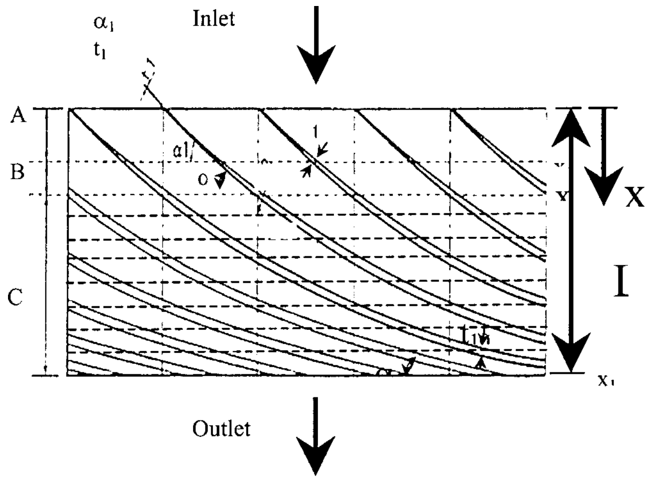

Fig. 2 Physical dimensions of the rotor: A: turbo blade design area (x/L: 0.0∼0.229) B: connection area (x/L:0.229∼0.403) C: helical-grooved design area (x/L:0.403∼1.0) L: axial length of rotor (201 mm) X, x_1, x_2, . . . ,x_{10}: axial distance downstream of the pump inlet port t_1, t_2, . . . ,t_{10}: blade thickness (A:2 mm, B: 2∼5.6 mm, C: 5.6 mm) α_1, α_2, . . . ,α_{10}: spiral angle of blade (A, B: 30°, C: 30° ∼12.5°)

different elements, attached together continuously, i.e., turbo blade design area, connection area, and helical-grooved design area. These three sections, A, B and C, are described in Fig. 2. The radial depth of flow channel is 58.4 to 4 mm from the rotor inlet to the outlet.

The flow in the pump is laminar because of the low Reynolds number, less than 10, which is defined as mean velocity (120.0 m/sec)×characteristic length (0.0584 m, the maximum radial depth of flow channel)×mean density (1.4×10^{-3} kg/m^3, the pressure of flow stream is less than 1.2 mbar)/viscosity (1.0×10^{-3} N·sec/m^2) for all testing cases. The computational coordinate system is fixed with the rotor and the centrifugal and coriolis forces are included in the source terms of the momentum equations. To reduce the computational time, only one single spiral flow passage is considered. Three subregions, as seen in Fig. 3, link the full computational domain. The generalized governing equations of mass, momentum, and energy in a rotating frame of reference can be written in curvilinear-transformed form as follows:

$$\frac{1}{J}\frac{\partial}{\partial t}(\rho q)=-\frac{\partial}{\partial \xi_i}(\rho U_i q)+\frac{\partial}{\partial \xi_i}\left(\mu G_{ij}\frac{\partial q}{\partial \xi_j}\right)+S_q \qquad (1)$$

where $q=1$ continuity equation
$=u$, v, w ξ_1, ξ_2, and ξ_3-momentum equation
$=h$ energy (static enthalpy) equation

where J, U_i, and G_{ij} represent the Jacobian of coordinate transformation, the volume-weighted contravariant velocities, and diffusion metrics, respectively. An equation of state is employed to close the above system of equations.

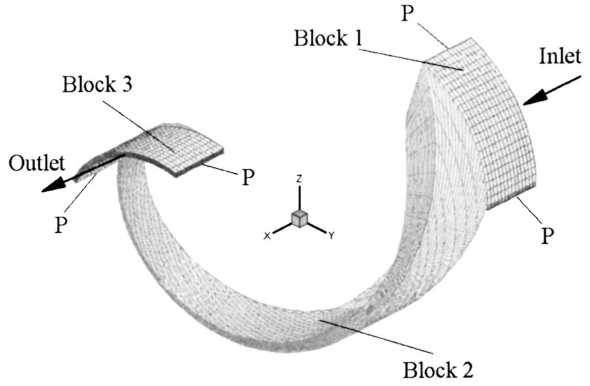

Fig. 3 Computational mesh: Block 1: upstream extended grid (vacuum chamber) Block 2: spiral flow passage of rotor Block 3: downstream extended grid P: periodical boundary condition

Boundary Conditions. In this study, the outlet pressure of the flow channel is assumed to Pe=0.665 mbar to imitate the operating situations of the pump in continuum and slip flow regions. Ten mass flow rates are given at the pump inlet, and the associated pumping volume flow rates can be obtained from the ratio of inlet mass flow rate to calculated inlet density. Isothermal (300 K) boundary condition was specified at the solid surfaces. The periodical treatment, [7], is imposed at all P-planes, as seen in Fig. 3. The slip and no-slip treatments, [7], are automatically imposed on the wall surface, depending on the values of the local Knudsen number (Kn). The Kn is defined as the ratio of mean free path to the radial depth of flow channel. The mean free path is defined as 0.0665/P, [5], and the unit is mm, where the P is the arithmetic mean pressure at axial plane and the unit is mbar. For the slip boundary condition, the perfectly diffuse reflection is assumed at the wall.

Numerical Schemes. A commercial CFD code, [7], is used here to calculate the flow field in the TBP. Finite difference approximations are employed to discretize the transport equations on nonstaggered grid mesh systems. A third-order upwind TVD (total variation diminishing) scheme is used to approximate the convective terms of the governing equations. A second-order central difference scheme is used for the viscous and source terms. For time advancing, an efficient noniterative time-marching scheme with a predictor/corrector solution algorithm is employed.

Before carrying out the investigations, a careful check for the grid-independence of the numerical solutions has been made to ensure the accuracy and validity of the numerical results. For this purpose, three different grid systems (33,831, 57,876, and 91,171 nodes) for case 5 were tested. It was found that the relative errors of the arithmetic mean pressure at axial plane are less than 3% for 57,876 and 91,171 grid systems. In order to shorten

Table 1 Mass flow rates and rotational speeds of cases

Case	SCCM	N (rpm)
1	154	24 000
2	308	24 000
3	462	24 000
4	616	24 000
5	770	24 000
6	924	24 000
7	1078	24 000
8	1232	24 000
9	1386	24 000
10	1540	24 000
11	770	20 000
12	770	28 000
13	770	32 000
14	1540	20 000
15	1540	28 000
16	1540	32000

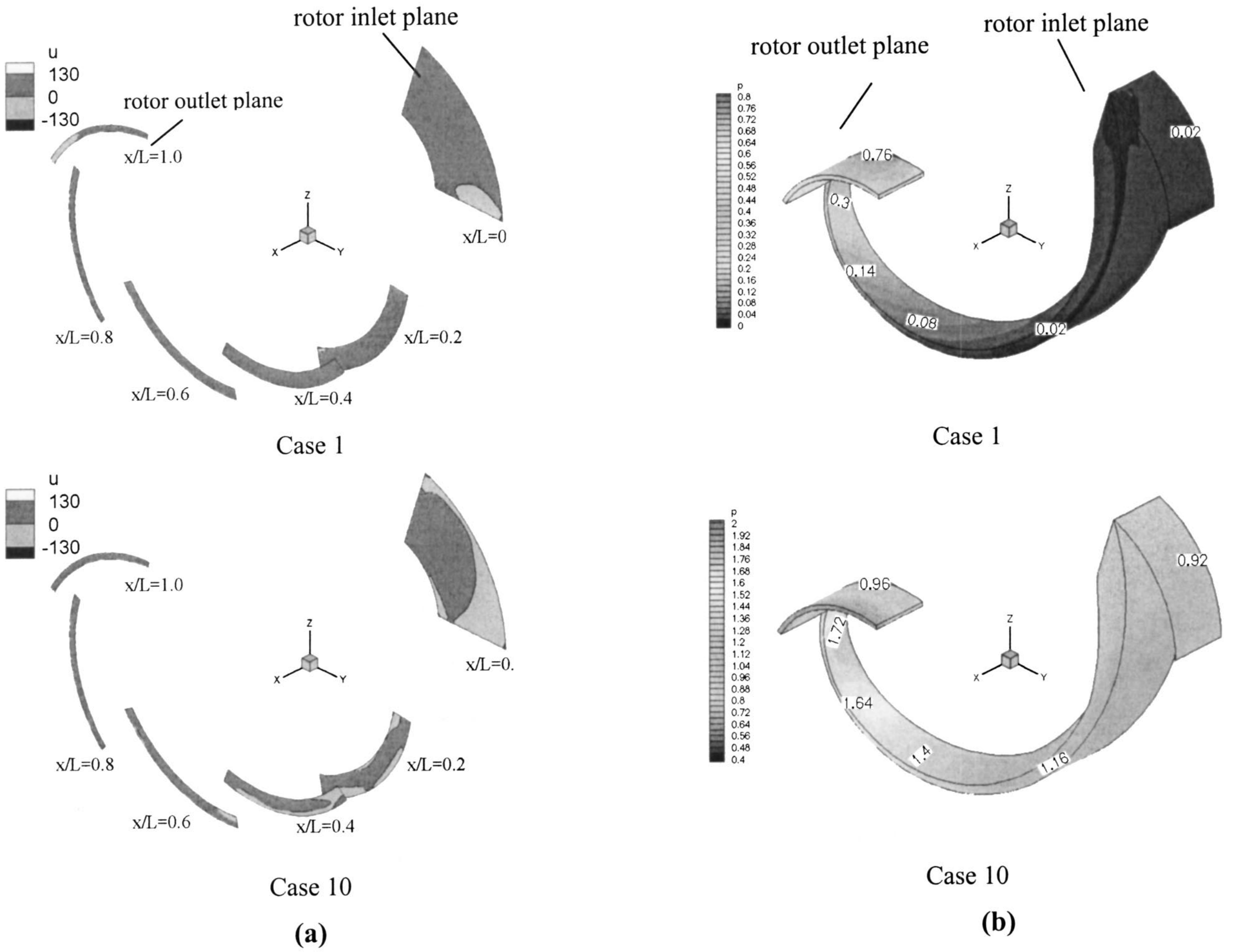

Fig. 4 (*a*) Axial velocity contours for cases 1, and 10 (*N*=24,000 rpm); (*b*) pressure distributions for cases 1, and 10 (*N*=24,000 rpm)

the computational time, the total grid 57,876 was adopted in this study.

Results and Discussion

Ten mass flow rates and four rotor rotational speeds are investigated in this study, and are described in Table 1. Basically, all cases 1 through 10 were in the slip $(0.01<\mathrm{Kn}<0.1)$ and continuum $(\mathrm{Kn}<0.01)$ flow regions except for the region near the rotor middle of case 1. Figure 4(*a*) shows the sectional contours of the axial velocity for cases 1, and 10. The darker area indicates that the flowing direction of gas is from the pump inlet to the outlet, while the lighter area is from the pump inside back to the

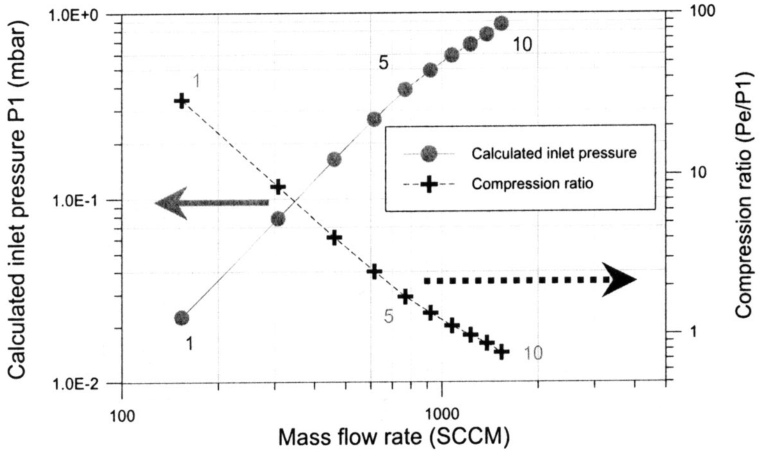

Fig. 5 Calculated inlet pressure (P1) and compression ratio as a function of the throughput for cases 1 to 10 (*N*=24,000 rpm, Pe=0.665 mbar)

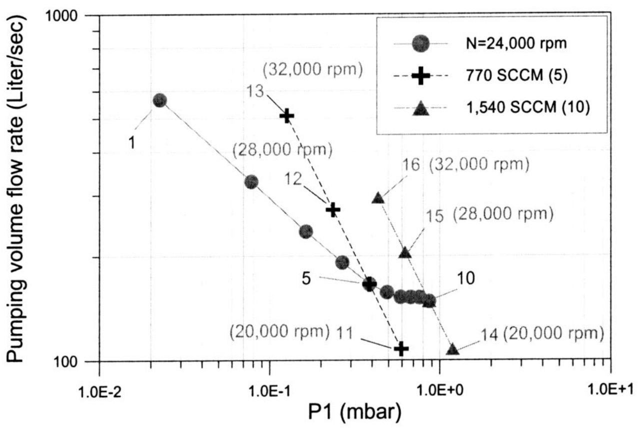

Fig. 6 Pumping volume flow rate as a function of calculated inlet pressure (P1) for cases 1 to 16—Parameters: rotor rotational speed (rpm) and mass flow rate (SCCM)

vacuum chamber. The gas backflow to vacuum chamber is more evident when the inlet mass flow rate is increased. The pressure distributions for cases 1 and 10 are shown in Fig. 4(*b*). The figure shows the pressure is increased from the inlet towards the outlet for case 1. But for case 10, the pressure is increased then decreased near the end of the rotor.

The calculated inlet pressure (P1) and compression ratio (Pe/P1) as a function of mass flow rate for cases 1 to 10 is shown in Fig. 5. A log-log scale is adopted for the vertical and horizontal axis with base-10 logarithm. The figure shows P1 is increased quite linearly in the log-log scale when the mass flow rate is increased, while the compression ratio is decreased. The slope of these two curves is nearly constant for cases 1 to 4, while the slope is decreased slightly for cases 5 to 10.

Figure 6 shows the pumping volume flow rate as a function of P1 for cases 1 to 16. The commercial TMP uses this type of plot to show its pumping performance. The vertical and horizontal axes are in a decimal log-log scale. As the figure shows, the pumping volume flow rate is decreased dramatically from case 1 to case 5. When the inlet pressure is increased continuously, from case 6 to case 10, the pumping volume flow rate is decreased gently. Compared with other commercial products, the pumping volume flow rate of this TBP (from 200 to 150 liter/sec at entry) is higher than that of other pumps with the similar rotor size when the pump inlet pressure is larger then 0.1 mbar. The figure also shows the relationship between the pumping volume flow rate and the rotor rotational speed. For cases 5, 11, 12, and 13 the pumping volume flow rate is increased linearly when the rotor rotational speed is increased. The results of cases 10, 14, 15, and 16 are similar to that of previous cases 5, 11, 12, and 13.

Conclusions

Computations of the detailed flow in a new developed turbo booster pump have been performed using a CFD approach. Major findings are as follows:

1 There is an axial vortex dominating the flow passage and the gas flowing from the pump inside back to vacuum chamber is evident when the inlet mass flow rate is increased.

2 The pressure is increased from the pump inlet to the outlet for the low mass flow rate cases. For high mass flow rate cases, the pressure is increased until the region near the end of the rotor then decreased.

3 The calculated inlet pressure, compression ratio, and pumping volume flow rate is increased, decreased, and decreased, respectively, when the inlet mass flow rate is increased.

4 The pumping volume flow rate is increased linearly when the rotor rotational speed is increased with constant mass flow rate.

Acknowledgments

This work was supported by the National Science Council under Contract NSC 90-2626-E-027-002.

Nomenclature

D = outer diameter of rotor (mm)
G_{ij} = diffusion metrics
h = static enthalpy (J/kg)
J = Jacobian of coordinate transformation
K = Kelvin degree
Kn = Knudsen number
L = axial length of rotor (mm)
N = rotor rotational speed (rpm)
P = calculated local arithmetic mean pressure at axial plane (mbar)
P1 = calculated inlet arithmetic mean pressure of vacuum pump (mbar)
Pe = outlet pressure of vacuum pump (0.665 mbar)
q = properties of transport equations
S_q = source term
SCCM = standard cubic centimeter per minute (atm·cm^3/min)
t = time (sec)
$t_1, t_2, \ldots t_{10}$ = blade thickness (mm)
u, v, w = velocities in the directions of ξ_1, ξ_2, and ξ_3
U_i = volume-weighted contravariant velocities (m/sec)
$X(x_1, x_2, \ldots, x_{10})$ = axial distance downstream of the pump inlet port (m)
ρ = density (kg/m^3)
$\alpha_1, \alpha_2, \ldots, \alpha_{10}$ = spiral angle of blade
$\xi_i(\xi_1, \xi_2, \xi_3)$ = coordinates for three directions (rotating frame with rotor)
μ = viscosity (N·sec/m^2)

References

[1] Ino, K., Sekine, K., Shibata, T., Ohmi, T., and Maejima, Y., 1998, ‘‘Improvement of Turbomolecular Pumps for Ultraclean, Low-Pressure, and High-Gas-Flow Processing,’’ J. Vac. Sci. Technol. A, **16**, pp. 2703–2710.
[2] Holweck, F., 1923, ‘‘Pompe Moléculaire Hélicoidale,’’ C. R. Acad. Sci, **43**, pp. 177–124.
[3] Levi, G., 1992, ‘‘Combination of Turbomolecular Pumping Stages and Molecular Drag Stages,’’ J. Vac. Sci. Technol. A, **10**, pp. 2619–2622.
[4] Sawada, T., Nakamura, M., and Abumiya, A., 1992, ‘‘Spiral Grooved Vacuum Pump Working in High Pressure Range,’’ Vacuum, **43**, pp. 1097–1099.
[5] Nanbu, K., and Igarashi, S., 1992, ‘‘Three-Dimensional Low-Density Flows in the Spiral Grooves of a Turbo-Molecular Pump,’’ Comput. Fluids, **21**, pp. 221–228.
[6] Spagnol, M., Cerruti, R., and Helmer, J. C., 1998, ‘‘Turbomolecular Pump Design for High Pressure Operation,’’ J. Vac. Sci. Technol. A, **16**, pp. 1151–1156.
[7] UNIC, 1995, *UNIC General Purpose CFD Design Tool*, Engineering Sciences, Inc., AL.

Prediction Relations for Pressure Drop Across Finned Sections[1]

Daeho Im

H. S. Ghazi
e-mail: hassan_ghazi@sdstate.edu

Mechanical Engineering Department, South Dakota State University, Brookings, SD 57007

Introduction

The enhancement of heat transfer is a design consideration in many electrical and mechanical engineering applications. Different methods for increasing the heat transfer rate have been investigated. Among these, the usage of extended surfaces, or fins, is common in engineering practice. The subject matter has been dealt with extensively and the results published in the literature, [1–11]. Associated with the different methods for enhancing the heat transfer by forced convection, is an increase in the pressure drop and the power required for moving the fluid. The focus of the published literature, however, has been on the heat transfer aspect. Even though a number of publications also included findings on the pressure drops, the available data do not lend themselves to analysis and correlation with geometric and flow parameters.

The purpose of this study was to develop relations for predicting pressure drops across finned sections as a function of the Reynolds number and the geometry of the array. This was accomplished by running sets of experiments with systematic variation in the thickness, length, height and number of fins within an array, and developing empirical relations for predicting the pressure drop in terms of a dimensionless loss coefficient. The experiments were run with rectangular fins placed in a rectangular channel with air as the fluid.

Experimental Apparatus and Procedure

The experimental apparatus consisted of a blower which supplied the air flow, an orifice metering section for determining the air flow rate, a test section, manometers for measuring pressures, mercury thermometers for measuring air temperatures, and a barometer for measuring the local atmospheric pressure. The orifice plate and pressure taps were constructed and installed according to ASME fluid measurement standards, [12]. Airflow rate was controlled by an adjustable damper covering the inlet to a radial wheel centrifugal blower. Air temperatures at blower inlet and duct outlet were measured. A mercury barometer with an attached mercury thermometer gave the local atmospheric pressure and temperature.

The test section was located in a rectangular duct 20.32 cm wide with a movable lower surface to accommodate fins of different heights. The sides and top were fixed. Pressure taps for measuring the pressure drop across the fins were placed 15.24 cm upstream of the inlet to the finned section and 13.97 cm downstream of the outlet. The upstream pressure was measured by a single tap located at the center of the top surface of the duct. The downstream pressure was an average of five pressure readings—three readings from taps spaced equally along the top surface and two from taps located on each side of the duct wall.

The finned array was constructed of individual fins mechanically attached to a base plate with spring pins inserted into holes drilled in the fin and the base plate. The finned array was placed upside down in the duct, with the base plate resting on the vertical duct walls and the tips of the fins flush with the bottom surface of the duct. Fins were spaced to give equal flow passages across the duct width.

Pressure and temperature measurements were then taken at six flow rates. The number of fins in the array was then changed and the experiments repeated. Similar experiments were repeated after making the following changes in turn: the length of the array, the thickness of the fins, and lastly the height. A total of 432 test runs were made.

Data Reduction

The pressure drop across the finned arrays is expressed in terms of a dimensionless ratio,

$$K=\frac{\Delta P}{\frac{1}{2}\rho_d V_d^2}. \tag{1}$$

ΔP is the total pressure drop and represents the frictional effects and entrance/exit effects of the finned array. The velocity in Eq. (1) is the flow velocity in the duct. The Reynolds number against which K is plotted is based on the duct hydraulic diameter.

Results and Discussion

Figures 1, 2, and 3 are plots of the loss coefficient, K, versus the duct Reynolds number, Re_d. Figure 1 is for 15.24 cm long fins, Fig. 2 for 7.62 cm fins, and Fig. 3 for 2.54 cm fins. Each of the figures has four separate plots corresponding to fin heights of (a) 1.905 cm, (b) 2.54 cm, (c) 3.175 cm, and (d) 3.81 cm. There are six curves of each of these four plots, three for fins 0.3175 cm thick in combination with arrays of eight fins, four fins, and two fins, and three similar curves for fins 0.635 cm thick. The parameters that relate to a particular curve are identified above each of the plots.

Figure 1 shows the variation of the loss coefficient with the Reynolds number for different combinations of fin height, fin thickness, and number of fins. The pattern of the variation of K is similar in Figs. 2 and 3 with the loss coefficient decreasing with increasing Reynolds number. The indication is that the kinetic energy increases at a faster rate than the corresponding increase in the pressure drop with a net result of a decrease in the ratio of the two. These plots give an overall sense of the effect of the Reynolds number, fin height, fin thickness, and number of fins, on the loss coefficient.

Empirical Equations

The objective of the study was to obtain a general prediction equation for the loss coefficient, that is

$$K=f(t,N,L,H,\mathrm{Re}_d). \tag{2}$$

It may be useful, however, to have less restrictive prediction equations where some of the variables are fixed. The first of these simpler equations are those that predict the loss coefficient as a function of only the Reynolds number, while holding the other variables constant. These equations were obtained by drawing curves through the data in Figs. 1–3 using linear regression. The prediction equations are of the form

$$K=C_1(\mathrm{Re}_d)^{C_2} \tag{3}$$

---

[1] JFE Databank Contribution.

Contributed by the Fluids Engineering Division for publication in the JOURNAL OF FLUIDS ENGINEERING. Manuscript received by the Fluids Engineering Division May 16, 2000; revised manuscript received Nov. 27, 2002. Associate Editors: J. Bridges and J. Katz.

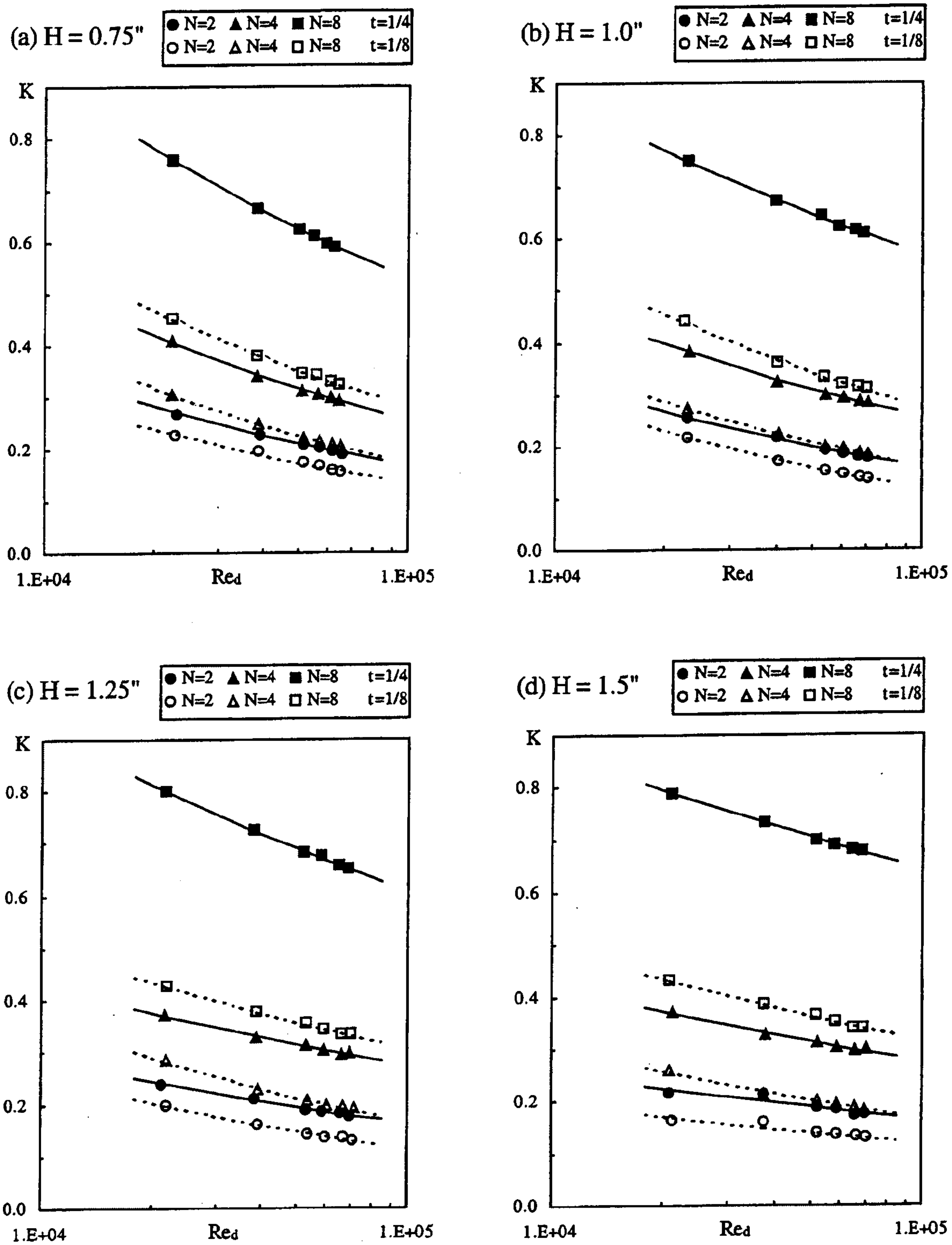

Fig. 1 Loss coefficient, K, versus Re_d, 15.24 cm long fins

where the coefficients C_1 and C_2 are functions of t, N, L, H. C_1 and C_2 are tabulated in Table 1. The correlation coefficients for the curve fits are also given. The predictions from Eq. (3), except for a few cases, are within ±5% of the experimental values with most being within ±2.5%

A prediction equation at a second level of generality is obtained by curve fitting cross plots of the data. The curves are of the form

$$K = C_3(\mathrm{Re}_d)^{C_4} \tag{4}$$

and were drawn using linear regression with the coefficients C_3 and C_4 being independent of fin height and given in Table 2. Equation (4) is simpler in that one of the variables has dropped out. Predictions from this equation are within ±20% of the experimental values.

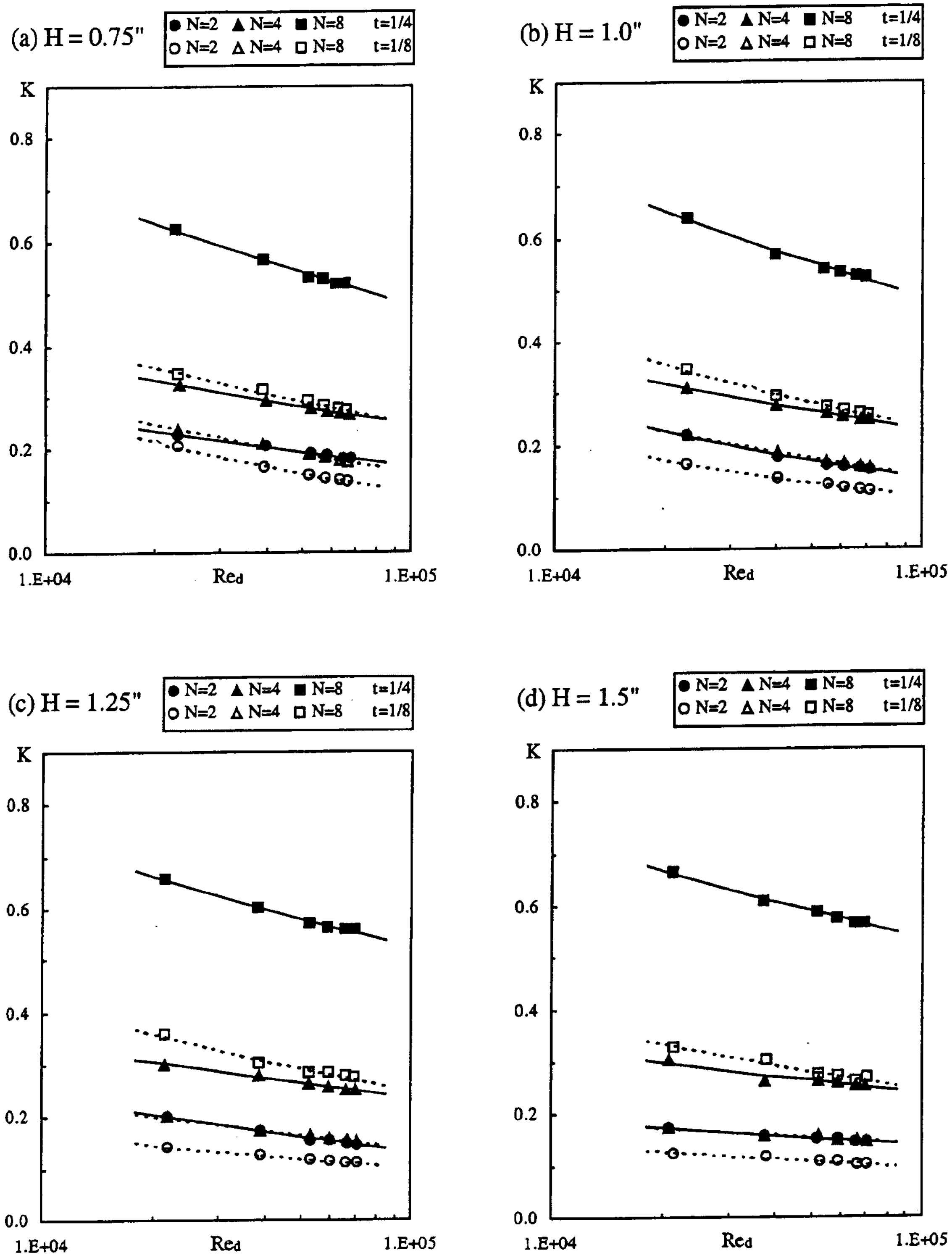

Fig. 2 Loss coefficient, K, versus Re_d, 7.62 cm long fins

A prediction equation at the most general level was also obtained and is

$$K=\left(\frac{L}{H}\right)^{0.2}[0.09+1.92(B)-3.277(B)^{0.36}\,\mathrm{Re}_d\times10^{-6}]. \quad (5)$$

Except for a very few cases, the predictions from this equation are within ±20% of the experimental values. In the absence of other information, Eq. (5) is useful as a guide in predicting the general levels of the pressure drop to be expected.

Uncertainty Analysis

The relative uncertainties in the results were obtained using the procedure described by Moffat [13]. The uncertainties depend on

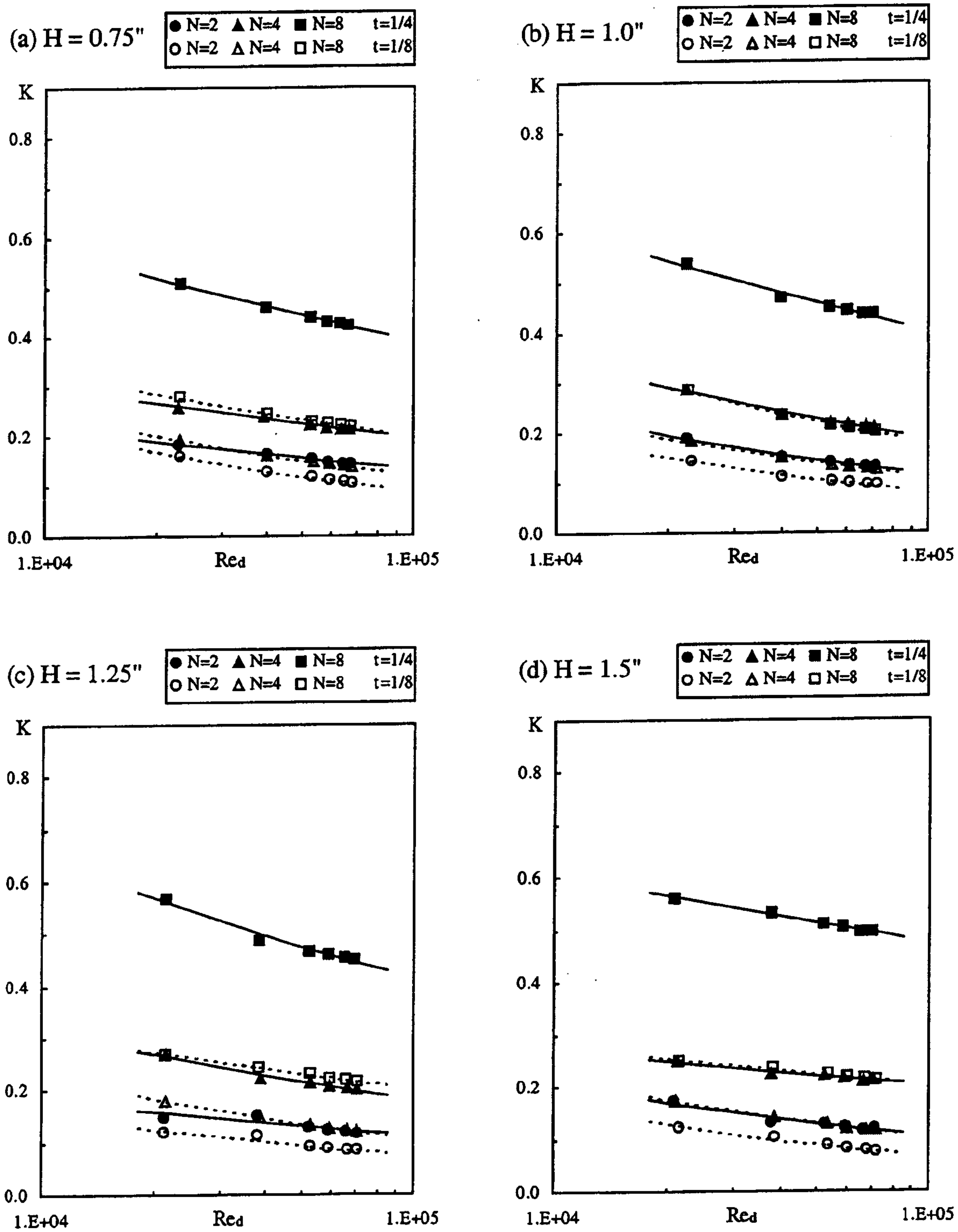

Fig. 3 Loss coefficient, K, versus Re_d, 2.54 cm long fins

the conditions of the test runs. The relative uncertainty in K was highest for test runs on two fin sections and low Reynolds number and smallest for the runs with eight fins and high Reynolds number. Using ±15% relative uncertainty as a reference, 96% of the results from eight fin sections were below this value, 89% from the four fin sections, and 83% from the two fin sections. Overall, about 90% of the results were below this value. Using ±10% relative uncertainty as a reference, the corresponding results are 91%, 81%, and 74% for eight fin, four fin, and two fin sections respectively. Overall, about 82% of the results were below a relative uncertainty of ±10%.

Conclusions

The results from the experiments showed that the number of fins had the largest effect on the loss coefficient. The fin thickness showed the second largest effect followed by the length and Reynolds number. The fin height appeared to have little effect. Three

Table 1 Coefficients and correlation coefficients for Eq. (3)

			1/4″ Thickness			1/8″ Thickness		
Length	Height	Fins	C_1	C_2	R_{val}	C_1	C_2	R_{val}
6″	1.5″	2	1.5273	−0.1933	0.9204	1.5054	−0.2191	0.9457
		4	2.3573	−0.1863	0.9948	3.7241	−0.2692	0.9942
		8	2.9785	−0.1333	0.9994	3.1942	−0.2010	0.9978
	1.25″	2	2.9689	−0.2521	0.9970	7.2982	−0.3601	0.9990
		4	2.6659	−0.1975	0.9974	8.5535	−0.3409	0.9972
		8	4.8003	−0.1793	0.9993	3.7912	−0.2180	0.9992
	1.0″	2	6.6073	−0.3238	0.9993	13.9405	−0.4136	0.9992
		4	6.0788	−0.2755	0.9987	9.6672	−0.3546	0.9997
		8	5.0031	−0.1891	0.9984	9.5315	−0.3074	0.9971
	0.75″	2	6.9452	−0.3233	0.9991	7.9168	−0.3524	0.9929
		4	8.8089	−0.3072	0.9984	13.2897	−0.3762	0.9993
		8	8.7016	−0.2434	0.9998	10.4420	−0.3132	0.9989
3″	1.5″	2	0.6595	−0.1352	0.9928	0.6674	−0.1674	0.9664
		4	1.1237	−0.1341	0.9461	0.6178	−0.1284	0.9743
		8	2.5855	−0.1367	0.9966	2.1640	−0.1885	0.9824
	1.25″	2	2.9027	−0.2675	0.9969	1.3451	−0.2238	0.9970
		4	1.4691	−0.1588	0.9959	1.9820	−0.2297	0.9961
		8	2.8460	−0.1470	0.9949	3.3971	−0.2267	0.9872
	1.0″	2	5.4045	−0.3203	0.9954	4.4788	−0.3289	0.9988
		4	2.3945	−0.2036	0.9979	4.4910	−0.3005	0.9996
		8	3.9515	−0.1820	0.9947	4.8328	−0.2628	0.9983
	0.75″	2	2.1185	−0.2218	0.9956	8.7319	−0.3743	0.9981
		4	2.1361	−0.1877	0.9994	4.3375	−0.2885	0.9966
		8	3.7570	−0.1792	0.9984	3.3802	−0.2263	0.9940
1″	1.5″	2	3.2329	−0.2976	0.9692	6.4593	−0.3947	0.9944
		4	0.9311	−0.1333	0.9775	4.2213	−0.3210	0.9979
		8	1.6511	−0.1080	0.9937	0.9481	−0.1331	0.9887
	1.25″	2	1.3363	−0.2153	0.9071	2.7086	−0.3092	0.9585
		4	3.0278	−0.2442	0.9867	4.8435	−0.3304	0.9993
		8	3.9679	−0.1961	0.9869	1.6781	−0.1829	0.9964
	1.0″	2	4.8290	−0.3239	0.9892	6.1874	−0.3741	0.9962
		4	4.4376	−0.2747	0.9891	4.7020	−0.3239	0.9983
		8	3.2779	−0.1815	0.9909	5.7378	−0.2998	0.9956
	0.75″	2	1.6615	−0.2187	0.9958	7.5152	−0.3822	0.9994
		4	1.7650	−0.1904	0.9930	4.3087	−0.3087	0.9995
		8	2.8529	−0.1721	0.9987	2.6673	−0.2245	0.9985

Table 2 Coefficients and correlation coefficients for Eq. (4)

		1/4″ Thickness			1/8″ Thickness		
Length	Fins	C_3	C_4	R_{val}	C_3	C_4	R_{val}
1″	2	2.3553	−0.2612	0.7758	5.0952	−0.3607	0.7827
	4	2.1338	−0.2093	0.9303	4.4834	−0.3204	0.9129
	8	2.8237	−0.1653	0.7648	2.1877	−0.2087	0.9282
3″	2	2.0337	−0.2305	0.7076	2.2782	−0.2675	0.6291
	4	1.6680	−0.1690	0.9077	2.0447	−0.2297	0.7237
	8	3.1985	−0.1603	0.8699	3.3183	−0.2263	0.9626
6″	2	3.5717	−0.2673	0.8991	5.8069	−0.3349	0.8240
	4	4.1782	−0.2393	0.9693	7.8672	−0.3337	0.9397
	8	4.7168	−0.1809	0.8245	5.7704	−0.2580	0.9615

prediction equations for the pressure drop across rectangular finned arrays were obtained. The most general equation predicted the loss coefficient to within ±20% of the experimental values. Predictions from two other less restrictive equations were within ±10% and ±5% of the experimental values.

Nomenclature

A_d = duct area
A_f = open flow area between fins
B = blockage ratio, $(A_d - A_f)/A_d$
H = height of fins
K = total loss coefficient, Eq. (1)
L = length of fins
N = number of fins
Re_d = Reynolds number in duct, based on duct hydraulic diameter
t = fin thickness
V_d = velocity of the air in the duct
ΔP = total pressure drop across fins
ρ_d = density of air at inlet to test section

References

[1] Korotky, G. J., and Taslim, M. E., 1998, ''Rib Heat Transfer Coefficient Measurements in a Rib-Roughened Square Passage,'' ASME J. Turbomach., **120**, pp. 376–385.

[2] Taslim, M. E., and Lengkong, A., 1998, ''45° Staggered Rib Heat Transfer Coefficient Measurements in a Square Channel,'' ASME J. Turbomach., **120**, pp. 571–580.

[3] Hwang, J. J., and Liou, T. M., 1994, ''Augmented Heat Transfer in a Rectangular Channel With Permeable Ribs Mounted on the Wall,'' ASME J. Turbomach., **116**, pp. 912–920.

[4] Molki, M., Faghri, M., and Ozbay, O., 1994, ''A New Correlation for Pressure Drop in Array of Rectangular Blocks in Air-Cooled Electronic Units,'' ASME J. Fluids Eng., **116**, pp. 856–861.

[5] Hong, J. C., and Hsieh, S. S., 1993, ''Heat Transfer and Friction Factor Measurements in Ducts With Staggered and In-Line Ribs,'' ASME J. Heat Transfer, **115**, pp. 58–65.

[6] Greiner, M., Chen, R. F., and Wirtz, R. A., 1991, ''Enhanced Heat Transfer and Pressure Drop Measured From a Flat Surface in a Grooved Channel,'' ASME J. Heat Transfer, **113**, pp. 498–501.

[7] Garimella, S. V., and Schlitz, D. J., 1992, ''Influence of Fin Aspect Ratio on Heat Transfer Enhancement,'' SAE Journal of Materials and Manufacturing, **101**, pp. 467–472.

[8] Sparrow, E. M., and Hajiloo, A., 1980, ''Measurements of Heat Transfer and Pressure Drop for an Array of Staggered Plates Aligned Parallel to an Air Flow,'' ASME J. Heat Transfer, **102**, pp. 426–432.

[9] Cur, N., and Sparrow, E. M., 1978, ''Experiments on Heat Transfer and Pressure Drop for a Pair of Collinear, Interrupted Plates Aligned With the Flow,'' Int. J. Heat Mass Transf., **21**, pp. 1069–1080.

[10] Halle, H., Chenoweth, J. M., and Wambsganss, M. W., 1988, ''Shellside Waterflow Pressure Drop Distribution Measurements in an Industrial-Sized Test Heat Exchanger,'' ASME J. Heat Transfer, **110**, pp. 60–67.

[11] Kim, J. Y., Lai, M. C., Li, P., and Chui, G. K., 1995, ''Flow Distribution and Pressure Drop in Diffuser-Monolith Flows,'' ASME J. Fluids Eng., **117**, pp. 362–368.

[12] ASME, 1959, ''Fluid Meters—Their Theory and Applications,'' Report of ASME Research Committee on Fluid Meters, New York.

[13] Moffat, R. J., 1985, ''Using Uncertainty Analysis in the Planning of an Experiment,'' ASME J. Fluids Eng., **107**, pp. 173–185.

Oxidation Effect on the Monosized Droplets Generation of the Liquid Metal Jet

Wei-Hsiang Lai
e-mail: whlai@mail.ncku.edu.tw

Chia-Chin Chen

Department of Aeronautics and Astronautics, National
Cheng Kung University, 1 University Road,
Tainan 701, Taiwan, R.O.C.

The oxide formation on the surface of the molten metal jet was shown to have a drastic effect on the droplet formation process according to the description of some publication. Thus, the main objective of this research is to investigate the influence of oxygen concentration on the breakup and the monosized droplets generation of molten metal jet (Sn63 Pb37 alloy). The breakup phenomena of molten metal jet can be approximately divided into three regimes. They are "breakup regime" for oxygen concentration below C_1, "transition regime" for oxygen concentration between C_1 and C_2, and "breakup failing regime" for oxygen concentration beyond C_2, respectively. [DOI: 10.1115/1.1566044]

1 Introduction

The generation of monosized droplets has been a topic of interest for many decades. It is relevant to many research areas and engineering applications from basic research on atomization and sprays, which may include evaporation, combustion, or solidification, to various applications including rapid prototyping, soldering, spray deposition, or agricultural applications. The phenomena of uniform droplets formation from a stream of liquid issuing from an orifice were initially described mathematically by Lord Rayleigh [1]. According to Rayleigh's theory, a liquid cylinder is unstable to axisymmetric perturbations with a wavelength, λ, greater than

$$\lambda_{\min}=\pi D \tag{1}$$

where D is the jet diameter, and the fastest-growing disturbance is

$$\lambda_{\mathrm{opt}}=4.51D. \tag{2}$$

The size and spacing of the droplets produced by this instability, first identified by Lord Rayleigh [1–2], can be controlled if a forced sinusoidal perturbation is used. In that case, the droplets are monosized and the diameters are

$$d=1.145\sqrt[3]{4Q/f\pi} \tag{3}$$

where Q is the jet volume flow rate and f is the perturbation frequency, with constant spacing (=λ). Rayleigh's analysis was limited to inviscid fluids. The effect of viscosity was later included by Weber [3], which led to an improved expression. For viscous liquids

$$\lambda_{\mathrm{opt}}=\sqrt{2}\pi D\left(1+\frac{3\mu}{\sqrt{\rho\sigma D}}\right)^{0.5} \tag{4}$$

where μ is the viscosity, ρ the density, and σ the surface tension coefficient of the liquid. Weber next examined the effect of air resistance on the disintegration of jets. At 15 m/s relative air velocity

$$\lambda_{\min}=2.2D \tag{5}$$

$$\lambda_{\mathrm{opt}}=2.8D. \tag{6}$$

The phenomena of monosized droplets generation can be obtained from the typical literatures [4–6]. In this research, the oxygen contamination on the surface of the molten metal jet is the other problem which should be considered. There are many literatures relating to the oxidation. Wallace [7] points out that oxide formation on the surface of the molten solder jet was shown to have a drastic effect on the droplet formation process, i.e., if the oxygen is not removed from the environment, no jet breakup occurs. Passerone et al. [8,9] described the many phenomena of oxidation of molten metal surface. The jet breakup of molten liquid metal are investigated by Haj-Hariri [10], Artem ev [11], and Ankudinov et al. [12]

2 Experimental Setup and Methods

A schematic diagram of the experimental setup is shown in Fig. 1, it includes the following subsystems: droplet generator, observation chamber, pressurization gas supply, vacuum pump, perturbation signal generation and monitoring, and image acquisition. The experimental procedures are described as follows: First the vacuum pump system pumps air out of the generator and observation chamber to a certain vacuum pressure. Then nitrogen is supplied into both chambers to produce desired oxygen concentration. Both chambers are filled to 0.5 kg/cm^2 gage pressure and then discharged to 1 atm absolute pressure. This procedure is repeated several times until the desired oxygen concentration is obtained. The oxygen concentration is measured by a oxygen analyzer (Teledyne analytical instrument 311D) which can measure oxygen concentration as low as 0–10,000 ppm with accuracy of ±0.2% of full scale at constant temperature. Secondarily, the heater heats the metal in generator. The temperature is maintained at 350°C. The thermocouple is arranged at the bottom of the furnace of generator. After the metal is molten, the generator is pressurized by nitrogen. The liquid metal flows out of a nozzle located at the bottom of the generator. The velocity of jet is about 3.6 m/s, which is obtained from the measured perturbation wavelength and the known perturbation frequency ($v=f\lambda$). It is maintained at constant to avoid its effect. Thus, the oxidation effect can be studied clearly. The orifice of the nozzle is made of ruby with diameter 102 μm (0.004 in.), 152 μm (0.006 in.), and 203 μm (0.008 in.) with thickness 254 μm (0.01 in.). Without considering the influence of oxidation, the viscosity is 1.9×10^{-3} Ns/m^2, which is estimated by viscosity equation [13]. Both surface tension and density are 480×10^{-3} N/m and 7870 kg/m^3, which are estimated by White's [14] and Fisher's [15] data, respectively. Finally, the perturbations are applied into the jet upstream to excite it. The sinusoidal signals are generated by a function generator (HP 33120A), amplified by a transformer and applied to the piezoelectric disk. While a run proceeds, the images of the droplets produced are acquired by CCD and recorded by videocassette recorder. The light source is a PIONEER DS-303 digital strobe light.

3 Results

The Figs. 2(*a*) to (*c*) show that the effect of oxygen concentration on liquid metal jet without excitation. Figure 2(*a*) shows that the jet break up to generate metal droplets at oxygen concentration 10 ppm. Figure 2(*b*) shows that the jet break up in strip or droplet shape at oxygen concentration 560 ppm. Figure 2(*c*) shows that the jet does not break up at oxygen concentration 910 ppm. Figures 2(*d*) to 2(*f*) show the effect of oxygen concentration on liquid metal jet with excitation frequency 6 kHz. Figure 2(*d*) shows that the jet break up to produce monosized metal droplets at oxygen concentration 10 ppm. Figure 2(*e*) shows that the jet break up to produce monosized metal droplets at oxygen concentration 560 ppm. Figure 2(*f*) shows that the jet does not break up at oxygen concentration 910 ppm in spite of applying excitation perturba-

---

Contributed by the Fluids Engineering Division for publication in the JOURNAL OF FLUIDS ENGINEERING. Manuscript received by the Fluids Engineering Division Oct. 11, 2001; revised manuscript received Nov. 14, 2002. Associate Editor: S. Ceccio.

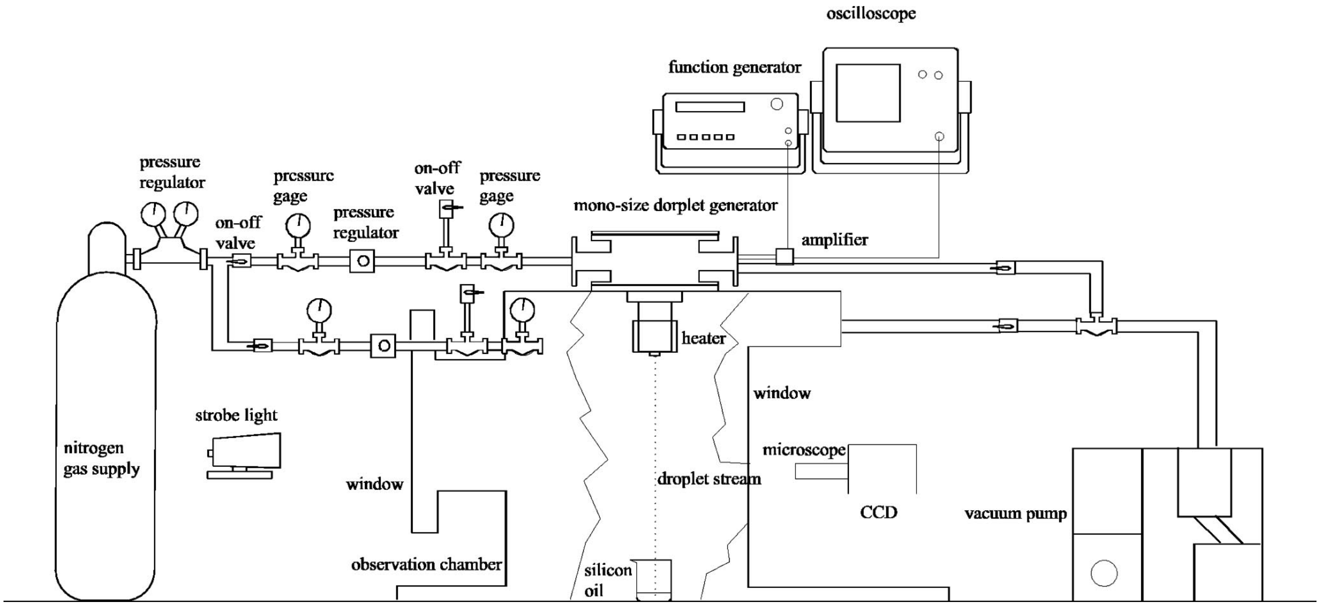

Fig. 1 Schematic diagram of monosized droplet generator

tion. These phenomena can be summarized in Table 1, which is the final results after many runs. The C_1 is the first critical value of oxygen concentration. Below this value, the jet can break up to generate liquid metal droplets without excitation. The monosized metal droplet can be generated with excitation. The C_2 is the second critical value of oxygen concentration. Beyond this value, the perturbations are damped out. The jet cannot break up to generate liquid metal droplets, whether the excitation has been applied or not. Certainly the monosized droplets cannot be produced and even breakup fails in spite of applying excitation perturbation. Between oxygen concentration C_1 and C_2, the jet breaks up in strip and droplet shape. However, as the excitation is applied to the jet, the monosized metal droplet can still be formed. Both the critical values increase with the decrement of orifice diameter. The differences result from the circumference of jet, breakup length and capillary force, which are caused by the variation of orifice diameter.

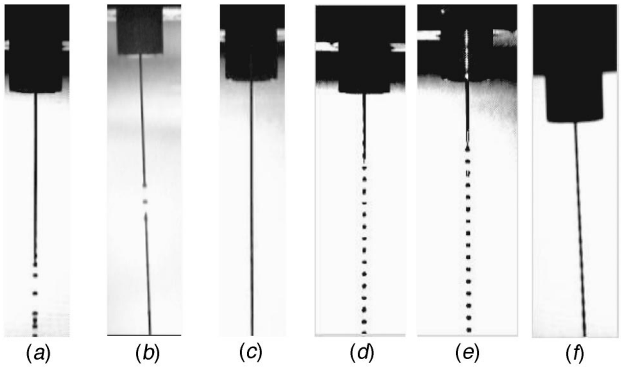

Fig. 2 The effect of oxygen concentration on metal jet around nozzle without excitation frequency; (*a*) $[O_2]=10$ ppm; (*b*) $[O_2]=560$ ppm; (*c*) $[O_2]=910$ ppm; and with excitation frequency 6 kHz (*d*) $[O_2]=10$ ppm; (*e*) $[O_2]=560$ ppm; (*f*) $[O_2]=910$ ppm (at 350°C)

Table 1 The effect of orifice diameter on C_1 and C_2

Orifice Diameter\Critical Value	C_1 (ppm)	C_2 (ppm)
102 μm	590	1020
152 μm	490	910
203 μm	310	700

4 Conclusion

According to above results, the situations of molten metal jet can be approximately divided into three regimes. They are breakup regime for oxygen concentration below C_1, transition regime for oxygen concentration between C_1 and C_2, and breakup failing regime for oxygen concentration beyond C_1, respectively. The bound of these regimes slightly shift with the variation of orifice diameter.

References

[1] Rayleigh, Lord J. W. S., 1878, ‘‘On the Instability of Jets,’’ Proc. London Math. Soc., **10**, pp. 4–13.
[2] Stricker, J., and Sofer, D., 1991, ‘‘Monosize Droplet Stream Generator,’’ Rev. Sci. Instrum., **62**(12), pp. 3047–3050.
[3] Weber, C., 1931, ‘‘Disintegration of Liquid Jets,’’ Z. Angew. Math. Mech., **11**(2), pp. 136–159.
[4] Schnieder, J. M., and Hendricks, C. D., 1964, ‘‘Source of Uniform-Sized Liquid Droplets,’’ Rev. Sci. Instrum., **35**, p. 1349.
[5] Connon, C. S., and Dunn-Rankin, D., 1996, ‘‘Droplet Stream Dynamics at High Ambient Pressure,’’ Atomization Sprays, **6**, pp. 485–497.
[6] Lai, W. H., and Chen, C. C., 2000, ‘‘Influence of Fluid Properties on Mono-Size Droplet Generation,’’ *Eighth International Conference on Liquid Atomization and Spray Systems*, Pasadena, CA, pp. 1326–1333.
[7] Wallace, D. B., 1993, ‘‘Capillary Instability of a Jet of Liquid Metal,’’ ASME J. Fluids Eng., **115**, pp. 529–532.
[8] Passerone, A., Ricci, E., and Sangiorgi, R., 1990, ‘‘Influence of Oxygen Contamination on the Surface Tension of Liquid Tin,’’ J. Mater. Sci., **25**, pp. 4266–4272.
[9] Ricci, E., and Passerone, A., 1993, ‘‘Review: Surface Tension and Its Relations With Adsorption, Vaporization and Surface Reactivity of Liquid Metals,’’ Mater. Sci. Eng., **A161**, pp. 31–40.
[10] Haj-Hariri, H., and Poulikakos, D., 2000, ‘‘Capillary Instability of a Cylindrical Jet With an Shroud: A Model for the Breakup of an Oxidized Metal Jet,’’ ASME J. Appl. Mech., **67**, pp. 626–628.
[11] Artem ev, B. V., and Kochetov, S. G., 1991, ‘‘Capillary Breakup of a Liquid-Metal Jet in an Oxidizing Medium,’’ J. Eng. Phys., **60**, pp. 425–429.
[12] Ankudinov, V. B., 1991, ‘‘An Experimental Investigation of Capillary Breakup of a Liquid,’’ J. Eng. Phys., **60**, pp. 416–419.
[13] Ejima, T., Asto, Y., Yamamura, T., Hayashi, A., and Yamazaki, T., 1990, ‘‘Viscosity Measurement of Pb-Sn Binary Metals and the Effect of Melting and Solidification on the Measurement,’’ J. Jpn. Inst. Met., **54**(9), pp. 1005–1012.
[14] White, D. W. G., 1971, ‘‘The Surface Tensions of Pb, Sn, and Pb-Sn Alloys,’’ Metall. Trans., **2**, pp. 3067–3071.
[15] Fisher, H. J., and Phillips, A., 1954, ‘‘Viscosity and Density of Liquid Lead-Tin and Antimony-Cadmium Alloys,’’ J. Met., pp. 1060–1070.

The Shear Layers of a Two-Dimensional Jet Excited by Flexible Wires

Ming-huei Yu[1]
Associate Professor
e-mail: mhyu@mail.nsysu.edu.tw

Yi-chun Liao
Graduate Student

Chung-ho Tseng
Graduate Student

Department of Mechanical Engineering, National Sun Yat-sen University, 804 Kaohsiung, Taiwan R.O.C.

A two-dimensional air jet, heated at a density ratio of 0.8, under external forcing by flexible wires is investigated experimentally. In each shear layer of the hot jet flow, a wire of diameter 0.23 mm (0.015 jet width) is flexibly mounted along the spanwise direction. By flow visualization, temperature measurements, and spectral analysis, the study demonstrates that the wires have quite different effects on the jet flow depending on that the wires are motionless or vibrating in the flow, and the shear layers of the heated plane jet can be manipulated by means of flexible wires.
[DOI: 10.1115/1.1566045]

1 Introduction

A lot of information on the phenomena of shear layer structures has been accumulated, but methods of manipulating the shear layer, for the purpose of, say, enhancing/reducing the turbulence intensity of a jet, have not been completely documented. Small cylinders (wires), among other means for flow control, have been proven to be effective in changing the turbulence intensity of jet flows, [1,2]. The two examples used rigidly fixed wires that were motionless in the jet flows. Vandsburger and Ding [3] used flexible wires that could vibrate in the flow, for turbulence control of mixing layers. These previous studies were, however, of cold flows. It has been shown that a jet with density gradient has different characteristics from a homogeneous jet, [4–8]. From the stability point of view, a homogeneous jet flow without density gradient is globally stable while a low-density jet may exhibit global instability, [4,5]. With the different flow nature, a heated jet may response to external forcing differently from a cold jet. It is therefore of interest to investigate a hot jet under external forcing by flexible wires. By flow visualization, temperature measurements, and spectral analysis, the present study demonstrates that the shear layers of a heated plane jet can be manipulated by means of flexible wires.

2 Experimental Apparatus

The facility used to produce a plane hot jet is shown in Fig. 1. The nozzle, pointing vertically upwards, has a size of 15×300 mm, giving an aspect ratio of 20:1. The streamwise, transverse, and spanwise coordinates are denoted by X, Y, and Z, respectively, which are normalized by the jet width $H=15$ mm. In each shear layer of the jet, a metal wire 0.23 mm in diameter (0.015 jet width) and 540 mm long was mounted along the jet spanwise direction. The wires were flexibly mounted so that they could vibrate in the flow. Adjusting the wire tension could change the nature frequency of the wire. In the present experiment, both the wires were set at the same natural frequency, f_n, for each test.

The hot jet flow was visualized by using a typical Schlieren optical system. The wire vibration was detected by a detector coil, PASCO Model WA-9613. A DANTEC hot wire anemometer in constant current mode was used to collect local unsteady temperature data. The sensor was platinum-plated tungsten wire of 1 μm in diameter and 0.4 mm long. The frequency response of the sensor in constant current mode for temperature measurement was about 2 kHz, which was adequate for the present experiments. The temperature signals were digitized at a sampling rate of 2048 samples/second by a 12 bit A/D converter. The uncertainty of the output voltage collected from the anemometer due to digitization is 3×10^{-4} Volt, and the uncertainty of temperature measurements was 0.26°C.

3 Results and Discussion

Throughout the experiments, the jet exit temperature T_j was fixed at 110°C, and the ambient temperature T_∞ was 27°C, giving a density ratio S of about 0.8. The jet exit velocity U_j was fixed at 4 m/s. The Reynolds number, $\mathrm{Re}=(U_jH/\nu)$, is 3000 approximately, where the kinematic viscosity, ν, is evaluated at the average of the jet exit and the ambient temperatures. The jet is initially laminar. The corresponding Richardson number, defined as $gH(1-S)/(SU_j^2)$ is about 2×10^{-3}. Hence, buoyancy forces are insignificant in the near field of the hot jet.

3.1 Flow Visualization. It was found that the wire had no impact on the jet flow, when it was mounted in the potential core or in the shear layer region with small mean velocity gradient. To influence the jet flow, the wire was mounted in the shear layer at a location with high velocity mean gradient, $Y=0.5$. Typical Schlieren images for four conditions are shown in Fig. 2. When the two wires were rigidly fixed and hence motionless in the shear layers at $Y=\pm0.5$, the vortical structures appeared smaller and form slightly downstream, and the potential core looked longer compared with the jet without the wires (see Figs. 2(*a*) and 2(*b*), for instance).

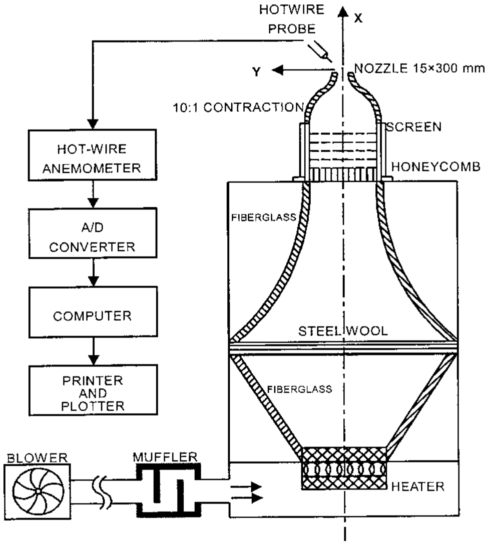

Fig. 1 The jet facility

---

[1] To whom correspondence should be addressed.

Contributed by the Fluids Engineering Division for publication in the JOURNAL OF FLUIDS ENGINEERING. Manuscript received by the Fluids Engineering Division Nov. 26, 2001; revised manuscript received Dec. 16, 2002. Editor: M. Plesniak.

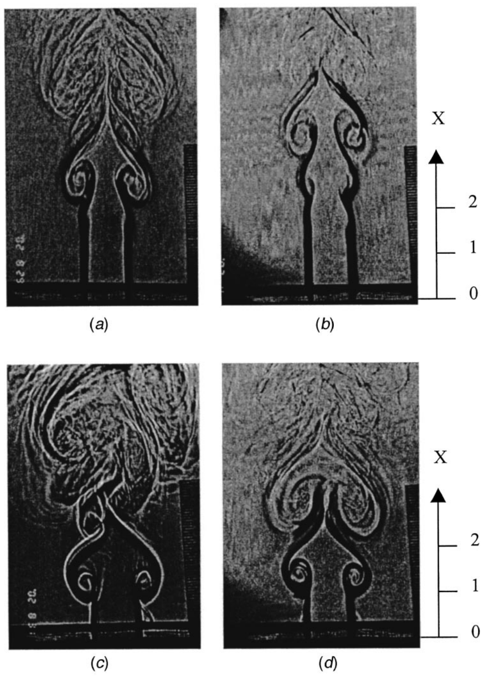

(*a*) (*b*)

(*c*) (*d*)

Fig. 2 Typical Schlieren image of the hot jet, (*a*) without wires (*b*) with two still wires at $X=0.48$ and $Y=\pm 0.5$ ($Y=0$ corresponds to the centerline of the jet on each Schlieren image), (*c*) with flexible wires, $f_n=37$ Hz, (*d*) with flexible wires, $f_n=83$ Hz

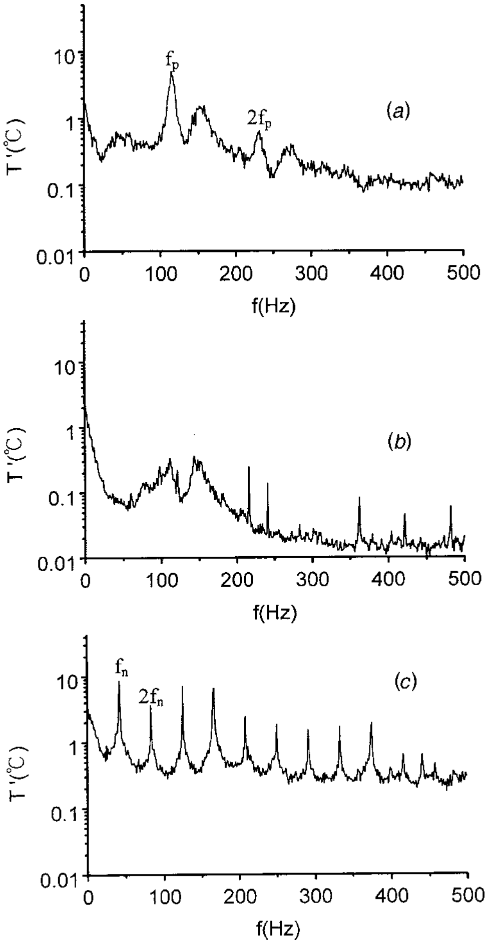

Fig. 3 Temperature spectra of the hot jet, temperature probe at $X=2.4$, $Y=0.5$, (*a*) without wires (*b*) with still wires at $X=0.48$ and $Y=\pm 0.5$, (*c*) with vibrating wires, $f_n=37$ Hz

In the cases of flexible wires, the wires were found to vibrate at the natural frequency of the wires and the vibration amplitude decreased as the natural frequency was increased. Once the wire natural frequency was above 143 Hz, no wire vibration was observed in the jet flow. With the wires vibrating in the flow, big coherent vortices developed much closer to the nozzle and the originally laminar jet became turbulent after a shorter transition region (compare Figs. 2(*c*)–(*d*) and Figs. 2(*a*)–(*b*)), while the jet flows in Figs. 2(*c*)–(*d*) looked similar for different natural frequencies of the wires.

3.2 Spectral Data. The corresponding temperature spectra for the jets of Figs. 2(*a*)–(*c*) are shown in Figs. 3(*a*)–(*c*), respectively. As illustrated in Figs. 3(*a*) and (*b*), the spectral peak $f_p = 116$ Hz, originally dominant in the unexcited jet flow, was suppressed by the still wires. Spectral analysis for different streamwise locations showed that the growth of the dominant mode f_p along the X-direction was subdued in the developing region by the still wires. As a result, the development of large vortical structures was deferred, as already seen in the Schlieren images.

With the wires vibrating in the shear layers, the jet shows line-dominated spectra with peaks at multiples of the natural frequency of the wires, as shown in Fig. 3(*c*). The dominant frequency of the flow is now related to the natural frequency of the wires, while the original dominant mode, $f_p = 116$ Hz, of the natural hot jet disappears in the spectra. This finding suggests that adjusting the nature frequency of the wires can control the dominant frequency in the flow.

3.3 Temperature Field. The temperature distributions of the jet along the centerline are shown in Fig. 4. The mean temperatures decayed, after $X \approx 4$, slightly downstream with the wires motionless in the shear layers than without any wire. The temperature fluctuations also occurred more downstream suggesting a slightly longer potential core. With the wires vibrating in the shear layers, analysis of the temperature field in the streamwise direction showed the mean temperature dropping significantly upstream of the case with no perturbation and corresponding temperature fluctuations to increase significantly at this point. Calculations revealed that the length of the potential core is reduced by as much as 50% when compared to the unperturbed jet. The mean and fluctuation temperature distributions for different natural frequencies of the wire are almost similar in spite of change in the dominant frequency.

The temperature distributions along the transverse (Y) direction, at $X=3$, for example, are shown in Fig. 5. With the wires motionless in the flow, the spreading of mean temperature in the Y-direction was slightly restricted, while the temperature fluctuations were suppressed significantly. On the contrary, with the wires vibrating in the flow, temperature fluctuations were increased in a wider region. The mean and fluctuation temperature distributions in the transverse direction can be used to get an idea about the jet spreading. As an indication of jet spreading, the half-jet width of temperature, $Y_{1/2}$ is defined as the Y-location where the temperature is the average of the centerline temperature and the ambient. The half-jet widths along the streamwise direction are shown in Fig. 6. It becomes clear that the vibrating wires in the shear layers can enhance the jet spreading, while the still wires have little effect on the jet spreading.

4 Conclusion

Two small wires were used to excite a two-dimensional hot jet flow. When the wires rigidly mounted in the shear layers having high mean velocity gradient, they acted as a perturbation and resulted in reduced natural shear layer vortical structures that formed slightly downstream when compared to the structures with

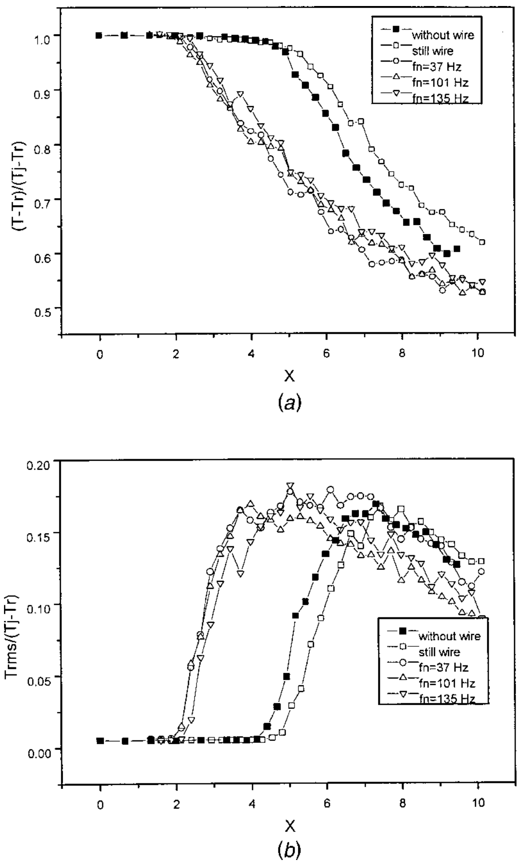

Fig. 4 Temperature distributions along the centerline (*a*) mean values (*b*) temperature fluctuations

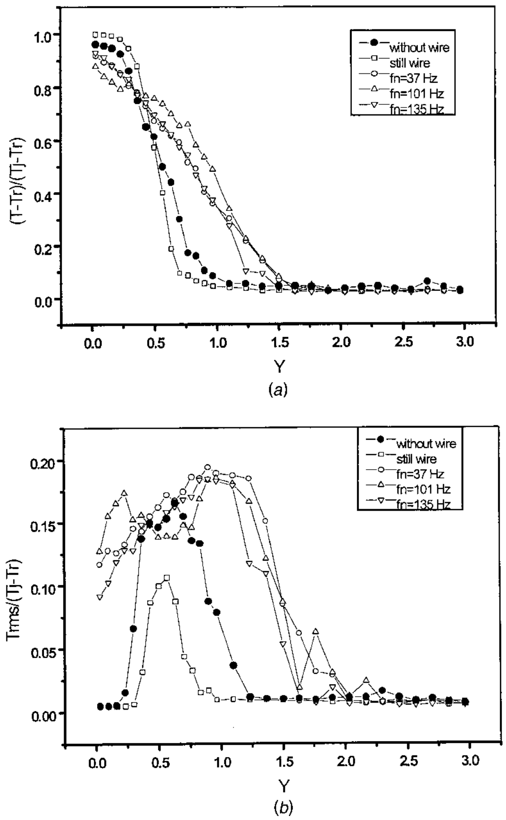

Fig. 5 Temperature distributions along the *Y*-direction, at *X* = 3 (*a*) mean values (*b*) temperature fluctuations

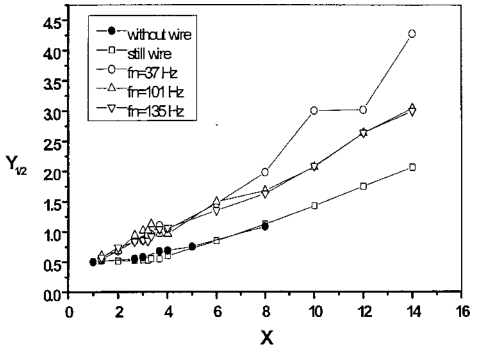

Fig. 6 The jet-half width versus the *X*-coordinate

no wire attached. Moreover, the length of the potential core also seems to have increased. The spectral analysis of this condition revealed considerable suppression of the spectral peak which is linked to the reduction of the vortical structures observed in the flow visualization images.

Attaching the wires flexibly in the region having high mean velocity gradient resulted in the wire vibrating at its natural frequency. This vibration was, however, observed only when the natural frequencies of the wires were below a certain cutoff (in this case 143 Hz), and above this frequency, no vibration of the wire was observed. The flow visualization images for this condition showed coherent vortices forming much closer to the nozzle and a much shorter transition region. The spectral analysis showed line-dominated spectra with peaks at multiples of the natural frequency of the wires. The original dominant mode of the jet completely vanishes and the dominant frequency is now related to the natural frequency of the wires. This means that adjusting the natural frequency of the perturbation can control the dominant frequency of the flow. Analysis of the temperature field revealed that the flexible wire configuration was effective in increasing the jet spreading and reducing the length of the potential core by as much as 50%, whereas still wires have little effect on the spreading.

Acknowledgments

We thank National Science Council, ROC, for the financial support.

References

[1] Tong, C., and Warhaft, Z., 1994, "Turbulence Suppression in a Jet by Means of a Fine Ring," Phys. Fluids, **6**(1).

[2] Rajagopalan, S., and Antonia, R. A., 1998, "Turbulence Reduction in the Mixing Layer of a Plane Jet Using Small Cylinders," Exp. Fluids, **25**, pp. 96–103.

[3] Vandsburger, U., and Ding, C., 1995, "Self-Excited Wire Method for the Control of Turbulent Mixing Layers," AIAA J., **33**, pp. 1032–1037.

[4] Monkewitz, P. A., and Sohn, K. D., 1988, "Absolute Instability in Hot Jets," AIAA J., **26**, pp. 911–916.

[5] Yu, M. H., and Monkewitz, P. A., 1990, "The Effect of Nonuniform Density on the Absolute Instability of Two Dimensional Jets and Wakes," Phys. Fluids A, **2**, pp. 1175–1181.

[6] Sreenivasan, K. R., Raghu, S., and Kyle, D., 1989, "Absolute Instability in Variable Density Round Jets," Exp. Fluids, **7**, pp. 309–317.

[7] Monkewitz, P. A., Bechert, D. W., Barsikow, B., and Lehmann, B., 1990, "Self-Excited Oscillations and Mixing in a Heated Round Jet," J. Fluid Mech., **213**, pp. 611–639.

[8] Yu, M. H., and Monkewitz, P. A., 1993, "Oscillation in the Near Field of a Heated Two-Dimensional Jet," J. Fluid Mech., **255**, pp. 323–347.